

## **General Disclaimer**

### **One or more of the Following Statements may affect this Document**

- This document has been reproduced from the best copy furnished by the organizational source. It is being released in the interest of making available as much information as possible.
- This document may contain data, which exceeds the sheet parameters. It was furnished in this condition by the organizational source and is the best copy available.
- This document may contain tone-on-tone or color graphs, charts and/or pictures, which have been reproduced in black and white.
- This document is paginated as submitted by the original source.
- Portions of this document are not fully legible due to the historical nature of some of the material. However, it is the best reproduction available from the original submission.

NASA CR-143643

22296-6001-RU-02

1 OCTOBER 1974

**FINAL  
REPORT**

**3**

**DESIGN/COST  
TRADEOFF STUDIES  
APPENDIX A.  
SUPPORTING ANALYSES  
AND TRADEOFFS**

BOOK 2

(NASA-CR-143643) DESIGN/COST TRADEOFF  
STUDIES. APPENDIX A. SUPPORTING ANALYSES  
AND TRADEOFFS, BOOK 2. EARTH OBSERVATORY  
SATELLITE SYSTEM DEFINITION STUDY (EOS)  
Final Report (TRW Systems Group) 678 p HC

N75-15689

Unclas

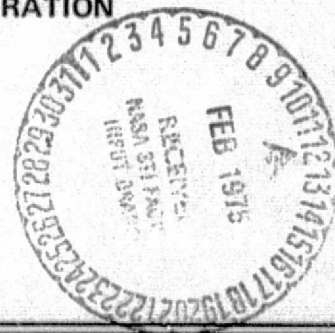
G3/18 09226

**EARTH OBSERVATORY SATELLITE  
SYSTEM DEFINITION STUDY (EOS)**

PREPARED FOR

**NATIONAL AERONAUTICS AND SPACE ADMINISTRATION  
GODDARD SPACE FLIGHT CENTER**

IN RESPONSE TO  
CONTRACT NAS5-20519





**Page intentionally left blank**

## CONTENTS

	Page
5.2 Attitude Determination and Control	5-217
5.2.1 Attitude Reference Design	5-217
5.2.2 Inertial Reference and Unit Design	5-232
5.2.3 Star Sensor Selection	5-238
5.2.4 Actuation Module Design	5-265
5.2.5 Pointing Error Budget Allocation	5-364
5.2.6 Safe Mode Definition	5-383
5.2.7 Reaction Wheel Selection	5-386
5.3 Propulsion	5-391
5.3.1 Propulsion System Design--Titan Configuration	5-391
5.3.2 Propulsion System Design--Thor-Delta	5-434
5.4 Electric Power and Electrical Integration	5-442
5.4.1 Power Budgets and Profiles	5-442
5.4.2 Battery Studies	5-454
5.4.3 Electrical Power Control Configuration	5-464
5.4.4 On-Board Computer Power Management	5-494
5.4.5 Power Module Electrical Design	5-499
5.4.6 Solar Array Design	5-519
5.5 Thermal Control	5-535
5.5.1 Active Thermal Control	5-535
5.5.2 Modular Thermal Design Validation	5-543
5.5.3 Thermal Design of Modules	5-549
5.5.4 Structure Thermal Design	5-581
5.5.5 Impact of Sun-Orbit Geometry	5-602
5.5.6 General Information Used in Thermal Design, Analysis, and Trades	5-607
5.6 Structure	5-610
5.6.1 Modal Analysis	5-610
5.6.2 Stress and Distortion Analyses	5-632
6. OBSERVATORY INTEGRATION AND TEST	6-1
6.1 Test Plan and Test-Cost Reduction	6-1
6.1.1 Assumptions	6-2
6.1.2 Analysis and Tradeoffs	6-2
6.1.3 Conclusions	6-3
6.2 Low-Cost Test Designs	6-17
6.2.1 Assumptions	6-17
6.2.2 Analysis and Tradeoffs	6-17
6.2.3 Conclusions	6-19
6.3 Ground Support Equipment	6-21
6.3.1 Assumptions	6-21
6.3.2 Analysis and Tradeoffs	6-21
6.3.3 Conclusions	6-23

## CONTENTS (Continued)

	Page
<b>7. GROUND DATA PROCESSING SYSTEM</b>	<b>7-1</b>
<b>7.1 Control Center System Analysis and Design</b>	<b>7-1</b>
7.1.1 Problem Discussion	7-1
7.1.2 Assumptions	7-1
7.1.3 Analysis and Tradeoffs	7-5
7.1.4 Conclusions	7-16
<b>7.2 Software Sizing</b>	<b>7-19</b>
7.2.1 Problem Discussion	7-19
7.2.2 Assumptions	7-19
7.2.3 Analyses and Tradeoffs	7-20
7.2.4 Conclusions	7-22
<b>7.3 Control Center Support to Low-Cost Ground Station</b>	<b>7-23</b>
7.3.1 Problem Discussion	7-23
7.3.2 Assumptions	7-23
7.3.3 Analysis and Tradeoffs	7-23
7.3.4 Conclusions	7-25
<b>7.4 Control Center Man-Machine Interfaces</b>	<b>7-27</b>
7.4.1 Problem Discussion	7-27
7.4.2 Assumptions	7-27
7.4.3 Analysis and Tradeoffs	7-27
7.4.4 Conclusions	7-31
<b>7.5 Use of ERTS Control Center</b>	<b>7-32</b>
7.5.1 Problem Discussion	7-32
7.5.2 Assumptions	7-32
7.5.3 Analysis and Tradeoffs	7-32
7.5.4 Conclusions	7-33
<b>7.6 Non-Orthogonal Scan Impact</b>	<b>7-35</b>
7.6.1 Conical Scan Linearization	7-35
7.6.2 Conical Coordinate System Processing	7-36
<b>7.7 Applicability of ERTS Equipment to CDPF</b>	<b>7-39</b>
<b>7.8 CDPF Software Functions</b>	<b>7-44</b>
7.8.1 CDPF	7-44
7.8.2 Problem Discussion and Assumptions	7-44
7.8.3 Analysis	7-46
<b>7.9 Image Processing Algorithms</b>	<b>7-86</b>
7.9.1 Image Data Quality Requirements	7-86
7.9.2 Geometric Correction and Temporal Registration	7-90
7.9.3 Image Correction Implementation for High Throughput	7-114

## CONTENTS (Continued)

	Page
7.9.4 Temporal Registration Process and RCP Library Maintenance	7-115
7.9.5 Special Processing	7-119
7.10 Registration Control Points	7-123
7.10.1 Assumptions	7-125
7.10.2 Analysis and Tradeoffs	7-125
7.10.3 Conclusions	7-129
7.11 CDPF System Synthesis	7-130
7.11.1 Input/Output Characteristic Used for Sizing CDPF Design	7-130
7.11.2 Image Processing System Functional Design	7-138
7.11.3 Image Processing System Hardware Design	7-151
7.11.4 Image Processing Operational Considerations	7-172
7.12 Data Processing for Other Missions	7-177
7.13 Ground Wideband Tape Recorders	7-182
7.13.1 Problem Discussion	7-182
7.13.2 Assumptions	7-182
7.13.3 Analysis and Tradeoffs	7-182
7.13.4 Conclusions	7-186
7.14 LCGS Configuration	7-187
7.14.1 Problem Discussion	7-187
7.14.2 Assumptions	7-188
7.14.3 Analysis and Tradeoffs	7-188
7.14.4 Conclusions	7-190
7.15 Tape Format Compatibility	7-192
7.15.1 Problem Discussion	7-192
7.15.2 Assumptions	7-192
7.15.3 Analysis and Tradeoffs	7-192
7.15.4 Conclusions	7-194
7.16 Filmwriter Technology	7-195
7.16.1 Problem Discussion	7-195
7.16.2 Assumptions	7-195
7.16.3 Analysis and Tradeoffs	7-196
7.16.4 Conclusions	7-197
7.17 Impact of Other System Elements	7-198
7.17.1 Assumptions	7-198
7.17.2 Analyses and Tradeoffs	7-198
7.17.3 Conclusions	7-200



## CONTENTS (Continued)

	Page
7.18 Orbit Determination	7-201
7.18.1 Analyses and Tradeoffs	7-201
7.18.2 Conclusions	7-202
7.19 LCGS RF Equipment	7-203
7.19.1 Equipment Description	7-205

## 5.2 ATTITUDE DETERMINATION AND CONTROL

### 5.2.1 Attitude Reference Design

This study activity compares candidate attitude reference approaches in the light of EOS-A and future missions, considering fixed and gimballed star trackers, star mappers, and digital sun sensors. Covariance analyses were performed to determine performance for the most promising candidate in low altitude and synchronous orbits.

#### 5.2.1.1 Motivation

The purpose of this study task was to identify and then analyze in detail the most promising low cost approach to EOS attitude estimation that will meet the required performance. Sun synchronous, geosynchronous and inertial point missions were considered.

#### 5.2.1.2 Methodology

The performance of attitude estimators employing gyros that are periodically updated by a star sensor can be accurately established by a single axis covariance analysis. The gyros are considered to possess a nonconstant drift rate bias in addition to float torque noise, and the star sensor output is taken to be both biased and noisy. Attitude estimation performance is established by using normalized results, such as presented in "Generalized Results for Precision Attitude Reference Systems Using Gyros" by R. L. Farrenkopf (AIAA Mechanics and Control of Flight Conference, Anaheim, California - August 5-9, 1974).

#### 5.2.1.3 Results

##### 5.2.1.3.1 Performance Requirements

The Pointing Error Budget Allocation task has defined the one sigma accuracies of the Inertial Attitude Estimator and the Ephemeris Estimator to be that given by, respectively, Tables 5-22 and -23. The error sources (bias, drift, drift rate deviation, jitter) are defined in Section 5.2.5 of Appendix A.

Table 5-22. Low Altitude Inertial Attitude Estimation Specification<sup>(A)</sup>  
(1  $\sigma$ )

	Earth Pointing		Stellar Inertial or Sun <sup>(B)</sup> Pointing. (per axis)
	Roll, Pitch	Yaw	
Bias	15 $\widehat{\text{sec}}$	25 $\widehat{\text{sec}}$	0.5 $\widehat{\text{min}}$
Drift	.009 deg/hr	.04 deg/hr	.004 deg/hr over 1 hr
Drift Rate Deviation	.005 deg/hr over 2 minutes	.015 deg/hr over 2 minutes	.004 deg/hr for 30 $\widehat{\text{sec}} < t < 1 \text{ hr}$
Jitter	0.30 $\widehat{\text{sec}}$ rms over 2 minutes	1.0 $\widehat{\text{sec}}$ rms over 2 minutes	2 $\widehat{\text{sec}}$ rms for times up to 1 hr

(A) Refers to the Accuracy of Estimate of Attitude of Star Tracker Mounting Surface

(B) GSFC/NASA RFP Spec

Table 5-23. Ephemeris Specification <sup>(A)</sup>  
(Earth Pointing Mode — 1  $\sigma$ )

	Along Roll or Pitch Axes	Along Yaw Axis
Bias	120 m	900 m
Drift	0.15 m/sec	0.50 m/sec

(A) Accuracy of the ephemeris data utilized  
by the CDPF



#### 5.2.1.3.2 Attitude Reference System Tradeoffs

A qualitative comparison of candidate attitude determination approaches is given in Table 5-24. It illustrates that the systems whose attitude estimates are based upon using an earth sensor lack the necessary mission flexibility and performance. A star sensor of some sort is thus indicated. Star mappers, a natural choice for orbiting spacecraft, are ruled out by the inertial point requirement of future EOS missions. Use of a sun sensor-star sensor combination is a viable possibility, but the sun sensor's mounting orientation would be dependent upon the orbit flown undermining the desire for a "universal" attitude reference module. The gimbale trackers easily meet the performance and mission flexibility requirements, but are at a disadvantage from a weight, power, and cost standpoint. The most reasonable selection turns out to be that involving the use of multiple body-fixed star trackers in conjunction with the gyros. This system is easily within the state of the art, and, as will be shown, meets the EOS requirements for both earth-pointing and inertial-pointing missions.

Table 5-24. Candidate Attitude Determination Approaches

ATTITUDE DETERMINATION SYSTEM	LEGEND									
	PERFORMANCE	MISSION FLEXIBILITY	HARDWARE COMPLEXITY	SOFTWARE COMPLEXITY	SPACECRAFT INTEGRATION	WEIGHT	POWER	DEVELOPMENT STATUS	COST	
EARTH SENSOR GYROCOMPASS	+	+	+	+	+	+	+	+	+	
EARTH SENSOR/IRU/SOFTWARE	-	+	+	-	+	0	0	-	0	
STAR MAPPERS/IRU/SOFTWARE	+	-	+	-	-	0	0	0	0	
SUN SENSOR/FIXED STAR SENSOR/IRU/SOFTWARE	0	-	0	0	-	0	0	0	0	
FIXED STAR SENSORS/IRU/SOFTWARE	0	0	0	0	-	0	0	0	0	
ONE-GIMBAL TRACKER/IRU/SOFTWARE	+	0	-	0	0	-	-	0	-	
TWO-GIMBAL TRACKER/IRU/SOFTWARE	+	+	-	0	0	-	-	0	-	

#### 5.2.1.3.3 Attitude Reference System Description

The selected system will now be described in detail. Figure 5-76 illustrates star tracker geometry requirements.

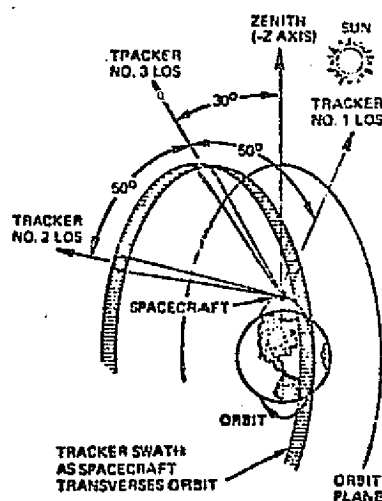


Figure 5-76. Earth Pointing Attitude Determination Operation

The TRW attitude determination design uses as sensors a three-axis rate gyro package, and three body-fixed 8 x 8 degree field-of-view star trackers to provide occasional attitude and gyro rate bias updates. The sensor information is processed by an on-board digital computer which integrates the gyro rates to provide attitude and establishes optimal estimates at the update times. Normal operation requires Trackers No. 1 and 2, with No. 3 in a standby mode. As Figure 5-76 indicates, the star sensors are positioned on the spacecraft so that a large swath (including many stars) is cut on the celestial sphere with minimum radiant interference from the sun.

The inertial-point mode, illustrated in Figure 5-77, operates in the same manner (provided that at least one star appears in the field of view of two trackers). This likelihood is very high for the chosen BBRC unit, and with a small rotation about the experiment, line of sight is virtually assured. If mission constraints require, attitude estimates based upon the IRU alone can be used for up to one hour. Then a spacecraft maneuver is needed to seek stars to update attitude and gyro drift rates.

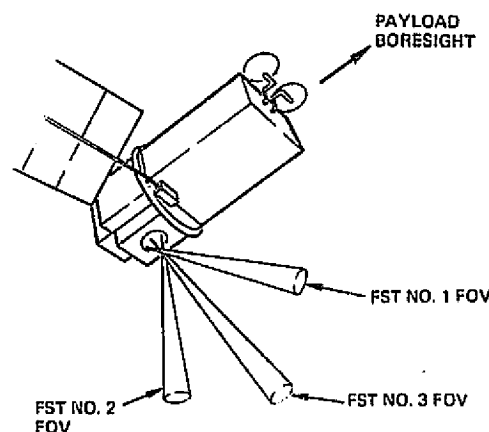


Figure 5-77. Typical Inertial Pointing Operating Geometry

The algorithm employed by the on-board computer in processing the gyro and star tracker data is illustrated by the block diagram of Figure 5-78.

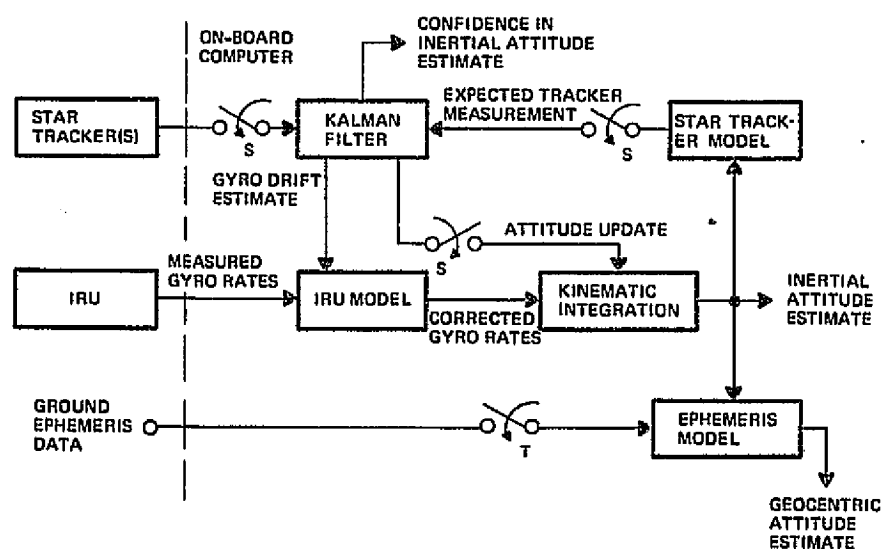


Figure 5-78. Attitude Determination Block Diagram

The digital computer receives IRU data input every 200 msec and star tracker information every 30 minutes. The IRU-measured gyro rates are corrected within the computer for their bias drift rates and the result kinematically integrated to yield an inertial attitude estimate. When a predetermined star enters a tracker field of view, the symbolic switch "S" closes and both the inertial attitude and the gyro drift rates are updated.

Ground ephemeris data is provided periodically to a time-dependent ephemeris model which, along with the inertial attitude estimate, yields an estimate of spacecraft attitude in geocentric coordinates.

#### 5.2.1.3.4 Sensor Error Sources

Error sources of the baseline BBRC star tracker are indicated in Table 5-25.

Table 5-25. BBRC Star Sensor Error Analysis

Unit Type: 8 x 8 deg field-of-view fixed head tracker  
 Usable Input Range: Stars from third to sixth magnitude  
 Manufacturer: Ball Brothers Research Center

Error Type	Error ( $\widehat{\text{sec}}$ ) $1\sigma$	
	Before Calibration	After Calibration
A. "Noise" from update to update		
Distortion	180	5
Magnetic field influence	38	5
Star magnitude variation	2	2
Star color	2	2
Power supply variations	2	2
Electronic noise	10	10
Total "Noise" (RSS)	184	12.7
B. Slowly Varying Biases		
Mechanical offsets	19	3.5
Null shift	4	4
Temperature effects (40°C range)	80	3
Aging	12	3
Total Bias (RSS)	83.2	6.8
Total Error (RSS)	202	14.4

Its error consists basically of two types, biases which change only over long periods of time; and "noise" which represents error fluctuations from star update to update. These error sources enter directly into the attitude estimation accuracy, as will be seen later.



The predominant gyro error sources, aside from its drift rate, consist of float torque noise of variance  $\sigma_v^2$ , drift rate variation noise of variance  $\sigma_u^2$ , and equivalent angle noise of variance,  $\sigma_e^2$ . If the one sigma knowledge of the drift rate is  $\sigma_b$ , then the standard deviation of the attitude uncertainty after T seconds is given by

$$\sigma_\theta = \left[ \sigma_e^2 + \sigma_v^2 T + \sigma_b^2 T^2 + \frac{1}{3} \sigma_u^2 T^3 \right]^{1/2}$$

The Kalman Filter reduces  $\sigma_b$  to a very low value, but can do little to combat  $\sigma_u$ ,  $\sigma_e$ , and  $\sigma_v$ . Table 5-26 cites these values for the baseline Bendix 64 PM RIG gyro. The influence of  $\sigma_e$  is fairly negligible, but float torque noise and drift rate variation noise are influential as lengthy star update times are reached. These influences will be considered in the next section.

Table 5-26. Sensor Numerical Values

Gyro (Bendix 64 PM RIG)	
$\sigma_e$	.1667 $\widehat{\text{sec}}$
$\sigma_v$	.025 $\widehat{\text{sec/sec}}/(\text{rad/sec})^{1/2}$
$\sigma_u$	$1.67 \times 10^{-5} \widehat{\text{sec/sec}^2}/(\text{rad/sec})^{1/2}$
Star Tracker (BBRC)	
$\gamma$	60 deg
$\eta$	8 deg
$\sigma_h$	12.7 $\widehat{\text{sec}}$
$\sigma_s$	6.8 $\widehat{\text{sec}}$

#### 5.2.1.3.5 Inertial Attitude Estimation Performance

Performance of the Inertial Attitude Estimator and the on-board Ephemeris Estimator will now be considered and compared to the requirements noted in Tables 5-22 and 5-23.

### Inertial Attitude Estimation

A single axis analysis using one tracker with a single readout variable will now be initiated. Simulation runs have shown that this is indicative of the per axis behavior of the EOS 3-axis estimator using two trackers, each with two output variables. From Figure 5-76, it is clear that the angle,  $\gamma$ , between the tracker boresight and the orbit rate vector is 60 degrees. Also, as noted before, the tracker field of view,  $\eta$ , is 8 degrees. Table 5-26 summarizes the assumed sensor values, noting previous considerations.

It can be shown that jitter is given by

$$\bar{\sigma}_\beta(t) = \left[ \sigma_e^2 + \frac{T}{9} \sigma_v^2 + \frac{T^3}{180} \sigma_u^2 \right]^{\frac{1}{2}}$$

and drift rate deviation by

$$\sigma_e(t) = \left[ \frac{4\sigma_e^2}{T^3} + \frac{4\sigma_v^2}{3T} + \frac{\sigma_u^2}{5} \right]^{\frac{1}{2}}$$

Table 5-27 documents values of these errors for  $t$  equal to 30, 120, and 3600 sec.

Table 5-27. Low Altitude Attitude Estimation Performance  
(Per Axis,  $1\sigma$ )

	$t = 30 \text{ sec}$	$t = 120$	$t = 3600$
Jitter ( $\widehat{\text{sec}}$ )	.173	.190	.592
Drift Rate Deviation (deg/hr)	.0056	.0026	$5.5 \times 10^{-4}$

Bias ( $\widehat{\text{sec}}$ )	11.19
Drift Rate (deg/hr)	.00145

Key to establishing the attitude and drift rate bias estimation accuracies are Figures 5-79 through -81. Given  $\gamma$ ,  $\eta$ , and an assumed star tracker sensitivity, Figure 5-79 yields the average and 95 percent likely update times,  $T_{av}$  and  $T_{95}$  respectively, in terms of the orbit period,  $P_o$ . Setting  $T = T_{95}$ , the ordinate and abscissa values of Figure 5-80 can be computed and a print located on an appropriate  $\sigma_z/\sigma_h$  curve.  $\sigma_z$  represents the standard deviation of the attitude uncertainty just prior to an update if there were no tracker bias. Computing  $\sigma_z$ , the actual attitude estimation uncertainty is then given by

$$\sigma_\theta = \sqrt{\sigma_z^2 + \sigma_b^2}$$

In a similar way, the gyro drift rate uncertainty is established from Figure 5-81.

#### Low Altitude Attitude Estimation

Assuming a 386 nm circular orbit and a star tracker sensitivity,  $m$ , of 4.0, the recipe described above yields

$$\begin{aligned}\sigma_\theta &= 11.19 \text{ sec} \\ \sigma_b &= .00145 \text{ deg/hr}\end{aligned}$$

These results are repeated in Table 5-27, and meet the requirements specified in Table 5-22.

#### Geosynchronous Attitude Estimation

Here stars stay within the tracker field of view for about one-half hour and  $m$  can realistically be taken as 5.5. It follows that

$$\begin{aligned}\sigma_\theta &= 14.41 \text{ sec} \\ \sigma_b &= .00128 \text{ deg/hr}\end{aligned}$$

performance comparable to that at the low altitude.

#### 5.2.1.3.6 Ephemeris Estimation

On-board ephemeris estimation is necessary so that the spacecraft attitude relative to geocentric coordinates can be established and ultimately used to control the vehicle. If  $\bar{R}(t)$  defines the spacecraft position at time  $t$  and  $\bar{V}(t)$  its velocity, then the geocentric coordinate set  $(y_1, y_2, y_3)$  is defined by

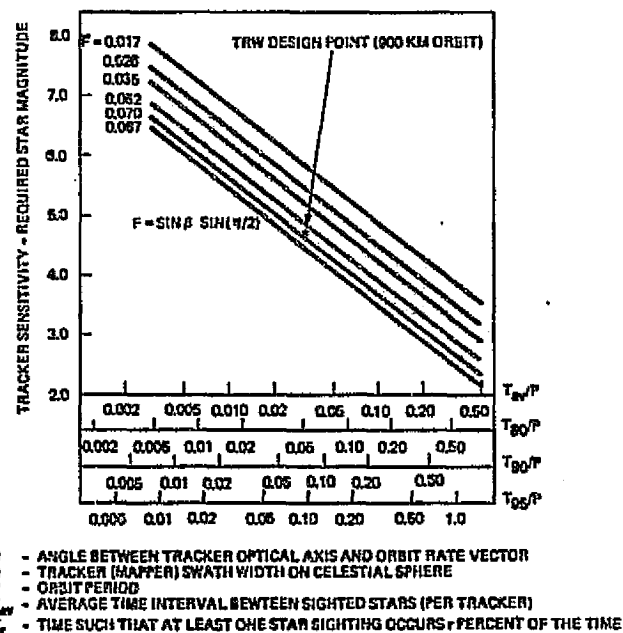


Figure 5-79. Star Magnitude as a Function of Normalized Update Time

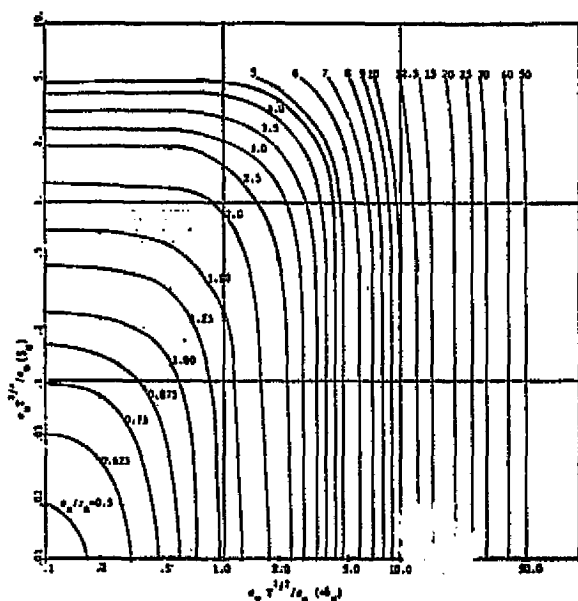


Figure 5-80. Normalized Prefilter Attitude Estimation Error

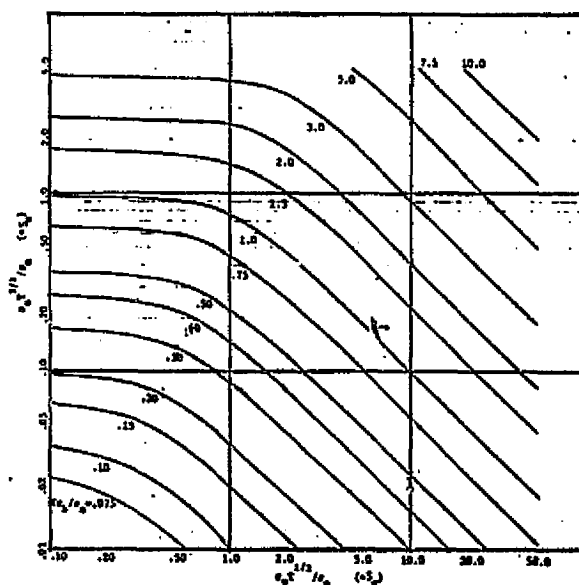


Figure 5-81. Normalized Post-Filter Gyro Drift Rate Error Over the Time Interval  $0 < t < T_f$  for  $T_f = 4T$



$$\bar{y}_3 = -\bar{R}/|\bar{R}|$$

$$\bar{y}_2 = \bar{R} \times \bar{V}/|\bar{R} \times \bar{V}|$$

$$\bar{y}_1 = \bar{y}_2 \times \bar{y}_3$$

Given the components of  $\bar{R}$  and  $\bar{V}$  in ECI coordinates, the transformation from this inertial set to  $(y_1, y_2, y_3)$  follows immediately.

The accurate on-board estimation of  $\bar{R}(t)$  and  $\bar{V}(t)$  is no easy task, and several approaches are possible. Clearly the most accurate estimation of present and future spacecraft ephemeris is performed by a ground based computer employing a sophisticated filter operating on a complex model that includes earth oblateness effects, aerodynamic drag, etc. Unfortunately, this high quality ephemeris estimate cannot be continually provided to the spacecraft due to mission constraints. It is assumed that ephemeris data is provided to the spacecraft on a once per day basis, indicating to the vehicle its predictions of  $\bar{R}(t)$  and  $\bar{V}(t)$  at orbit angles of, say, 60 degrees over the next 24-hour period. Including also the time benchmarks, this amounts to a computer memory requirement of about 600 words.

Figure 5-82 illustrates the on-board estimation philosophy, assuming that the time  $t$  lies between the  $i$ th ground supplied benchmark,  $t_i$ , and the  $i$ th st benchmark,  $t_{i+1}$ . Using  $\bar{R}(t)$  and  $\bar{V}(t)$ , the on-board computer generates a Kepler trajectory  $\bar{R}_1(t)$ ,  $\bar{V}_1(t)$  that matches the benchmark at  $t_i$ . In a similar fashion, a Kepler curve  $\bar{R}_2(t)$ ,  $\bar{V}_2(t)$  is fit through the reference at  $t_{i+1}$ . These curves may correspond to slightly different orbital parameters (e.g., eccentricity) due to perturbations introduced, for example, by aerodynamic drag. The spacecraft's estimate of ephemeris at  $t$  is then taken to be

$$\bar{R}(t) = \bar{R}_1(t) + [\bar{R}_2(t) - \bar{R}_1(t)] (t-t_i)/(t_{i+1}-t_i)$$

$$\bar{V}(t) = \bar{V}_1(t) + [\bar{V}_2(t) - \bar{V}_1(t)] (t-t_i)/(t_{i+1}-t_i)$$

The amount of computation involved in this process is not severe, and leads directly to a definition of the estimated transformation relating ECI and geocentric coordinate systems.

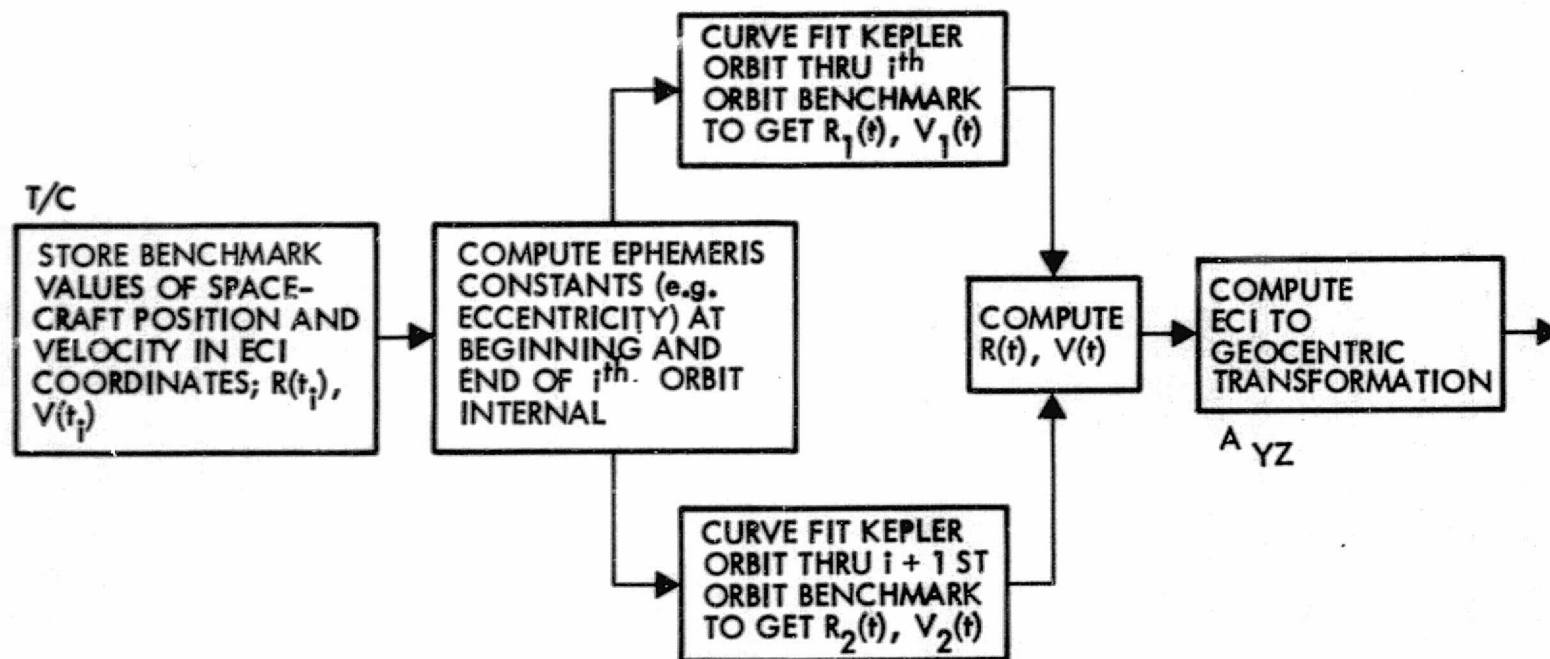


Figure 5-82. Functional Block Diagram of Spacecraft On-Board Ephemeris Estimator

Quantitative results regarding the accuracy of the above estimation approach are not available at this time. Clearly, errors will exist in:

- (i) the ground supplied ephemeris data
- (ii) the on-board interpolation algorithm.

Numbers as low as 30-50 m have been associated with (i), but this relates to post-facto data smoothing efforts rather than the predictive estimates that must be provided here. Errors associated with (ii) can be established by comparison with presently available ephemeris tapes (e.g., ERTS). If these errors are severe, they can be reduced to acceptable values by additionally incorporating polynomial correctors in  $t$  in estimating  $\bar{R}(t)$  and  $\bar{V}(t)$ ; or, perhaps better, using ground-supplied benchmarks at, say, 30 degree intervals instead of 60 degrees. Of course there is a computer impact in such refinements. Nevertheless, the accuracy of the ground supplied data ultimately limits the accuracy of the on-board ephemeris estimator, and if the technology is such that daily updates are too error prone, more frequency ground transmissions may be required.

The requirements of Table 5-23, while challenging, should be within the present state of the art if the ground update frequency is not too low. Whether one update per day is adequate, or even desirable, is a topic for further study. On-board induced errors, which peak at about 5 min. subsequent to each benchmark for low altitude orbits, probably can be made to contribute little to the 120 m allotment, at least on an RSS basis. Thus, Table 5-23 represents primarily a specification upon the ground based ephemeris estimation system.

#### 5.2.1.3.7 Spacecraft Antenna Gimbal Commands

Figure 5-83 illustrates the methodology used in establishing the antenna gimbal angle commands necessary to track a given ground station. If the spacecraft undergoes a commanded yaw profile in order to compensate for earth rotation effects, this yaw angle must, of course, be considered in the gimbal angle computations. Since the required tracking accuracy is not severe (0.25 degree or so), spacecraft pitch and roll errors can be ignored due to their extremely small values (.01 degree (1  $\sigma$ )).

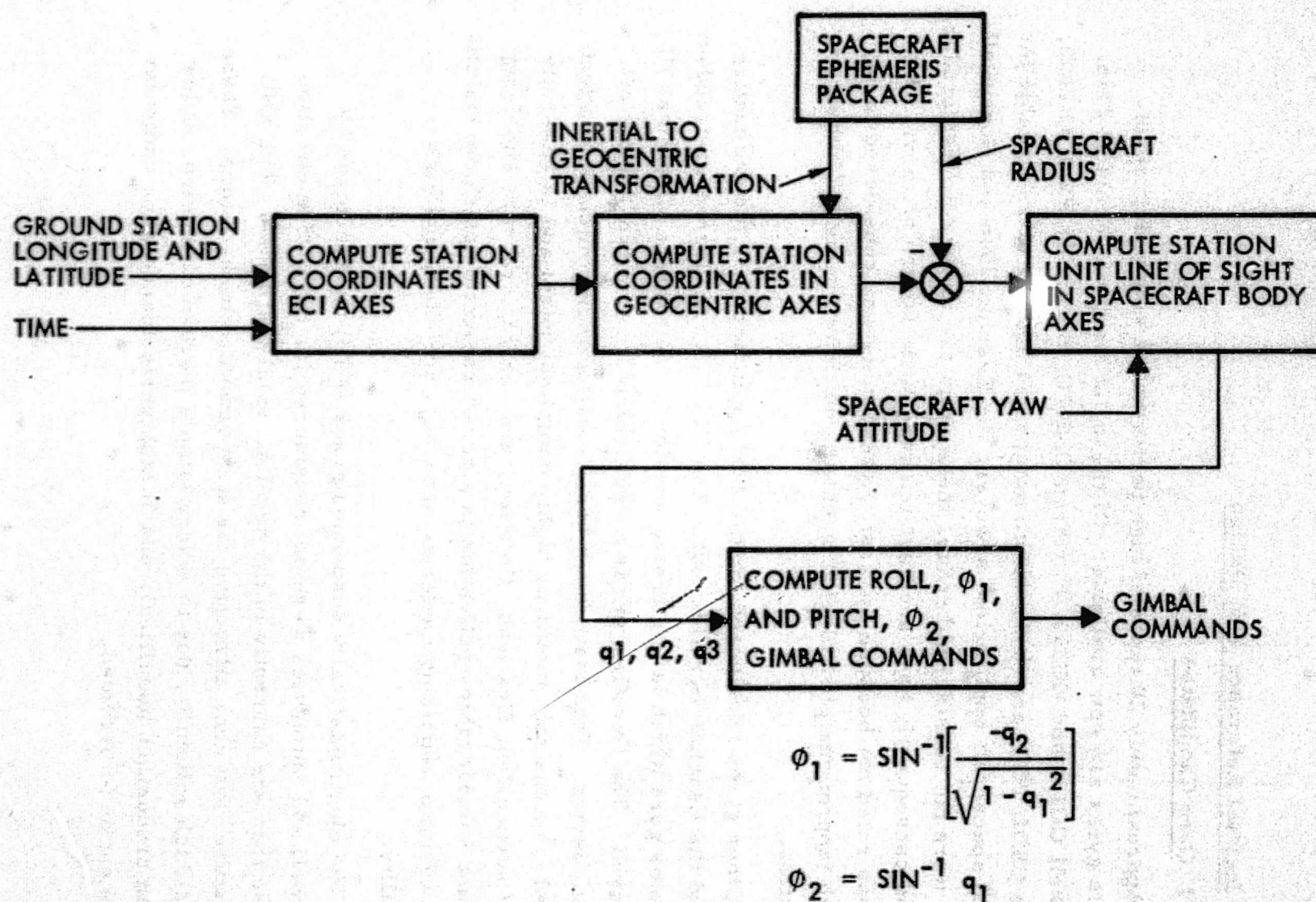


Figure 5-83. Block Diagram of Antenna Gimbal Commands

## 5.2.2 Inertial Reference Unit Design

### 5.2.2.1 Gyro Candidates

Approximately 20 types of high performance single-degree-of-freedom gyros are now available. Of these, at least six (Kearfott 2546, Honeywell GG134 and GG334, Northrop GI-K7G, Bendix 64 PM RIG-2000, and the CSDL TGG) are in the subminiature gas bearing class suitable for the EOS spacecraft application; however, the Kearfott 2546 and Honeywell GG134 were not considered because these units are in very limited production and consequently have accumulated very little failure history. The TGG was ruled out because the cost of these units was considered to be too high (approximately \$100,000 each) in addition to being in limited production.

Other gyros considered for the EOS application are the Autonetics G21 and the Kearfott Gyroflex unit. The G21 is a two-degree-of-freedom free rotor gyro which is a half size version of the present Minuteman III G6B4 gyro. The Gyroflex unit is a dry (isolated rotor) two-degree-of-freedom device. This instrument has a rotating mass which is in effect isolated from the spin motor by highly compliant joints and is generally free of suspension, flex lead, flotation, and bearing errors. The design has found considerable application in aircraft navigation platform stabilization systems requiring moderate accuracy, low cost, and high reliability.

The electrostatically suspended gyros (ESG) manufactured by Honeywell and Autonetics were not considered for the EOS application because they are currently in the developmental test phase. The ESG has features that look attractive for strapdown use in the future. These are: 1) high reliability due to a very simple mechanical design, 2) low cost (in production quantities), and 3) high performance when computer compensation is provided.

#### 5. 2. 2. 2 Cost

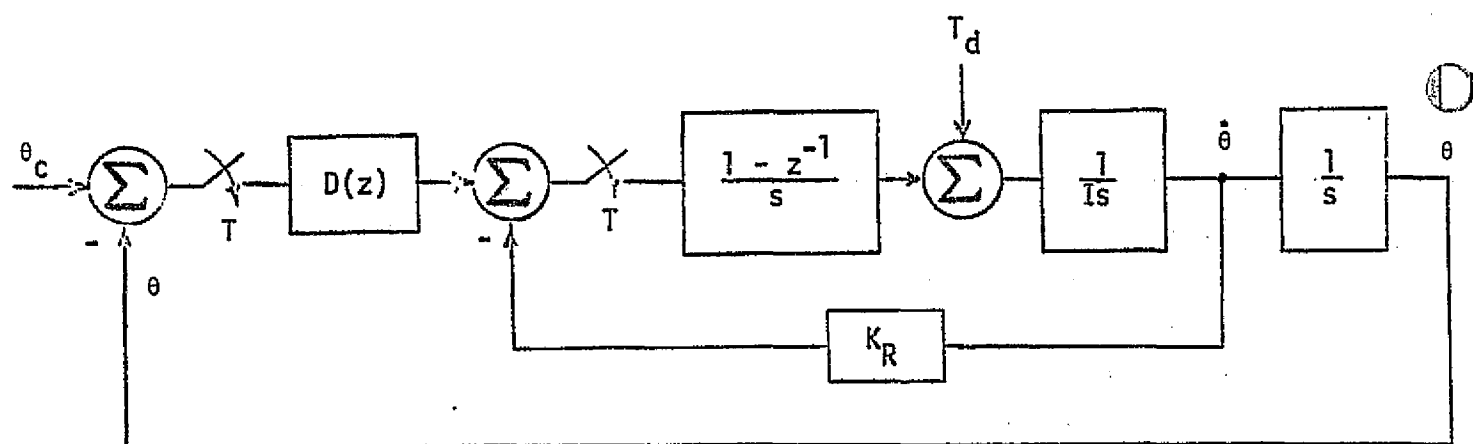
Accurate cost information of attitude reference systems is difficult to obtain because the cost is a function of both the gyro and its associated electronics. The gyro manufacturer is reluctant to give out meaningful estimates without first seeing a specification. In general, analog systems are less expensive than digital systems because the electronics design is less complex; however digital systems are capable of higher accuracy. The cost data presented in Table 5-28 are estimates based on 1) information obtained from gyro sales representatives, 2) proposals submitted to TRW for various attitude reference systems, and 3) past experience obtained during other gyro procurements.

#### 5. 2. 2. 3 Reliability

The major problem in the prediction of gyro reliability is in finding valid data as to gyro failure rates under mission conditions. There is no standard gyro, so information about one gyro cannot be transferred directly to predict the failure rate of another.

Most inertial quality gyros are used in small quantity and, therefore, the rate of accumulation of operating time for gyros is small. It is significant to note that the gyros having the lowest failure rates are those which have been used on very large programs using hundreds of gyros and involving long times in development and qualification.

The reliability data presented in Table 5-28 was obtained from brochures, technical reports, and proposals.



$T \triangleq$  SAMPLE PERIOD  
 $\theta_c \triangleq$  COMMANDED ATTITUDE

#### SAMPLED DATA FILTER

$$D(z) = \left[ 1 + K_I \frac{T}{2} \frac{(1 + z^{-1})}{(1 - z^{-1})} \right] K_P K_L \frac{(1 - az^{-1})}{(1 - bz^{-1})} z^{-1}$$

$K_P \triangleq$  Position Gain

$K_L \triangleq$  Lead Filter Gain

$K_I \triangleq$  Integrator Gain

#### DISTURBANCE TORQUE

$$T_D = \left. \begin{aligned} &A_0 + A_1 \sin \omega_0 t + A_2 \cos \omega_0 t \\ &+ B_1 \sin 2\omega_0 t + B_2 \cos 2\omega_0 t \end{aligned} \right\} \text{GENERAL FORM}$$

$\omega_0 \triangleq$  Orbit Rate

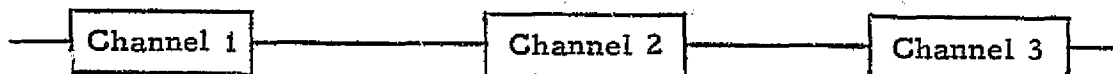
$I \triangleq$  Axis Inertia

Figure 5-126. Single Axis Model of Wheel Controller

A minimum of three gyro channels per spacecraft are required, one for each of the three control axes. A number of redundant configurations can be considered for improved reliability. These are evaluated below.

● Basic Orthogonal triad (no redundancy)

$$\lambda = 16,682 \times 10^{-9*}$$

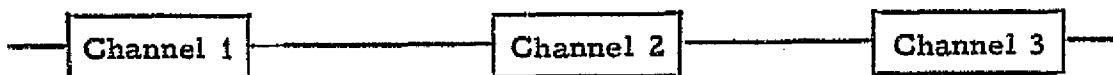


<u>Time (yrs)</u>	<u>Reliability</u>
1	0.6451
2	0.4161
3	0.2684
4	0.1732
5	0.1117

\*Gyro plus associated electronics

● Orthogonal triad (6 gyros in redundant pairs)

$$\lambda = 16,682^{-9}$$

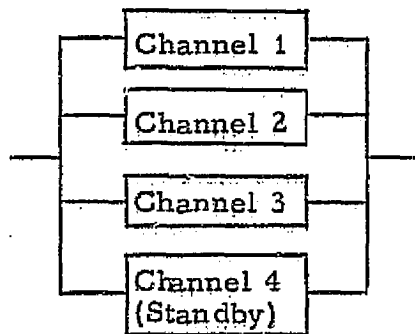


<u>Time (yrs)</u>	<u>Reliability</u>
1	0.9685
2	0.8892
3	0.7832
4	0.6672
5	0.5532



- Orthogonal triad plus standby skewed unit  
(4 gyros, any 3 out of 4 required)

$$\lambda = 16,682 \times 10^{-9}$$



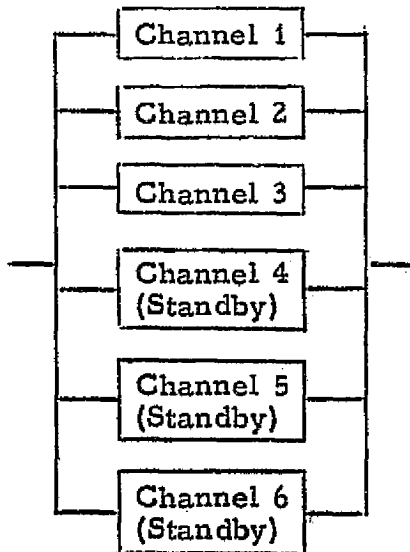
Time (yrs)

Reliability

1	0.9258
2	0.7757
3	0.6138
4	0.4681
5	0.3478

- Dodecahedron (6 gyros, any 3 out of 6 required)

$$\lambda = 16,682 \times 10^{-9}$$



Time (yrs)

Reliability

1	0.9989
2	0.9877
3	0.9554
4	0.8987
5	0.8209

These results show that the 6-gyro dodecahedron configuration is significantly more reliable for extended missions than the other configurations. The use of a single-standby skewed gyro with the basic orthogonal triad is a minimum cost redundancy configuration and provides a substantial reliability improvement over the basic nonredundant configuration.

#### 5.2.2.4 Gyro Package Selection

An inertial reference unit (IRU) package containing a single gyro and associated electronics is recommended in order to provide maximum flexibility in tailoring the level of redundancy to mission requirements. Based on cost, performance, and development status for space programs, an IRU design based on the Bendix design for the IUE and HEAO programs is suggested for EOS application. This package uses the Bendix gas bearing gyro model 64 PM RIG-2000 and has the following basic performance:

- Dynamic rate range (about gyro input axis)  $\pm 2.5$  deg/sec (without scale factor or gyro speed switching)
- Output angle resolution  $0.1 \text{ } \overline{\text{sec}}/\text{bit}$
- Bandwidth  $>10$  Hz (-3 dB)
- Random drift ( $3\sigma$ )  $0.006^\circ/\text{hr}$

### 5.2.3 Star Sensor Selection

#### 5.2.3.1 Summary

To establish star tracker requirements based on mission constraints, an algorithm has been developed that consists of the following five major components:

- 1) Relationship between required star tracker field-of-view and sensitivity as a function of maximum stellar update period and star availability probability.
- 2) Dependence of digital star tracker sensitivity on such tracker parameters as field-of-view, aperture, output time constant and random noise angle.
- 3) Sensitivity of digital tracker rate error to input rate and track parameters, particularly track time constant.
- 4) Dependence of tracker bias errors and stabilities on field-of-view.
- 5) Limiting volume (maximum length and diameter) of a two-stage stray light shade as a function of star tracker aperture and field-of-view, and mission minimum sun angle (or earth limb) constraints.

The first and last relations may be used to evaluate an existing star tracker design, such as the Ball Brothers SAS-C unit discussed herein.

This algorithm has been used to conceptualize an alternate EOS star tracker design based on the TRW digital "photon counting" technique that has been developed to the breadboard stage. Advantages of the digital star tracker approach include improved noise performance and acquisition capability for a given aperture, field-of-view and star in comparison to an analog tracker, such as the SAS-C unit. In addition, the dynamic range capability is significantly greater. As an alternative, this digital technique allows a considerable reduction in star tracker aperture and field-of-view with corresponding reduction in stray light shade volume and weight.

### 5.2.3.2 Star Availability Constraints

The star tracker must have a field-of-view and sensitivity that is consistent with mission and attitude determination constraints. The primary constraints are spacecraft orbital rate and the required stellar update frequency, which is a function of the quality of the gyro rate information and attitude determination filter. Other limitations include minimum sun and earth limb angles relative to the tracker field, required accuracy, size and weight restrictions, and star catalog accuracy and complexity. Certain general comments may be made regarding these latter limitations.

1) It is desirable to maximize the sun and earth limb angles. The sun problem is readily accommodated in a sun-synchronous orbit and earth limb restrictions may be minimized by proper orientation of the star tracker field with respect to earth nadir.

2) For a given sun angle constraint, the light shade volume is proportional to the star tracker aperture area (see Section 5). From shade size and weight considerations, it is desirable to minimize tracker aperture.

3) Star tracker accuracy is generally improved by minimizing the field-of-view. Since the available stars for a given field increases with tracker sensitivity, decreasing the star tracker field-of-view implies higher sensitivity (ability to track dimmer stars) which is approximately proportional to aperture diameter.

4) A requirement to track dim stars complicates the necessary star catalog. The star position and intensity accuracies available degrade for dimmer stars and the number of stars in the catalog necessarily increases.

The previous comments present conflicting requirements for a star tracker design. However, it appears that the optimum general approach is to:

- 1) Select the largest star tracker field-of-view consistent with overall accuracy requirements.
- 2) Determine the required star tracker sensitivity for that field based on orbital rate and stellar update frequency constraints.
- 3) Design the star tracker aperture for these sensitivity and accuracy requirements.

For an earth-pointing mission the relation between required tracker field-of-view and sensitivity may be described by:

$$N_p \geq 360 \text{ FOV } \cos \phi N_m T_u/T_p \quad (1A)$$

where,

$N_p$  = number of stars per stellar update period required for probability of one or more stars,  $P_s$

FOV = star tracker field-of-view, deg.

$\phi$  = angle between tracker boresight axis and orbit plane

$N_m$  = density of stars brighter than a given visual magnitude (m), stars/deg.<sup>2</sup>

$T_u$  = stellar update period

$T_p$  = orbital period

Since  $N_p \rightarrow \infty$  for  $T_p \rightarrow 0$ , equation (1) does not realistically describe an inertial-pointing mode, since only a single-axis (slit) field is implied. For random inertial pointing the average FOV-sensitivity relationship may be limited to:

$$N'_p = N_m(\text{FOV})^2 \quad (1B)$$

From equations (1A) and (1B) a realistic relation between required star tracker FOV and sensitivity results. This relationship is shown in Figure 5-84 using mean stellar density data from Allen\* and assuming star density to be a Poisson distribution, so that  $N_p = 3$  for  $P_s = 95$  degrees.

The earth-pointing limits are plotted as a function of the ratio of update period to orbit period ( $T_u/T_p$ ). For high quality gyros,  $T_u$  is reasonably twenty minutes or longer. Therefore, for a low altitude orbit ( $\sim 750$  Km),  $T_u/T_p \geq 0.2$  and for a synchronous orbit  $T_u/T_p \approx 0.014$ .

An adequate star tracker design for all three types of missions (1. low altitude earth point, 2. synchronous orbit and 3. inertial pointing) would have a FOV of at least  $5^\circ$  and a minimum sensitivity of  $6^m$ . Reducing the FOV to  $2^\circ$  necessitates a sensitivity of  $5^m$  for mode 1,  $7^m$  for mode 2, and  $8^m$  for mode 3. The latter design is feasible if it is possible to command different track bandwidths (or output signal time constants) for each mode.

\* \* Allen, C. W., Astrophysical Quantities, Athlone Press, 1963.

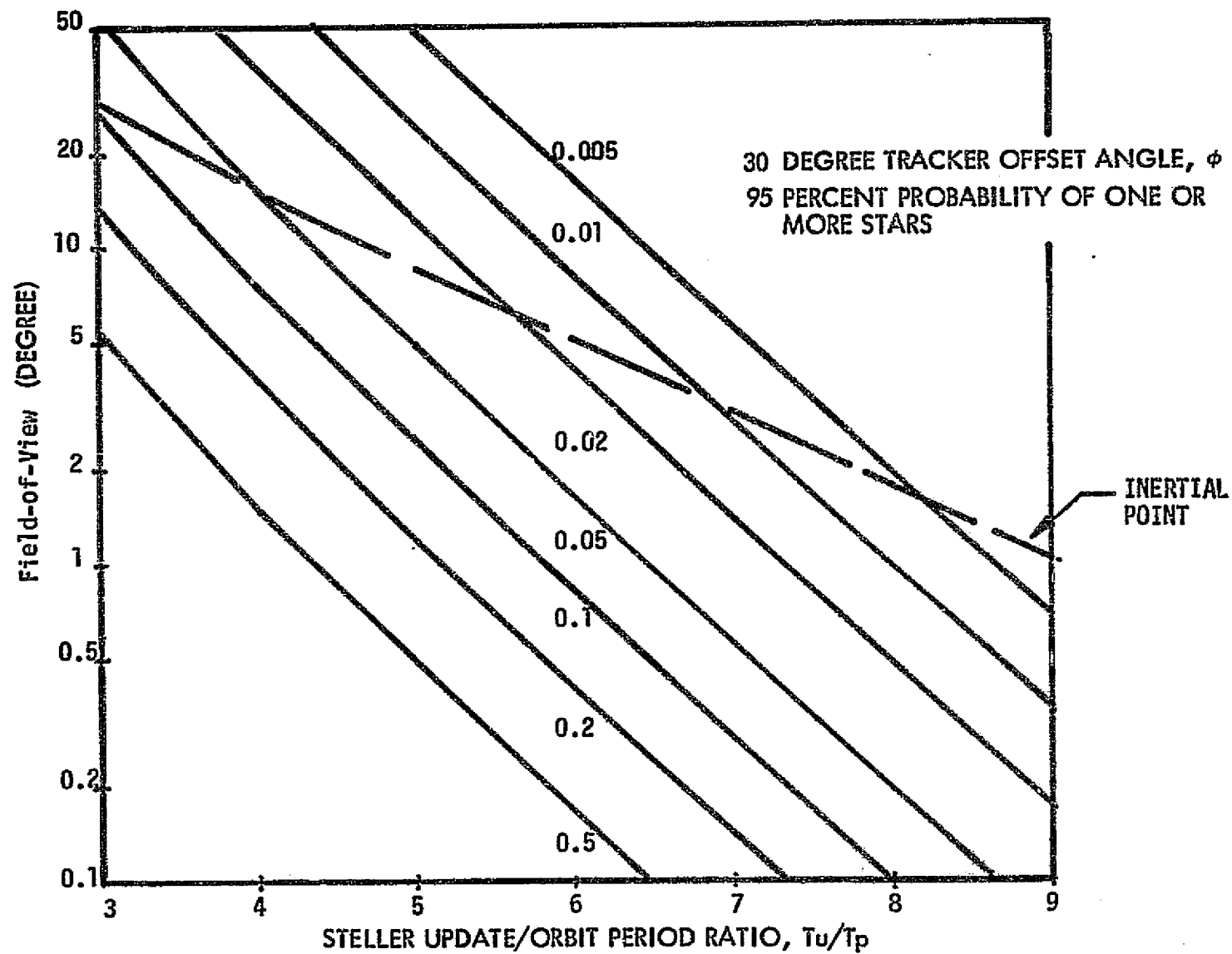


Figure 5-84. Star Availability as a Function of Tracker Field-of-View and Sensitivity

The following sections describe two candidate designs that satisfy the above constraints. One is an analog tracker that is being developed for the SAS-C spacecraft. This unit has an 8° square field and 6<sup>m</sup> sensitivity. The other is a digital ("photon-counting") tracker based on TRW internally-funded development studies.

#### 5.2.3.3 BBRC SAS-C Star Tracker

The Ball Brothers Research Corporation (BBRC) CT-401 star tracker (STA) is presently being developed for the Small Astronomy Satellite (SAS-C), under a contract with the MIT Center for Space Research. This unit employs an electronically deflected image tube to search a star field, detect a star, and track that star until it leaves the STA field-of-view or a command is received to return to the search mode.

The salient features of this STA are summarized in Table 5-59, together with design parameters for the required STA shade.

The 10 arc second calibrated accuracy of the SAS-C STA is achieved using ground calibrations and computer analysis to remove nonlinear and environmental dependent effects.

The major error sources include:

- Lens and image dissector distortions
- Temperature variations
- External magnetic field
- Star intensity variations



Table 5-29. Summary of BBRC SAS-C STA Performance and Shade Design

STA

PHOTODETECTOR

TYPE	ITT F4012RP Image Dissector
DEFLECTION	Magnetic
FOCUS	Magnetic
SPECTRAL RESPONSE	S-20
CATHODE APERTURE	0.008 inch square

LENS

TYPE	Farrand Optical Super-Farron
FOCAL LENGTH	76 mm
APERTURE	f/0.87 (T/1.0)

FIELD-OF-VIEW

8° x 8°

INSTANTANEOUS FIELD-OF-VIEW

0.153° (9.2 arc min.)

STAR SIGNAL DYNAMIC RANGE  
VISUAL MAGNITUDE (GOV)

+ 6.0 to + 2.0

SEARCH MODE

TYPE	Raster
LINE TIME	50 ms
FRAME TIME	4.0 seconds

TRACK MODE

TYPE	Cross scan
SCAN PERIOD	100 ms

Table 5-29. Summary of BBRC SAS-C STA Performance and Shade Design (Continued)

OUTPUT TIME CONSTANT	
OUTPUT 1	62.5 ms
OUTPUT 2	0.4 second
RMS OUTPUT NOISE (NEA)	
OUTPUT 1	15 arc sec.
OUTPUT 2	6 arc sec.
UNCALIBRATED ACCURACY	10 arc min.
CALIBRATED ACCURACY (See discussion)	10 arc sec.
<u>SIGNAL INTERFACE</u>	
DIGITAL COMMANDS:	Power on Power off Search Initialize
BI-LEVEL:	Set star threshold (2 bits) Enable star threshold (1 bit) Set bright object threshold (2 bits) Bright Object presence (1 bit) Track mode star presence (1 bit)
ANALOG:	High voltage; 0-5 VDC Star magnitude; 0-5 VDC Internal temperature (2); 0-5 VDC  Star Position (4); - 5 VDC to +5 VDC U position, wide band V position, wide band U position, narrow band V position, narrow band

Table 5-29. Summary of BBRC SAS-C STA Performance and Shade Design (Continued)

PHYSICAL CHARACTERISTICS

SIZE	6.0 in. x 5.25 in. x 12.0 in.
WEIGHT	11.5 lb.
POWER	6 W
RELIABILITY	0.979, 6 months 0.955, 1 year
TEMPERATURE RANGE	-10°C to +50°C

SHADE

<u>MINIMUM SUN ANGLE</u>	45°
--------------------------	-----

LENGTH X WIDTH

3 IN. APERTURE, 8°	
CIRCULAR FOV	20.7 in. x 10.6 in.
3.5 IN. APERTURE, 8° SQUARE FOV	19.2 in. x 21.1 in.

Each unit is calibrated over its field as a function of each of the above error sources, using a star simulator matrix (9 x 9 array of stars with 1° spacing between stars). A polynomial fit is then made to this data.

The distortions are removed with a fit of the form:

$$\theta(X,Y) = A_0 + A_1 X + A_2 Y + A_3 XY + \dots + A_9 Y^3$$

$$\phi(X,Y) = B_0 + B_1 X + \dots + B_9 Y^3$$

where  $\theta$  and  $\phi$  are the true input angles and  $X$  and  $Y$  are the unit output voltages. The fit is generally made only over a 6° x 6° field. Data is taken at five temperatures and the temperature effects are compensated by a quadratic fit of the  $A_i$  and  $B_i$  coefficients; for example:

$$A_i = \alpha_{i0} + \alpha_{i1} T + \alpha_{i2} T^2$$

The magnetic field effects are calibrated only along the longitudinal axis, since transverse fields ( $\pm$  earth's field) cause less than 2 arc seconds error. These axial field effects are fit linearly; that is:

$$\Delta X = C_0 + C_1 X + C_2 Y$$

$$\Delta Y = D_0 + D_1 X + D_2 Y$$

Star intensity effects are calibrated at five different intensities. The variations of position (X, Y) with intensity are quasi-linear. Therefore, a slope (change in position/unit intensity) is calculated for each star position and these slopes are fit as a function of position in the field using a quadratic fit.

A summary of these errors, before and after calibration, is shown in Table 5-30 (1.-4.) for the SAS-C tracker, as derived from data on the first two units. Several other potential error sources are estimated (5.-10.).

The shade design for the SAS-C star tracker is based on the two-stage shade concept described in Section 5, with a 45° minimum sun angle constraint. For the STA 8° square FOV and 3.5 inch aperture diameter, a minimum length shade design is 19.2 in. L x 21.1 in. W. By limiting the STA field to 8° circular and reducing the aperture to 3 inches (reducing sensitivity by about 0.3<sup>m</sup>) allows the shade width to be reduced to less than 11 inches with about the same length. A folded STA/shade combination, using a 45° plane mirror, allows room for the three STA/shade subassemblies in the Attitude Determination module.

Table 5-30. BBRC SAS-C STA Bias Error Summary

BIAS ERROR SOURCE	ERROR (ARC SEC. $1\sigma$ )	
	BEFORE CALIBRATION	AFTER CALIBRATION
1. DISTORTION BIAS	10 arc min.	3 ( $6^\circ \times 6^\circ$ field)
2. TEMPERATURE SENSITIVITY ( $-10^\circ\text{C}$ to $+50^\circ\text{C}$ )	2 arc sec./ $^\circ\text{C}$	3
3. EXTERNAL MAGNETIC FIELDS ( $\pm 0.5$ GAUSS EARTH FIELD)	2 (Transverse) 10 (Axial)	2 2.5
4. STAR INTENSITY ( $+3^m$ to $+6^m$ )	$> 30$	2.5
<hr/> (ESTIMATED)		
5. STAR COLOR VARIATIONS	2	2
6. POWER SUPPLY VARIATIONS	2	2
7. MECHANICAL OFFSETS	19	3.5
8. NULL SHIFT	4	4
9. AGING	12	3
10. RATE ERROR (DYNAMIC LAG)	14 (Output 1)	2
RSS TOTAL	$\sim 10$ arc min.	$< 10$

#### 5.2.3.4 Alternate Star Tracker Design

During the past year, significant advances in star tracker technology have been demonstrated at TRW. This performance improvement has been realized through the use of digital "photon counting" signal processing instead of the conventional analog signal processing. The digital counting technique reduces the tracker noise angle (NEA) and improves acquisition of dim stars for a given collection aperture and bandwidth. As an alternative, for a given NEA requirement, it allows a reduction in the tracker aperture, or field-of-view (improving overall accuracy), or both.

A reduction in star tracker aperture is desirable for two reasons. First, this reduces shade volume in proportion to the aperture area, and minimizes weight. For the limited Attitude Determination module volume the problems associated with packaging three star tracker/shade assemblies are eased and the restrictions of a folded tracker/shade eliminated. Second, the stray light scattering and multiple reflections of large relative aperture optics (f/0.87 for SAS-C tracker) are extremely difficult to limit. Since an overall stray light attenuation of at least  $10^{10}$  is required for a  $6^m$  star tracker, and a carefully designed and maintained two-stage shade is capable of  $10^7$  attenuation, the lens must provide the remaining  $10^3$  attenuation. This attenuation level is consistent with relatively simple lenses\* (three elements or less), but has not been verified for a lens as complex as the Super Farron.

---

\* cf. Leinert, C. and Kluppelberg, D., "Stray Light Suppression in Optical Experiments," Applied Optics, Vol. 13, No. 3, March 1974.

The design of a digital star tracker may be accomplished using the following equations that have been analytically derived and experimentally verified by a TRW breadboard tracker.

1) TRACK NEA

$$\sigma_{\theta}^2 = \left( \frac{K}{2-K} \right) \left( \frac{\lambda_s + 2\lambda_B}{\lambda_s^2} \right) \left( \text{IFOV} \right)^2 / \Delta t \quad (2)$$

where,  $\sigma_{\theta}$  = RMS track NEA, arc sec. ( $1\sigma$ )

$K$  = track loop gain ( $0 < K < 2$ )

$\lambda_s$  = signal count rate,  $\text{sec}^{-1}$

$\lambda_B$  = background noise count rate,  $\text{sec}^{-1}$

IFOV = tracker instantaneous field-of-view, arc sec.

$\Delta t$  = track mode time constant, sec.

Further,

$$\lambda_s = 3.25 \times 10^5 A_0 2.51^{-m} \quad (2A)$$

where,

$A_0$  = tracker aperture area,  $\text{cm}^2$

$m$  = star visual magnitude

assuming a GOV spectral class star, S-20 photocathode with 60 mA/w peak responsivity, and 90% transmission.

$$\lambda_B = 2.51 \times 10^{-4} A_0 (\text{IFOV})^2 + 1.12 \times 10^{13} \alpha_L \quad (2B)$$

where the first term is the star field background, assuming  $100 \times 10^m$  stars/deg.<sup>2</sup> and the second term is the scattered sunlight background for a 0.009 inch effective photocathode aperture, with  $\alpha_L$  the total shade and lens attenuation factor (assumed to be  $10^{-10}$ ).

### 3) BIAS ERRORS

The major bias errors sources are distortions over the star tracker field due to nonorthogonality of axes, non-linear deflections and optical distortion, and deflection null and scale factor instabilities due to temperature and aging. All of these errors are proportional to the tracker FOV. Other fixed bias errors, such as boresight and spacecraft alignments are readily compensated either before launch or on-orbit. Field distortion is by far the most significant error source, requiring calibration and compensation. Based on experience by MIT with the SAS-C tracker and similar studies by TRW, the distortion compensation by means of software requires at least a ten coefficient polynomial for each axis. For SAS-C about 30 terms per axis are used to compensate for temperature as well. An additional twelve terms are required for magnetic field and star intensity variations. The TRW breadboard digital tracker indicates negligible (<2 arc sec.) magnetic sensitivity (due to better magnetic shielding) and intensity variations (by virtue of digital processing method).

Based on the TRW digital star tracker experience, the following bias error estimate is made. The distortion compensation is conservatively estimated to be 1:20, although the SAS-C experience to date indicates that at least 1:50 is realistic.

$$e_T = e_B^2 + e_{SF}^2 + e_{DC}^2 \quad (4)$$

$$e_B = K_B \text{ FOV} \quad (4A)$$

$$e_{SF} = K_{SF} \text{ FOV} \quad (4B)$$

$$e_{DC} = e_{DU}/20 = K_D \text{ FOV}/20 \quad (4C)$$



The relationship between required star tracker aperture,  $A_0$ , and track time constant,  $\Delta t$ , as a function of star magnitude,  $m$ , is shown in Figure 5-85a ( $5^\circ \times 5^\circ$  FOV) and Figure 5-85b ( $2^\circ \times 2^\circ$  FOV) for  $\sigma_\theta = 10$  arc sec. and  $K = 1$  (unity track loop gain). The relationship between IFOV and FOV is a complicated function of tube aperture, optics resolution and acquisition mode requirements and parameters. However, for these two fields a reasonable assumption has been made that  $\text{IFOV} = \text{FOV}/40$ .

## 2) RATE ERROR (DYNAMIC LAG)

$$\sigma_L = \left[ \left( \frac{4}{3K} - \frac{1}{2} \right)^2 + \frac{1}{12} \right] \dot{\theta}_s \Delta t \quad (3)$$

where,

$\sigma_L$  = uncompensated rate error, arc sec.  $1\sigma$

$\dot{\theta}_s$  = input rate, arc sec./sec.

For a known rate, as given by the attitude determination filter, the rate error may be compensated. However, the stability of the track loop gain,  $K$ , limits the accuracy of this compensation. For  $K = 1$  it is estimated that this uncertainty, or compensated rate error ( $\sigma_L'$ ), is about 10% of  $\sigma_L$ . Figure 5-86 shows both  $\sigma_L$  and  $\sigma_L'$  for low altitude ( $\sim 750$  km) and synchronous earth-pointing orbits.

$A_o$ ,  
APERTURE AREA  
( $\text{CM}^2$ )

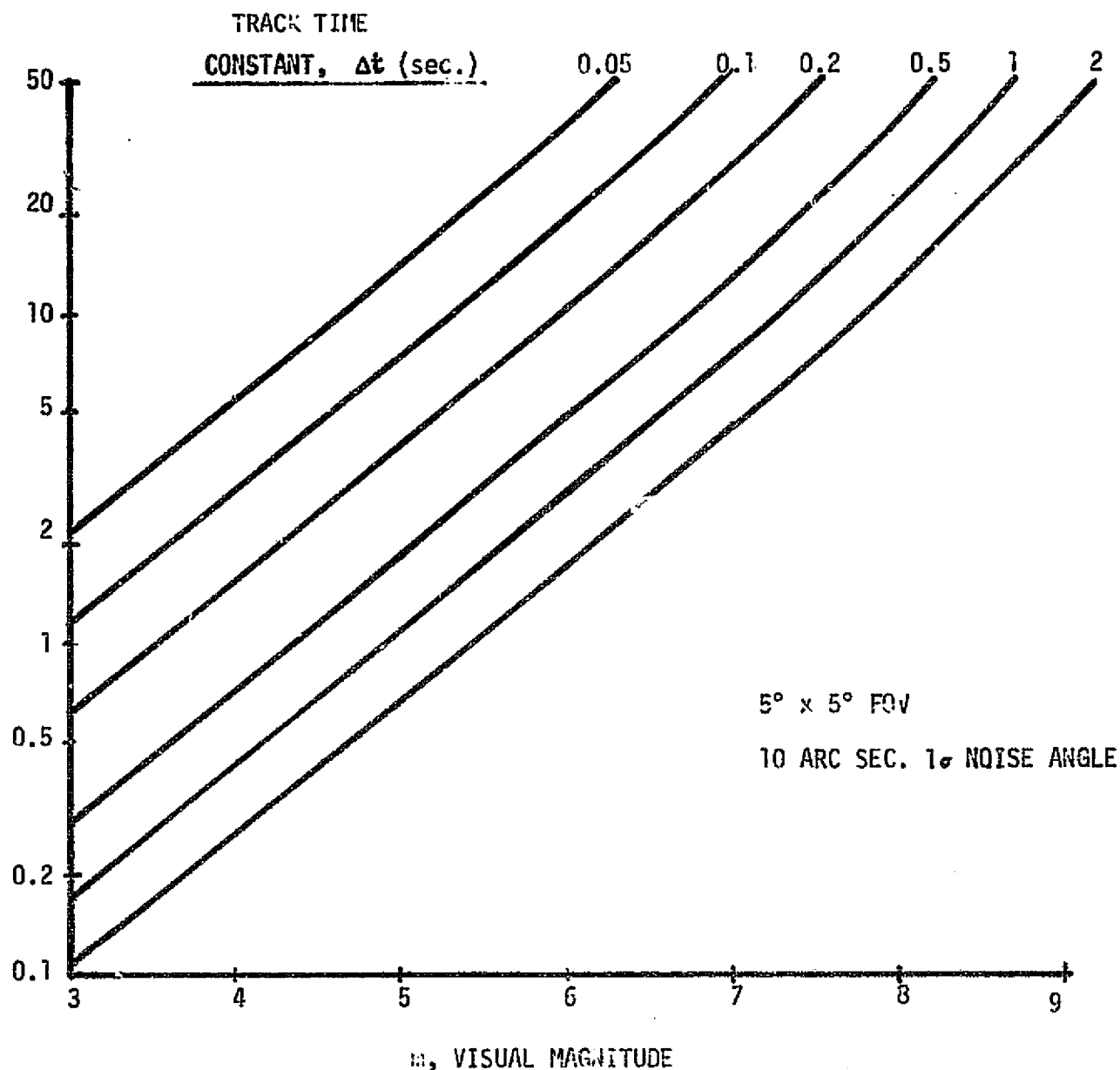


Figure 5-85a. Required Aperture and Track Time Constant as a Function of Sensitivity (5° x 5° Field)

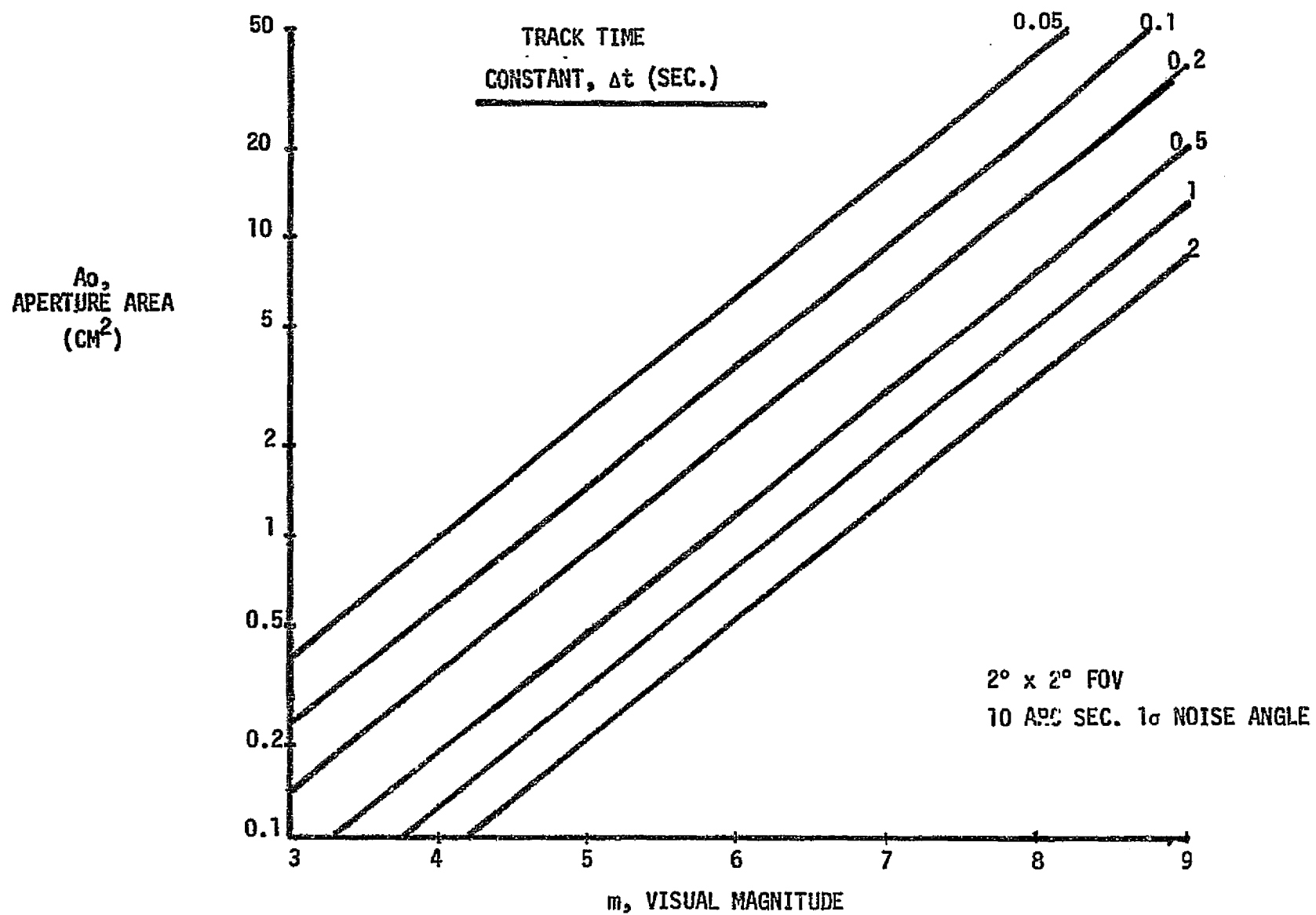


Figure 5-85b. Required Tracker Aperture and Track Time Constant as a Function of Sensitivity (2° x 2° Field)

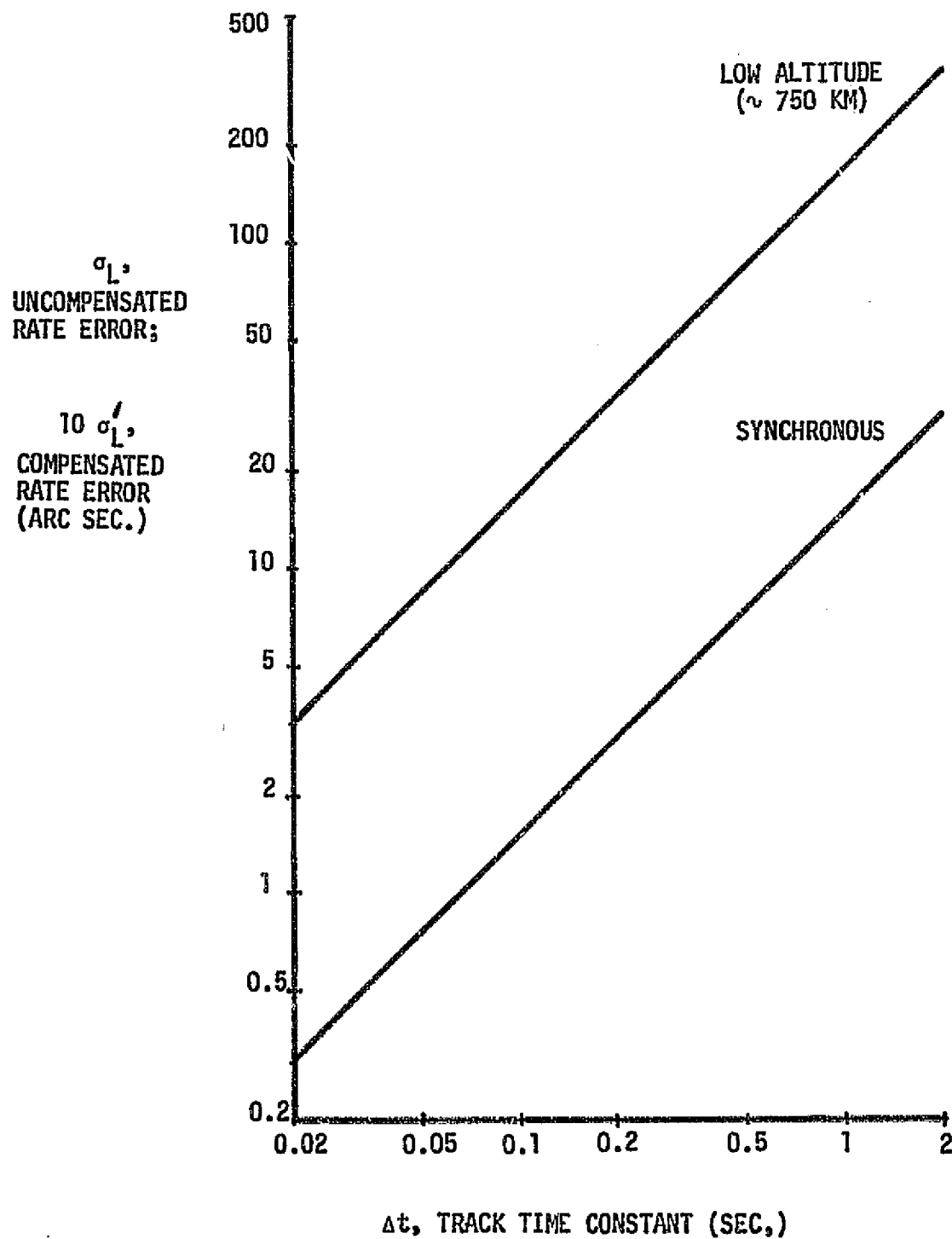


Figure 5-86. Tracker Rate Error (Uncompensated and Compensated) as a Function of Track Time Constant

where,

$e_T$  = total RSS bias uncertainty

$e_B$  = deflection bias error

$e_{SF}$  = deflection scale factor error

$e_{DC}$  = compensated distortion error

$e_{DU}$  = uncompensated field distortion

$K_B$  = deflection bias sensitivity  $\doteq 1.44$  arc sec./deg.

$K_{SF}$  = deflection scale factor sensitivity  $\doteq 0.72$  arc sec./deg.

$K_D$  = distortion sensitivity  $\doteq 24$  arc sec./deg.

The solution of equation (4) is shown in Figure 5-87 as a function of tracker overall field-of-view.

Using Figures 5-84 through -87 a digital star tracker design may be formulated. For an overall accuracy of 10 arc sec. the field-of-view should be limited to  $5^\circ$  or less (Figure 5-87). Two designs ( $5^\circ$  and  $2^\circ$  FOV) are summarized in Table 5-31 with the following constraints:

- 1) The stellar update period is at least ten minutes with a 95 percent probability of one or more stars per period.

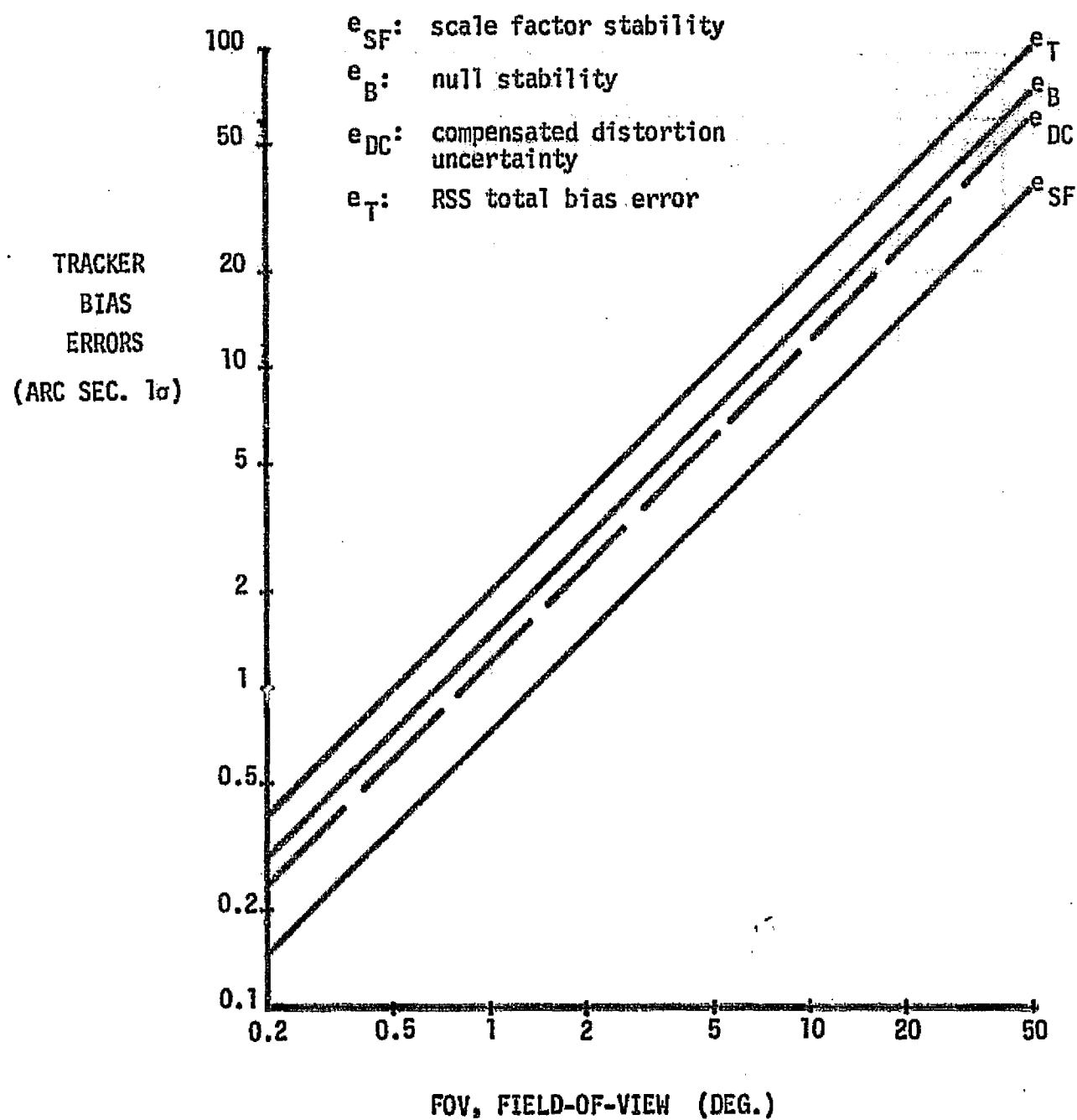


Figure 5-87. Tracker Distortion and Stability Uncertainty Variation with Field-of-View

Table 5-31. Alternate Star Tracker Design

REF. FIGURE		4		1	3	2
DESIGN	FOV (DEG. SQ.)	BIAS STABILITY (ARC SEC. $1\sigma$ )	MISSION MODE(1)	REQUIRED SENSITIVITY (VISUAL MAG)	MAX. TRACK TIME CONSTANT (SEC.)	MIN. APER- TURE AREA (cm <sup>2</sup> )
1	5	10	A	5	0.1	7.4
			B	7	1	7.5
			C	<7	> 1	<7.5
2	2	4	A	6	0.1	3.8
			B	8	1	5.1
			C	8	> 1	<5.1

(1) Mission Modes: Low altitude earth point (A); synchronous earth point (B); inertial point (C)

2) Tracker output noise is 10 arc sec. ( $1\sigma$ ), or less, with a track period (output bandwidth) limited by a compensated rate error of no more than 2 arc sec.

Based on this summary, Design 1 could be conservatively achieved using a 1.3 inch aperture (8.6 cm<sup>2</sup>), while Design 2 would meet all requirements with a 1.1 inch aperture. Therefore, a 1.3 inch (8.6 cm<sup>2</sup>) aperture is selected as the basis for the shade design.

The physical characteristics of the digital tracker include:

Size - 6 in. x 6 in. x 12 in.  
Weight - 12 lb.  
Power - 10 W

#### 5.2.3.5 Stray Light Shade Design

The shade attenuation required is assumed to be  $10^7$  or greater for all light sources greater than  $45^\circ$  from the star tracker optical axis. This is based on an estimated  $10^{10}$  total required attenuation of stray light by the shade and tracker for stars of  $5^m$  or dimmer, and the desire to limit the required tracker attenuation to  $10^3$ .

Shade attenuation factors of  $10^7$  are feasible in two-stage shades with careful design and production of baffle edges and inner surface coatings. Martin Marietta, for example, has developed special black coating and baffle processes that have achieved measured attenuations of  $10^8$  or more. A single-stage shade is not likely to achieve  $10^7$  attenuation except at stray light angles approaching  $90^\circ$ .

The criteria for a two-stage shade design are given in Figure 5-88, together with equations for overall length and width. The overall shade length is minimized by selection of the cone angle,  $\phi$ , of the outer baffle section by:

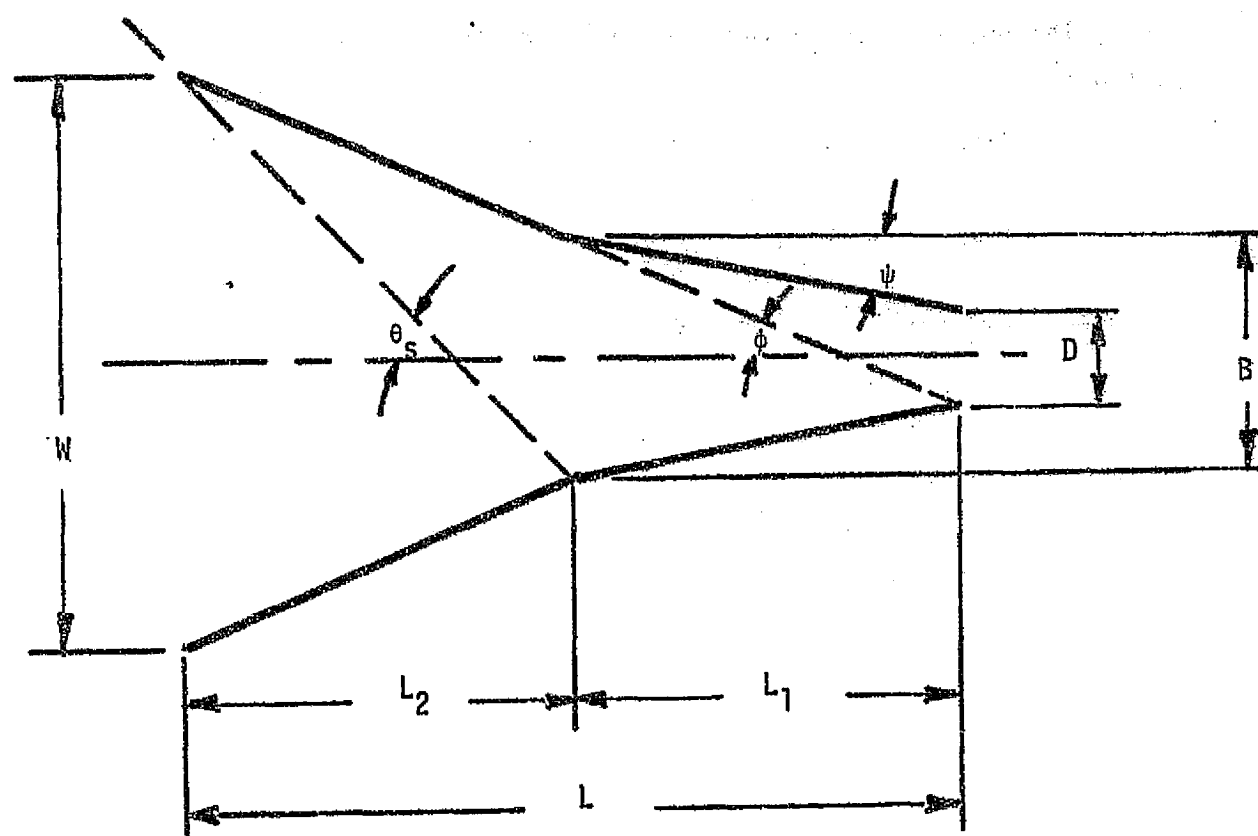
$$\tan \phi = 1/2 (\tan \theta_s + \tan \psi) \quad (5)$$

where,

$\theta_s$  = minimum sun angle

$\psi$  = FOV diagonal half-angle





#### DESIGN EQUATIONS

$D$  = Tracker Aperture Diameter  
 $B$  = Inner Baffle Width  
 $W$  = Outer Baffle Width  
 $L_1$  = Inner Baffle Length  
 $L_2$  = Outer Baffle Length  
 $L$  = Total Shade Length  
 $\theta_s$  = Minimum Sun Angle  
 $\phi$  = Outer Baffle Cone Angle  
 $\psi$  = 1/2 Field-of-View (Diagonal)

$$L_1 = \frac{D}{\tan \phi - \tan \psi}$$

$$L_2 = \frac{B}{\tan \theta_s - \tan \phi}$$

$$B = D + 2 L_1 \tan \psi$$

$$W = B + 2 L_2 \tan \phi$$

Figure 5-88. Light Shade Design Chart

For this choice of  $\phi$ , the shade length and baffle width are given by:

$$L = \frac{4 D (\tan \theta_s + \tan \psi)}{(\tan \theta_s - \tan \psi)^2} \quad (6A)$$

$$W = 3D + \frac{16 D \tan \theta_s \tan \psi}{(\tan \theta_s - \tan \psi)^2} \quad (6B)$$

where,

L = overall shade length

W = width of outer baffle aperture

D = star tracker aperture (shade exit diameter)

The relationships for  $\theta_s = 45^\circ$  are shown in Figure 6 for tracker FOV of  $5^\circ$  ( $\psi = 5\sqrt{2}/2$  deg.) and  $2^\circ$  ( $\psi = \sqrt{2}$  deg.), with the following allowances:

- 1) 20% is added to the outer baffle width (W) to allow for the baffles and outer shade structure.
- 2) 0.1 inch is added to the tracker aperture diameter to determine the shade exit diameter (D) with allowance for manufacturing and alignment tolerances.

From Figure 5-89, for  $5^\circ$  and  $2^\circ$  FOV with a 1.3 inch tracker aperture, and using equation (6) for the SAS-C tracker the required shade dimensions are determined, as summarized in Table 5-31a. Due to the large shade volume required for the SAS-C tracker, an alternate design is also shown that limits shade outside diameter by restricting that tracker's FOV to  $8^\circ$  diameter, rather than square, and decreasing the aperture to 3 inches, which decreases sensitivity by about  $0.3^m$ .

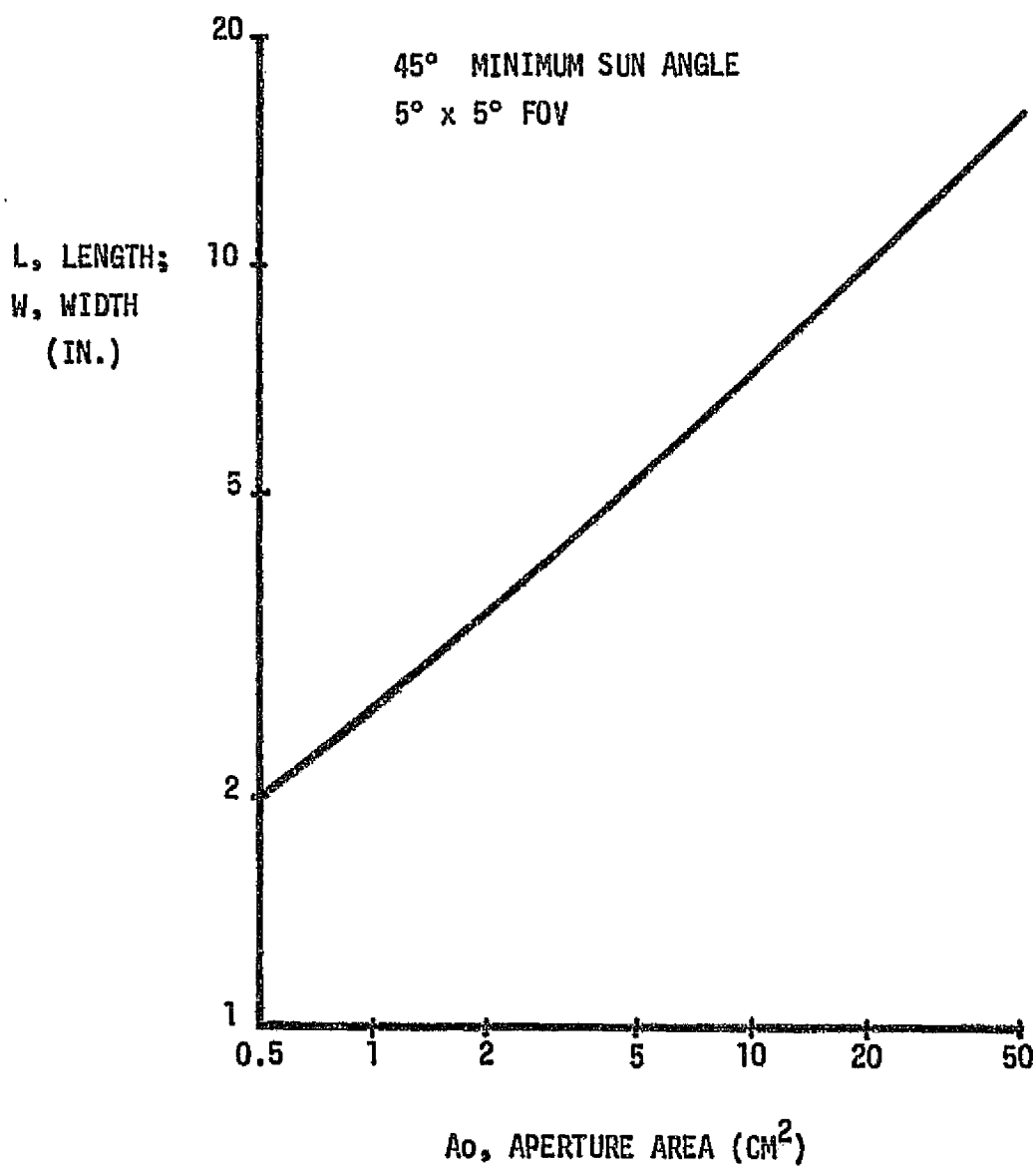


Figure 5-89a. Shade Limiting Size as a Function of Tracker Aperture (5° x 5° Field)

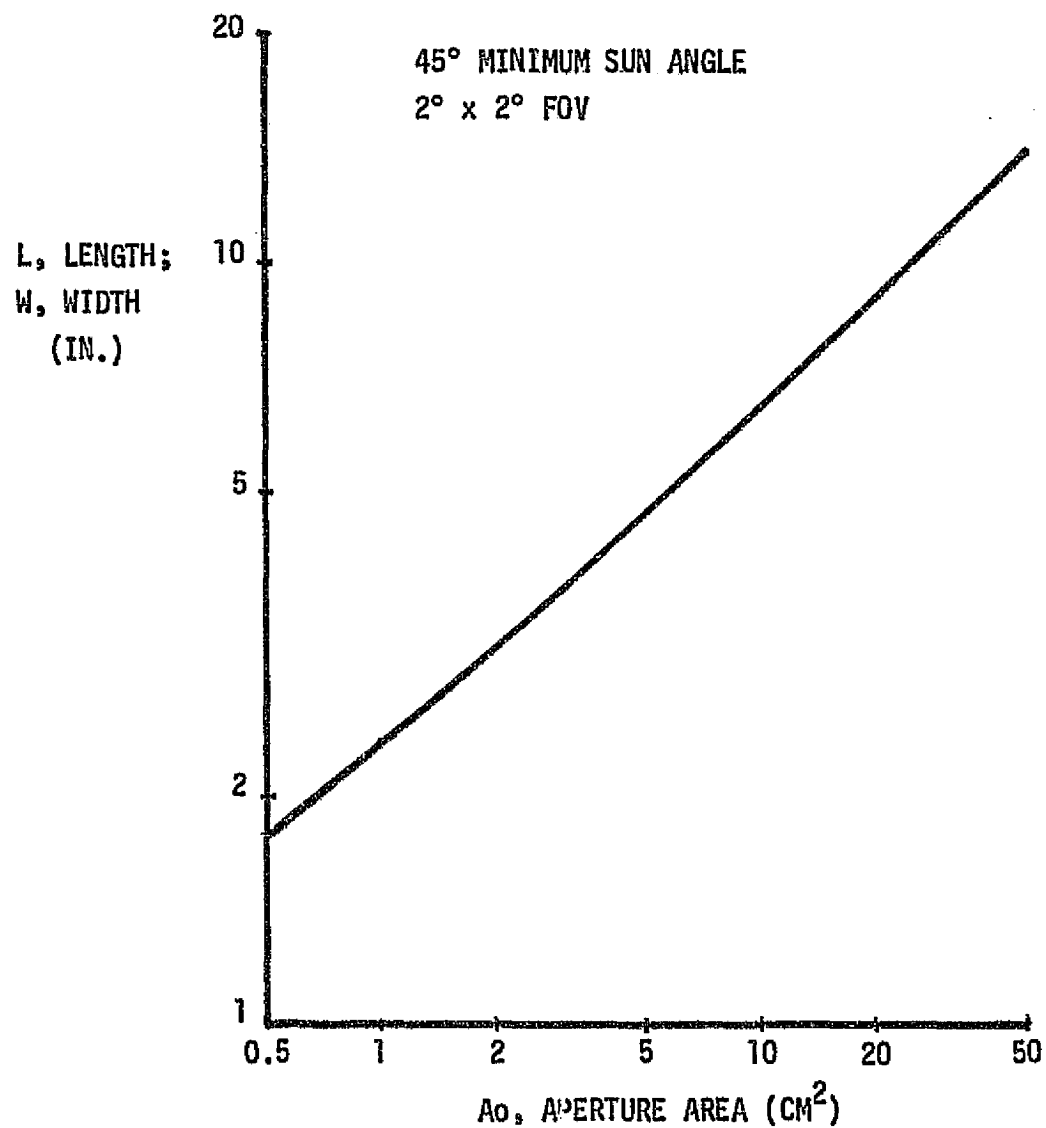


Figure 5-89b. Shade Limiting Size as a Function of Tracker Aperture (2° x 2° Field)

Table 5-31a. Shade Limiting Volume Summary

STAR TRACKER				SHADE	
TYPE	APERTURE DIAMETER (IN.)	APERTURE AREA (cm <sup>2</sup> )	FOV (DEG.)	LENGTH (IN.)	WIDTH (IN.)
BBRC SAS-C	3.44	60	8°	19.2	21.1
	3	45.6	8° (dia.)	20.7	10.6
TRW Digital	1.3	8.6	5°	6.8	7.0
	1.3	8.6	2°	6.1	5.8

#### 5.2.4 Actuation Module Design

##### 5.2.4.1 Perturbation and Dynamic Modeling

Modeling the EOS-A environmental and internal disturbance torques for Thor-Delta and Titan configurations, considering gravity gradient, solar pressure, magnetic moments, and aerodynamics. The effects of internal moving parts were identified. Reaction wheels and magnetic torquers were sized for disturbance models of several orbits and missions. Performance of the magnetic unloading law was evaluated.

###### 5.2.4.1.1 Motivation

The sizing of reaction wheels and magnetic torquers is dependent on disturbances experienced by the spacecraft and the selection of the proper actuation module size is directly related to the mission environment. The purpose of this task was to examine a range of spacecraft size and missions on a parametric basis to allow the selection of the "optimum" actuation module sizes consistent with their availability from an inventory of off-the-shelf hardware.

###### 5.2.4.1.2 Methodology

###### a. Environmental and System Models

The determination of environmental disturbance torques and the design of the momentum unloading control system were accomplished using a detailed digital computer simulation. The simulation modelled the spacecraft 3-axis rigid body dynamics and kinematics, the control system dynamics, the time-varying inertias (due to the rotating solar array paddle), the earth's magnetic field, and the solar, aero, gravity gradient, and magnetic disturbance torques as a function of orbit position and spacecraft orientation. The pertinent equations are provided in the following section.

Preliminary sizing for the Delta/Titan reaction wheels, magnets, and magnetic unloading gain was performed by assuming a simple proportionality input/output characteristic (no saturation) for the unloading magnetics and

then varying the unloading gain  $K_u$  over several orders of magnitude. In this manner, curves establishing requirements for total wheel momentum, wheel torque, and magnetic moment were generated. An "optimal" unloading gain was chosen to minimize the wheel momentum and magnetic torquer size. Having established the unloading design requirements, the effects of magnet saturation were studied and point designs were chosen for the nominal EOS-A missions.

Substantial design margin was assured by designing to worst case disturbances and vehicle orientation. Allowance was also made for potential growth in the spacecraft size, particularly, growth in the solar array paddle.

### 1. Rigid Body Dynamics and Kinematics

The total spacecraft momentum,  $\bar{H}$ , is the result of the reaction wheel momenta and the spacecraft body rates:

$$\bar{H} = \bar{I} \bar{\omega} + \bar{H}_W \quad (1)$$

where

$\bar{\omega} = (\omega_x, \omega_y, \omega_z)^T$  = the spacecraft angular rates about the roll, pitch, and yaw body axes

$\bar{H}_W = (H_{wx}, H_{wy}, H_{wz})^T$  = the reaction wheel momentum vector due to the three orthogonal reaction wheels

and

$$\bar{I} = \begin{bmatrix} I_{xx} & -I_{xy} & -I_{xz} \\ -I_{xy} & I_{yy} & -I_{yz} \\ -I_{xz} & -I_{yz} & I_{zz} \end{bmatrix} = \text{the spacecraft inertia tensor in body coordinates.}$$

From Euler's equations of motion, the rate of change of total momentum is related to the applied external torque  $\bar{T}$  by

$$\frac{d\bar{H}}{dt} = \bar{T} \quad (2)$$

or

$$\bar{I} \dot{\bar{\omega}} + \dot{\bar{H}}_W + \bar{\omega} \times [\bar{I} \bar{\omega}] - \bar{\omega} \times \bar{H}_W = \bar{T}_d + \bar{T}_M \quad (3)$$

where

$\bar{T}_d = (T_{dx}, T_{dy}, T_{dz})^T$  = the total disturbance torque vector about the spacecraft body axes.

$\bar{T}_M = \bar{M} \times \bar{B}$  = the magnetic unloading torque.

$\bar{M} = (M_x, M_y, M_z)^T$  = the magnetic moment vector in body coordinates.

and

$\bar{B} = (B_x, B_y, B_z)^T$  = the earth's magnetic field in body coordinates.

Note that Equation (3) neglects the term  $\dot{\bar{T}} \bar{\omega}$  which is a result of the rotating solar array paddle.

The spacecraft kinematics are expressed in terms of Euler symmetric parameters, or quaternions. The differential equation for the spacecraft kinematics, assuming a circular orbit, is given by

$$\begin{bmatrix} \dot{\xi} \\ \dot{\eta} \\ \dot{\zeta} \\ \dot{\chi} \end{bmatrix} = \frac{1}{2} \begin{bmatrix} 0 & \omega_z & -(\omega_y - \omega_0) & \omega_x \\ -\omega_z & 0 & \omega_x & \omega_y + \omega_0 \\ \omega_y - \omega_0 & -\omega_x & 0 & \omega_z \\ -\omega_x & -(\omega_y + \omega_0) & -\omega_z & 0 \end{bmatrix} \begin{bmatrix} \xi \\ \eta \\ \zeta \\ \chi \end{bmatrix} \quad (4-a)$$

where  $\omega_0$  is orbit rate.

The direction cosines for the transformation from orbital reference coordinates to spacecraft body coordinates are, in turn, related to the symmetric parameters by



$$a_{11} = \xi^2 - \eta^2 - \zeta^2 - \chi^2$$

$$a_{21} = 2(\xi\eta - \zeta\chi)$$

$$a_{31} = 2(\xi\eta + \eta\chi)$$

$$a_{12} = 2(\xi\eta + \eta\chi)$$

$$a_{22} = -\xi^2 + \eta^2 - \zeta^2 + \chi^2$$

(4-b)

$$a_{32} = 2(\eta\zeta - \xi\chi)$$

$$a_{13} = 2(\xi\zeta - \eta\chi)$$

$$a_{23} = 2(\xi\chi + \eta\zeta)$$

$$a_{33} = -\xi^2 - \eta^2 + \zeta^2 + \chi^2$$

The orbital reference coordinate system is defined in the usual way, namely,  $\hat{x}_r$  is in the direction of the spacecraft velocity vector,  $\hat{z}_r$  points at the geo-center, and  $\hat{y}_r$  completes the right handed coordinate set.

## 2. Magnetic and Attitude Control System Models

Figure 5-92 provides block diagrams of the momentum unloading and attitude control systems as implemented in the EOS simulation. The TRW proposed magnetic control law is given by

$$\bar{M} = \frac{K_u}{B_0^2} H_w \times \bar{B} \quad (5)$$

where  $B_0$  = the minimum earth's magnetic field. The above control law generates a magnetic moment vector  $\bar{M}$  proportional to the stored wheel momenta.  $\bar{M}$ , in turn, interacts with the earth's magnetic field to produce torques to reduce wheel speed.

The attitude control system in Figure 5-92 is similar, but not identical to the proposed EOS control system. Its purpose in the simulation was merely to provide control dynamics. Hence, gains were chosen only to produce stable pointing and no effort was made, in this part of the study, to verify pointing accuracy.

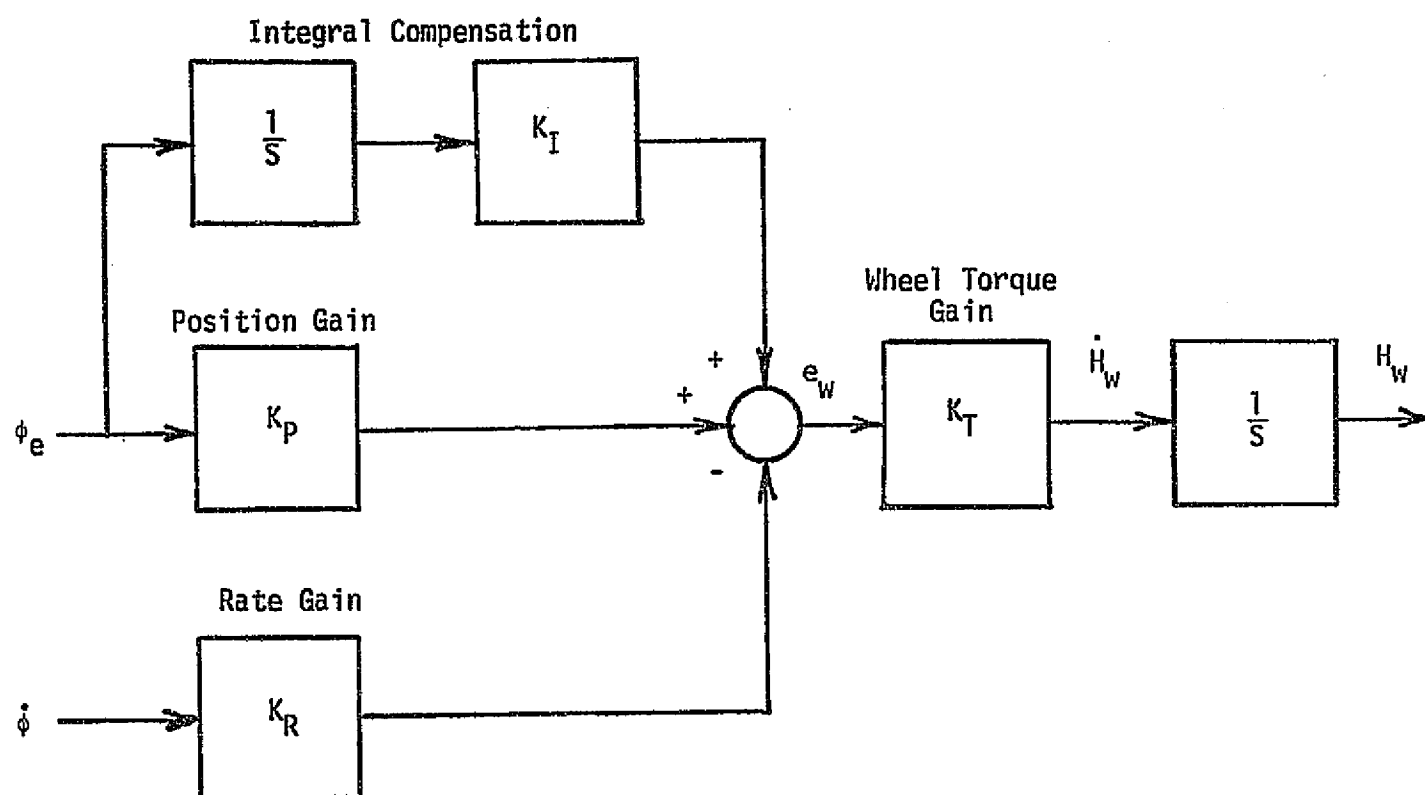


Figure 5-92a. Generic Attitude Control System  
Used In Disturbance Torque/  
Magnetic Unloading Simulation

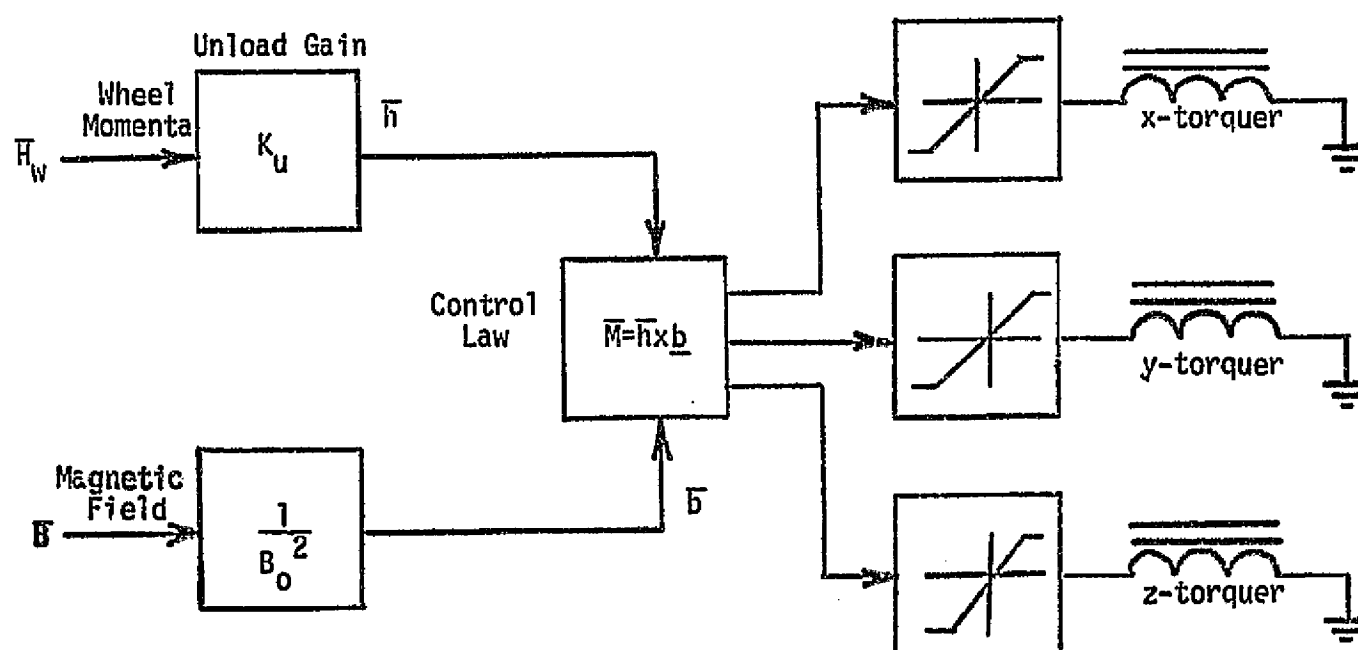


Figure 5-92b. Magnetic Unloading Control System

### 3. Magnetic Field Model

The Earth's magnetic field in orbit reference coordinates is given by

$$\begin{bmatrix} B_{ex} \\ B_{ey} \\ B_{ez} \end{bmatrix} = \left( \frac{-M_e}{R_0^3} \right) \begin{bmatrix} -\cos \alpha \sin i \cos \epsilon - \frac{1}{2} \sin \epsilon [-(1+\cos i) \cos(\alpha - \mu') + (1 - \cos i) \cos(\alpha + \mu')] \\ \cos i \cos \epsilon + \sin i \sin \epsilon \cos \mu' \\ -2 \sin \alpha \sin i \cos \epsilon - \sin \epsilon [-(1+\cos i) \sin(\alpha - \mu') + (1 - \cos i) \sin(\alpha + \mu')] \end{bmatrix} \quad (6)$$

where  $M_e = 2.845 \times 10^{21}$  gauss/ft<sup>3</sup>

$R_0$  - radius from center of Earth to spacecraft c.g.

$i$  - orbit plane inclination

$\epsilon$  - tilt of magnetic dipole (11.0 deg nominal)

$\alpha$  - angular displacement of spacecraft from ascending line of nodes

$\mu' = (\alpha_e + \Delta - \Omega)$

$\alpha$  - angular displacement of prime meridian from the vernal equinox (time of day)

$\Delta$  - angular displacement of magnetic X-axis measured at the equator (20.0 deg nominal)

$\Omega$  - displacement of ascending line of nodes from the vernal equinox

Finally, the time of day is given by

$$\alpha_e = \omega_e t + \alpha_{e0} \quad (7)$$

where  $\alpha_{e0}$  - initial time of day for  $t=0$   
(0. rad nominal)

$\omega_e$  - earth's rotational rate  
(0.00416667 rad/sec = 15 deg/hr)

Note that the spacecraft magnetometers were assumed to be ideal and with no dynamics.

#### 4. Environmental Disturbance Torques

In this section, the necessary equations are presented for the computation of the environmental disturbance torques ( $\bar{T}_d$  of Equation 1). The environmental disturbance torque is given by

$$\bar{T}_d = \bar{T}_s + \bar{T}_a + \bar{T}_g + \bar{T}_M \quad (8)$$

where

$\bar{T}_s$  = the disturbance torque due to solar pressure

$\bar{T}_a$  = the disturbance torque due to aerodynamic pressure

$\bar{T}_g$  = the gravity gradient disturbance torque

$\bar{T}_M$  = the magnetic disturbance torque due to the residual magnetism of the spacecraft.

##### Solar Torque Model

The general approach taken in developing the solar torque (and aero disturbance) model was to decompose the spacecraft into surfaces that could be easily modelled as plates and cylinders. The torque about the spacecraft center of mass for each surface was computed, and then all the torque contributions were summed to obtain the total solar disturbance torque acting on the spacecraft.

The primary assumptions that were made in the development of the solar disturbance torque model are as follows:

- 1.) All reflectivity is specular
- 2.) The reflectivity of all surfaces covered with solar cells is 0.2 while the reflectivity of all other surfaces is 0.5.
- 3.) The reflectivity is uniform over any given surface
- 4.) The normal and tangential reflectivity  $v_t$  and  $v_n$  are assumed to be equal
- 5.) The solar pressure coefficient  $V_s$  ( $9.4 \times 10^{-8}$  lbs/ft<sup>2</sup>) is spatially constant and time invariant.

In addition to these assumptions, the effects of shading and reflections between spacecraft surfaces were not considered.

The equations for solar forces and moments on individual plate surfaces are

$$\begin{aligned} \bar{F}_p &= \begin{cases} V_s A \cos \eta_p \left[ (1-v_t) \underline{\delta}_s + (v_n+v_t) \cos \eta_p \underline{n}_p \right] & \text{for } \cos \eta_p > 0 \\ 0 & \text{for } \cos \eta_p \leq 0 \end{cases} \\ \bar{M}_p &= 0 \end{aligned} \quad (9)$$

The equations for the cylindrical surfaces are

$$\begin{aligned} \bar{F}_c &= \frac{V_s}{3} LD \sin \eta_c \left[ \left( \frac{3}{2} + v_n - \frac{1}{2} v_t \right) \underline{\delta}_s - (v_n+v_t) \cos \eta_p \underline{\delta}_c \right] \\ \bar{M}_c &= \frac{\pi}{8} V_s LD^2 (1-v_t) \cos \eta_c (\underline{\delta}_s \times \underline{\delta}_c) \end{aligned} \quad (10)$$

where

$V_s$  - solar pressure constant ( $9.4 \times 10^{-8}$  lbs/ft<sup>2</sup>)

$A$  - surface area (ft<sup>2</sup>)

$\eta_p$  - angle between inward surface normal and photon flow ( $\underline{n}_p \cdot \underline{\delta}_F$ )

$v_t$  - tangential reflectivity

$v_n$  - normal reflectivity

$\underline{n}_p$  - inward pointing normal to the surface

$\underline{\delta}_s$  - unit flow vector from the sun

$L$  - cylinder height

$D$  - cylinder diameter

$\eta_c$  - angle between cylinder axis and photon stream ( $\underline{\delta}_c \cdot \underline{\delta}_F$ )

$\underline{\delta}_c$  - unit vector denoting cylinder axis.

The disturbance torque on the spacecraft is the sum of the torques produced by the force and moments on each surface

$$\bar{T}_S = \sum_{i=1}^N (\bar{R}_i \times \bar{F}_i + \bar{M}_i) \quad (11)$$

where

$N$  = the total number of surfaces composing the spacecraft surface area

$\bar{R}_i = \bar{R}_{ci} - \bar{R}_{cm}$

$\bar{R}_{ci}$  = the location of the  $i$ th centroid in body coordinates

$\bar{R}_{cm}$  = the location of the center of mass in body coordinates

The surface models for the nominal Titan III-D and Thor-Delta spacecrafts are given in Tables 5-32 and 5-33.

#### Aerodynamic Disturbances

The equations for the aerodynamic forces and moments on individual plates and cylinders are given in equations 12 and 13, respectively:

$$\bar{F}_p = \begin{cases} 2q A \cos \eta_p [ f_T \bar{\delta}_F + (2-f_N-f_T) \cos \eta_p \bar{n}_p ] & \text{for } \cos \eta_p > 0 \\ 0 & \text{for } \cos \eta_p \leq 0 \end{cases} \quad (12)$$

$$\bar{M}_p = 0$$

$$\bar{F}_c = \frac{2}{3} qLD \sin \eta_c [ (2 + \frac{f_N}{2} - f_T) \bar{\delta}_F - 2(2-f_N-f_T) \cos \eta_c \bar{\delta}_c ] \quad (13)$$

$$\bar{M}_c = \frac{\pi}{4} qLD^2 f_T \cos \eta_c (\bar{\delta}_F \times \bar{\delta}_c)$$

where

$q$  - dynamic pressure ( $\frac{1}{2} \rho v^2$ )

$A$  - surface area

$\eta_p$  - angle between inward surface normal and particle flow ( $\bar{n}_p \cdot \bar{\delta}_F$ )

$f_T$  - tangential accommodation coefficient

$f_N$  - normal accommodation coefficient

$\bar{n}_p$  - inward facing normal to surface area

Table 5-32. Surface Model Titan III-D Configuration

Surface	No.	Arca (In <sup>2</sup> )		R <sub>c</sub> (In.)			$\bar{n}_p$			u <sub>no</sub>	f <sub>N</sub>
				R <sub>cx</sub>	R <sub>cy</sub>	R <sub>cz</sub>	$\bar{n}_{px}$	$\bar{n}_{py}$	$\bar{n}_{pz}$		
End Plate (+x <sub>b</sub> )	1	4791		115.12	0	0	-1	0	0	.5	.85
Forward (+y <sub>b</sub> ) Plate	2	6562		52.62	45.62	0	0	-1	0	.5	.85
Forward (-y <sub>b</sub> ) Plate	3	6562		52.62	-45.62	0	0	1	0	.5	.85
Forward (+z <sub>b</sub> ) Plate	4	11406		52.62	0	26.25	0	0	-1	.5	.85
Forward (-z <sub>b</sub> ) Plate	5	11406		52.62	0	-26.25	0	0	1	.5	.85
End Plate (-x <sub>b</sub> )	6	3025		-95.50	0	0	1	0	0	.5	.85
Back (+y <sub>b</sub> ) Plate	7	1650		-80.50	27.50	0	0	-1	0	.5	.85
Back (-y <sub>b</sub> ) Plate	8	1650		-80.50	-27.50	0	0	1	0	.5	.85
Back (+z <sub>b</sub> ) Plate	9	1650		-80.50	0	27.50	0	0	-1	.5	.85
Back (-z <sub>b</sub> ) Plate	10	1650		-80.50	0	-27.50	0	0	1	.5	.85
Forward Cyl. Plate	11	4286		-9.88	0	0	-1	0	0	.5	.85
Back Cyl. End Plate	12	6051		-65.50	0	0	1	0	0	.5	.85
Solar Array (Front)	13	23328		*	*	*	*	*	*	.2	.85
Solar Array (Back)	14	23328		*	*	*	**	**	**	.5	.85
+y Antenna (Front)	15	240		228.37	31.25	83.75	0	0	+1	.5	.85
-y Antenna (Front)	16	240		228.37	-31.25	83.75	0	0	+1	.5	.85
+y Antenna (Back)	17	240		228.37	31.25	83.75	0	0	-1	.5	.85
-y Antenna (Back)	18	240		228.37	-31.25	83.75	0	0	-1	.5	.85
Cylinders		Dia.	Length								
Central Cylinder	18	107.5	55.62	-37.69	0	0	1.0	0	0	.5	.85

$$* \quad R_c(13) = (.33 - 123 \sin \theta_A \sin \phi_A, -40 - 123 \cos \phi_A, -33.75 - 123 \sin \phi_A \cos \theta_A)^T$$

$$\bar{n}_p(13) = (\sin \theta_A \cos \phi_A, -\sin \phi_A, \cos \theta_A \cos \phi_A)^T; \text{ where } \phi_A = \text{orbit declination (earth pointed missions)}$$

$$\text{and } \theta_A = \omega_0 t + \alpha_0$$

$$** \quad \bar{n}_p(14) = -\bar{n}_p(13)$$

Table 5-33. Surface Model Thor-Delta Configuration

Surface	No.	Area (In <sup>2</sup> )		$R_c$ (In.)			$\eta_p$			$u_{NO}$	$f_H$
				$R_{cx}$	$R_{cy}$	$R_{cz}$	$\eta_{px}$	$\eta_{py}$	$\eta_{pz}$		
Top Plate ( $-z_b$ )	1	5724		36.25	0	-26.25	0	0	1	.5	.85
Bottom Plate ( $+z_b$ )	2	6128		36.25	0	16.25	0	0	-1	.5	.85
Side Plate ( $+y_b$ )	3	3952		36.25	64.06	5.00	0	-.996	.087	.5	.85
Side Plate ( $-y_b$ )	4	3952		36.25	-64.06	5.00	0	.996	.087	.5	.85
End Plate ( $+x_b$ )	5	2723		82.50	0	-4.38	-1	0	0	.5	.85
Trans. Ring Plate	6	2623		-10.	0	0	-1	0	0	.5	.85
Att. Mod. End Plate	7	2827		-81.	0	0	1	0	0	.5	.85
Att. Control Mod. Plate	8	2518		-62.5	0	0	1	0	0	.5	.85
Solar Array (Front)	9	23328		*	*	*	*	*	*	.2	.85
Solar Array (Back)	10	23328		*	*	*	*	*	*	.5	.85
Antenna (+y) Front	11	240		109.	67.5	25.	0	0	-1	.5	.85
Antenna (-y) Front	12	240		109.	-15.	25.	0	0	-1	.5	.85
Antenna (+y) Back	13	240		109.	67.5	25.	0	0	1	.5	.85
Antenna (-y) Back	14	240		109.	-15.	25.	0	0	1	.5	.85
Cylinders		Dia.	Length								
Att. Control Mod.	15	82.5	52.5	-36.25	0	0	1	0	0	.5	.85
Actuation Mod.	16	30.	18.75	-81.	0	0	1	0	0	.5	.85

$$* \quad R_c(9) = (-6.12 - 90 \sin \theta_A \sin \phi_A, -70. - 90 \cos \phi_A, -26.25 - 90 \sin \phi_A \cos \theta_A)^T$$

$$\eta_p(9) = (\sin \theta_A \cos \phi_A, -\sin \phi_A, \cos \theta_A \cos \phi_A)^T; \text{ where } \phi_A = \text{orbit declination (earth pointed missions)} \\ \text{and } \theta_A = \omega_0 t + \alpha$$

$$** \quad \eta_p(10) = -\eta_p(9)$$



$\bar{\delta}_F$  - unit flow vector

L - cylinder height

D - cylinder diameter

$\eta_c$  - angle between cylinder axis and particle stream ( $\bar{\delta}_c \cdot \bar{\delta}_F$ )

$\bar{\delta}_c$  - unit vector denoting cylinder axis

The total aerodynamic disturbance is therefore given by

$$\bar{T}_a = \sum_{i=1}^N (\bar{R}_i \times \bar{F}_i + \bar{M}_i) \quad (14)$$

where

$$\bar{R}_i = \bar{R}_{ci} - \bar{R}_{cM}$$

$\bar{R}_{ci}$  = the location of the  $i$ th centroid in body coordinates

$\bar{R}_{cM}$  = the location of the center of mass in body coordinates

The aerodynamic pressure is the most uncertainty in the disturbance torque model. It is directly related to the atmospheric density,  $\rho$ , by the following equation

$$\begin{aligned} q &= \frac{1}{2} \rho V^2 \\ &= \frac{1}{2} \frac{\mu}{R_0 + h} \rho \end{aligned} \quad (15)$$

where

$\mu$  - gravitational constant ( $1.407 \times 10^{16}$  ft<sup>3</sup>/sec<sup>2</sup>)

$R_0$  - radius of the earth

h - spacecraft altitude

The density varies considerably with orbit position (diurnal), solar and magnetic activity. As a conservative estimate for  $\rho$ , peak values were chosen for the various altitudes considered over the period from March 21, 1978 to March 21, 1983. The resulting aerodynamic pressures are presented in Table 5-34.

Table 5-34. Aerodynamic Pressure

	Altitude (N.M.)			
	300	316	386	500
Aerodynamic Pressure (lb/ft <sup>2</sup> )	$1.0 \times 10^{-6}$	$8.09 \times 10^{-7}$	$1.45 \times 10^{-7}$	0.0

The aerodynamic surface models for the Titan III-D and Thor-Delta spacecrafts are essentially the same as those given for solar pressure, Tables 5-32 and 5-33. The accommodation coefficients  $f_N$  and  $f_T$  were assumed to have a common value of 0.85.

### Gravity Gradient Torques

The gravity gradient torques acting on the spacecraft are

$$\begin{aligned}
 T_{gx} &= 3 \omega_0^2 \left\{ (I_{zz} - I_{yy}) a_{23} a_{33} + I_{xy} a_{13} a_{33} \right. \\
 &\quad \left. - I_{xy} a_{13} a_{23} - I_{yz} (a_{23}^2 - a_{33}^2) \right\} \\
 T_{gy} &= 3 \omega_0^2 \left\{ (I_{xx} - I_{zz}) a_{13} a_{33} + I_{xy} (a_{13}^2 - a_{33}^2) \right. \\
 &\quad \left. + I_{yz} a_{13} a_{23} - I_{xy} a_{23} a_{33} \right\} \\
 T_{gz} &= 3 \omega_0^2 \left\{ (I_{yy} - I_{xx}) a_{13} a_{23} + I_{xy} (a_{23}^2 - a_{13}^2) \right. \\
 &\quad \left. + I_{xz} a_{23} a_{33} - I_{yz} a_{13} a_{33} \right\}
 \end{aligned} \tag{16}$$

where

$\omega_0$  = orbit rate

$\underline{a} = (a_{13}, a_{23}, a_{33})^T$  = gravity gradient vector in body coordinates

$I_{xx}, I_{yy}, \dots, I_{yz}$  = the moments and products of inertia.

If the differences between the principle moments of inertia are neglected, the above equations may be approximated by

$$\begin{aligned}
 T_{gx} &\cong c_x a_{23} a_{33} \\
 T_{gy} &\cong c_y a_{13} a_{33} \\
 T_{gz} &\cong c_z a_{13} a_{23}
 \end{aligned} \tag{17}$$

where

$$c_x \triangleq 3 \omega_0^2 (I_{zz} - I_{yy})$$

$$c_y \triangleq 3 \omega_0^2 (I_{xx} - I_{zz})$$

$$c_z \triangleq 3 \omega_0^2 (I_{yy} - I_{xx})$$

For a "worst case" pointing attitude we wish to maximize

$$T^2 = T_{gx}^2 + T_{gy}^2 + T_{gz}^2 \quad (18)$$

S.T.C.

$$a_{13}^2 + a_{23}^2 + a_{33}^2 = 1.0$$

$$-a_{13}^2 \leq 0$$

$$-a_{23}^2 \leq 0$$

$$-a_{33}^2 \leq 0$$

Define

$$L = T^2 = c_x^2 a_{23}^2 a_{33}^2 + c_y^2 a_{13}^2 a_{33}^2 + c_z^2 a_{13}^2 a_{23}^2 \quad (19)$$

S.T.C.

$$f_1 = a_{13}^2 + a_{23}^2 + a_{33}^2 - 1 = 0$$

$$f_2 = -a_{13}^2 \leq 0$$

$$f_3 = -a_{23}^2 \leq 0$$

$$f_4 = -a_{33}^2 \leq 0$$

Now

$$H \triangleq L + \sum \lambda_i f_i \quad (20)$$

where

$$\lambda_i \leq 0 \text{ and } \lambda_i = \begin{cases} 0 & f_i(a) = 0 \\ 0 & f_i(a) < 0 \end{cases} \quad i = 2, 3, 4$$

For a maximum the necessary conditions are

$$\frac{\partial H}{\partial a} = \frac{\partial L}{\partial a} + \sum \lambda_i \frac{\partial f_i}{\partial a} = 0 \quad (21)$$

$$= \begin{bmatrix} 2 c_y^2 a_{13} a_{33}^2 + 2 c_z^2 a_{13} a_{23}^2 + 2 \lambda_1 a_{13} - 2 \lambda_2 a_{13} \\ 2 c_x^2 a_{23} a_{33}^2 + 2 c_z^2 a_{13}^2 a_{23} + 2 \lambda_1 a_{23} - 2 \lambda_3 a_{23} \\ 2 c_x^2 a_{23}^2 a_{33} + 2 c_y^2 a_{13}^2 a_{33} + 2 \lambda_1 a_{33} - 2 \lambda_4 a_{33} \end{bmatrix} = \underline{0} \quad (21)$$

$$= \begin{bmatrix} c_y^2 a_{33}^2 + c_z^2 a_{23}^2 + \lambda_1 - \lambda_2 \\ c_x^2 a_{33}^2 + c_z^2 a_{13}^2 + \lambda_1 - \lambda_3 \\ c_x^2 a_{23}^2 + c_y^2 a_{13}^2 + \lambda_1 - \lambda_4 \end{bmatrix} \quad (22)$$

and  $\underline{f(a)} \leq 0$ .

Inspection of the constraint equations can yield considerable insight into the problem. First, the constraint  $f_1 = 0$  is simply the orthogonality condition. It represents a hard constraint and must therefore be included in all cases considered. However, any of the constraints,  $f_2$ ,  $f_3$ , or  $f_4$ , are included in the problem only if the constraint is imposed, because  $\lambda_i = 0$  otherwise ( $i = 2, 3, 4$ ). If any of the constraints  $f_2$ ,  $f_3$ , or  $f_4$  are in effect, they correspond to the conditions  $a_{13} = 0$ ,  $a_{23} = 0$  or  $a_{33} = 0$ , respectively. The optimum solution may therefore be determined by considering all combinations of the constraint equations.

The optimum solution is realized for  $a_{23}^2 = 0$ ,  $a_{13}^2 = a_{23}^2 = 0.5$ , which corresponds to a 45 deg rotation about the pitch axis with the x-z body plane containing the gravity gradient vector. By imposing the constraint  $f_2 = -a_{23}^2 = 0$  the worst case pointing attitude is evaluated through solution of the set of equations

$$\begin{bmatrix} c_y^2 & 0 & 1 \\ 0 & c_y^2 & 1 \\ 1 & 1 & 0 \end{bmatrix} \begin{bmatrix} a_{13}^2 \\ a_{33}^2 \\ \lambda_1 \end{bmatrix} = \begin{bmatrix} 0 \\ 0 \\ 1 \end{bmatrix} \quad (23)$$

It should be noted, that if analysis proves that the residual magnetism is moderate, then the magnetic torquers could possibly be used to bias out the residual effects.

#### Magnetic Disturbance Torque

Disturbance torques will result when the earth's magnetic field interacts with the spacecraft residual magnetic moments. The sources of these magnetic moments include the on-board experiments, residual magnetism in the magnetic torquers, and current loops in the solar array paddle and spacecraft electronics.

If  $\bar{M}_R = (M_{Rx}, M_{Ry}, M_{Rz})^T$  is the spacecraft residual magnetic moment vector, then the torque is simply

$$\bar{T}_M = \bar{M}_R \times \bar{B} \quad (24)$$

No analysis of the EOS spacecraft residual magnetism has been performed at this time. Hence, the estimate of residual magnetic moment was based upon empirical data from SATS. The magnetic moments for the various EOS spacecrafts were extrapolated on the basis of spacecraft weight. For SATS, a magnetic moment to weight ratio of about .667 pole - cm/lb was determined. A ratio of 1 pole-cm/lb was chosen to guarantee conservatism.

For the Titan III-D, the total weight is

$$\begin{aligned} W_S &= \text{wt of main body} + \text{wt}_0 \text{ of array} \\ &= 5360 + 90 \\ &= 5450 \text{ lb} \end{aligned}$$

Hence,

$$M_x = M_y = M_z \approx 5450 \text{ pole-cm}$$

The residual magnetism in the 100,000 pole-cm magnetic has been estimated to be less than 688 pole-cm. Hence, an additional 1000 pole-cm was lumped into residual magnetic moment yielding, what should be a very conservative estimate of spacecraft magnetic moment, namely

$$M_{xR} = M_{yR} = M_{zR} = 6500 \text{ pole-cm}$$

Similarly, the Thor-Delta residual magnetic moment was estimated at

$$M_{xR} = M_{yR} = M_{zR} = 3200 \text{ pole-cm}$$

### 5. Mass Properties

The spacecraft mass properties geometry is depicted in Figure 5-93. The coordinate sets  $(x_b, y_b, z_b)$  and  $(x_a, y_a, z_a)$  are located at the center of mass of the spacecraft main body and solar array, respectively. The coordinate set  $(xT, yT, zT)$  has its axes parallel to the body coordinate set and its origin at the total spacecraft (body + array) center of mass. The  $(xT, yT, zT)$  coordinate set, obviously not to scale, has been depicted in the position shown for clarity. The main body coordinate set  $(x_b, y_b, z_b)$  was chosen as the spacecraft body reference coordinate system used throughout this part of the study.

The appropriate equations for the spacecraft mass properties about the center of mass are

$$\begin{aligned} I_{xT} &= I_{x1} + I'_{x2} + M_1 (r_{12}^2 + r_{13}^2) + M_2 (r_{22}^2 + r_{23}^2) \\ I_{yT} &= I_{y1} + I'_{y2} + M_1 (r_{11}^2 + r_{13}^2) + M_2 (r_{21}^2 + r_{22}^2) \\ I_{zT} &= I_{z1} + I'_{z2} + M_1 (r_{11}^2 + r_{12}^2) + M_2 (r_{21}^2 + r_{22}^2) \quad (25) \\ P_{xyT} &= P_{xy1} + P'_{xy2} + M_1 r_{11} r_{12} + M_2 r_{21} r_{22} \\ P_{xzT} &= P_{xz1} + P'_{xz2} + M_1 r_{11} r_{13} + M_2 r_{21} r_{23} \\ P_{yzT} &= P_{yz1} + P'_{yz2} + M_1 r_{12} r_{13} + M_2 r_{22} r_{23} \end{aligned}$$

where

$$I'_2 = A^T I_2 A$$

$$\bar{r}_1 = - \frac{M_2}{M_1 + M_2} \bar{R}_{cp}$$

$$\bar{r}_2 = \frac{M_1}{M_1 + M_2} \bar{R}_{cp}$$

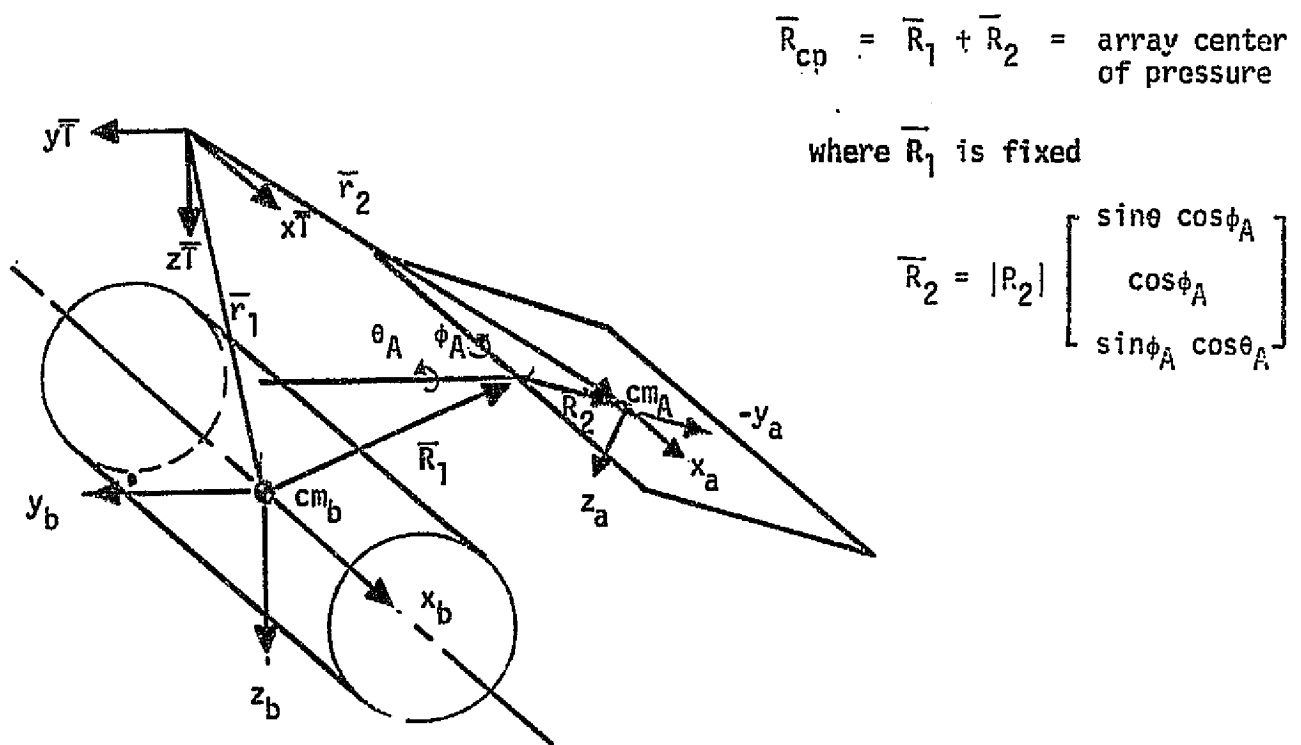


Figure 6-93. Mass Properties Geometry



$$A = \begin{bmatrix} \cos\theta_A & 0 & -\sin\theta_A \\ \sin\theta_A \cos\phi_A & \cos\phi_A & \sin\phi_A \cos\theta_A \\ \sin\theta_A \sin\phi_A & -\sin\phi_A & \cos\phi_A \cos\theta_A \end{bmatrix} = \text{transformation from main body to array coordinates}$$

$$I_1 = \begin{bmatrix} I_{x1} & 0 & 0 \\ 0 & I_{y1} & 0 \\ 0 & 0 & I_{z1} \end{bmatrix} = \text{spacecraft main body inertias (body coordinates)}$$

$$I_2 = \begin{bmatrix} I_{x2} & 0 & 0 \\ 0 & I_{y2} & 0 \\ 0 & 0 & I_{z2} \end{bmatrix} = \text{array inertias, (array coordinates)}$$

$\bar{R}_{cp} = \bar{R}_1 + \bar{R}_2 =$  vector from body coordinates origin to array center of mass.

$M_1 =$  mass of spacecraft main body

$M_2 =$  mass of array

and, finally,

$\bar{r}_{cm} = -\bar{r}_1 =$  total spacecraft center of mass with respect to body coordinates.

These equations were implemented in the EOS simulation to compute the spacecraft mass properties as a function of array orientation. The numerical values of the mass properties are summarized in Table 5-35.

Table 5-35. Mass Properties

Description	Sym.	Titan III D	Thor-Delta	Units
Main Body Inertias (Body Coordinates)	$I_{x1}$ $I_{y1}$ $I_{z1}$	1077 4369 4487	380 1560 1650	Slug-Ft <sup>2</sup>
Array Inertias (Array Coordinates)	$I_{x2}$ $I_{y2}$ $I_{z2}$	41 76 117	41 76 117	Slug-Ft <sup>2</sup>
Array Weight	AWT	130	130	Lb
Spacecraft Body Weight	BWT	5360	2545	Lb
Vector From Body Co-ordinates Origin to Array Hinge	$R1_x$ $R1_y$ $R1_z$	0.33 -40.00 -33.75	-6.12 -70.00 -26.25	In.
Vector For Array Hinge To Array Center of Mass	$R2_x$ $R2_y$ $R2_z$	0. -123. 0.	0. -90. 0.	In.
Distance From Station 0 To Body Coord. Origin	$\bar{x}$	95.5	81.0	In.

b. Internal Disturbances

Moving parts on the EOS-A observatory include 1) reaction wheels, 2) rate gyros, 3) the solar array, 4) dish antennas, 5) parts of the HRPI, and 6) parts of the Thematic Mapper. Their movements impart torques to the main body of the observatory which produce main body motions of two types: a) rotations of the whole observatory and b) structural vibrations.

To assess the magnitude of these effects, simple hand calculations have been performed to estimate resulting main body rotations at the attitude determination module assuming that the main body is uncontrolled. Only rapid disturbances, i.e., those whose frequencies are high compared to the control system band pass of .1 hz, are considered.

Two analysis techniques have been used. For motions of parts which are non-periodic, the observatory is modeled as a rigid body containing a hinged moving part. Only motion in a plane normal to the hinge line is considered. The motion is governed by the following physical properties:

- $\theta$  = Rotation of the main body
- $\phi$  = Rotation of the moving part relative to the main body
- $I$  = Centroidal moment of inertia of main body
- $J$  = Centroidal moment of inertia of moving part
- $R$  = Distance from main body mass center to hinge
- $L$  = Distance from appendage mass center to hinge
- $M$  = Main body mass
- $m$  = appendage mass

Figure 5-94 depicts the system. Assuming zero system angular momentum, the main body rotation is given by

$$\theta = \frac{\phi \left[ J + \frac{Mm}{M+m} (R+L)L \right]}{I + J + \frac{Mm}{M+m} (R^2 + L^2 + 2RL \cos \phi)}$$

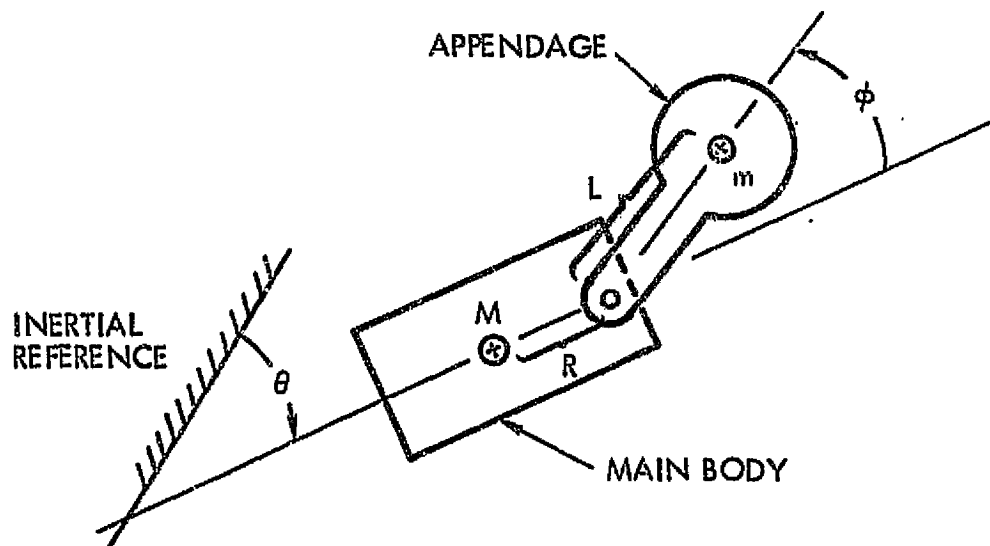


Figure 5-94. Model for Non-Oscillatory Moving Parts

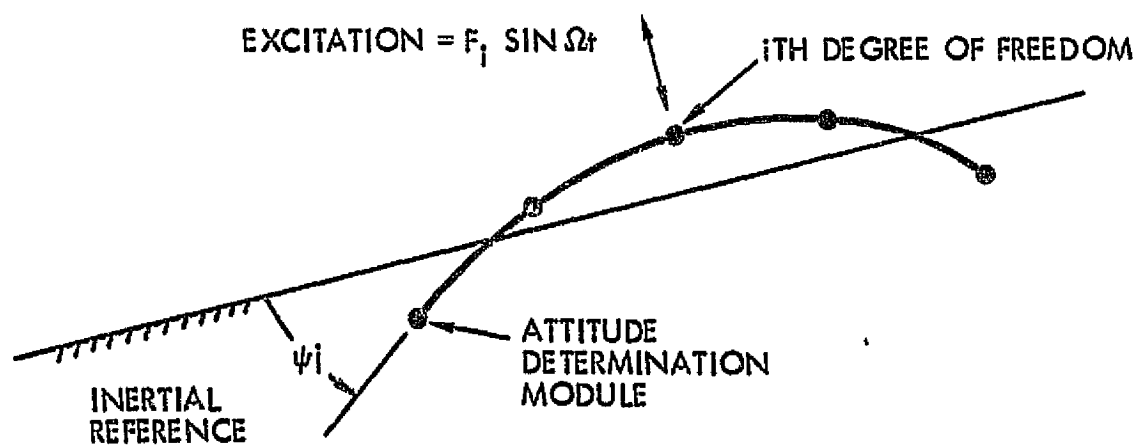


Figure 5-95. Model for Periodic Excitation of Structure

Here, the relative motion  $\phi$  is prescribed and main body rotation  $\theta$  is determined. This equation can be used to assess the effects of antenna slowing, solar array motion, and offset pointing of HRPI mirrors.

A second technique is used to estimate the effect of periodic motions of internal moving parts. Periodic excitations can cause significant structural vibration of the observatory (with no mean attitude drift) if the excitation is tuned to a structural resonance and damping is sufficiently low. For a conservative approach, structural damping has been taken as .1% of critical (i.e.,  $\zeta = .001$ ). Peak rotational response  $\psi_j$  of structural degree-of-freedom  $j$  is then given by

$$\psi_j = \frac{\phi_{jr} (F_i \phi_{ir})}{\omega_r^2 \sqrt{(1 - \Omega^2/\omega_r^2)^2 + (2\zeta\Omega/\omega_r)^2}}$$

where

- $\Omega$  = Excitation frequency
- $\phi_{jr}$  = Modal rotation at degree-of-freedom  $j$  in mode  $r$
- $\omega_r$  = Natural frequency of mode  $r$
- $\zeta_r$  = Damping coefficient for mode  $r$
- $F_i$  = Force (or moment) at  $i$ th structural degree-of-freedom
- $\phi_{ir}$  = Modal deflection (or rotation) at  $i$ th structural degree-of-freedom in mode  $r$

Figure 5-95 illustrates the system. Degree-of-freedom  $j$  is always taken as a rotation of the Observatory's attitude determination module. In most cases,  $F_i$  is a sinusoidal force or moment induced by static or dynamic imbalance, respectively, in a rotating part. Then

$$F_i/\Omega^2 = P$$

where  $P$  is imbalance. This technique also requires knowledge of mode shapes of the structure. Crude estimates of these shapes were developed for preliminary analysis as shown in Table 5-36. These estimates preceeded development of detailed structural models of EOS-A and hence only roughly resemble the current structural design. Whenever possible, the excitation was assumed to occur at a resonant frequency. However, when this assumption produced high responses, frequency separation of 1 hz was assumed. The latter assumption was not made for moving parts which operate at variable frequency.

Moving parts producing periodic disturbances include the reaction wheels, rate gyros, spinning wheels and oscillating mirrors in the TM and HRPI, and a stepping solar array drive.

Table 5-36. EOS-A Thor-Delta On-Orbit Dynamic Model for Structural Vibration

Location	Deflection or Rotation	Mode Shapes *					
		Solar Array Modes ***			Main Body Modes		
		--- Bending ----		Torsion	---Bending---		Torsion
		1.9 hz	2.2 hz	3.7 hz	15 Hz	15 hz	18 hz
Attitude	$u_x$	-.0053	-.00031	.0048	0	0	0
Determination	$u_y$	-.18	.011	-.0062	.33	0	0
and Actuation	$u_z$	-.051	-.26	.0030	0	.33	0
Modules	$\theta_x$	-.00028	-.010	.00071	0	0	.0167
	$\theta_y$	-.00053	-.00011	-.00019	0	-.032	0
	$\theta_z$	.0022	-.00011	.000084	.032	0	0
Experiment	$u_x$	.052	-.0040	.00019	0	0	0
Modules **	$u_y$	.011	.0067	-.00042	.33	0	0
	$u_z$	.0028	.036	.0024	0	.33	0
	$\theta_x$	-.00028	-.011	.00080	0	0	-.0167
	$\theta_y$	-.00051	-.00019	-.00079	0	.032	0
	$\theta_z$	.0027	-.00018	.000010	-.032	0	0
Array	$u_x$	-1.9	.15	-.0071			
Mass	$u_y$	-.40	-.25	.015			
Center	$u_z$	-.10	-1.3	-.039	N/A	N/A	N/A
	$\theta_x$	.0015	.022	-.012			
	$\theta_y$	-.00028	.0082	.063			
	$\theta_z$	-.026	.0019	-.00030			

\* Mode shapes are normalized to a generalized mass of 1 lb-sec<sup>2</sup>/in.

\*\* At the time this model was generated, locations of the TM & HRPI were not resolved, so one location was used for both.

\*\*\* Solar array in maximum +X position.

c. On-Orbit Dynamic Model (Thor-Delta Version)

Control system/structural interactions are assessed using a flexible model of the observatory. Modal rotations at the attitude determination module and translations and rotations at the actuators can be used to verify that the controllers do not excite observatory bending.

A dynamic model for EOS-A (Thor-Delta 2910 version) was developed by regarding the main body as rigid with flexibility present in the solar array boom and panels. The boom thickness (3" square with .050" wall) was chosen to keep first bending frequencies on the order of 1 hz and, hence, well above the control system band pass of .1 hz. The four 63" by 69" array panels were modeled as a honeycomb substrate surrounded by a frame and tied to the boom via rigid hinges. (See Figure 5-96.)

Bending frequencies and main body rotations are listed in Table 5-37. Due to the 15° bend in the boom and the large offset mass of the arrays, most bending modes produce significant main body rotations about more than one axis. For this analysis, the boom was positioned with the solar array mass center in its maximum +X position. This produces the largest modal rotations of the main body about the roll (X) axis which is the critical axis due to the corresponding low main body moment of inertia.



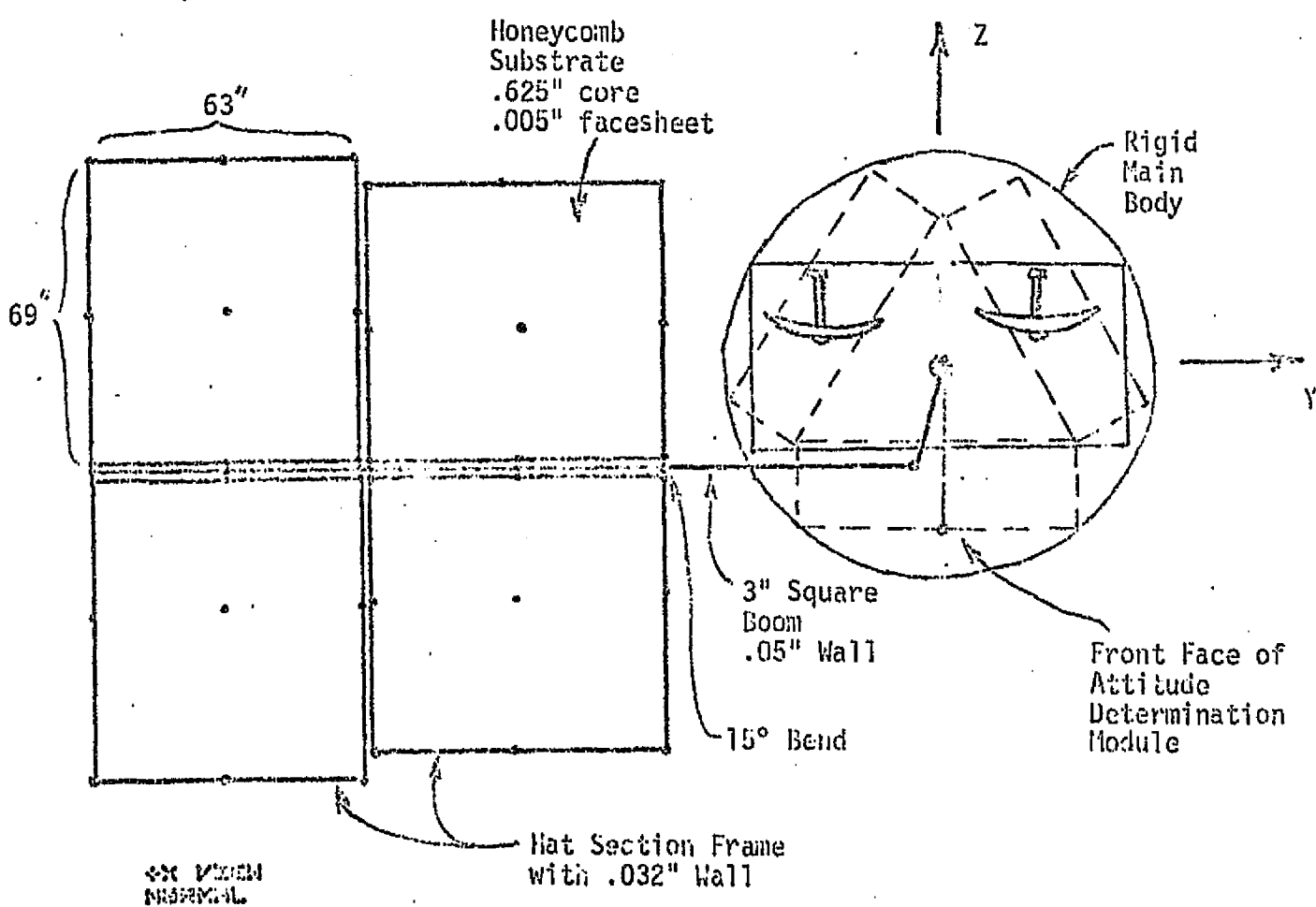


Figure 5-96. Deployed Dynamic Model (Thor-Delta Version)

Table 5-37. Main Body Rotations in Deployed Bending Modes

Mode No.	Frequency (Hz)	----Rotations (rad/in)*----			Mode Description
		$\theta_x$	$\theta_y$	$\theta_z$	
1	.93	-.000017	.00047	-.0033	1st Bending about Z
2	1.4	.012	.00059	.000084	1st Bending about X/Torsion
3	1.7	-.0029	.00095	-.000025	1st Torsion
4	4.4	.00050	-.00019	-.000005	2nd Torsion
5	4.5	-.000065	-.00024	.000051	Panel Bending (Inboard +X, Outboard -X)

\*Modes are normalized to a generalized mass of 1 lb-sec<sup>2</sup>/in.

#### 5.2.4.1.3 Results

##### a. Environmental

##### Thor-Delta Spacecraft, Earth Point

##### Orbit/Disturbance Torques

The first case considered is the Thor-Delta spacecraft with an orbit of the following specifications:

- Sun - synchronous
- Altitude 316 n.m.
- Inclination 100 deg
- Right ascension of the ascending node 345 deg.

The spacecraft configuration, as previously defined in Table 5-33, had a 1 KW solar array paddle (162 ft<sup>2</sup>). The same basic configuration with a 580 watt array (96 ft<sup>2</sup>) was also considered.

The environmental disturbance torques acting on the spacecraft with the large array are presented graphically in Figure 5-97.  $T_{dx}$ ,  $T_{dy}$ , and  $T_{dz}$  are the disturbance torques about the roll, pitch and yaw body axes due to the combined effects of solar pressure, aerodynamic pressure, gravity gradient, and residual magnetic moment.

The predominant torque, which is about the yaw axis, is due to aerodynamic effects and tends to be 1 to 2 orders of magnitude greater than the other disturbances. For the disturbances about the roll and pitch axes, the disturbances arising from the various sources are of nearly equal magnitude.

A comparison of Figure 5-97 and -98 shows the relative effects of the different array sizes. The magnitudes of all components of the disturbance torques for the small array configuration are approximately 50 percent smaller than those for the large array, while the relative shape is quite similar in both cases.

DELTA DIS. TORQUES, 1KW ARRAY  
 NOM. ORBIT  
 ALT = 316 N.M.

TOTAL DIST. (FT-LES)

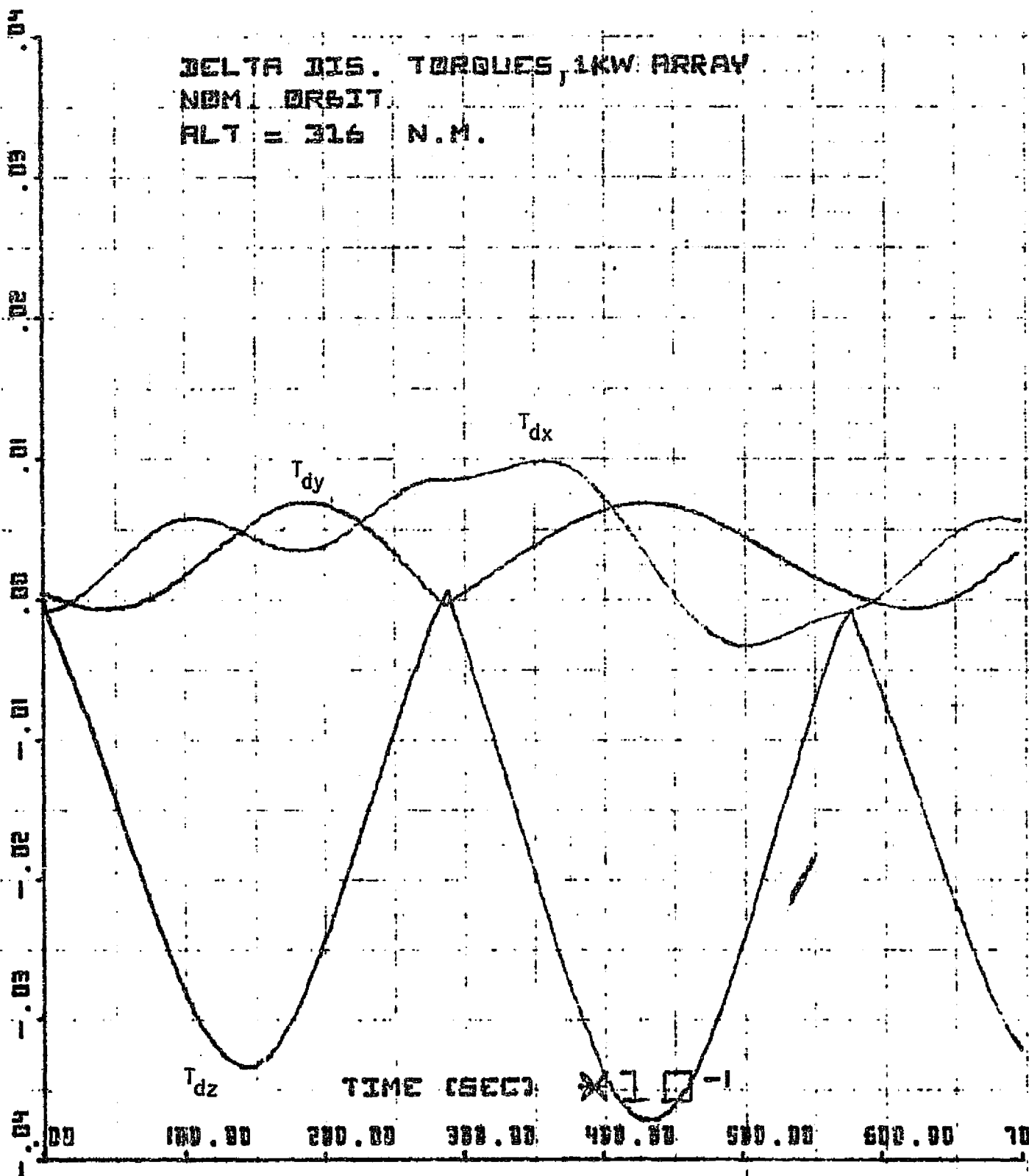


Figure 5-97. Delta Disturbance Torques,  $\overline{T}_d$ , Large Array

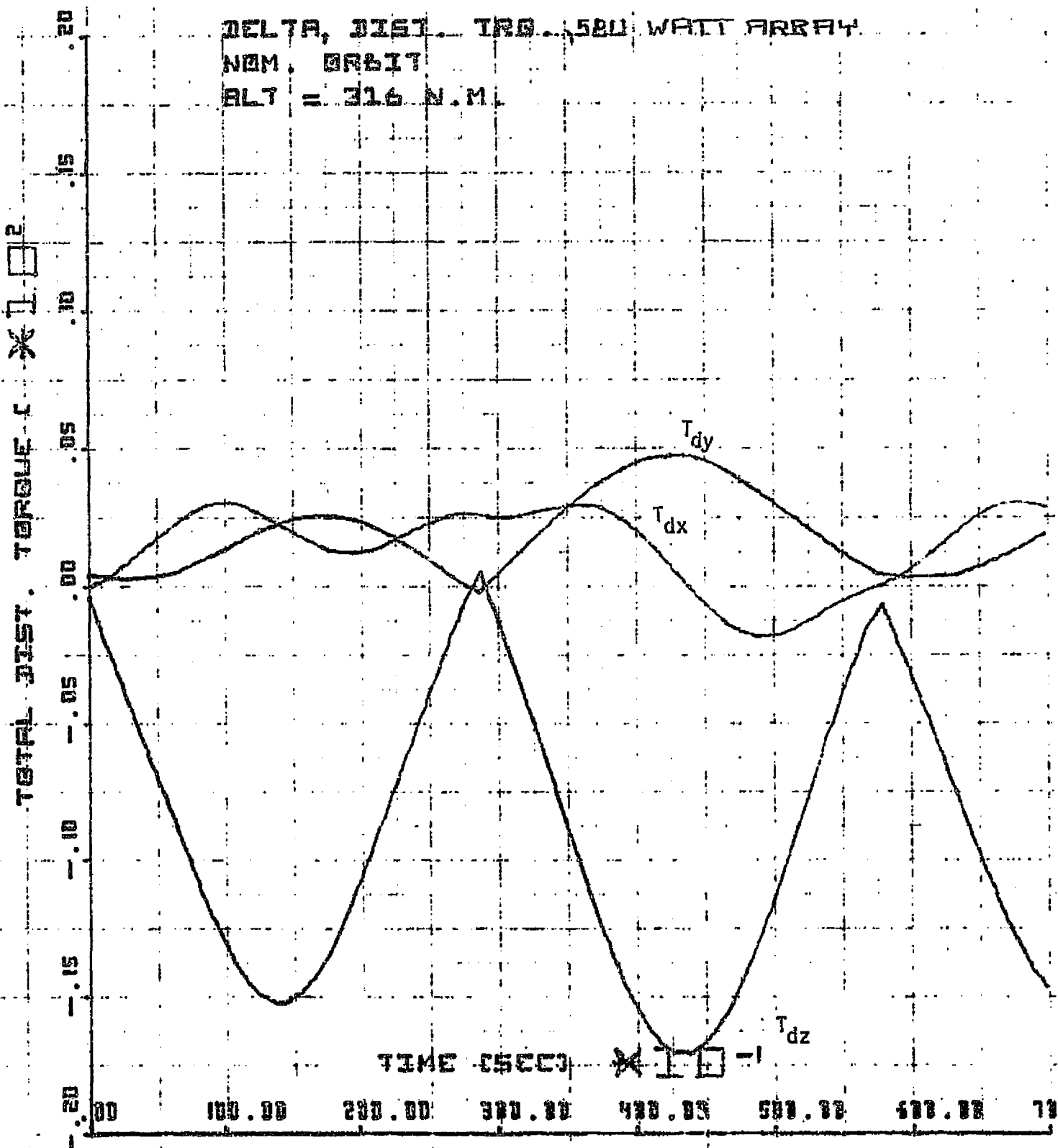


Figure 5-98. Delta Disturbance Torques,  $\bar{T}_d$ , Small Array

A fourier series approximation for the 1 KW array is given by

$$\begin{aligned} T_{dx} &= 0.5 \times 10^{-3} - 0.5 \times 10^{-3} \cos \omega_0 t + 0.45 \times 10^{-3} \sin \omega_0 t \\ T_{dy} &= 0.4 \times 10^{-3} - 0.4 \times 10^{-3} \cos 2 \omega_0 t \\ T_{dz} &= -1.9 \times 10^{-3} + 0.2 \times 10^{-3} \sin \omega_0 t + 1.90 \times 10^{-3} \cos 2 \omega_0 t \end{aligned} \quad (26)$$

and for the 580 watt array by

$$\begin{aligned} T_{dx} &= 0.2 \times 10^{-3} - 0.2 \times 10^{-3} \cos \omega_0 t + 0.125 \times 10^{-3} \sin 2 \omega_0 t \\ T_{dy} &= 0.187 \times 10^{-3} - 0.125 \times 10^{-3} \sin \omega_0 t - 0.187 \times 10^{-3} \cos 2 \omega_0 t \\ T_{dz} &= -0.8 \times 10^{-3} + 0.1 \times 10^{-3} \sin \omega_0 t + 0.8 \times 10^{-3} \cos 2 \omega_0 t \end{aligned} \quad (27)$$

#### Reaction Wheel Magnet Sizing

Simulation studies have provided the wheel/magnet requirements for the Thor-Delta spacecraft as summarized in Table 5-38. A 7.2 ft-lb/sec OGO reaction wheel in conjunction with a 120K pole-cm magnet will handle the requirements for both the large and small solar array configurations with ample margin. Since the slew mode momentum storage requirement is about 1 (ft-lb/sec), we see that the wheel sizes in these cases are dictated by the normal mode requirements.

Table 5-38. Thor-Delta Wheel/Magnet Requirements

Configuration	Momentum Storage (Ft-lb/sec)	Wheel Torque (Ft-lb)	Magnetic Moment (Pole-CM)	Unloading Gain, $K_u$ (Gauss-Pole CM/Ft-Lb - Sec)
1 KW Array	4.2	$4.8 \times 10^{-3}$	100 K	$4.2 \times 10^3$
580 W Array	1.85	$2.03 \times 10^{-3}$	100 K	$1.4 \times 10^4$

Figures 5-99 and 5-100 provide the reaction wheel and magnet requirements as a function of the unloading gain  $K_u$ . The appropriate unloading gains were chosen so as to minimize the required momentum storage with a required magnetic moment

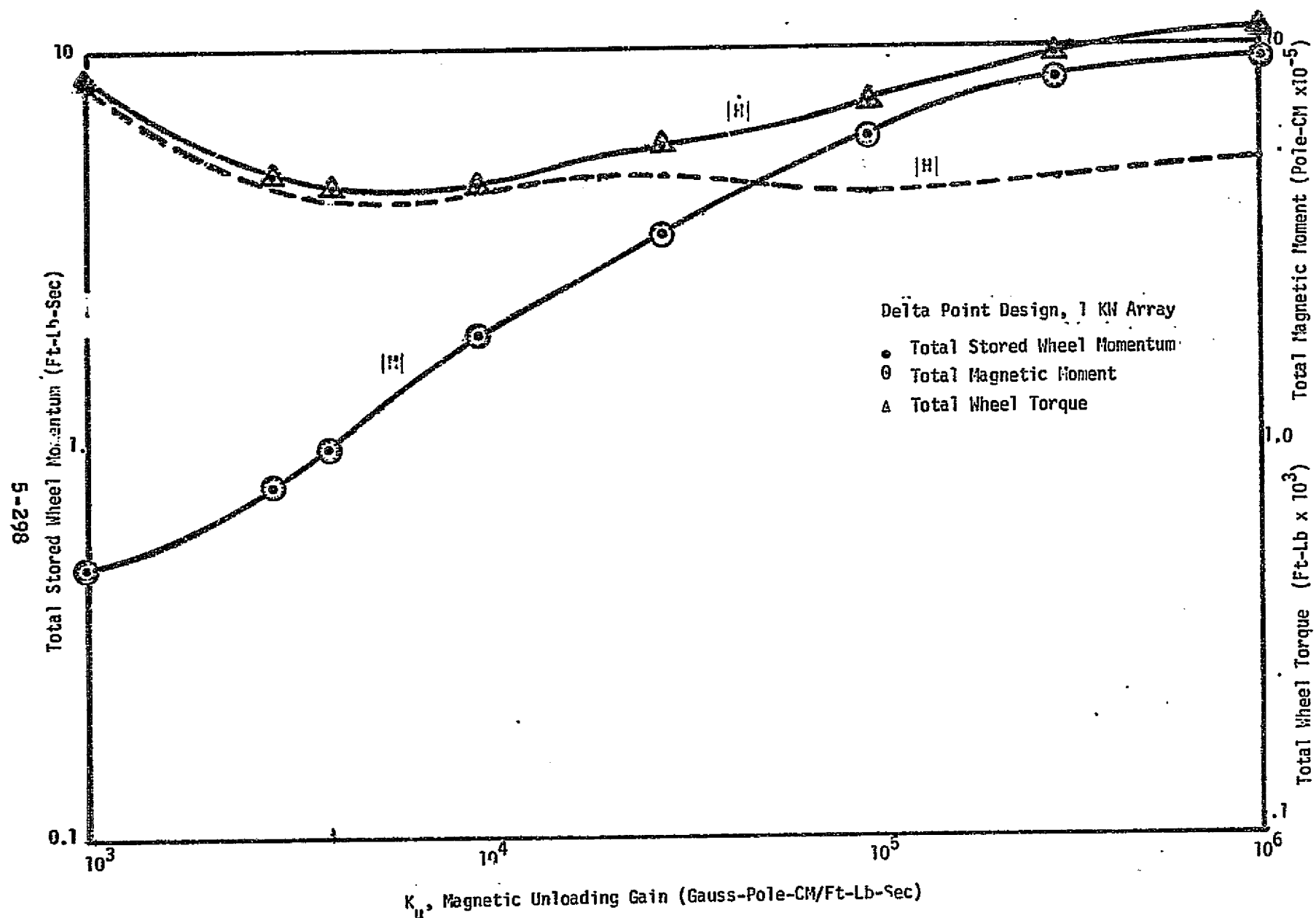


Figure 5-99. Wheel/Magnet Requirements Thor-Delta, 1 KW Array

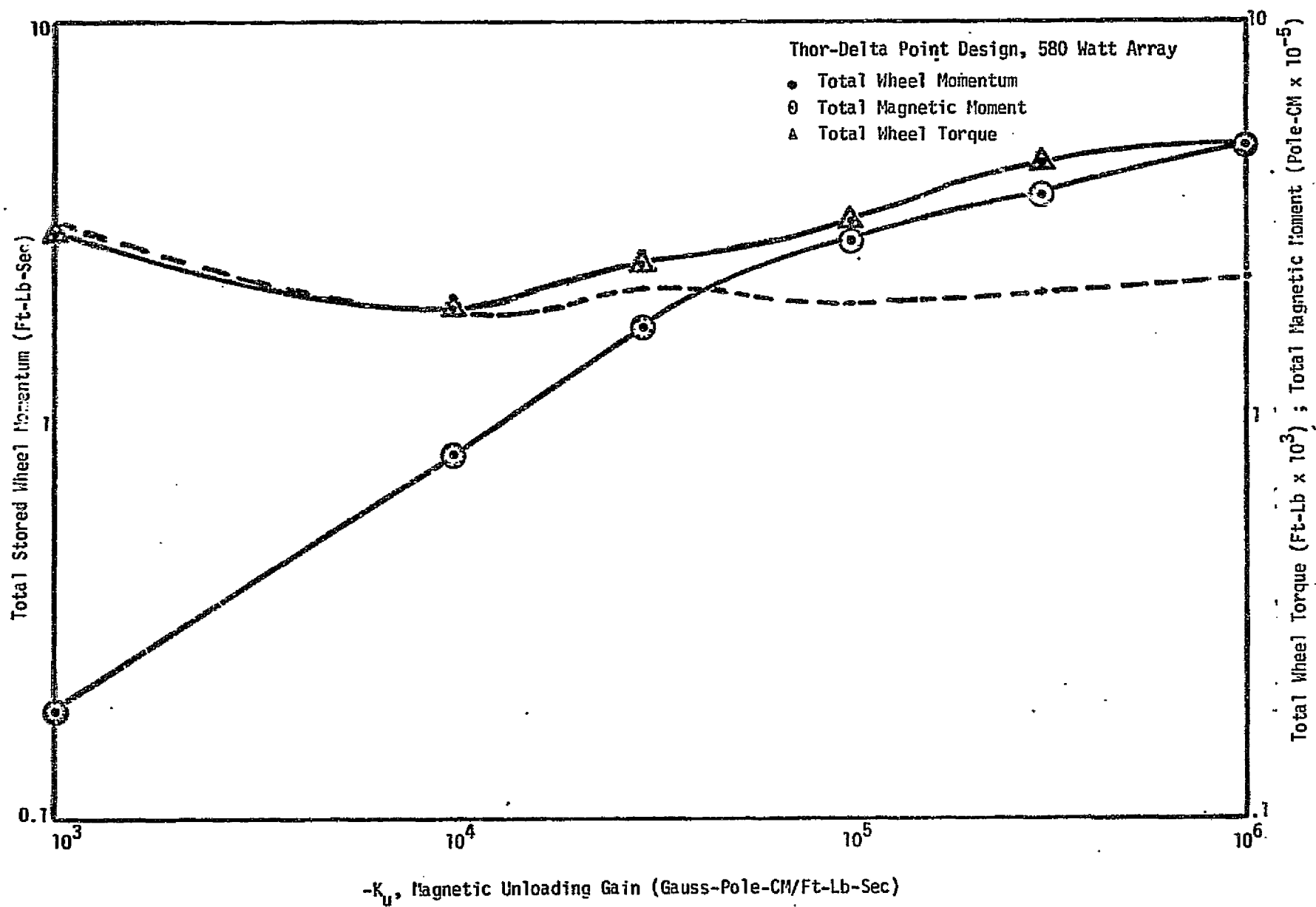


Figure 5-100. Wheel/Magnetic Requirements Thor-Delta, 580 W Array



of no greater than 100K pole-cm. The quantities plotted in Figure 5-99 and -100 are the vector magnitudes of wheel momentum, wheel torque, and magnetic moment and, therefore, provide an upper bound on the normal mode wheel/magnet requirements for each axis.

#### Thor-Delta Magnetic Unloading Performance

Figures 5-101 and -102 show the Thor-Delta Wheel and magnet response characteristics, respectively, for the nominal design with the 1 KW array. Approximately 2 orbits are required before steady-state unloading is obtained. Note that for the chosen unloading gain no overshoot results. Required momentum storage in roll and yaw is nearly an order of magnitude greater than that required in pitch. Similarly, the magnetic moment in pitch is greater than 4 times that in either roll or yaw. This indicates, however, that substantially smaller magnetics could be used for the roll and yaw magnetic torquers, say 35K pole-cm.

Figures 5-103 and -104 show the effects of magnet saturation on the nominal Thor-Delta design. A saturation level of 75K pole-cm increased the momentum unloading steady-state response to greater than 4 orbits with an increase in peak momentum of approximately 20 and 30 percent in yaw and roll. These results indicate that magnets of at least 100K poles-cm are necessary to provide good unloading performance.

The qualitative effects of unloading gain variations are to produce large overshoots and long settling times for excessively high gains and inadequate unloading capability and long settling times for excessively low gains. Representative plots showing the effects of gain variations are given in Figure 5-103, through 5-110 for the small array Thor-Delta configuration.

Previous analytical results\* have shown that an effective gain reduction exists in the yaw channel. To compensate for this effect, the yaw wheel error signal gain was increased by a factor of 3 in one of the cases simulated. The resulting effects on wheel response and magnetic moment response are shown in Figures 5-111 and -112. Some improvement in wheel performance was realized. In particular, the peak roll momentum was reduced by nearly 30 percent and the peak yaw momentum by about 12 percent. The associated peak pitch magnetic moment, however, increased substantially (about 60 percent).

---

\* Work memo.

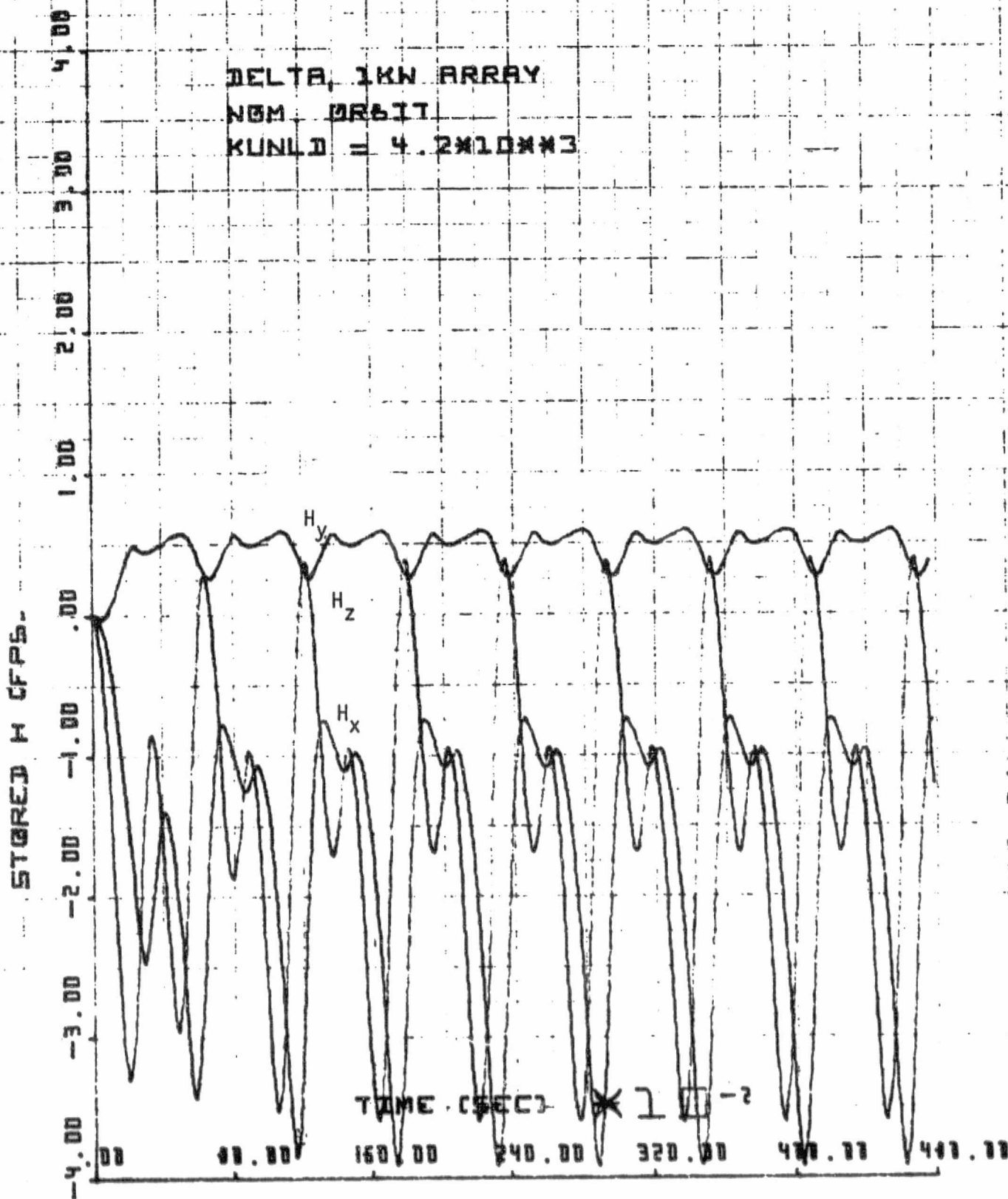


Figure 5-101. Nominal Thor-Delta Wheel Response, 1 KW Array

DELTA, 1KW ARRAY  
 NOM. ORBIT  
 $KUNLD = 4.2 \times 10^{-3}$

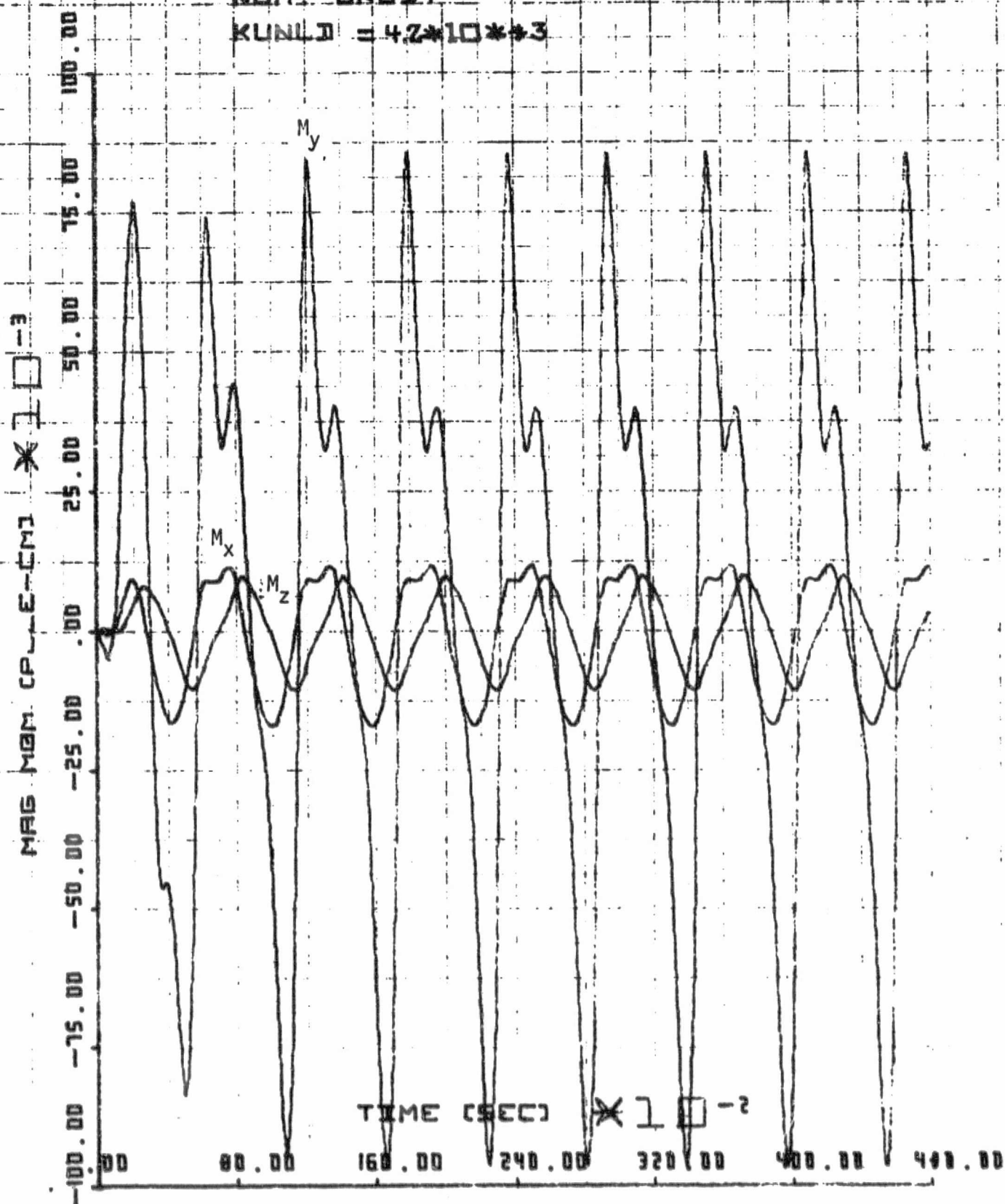


Figure 5-102. Nominal Thor-Delta Magnetic Response, 1 KW Array

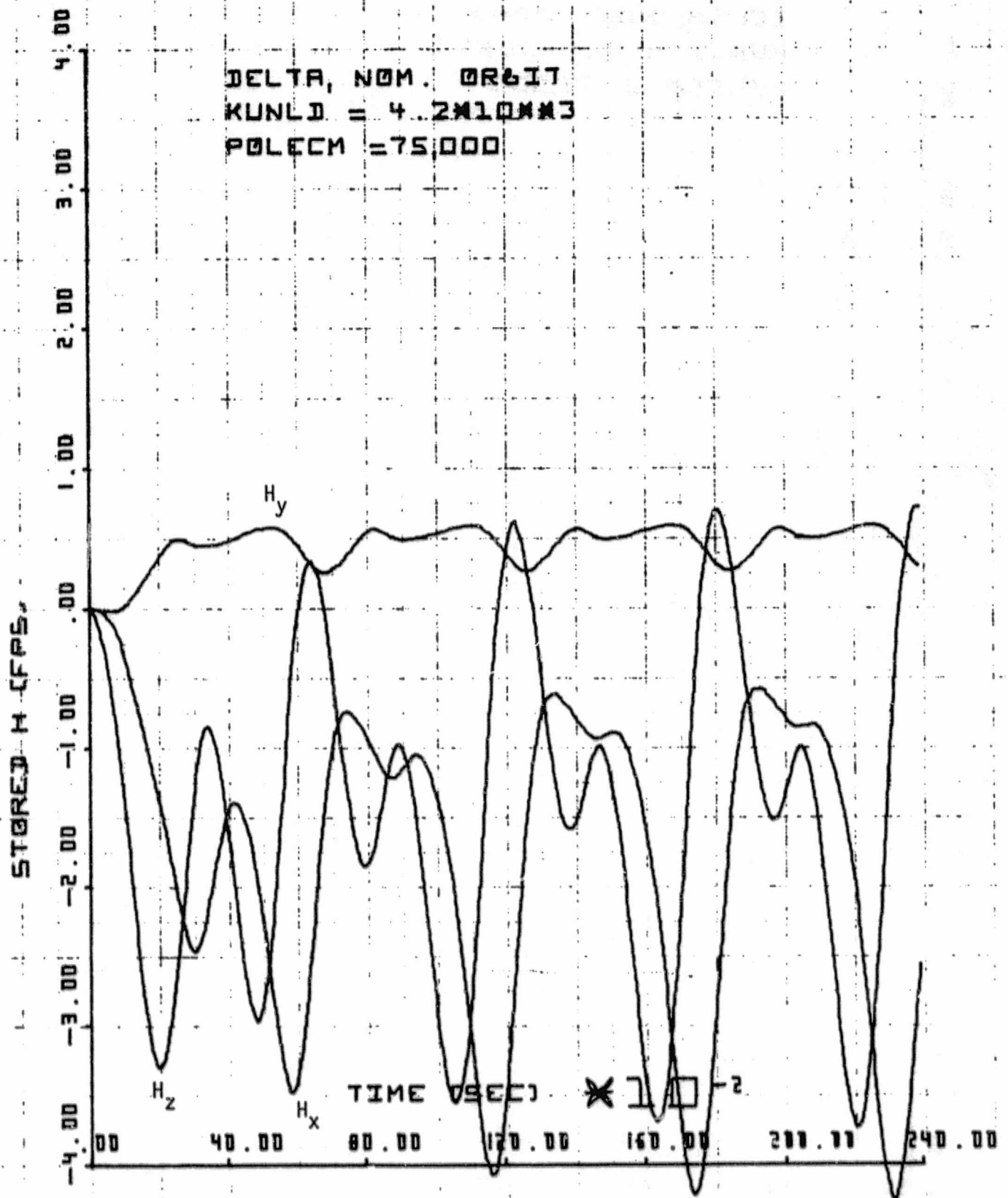


Figure 5-103. Thor-Delta Design with Magnetic Saturation Wheel Dynamics



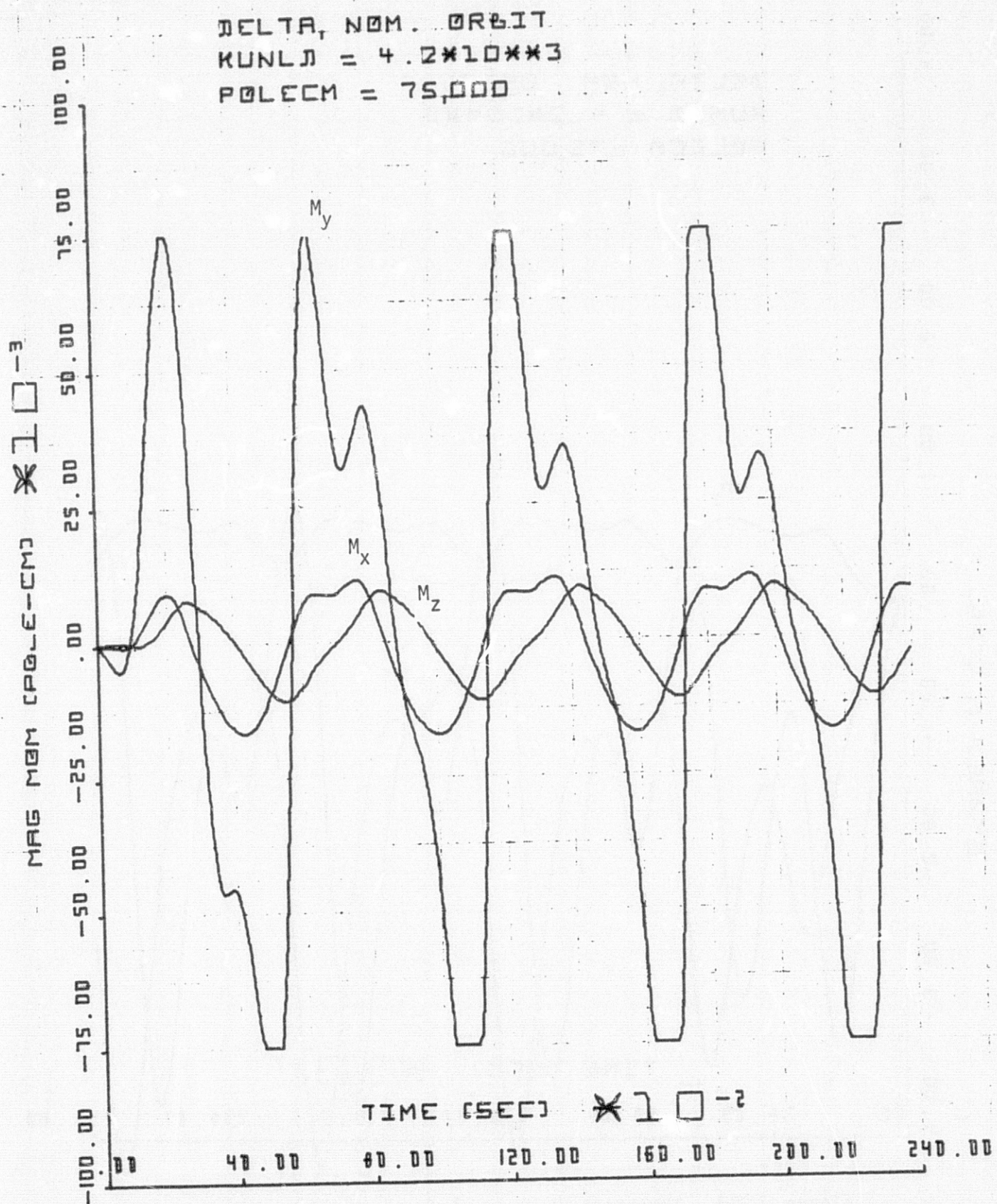


Figure 5-104. Thor-Delta Design with Magnetic Saturation, Magnet Dynamics

DELTA, NOM. ORBIT  
KUNLD = 10M#3

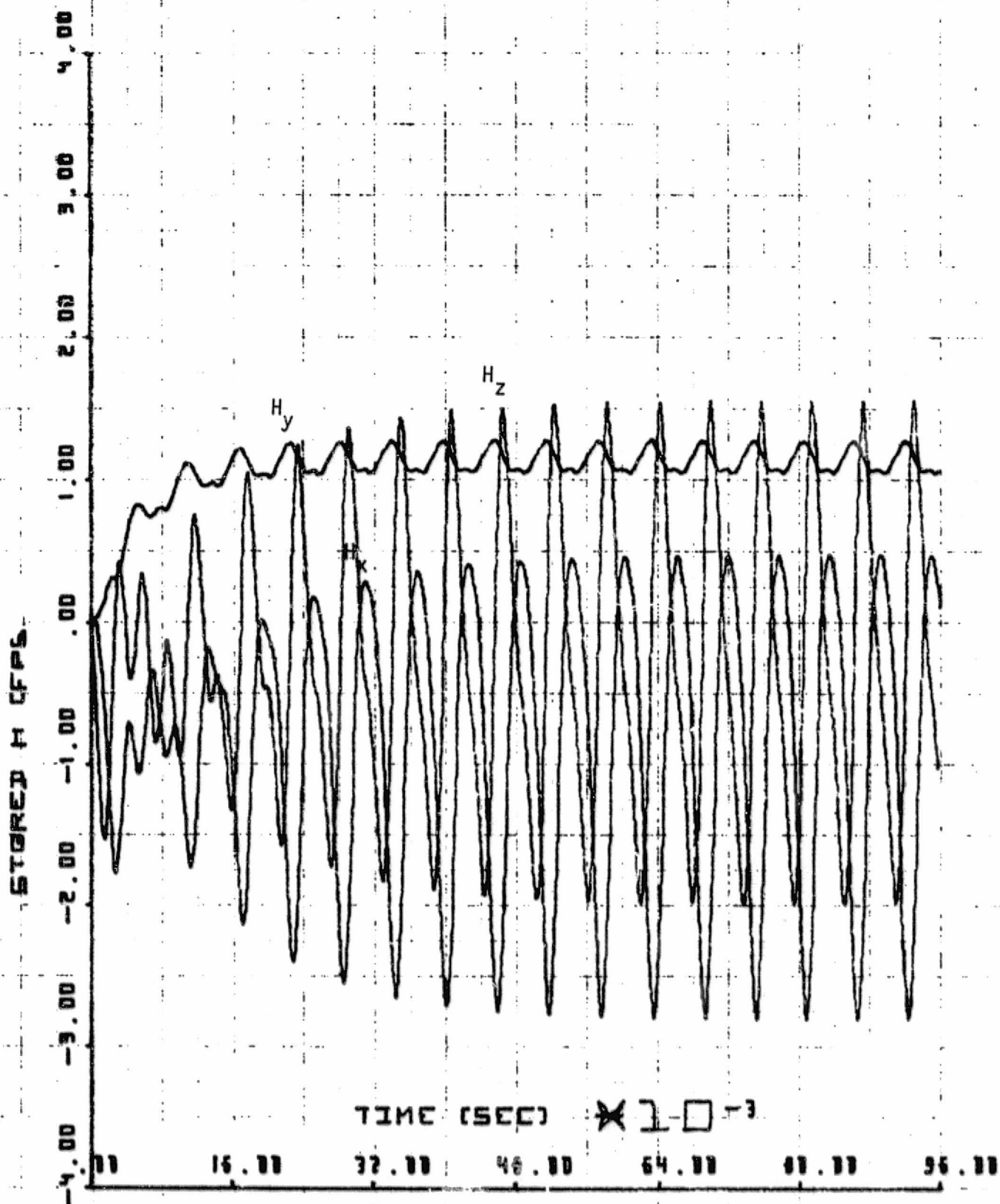


Figure 5-105. Wheel Response, Thor-Delta With Small Array,  $K_u = 10^3$

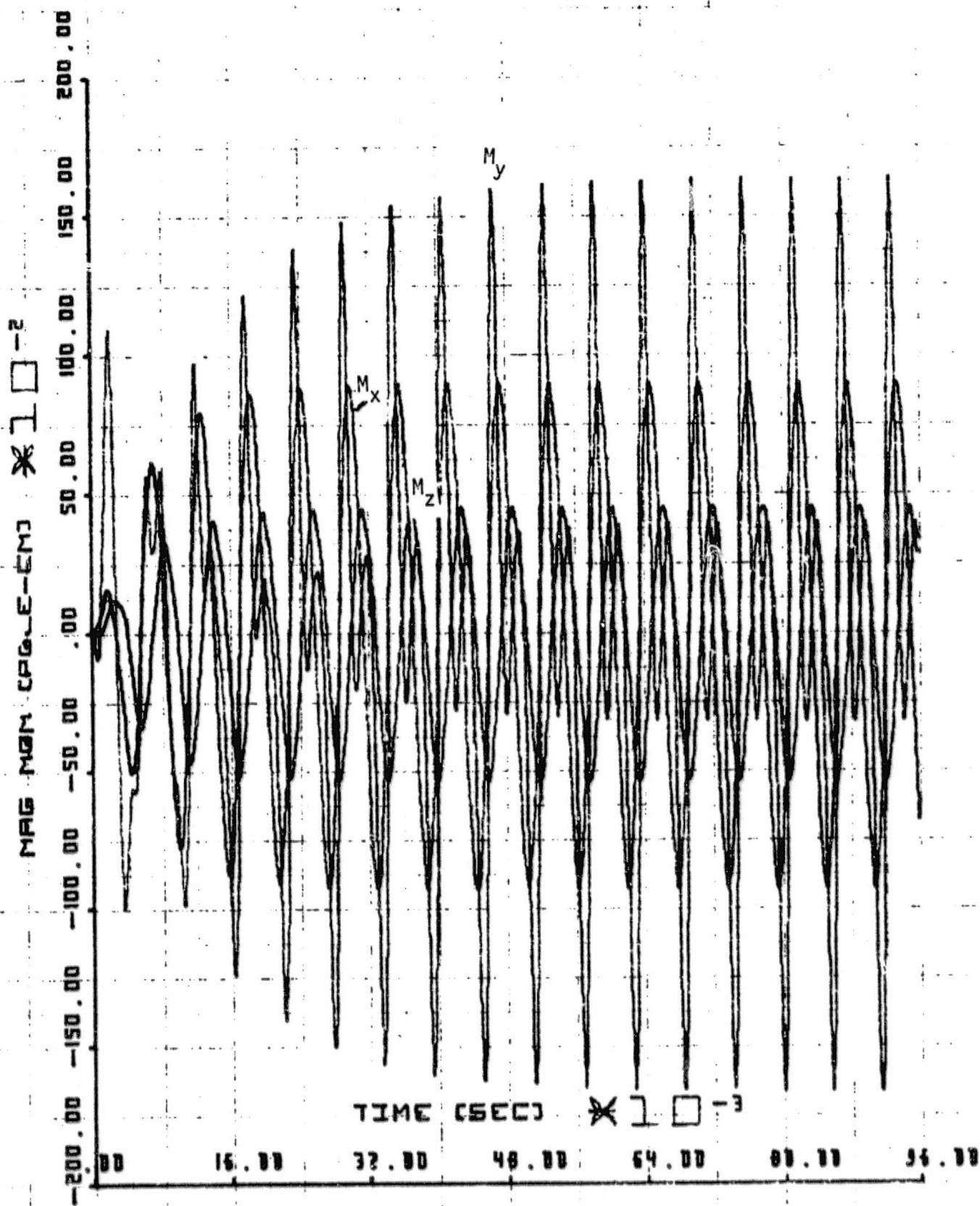


Figure 5-106. Magnet Response, Thor-Delta With Small Array,  $K_u = 10^3$



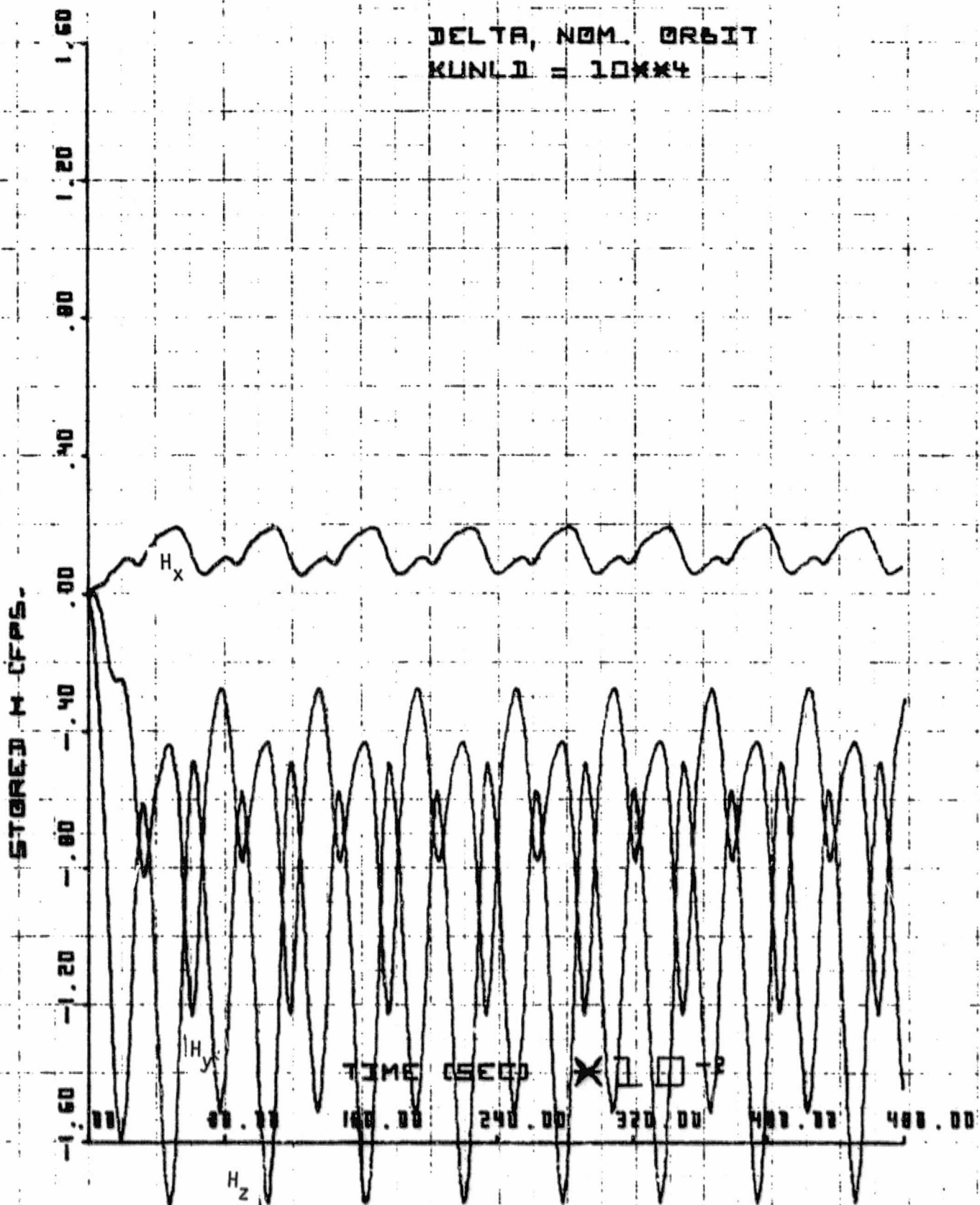


Figure 5-107. Wheel Response, Thor-Delta, Small Array,  $K_u = 10^4$



DELTA, NOM. ORBIT  
KUNLI = 10MM4

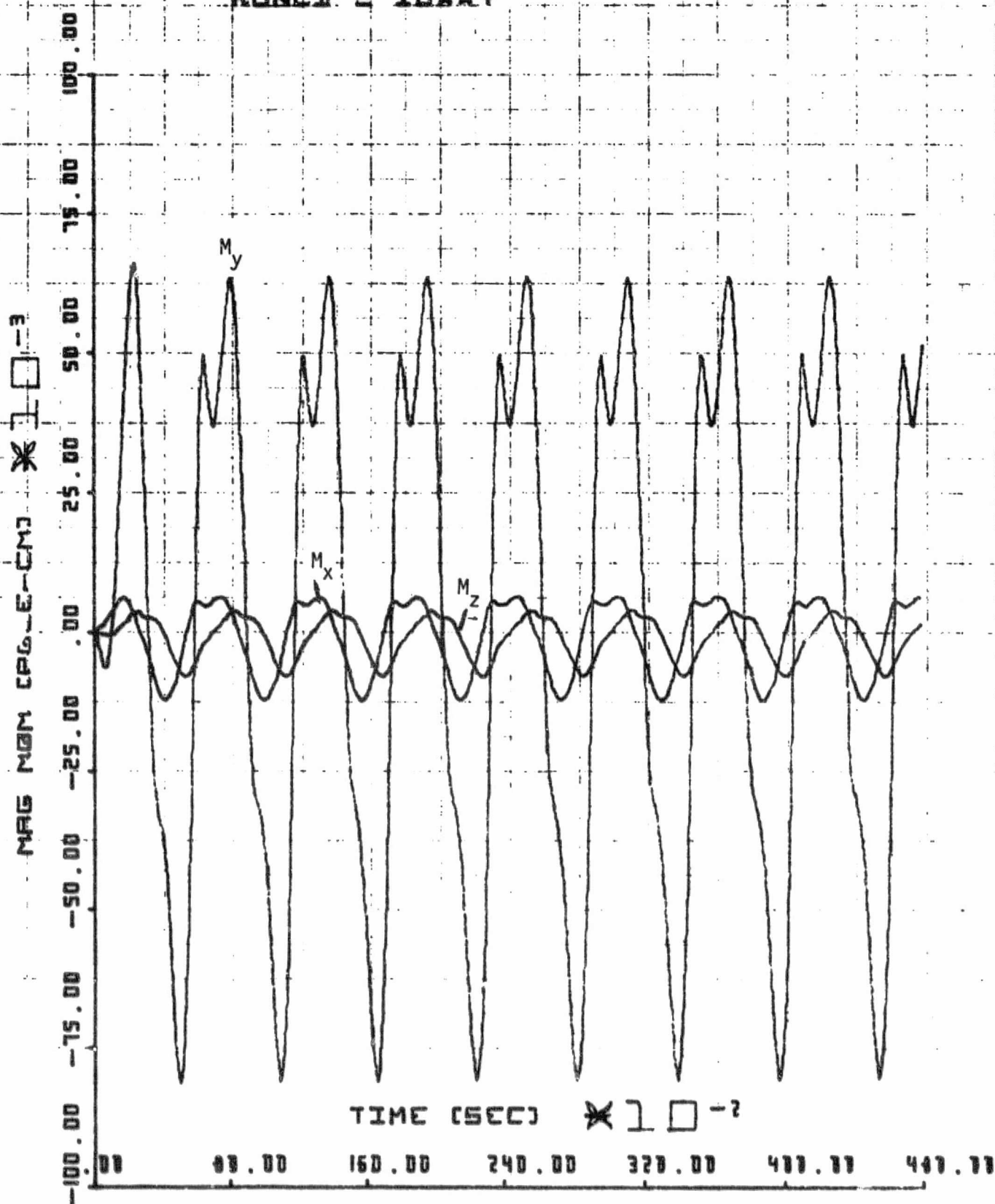


Figure 5-108. Magnet Response, Thor-Delta, Small Array,  $K_u = 10^4$

DELTA, NOM. ORBIT  
KUNLD = 10XK6

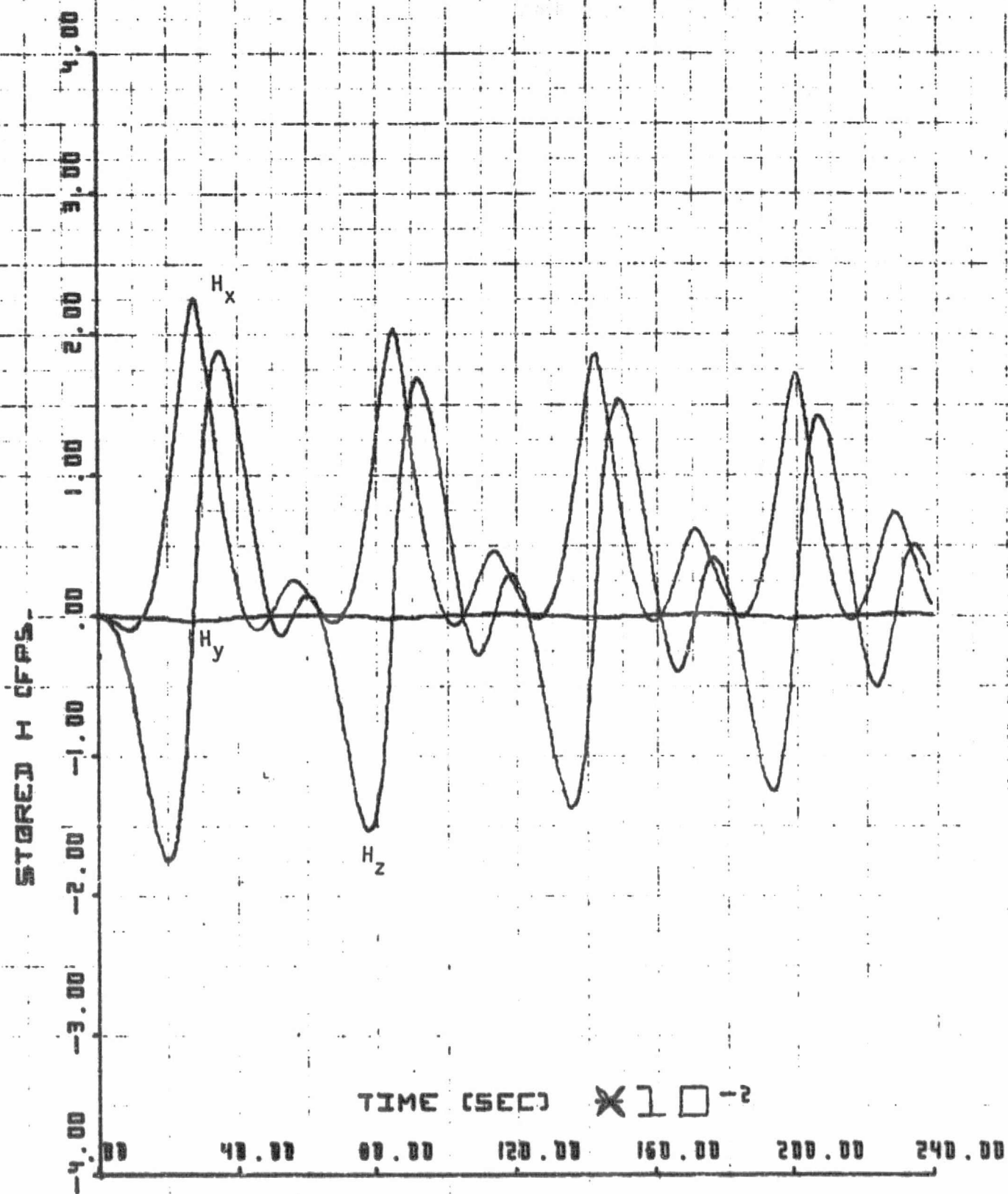


Figure 5-109. Wheel Response, Thor-Delta With Small Array,  $K_u = 10^6$

DELTA, NOM. ORBIT  
KUNLD = 10#6

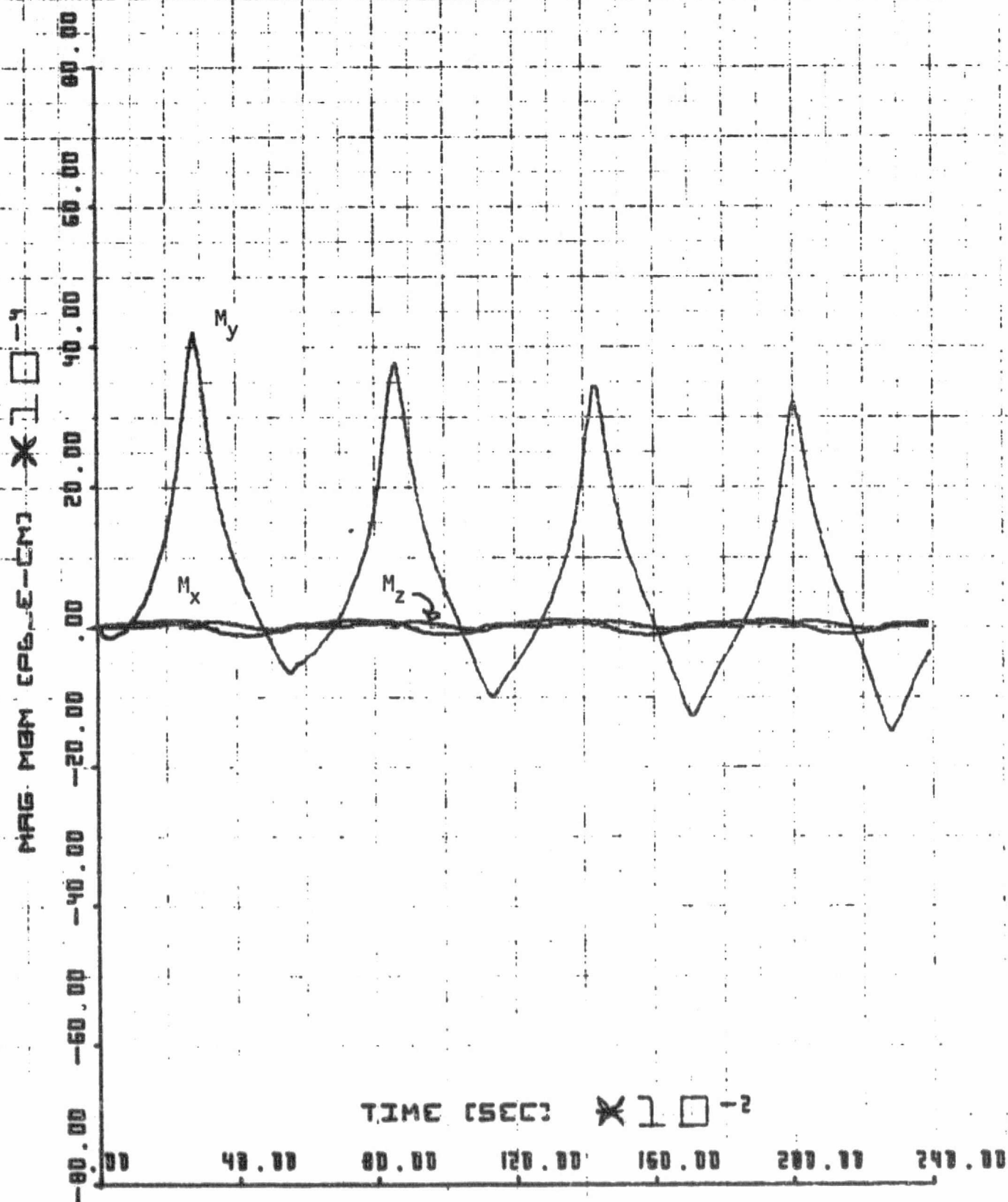


Figure 5-110. Magnet Response, Thor-Delta With Small Array,  $K_u = 10^6$

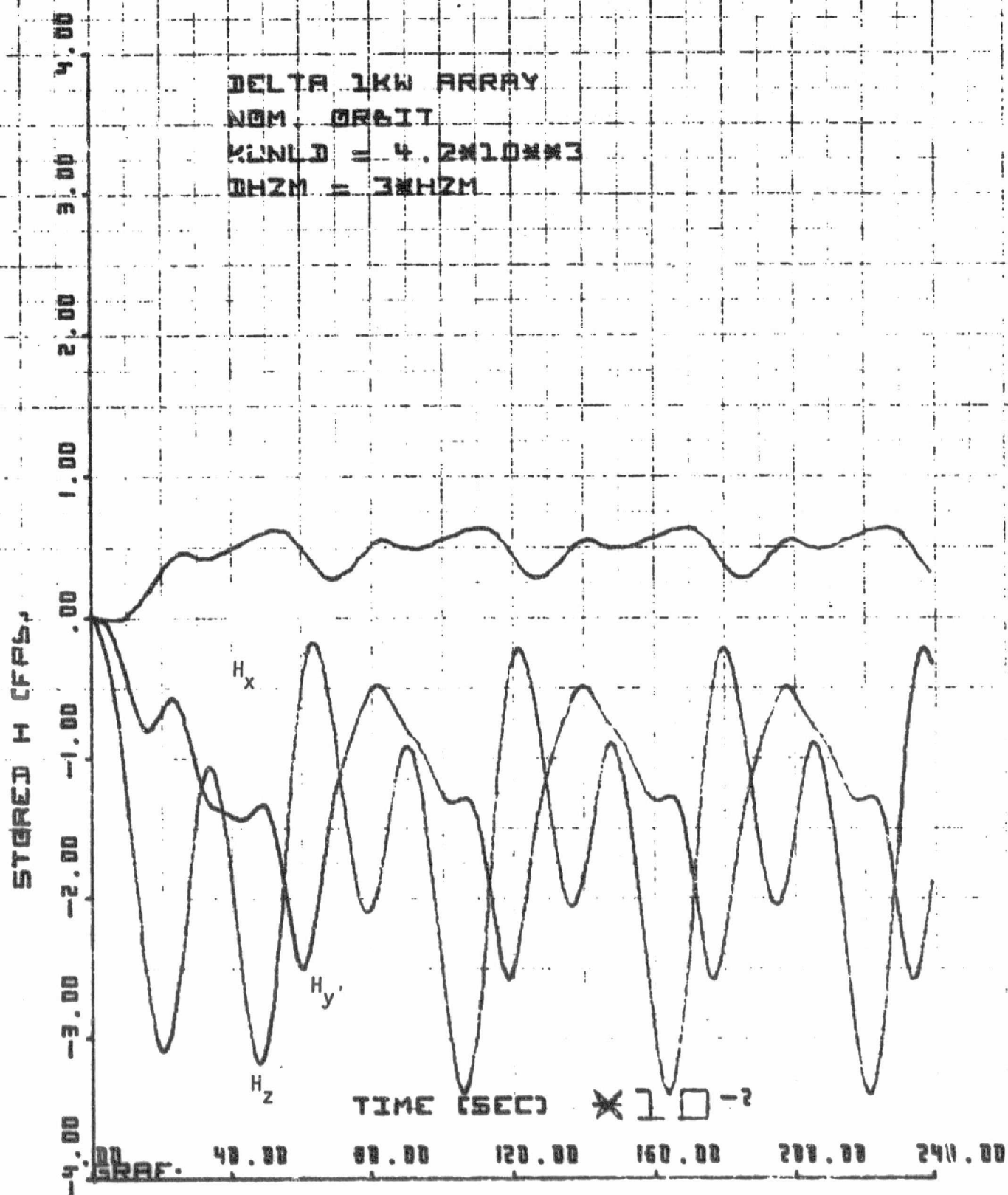


Figure 5-111. Thor-Delta Wheel Momentum With Increased Wheel Error Gain

MAG MOM (PUL-E-CM)  $\times 10^{-3}$

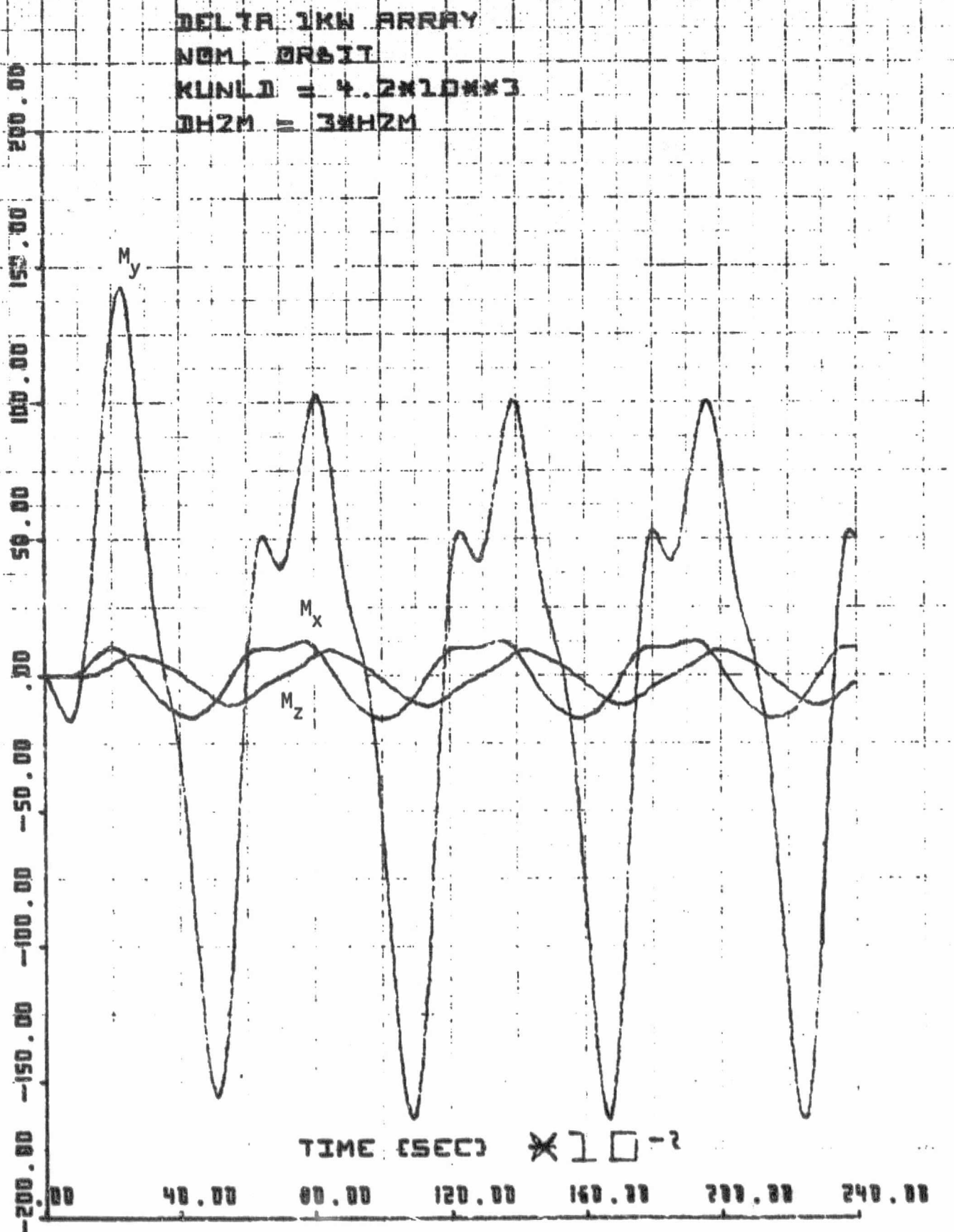


Figure 5-112. Thor-Delta Magnetic Moment With Increased Wheel Error Gain

## 2. Titan III-D, Earth Point

### Orbit/Disturbance Torques

In this section the Titan III-D configurations is considered with the following orbit:

- o Sun - Synchronous
- o Altitude 386 n.m.
- o Inclination 99.15 deg
- o Right ascension of the ascending node 345 deg

As with the Delta configuration, the Titan II-D spacecraft was considered with the large 1 KW array and the small 580 W array.

Plots presenting the total disturbance torques about the spacecraft roll, pitch, and yaw body axes are given Figures 5-113 and -114 for the large array and small array cases, respectively. The corresponding Fourier series approximation are, for the 1 KW array case,

$$\begin{aligned}T_{dx} &= 4.75 \times 10^{-4} + 6.25 \times 10^{-4} \sin[\omega_0 t - 60 \text{ deg}] \\T_{dy} &= 1.00 \times 10^{-4} - 3.00 \times 10^{-4} \sin 2 \omega_0 t \\T_{dz} &= -6.75 \times 10^{-4} + 2.00 \times 10^{-4} \sin \omega_0 t + 5.75 \times 10^{-4} \cos 2 \omega_0 t\end{aligned} \tag{28}$$

and, for the 580 W array case,

$$\begin{aligned}T_{dx} &= 2.8 \times 10^{-4} + 3.6 \times 10^{-4} \sin (\omega_0 t - 45 \text{ deg}) \\T_{dy} &= 0.5 \times 10^{-4} - 2.5 \times 10^{-4} \sin \omega_0 t \\T_{dz} &= -2.4 \times 10^{-4} + 1.15 \times 10^{-4} \sin \omega_0 t + 1.4 \times 10^{-4} \cos 2 \omega_0 t\end{aligned} \tag{29}$$

### Reaction Wheel/Magnetic Sizing

Through simulation the normal mode reaction wheel/magnet requirements given in Table 5-39 were established for the Titan III-D, 386 n.m. orbit. For the Titan mission, the wheel size is actually dictated by the 2 deg/min slew speed which requires about 3 ft-lb/sec of momentum storage. Hence, 7.2 ft-lb/sec OGO wheel and 120K pole-cm magnets will also suffice for either of the Titan missions given above.



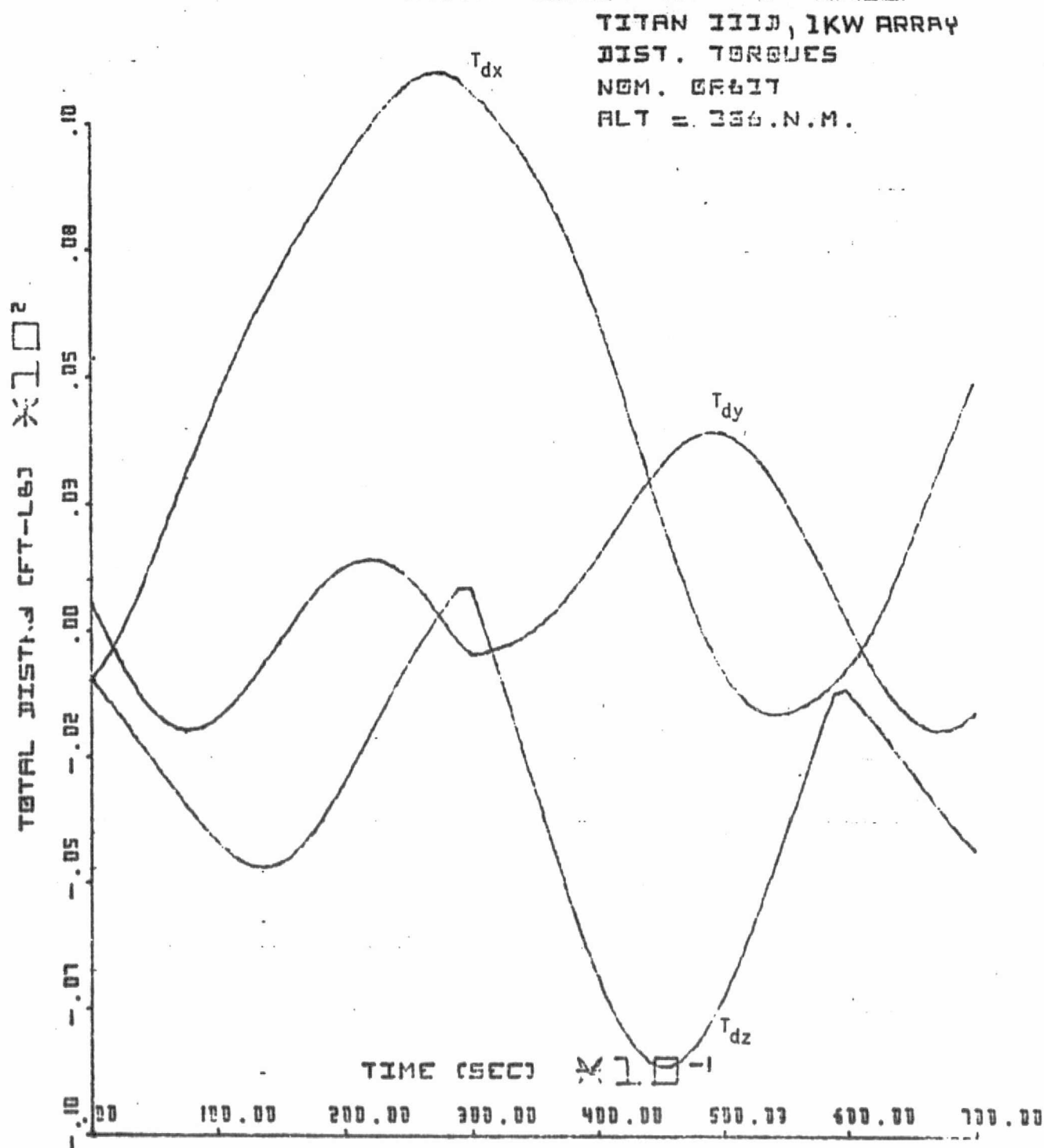


Figure 5-113. Titan III-D Disturbance Torques, 1 KW Array

NOM. TITAN III-D  
ALT = 386 NM

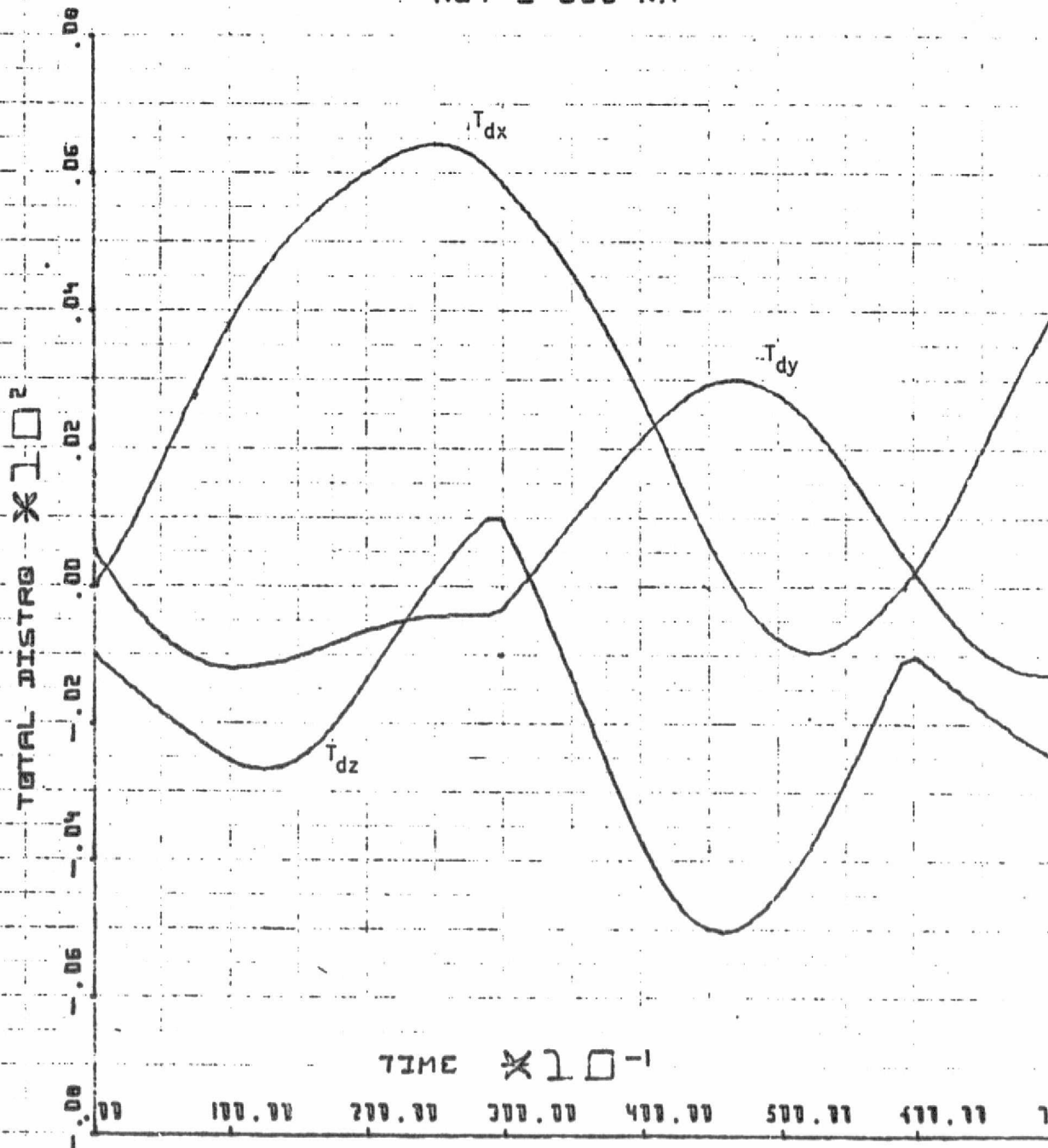


Figure 5-114. Titan III-D Disturbance Torques, 580 W Array



Table 5-39. Titan III Wheel/Magnet Requirements

Configuration	Momentum Storage (Ft-lb/sec)	Wheel Torque (Ft-Lb)	Magnetic Moment (Pole-CM)	Unloading Gain, $K_u$ (Gauss-Pole CM/Ft-Lb/Sec)
1 KW Array	1.4	$1.6 \times 10^{-3}$	100 K	$1.7 \times 10^4$
580 W Array	0.68	$10^{-3}$	100 K	$5.4 \times 10^4$

Figures 5-115 and -116 give the reaction wheel/magnet requirements as a function of unloading gain  $K_u$  for the 1 KW and 580 watt arrays, respectively. As with the Thor-Delta configuration, the criteria employed in choosing the unloading gain was to minimize wheel momentum with an upper bound on the magnet size of 100K pole-cm.

#### Titan III-D Magnetic Unloading Performance

The reaction wheel and magnet responses for the nominal Titan III-D design are given in Figures 5-117 and -118. The response is quite good with steady-state response achieved within one orbit. The system in this case, appears to be nearly critically damped. As with the Thor-Delta spacecraft, the roll and yaw reaction wheels experience the greatest loading with the y-axis magnet performing most of the unloading.

This design appears to be quite insensitive to the effects of magnet saturation. Magnetic saturation levels of 75K and 50K pole-cm were considered with relatively small degradation in system performance. Figures 5-119 and -120 show the wheel and magnet responses with the 50K pole-cm saturation level. The increase in peak yaw momentum is only about 10 percent. This indicates that 50K pole-cm magnets could be used quite effectively with the 7.2 ft-lb/sec OGO wheel.

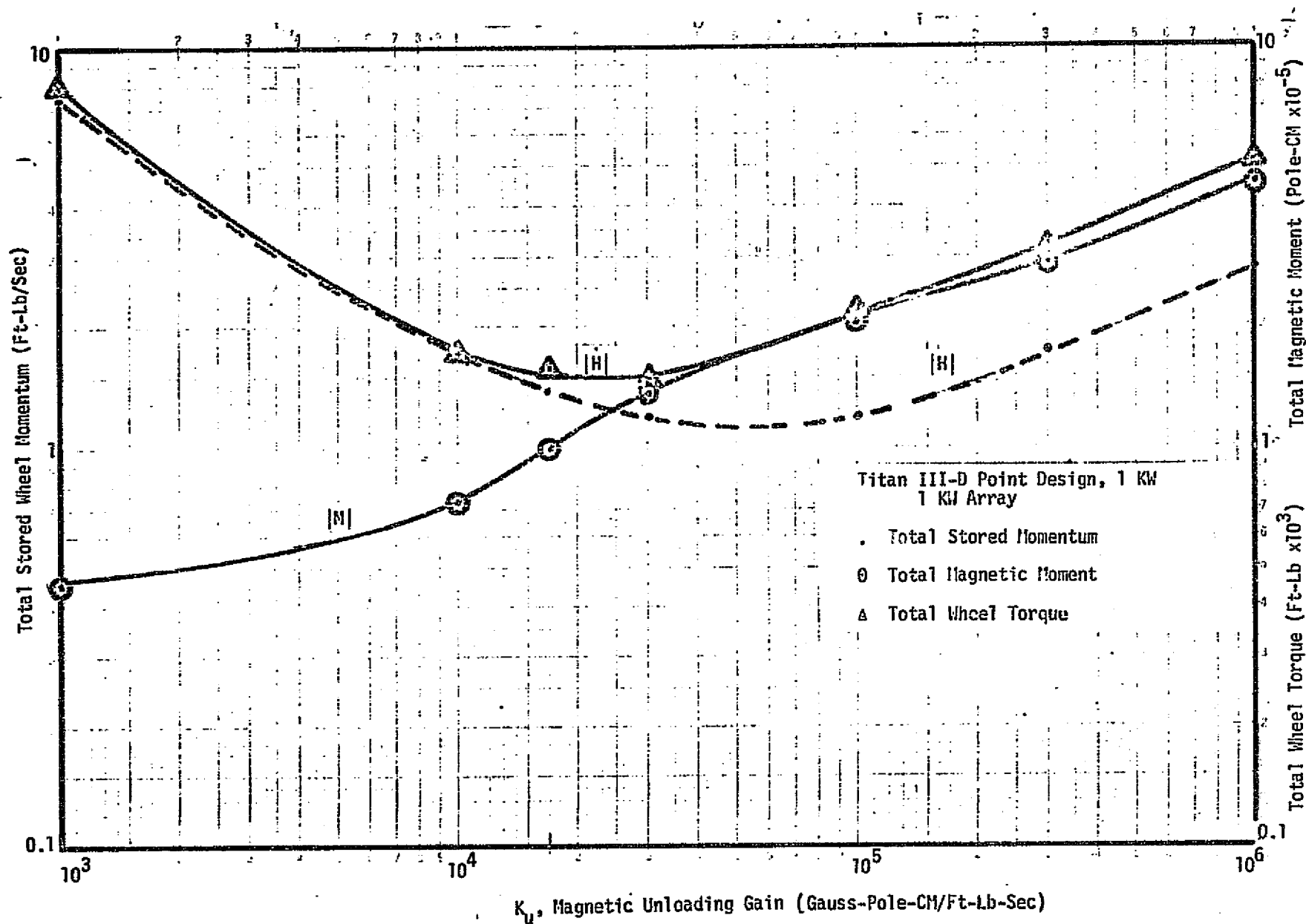


Figure 5-115. Titan III-D Wheel/Magnetic Requirements, 1 KW Array

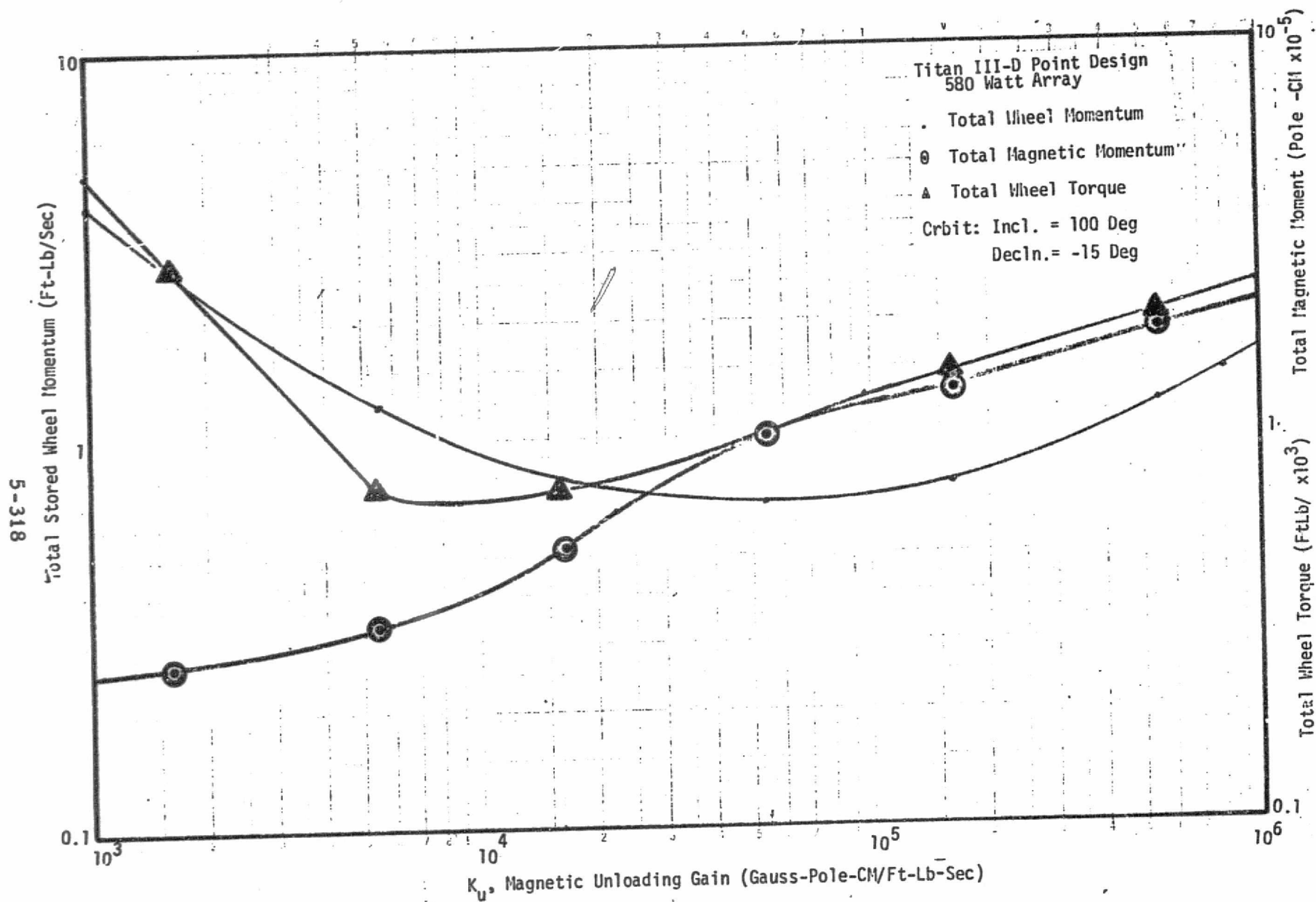


Figure 5-116. Titan III-D Wheel/Magnet Requirements, 580 Watt Array

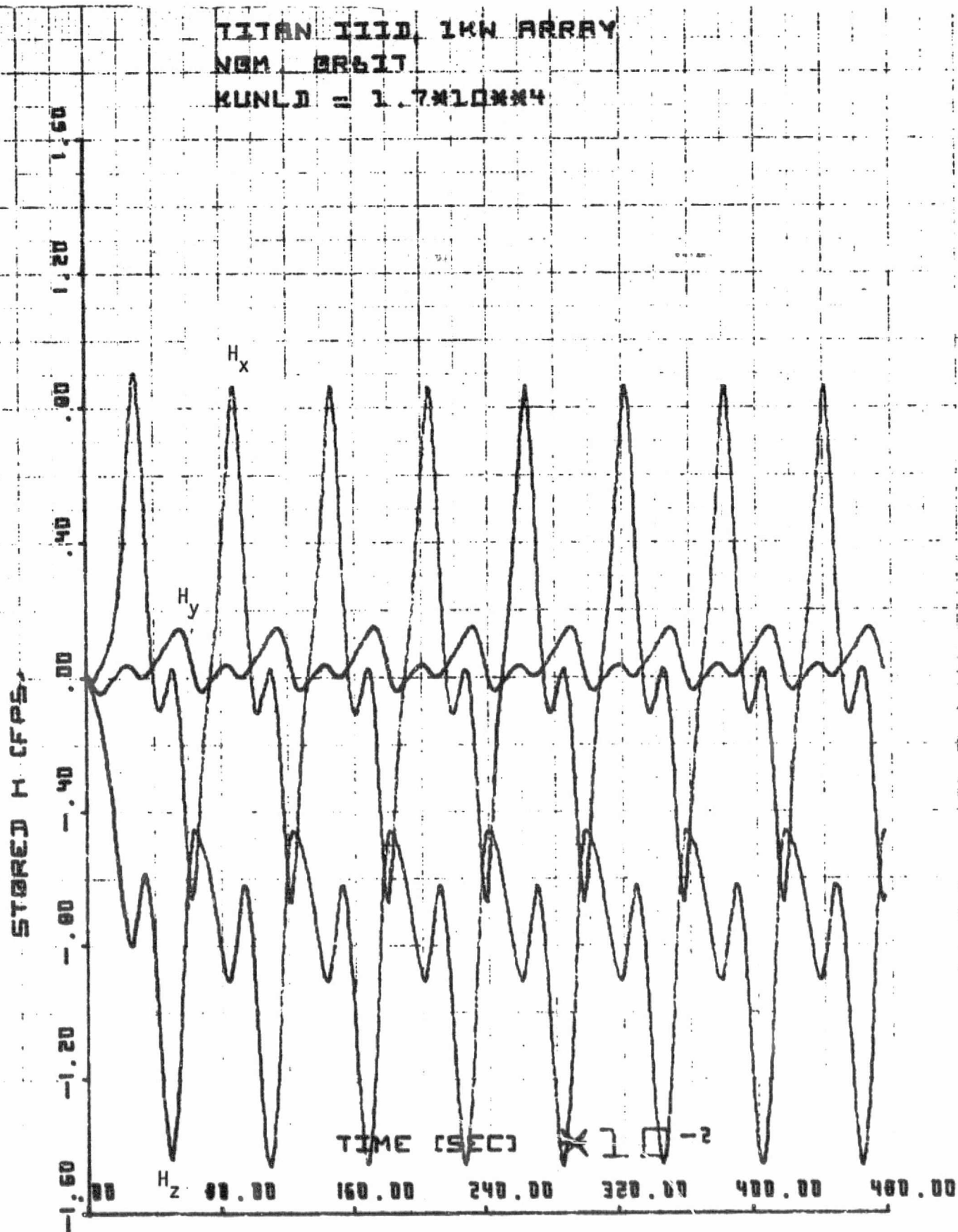


Figure 5-117. Nominal Titan III-D Wheel Response, 1 KW Array

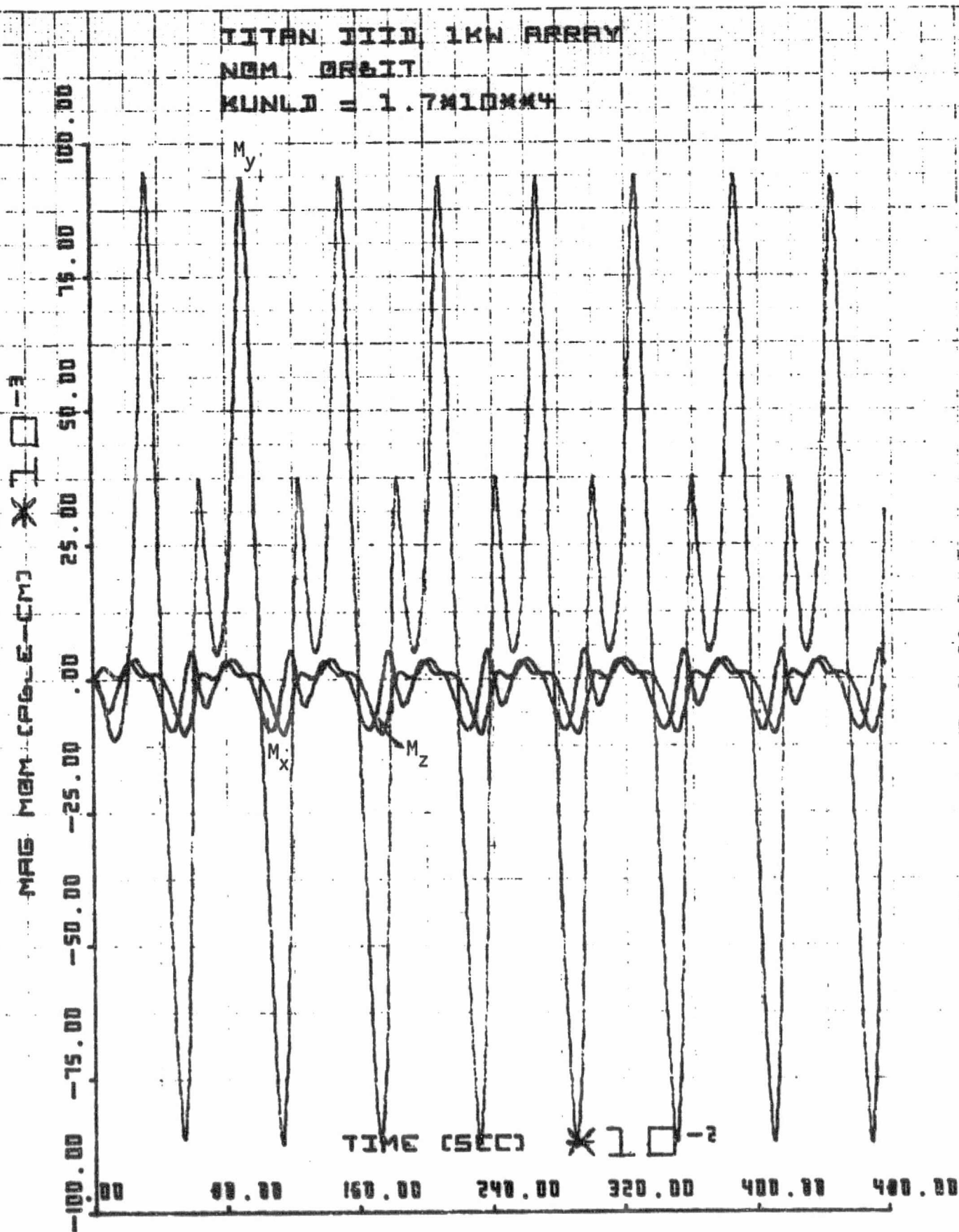


Figure 5-118. Nominal Titan III-D Magnet Response, 1 KW Array

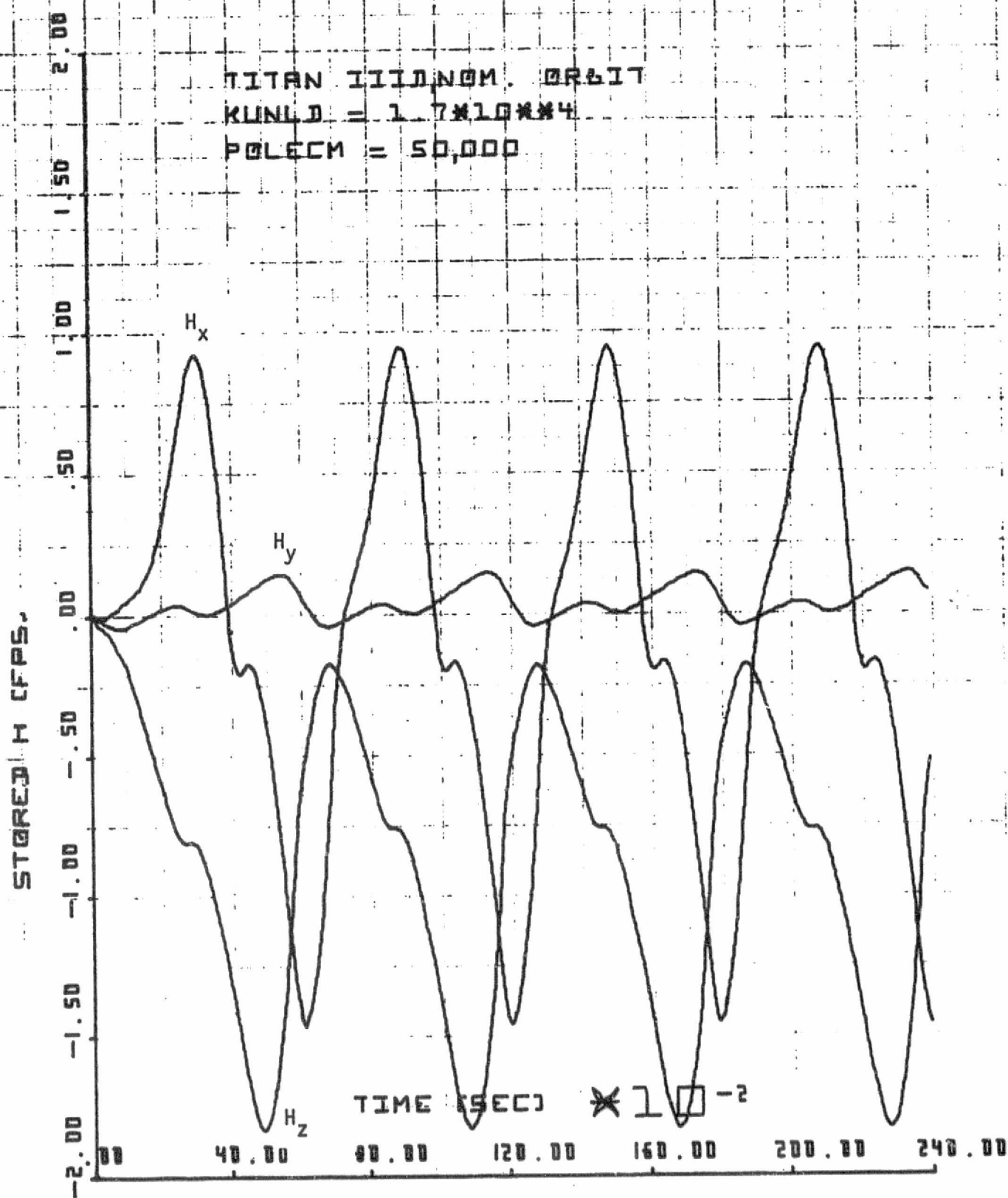


Figure 5-119. Wheel Response For Nominal Titan III-D Design  
 With 50K (Pole-CM) Magnets



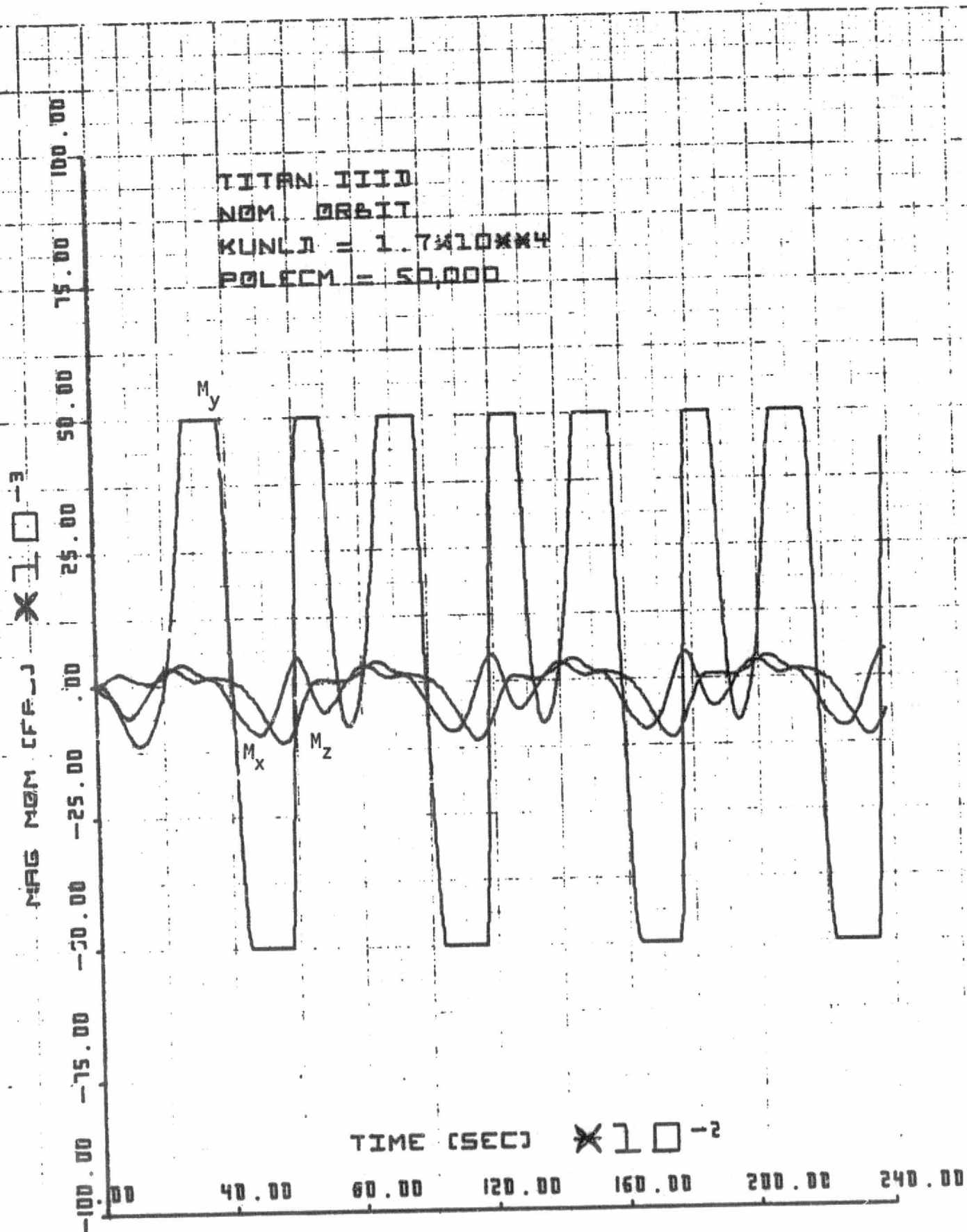


Figure 5-120. Magnet Response For Nominal Titan III-D Design With 50K (Pole-CM) Magnets

### 3. Titan III-D, 494 N.M. Altitude

#### Orbit/Disturbance Torques

The second Titan orbit considered is described as follows:

- Attitude 494 N.M.
- Sun-synchronous
- Inclination 99.15 deg
- Right ascension of ascending node 345 deg

During this orbit the spacecraft is earth pointed.

The environment/disturbance torques for this orbit are given in Figure 5-121. The large roll disturbances are the result of gravity gradient torques. At an orbit position of approximately 160 deg,  $I_{xz} = 270 \text{ slug-ft}^2$ . Note that this configuration was considered with a 1 KW solar array.

The disturbance torques of Figure 5-118 may be approximated by

$$\begin{aligned} T_{dx} &= 4.325 \times 10^{-4} - 6.05 \times 10^{-4} \cos(\omega_0 t + 20) \\ T_{dy} &= 2.250 \times 10^{-4} \sin(\omega_0 t - 20) \\ T_{dz} &= -1.414 \times 10^{-4} \sin \omega_0 t - 2.0 \times 10^{-4} \sin 2 \omega_0 t \end{aligned} \quad (30)$$

#### Reaction Wheel/Magnet Sizing/Performance

Figure 5-122 gives the wheel momentum, wheel torque, and magnet requirements as a function of the unloading gain. The minimum wheel momentum is obtained for an unloading gain of  $7.5 \times 10^{-4}$  (gauss-pole-cm/ft-lb-sec) with corresponding wheel torque and magnetic moment requirements of  $1.4 \times 10^{-3}$  ft-lb and 155 K pole-cm, respectively.

Figures 5-123 and -124 give the wheel and magnet time responses for the unloading gain of  $7.5 \times 10^{-4}$  (gauss-pole-cm/ft-lb-sec). The magnetic moment requirements may be reduced by selecting a smaller unloading gain, say  $1.7 \times 10^{-4}$  (gauss-pole-cm/ft-lb-sec) for a 100 K pole-cm magnetic moment requirement.



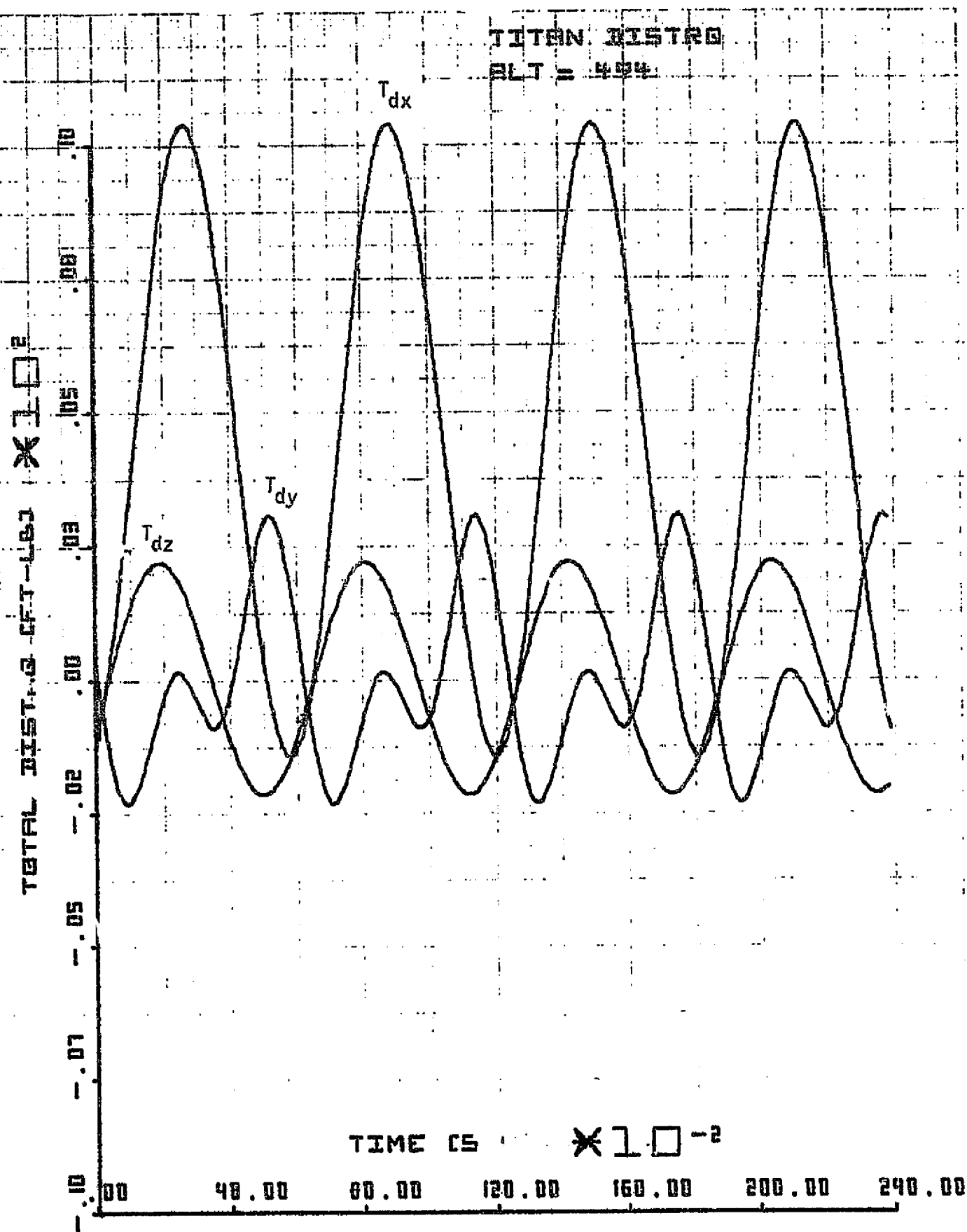


Figure 5-121. Titan Disturbance Torques, 494 N.M. Orbit

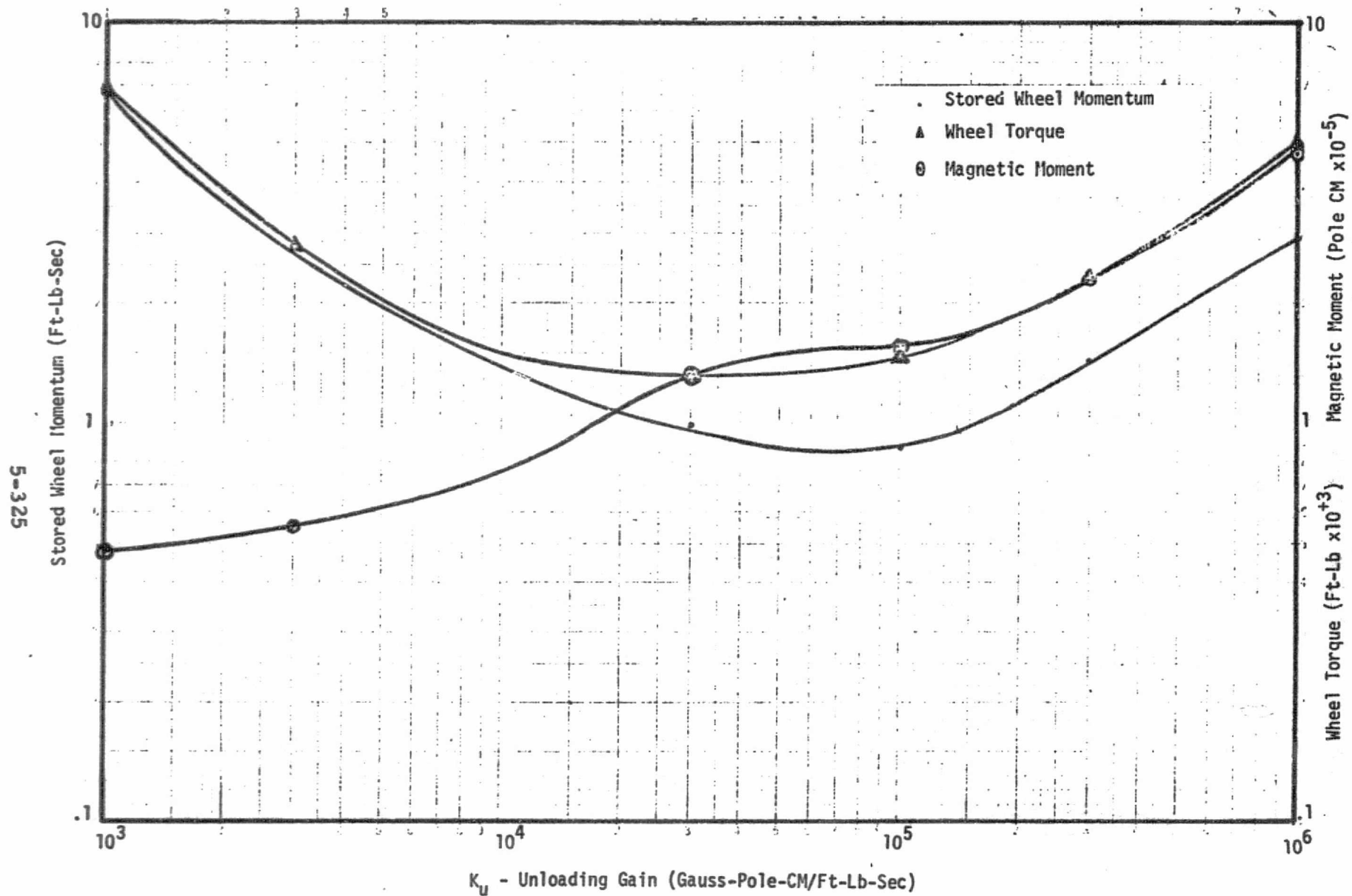


Figure 5-122. Reaction Wheel/Magnet Requirements for Titan Spacecraft 494 N.M. Orbit

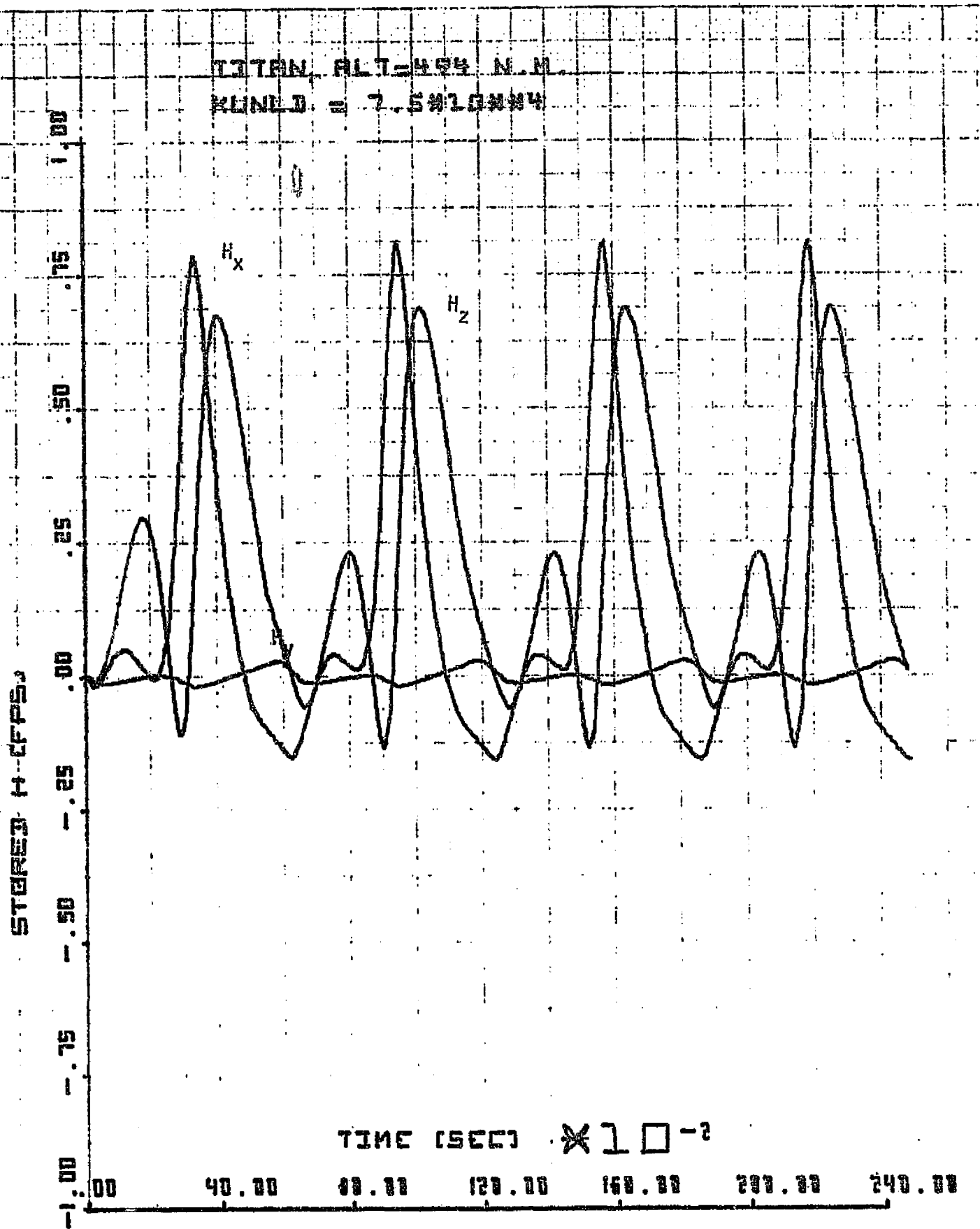


Figure 5-123. Reaction Wheel Response, Titan III, 494 N.M. Orbit

TITAN, ALT = 494  
 KUNL II = 7.510214

MAGNET RESPONSE - GMS  $\times 10^{-3}$

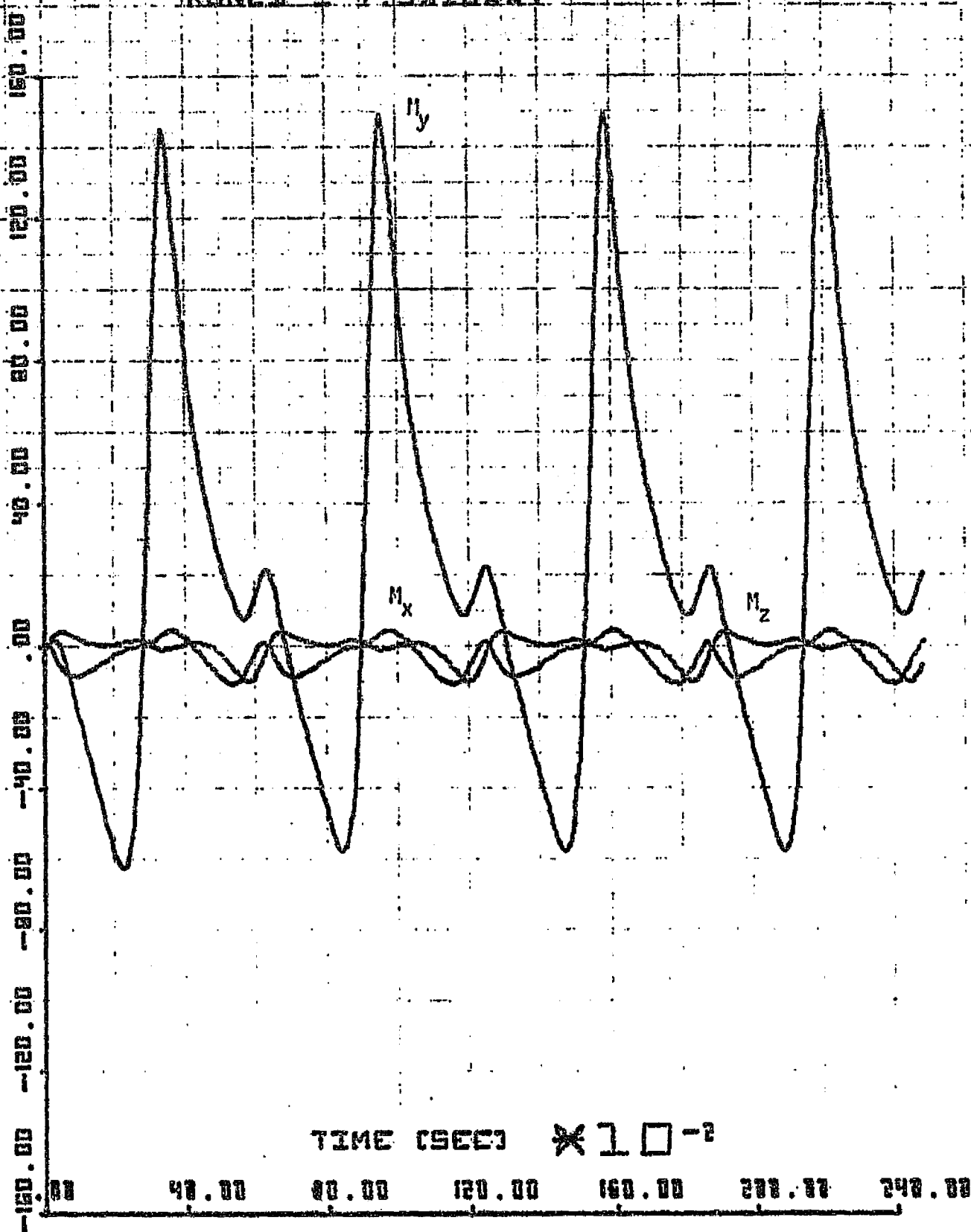


Figure 5-124. Magnet Response, Titan III-D, 494 N.M. Orbit

### b. Internal Disturbances

Based on a preliminary allocation of attitude errors, .15 arc seconds of rms jitter ( $1\sigma$ ) have been allocated to the attitude control system and .3 arc seconds to the structure (which is interpreted here as including the experiments). Errors of this magnitude correspond to .6 and 1.2 arc seconds (zero-to-peak  $3\sigma$ ) of sinusoidal oscillation, respectively. Jitter here is defined loosely as rotational oscillations of the attitude determination module at frequencies exceeding the control system band pass of .1 hz. Thus, the requirements on spacecraft jitter are interpreted as follows:

<u>Jitter Source</u>	<u>Zero-to-peak <math>3\sigma</math> Rotations of the Attitude Determination Module</u>
Attitude Control and Solar Array Drive Motions	< .6 sec
Experiment and Antenna Motions	<1.2 sec

Using these requirements as a yardstick, disturbances due to moving parts on the Thor-Delta observatory were assessed. Conclusions are as follows:

<u>Jitter Source</u>	<u>Conclusion</u>
Low level thrusters Reaction wheels Dish antennas Rate gyros	No problems
HRPI TM	Potential specification exceedance in Roll if mirror motions are synchronized to spacecraft modes, particularly the primary torsion mode. More detailed dynamic modelling is required to confirm this. Potential solution is to make greater use of momentum compensation in experiments. Vibration isolation of particular moving parts is probably not feasible. The Hughes TM, without added momentum compensation, is unacceptable.

Jitter  
Source

Conclusion

Solar  
Array  
Drive

Potentially serious specification exceedance in Roll due to bend in array boom. Disturbances in Pitch and Yaw are acceptable. Problem is minimized by using small (i.e.,  $\approx .001^\circ$ ) solar array drive stepsize or by using a continuous drive. Problem can be alleviated by straightening solar array boom or minimized by altering boom configuration so that the array mass center lies on the drive axis.

In general, problems arise only about the roll axis. This is due to three items: 1) The roll axis is the axis of minimum inertia. 2) The oscillation axes for experiment mirrors is also the roll axis. 3) The bend in the solar array boom produces pitch/roll coupling when the boom lies parallel to the observatory pitch-yaw plane. Table 5-40 lists calculated values of jitter and specifies assumptions on which they're based.

In summary, the inducement of even small vibrations in the solar array (i.e., those induced by an instantaneous  $.001^\circ$  step) will induce roll oscillations of about 1 arc second. This suggests that the present solar array boom configuration requires further study. Other potential disturbance sources are parts of the TM and HRPI. Momentum compensation can be used to render them acceptable.

Table 5-40. On-Orbit Jitter of the Attitude Determination Module  
(Thor-Delta Version of EOS-A)

Disturbance	Jitter (Max. or $3\sigma$ ) Arc-Seconds (Zero-to-Peak)			Assumptions
	Roll $\theta_x$	Pitch $\theta_y$	Yaw $\theta_z$	
1 Minimum Impulse of Thrust	.13	.06	.06	.050 sec; .050 lbf; $\zeta = 0$ ; Array & body flexible; worst-case thrust direction
Reaction Wheel:				
Static Imbalance	.003	.009	.009	Single wheel; $5 \times 10^{-5}$ in-oz imbalance; $\zeta = .001$ ; Synchronized to 1st main body bending frequency
Dynamic Imbalance	.001	.009	.009	Single wheel; $5 \times 10^{-4}$ oz-in <sup>2</sup> imbalance; $\zeta = .001$ ; Synchronized to 1st main body bending frequency
Solar Array Drive	0.1	.003	.006	"Continuous Drive"
Rate Gyros	--	--	--	Gyros are balanced even better than reaction wheels; Floated gyros permit spin about CM and principal axis; Frequency 4000 hz
Dish Antennas	.09	.12	--	Single .0315° Step; Stepping rate varies from 0 to 21 hz. Potential for resonance unexplored.
HRPI (Te)				
Wheel & Compensation	.12	--	--	Wheel spins at 1 hz; Static Balance < .02 in-oz; Dynamic Balance < .3 oz-in <sup>2</sup>
Oscillating Mirror	.21*	--	--	2 lb Mirror; 4" dia.; 18 hz sinusoidal oscillation; 1 hz separation between excitation and torsion mode frequency
Pointing Mirror	.16	--	--	60° Sweep; 70 lb, 24" dia. mirror; < 1.12 in-oz static imbalance; non-oscillatory
HRPI (Westinghouse)				
Pointing Mirror	.16	--	--	60° Sweep; 70 lb, 24" dia. mirror; < 1.12 in-oz static imbalance; non-oscillatory
TM (Te)				
Wheel & Compensation	.12	--	--	Wheel spins at 1 hz; Static Balance < .02 in-oz; Dynamic Balance < .3 oz-in <sup>2</sup>
Oscillating Mirror	.21*	--	--	2 lb Mirror; 4" dia; 18 hz sinusoidal oscillation; 1 hz separation between excitation and torsion mode
TM (Hughes)				
Primary Mirror	7.8	--	--	.25 in-lb-sec <sup>2</sup> Mirror inertia; No momentum compensation; Drive Frequency 9.8 hz; Torsional Mode @ 13 hz
Compensation Mirror	.21*	--	--	2 lb Mirror; 4" dia; 9.8 hz sinusoidal oscillation; 1 hz separation between excitation and torsion mode
TX (Honeywell)				
Wheel & Compensation	.2	--	--	Wheel spins at 2.1 hz; Static Balance < .016 in-oz; Dynamic Balance < .05 oz-in <sup>2</sup>

\*If perfect resonance were assumed with  $\zeta = .001$ , these roll errors would be 11.5 arc seconds. In this case, momentum compensation would be required.

ORIGINAL PAGE IS  
OF POOR QUALITY

#### 5.2.4.2 Normal and Slew Mode Design

##### 5.2.4.2.1 Task Statement

Normal and slew mode reaction wheel control system loops to satisfy EOS-A requirements for both the Thor-Delta and Titan launched configurations were designed. Appropriate loop parameters (including gains, shaping, etc.) were defined.

##### 5.2.4.2.2 Motivation

In order to demonstrate the feasibility of satisfying the performance requirements imposed by the EOS-A mission, a typical normal and slew mode reaction wheel control system is synthesized.

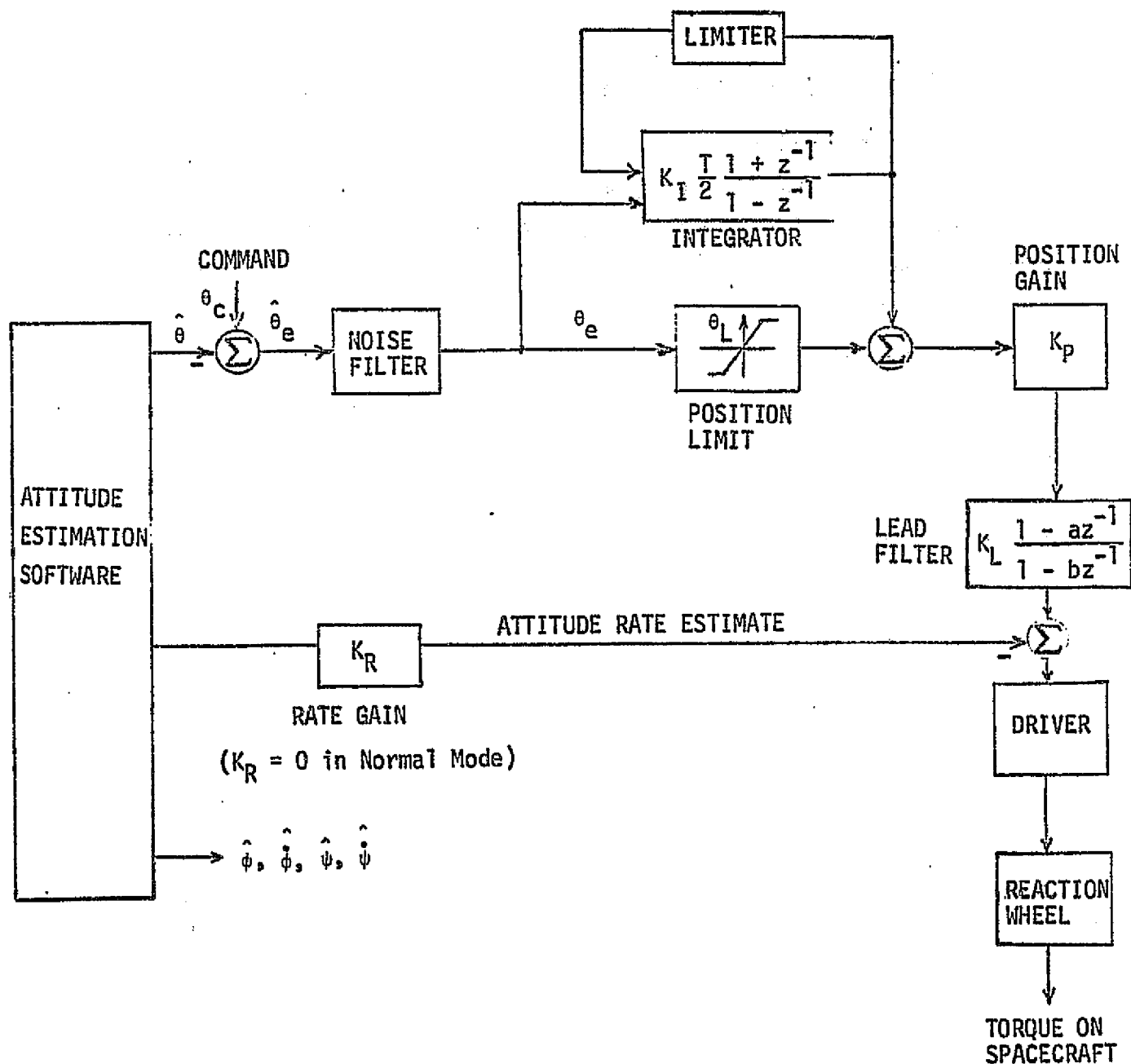
##### 5.2.4.2.3 Methodology

Standard sampled data techniques are used to select the controller parameters to design a loop with reasonable response characteristics. A design goal of a loop with 0.6 damping ratio and cutoff frequency of 0.1 hz is synthesized. Nonlinear simulation is used to evaluate dynamic performance.

##### 5.2.4.2.4 Results

The reaction wheel control laws are illustrated in Figure 5-125. The control law is a digital implementation of proportional-plus integral-plus-rate control. In the normal mode of operation the attitude rate estimate is not used in order to reduce noise amplification, while in the slew mode the input and output of the integrator loop is set to zero. The integrator is utilized in the normal mode in order to eliminate constant position "hangoff" errors associated with wheel controllers. Trapezoidal integration is implemented. A digital lead filter is used to approximate rate and add phase margin to the linear system. The position limit is used to implement rate limiting during the slew mode. The rate of slew will be  $\geq 2.0$  degrees per minute.





The Reaction Wheel Control Laws are implemented in the On-Board Computer, and employ conventional proportional-plus-integral-plus rate control in each axis. In Normal Mode Operation  $K_R = 0$  and in the Slew Mode  $K_I$  is set to zero. Rate limiting in the slew mode is implemented by suitably selecting  $\theta_L$  and  $K_R$ . Since the control of relative rather than absolute error is sometimes of prime importance, provision for a non-zero attitude command is included. Also shown is a noise filter for limiting attitude rate excursions.

Figure 5-125. Reaction Wheel Control Laws

The wheel control laws are essentially the same for the pitch, yaw and roll axes, with the position and rate gain both normalized by the respective inertia axis. Although the reaction wheel characteristics may be square law, in order to utilize linear analysis techniques, the transfer function is approximated by a constant gain which when combined with the "driver gain" results in unity gain. The three axes are considered to be uncoupled with each other and with the magnetic momentum unloading system. With the control model described above, standard sampled data techniques are used to select the controller parameters to design a loop with reasonable response characteristics.

a. Frequency Domain Investigation

A linear stability analysis of the one axis reaction wheel control system is considered in this section. The combined analog-digital control system is displayed in Figure 5-126. For normal mode operation standard sampled data techniques are used to design a loop with a damping ratio of 0.6 and cutoff frequency of 0.1 hz. Note that  $K_R$  is set to zero during this mode to reduce noise amplification. For slew mode operation the integrator loop gain  $K_I$  is set to zero. The values of  $K_R$  and the position limit  $\theta_L$  are chosen in order to realize a slew rate of .05 degrees per second. The evaluation of  $K_R$  is based upon the nonlinear characteristics of the control system.

NORMAL MODE

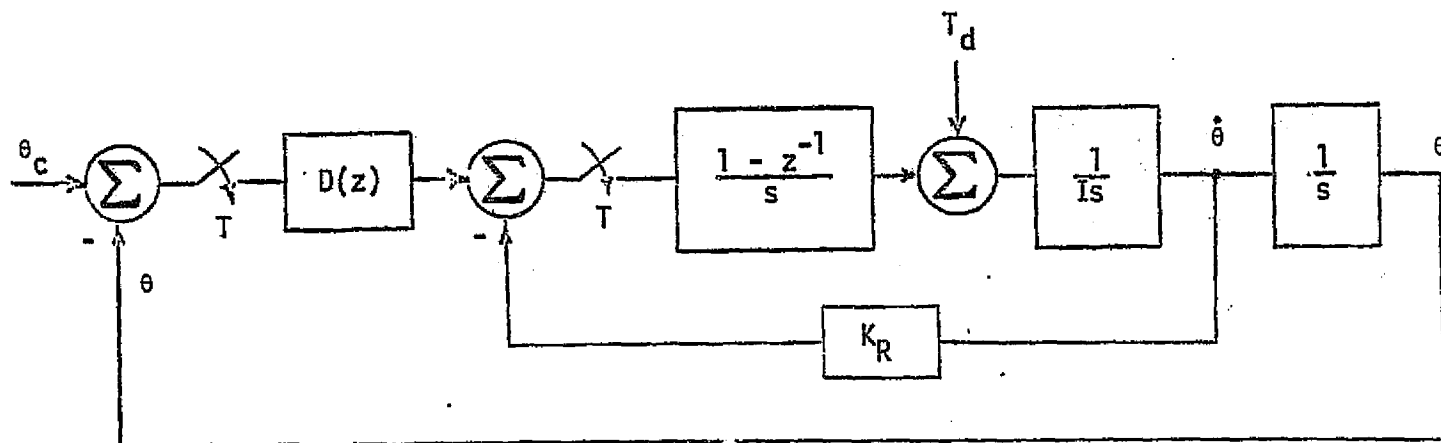
Making the rate gain zero, the closed loop transfer function is derived in Figure 5-127. Although the open loop transfer function is developed in the z domain, the open loop w-plane frequency responses for nominal  $K_I$  and zero  $K_I$  are displayed in Figure 5-128. The w-domain is a bilinear transformation of the z-domain where

$$z = e^{sT} \qquad z = \frac{1 + w}{1 - w}$$

The frequency in the s and w plane is related by the equation

$$\omega = \frac{2}{T} \tan^{-1}(V)$$

where  $\omega$  is the frequency in the s plane and  $V$  is the frequency in the w plane.



$T \triangleq$  SAMPLE PERIOD  
 $\theta_c \triangleq$  COMMANDED ATTITUDE

#### SAMPLED DATA FILTER

$$D(z) = \left[ 1 + K_I \frac{T}{2} \frac{(1 + z^{-1})}{(1 - z^{-1})} \right] K_P K_L \frac{(1 - az^{-1})}{(1 - bz^{-1})} z^{-1}$$

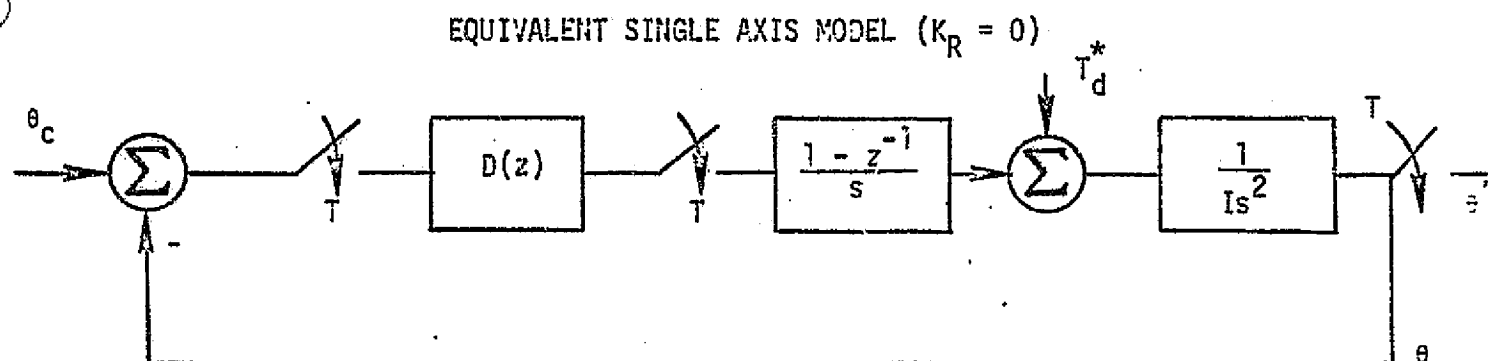
$K_P \triangleq$  Position Gain  
 $K_L \triangleq$  Lead Filter Gain  
 $K_I \triangleq$  Integrator Gain

#### DISTURBANCE TORQUE

$$T_D = \left. \begin{aligned} &A_0 + A_1 \sin \omega_0 t + A_2 \cos \omega_0 t \\ &+ B_1 \sin 2\omega_0 t + B_2 \cos 2\omega_0 t \end{aligned} \right\} \text{GENERAL FORM}$$

$\omega_0 \triangleq$  Orbit Rate  
 $I \triangleq$  Axis Inertia

Figure 5-126. Single Axis Model of Wheel Controller



CLOSED LOOP TRANSFER FUNCTION

$$\theta(z) = \frac{D(z) G(z) \theta_c(z) + G(z) T_D(z)}{1 + D(z) G(z)}$$

where

$$G(z) = z \left\{ \frac{1 - z^{-1}}{Is^3} \right\} = \frac{T^2}{2I} \frac{(z + 1)}{(z - 1)^2}$$

$$D(z) = K_P K_L (1 + K_I \frac{T}{2}) \frac{(z - c)(z - a)}{z(z - 1)(z - b)}$$

$$c \triangleq (1 - K_I T/2)/(1 + K_I T/2)$$

OPEN LOOP TRANSFER FUNCTION

$$D(z) G(z) = K_P' K_L (1 + K_I \frac{T}{2}) \frac{T^2}{2} \frac{(z - c)(z + 1)(z - a)}{z(z - 1)^3(z - b)}$$

$$K_P' \triangleq K_P / I$$

RESPONSE CHARACTERISTICS

$$\lim_{n \rightarrow \infty} \theta(n) = \lim_{z \rightarrow 1} (z - 1) \theta(z) \quad \left\{ \begin{array}{l} \text{If } \theta_c \text{ or } T_D \text{ are constant} \\ \text{then } \theta(n) \rightarrow 0. \end{array} \right.$$

Figure 5-127. Normal Mode Transfer Function

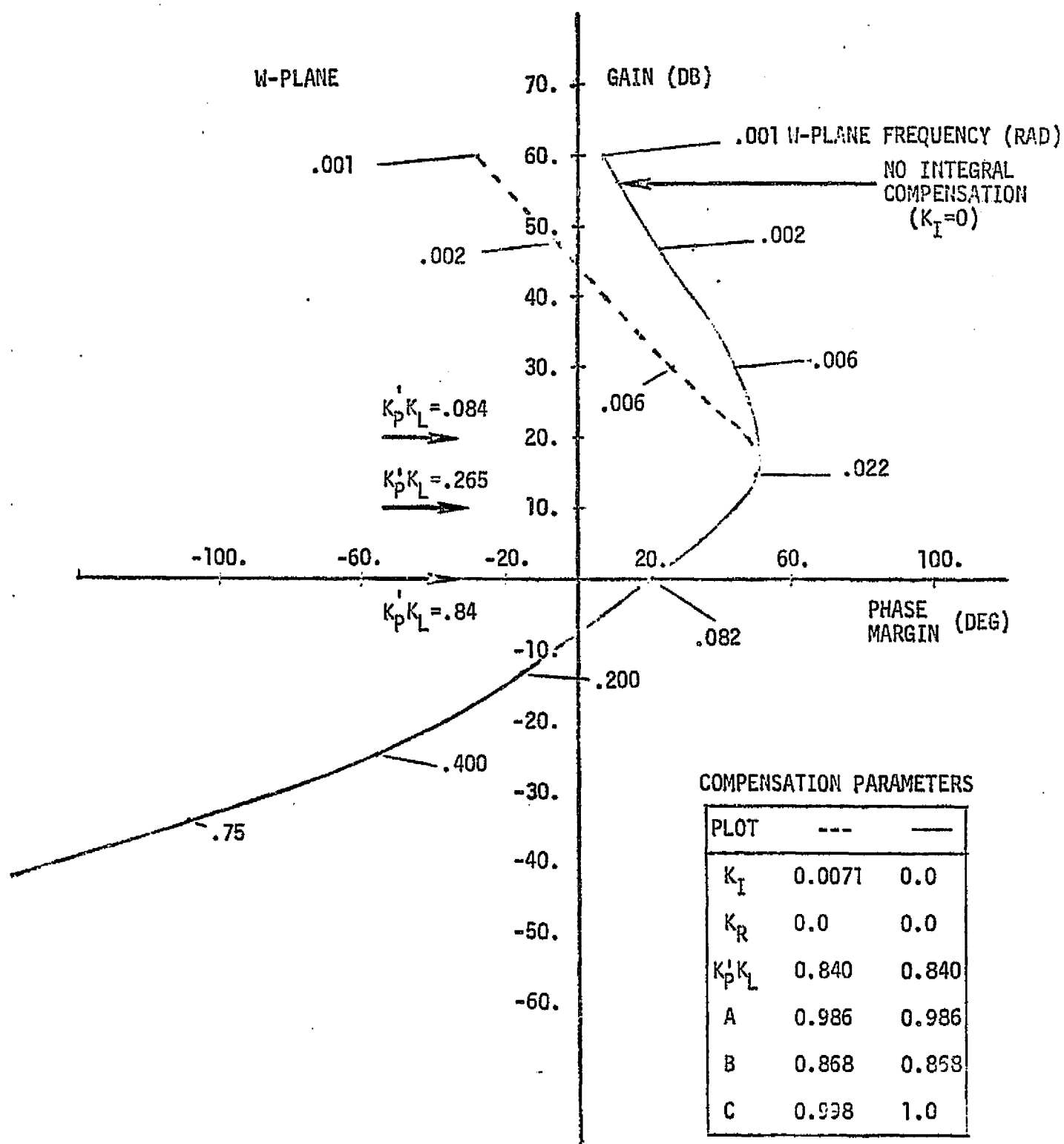


Figure 5-128. W Plane Open Loop Frequency Response for the Single Axis Wheel Controller

Both frequency responses indicate system stability for a wide range of gains. The nominal gains which result in the desired closed loop response characteristics are indicated. In both plots the normalized position gain can be changed by shifting the zero db line. The frequency characteristics are independent of the position gain. In both cases a one sample period computational delay is assumed.

The filter parameters and spacecraft mass properties are summarized in Table 5-41. The gains for any one axis can be obtained by multiplying the normalized gains with the axis inertia. In the linear region this filter yields a closed loop damping ratio of 0.6 with the cutoff frequency (-3 db) approximately 0.1 hz. Environmental disturbance torques for both the Titan III and Delta launch vehicle configurations are also summarized in Table 5-41. The internal disturbances caused by the solar array drive are not unusually large and therefore neglected. The system response to both position commands and nominal disturbance torques are considered in Section 2.4.2. Since the highest frequency component in the disturbance torques is twice orbit rate, the disturbance torque is approximately constant relative to the fast responding control system.

#### SLEW MODE

The major requirement of single axis rotations, slew mode, is that the slew rate is sufficiently large, i.e.,

$$K_R/K_P \triangleq |\dot{\theta}_L|/|\dot{\theta}|$$

$$K_R/K_P = \frac{.5 \text{ degree}}{.05 \text{ degree/sec}} = 10 \text{ sec}$$

This rate gain results in a lightly damped system which is desirable since the control system should not respond to rate noise disturbances. The breakaway point from constant rate is defined by  $\theta_L$ . When the attitude and attitude rate errors are sufficiently small, the rate gain is set to zero and the integrator gain is reset. This means that the response damping ratio is then approximately 0.6. Phase plane time trajectories will be presented in the simulation results section.

Table 5-41. Filter Design and System Parameters

Mass Properties

<u>Inertia</u>	<u>Delta</u>	<u>Titan</u>
$I_{xx}$ (Roll)	586 slug ft <sup>2</sup>	1504 slug ft <sup>2</sup>
$I_{yy}$ (Pitch)	1584 slug ft <sup>2</sup>	4451 slug ft <sup>2</sup>
$I_{zz}$ (Yaw)	1862 slug ft <sup>2</sup>	4864 slug ft <sup>2</sup>

Control Filter Parameters (Roll, Pitch and Yaw)

Sample Period -  $T = 0.2$  sec

Normalized Position Gain -  $K_p K_L / I = 0.84$

Integrator Gain -  $K_I = \begin{cases} 0.0071 & \text{Normal Mode} \\ 0.0 & \text{Slew Mode} \end{cases}$

Lead Filter Zero -  $a = \begin{cases} 0.986 & \text{Normal Mode} \\ 0.0 & \text{Slew Mode} \end{cases}$

Lead Filter Pole -  $b = \begin{cases} 0.8678 & \text{Normal Mode} \\ 0.0 & \text{Slew Mode} \end{cases}$

Normalized Rate Gain -  $K_R / I = \begin{cases} 0.0 & \text{Normal Mode} \\ 10.0 & \text{Slew Mode} \end{cases}$

Position Limit -  $\theta_L = 0.5$  degrees

Environmental Disturbance Torques (External)

Titan Configuration

$$T_{dx} = 4.75 \times 10^{-4} + 6.25 \times 10^{-4} \sin(\omega_0 t - 60^\circ) \text{ ft-lbs}$$

$$T_{dy} = 1.0 \times 10^{-4} - 3.0 \times 10^{-4} \sin 2\omega_0 t$$

$$T_{dz} = -6.75 \times 10^{-4} + 2.0 \times 10^{-4} \sin \omega_0 t + 5.75 \times 10^{-4} \cos 2\omega_0 t$$

Delta Configuration

$$T_{dx} = 5.0 \times 10^{-4} - 5.0 \times 10^{-4} \cos \omega_0 t + 4.5 \times 10^{-4} \sin 2\omega_0 t$$

$$T_{dy} = 4.0 \times 10^{-4} - 4.0 \times 10^{-4} \cos 2\omega_0 t$$

$$T_{dz} = -1.9 \times 10^{-3} + .2 \times 10^{-3} \sin \omega_0 t + 1.9 \times 10^{-3} \cos 2\omega_0 t$$

### b. Time Domain Investigation

A stability analysis of the single axis reaction wheel control system was considered in the previous section. Standard sampled data techniques are used to select the controller parameters which result in a loop with reasonable response characteristics. A single axis time simulation has been developed which steps at the sampling frequency. The forward loop compensation is developed in Figure 5-126 in the z-domain. The compensation,  $D(z)$ , yields a set of linear difference equations. A closed form solution to the dynamics is easily obtained since the control and disturbance torques are essentially constant during one sample period. The simulation utilizes normalized position and rate gains and therefore the effective disturbance torque is normalized. Both normal mode and slew mode time response characteristics are considered in this section. The frequency domain analyses established filter pole and zero locations along with the total forward loop gain. The rate gain is selected for rate limiting during the slew mode.

#### NORMAL MODE

During normal mode operation the rate gain is set to zero. The open loop frequency response is illustrated in Figure 5-128. The effect of gain variations on the system's frequency response characteristics is examined by merely changing the zero DB line in those curves by an amount proportional (in DB) to the relative gain variation. This has been done for selected gain levels in Figure 5-128. The step response for each gain level is displayed in Figure 5-129. The compensation parameters, with the integrator loop closed, is tabulated in Figure 5-128. The system response to a step in the disturbance torque is displayed by the position-time trajectory of Figure 5-130. The dominant time constant is determined by the integrator rate gain  $K_I$  which is required to negate constant disturbance torques.



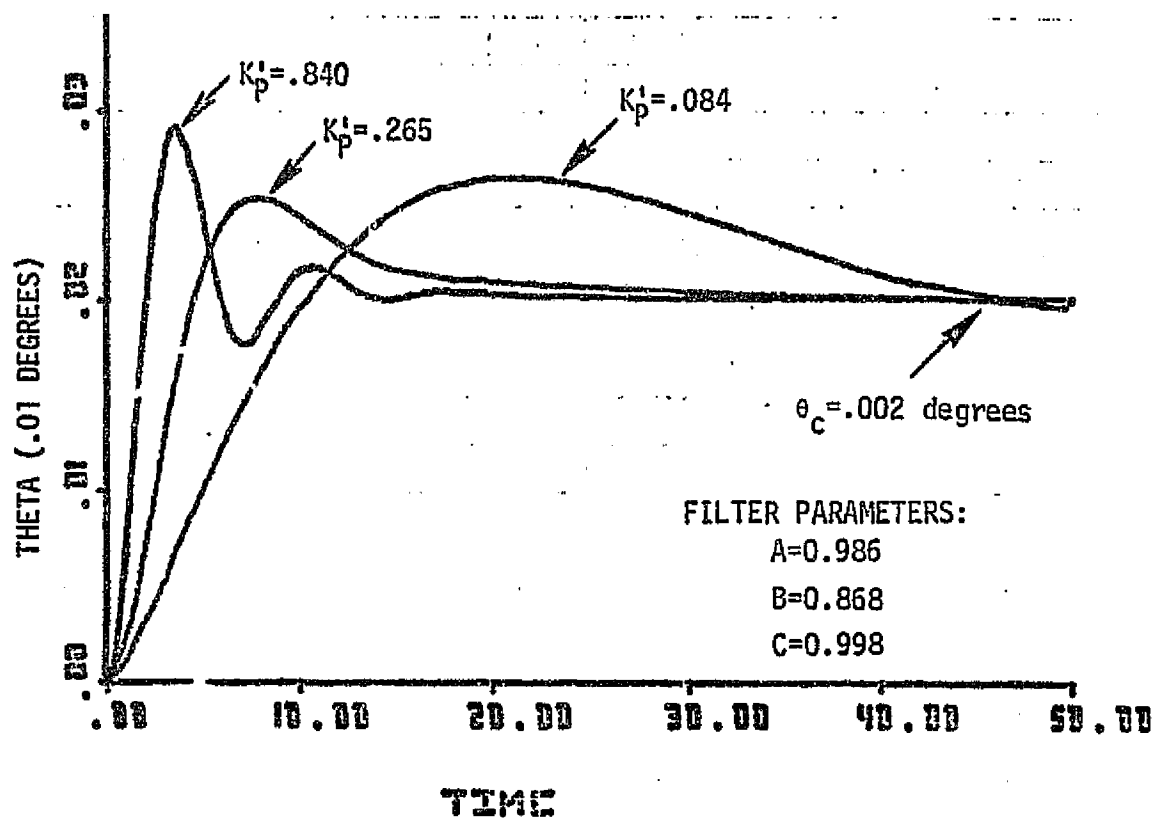


Figure 5-129. Normal Mode Time Response Characteristics  
Step Change in Commanded Position

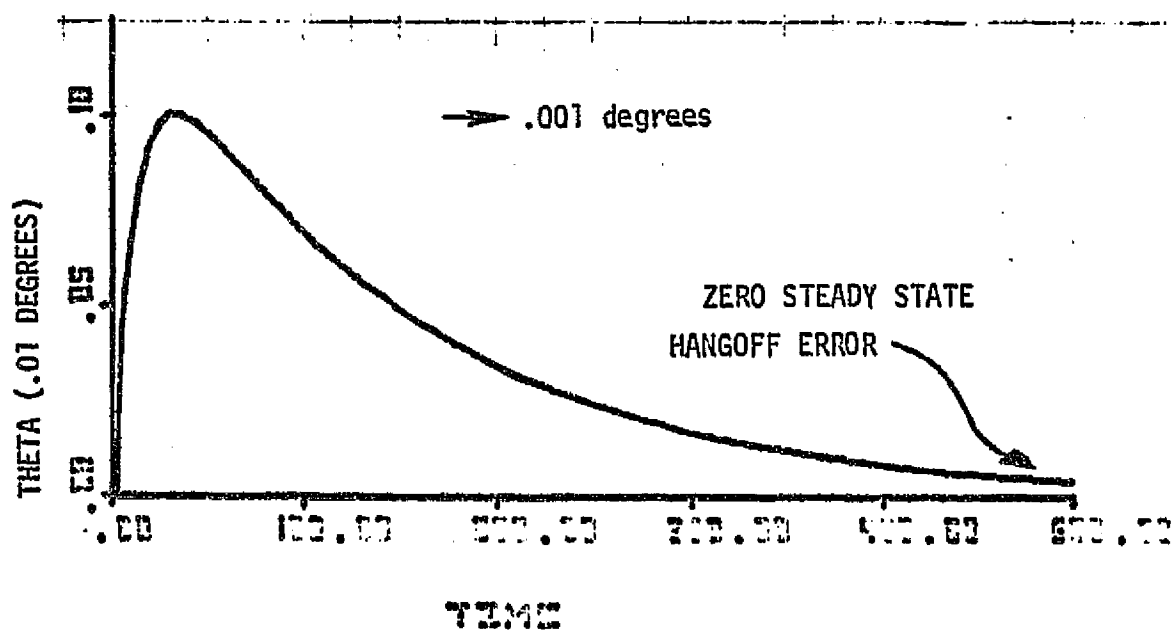


Figure 5-130. Normal Mode Time Response - Step  
Change in Disturbance Torque

### SLEW MODE

The slew rate about any one axis is required to be greater than 2.0 degrees per minute. Nominal rate limiting is selected as 0.05 degrees per second. Rate limiting is implemented by utilizing position limiting with rate feedback. The position limit  $\theta_L$  and rate gain  $K_R$  determine the rate limit. Representative slew mode operation is illustrated in Figure 5-131. The maneuver initial conditions are given by

$$\theta = 0 \text{ degrees} \quad \dot{\theta} = -0.04 \text{ deg/sec}$$

with a commanded position  $\theta_c = 5.0$  degrees. The slew maneuver terminates with  $\theta = \theta_c$  and  $\dot{\theta} = 0$ . The integrator gain is set to zero during the maneuver and the nominal rate gain is preset. When the maneuver is completed the system is returned to normal mode, i.e., the integrator gain is reset and the rate gain is set to zero. Torque is limited to a maximum of 20 in-oz. For a worst case investigation the torque limit has been normalized by the Titan yaw inertia which minimizes the control authority.

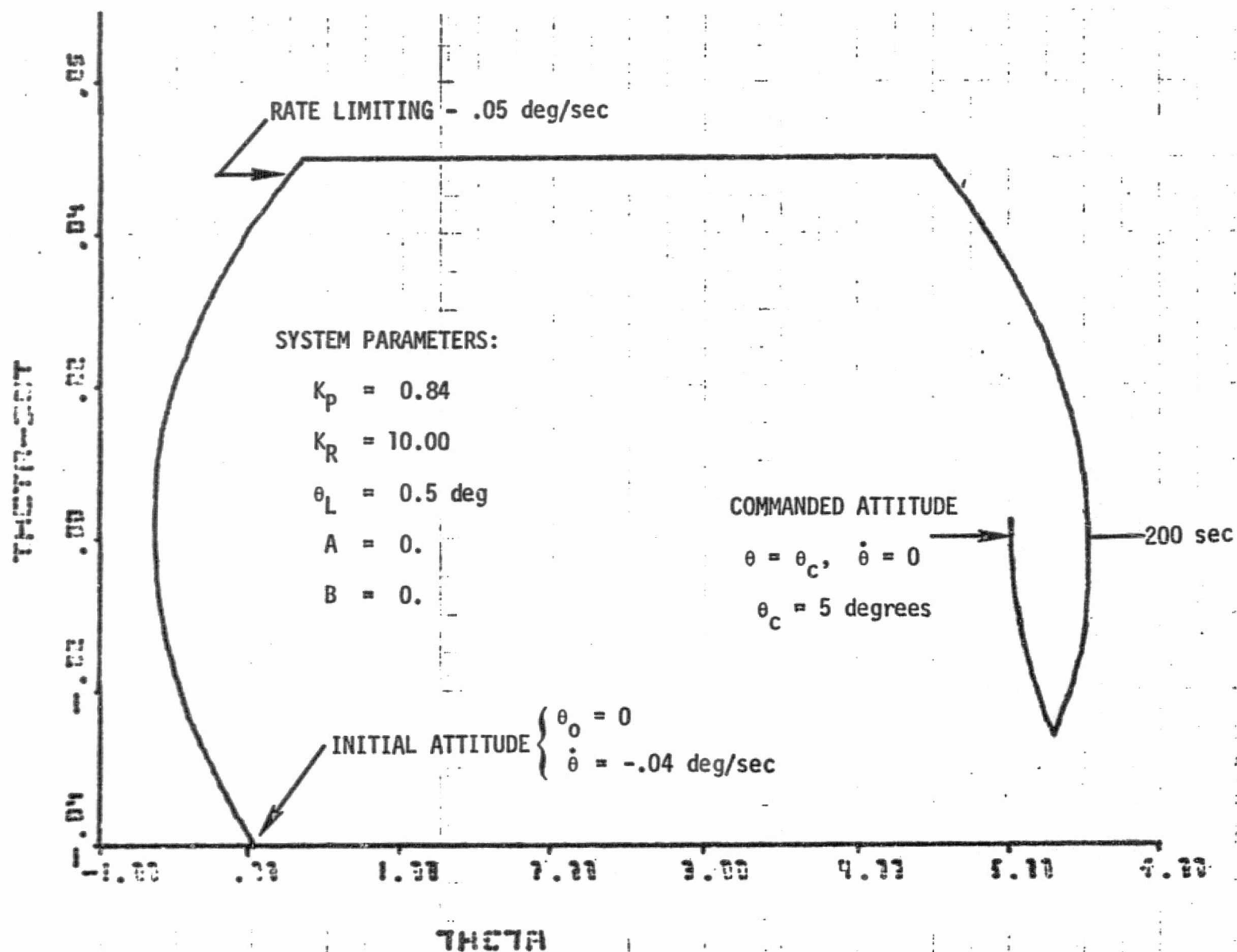


Figure 5-131. Slew Mode Phase Plane Trajectory

#### 5.2.4.3 Thruster Controlled Mode Design

##### 5.2.4.3.1 Task Statement

Design control loops for thruster controlled modes for both primary and backup acquisition, orbit adjust, and transfer orbit operation to satisfy EOS-A mission using Thor-Delta and Titan launched vehicles. Select controller parameters including gains, shaping, thrust level, etc. Evaluate control loop performance and review the feasibility of using unloading magnetics for acquisition.

##### 5.2.4.3.2 Motivation

The examination of several techniques to accomplish acquisition and attitude control during various maneuvers is important to the selection of viable primary and alternate control methods. Demonstration of the adequacy of a system with and without gyros, limited field-of-view sensors, etc. will aid in the selection of a simple, modular design to satisfy EOS-A mission objectives.

##### 5.2.4.3.3 Methodology

Standard linear techniques are used to establish preliminary controller parameters. Performance evaluation is by nonlinear simulation to demonstrate compliance with various requirements imposed by the EOS-A mission.

##### 5.2.4.3.4 Results

For each of the two thruster modes of operation, primary and backup, there is a set of specifications. The primary mode control system, which makes use of the on-board gyros, is required to maintain the attitude of the spacecraft within  $\pm 2$  deg of sun pointing and the body rates within  $\pm 0.03$  deg/sec. The backup or "safe" mode control system must function without gyro inputs (to allow for the possibility of gyro failure), and it must maintain spacecraft attitude within  $\pm 7$  deg of sun pointing.

Analytical and simulation studies indicate that all of the above specifications are met by the proposed control system designs. For the Thor-Delta EOS configuration, initial sun acquisition using the primary control system is accomplished within 230 sec from initial attitude and 1 deg/sec initial

rate about each body axis. During this time 19.1 lb-sec of thruster impulse is required. Within the next 370 sec (total 600 sec), only 0.4 lb-sec additional impulse is required to maintain sun pointing (total 19.5 lb-sec).

For the Titan EOS configuration, sun acquisition using the primary mode control system takes 350 sec and requires 66.8 lb-sec thruster impulse. During the next 650 sec (total 1000 sec), impulse requirements are only 0.9 lb-sec more (total 67.7 lb-sec).

In the backup mode with the Thor-Delta configuration, 455 sec is required to acquire the sun using the same initial conditions. 75.7 lb-sec thruster impulse is expended within this period. During the following 745 sec (total 1200 sec), 4.3 lb-sec additional impulse is required (total 80.0 lb-sec).

Backup mode sun acquisition with the above initial conditions for the Titan configuration fails to acquire the sun. Instead, the spacecraft tumbles indefinitely, expending more thruster propellant each time the sun passes through the sun sensor field-of-view. This problem can be resolved by giving more control authority to the roll system. For instance, if the roll thrusters are increased in size from 0.05 lb to 0.5 lb, then the Titan backup control system easily acquires the sun in 200 sec (187 lb-sec impulse).

When the spacecraft's view of the sun is eclipsed, control system activity is inhibited, due to loss of attitude reference from the sun sensor. Disturbance torques acting upon the spacecraft during eclipse induce undesired body rates and attitude errors which must be nulled by the primary or backup system upon regaining the sun. Under the conditions of maximum eclipse time (70 min), worst case disturbance torques (which combine to produce large rates), and worst possible attitude upon leaving eclipse, the backup mode of the Thor-Delta configuration requires 850 sec to re-acquire sun pointing. Total thruster impulse required is 91.4 lb-sec. (Primary mode would take far less time and require far less thruster impulse.) The Titan configuration has different body rates following the same eclipse, and the backup mode takes 1700 sec (160 lb-sec thruster impulse) to acquire the sun.

In the event of a major power failure in normal mode, all reaction wheels will run down, dumping their stored momenta into unwanted body rates. These rates (and resulting attitude errors) must be nulled by the backup system. Under the conditions that a maximum 7.2 ft-lb-sec wheel momentum has been dumped in each axis and the spacecraft is anti-sun pointing, the backup controller with the Thor-Delta configuration takes 570 sec and consumes 76.3 lb-sec thruster impulse during re-acquisition. With the Titan configuration, the same wheel rundown induces different body rates, and backup acquisition takes 1460 sec and requires 168 lb-sec thruster impulse.

In all cases the backup mode system response can be improved by tuning the parameters of the proposed design. This task was beyond the scope of the present preliminary investigation.

All of the above reported results are based on using high thrust (1 lb) thrusters for pitch and yaw control. When the low thrust (0.05 lb) thrusters are used in the primary mode, sun acquisition requires 200 sec (23.4 lb-sec impulse) for the Thor-Delta configuration and 520 sec (98.2 lb-sec impulse) for the Titan configuration (initial conditions are anti-sun pointing attitude and 1 deg/sec rates about each axis). The backup mode with the Thor-Delta configuration acquires the sun from the same initial conditions in 520 sec (59.4 lb-sec), but with the Titan configuration the backup mode fails to acquire (tumbles indefinitely). It is recommended that either the contemplated use of low thrust levels be abandoned or the backup mode be redesigned for such low thrust levels.

During orbit adjust, the action of the 50-lb thruster is expected to induce unwanted body torques. Under the assumptions that the spacecraft center of mass is offset 0.25 in. and the 50-lb thruster is misaligned 0.1 deg, the induced torques (about 1.6 ft-lb) will cause the control system to command pitch and yaw (1 lb) thruster pulses on approximately a 25% duty cycle basis during each orbit adjust burn. Using smaller thrusters (0.05 lb), insufficient control torque is generated and the spacecraft would be uncontrollable during orbit adjust.

All of the proposed control system designs are stable and can be implemented simply using standard hardware.

Regarding the possibility of using the normal mode unloading magnets for sun acquisition, it is noted that the EOS Titan configuration is similar in mass properties to the HEAO-A configuration, for which extensive magnetic control investigation has been performed. The HEAO study established that sun acquisition is sensitive to magnetic coupling between the electromagnets and the magnetometer, that it is impossible to generate control torques in any plane parallel to the instantaneous earth magnetic field vector, that sun acquisition would require a very long time period (up to three HEAO orbits), and that the practicality of the backup mode design (similar to the one proposed for EOS) would be significantly imperiled. For these reasons, magnetic sun acquisition is not recommended.

a. Thruster Mode General Properties

For both primary and backup modes, the attitude reference device is a sun sensor mounted along the -z-axis (yaw). The maximum field-of-view for a sensor in this location is a hemisphere ( $2\pi$  steradians); thus when the -z-axis is pointing anywhere in the other hemisphere, there is no attitude signal to be fed to the control system. In either case, the spacecraft must be rotated such that its -z-axis is pointed toward the sun and remains sun pointed within the specified limits.

Two EOS configurations are considered: the Thor-Delta configuration, designed for a nominal orbit of 316 n.m., and the Titan configuration, designed for a nominal orbit of 388 n.m. Thruster mode related mass properties for the two configurations are tabulated in Table 5-42.

Two sets of thrusters are available for EOS. Four high thrust (1 lb) thrusters are positioned to provide pitch and yaw control torques, and four low thrust (0.05 lb) thrusters are positioned such that they nominally provide roll control torques, but can also produce pitch and yaw control torques by appropriate commands. The control torques available for the two configurations are also listed in Table 5-42.

Table 5-42. EOS Thruster Modes Mass Properties

Configuration	Axis	Moment of Inertia (slug ft <sup>2</sup> )	Thruster Lever Arm (in)	Torque (ft/lb)
Thor-Delta	Roll x	586 380*	31.25**	0.1841
	Pitch y	1604 1560*	72.5 71.25***	6.042 0.4198***
	Yaw z	1862 1650*		
Titan	Roll x	1504 1077*	22.5**	0.1326
	Pitch y	4451 4369*	85 83.75***	7.083 0.4935***
	Yaw z	4864 4487*		

\*Moments of inertia prior to array deployment (first acquisition)

\*\*Roll thruster lever arms must be multiplied by  $\sqrt{2}/2$  due to angular offset

\*\*\*Low thrust (0.05 lb) thrusters optional for pitch and yaw control



Simulation results shown below are obtained from a digital computer simulation of EOS which models the gyroscopic torque coupling between the three body axes. Analytical results and block diagrams, however, utilize only decoupled dynamics for simplicity. The simulation results validate the analytical approach.

In the simulation, an off-the-shelf Bendix sun sensor is modelled. This sensor, which has a field-of-view of one complete hemisphere, is used in lieu of fine and coarse sun sensors mentioned in the proposal. The sensor outputs are corrupted with random noise ( $\sigma = 0.025$  deg). The gyros are modelled with ideal properties (no noise, no biases).

#### b. Sun Acquisition

A block diagram of the proposed primary mode thruster control system for pitch and roll is shown in Figure 5-132.

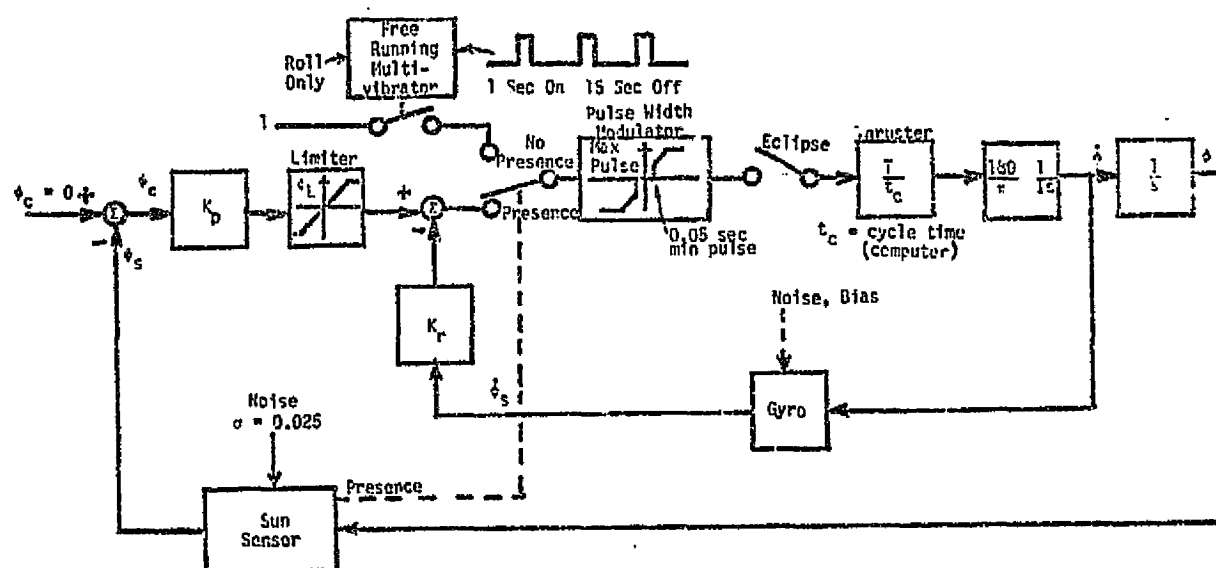


Figure 5-132. Pitch and Roll Primary Thruster Mode Control System (Roll Variables Shown)

Assuming linear and ideal sun sensor, gyro, and pulse width modulator and uncoupled dynamics (as shown), the open-loop transfer function of the system is

$$GH(s) = \frac{\frac{180}{\pi} \frac{T K_p}{t_c I}}{s \left( s + \frac{180}{\pi} \frac{T K_r}{t_c I} \right)}$$

where  $t_c$  is the onboard computer cycle time (200 msec). Since the attitude error specification is  $\pm 2$  deg, this combines with the minimum pulse width of the modulator to fix  $K_p$ :

$$K_p = \frac{0.05 \text{ sec}}{2 \text{ deg}} = 0.025 \text{ sec/deg}$$

Similarly, the  $\pm 0.03$  deg/sec rate specification determines  $K_r$ :

$$K_r = \frac{0.05 \text{ sec}}{0.03 \text{ deg/sec}} = 1.667 \text{ sec}^2/\text{deg}$$

The open-loop transfer function becomes

$$GH(s) = \frac{\frac{180}{\pi} \frac{T}{(0.2) I} (0.025)}{s \left[ s + \frac{180}{\pi} \frac{T}{(0.2) I} (1.667) \right]}$$

$$GH(s) = \frac{K}{s(s+\alpha)}$$

This system is always stable, as the root locus of Figure 5-133 indicates. Furthermore, the system may be either overdamped or underdamped, depending on the magnitudes of  $T$  and  $I$ . For the EOS values for  $T$  and  $I$  (see a.), the system is overdamped (Thor-Delta and Titan, pitch and roll). The dominant time constant ranges from 30 sec (roll) to 60 sec (pitch), implying that primary mode sun acquisition will require about 200 sec.

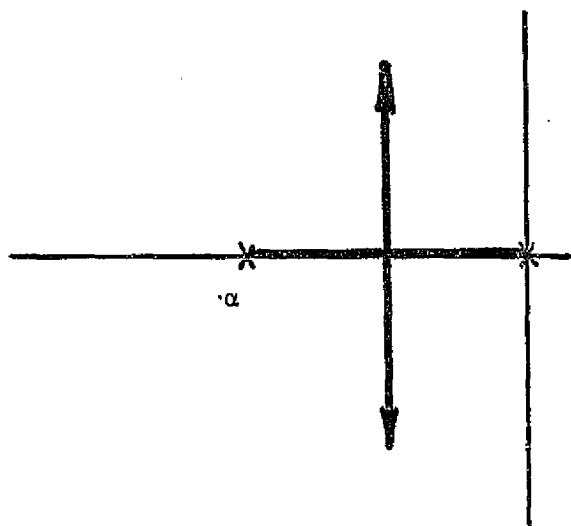


Figure 5-133. Root Locus of Linearized Pitch and Roll Primary Thruster Mode Control Systems

The limiter shown in the forward attitude loop is designed to prevent the control system from commanding excessive body rates. The limiter value  $\phi_L$  is related to the desired maximum rate  $\phi_{\max}$  by

$$\phi_L = K_r \phi_{\max}$$

For this study,  $\phi_{\max}$  is 1 deg/sec; thus

$$\phi_L = K_r = 1.667$$

Since the sun sensor is mounted along the yaw axis, it generates no attitude information about yaw. The primary mode thruster control system utilizes only the yaw axis gyro information to control yaw motion, as shown in Figure 5-134.

As before,  $K_r$  is determined from the specification on yaw rate ( $\pm 0.03$  deg/sec) and the minimum pulse width (0.05 sec).

$$K_r = \frac{0.05 \text{ sec}}{0.03 \text{ deg/sec}} = 1.667 \text{ sec}^2/\text{deg}$$

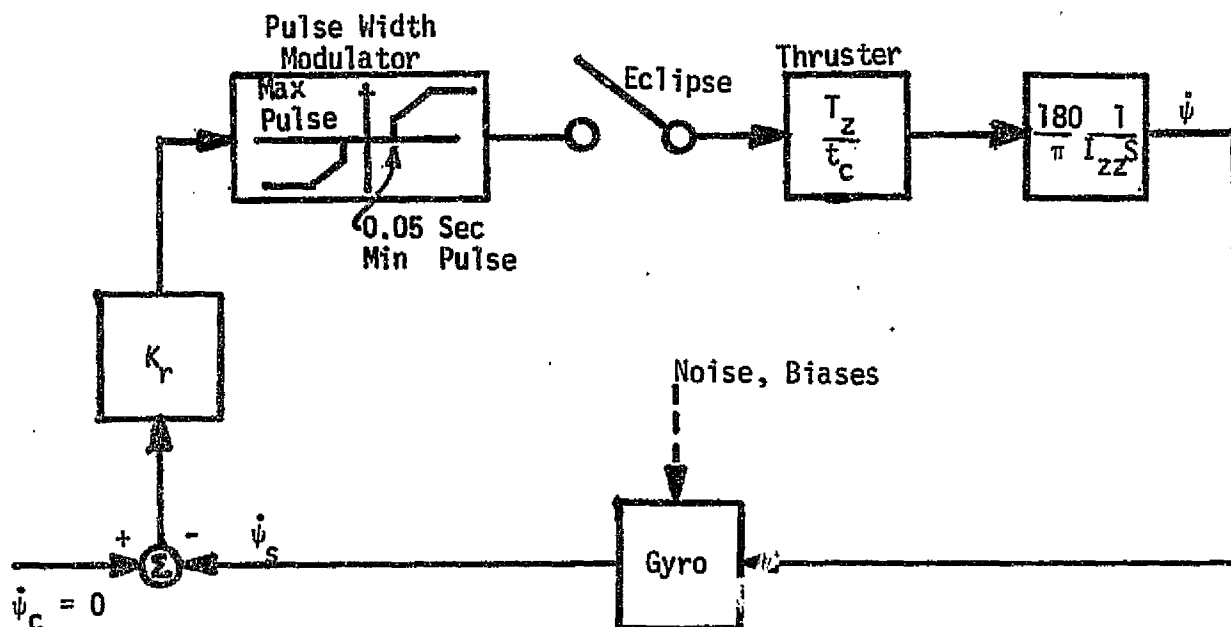


Figure 5-134. Yaw Primary Thruster Mode Control System

This system is always stable (over damped). Its dominant time constant is

$$\tau = \frac{\pi t_c I_{zz}}{180 T_z K_r} = \begin{cases} 0.6 \text{ sec Thor-Delta} \\ 1.3 \text{ sec Titan} \end{cases}$$

Thus, yaw rate will be nulled long before pitch and roll attitude and rates are brought under control.

Simulation studies utilizing the proposed pitch, roll, and yaw control systems in sun acquisition tests are summarized in Table 5-43, followed by plots of significant variables in Figure 5-135. The results were discussed in Section 5.2.4.3.4.

Table 5-43. Sun Acquisition Simulation Results (Primary Mode)

Run	Configuration	Initial Conditions						Time to Acquire (sec)	Final Conditions						Thruster Activity					
		Attitude (deg)			Rates (deg/sec)				Time (sec)	Attitude (deg)			Rates (deg/sec)			Time (sec)	Impulse (lb-sec)			
		Roll	Pitch	Yaw	Roll	Pitch	Yaw			Roll	Pitch	Yaw	Roll	Pitch	Yaw		Roll	Pitch	Yaw	Roll
1	Thor-Delta	180	180	1	1	1	230	200	.67	.31	.018	.016	-.020	230 300 600	6.4 6.5 6.4	10.7 10.7 10.7	2.5 2.5 2.5	19.1 19.4 19.5		
2	Titan	180	180	1	1	1	350	1060	-.906	1.28	.007	-.001	-.027	200 250 400 1000	13.4 21.2 21.7 22.0	21.9 22.9 22.9 22.9	22.0 22.0 22.8 22.8	66.0 66.3 67.1 67.7		

Note: Array stored

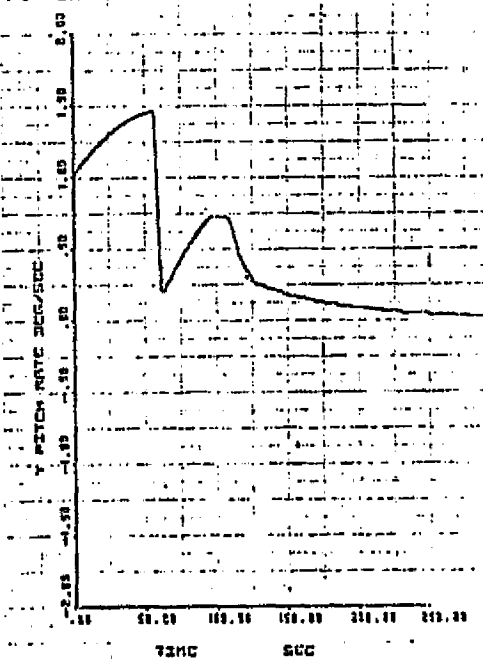
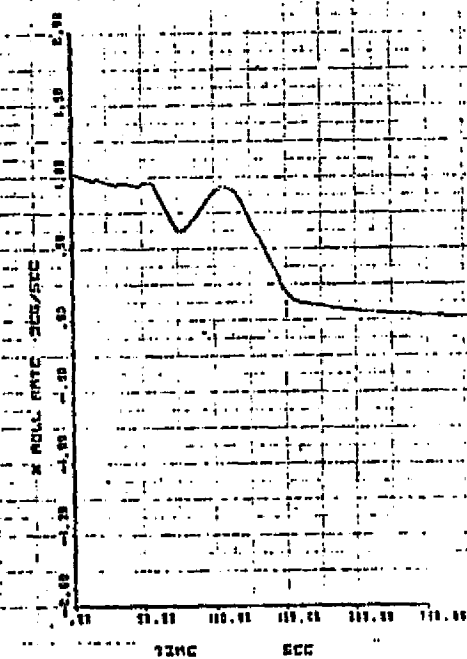
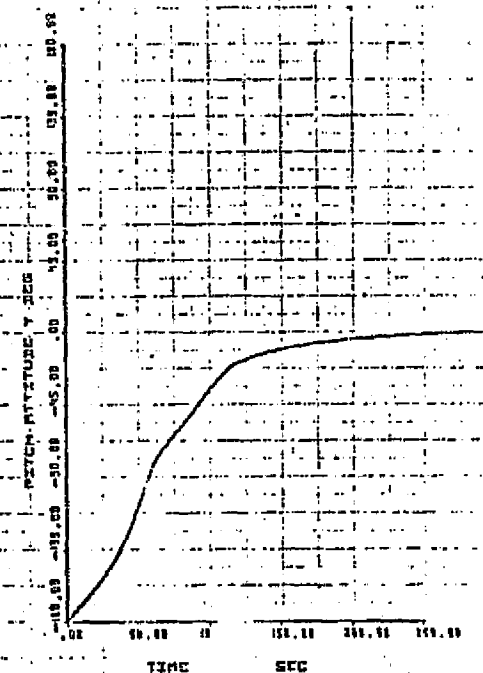
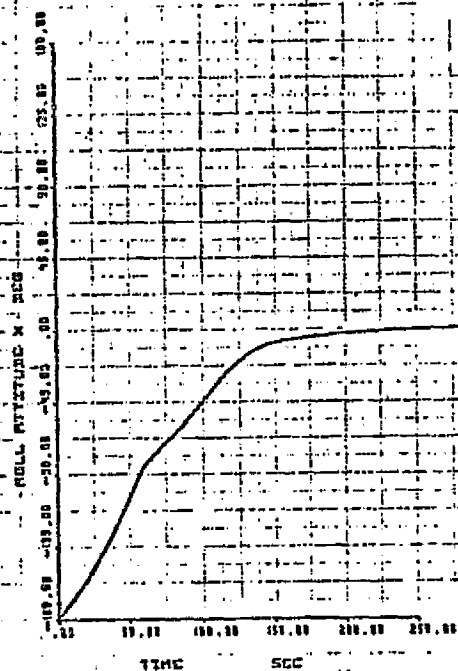


Figure 5-135a. Simulation plots of a Thor-Delta Primary Mode acquisition (Run 1).

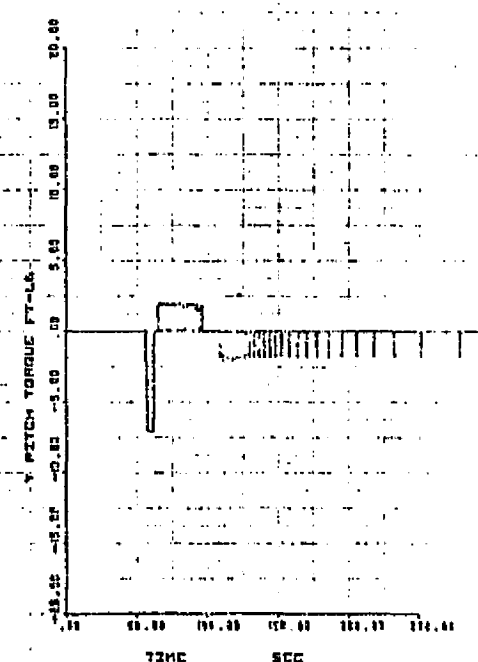
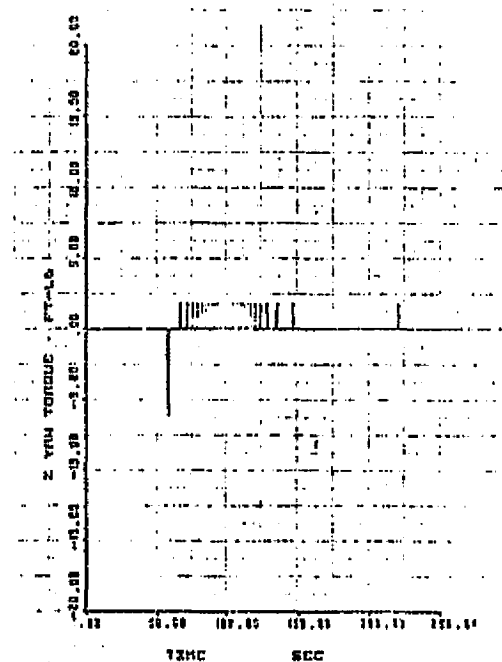
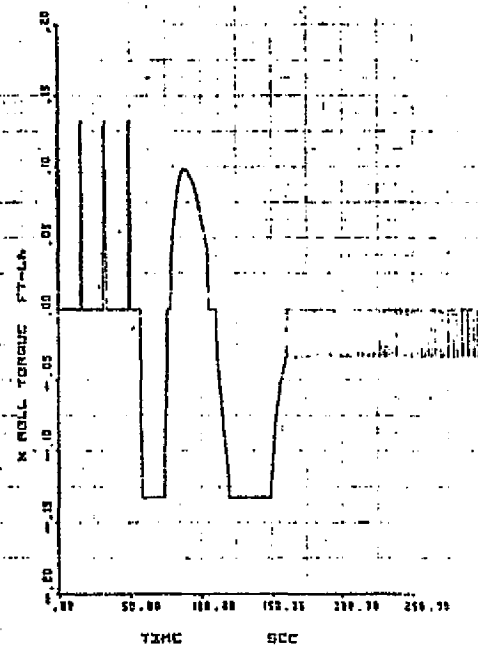
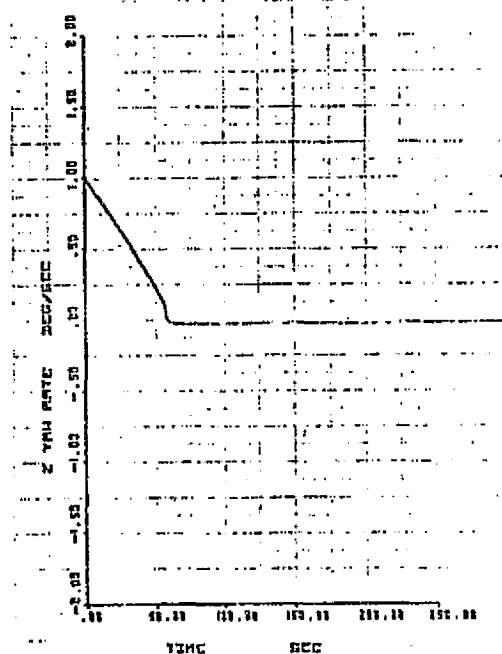


Figure 5-135b. Simulation plots of a Thor-Delta Primary Mode sun acquisition (Run 1).

### c. Backup or "Safe" Mode Thruster Control System

The backup or "safe" mode is designed for use during a catastrophic failure, when neither the gyros nor the on-board digital computer may be operational. Thus, the backup control system must be constructed of simple analog hardware and cannot rely on the gyros for rate feedback information.

A block diagram of the proposed backup mode thruster control system is shown in Figure 5-136.

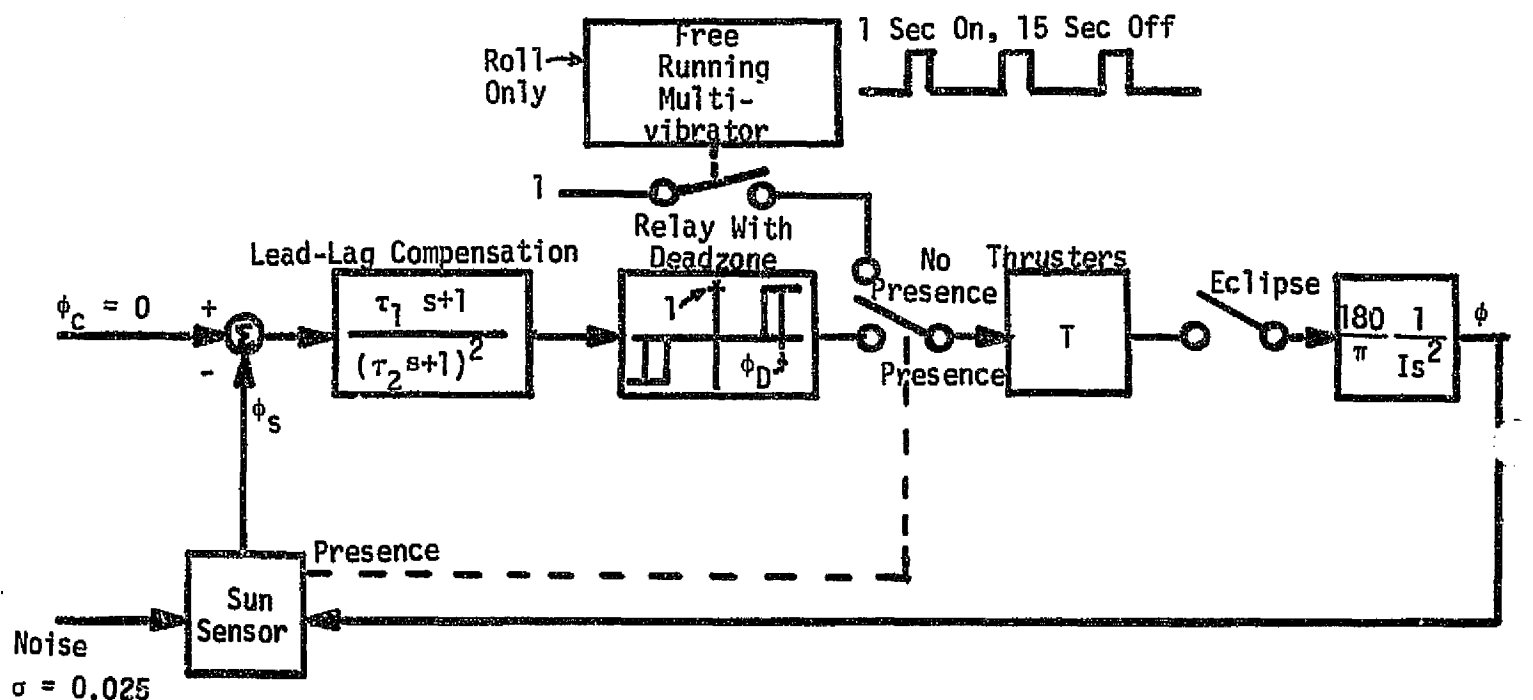


Figure 5-136. Pitch and Roll Backup Mode Control System  
(Roll Variables Shown)

The lead-lag filter is designed to introduce damping in the control loop, while simultaneously filtering out noise from the sun sensors. The deadzone  $\phi_D$  is set at the backup attitude specification,

$$\phi_D = 7 \text{ deg}$$

The open-loop transfer function of the system is (assuming relay can be linearized to an equivalent gain  $K_e$ )

$$GH(s) = \frac{(\tau_1 s + 1) K_e T}{(\tau_2 s + 1)^2} \cdot \frac{180}{\pi I s^2}$$

$$GH(s) = K \frac{(s + \frac{1}{\tau_1})}{s^2 (s + \frac{1}{\tau_2})^2}$$

where  $\tau_1 > \tau_2$ . A typical root locus for this function (Figure 5-137) shows that the linearized system is conditionally stable, depending on the placement of the lead-lag zero and poles and the equivalent gain  $K_e$ . Since it is difficult to predict accurately an equivalent  $K_e$ , and since the backup system is really nonlinear, its exact operating properties are best established by simulation.

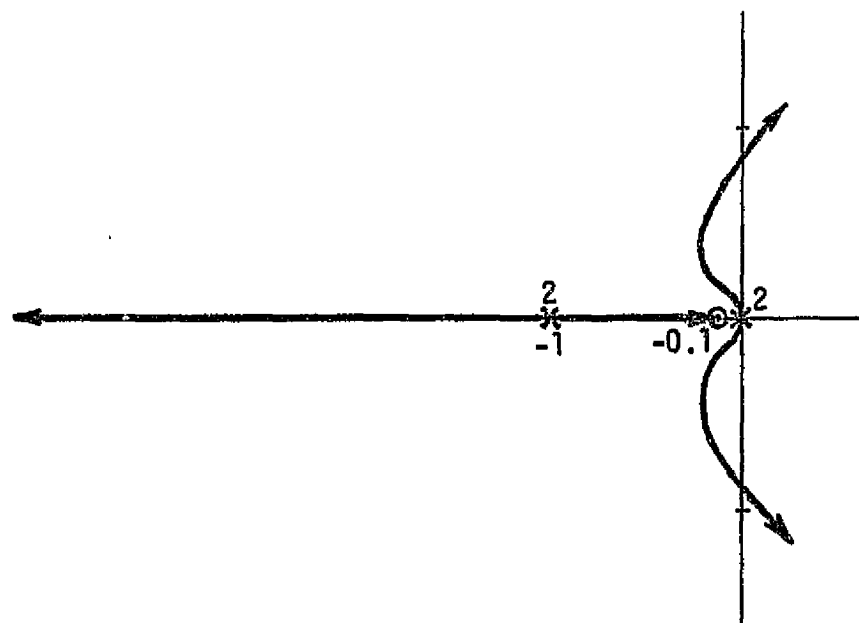


Figure 5-137. Root Locus of Linearized Backup System When  $\tau_1 = 10$ ,  $\tau_2 = 1$ .

Because the sun sensor does not give yaw information and the yaw gyro is not available in the backup mode, no yaw backup control system is possible. Whatever yaw rates accumulate through initial conditions or gyroscopic torque coupling from the pitch and roll axes must be simply accepted. Typically these will be small, since yaw moment of inertia is large.



Results of simulation studies conducted on the backup mode are shown in Table 5-44, followed by plots of Run 3 in Figure 5-138. The plots indicate that the pitch axis control system is very well behaved, since it converges to the  $\pm 7$  deg deadzone within about 60 sec after sun presence is obtained. The roll axis control system, on the other hand, is too underdamped, wasting time and thruster fuel. This problem could be corrected by tuning the roll control system parameters.

Table 5-44. Backup Mode Simulation Results

Run	Configuration	Initial Conditions					Time to Acquire (sec)	Final Conditions					Thruster Activity					
		Attitude (deg)		Rates (deg/sec)				Time (sec)	Attitude (deg)		Rates (deg/sec)			Time (sec)	Impulse (lb-sec)			
		Roll	Pitch	Roll	Pitch	Yaw			Roll	Pitch	Roll	Pitch	Yaw		Roll	Pitch	Yaw	Total
3	Thor-Delta	180	100	1	1	1	455	600	-1.65	1.00	.063	.045	-.311	455	33.5	42.2	0	75.7
														600	35.7	42.2	0	77.9
														1200	36.0	43.6	0	80.0
4	Titan Roll Thrust equals .05 lb	180	180	1	1	1	Failed To Acquire	1500	Tumbling		.790	-.047	-.042	420	17.5	64.0	0	81.5
														600	18.9	64.0	0	82.9
														900	31.3	106	0	138
														1200	55.7	134	0	189
5	Titan Roll Thrust equals 0.5 lb	180	180	1	1	1	200	600	-6.66	1.68	.019	.176	-1.24	100	57.4	53.2	0	121
														200	124	63.4	0	187
														400	124	64.6	0	189
														600	129	64.6	0	193

Note: Array Deployed

#### d. Backup Mode Following Eclipse

During eclipse of the sun's rays from the spacecraft all control thrusting is inhibited in both primary and backup modes, as indicated in Figures 5-132, -134, and -136. While eclipsed, disturbance torques act upon the spacecraft to produce unwanted attitude errors and body rates. Estimates of average disturbance torques (from Section 5.2.4.1.3) for low altitude orbits are shown in Table 5-45.

Table 5-45. Average EOS Disturbance Torques  
(Neglecting Solar Effects)

Configuration	Torques		
	Roll x	Pitch y	Yaw z
	(x10 <sup>-4</sup> Ft-Lb)		
Thor-Delta (316 n.m.)	5	2.5	-20
Titan (386 n.m.)	5	3.0	- 4

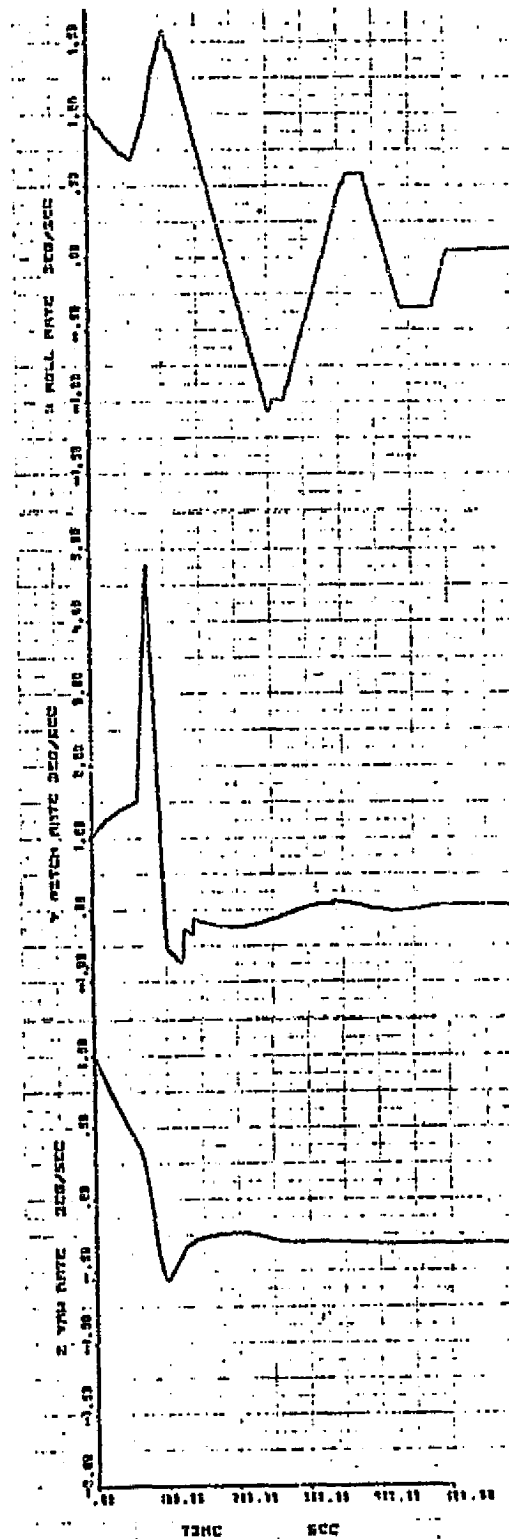
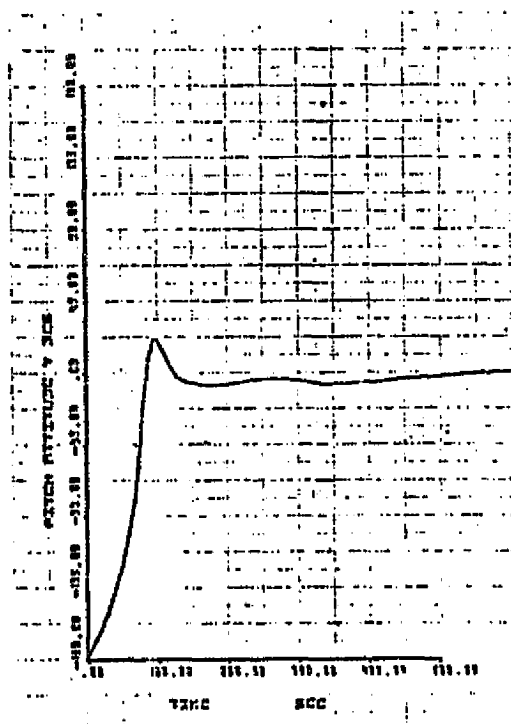
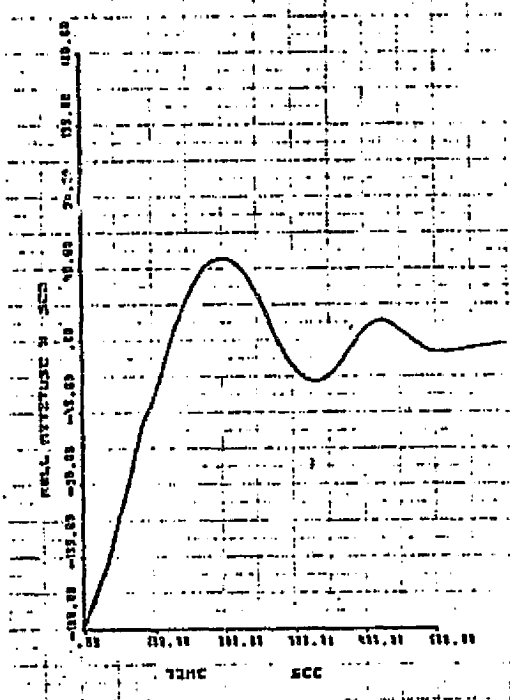


Figure 5-138. Simulation plots of a Thor-Delta Backup Mode sun acquisition (Run 3).

ORIGINAL PAGE IS  
OF POOR QUALITY

Newton's Second Law states that the net change in angular momentum of the spacecraft must equal the net torques applied.

$$\Sigma \dot{H} = \Sigma T$$

For one axis,

$$I \ddot{\theta} = T_d$$

where disturbance torque  $T_d$  is assumed to be the only torque present.

Integrating,

$$I \dot{\theta} + H_0 = \int T_d dt$$

Assuming initial angular momentum  $H_0$  is zero and that  $T_d$  is constant,

$$I \dot{\theta} = T_d \Delta t$$

$$\dot{\theta} = \frac{T_d \Delta t}{I}$$

Thus, the undesired rate built up during eclipse is related to the magnitude of disturbance torque  $T_d$ , the length of the eclipse  $\Delta t$ , and the moment of inertia  $I$ .

The longest eclipse possible occurs during the proposed EOS synchronous orbit:  $\Delta t = 70$  min. Although the disturbance torques at synchronous altitude are far less than those at the altitudes indicated in Table 5-45, and the disturbance torques would not act constantly in one direction on a tumbling spacecraft, a worst case can be obtained by combining the torques from Table 5-45 with  $\Delta t = 70$  min in the above formula. Results are shown in Table 5-46.

Table 5-46. Worst Case Rates Upon Leaving Eclipse

Configuration	Body Rates (Deg/Sec)		
	Roll x	Pitch y	Yaw z
Thor-Delta	0.205	0.0375	-0.258
Titan	0.080	0.0162	-0.0198

These rates were used as initial conditions for simulation runs tabulated in Table 5-47. It was further assumed that the spacecraft were initially anti-sun pointing. Plots of a simulation run for Thor-Delta (Figure 5-139) show that sun presence was not obtained for 301 sec due to low initial rates. Acquisition took another 550 sec (850 sec total). Again, the pitch backup system has better damping than the roll (cf Section 3.4.3).

Table 5-47. Backup Acquisition Following 70 Min. Eclipse

Run	Configuration	Initial Conditions					Time to Acquire (sec)	Final Conditions					Thruster Activity					
		Attitude (deg)		Rates (deg/sec)				Time (sec)	Attitude (deg)		Rates (deg/sec)			Time (sec)	Impulse (lb-sec)			
		Roll	Pitch	Roll	Pitch	Yaw			Roll	Pitch	Roll	Pitch	Yaw		Roll	Pitch	Yaw	Total
6	Thor-Delta	180	180	.205	.038	-.258	850	1200	-3.42	5.51	.008	.139	-1.06	790	37.0	43.8	0	56.8
														850	47.2	44.2	0	91.4
														1200	47.9	45.4	0	93.3
7	Titan	180	180	.080	.0162	-.0192	1700	2000	-4.02	2.01	.012	.118	-.654	750	20.5	43.8	0	64.2
														1000	47.5	51.6	0	99.1
														1500	90.8	56.0	0	147
														1750	103	57.2	0	160
														2000	104	58.2	0	162

Note: Array deployed

e. Backup Mode Following Wheel Failure (Rundown)

If the reaction wheel used in normal mode should lose power and subsequently run down, all of their stored momenta would be dumped into body rates. Newton's second law again requires

$$\Sigma \dot{H} = \Sigma T$$

In one axis,

$$I\ddot{\theta} + \dot{H}_W = \Sigma T$$

where  $H_W$  is the stored momentum of one wheel. Integrating

$$I\dot{\theta} + H_W + H_0 = \int \Sigma T dt$$

where  $H_0 = -H_W$  ideally. Assuming external torques are negligible during wheel run down

$$I\Delta\dot{\theta} = \Delta H_W$$

$$\Delta\dot{\theta} = \frac{\Delta H_W}{I}$$

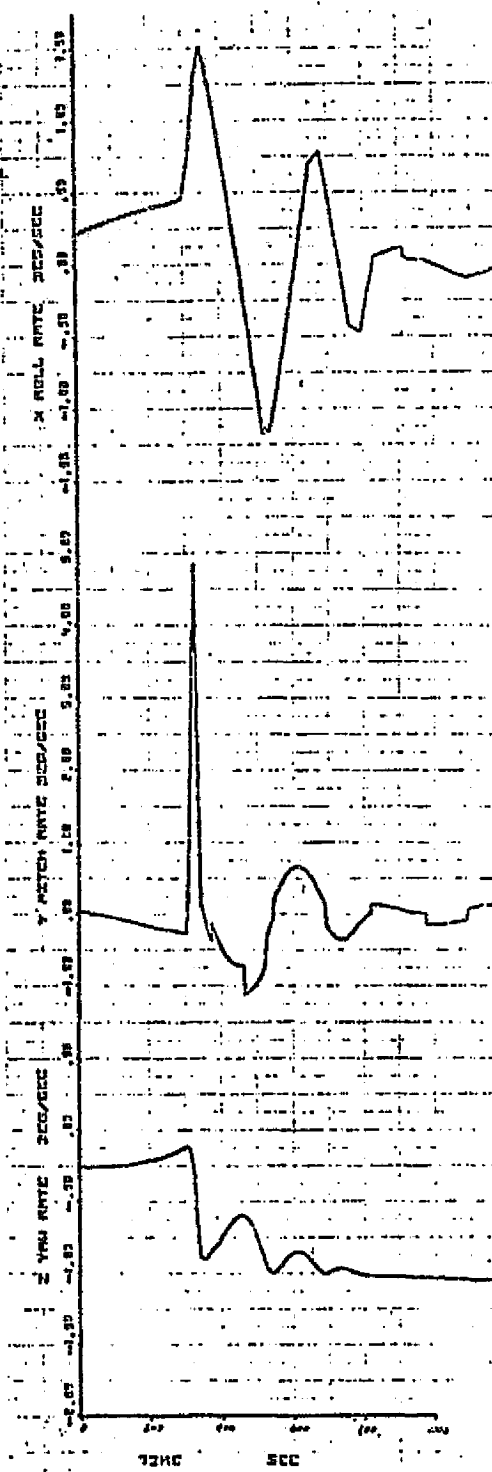
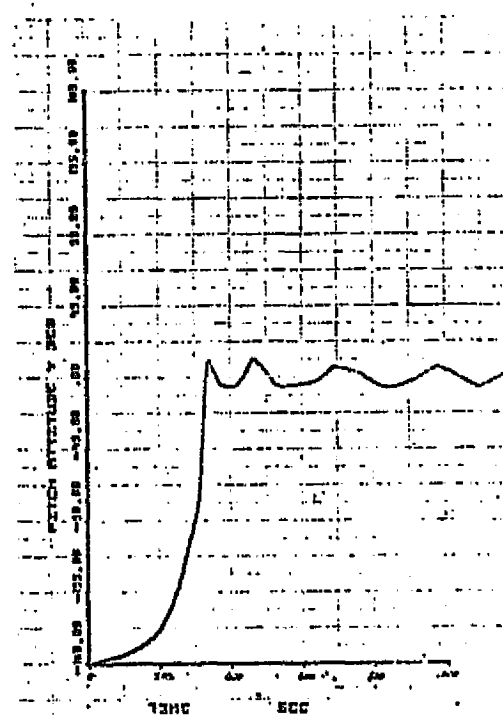
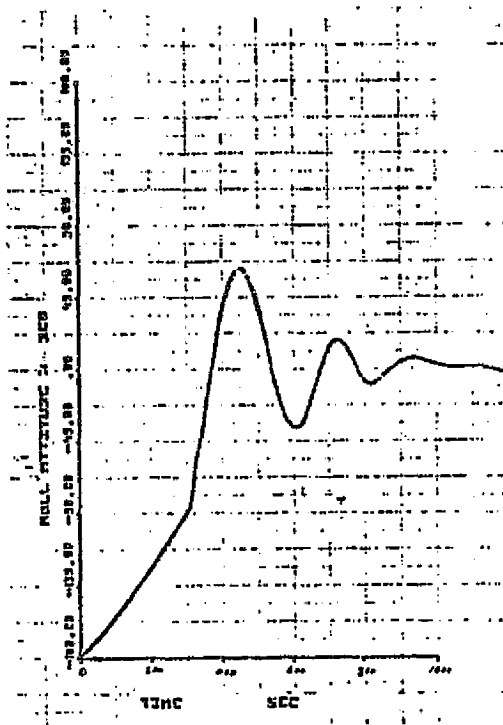


Figure 5-139. Simulation plots of a Thor-Delta Backup Mode sun acquisition following a 70 min eclipse (Run 6).

Since initial rate  $\dot{\theta}$  is zero, the rate after wheel rundown is equal to wheel momentum divided by inertia. In Table 5-48, rates computed according to the above relation (assuming maximum wheel momentum is 7.2 ft-lb-sec) are tabulated.

Table 5-48. Body Rates After Wheel Rundown

Configuration	Body Rates (Deg/Sec)		
	Roll x	Pitch y	Yaw z
Thor-Delta	0.704	0.257	0.222
Titan	0.274	0.0927	0.0848

Simulation runs using these rates for initial conditions (and anti-sun pointing initial attitude) are summarized in Table 5-49, followed by plots of a Thor-Delta run in Figure 5-140. From the plots it is seen that sun presence was obtained after 110 sec had elapsed, and sun acquisition required another 460 sec (total 570 sec).

Table 5-49. Backup Operation Following Wheel Failure (Rundown)

Run	Configuration	Initial Conditions						Time to Acquire (sec)	Final Conditions						Thruster Activity				
		Attitude (deg)		Rates (deg/sec)			Time (sec)		Attitude (deg)		Rates (deg/sec)			Time (sec)	Impulse (lb-sec)				
		Roll	Pitch	Roll	Pitch	Yaw			Roll	Pitch	Roll	Pitch	Yaw		Roll	Pitch	Yaw	Total	
8	Thor-Delta	180	130	.704	.257	.222	570	1200	5.83	3.07	.042	.012	-1.06	420	30.2	34.7	0	64.6	
														570	41.1	39.2	0	76.3	
														990	46.1	37.0	0	83.1	
														1200	46.1	36.0	0	84.1	
9	Titan	180	100	.274	.0927	.0848	1460	2000	-4.51	1.31	.063	-.014	-.727	1000	67.7	66.6	0	134	
														1400	91.1	68.6	0	156	
														1700	103	69.8	0	174	
														2000	104	70.6	0	175	

Note: Array deployed

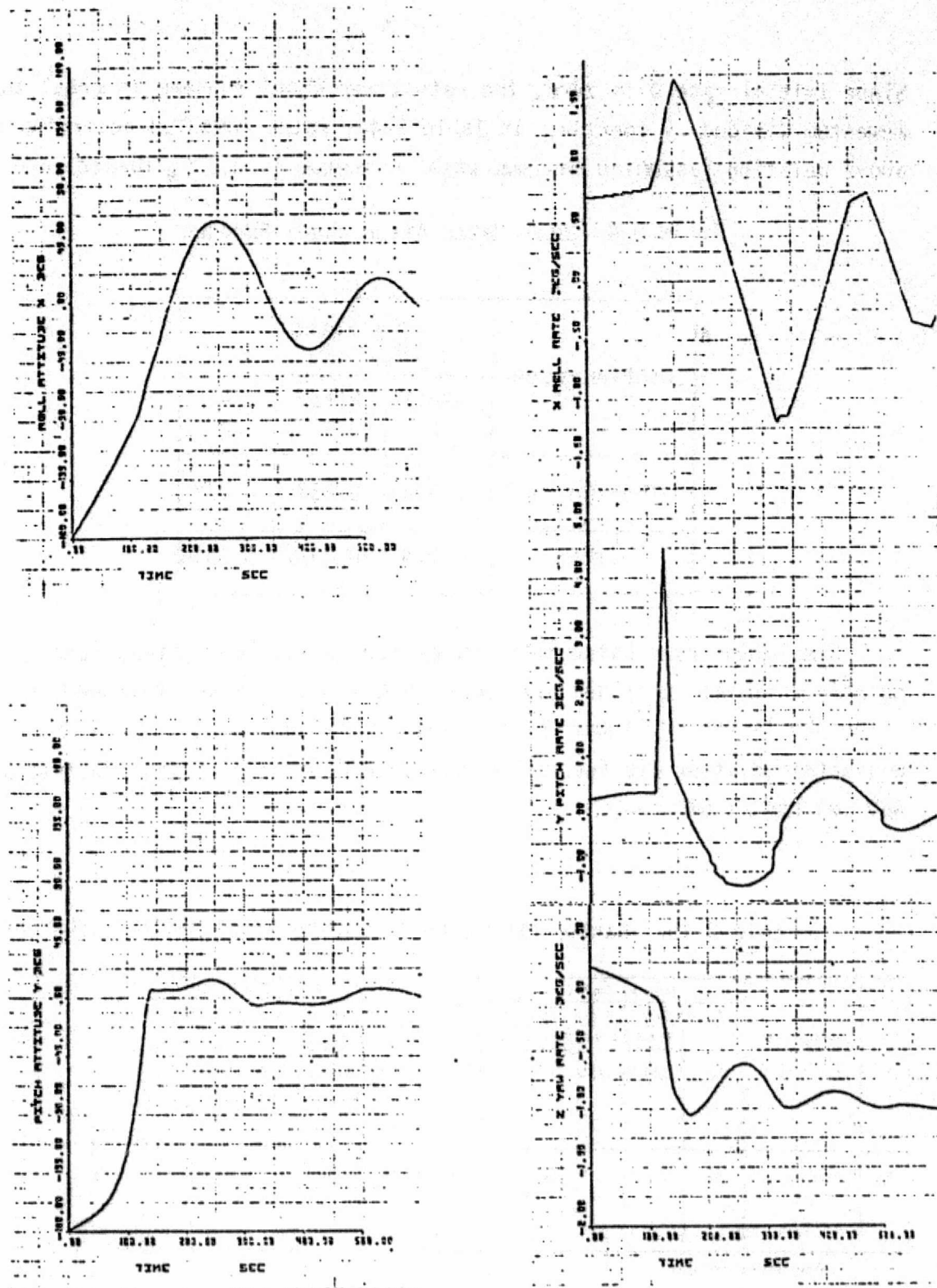


Figure 5-140. Simulation plots of a Thor-Delta Backup Mode sun acquisition following wheel rundown (Run 8).



## b. Low Thrust Operation

All of the previous analysis and simulation was done under the assumption that the high thrust (1 lb) thrusters would be used for pitch and yaw control, with the low thrust (0.05 lb) thrusters used for roll control only. In this section, consideration is given to using the 0.05 lb thrusters for controlling all three axes. The results are tabulated in Table 5-50.

Table 5-50. Low Thrust Operation

Run	Configuration	Initial Conditions					Time to Acquire (sec)	Final Conditions					Thruster Activity						
		Altitude (deg)		Rates (deg/sec)				Time (sec)	Altitude (deg)		Rates (deg/sec)			Time (sec)	Impulse (lb-sec)				
		Roll	Pitch	Roll	Pitch	Yaw			Roll	Pitch	Roll	Pitch	Yaw		Roll	Pitch	Yaw	Total	
10	Thor-Delta Primary Mode Array Deployed	180	180	1	1	1	260	600	1.85	1.97	.001	-.001	-.030	200 300 600	7.1 7.3 7.4	7.9 8.1 8.2	8.4 8.7 8.4	23.4 23.9 24.1	
11	Thor-Delta Backup Mode Array Deployed	180	180	1	1	1	520	1200	-5.82	2.78	.019	.069	-.593	520 600 1200	21.3 22.3 23.0	36.0 39.8 39.3	0 0 0	59.4 62.1 62.8	
12	Titan Primary Mode Array Stowed	180	180	1	1	1	520	1000	-1.48	1.82	.005	.001	-.030	300 520 600 1000	22.9 39.0 39.0 39.0	34.0 36.8 37.4 37.6	21.4 22.4 22.4 22.4	67.4 98.2 98.8 99.1	
13	Titan Backup Mode Array Deployed	180	180	1	1	1	Failed to Acquire	2400	Tumbling		.705	-1.36	-.376	500 2000 2400	16.0 21.0 107	20.0 76.4 91.9	0 0 0	36.0 168 199	

As discussed in Section 5.2.4.3.4, it is recommended that either the thrust of these small thrusters be increased or the backup mode be redesigned to ensure acquisition for all expected initial conditions.



## 5.2.5 Pointing Error Budget Allocation

### 5.2.5.1 Summary

This appendix presents the detailed development of pointing error allocations as required to specify performance. Total system performance (i.e., output quality) is considered as the main driver. Future mission requirements are also considered.

### 5.2.5.2 Motivation

This task is motivated by the need to define subsystems specifications for various components of the EOS spacecraft, and to establish the impact of subsystem error sources upon overall geometric/geodetic pointing accuracy.

### 5.2.5.3 Methodology

The geometric impact of each error source upon in-track and cross-track errors in locating ground points from the spacecraft is established. This directly influences the LCGS user. The improvement in performance that results from the use of ground control points whose geodetic location is known is then assessed. This is indicative of the accuracy available to the CDPF user, whose ground-based optimal filter essentially removes the predominant source errors.

### 5.2.5.4 Results

This section considers EOS spacecraft subsystem specifications to meet overall payload pointing requirements. The subsystems considered are:

- a) attitude control
- b) inertial attitude estimation
- c) ephemeris estimation

- d) thermal/structural control
- e) payload (Thematic Mapper)

Imperfections in these subsystems all contribute to payload pointing errors in geocentric coordinates. The overall system performance requirements depend upon which of the several control modes the spacecraft is in. These modes are: Earth Pointing, Inertial Pointing, Sun Pointing, and Stellar Pointing. Each of these modes and their requirements will be described shortly. As a reference, Table 5-51 documents the one sigma pointing requirements suggested by GSFC/NASA in their EOS Study RFP. This section will define a similar set of requirements for each subsystem, focusing primarily upon the primary mode, Earth Pointing.

Table 5-51. GSFC/NASA EOS RFP Performance Requirements

Mode	Pointing Accuracy ( $1\sigma$ )	Pointing Stability ( $1\sigma$ )	
		Average Rate Deviation <sup>(c)</sup>	Jitter (b)
Earth Oriented	0.01 deg	$10^{-6}$ deg/sec	0.0003 deg for $t \leq 30$ sec <sup>(a)</sup> 0.0006 deg for $t \leq 20$ min
Stellar Inertial	0.01 deg	$10^{-6}$ deg/sec	0.0006 deg for $t \leq 1$ hr
Normal	$3 \times 10^{-6}$ deg	N/A	$10^{-7}$ deg for $t \leq 1$ hr
Ideal Sensors			

(a)  $t$  = time

(b) Relative to Average Baseline

(c) for  $t \geq 30$  min

#### 5.2.5.1 Mission Normal Modes

##### a. Earth Pointing Mode

This mode receives primary attention as it is the basic mode for EOS-A with a clear definition of its payload sensors. These sensors comprise a Thematic Mapper (TM) and a High Resolution Pointable Imager (HRPI). The former is assumed to have the more stringent geometric/geodetic accuracy requirements, thus the HRPI will not be considered in the sequel. The TM is assumed to point nominally along the spacecraft yaw axis when its scan angle is zero, and to sweep about an axis colinear

with the spacecraft roll axis. Other significant characteristics associated with the TM are given in Table 5-52. Each TM image consists of approximately 38 million pixels in order to meet the radiometric resolution requirements. Geodetic accuracy denotes the degree to which the TM image can be located upon the surface of the earth. Important to cartographers, a one pixel accuracy (30 m,  $1\sigma$ ) is desirable. More stringent is the required geometric accuracy, namely the fidelity or distortion free characteristic of each image. In order to accurately note changes in comparable scenes imaged at different times (e.g., 17 days) a one sigma error less than 1/4 pixel, or 7.5 m, is the goal.

Table 5-52. Thematic Mapper Data Characteristics

Item	Range	Nominal Value
Orbital Altitude	556 - 1668 km	914 km
Picture Size	185 x 185 km	185 x 185 km
Picture Time	26.5 - 33.2 sec	28.6 sec
Pixel Size	30 x 30 m	30 x 30 m
Number of Channels	14	14
Number of Radiation Bands/ Channels	6	6
Scan Rate	16 Hz	16 Hz
Scan Amplitude	$\pm 9.4$ deg to $\pm 3.1$ deg	$\pm 5.8$ deg
Data Storage per Sweep	$\sim 5 \times 10^6$ bits	$5 \times 10^6$ bits
Time for One Pass	8.8 to 11.1 min	10 min

Data from both the TM and the HRPI is telemetered via a wideband communications system to a Central Data Processing Facility (CDPF). The primary burden placed upon the CDPF concerns the formation of a "continuous" radiometric image given the 38 million discrete samples. Additionally the CDPF removes any causal geometric/geodetic effects of significance (e.g., skew caused by earth rotation). To aid in improving its image fidelity, the CDPF makes use of the known locations of 10 or so imaged points per pass. These Ground Control Points (GCP) are assumed

uncorrelated and known to 30 m ( $1\sigma$ ). Since this accuracy far exceeds that which a spacecraft fixed observer could predict, such points actually aid in calibrating spacecraft error sources. Once calibrated, the geometric/geodetic accuracy of every pixel can be vastly improved. This improvement depends, of course, upon the number and location of the GCPs chosen. As a baseline approach, it is assumed that ground control points are established at a variety of TM scan angles, and separated in time by no more than 2 minutes. In fact, the first three such points will be assumed about 10 seconds apart so that the predominant bias errors can be removed early in the data taking pass. The way in which these GCPs are used will be described in detail later.

Besides the CDPF, there exist several other downlink processors of the TM and HRPI radiometric data. These Low Cost Ground Stations (LCGS) perform neither radiometric nor geometric/geodetic corrections. Pictures are formed from the data in an "as received" condition. Apparently for many applications, there is sufficient accuracy to warrant the cost savings and flexibility (e.g., mobile) of LCGS units. For more exacting needs, the CDPF is always available. One assumption regarding the LCGS will be made, however: it is assumed that ground points in two comparable 185 km by 185 km scenes can be visually established in order to fix four "almost constant" error sources which largely dominate the geometric/geodetic accuracy. The influence of these parameters,  $x_1$  to  $x_4$ , will be established shortly in the specification of Equations (1) and (2).

b. Stellar Inertial Mode

The normal stellar inertial mode uses the same gyro package and star tracker used for the earth-pointing mode. Here it becomes particularly important that the spacecraft exhibit a repeatable attitude in order to observe the emission of very dim stars. Since stellar payloads and the accuracy of their information have not been defined, the required attitude control performance in this mode will be assumed given by the GSFC/NASA values suggested in Table 5-51.

c. Sun Pointing Mode

In a sun pointing mission, it is likely that the star trackers would be removed from the attitude determination module in favor of an accurate sun sensor in order to effect a cost savings. However, no change in the

performance specs is anticipated. During sunlit times, the pointing accuracy in each axis shall still be 0.01 deg (1 $\sigma$ ), with the stability specs of Table 5-51 holding during eclipse intervals.

d. Stellar Inertial Mode Using Ideal Sensors

In some future missions, it is anticipated that spacecraft attitude information will be derived from the payload itself, rather than using separate body fixed trackers. Such an attitude reference would, of course, be very accurate, and any significant spacecraft attitude errors would only be the result of non-ideal control system components. The GSFC/NASA spec of Table 5-51 cites allowable errors attributed to the control system in such applications.

5.2.5.4.2 Ground Point Location Errors

When ground control points are not used to improve image geometric/geodetic quality, but rather ground points are located entirely by noting spacecraft attitude, ephemeris etc., then it can be shown that the location error of a ground target in the nominal spacecraft pitch-yaw plane at a TM scan angle of  $\phi$  is given by:

In track:

$$\epsilon_{x_1} = x_1 + \phi x_2 \quad (1)$$

Cross track:

$$\epsilon_{x_2} = x_3 + \phi x_4 \quad (2)$$

where

$$x_1 = h_o \theta^{(2)} + z^{(1)} \quad (3)$$

$$x_2 = h_o \theta^{(3)} \quad (4)$$

$$x_3 = z^{(2)} - h_o (\theta^{(1)} + \phi') \quad (5)$$

$$x_4 = z^{(3)} + kr \quad (6)$$

where  $h_o$  is the spacecraft altitude.  $\theta^{(1)}$ ,  $\theta^{(2)}$ ,  $\theta^{(3)}$  are, respectively, the errors in the assumed inertial roll, pitch and yaw attitude of the thematic mapper mounting surface;  $z^{(1)}$ ,  $z^{(2)}$ ,  $z^{(3)}$  are ephemeris errors in-track, cross-track, and radially, respectively;  $\phi'$  is the gimbal angle



readout error;  $r$  is the error in the assumed terrain height; and  $k$  is the ratio of spacecraft orbit to earth radius.

Sometimes of greater interest are the tracking errors,  $\epsilon_{x_1}^i$ ,  $\epsilon_{x_2}^i$  relative to that of a previous pass. It is easy to demonstrate that for previous errors  $\epsilon_{x_1P}$ ,  $\epsilon_{x_2P}$

$$\epsilon_{x_1}^i = x_1 - \epsilon_{x_1P} + \phi x_2 \quad (1a)$$

$$\epsilon_{x_2}^i = x_3 - \epsilon_{x_2P} + \phi x_4 \quad (2a)$$

Clearly, cartographic data involving  $\epsilon_{x_1}^i$  and  $\epsilon_{x_2}^i$  should be for more accurate than that involving  $\epsilon_{x_1}$  and  $\epsilon_{x_2}$ .

#### 5.2.5.4.3 Error Sources

Now the individual error sources contributing to the  $\theta^{(i)}$ ,  $z^{(i)}$ ,  $\phi^i$ , and  $r$  will now be considered and mathematical models derived.

##### a. Spacecraft Attitude Uncertainty, $\theta^{(a,k)}$ $k = 1, 2, 3$

Define  $\theta_i^{(a,k)}$  as the error at time  $t_i$  in the assumed inertial attitude of the star tracker  $x_k$  ( $k = 1, 2, 3$ ) axis where  $x_1$  is nominally along the spacecraft roll axis and  $x_2$  nominally along its pitch axis. This error will grow according to the model

$$\tilde{\theta}_{i+1}^{(a,k)} = \theta_i^{(a,k)} + b_i^{(a,k)} \tau_{i+1} + n_{v,i+1}^{(a,k)} + n_{e,i+1}^{(a,k)} \quad k = 1, 2, 3 \quad (7)$$

where the  $\sim$  indicates conditions at  $t_{i+1}$ ;  $b_i^{(a,k)}$  reflects the uncertainty in the spacecraft drift rate;

$$\tau_{i+1} = t_{i+1} - t_i \quad (8)$$

and  $n_v^{(a,k)}$  and  $n_e^{(a,k)}$  are white noise processes of variances  $\sigma_v^2 \tau_{i+1}$  and  $\sigma_e^2$ , respectively. While Equation (7) describes the entire attitude error model, it should be noted that the predominant portion of this error is caused by imperfections in the attitude and attitude rate sensors. The capability of the proposed control system exceeds by a considerable amount that of its sensors.

b. Thermal/Structural Uncertainties,  $\theta^{(\tau, k)}$

$$\tilde{\theta}_{i+1}^{(\tau, k)} = \theta_i^{(\tau, k)} + b_i^{(\tau, k)} \tau_{i+1} + n_{i+1}^{(\tau, k)} \quad k = 1, 2, 3 \quad (10)$$

Thermal deformation is assumed to vary sinusoidally at orbit rate, so that over any short time span (e.g., 10 minutes)  $b^{(\tau, k)}$  represents the local rate of change of deformation.  $n^{(\tau, k)}$  is a random process of variance  $\sigma_\tau^2$ , and represents structural vibration.

c. Thematic Mapper Scan Angle Uncertainty

$$\phi_{i+1}' = L_{i+1}^{(\tau)} + n_{i+1}^{(p)} \quad (11)$$

where  $b^{(p)}$  is some fixed bias angle and  $n^{(p)}$  represents local "noise" fluctuation from any of a number of sources. The latter is assumed random of variance  $\sigma_p^2$ .

d. Spacecraft Ephemeris Uncertainties,  $z^{(k)}$

It is assumed that present ephemeris data and a number of future bench marks are periodically transmitted to the spacecraft, with an on-board model providing interpolation. Errors can be assumed to arise from two causes

- a) Ground ephemeris errors for predicted benchmarks
- b) Spacecraft ephemeris modeling errors.

A simple model represents these errors over short time intervals as

$$z_{i+1}^{(k)} = z_i^{(k)} + b_i^{(e, k)} \tau_{i+1} \quad k = 1, 2, 3 \quad (12)$$

e. Terrain Height Uncertainty,  $r$

This is assumed to consist of a bias plus a random variation.

$$r_{i+1} = b_{i+1}^{(r)} + n_{i+1}^{(r)} \quad (13)$$

where the latter has variance  $\sigma_r^2$ .

#### f. Location Uncertainties of Ground Control Points

Errors in the absolute location of these points are assumed independent and are random, zero mean and variance  $E[\epsilon_{x_1}^2] = E[\epsilon_{x_2}^2] = \sigma_L^2$ . For errors relative to a previous comparable measurement,  $E[\epsilon'_{x_1}] = E[\epsilon'_{x_2}] = \sigma_L'^2$ .

#### 5.2.5.4.4 Kalman Filter Definition

Noting Equations (1) and (2), it follows that

$$x_1 = h_o (\theta^{(a, 2)} + \theta^{(\tau, 2)}) + z^{(1)} \quad (14)$$

$$x_2 = h_o (\theta^{(a, 3)} + \theta^{(\tau, 3)}) \quad (15)$$

$$x_3 = -h_o (\theta^{(a, 1)} + \theta^{(\tau, 1)} + b^{(p)}) + z^{(2)} \quad (16)$$

$$x_4 = z^{(3)} + k b^{(r)} \quad (17)$$

We also define

$$x_5 = h_o (b^{(a, 2)} + b^{(\tau, 2)}) + b^{(e, 1)} \quad (18)$$

$$x_6 = h_o (b^{(a, 3)} + b^{(\tau, 3)}) \quad (19)$$

$$x_7 = h_o (b^{(a, 1)} + b^{(\tau, 1)}) - b^{(e, 2)} \quad (20)$$

$$x_8 = b^{(e, 3)} \quad (21)$$

and the state vector

$$x = (x_1, x_2, \dots, x_8)^T \quad (22)$$

Also defining the state error covariance matrix at  $t_i$  - by

$$S_i = E[\tilde{x}_i^T x_i] \quad (23)$$

and at  $t_i +$  by

$$P_i = E[x_i^T x_i] \quad (24)$$



It follows that the state transition matrix is

$$\Phi_{i+1} = \begin{bmatrix} 1 & 0 & 0 & 0 & \tau_{i+1} & 0 & 0 & 0 \\ 0 & 1 & 0 & 0 & 0 & \tau_{i+1} & 0 & 0 \\ 0 & 0 & 1 & 0 & 0 & 0 & -\tau_{i+1} & 0 \\ 0 & 0 & 0 & 0 & 0 & 0 & 0 & \tau_{i+1} \\ 0 & 0 & 0 & 0 & 1 & 0 & 0 & 0 \\ 0 & 0 & 0 & 0 & 0 & 1 & 0 & 0 \\ 0 & 0 & 0 & 0 & 0 & 0 & 1 & 0 \\ 0 & 0 & 0 & 0 & 0 & 0 & 0 & 1 \end{bmatrix} \quad (25)$$

The state noise covariance matrix is

$$Q_{i+1} = \text{diag} [L_{i+1} \ L_{i+1} \ L_{i+1} \ 0 \ 0 \ 0 \ 0 \ 0] \quad (26)$$

where

$$L_{i+1} = h_o^2 [\sigma_r^2 \tau_{i+1} + \sigma_e^2 + \sigma_\tau^2] \quad (27)$$

The measurement matrix is

$$M_{i+1} = \begin{bmatrix} 1 & \phi_{i+1} & 0 & 0 & 0 & 0 & 0 & 0 \\ 0 & 0 & 1 & \phi_{i+1} & 0 & 0 & 0 & 0 \end{bmatrix} \quad (28)$$

and the measurement noise covariance matrix

$$R_{i+1} = \begin{bmatrix} \sigma_L^2 & 0 \\ 0 & \sigma_{L_1}^2 \end{bmatrix} \quad (29)$$

where

$$\sigma_{L_1}^2 = \sigma_L^2 + h_o^2 \sigma_P^2 + k^2 \phi_{i+1}^2 \sigma_r^2 \quad (30)$$

Fitted with appropriate initial conditions, the following equations define the errors in the optimal estimator of the state  $x$  at  $t_{i+1}$

$$S_{i+1} = \Phi_{i+1} P_i \Phi_{i+1}^T + Q_{i+1} \quad (31)$$

$$K_{i+1} = S_{i+1} M_{i+1}^T [M_{i+1} S_{i+1} M_{i+1}^T + R_{i+1}]^{-1} \quad (32)$$

$$P_{i+1} = [I - K_{i+1} M_{i+1}] S_{i+1} \quad (33)$$

Noting Equations (1) and (2), the resulting ground track errors are

$$E \begin{bmatrix} 2 \\ \epsilon_{x_1} \end{bmatrix} = \begin{cases} S(3,3) + \phi^2 S(2,2) + 2\phi S(1,2) \\ P(1,1) + \phi^2 P(2,2) + 2\phi P(1,2) \end{cases}_{i+1} \quad ; \quad t_{i+1}^- \quad (34)$$

$$; \quad t_{i+1}^+ \quad (35)$$

$$E \begin{bmatrix} 2 \\ \epsilon_{x_2} \end{bmatrix} = \begin{cases} S(3,3) + \phi^2 S(4,4) + 2\phi S(3,4) \\ P(3,3) + \phi^2 P(4,4) + 2\phi P(3,4) \end{cases} \quad ; \quad t_{i+1}^- \quad (36)$$

$$; \quad t_{i+1}^+ \quad (37)$$

with, of course, similar expressions for relative rather than absolute errors.

#### 5.2.5.4.5 Error Allocations

The above equations were programmed on the timeshare system in order to conduct rigorous covariance analyses. In fact, simple observation of the above equations leads rather directly to a fairly accurate allocation of errors, as the more detailed simulation results testify. The latter will thus not enter into the ensuing discussion.

It should be noted that a considerable number of judgements must be made in this allocation task, not all of which can be solidly defended, as the performance requirements and desires are, themselves, somewhat vague. Thus these judgements and assumptions will be developed in a controlled fashion, so that it will be easy to backtrack should a significant issue arise regarding one or more of these assumptions. In other words, reallocations can be quickly and easily performed.

The three most basic assumptions which drive the overall error allocations are the following:

- I) The relative shift of the same ground point over a 17-day period is 5m ( $1\sigma$ ). This is undoubtedly a conservative estimate for most ground points, but is adequate for our purposes here.
- II) The computational effort required by the software in order to correlate the same ground point on two images depends heavily upon the anticipated size of the search region. It will be assumed that this region is governed by the fact that the anticipated initial in-track and cross-track relative location is 300m ( $1\sigma$ ).
- III) Ground software memory requirements are adversely affected whenever the Thematic Mapper scan trace is not orthogonal to the projection of the spacecraft orbital velocity vector upon the surface of the earth. Estimation errors in spacecraft attitude yaw and ephemeris rates govern the degree of this orthogonality, and it is assumed that a 0.01 deg ( $1\sigma$ ) "effective" yaw estimation error is acceptable.

a. Bounding  $x_i$  ( $i = 1, 8$ ),  $L$  and  $R$

Table 5-53 documents the bounds on the important system variables. The following sub-paragraphs document the reasoning.

1. CDPF User





$x_1$  to  $x_8$  are accurately calibrated by the ground software Kalman Filter after use has been made of 3 to 5 ground control points. A reasonable estimate of the per axis error variance just prior to an update is (measurement accuracy)<sup>2</sup> +  $L$ . Allotting to  $\sqrt{L}$  the same 5 m uncertainty as exists according to (I), the pre-filter estimate assumes a reasonable value of 7.1 m.  $h_o \sigma_p$  is chosen as 3.5 m so that in Equation (30) it has a negligible effect upon  $\sigma_{L_1}$  with its 5 m error in  $\sigma_L$ .

2. LCGS User

Neither the CDPF or the LCGS can do much to combat the effect of  $\sqrt{L}$  and  $h_o \sigma_p$ . The latter system, being the less precise, will not introduce more stringent requirements, but will instead, assume those values previously noted. The LCGS user compensates (calibrates) the significant terms  $x_1$  to  $x_4$ , but cannot easily overcome the fixed drift rates that form

$x_5$  to  $x_8$ . As Equation (25) shows,  $x_5$  directly affects  $x_1$  (and thus  $\epsilon_{x_1}$ ) and is thus permitted the same error as already accepted for a similar degradation,  $\sqrt{L}$ . Since an image covers about 30 sec of elapsed time,  $x_5 = 5/30 \approx 0.17$  m/sec. Similar comments apply to  $x_7$ .  $x_6$  and  $x_8$  have a similar influence as  $x_5$  and  $x_7$  but get involved in multiplication by the scan angle,  $\phi$ , before affecting respectively  $\epsilon_{x_1}$  and  $\epsilon_{x_2}$ . Permitting the latter effects to be but one-half of the former and noting that  $|\phi| < 0.16$ , it follows that  $x_6$  and  $x_8$  have about three times the freedom (0.53 m/sec) of  $x_5$  and  $x_7$ .

Table 5-53. One Sigma Bounds On Error Sources

Variable	CDPF User	LCGS User	Ground Software
$x_1(t_0)$ (m)	<div style="text-align: center;">             Calibrated by Filter    </div>	<div style="text-align: center;">             Two Point User Calibration    </div>	300
$x_2(t_0)$ (m)			250
$x_3(t_0)$ (m)			300
$x_4(t_0)$ (m)			900
$x_5(t_0)$ (m/sec)		.17	-
$x_6(t_0)$ (m/sec)		.53	-
$x_7(t_0)$ (m/sec)		.17 (.33)*	-
$x_8(t_0)$ (m/sec)		.53	-
$\sqrt{L}$ (m)	5	5	-
$h_o \sigma_p$ (m)	3.5		-

\*0.33 m/sec corresponds to an ephemeris velocity error (out-of-plane) equivalent to a 0.0025 deg yaw rotation. This is insignificant when compared to the 0.01 deg allowed by assumption III.

### 3. Ground Software Constraints

$x_1$  and  $x_3$  at the initial time,  $t_0$ , enter directly into the ground errors  $\epsilon_{x_1}$  and  $\epsilon_{x_2}$ , respectively, and thus are set to 300 m by assumption (II). Noting Equations (2),  $x_4$  has less effect upon  $\epsilon_{x_2}$  due to the multiplication by  $\phi$  which is bounded by 0.16 rad. Letting  $x_4$  have, at most, half the effect of  $x_3$ , the spec on  $x_4$  becomes 900 m.  $x_2$  involves the yaw angle which by (III) must be held to 0.01 deg. Multiplying by  $h_0$  for a 900 n.mi. orbit,  $x_2$  is limited to 250 m.

#### b. Subsystem Specifications

Table 5-54 displays the partitioning of the error sources given in Table 5-53 into their various components. Factors based upon judgment are assigned to each of the latter with the resultant allowance then appearing in the right hand column. These results will now be translated into more familiar terms for each of the subsystems.

#### 1. Definition of Error Terms

Given the general error signal  $\theta(t)$  defined on  $0 \leq t \leq T$ , the following basic error terms are defined

##### Bias

$$\theta(0)$$

##### Drift Rate

Define the drift rate,  $b$ , to satisfy

$$\int_0^T [\theta(t) - \theta(0) - c_d t] dt = 0 \quad (38)$$

for  $T$  very large

Then

$$b = \frac{1}{T^2} \int_0^T [\theta(t) - \theta(0)] dt \quad (39)$$

$T$  large

Table 5-54. Primary Error Allocations

	Symbol	Factor	Result
$x_1$ (300 m)	$z^{(1)}$	0.5	120
	$h_o \theta^{(a, 2)}$ attitude estimate	0.5	120
	$h_o \theta^{(a, 2)}$ attitude control	0.25	60
	$h_o \theta^{(\tau, 2)}$	1	240
$x_2$ (250 m)	$h_o \theta^{(a, 3)}$ attitude estimate	0.5	109
	$h_o \theta^{(a, 3)}$ attitude control	0.25	55
	$h_o \theta^{(\tau, 3)}$	1	218
$x_3$ (300 m)	$z^{(2)}$	0.5	117
	$h_o \theta^{(a, 1)}$ attitude estimate	0.5	117
	$h_o \theta^{(a, 1)}$ attitude control	0.25	58
	$h_o \theta^{(\tau, 1)}$	1	235
	$h_o b(p)$	0.25	58
$x_4$ (900 m)	$z^{(3)}$	1	900
	$k b(r)$	-	30
$x_5$ (0.17 m/s)	$h_o b^{(a, 2)}$ Attitude estimate	0.5	0.07
	$h_o b^{(a, 2)}$ Attitude control	0.25	0.035
	$h_o b^{(\tau, 2)}$	0.5	0.07
	$b(e, 1)$	1	0.14
$x_6$ (0.53 m/s)	$h_o b^{(a, 3)}$ Attitude estimate	1	0.35
	$h_o b^{(a, 3)}$ Attitude control	0.5	0.17
	$h_o b^{(\tau, 3)}$	1	0.35
$x_7$ (0.17 m/s)	$h_o b^{(a, 1)}$ Attitude estimate	0.5	0.07
	$h_o b^{(a, 1)}$ Attitude control	0.25	0.035
	$h_o b^{(\tau, 1)}$	0.5	0.07
	$b(e, 2)$	1	0.14
$x_8$ (0.53 m/s)	$b(e, 3)$	1	0.53
$\sqrt{L}$ (5 m)	$h_o \sigma_v \sqrt{\tau}$	1	3.33
	$h_o \sigma_e$	0.5	1.67
	$h_o \sigma_r$	1.0	3.33
$\sigma_{L_1}$	$\sigma_L$	1	5(A)
	$h_o \sigma_p$	0.5	3.5
	$k \phi \sigma_r$	-	3.2(B)

(A) Assumption (I)

(B) Worst Case for  $\sigma_x = 10$  m

### Drift Rate Deviation

For  $0 \leq T_1 < T_2 \leq T$ , define the apparent drift rate as

$$c(T_1, T_2) = \frac{2}{(T_2 - T_1)^2} \int_{T_1}^{T_2} [\theta(t) - \theta(T_1)] dt \quad (40)$$

Then the drift rate deviation over  $[T_1, T_2]$  is simply

$$\Delta c(T_1, T_2) = c(T_1, T_2) - b \quad (41)$$

Whereas drift rate can be considered as a stationary effect, drift rate deviation arises due to noise sources in the system, and is thus a random variable. The CDPF Kalman Filter can successfully calibrate drift rates, but is somewhat at the mercy of drift rate variations.

### Jitter

$$\sigma_{\beta}(T_1, T_2) = \left\{ \frac{1}{T_2 - T_1} \int_{T_1}^{T_2} [\theta(t) - \theta(T_1) - c(t - T_1)]^2 dt \right\}^{1/2} \quad (42)$$

A general error model inclusive of all the models considered above is given by

$$\theta(t) = \theta(0) + bt + n_v + n_e \quad (43)$$

where  $n_v$  and  $n_e$  are the noise processes described previously. Setting

$$T_d = T_2 - T_1 \quad (44)$$

it can be shown that

$$\sigma_{\beta}(T_1, T_2) = \left[ \sigma_e^2 + \frac{\sigma_v^2 T_d}{9} \right]^{1/2} \quad (45)$$

and that the apparent drift rate,  $c(T_1, T_2)$  has the statistics

$$E\{c(T_1, T_2)\} = b \quad (46)$$

$$E\left\{\left[c(T_1, T_2) - b\right]^2\right\} = \frac{4\sigma_v^2}{3T_d} + \frac{4\sigma_e^2}{T_d^3} \quad (47)$$

Thus when  $T_d$  is large, the apparent drift rate equals the drift rate which equals  $b$ , as the second moment becomes negligible. When  $T_d$  is not large (e.g., 2 minutes), drift rate variation can be significant, the variance of  $\Delta c$  being given by Equation (43).

## 2. Resultant Specifications

The values of Table 5-54 lead directly to specifications upon  $z^{(1)}$ ,  $\theta^{(a, 2)}$ ,  $\sigma_v$ ,  $\sigma_e$ ,  $\sigma_T$  . . . etc. Noting Equations (45) and (47), it is now a simple matter to detail each error source for the five subsystems noted. The results appear in Tables 5-55 through -59. Should any of these specifications be particularly tight, it is, of course, possible to alter the factors noted in Table 5-54. If larger relief is required, one or more of assumptions (I) to (III) may have to be relaxed.



Table 5-55. Attitude Estimation Specification<sup>(A)</sup>  
(1 $\sigma$ )

	Earth Pointing		Stellar Interial or Sun <sup>(B)</sup> Pointing (per axis)
	Roll, Pitch	Yaw	
Bias	15 $\widehat{\text{sec}}$	25 $\widehat{\text{sec}}$	0.05 $\widehat{\text{min}}$
Drift	0.009 deg/hr	0.04 deg/hr	0.004 deg/hr over 1 hr
Drift Rate Deviation	0.004 deg/hr over 2 minutes	0.012 deg/hr over 2 minutes	0.004 deg/hr for 30 sec $\leq t < 1$ hr
Jitter	0.25 $\widehat{\text{sec}}$ rms	0.75 $\widehat{\text{sec}}$ rms	2 $\widehat{\text{sec}}$ rms for times up to 1 hr

(A) Refers to the Accuracy of Estimate of Attitude of Star Tracker Mounting Surface.

(B) GSFC/NASA RFP Spec.

Table 5-56. Attitude Control Specification<sup>(A)</sup>

	Earth Pointing		Stellar Inertial or Sun <sup>(B)</sup> Pointing (per axis)	Stellar Inertial (C) Using Experiment as Sensor
	Roll, Pitch	Yaw		
Bias	7.5 $\widehat{\text{sec}}$	12.5 $\widehat{\text{sec}}$	0.25 $\widehat{\text{min}}$	0.01 $\widehat{\text{sec}}$
Drift	0.005 deg/hr	0.02 deg/hr	0.002 deg/hr over 1 hr	N/A
Draft Rate Deviation	0.002 deg/hr over 2 minutes	0.006 deg/hr over 2 minutes	0.002 deg/hr for 30 sec $\leq t \leq$ 1 hr	N/A
Jitter	0.12 $\widehat{\text{sec}}$ rms over 2 minutes	0.37 $\widehat{\text{sec}}$ rms over 2 minutes	1 $\widehat{\text{sec}}$ rms for times up to 1 hr	0.004 $\widehat{\text{sec}}$ rms for times up to 1 hr

(A) Refers to control using ideal sensors of Star Tracker Mounting Surface.

(B) GSFC/NASA RFP Spec when separate Attitude Estimation Module is used.

(C) GSFC/NASA RFP Spec when the experiment becomes the attitude sensor.

Table 5-57. Ephemeris Specification<sup>(A)</sup>

(Earth Pointing Mode— $1\sigma$ )

	Along Roll or Pitch Axes	Along Yaw Axis
Bias	120 m	900 m
Drift	0.15 m/sec	0.50 m/sec

(A) Accuracy of the ephemeris data utilized by the CDPF

Table 5-58. Thematic Mapper Scan Angle

( $1\sigma$ )

Bias	$7 \text{ sec}$
Jitter (e.g., non-linearity)	$0.45 \text{ sec rms}$

Table 5-59. Thermal/Structural Specification<sup>(A)</sup>

	Earth-Pointing		Stellar-Inertial/Sun Pointing
	Roll, Pitch	Yaw	
Bias	$30 \text{ sec}$	$30 \text{ sec}$	$0.25 \text{ min}$
Drift	0.009 deg/hr	0.04 deg/hr	0.002 deg/hr
Jitter	$1.0 \text{ sec rms}$ <sup>(B)</sup>	$3.0 \text{ sec rms}$	$1 \text{ sec rms}$

(A) Refers to error in the estimate of the attitude of the Thematic Mapper mounting surface relative to that of the star tracker. A fixed bias in yaw can be compensated by an attitude yaw command.

(B) A + baseline altitude of 386 nmi.

#### 5.2.6 Safe Mode Definition

This section defines the general characteristics of the SAFE mode, and the associated implications for EOS spacecraft and payload modules.

The SAFE mode is intended to ensure the survival of the spacecraft in the event of on-board component failures in order to permit either:

- (i) Switching in of redundant hardware by ground command (following ground-based failure diagnosis) as a non-(time) critical operation; or
- (ii) Observatory retrieval (or resupply) using Space Shuttle (allowing for realistic space servicing delay times).

Necessary functions for survival include:

- Maintenance of some nominal level of electric power
- Avoidance of temperature extremes which would threaten survival
- Attitude control as required by other functions (in particular, electric power)
- For a redundant spacecraft (or one which requires de-orbiting for servicing, i.e., elliptical orbit servicing), maintenance of command and telemetry capability

The primary stay-alive function, without which no other functions will operate, is generation of electric power; this consideration has been paramount in defining the SAFE mode.

#### 5.2.6.1 Safe Mode: General Description

The SAFE mode will be entered when there is a clear indication that the spacecraft is in a long-term negative energy balance condition. When this occurs, the observatory will be powered down, the solar array drive will be driven to give an appropriate array angle (i.e., so that the array face normal is at its minimum angle relative to the minus yaw axis). The payload (DCS and Wideband Communications and Data Handling) will be powered down. The attitude control system will sun-point the minus yaw (-Z) axis using cold gas thrusters, data from a coarse sun sensor, and special-purpose backup control electronics. All SAFE mode functions will be implemented without use of the On-Board Computer or the Data Bus.

#### 5.2.6.2 Safe Bus

A common SAFE bus will terminate in the module connector of each (payload and spacecraft) module. So long as this bus is "high" (e.g., ungrounded), each module will remain in its normal operational configuration. If the SAFE bus goes "low", the appropriate payload and spacecraft elements are switched (internally) into their SAFE configuration (defined below). The SAFE bus can be returned to the "high" condition only by ground command.

#### 5.2.6.3 Safe Mode Entry

The SAFE mode will be entered (SAFE bus driven low) after a clear and persistent indication of a continuing negative energy balance condition. The logic to make this determination will be incorporated within the Power Module. The selected approach, based on a previous design, enables the SAFE mode if either of two conditions occurs:

- 1) Battery discharge occurs for a time exceeding the maximum eclipse, plus some additional time period (TBD); or
- 2) Two eclipses occur without two of the three being recharged (for a three-battery configuration).

#### 5.2.6.4 Safe Mode Configurations

The SAFE mode status of all observatory elements will be as described (in summary form) below.

- (a) Thematic Mapper: The TM will remain heated or fully powered to avoid degradation due to thermal extremes. Power consumption will be unchanged.
- (b) HRPI: Same as TM.
- (c) Data Collection System: The DCS will be unpowered.
- (d) Wideband Communications and Data Handling: The WBC & DH will be unpowered.
- (e) Payload Structure: Thermal control will be disabled (unpowered).
- (f) Spacecraft Structure: Thermal control will be disabled (unpowered).
- (g) Communications and Data Handling Module: The On-Board Computer will be unpowered.
- (h) Power Module: No change from operational.
- (i) Array and Drive Module: Array drive will drive array to maximum power condition with sun along -Z axis.
- (j) Attitude Determination Module: Gyro packages unpowered\*. Backup control electronics employed to control attitude via direct lines to Actuation Module.
- (k) Actuation Module: Wheels, magnetic torquers disabled. Pneumatics enabled by SAFE bus\*\*. Hydrazine system thermal control maintained.

---

\* Gyro integrity to be reviewed.

\*\* Pneumatics will normally be disabled via latching valves in normal operation.

### 5.2.7 Reaction Wheel Selection

#### 5.2.7.1 Definition

In this section we will determine reaction wheel requirements (torque, momentum, etc.), review existing designs and current developments that are compatible with EOS-A and follow-on missions, consider redundant wheel configurations, perform tradeoffs to select reaction wheels for standard actuation inventory, and identify any wheel developments required.

#### 5.2.7.2 Motivation

In order to minimize non-recurring development costs, it is necessary to determine if EOS-A and follow-on mission requirements can be met with existing "off-the-shelf" reaction wheel designs. The selection of a minimum number of standard reaction wheel types for the EOS inventory will minimize program costs.

#### 5.2.7.3 Methodology

Reaction wheel performance requirements have been assessed in Section 5.2.4, Part 1. The performance of existing wheel designs was compared with the range of EOS requirements and candidate wheel designs were selected as the standard inventory for the spectrum of EOS missions. Attitude control performance was verified with the selected wheel designs in Section 5.2.4, Part 2. Reliability trades were performed to establish the numerical reliability as a function of redundancy level for both orthogonal and non-orthogonal wheel configurations.

#### 5.2.7.4 Results

##### 5.2.7.4.1 Reaction Wheel Selection

A large number of flight proven reaction wheel designs are available from two major suppliers - Bendix and Sperry. These candidate reaction wheels and associated performance data are summarized in Table 5-58.

Reaction wheel torque and momentum requirements are summarized in Table 5-59 based on the analyses compiled in Section 5.2.4. In the interest of standardization for minimum cost, a single wheel design which is compatible with the most stringent mission requirements from Table 5-59 has



Table 5-58. Candidate Reaction Wheels

Mfg. & Part No.	Program Usage	Momentum Ft-Lb-Sec@RPM	Torque (In-Oz)	Peak Power (Watts)	Weight (Lb)	Size (In.)
BENDIX 1898720	NIMBUS	.33 @ 1250	4	10.5	5.0	6.5 Dx3.5
177860	NIMBUS	.4 @ 1250	2	4.6	4.8	6 D x 3.0
1871380	NIMBUS	.57 @ 1250	4	10.5	8.0	6 D x 6.9
180164	NIMBUS	1.44 @ 1250	4	10.5	8.8	7.5Dx 3.5
1778770	ADVENT	1.17 @ 1250	4	9.5	7.6	6.5Dx 3.0
1791290	ADVENT	1.46 @ 1000	2	4.6	10.1	7.5Dx 3.5
1823407	OGO	1.44 @ 1250	7	25	9.1	7.5Dx 3.9
1823408	OGO	7.2 @ 1250	20	53	16.5	12 Dx 4.7
1880272	OA0	2.1 @ 900	2	3.3	10.0	10.5Dx 4.3
1804280	OA0	3.56 @ 1000	33	62	16.6	12 Dx 4.8
1880026	VELA	8.47 @ 1250	20	53	17.0	12 Dx 4.7
SPERRY 1	—	1 @ 2000	5	6.0	20	8.8Dx 4.9
15	FLTSATCOM	8 @ 3600	15	115	14.5	11 Dx 5.5
	SPAR	15 @ 3750	7	50	14.8	11 Dx 8.5
30	—	30 @ 4750	10	56	17.8	14.5Dx 7.4
45	—	45 @ 5200	8	70	21.8	15.5Dx 7.5
400	MODEL-35	420 @ 4100	10	88	70	24D x 9



Table 5-59. EOS-A Reaction Wheel Requirements

		Momentum (ft-lb-sec)	Torque (in-oz)
Slew Mode <sup>(1)</sup>	Thor/Delta	1	3.0
	Titan	3	10.0
Disturbance Torques	Thor/Delta	2	0.4
	Titan	1	0.2

(1) Slew rate of 2 degrees/minute achieved in one minute time interval

been selected for use on all three control axes. This minimum cost approach may result in a modest weight penalty ( $\approx 10$  lbs per spacecraft).

From the candidate wheels listed in Table 5-58, the Bendix OGO unit (1823408) (7 ft-lb-sec momentum and 20 in-oz torque) has been selected for the baseline design. This selection may result in excess wheel performance capability for some missions but permits a single design with adequate design margin which is compatible with a broad spectrum of EOS mission applications.

#### 5.2.7.4.2 Reliability Tradeoffs

Orbital experience and ground test programs have shown that the reliability and life expectancy for the Bendix and Sperry reaction wheels is extremely high. On-going life test programs with Bendix OGO and Sperry DSP wheels have completed in excess of 10 years and 5 years, respectively, of continuous running without failure. Successful orbital operation in excess of four years has been accumulated to date on individual wheels.

A reliability assessment was performed for the candidate wheel/electronics redundancy configurations shown in Figure 5-141. The assessed reliability versus time results are shown in Table 5-60.

These results show as expected, that adding redundant wheels doesn't significantly improve reliability, whereas incorporating redundant wheel drive electronics results in a significant improvement. Based on

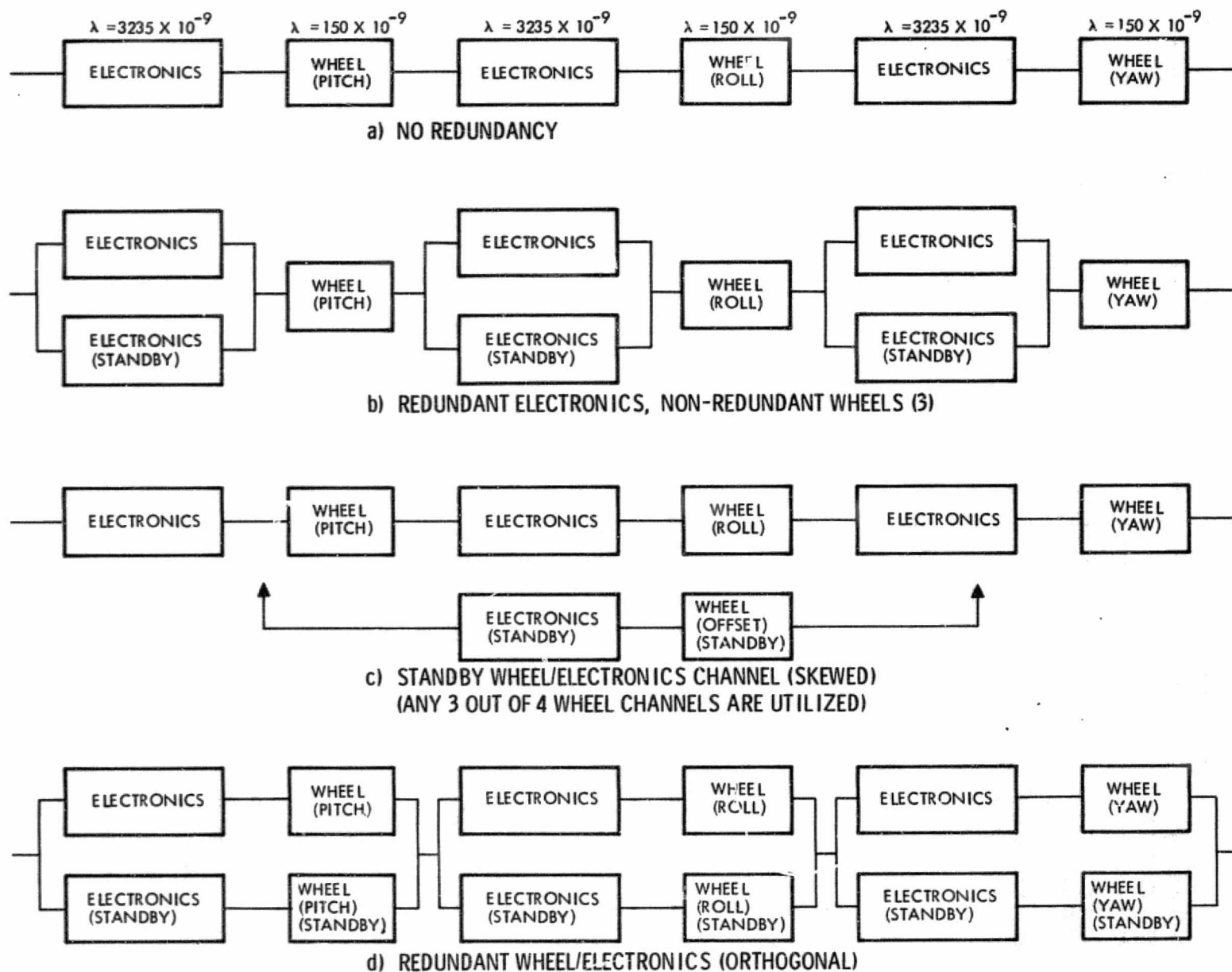


Figure 5-141. Redundant Wheel Configurations

Table 5-60. Wheel/Electronics Reliability

Redundancy Configuration	Years				
	1	2	3	4	5
No Redundancy	.9301	.8650	.8046	.7483	.6960
Redundant Electronics/ Non-Redundant Wheels(3)	.9948	.9871	.9772	.9652	.9513
4-Wheel/Electronics Channels (3 out of 4 required)	.9961	.9855	.9692	.9484	.9239
3 Orthogonal Redundant Wheel/Electronics Channels (six wheels)	.9986	.9944	.9878	.9788	.9676

this reliability analysis, the recommended wheel/electronics configuration for EOS-A incorporates a single reaction wheel for each of the three control axes, with each wheel being driven by a set of standby redundant electronics.

#### 5.2.7.4.3 Advanced Missions

The actuation module can easily accommodate larger reaction wheels which may be required for advanced EOS missions. An example of a large reaction wheel for potential application in advanced missions is the unit to be developed for the HEAO spacecraft. The HEAO reaction wheel design parameters are the following:

- Angular momentum                      30 ft-lb-sec
- Torque                                      20 in-oz
- Weight                                      28.5 lbs
- Size                                        14" dia. x 8" height
- Power                                       100 watts, peak

### 5.3 PROPULSION

#### 5.3.1 Propulsion System Design — Titan Configuration

##### 5.3.1.1 Orbit Transfer Sizing

##### 5.3.1.1.1 Task Description

Evaluate propulsion system alternatives and select a system to perform the orbit transfer maneuver. Consider incorporating orbit adjust capability into the system. Three categories of systems will be considered:

- 1) A system consisting of four solid rocket motors to provide impulse for the two transfer maneuvers and four hydrazine thrusters to provide impulse for orbit trim and orbit adjust.
- 2) An earth storable bipropellant system capable of performing both orbit transfer and orbit adjust maneuvers.
- 3) A monopropellant system similarly capable of performing the transfer and adjust maneuvers.

Each system will be compared on the basis of cost, weight, reliability, and operational considerations.

##### 5.3.1.1.2 Problem Discussion

The orbit transfer propulsion system must perform the dual functions of circularizing the elliptical orbit and subsequently returning from the circular orbit to the original elliptical orbit. In addition, it is desirable to incorporate orbit adjust capability into the system particularly if the same hardware can perform both functions.

Typical transfer orbit propulsion missions, which are used to provide impulse for a single transfer maneuver from elliptical to circular orbits, are generally achieved with a single solid rocket motor. The solid motor

provides approximately the correct total impulse with final trimming of the orbit achieved by secondary pneumatic or monopropellant hydrazine thrusters. The normal sequence of events for this type of transfer maneuver is to spin the spacecraft, fire the solid rocket motor, despin the spacecraft, orient the spacecraft, trim the orbit, and finally deploy the various spacecraft appendages.

For the EOS, which must perform a return mission, geometric considerations of the spacecraft dictated that each transfer maneuver be performed by a pair of diametrically opposed solid rocket motors as shown in Figure 5-142.

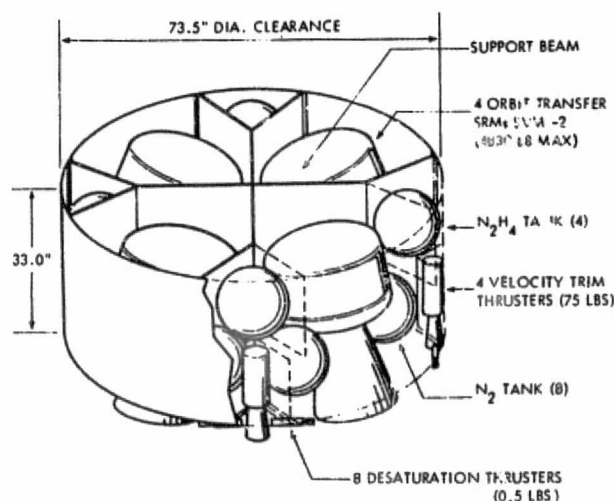


Figure 5-142. Solid Rocket Motor Orbit Transfer System

This arrangement of the solid rocket motors led to the configuration as shown in Figure 5-142, where the trim thrusters are located in the corners between each of the four solid rocket motors. This configuration has the desirable characteristic that these same trim thrusters can also be used to perform the orbit adjust maneuvers. In addition, the difference in impulse required to transfer into the circular orbit and to return to the elliptical

orbit can be made up by the trim thrusters. This capability makes it possible to standardize on the size of the solid motors. There are, however, disadvantages to this system. Primarily, the solid motors are inline and nonredundant such that a failure of any one of the four thrusters will result in loss of spacecraft. Secondly, because the system requires both solid motors and a hydrazine system, the cost will be significantly greater than either a bipropellant or monopropellant hydrazine system capable of performing the same functions.

Since the alternatives of an earth storable bipropellant system and a monopropellant hydrazine system have similar advantages and disadvantages, a trade study to compare the relative cost, weight, reliability, and operational characteristics was performed to determine the best type of system for EOS-A.

#### 5.3.1.1.3 Assumptions

Each of the three types of propulsion systems is shown schematically in Figures 5-143, -144, and -145. These systems each include a level of redundancy which was considered prudent within the constraints of vehicle geometry and the EOS-A mission objectives. The systems are representative of each category and were configured to permit comparisons on an equivalent basis. No specific attempt has been made at this point in the study to optimize the designs to maximize reliability and performance or to minimize cost.

In arriving at cost, weight, reliability, and performance characteristics, existing hardware was used throughout. The cost and weight values for component parts are sufficiently accurate to yield a high degree of confidence that the relative merits of each system has been accurately portrayed. The



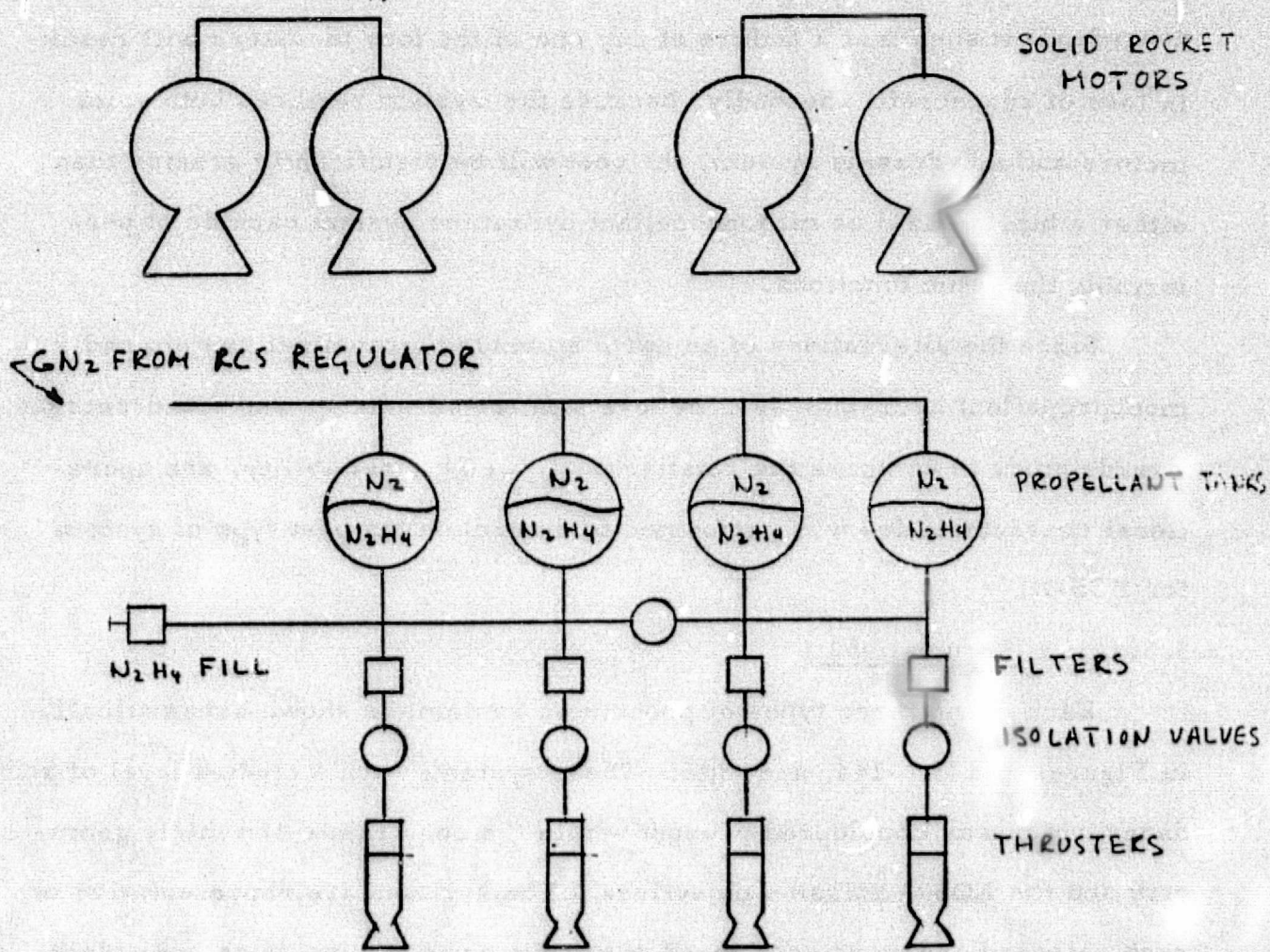


Figure 5-143. Solid Motor  $N_2H_4$  Trim and Orbit Adjust System

GN<sub>2</sub> FROM RCS REGULATOR

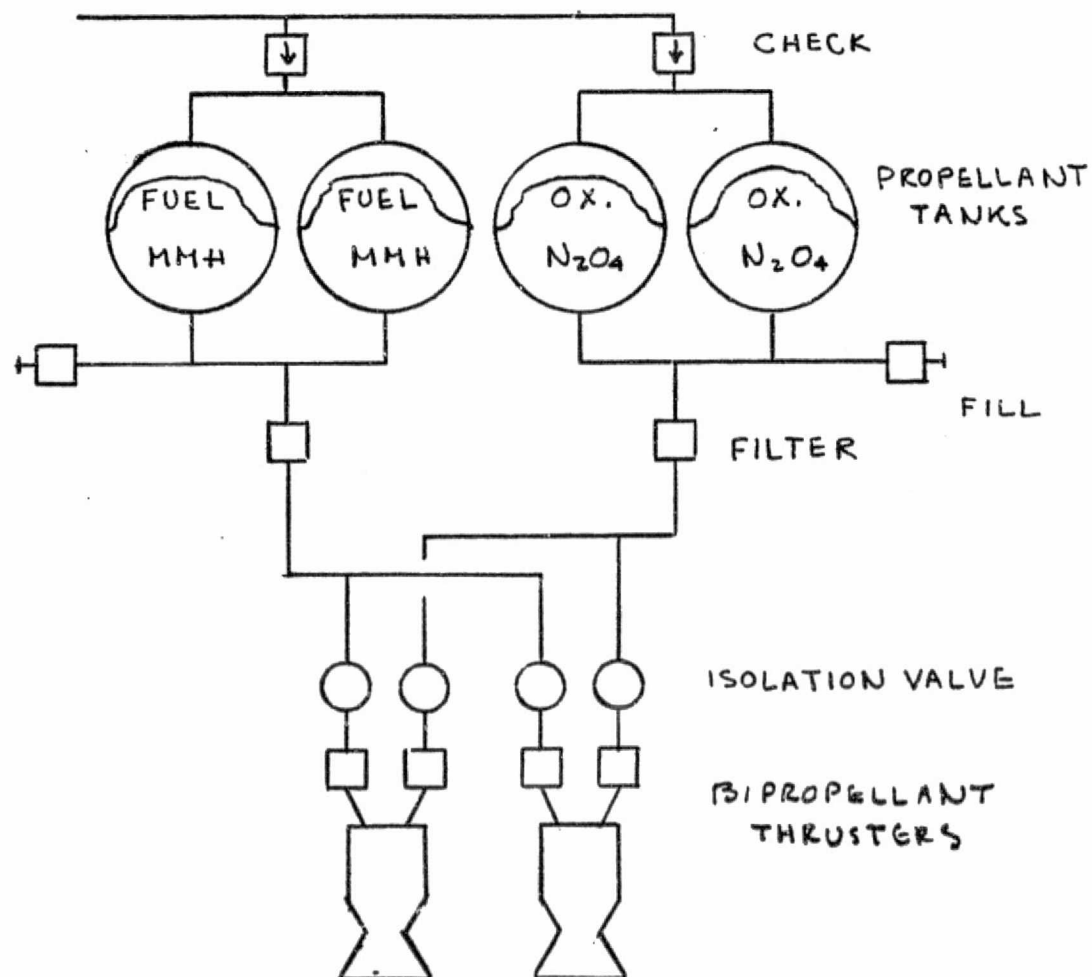


Figure 5-144. Bipropellant Orbit Transfer and Orbit Adjust System



GN<sub>2</sub> FROM RCS REG.

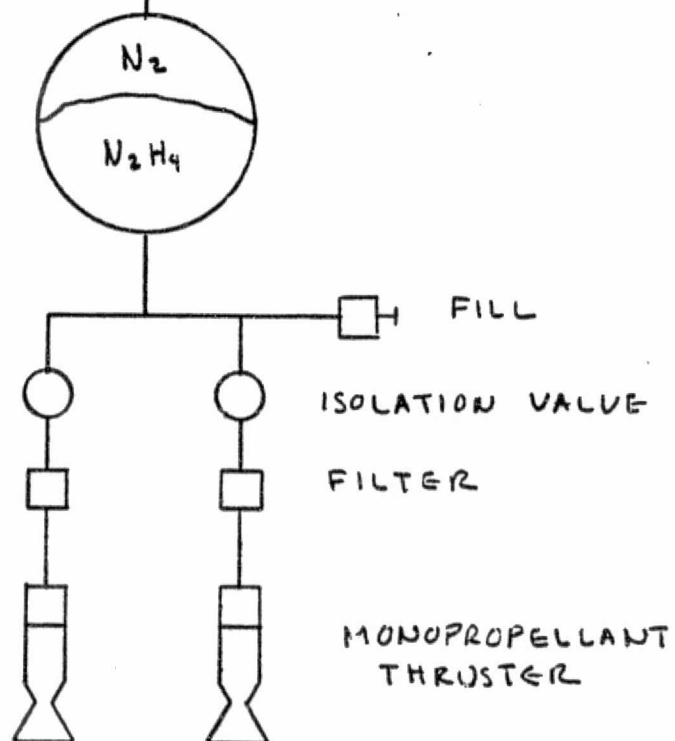


Figure 5-145. Monopropellant Orbit Transfer and Orbit Adjust System

supporting engineering and quality assurance costs are consistently factored based on similar programs and are representative of actual anticipated costs in 1974 dollars.

#### 5.3.1.1.4 Analysis and Tradeoffs

##### a. Cost Comparisons

Hardware lists for each of the three systems are shown in Tables 5-61, -62, and -63. Component costs were obtained from actual cost experience of on-going programs at TRW or from informal telecon quotations from vendors. The selected components have been qualified for use on previous programs. The one exception is the propellant tanks. Where optimum size tanks were not available, cost was interpolated from the two nearest available tank designs.

Table 5-61. Solid Motor -  $N_2H_4$  System

Component	Quantity	Unit Cost (000)	Total Cost (000)	Source
Solid Motors	4	75.0	300.0	Aerojet
Propellant Tanks	4	16.0	64.0	PSI
Thrusters	4	30.0	120.0	TRW
Filters	4	2.6	10.4	WINTEC
Isovalves	5	5.2	26.0	HRM
Fill Valve	1	3.9	3.9	TRW
Lines and Brackets			5.0	TRW
Integration and Test			15.0	
Engineering			70.0	
Q.A.			<u>21.0</u>	
Total			635.3	

Table 5-62. Bipropellant System

Component	Quantity	Unit Cost	Total	Source
Propellant Tanks	4	26.0	104.0	PSI
Thrusters	2	75.0	150.0	TRW
Filters	2	2.6	5.2	WINTec
Isovalves	4	5.2	20.8	HRM
Fill	2	3.9	7.8	TRW
Check	2	1.6	3.2	W.L. Leonard
Lines and Brackets			5.2	TRW
Integration and Test			15.0	
Engineering			70.0	
Q.A.			<u>27.0</u>	
Total			408.2	

Table 5-63. Monopropellant System

Component	Quantity	Unit Cost	Total	Source
Tank	1	47.0	47.0	PSI
Fill	1	3.9	3.9	TRW
Isovalves	2	5.2	10.4	HRM
Filter	2	2.6	5.2	WINTec
Thruster	2	30.0	60.0	TRW
Lines and Brackets			5.0	TRW
Integration and Test			15.0	
Engineering			60.0	
Q.A.			<u>15.0</u>	
Total			221.5	

The cost tradeoff study shows a significant cost advantage of the monopropellant system over the bipropellant system which in turn shows a significant advantage over the solid motor system.

b. Weight Comparison

Each of the three systems was sized on the basis of a 6000 lb initial weight vehicle and a  $\Delta V$  capability of 1142 ft/sec including orbit adjust. Specific impulse was assumed to be 288 seconds for the solid motors, 295 seconds for the bipropellant, and 230 seconds for the monopropellant. The solid motors are the Aerojet SVM-1, the bipropellant thruster is a TRW MMBPS 88 lb thrust motor operating on MMH +  $N_2O_4$ , and the monopropellant thruster is a TRW MRE-50. Weight comparisons of the three systems are shown in Table 5-64, -65, and -66.

Table 5-64. Solid Motor Weight

Item	Quantity	Unit Weight	Total
Solid Motors	4	192.8	771.2
$N_2H_4$ Tanks	4	3.5	14.0
Thrusters	4	3.5	14.0
Isovalves	5	0.6	3.0
Filters	4	0.5	2.0
Fill	1	0.5	0.5
Lines and Brackets			3.0
$N_2H_4$ Propellant			51.4
$GN_2$			1.3
$GN_2$ Tank (equiv)*			<u>1.6</u>
Total			862.0

\*Will be combined with RCS tanks

Table 5-65. Bipropellant System

Item	Quantity	Unit Weight	Total
Propellant			679.6
Tanks	4	10.0	40.0
Thrusters	2	7.5	15.0
Filters	2	0.5	1.0
Isovalves	4	0.6	2.4
Fill	2	0.5	1.0
Check	2	0.5	1.0
Lines and Brackets			3.0
GN <sub>2</sub>			12.3
GN <sub>2</sub> Tank (equiv)*			<u>15.0</u>
Total			770.3

Table 5-66. Monopropellant System

Item	Quantity	Unit Weight	Total
Propellant			857.4
Tank	1	56.0	56.0
Fill	1	0.5	0.5
Isovalves	2	0.6	1.2
Filter	2	0.5	1.0
Thruster	2	3.5	7.0
Lines and Brackets			3.0
GN <sub>2</sub>			23.7
GN <sub>2</sub> Tank (equiv)*			<u>28.5</u>
			978.3

\*Will be combined with RCS tanks

The weight comparison shows the bipropellant system has a significant weight advantage over the solid motor system which in turn has a similar advantage over the monopropellant system.

c. Operational Characteristics

Operational characteristics refer to considerations such as safety, impact of the propulsion system on other spacecraft subsystems, and long term space storability. These considerations were examined qualitatively to obtain a relative comparison between the three systems.

Solid Motor System Design Considerations

The solid rocket transfer motors adversely impact the design of several spacecraft subsystems. In order to compensate for the shift in the spacecraft center of gravity and the variability in thrust level between each motor, it is necessary to spin the spacecraft prior to firing the motors and to despin after shut down. In addition to spinning the spacecraft the relatively high thrust of the solid motors (approximately 6480 lbs as compared to less than 200 lbs for either liquid system) results in increased structural loads for appended equipment. Base heating and exhaust plume contamination are relatively more serious considerations with solid rocket motors than with the lower thrust, relatively cool and clean exhaust products of the liquid systems.

The long term space storability of solid rocket motors in a vacuum environment is not well characterized, but it is assumed that a suitable nozzle plug can be designed to circumvent this problem.

Handling and safety of solid motors as compared to the liquid systems would clearly be a plus factor except that trim and orbit adjust maneuvers require storage of pressurized  $N_2H_4$  as a necessary adjunct to the solid motors. Hence the safety and handling of the complete system is comparable to the  $N_2H_4$  system.

#### Bipropellant System

In general, the operational considerations related to the impact of the propulsion system on other vehicle subsystems is less severe than for the solid motor system. The lower thrust level and more precise control of the thrust level eliminates the need to spin the spacecraft or to retract appendages because of high "g" loads. The exhaust gases are cleaner and the base heating significantly lower than for solids. Long term storability of bipropellants may present corrosion and contamination problems which would degrade reliability. However, bipropellant systems are designed for storability of 10 to 20 years in military applications. There is a significant difference in the application because the EOS system would have to be capable of several usages over its lifetime whereas the military applications are one shot devices.

Corrosion and/or contamination resulting in leakage presents a potential safety hazard for shuttle operations significantly more serious than with monopropellants.

#### Monopropellant System

Operational considerations for the monopropellant system are less severe than either the solid motor system or the bipropellant system. Experience with monopropellants for long duration space missions has been demonstrated in a number of spacecraft. No significant operational drawbacks are evident for the monopropellant system.

#### 5.3.1.1.5 Conclusions

The monopropellant system is clearly superior to the solid motor / monopropellant system or the bipropellant system in the areas of cost, reliability, and overall operational characteristics. Because of the lower specific impulse of monopropellant hydrazine as compared to the solid rocket motor and the bipropellant motor, the propellant required and hence the system weight for the monopropellant system is approximately 100 lbs to 200 lbs greater than the solid or bipropellant systems. This weight disadvantage is not significant in the Titan configuration. Hence the selection of the monopropellant system is clearly justified.



#### 5.3.1.2 Orbit Transfer Design

##### 5.3.1.2.1 Task Description

Perform a preliminary modular design for the orbit transfer system. Select components, optimize performance, determine mass properties, and evaluate power requirements.

##### 5.3.1.2.2 Problem Discussion

Having selected the monopropellant system in Section c. the purpose of this task is to optimize the design to minimize cost and weight and to maximize reliability. The variables to be evaluated include the type of pressurization method - regulated or blow down; the operating pressure, the propellant orientation method, the type of propellant valve, and schematic arrangement of the components. After the variables have been evaluated, specific components will be recommended and the mass properties will be determined.

##### 5.3.1.2.3 Assumptions

As a general guideline, components were selected from existing qualified designs. Where optimization indicated the need for new components the designs were selected so that minimum development costs would be incurred.

##### 5.3.1.2.4 Analysis and Tradeoffs

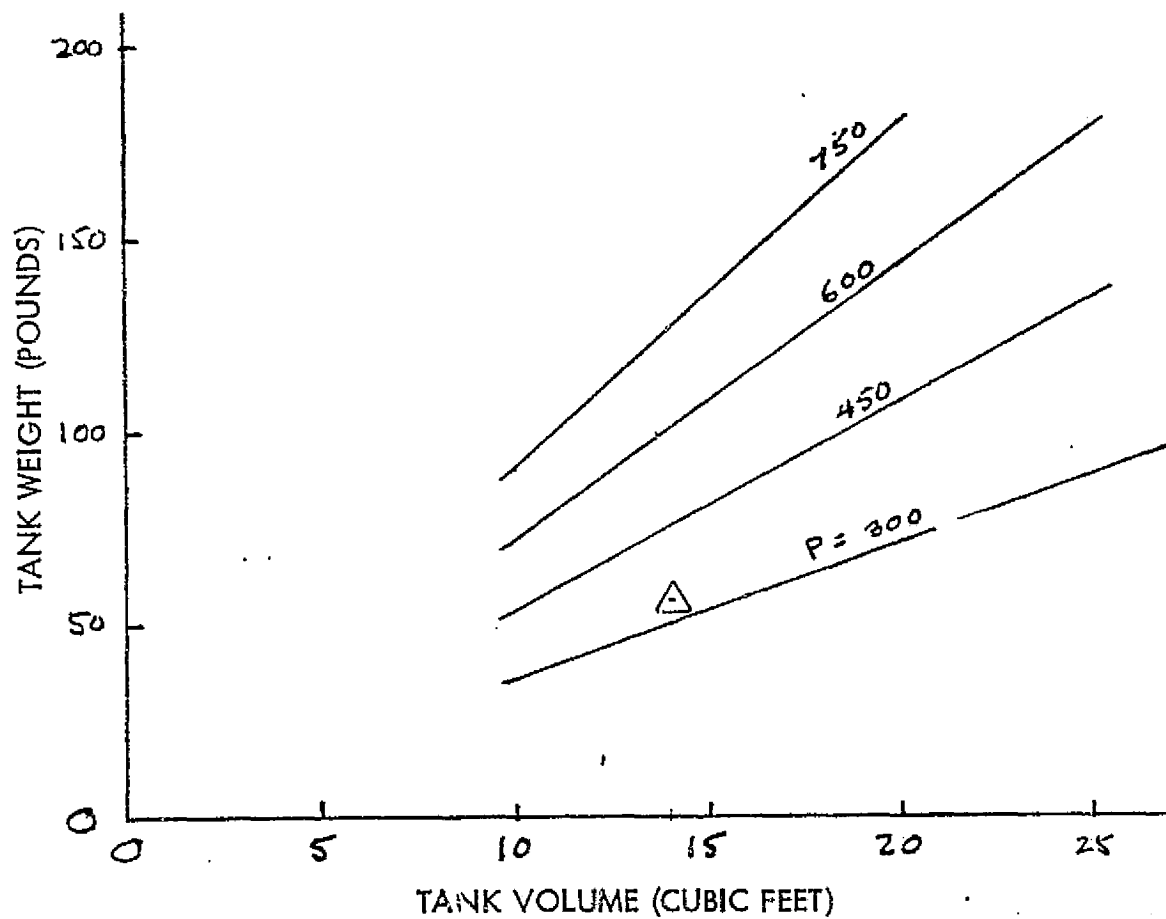
###### a. Pressurization Mode - Regulated versus Blowdown

Most current monopropellant systems use blowdown pressurization. The advantage of this mode of operation is that the pressurant storage tank and the regulator are eliminated in exchange for a modest weight penalty and increase in size of the propellant tank. In low total impulse systems

even this modest weight penalty tends to disappear. However, for the orbit transfer system which uses 857 pounds of propellant, the weight penalty is not insignificant and the additional volume required may be a problem. In addition, a regulated source of pressurant is available from the reaction control system which eliminates the need for an additional regulator.

For a pressure regulated system with a propellant capacity of 857 pounds, the tank volume required is 13.7 cubic feet corresponding to a tank diameter of 35.7 inches I.D. An existing hydrazine tank design, 36 inches in diameter, manufactured by PSI is ideally sized for this application. The tank is rated for 330 psia working pressure and weighs 56 pounds. This existing design provides a realistic base point for the pressure regulated system as well as a base point from which to compare the regulated system with various blowdown systems. Figure 5-146 shows estimated tank weights as a function of tank volume for various pressures using the 36 inch diameter tank as a base point and assuming that the tank weight varies directly with pressure and volume. For pressures below approximately 300 psi, minimum gage of the tank walls becomes a consideration such that the 300 psi line is essentially a minimum tank weight versus volume line in the size of interest.

For blowdown pressure fed systems the average specific impulse of the thruster decreases as the blowdown ratio increases, tank volume decreases with increased blowdown pressure ratio, tank pressure increases with increased blowdown pressure ratio, and pressurant weight decreases with increased blowdown pressure ratio. Combining all of these factors, as shown in Figure 5-147, results in system weight versus blowdown ratio that



△ BASE POINT  $P = 330$   $V = 19.1$   $W = 56$

Figure 5-146. Tank Weight versus Volume

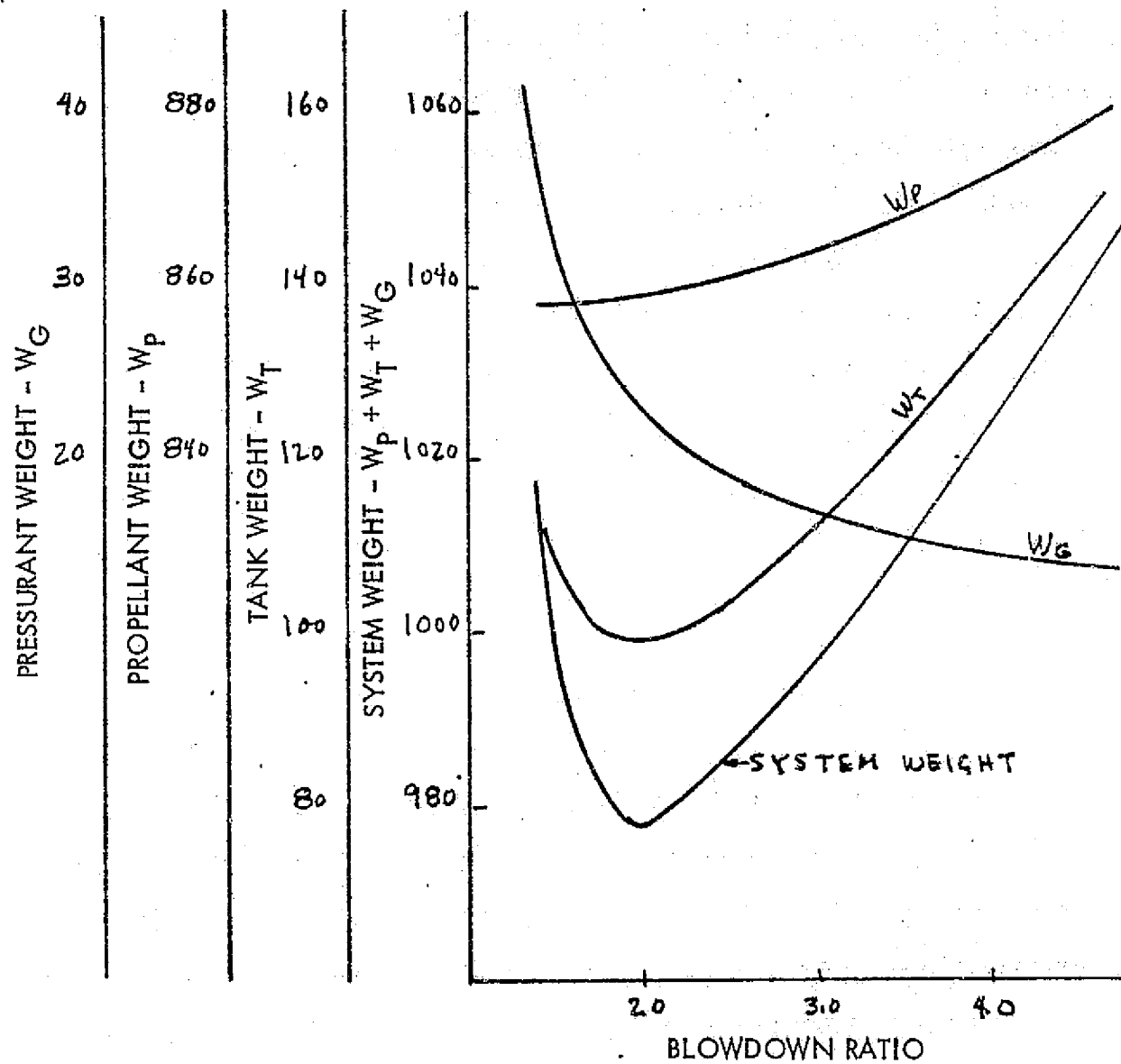


Figure 5-147. Blowdown System Optimization

optimizes in the region of 2.0:1 at a minimum weight of approximately 978 pounds for propellant plus pressurant plus tank.

For a pressure regulated system operating at a tank pressure of 300 psia the corresponding weight would be 956.1. This weight includes 858 pounds of propellant, 51 pounds for propellant tank, 21.4 pounds for pressurant gas, plus a gas storage tank weight of 25.7 pounds. Hence, the net weight savings for a regulated system would be approximately 22 pounds. However, more significant than the weight savings is the fact that the tank volume for the blowdown system would have to be increased by 13.7 cubic feet. This could be accomplished by adding a 23.2 inch cylindrical section between the 36 inch diameter hemispheres or increasing the tank diameter from 36 to 44.8 inches. Since the regulated system is lighter and more compact, and since the regulated gas supply is available from the RCS, there is no incentive to switch from the baseline regulated system to a blowdown system.

#### b. System Operating Pressure

The influence of system operating pressure on the weight of various system elements is shown in Figure 5-148. The break in the curves at 300 psi corresponds to the point beyond which the propellant tank wall thickness can practically be reduced because of manufacturing difficulties and increased cost. Taking into account the pressurant gas weight and the equivalent gas storage tank weight, which decrease with decreasing pressure, and thruster weight, which increases with decreasing pressure, the total pressure related system weight is relatively flat in the region below 300 psia tank pressure. As shown in Figure 5-148, system weight decreases

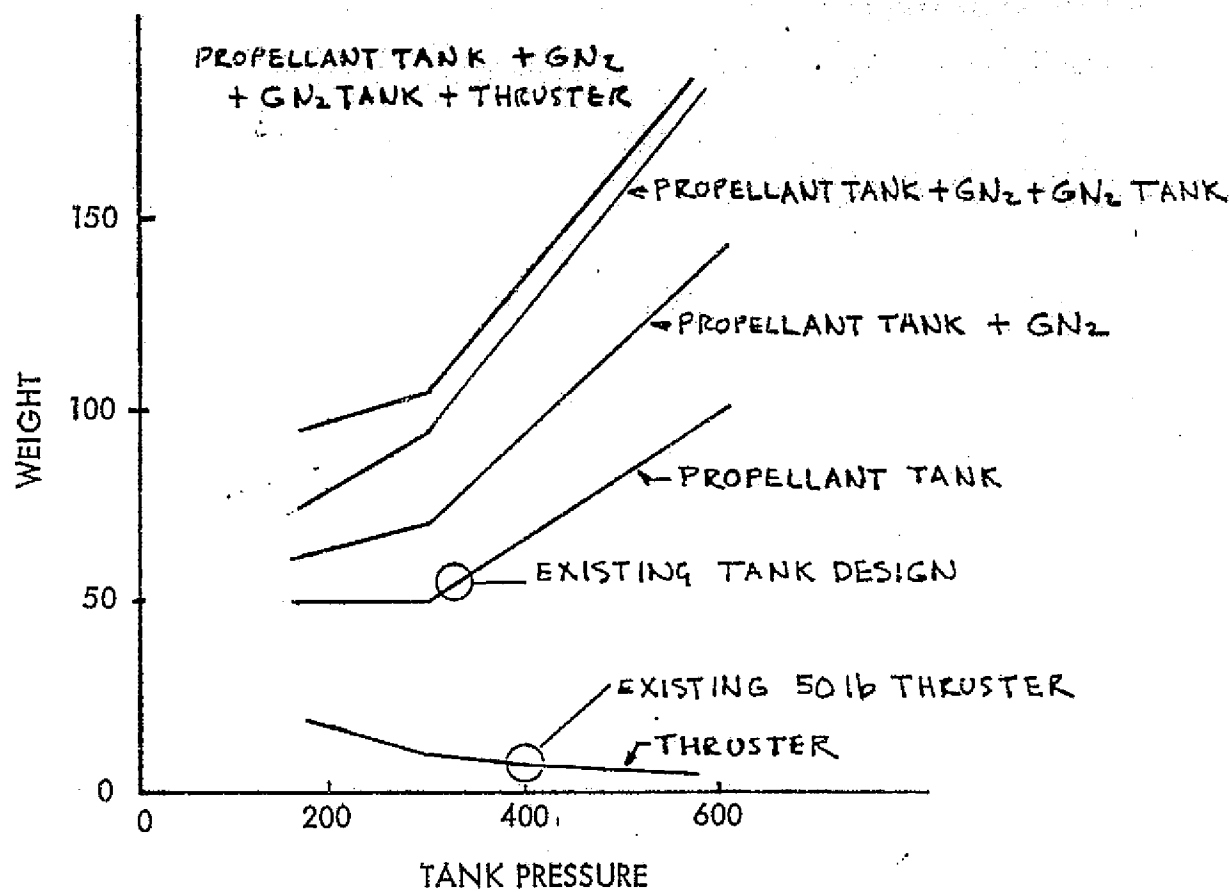


Figure 5-148. System Operating Pressure Weight Trade Off

only 5 pounds between 300 psia and 200 psia, and is probably flat below this point as the engine weight increase tends to offset the pressurant weight decrease.

Considering the availability of hardware and the effect on cost there is a trade between modifying the existing 50 lb thruster to operate at a lower pressure as opposed to redesigning and requalifying the tank for higher operating pressure. Neither of these options involves a significant engineering risk and the cost implications are approximately equal.

Therefore it appears that the best compromise considering both weight and cost is to select an operating pressure in the region of 300 psia and to modify the engine to operate at this pressure. Reducing pressure below 300 psia would require more extensive thruster modifications which do not appear warranted for the minimal weight savings that would be achieved.

c. Propellant Orientation Control

Three options were examined for propellant orientation: 1) positive expulsion devices such as diaphragms and bladders; 2) capillary propellant management devices; and 3) the use of auxiliary gas jets to create a "g" field to settle propellants. The Titan configuration for EOS-A uses the hydrazine system for performing orbit transfer and orbit adjust maneuvers. Typically the satellite will be fired once for the initial orbit insertion, up to 5 times for orbit adjust during operational life, and once for orbit transfer back to the Shuttle orbit. It is significant to note that with the selected pressure regulated system, the tank is initially full, and except for the first transfer maneuver, the tank is approximately half full for subsequent firings.

Two types of positive expulsion devices most commonly used for hydrazine systems are elastomeric (AF-E-332) diaphragms and bladders. The AF-E-332 material has demonstrated adequate compatibility with hydrazine and adequate cycle life to meet the requirements for the EOS mission; and therefore, the more complex and costly metallic devices generally considered for bipropellant systems were not considered. Tanks which use diaphragms shaped in the form of a hemisphere retain the diaphragm with a mechanical ring which is an integral part of the tank equatorial joint. Tanks which use bladders, particularly in the larger sizes, have a stand pipe in the core of the tank and a metallic frame which allows the bladder to fold around the frame in a manner which produces good expulsion efficiency. The stand pipe and the frame are inserted into the tank through a port in the base of the tank. For the Titan 36-inch diameter spherical tank, it is estimated that a diaphragm would weigh 6.7 pounds and the retaining ring would weigh 12 pounds, making a total weight of 18.7 pounds. A bladder for the same tank would weigh 13.5 pounds and the additional weight attributed to the stand pipe, support frame, and tank outlet configuration would be 7 pounds, making a total weight of 20.5 pounds. Expulsion efficiencies for both diaphragms and bladders generally exceed 99 percent; however, diaphragms tend to be slightly more efficient than bladders. Cost differences between the two devices are not significant; however, in this area also, the diaphragm and its retainer are less costly than the bladder and its stand pipe and frame. Hence, it appears that on all counts a diaphragm is slightly superior to a bladder for this particular tank configuration.

Two basic approaches are also used for capillary propellant management systems. The first approach is a partial retention design where a



small portion of propellant is contained near the tank outlet by a retention screen. This propellant is used to start the thrusters and to sustain flow until the propellant is settled by the "g" forces produced by the thrusters. The second approach is a total communication system. This approach is generally used when constraints associated with the partial retention designs become unacceptable. A typical case would be for a reaction control system which uses multi-directional thrusters for short pulses. In this application there could be no assurance that the propellant retainer of a partial retention screen would be refilled during any particular firing. Total communication systems are more complex, heavier, and more costly than partial retention screens particularly in the size tank required for this application. As previously pointed out, the EOS application is for unidirectional  $\Delta V$  maneuvers, and the main engines will fire for sufficient duration on all maneuvers to ensure that propellant is completely settled during each maneuver. Hence, a partial retention device is indicated as the better type of capillary device for the EOS type application.

A typical partial retention device, such as used by LMSC for the Agena spacecraft consists of a screen mesh trap at the tank outlet. The configuration used by LMSC for the large main tanks consists of a small sump at the base of the main tank; however, this configuration is costly, and would not be recommended for a tank of the size being considered for the EOS. A second configuration which uses a wire mesh partial retention screen device at the tank outlet appears more suitable for EOS. This device which weighs approximately 9 pounds is inserted in the tank before making the tank girth weld. Cost is comparable to a diaphragm expulsion system.

U The third option, the use of gas jets to settle propellants would require only a single additional gas valve to the RCS and an axially directed nozzle at the base of the vehicle. The gas jet would be used to settle propellants prior to each maneuver. Assuming a thrust of 1 pound for the jet and a weight of 6000 pounds for the spacecraft, the resultant "g" field would be approximately  $.005 \text{ ft/sec}^2$ . Further assuming that for nominal conditions the propellant in the tank would have to be settled a distance of 2 feet, the time to settle propellants would be approximately 30 seconds and the total impulse would be 30 lb-sec. Hence, the gas required per firing would be approximately 0.5 pounds and the equivalent tank weight requirement to store the gas would be .6 pounds. Assuming a total of 7 maneuvers, the gas plus tank weight would be approximately 7.7 pounds. Allowing an additional 2 pounds for the thruster valve, lines, supports, and electrical wiring, the total weight would be approximately 9.7 pounds. The total cost for the valve and for the larger gas tanks is probably of the same order as for the diaphragms or the surface tension screens. Hence, the gas jet approach appears to be competitive with the other options on the basis of weight and cost for this particular mission model. The disadvantages of this approach are: 1) that a change in the mission requirements which would increase the number of maneuvers required would increase the gas and weight requirements (not a factor in either of the other options); and 2) a failure of the gas valve so as not to permit settling of the propellant would make it impossible to retrieve the spacecraft.

Based on these considerations, the partial retention surface screens are considered to be slightly superior to either of the other options and have, therefore, been selected as the baseline design approach for propellant orientation control.

#### d. Thruster Design

The thruster is an MRE-50 modified to operate at a tank pressure of 300 psia. The MRE-50 nominally operates at an inlet pressure to the valve of 400 psi and a chamber pressure of 200 psia. The thruster uses a Marquardt R-4D valve and a thrust chamber consisting of a shower head injector and a two layered catalyst bed.

For the orbit transfer maneuver application, where the thruster will fire continuously for approximately 16 minutes, the Marquardt valve which requires 60 watts represents a significant power drain. In addition, the pressure drop of approximately 54 psid is undesirable for this case where the tank pressure will be reduced from 400 psia to 300 psia. To eliminate these shortcomings a latching solenoid type valve with a low pressure drop was evaluated to determine if a significant improvement was possible. The valve selected for comparison was the Hydraulics Research valve P/N 48002450. Table 5-67 compares the characteristics of the two valves.

Perhaps even more significant than the power savings is the low pressure drop of 5 psid for the Hydraulics Research valve. Because of this low pressure drop the only modification to the thruster required may be a small increase in the nozzle size. Since other factors including cost, weight, response and life are comparable and/or more than adequate for both valves, the Hydraulic Research valve is a clear choice for this application.

#### e. Other System Components

The remaining components for the system are a pair of isolation valves, a pair of filters, and a fill and drain valve. The pressure regulator and gas storage tank will be integrated into the RCS. The isolation valves are the same Hydraulic Research torque motor valves which are used for thruster propellant valves. Similar, but smaller valves of this type are

Table 5-67. Valve Comparison

	Marquardt	Hydraulic Research
Valve Type	Poppet, coaxial flow, normally closed, spring actuated to close	Torque motor latching type valve
Weight	0.98 lbs	0.8 lbs
Operating Voltage	27 VDC	22-32 VDC
Power	60 watts continuous	32 watts actuation only
Pressure Drop at Rated Flow	~54 psid	~5 psid
Proof Pressure	500 psig	3000 psig
Response		
Opening	~7 ms	~20 ms
Closing	~7 ms	~20 ms
Cycle Life	100,000 cycles	5000
Cost (approx)	\$3500	\$3500

used on several other TRW monopropellant systems. Use of the same valve for a propellant valve and an isolation valve is both cost effective and improves the commonality of the system. The filters are Wintec in line filters with a double dutch twill 15 micron element. Similar units of smaller capacity are used on all TRW monopropellant systems. The fill and drain valve is a standard valve manufactured at TRW and in use on all TRW monopropellant systems. The valve is manually operated with an ordinary open-end wrench. The poppet incorporates redundant seals. The valve has provisions for a redundant cap to provide additional protection against leakage and contamination.

Evaluation of these components during previous system design studies indicated that these components were the best available for long life mono-propellant systems.

f. System Schematic

The system schematic is the same as previously shown in Figure 5-145. Each of the two parallel legs of the system includes a thruster, a filter, and an isolation valve. Each leg is capable of firing the entire propellant load. Hence the system meets the single point failure criteria for these components. The fill valve is internally redundant in that in addition to the primary seal, the valve is capped off with a secondary seal after loading is accomplished. Redundant propellant tankage is not feasible from weight or volume consideration and even the option of dual or quad tank arrangements does not seem practical within the available envelope constraints. In addition, loss of a tank load of propellant during the mission would preclude recovery in any event.

g. Mass Property Analysis

The mass properties for the Titan-Orbit Transfer system are shown in Table 5-68. Propellant tank weight is for a tank with a surface tension screen rather than with a diaphragm as used in the previous task. The gas storage tank is shared with the RCS and will be included in the mass properties analysis for the RCS. The amount indicated for the gas storage tank is the equivalent weight which would be required to store the pressurant if it were an integral part of the orbit-transfer system.

Table 5-68. Orbit Transfer System Mass Properties\*

Item	Quantity	Unit Weight	Total	Source
Thrusters			7.6	TRW
Thruster Chamber	2	3.0		TRW
Propellant Valve	2	0.8		HRM
Filter	2	0.5	1.0	WINTEC
Isolation Valve	2	0.8	1.6	HRM
Fill Valve	1	0.5	0.5	TRW
Propellant Tank	1		35.0	PSI
Lines and Brackets			<u>3.0</u>	TRW
Total Dry Weight			48.7	
GN <sub>2</sub>			23.7	
GN <sub>2</sub> Tank			28.5	
Propellant (usable)			857.4	
Propellant Residuals			<u>8.6</u>	
Total Wet Weight			966.9	

\*Weight does not include structure, thermal insulation and heaters, or electrical wiring harness.

### 5.3.1.3 Reaction Control Sizing

#### 5.3.1.3.1 Task Description

Based on ACS acquisition analysis and orbit transfer and adjust stabilization requirements select a configuration and size the basic elements of the RCS. Compare baseline pneumatic system with monopropellant alternate. Develop schematic to ensure meeting reliability criteria.

#### 5.3.1.3.2 Problem Discussion

The baseline RCS, as shown in Figure 5-149, consists of 4 gas storage tanks, 2 fill valves, 2 filters, 1 high level regulator, 1 low level regulator, 2 pressure transducers, 5 isolation valves, 1 gas vent, and 16 thrusters.

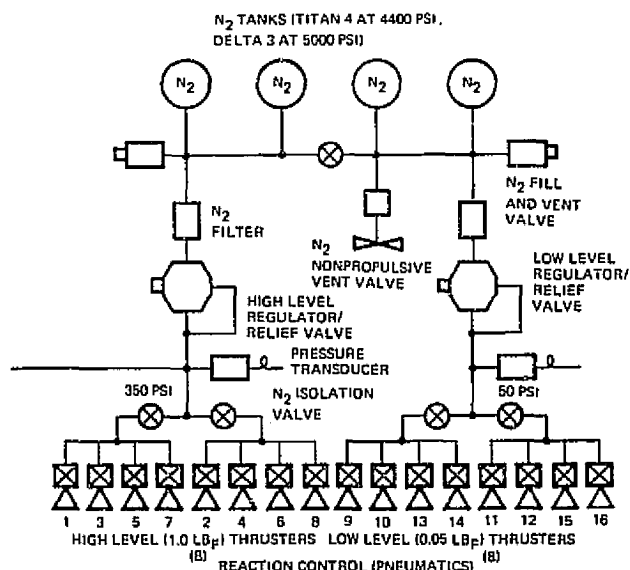


Figure 5-149. Baseline RCS

The purpose of this task is to review this design and to determine if alternates to this baseline design can provide a more cost effective or otherwise more efficient means of providing reaction control and to ensure that the reliability criteria related to reasonable single point failures are satisfied.

The major alternate to be considered is the use of hydrazine in place of  $\text{GN}_2$  as the propellant. The advantage of using hydrazine is that there will be a significant weight and volume savings as well as a simplification to the overall spacecraft structure. The disadvantage is the greater cost related to the cost of thrusters. The analysis will quantify the cost and weight differences. The interrelation between the transfer propulsion and the RCS will be examined to see if sharing of components between the two systems can be used as a means of effecting cost and weight savings.

A second alternate to be evaluated, should the pneumatic system be selected, is the use of bilevel thrusters in place of separate high level and low level thrusters. The apparent advantage of this alternate is that a higher level of redundancy and hence reliability may be possible at a reduced cost and total weight.

#### 5.3.1.3.3 Assumptions

For purposes of comparing the pneumatic system with the hydrazine system, a schematic configuration of each system which considers combining the RCS and orbit transfer systems to obtain the most cost effective combinations will be configured. Hardware weight and cost estimates will be based on typical components currently being used on similar spacecraft applications at TRW.



#### 5.3.1.3.4 Analysis and Tradeoff Studies

##### a. Hydrazine versus Pneumatic RCS

In Tasks 1 and 2, it was assumed that pressurant gas would be supplied from a common gas storage source in the pneumatic RCS. It was also assumed that the pressure used for the high thrust gas jets would be the same as that required to pressurize the main hydrazine tank. Figure 5-150a shows the combined RCS and orbit adjust system with these features. The schematic, as shown in Figure 5-150a, also shows both regulators at the same pressure as compared to the use of two different pressure level regulators in the baseline. This arrangement was selected to eliminate the regulator as a single point failure. Figure 5-150b shows the hydrazine RCS combined with the orbit transfer system. In this system, it was assumed that the main hydrazine tank could be used as a common propellant tank. Since the RCS propellant requirements are less than 2 percent of the transfer propellant requirements there is no cost impact on the main hydrazine tank.

##### Cost Analysis

Tables 5-69 and -70 list the component parts and the estimated recurring costs for each system. Components which are used for the orbit transfer system only and which are common to both systems have not been included in either table. Engineering and Q.A. costs were estimated based on previous experience. As seen in Tables 5-69 and -70, the significant difference is in the cost of the thrusters. This difference is partially offset by the savings in tank cost for the hydrazine system; however, the pneumatic system shows a clear cost advantage of approximately \$46K or 18 percent.



5-421

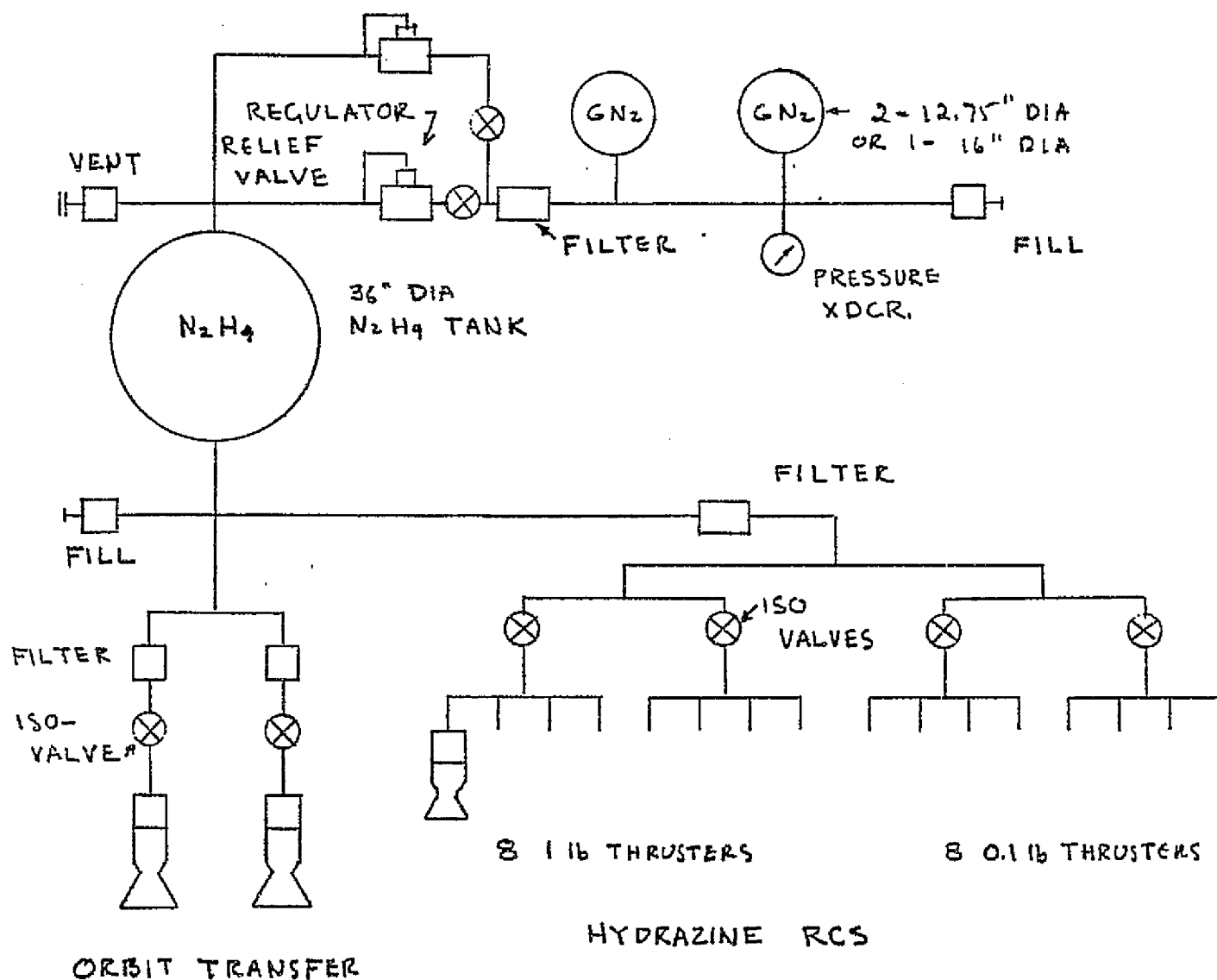


Figure 5-150b. Hydrazine RCS and Orbit Transfer

NOTE: EACH REGULATOR AND PROPELLANT VALVE IS  
PROTECTED WITH AN INTEGRAL FILTER

Table 5-69. Pneumatic RCS Cost Estimate

Item	Quantity	Unit Cost	Total	Source
GN <sub>2</sub> Fill	1	3.9	3.9	TRW
Pressure Transducer	1	5.2	5.2	Statham
GN <sub>2</sub> Tanks (20 in. dia.)	3	10.0	30.0	PSI
GN <sub>2</sub> Vent	1	3.0	3.0	Leonard
Filter	1	2.6	2.6	Wintec
Isolation Valves	6	5.2	31.2	HRM
Regulator	2	10.0	20.0	Sterer
Thruster	16	4.5	72.0	Sterer
Lines and Brackets			5.0	TRW
Engineering			70.0	
Quality Assurance			17.0	
			259.9*	

\*Does not include integration and test

Table 5-70. Hydrazine RCS Cost Estimate

Item	Quantity	Unit Cost	Total	Source
GN <sub>2</sub> Fill	1	3.9	3.9	TRW
Pressure Transducer	1	5.2	5.2	Statham
GN <sub>2</sub> Tanks (16-in. dia.)	1	8.0	8.0	PSI
Filter	2	2.6	5.2	Wintec
Isolation Valves	6	5.2	31.2	HRM
Regulator	2	10.0	20.0	Sterer
Thrusters	16	8.0	128.0	Sterer
Lines and Brackets			5.0	
Engineering			80.0	
Quality Assurance			20.0	
			<u>306.5*</u>	

\* Does not include integration and test

### Weight and Volume Comparison

The weight difference between the pneumatic RCS is basically the difference between the  $\text{GN}_2$  and  $\text{GN}_2$  storage tanks for the pneumatic system and the  $\text{GN}_2$ ,  $\text{GN}_2$  storage tanks, and hydrazine propellant for the hydrazine RCS. Other component parts are essentially equivalent. As shown in Table 5-71 the hydrazine system is approximately 73.6 pounds lighter than the pneumatic system. Some additional savings in spacecraft structural weight would also result because of the lighter smaller tanks of the hydrazine system.

Table 5-71. Weight Comparison  
Hydrazine RCS and Pneumatic RCS

Item	Pneumatic RCS	Hydrazine RCS
$\text{GN}_2$	60.3	21.4
$\text{GN}_2$ Tankage	72.4	25.7
$\text{N}_2\text{H}_4$		12.0
	132.7	59.1

The volume difference between the systems, assuming gas storage at 4000 psi, can be seen by referring back to Figures 5-150a and -b. For the hydrazine system  $\text{GN}_2$  storage can be accommodated by a single 16-inch diameter spherical tank. The pneumatic system requires three 16-inch diameter or four 14.4-inch diameter tanks for gas storage.

Therefore, on the basis of weight and volume the hydrazine system has a clear advantage over the pneumatic system for the Titan configuration.

### Reliability Comparison

Both systems contain essentially the same elements such that the difference in reliability is the difference between the gas jet and the hydrazine thruster. Unquestionably the gas jet will be more reliable than the hydrazine thruster. However, it should be pointed out that the duty cycle for this application is far less severe than that for which hydrazine thrusters of this class have been previously qualified. Therefore, hydrazine thrusters would readily satisfy the reliability requirements anticipated for the actuation module.

### Conclusions

Based on the cost difference of approximately \$46K per system, and the slight reliability advantage for the pneumatic system, the pneumatic system is recommended. However, should weight become a problem as the spacecraft design progresses, replacement of the pneumatic system with the hydrazine system should be reconsidered.

#### b. Schematic Arrangement of Thrusters

The thruster arrangement in the proposal baseline RCS is shown in Figures 5-151a and b. As shown in Table 1 of Figure 5-151b, this arrangement has no backup or redundant mode for low thrust torque in the Y and Z axis and no high thrust control about the X axis. Figures 5-151c and d show an alternate arrangement of thrusters which uses only 12 thrusters. This arrangement is capable of control about all three axes in both high and low thrust with complete redundancy. The improved capability and reliability is achieved with 2 less thrusters than were required by the baseline system. The advantages for this arrangement are apparent and it is recommended to replace the baseline system.

Figure 5-151a

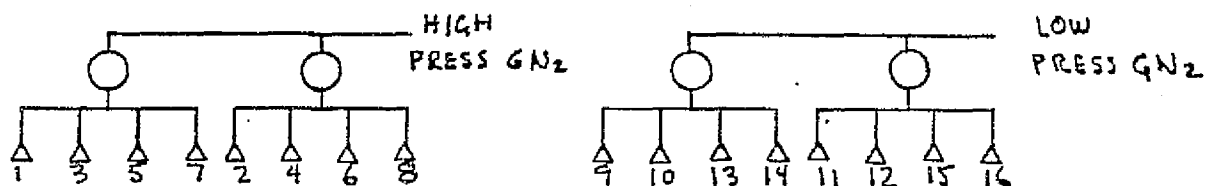


Figure 5-151b

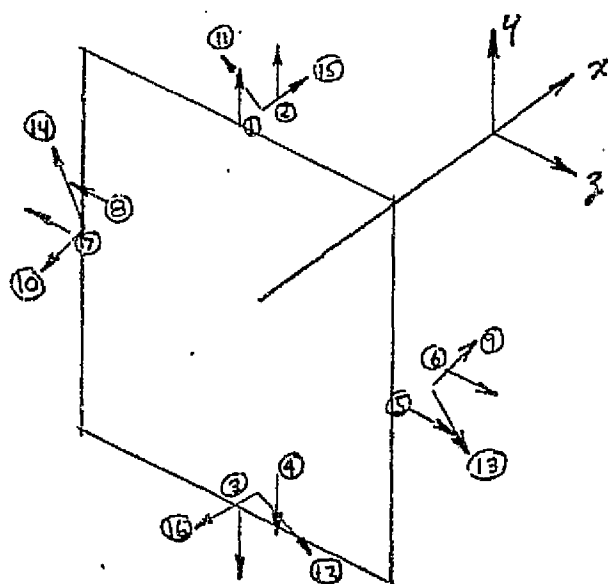


Table 1

Torque	Thrust	Thruster	
		Primary	Backup
+X	H	--	--
	L	9, 10	11, 12
-X	H	--	--
	L	13, 14	15, 16
+Y	H	1	2
	L	11, 15	--
-Y	H	3	4
	L	12, 16	--
+Z	H	5	6
	L	9, 13	--
-Z	H	7	8
	L	10, 14	--

Figure 5-151. Thruster Arrangement



Figure 5-151c

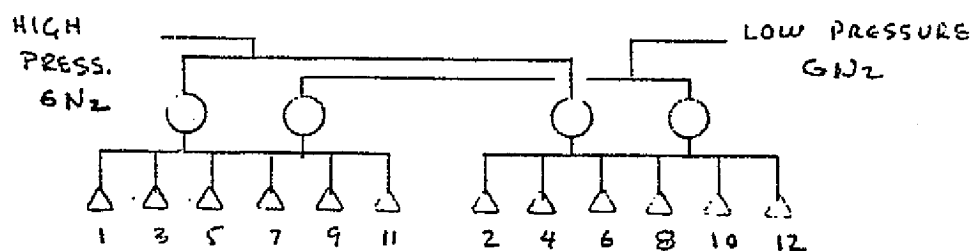


Figure 5-151d

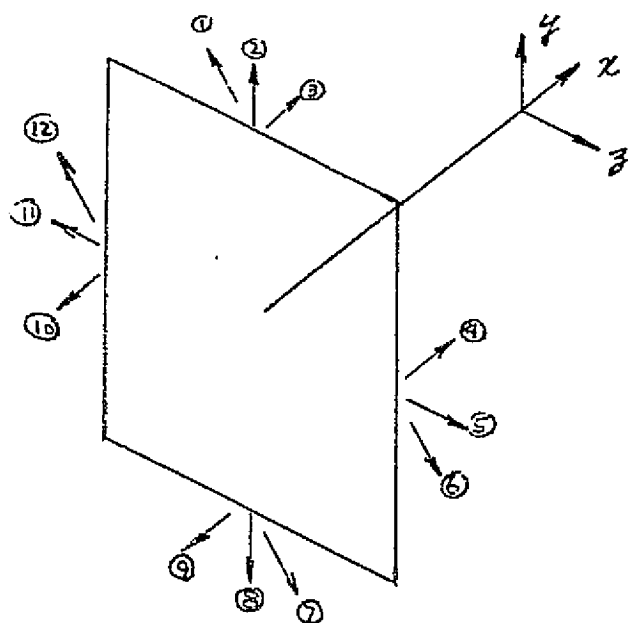


Table 2

Torque	Thrust	Thruster	
		Primary	Backup
+X	H L	1, 7	4, 10
-X	H L	3, 9	6, 12
+Y	H L	5	4, 6
-Y	H L	11	10, 12
+Z	H L	7, 9	8
-Z	H L	1, 3	2

Figure 5-151. Alternate Thruster Arrangement

#### 5.3.1.4 Reaction Control Design

##### 5.3.1.4.1 Task Description

Prepare an RCS preliminary design including a system schematic and a system layout with the system incorporated into the actuation module; size and select components; prepare a mass property statement.

##### 5.3.1.4.2 Problem Discussion and Assumptions

In Task 3, a pneumatic RCS with 12 thrusters was selected for the RCS configuration. This task will definitize the design. The system will be configured with two tank options. The first option will include sufficient tank volume for storing pressurization gas for the orbit transfer tank in addition to gas to provide impulse for the RCS; the second option will include only storage volume for gas to provide impulse for the RCS. Provision for leakage of 5 scc/min for a total of 4 pounds over the 5-year life has been included in the tank sizing. Redundancy has been applied to critical components to eliminate single point failures.

##### 5.3.1.4.3 Design Description

The schematic layout of the RCS is shown in Figure 5-152. The system includes two sets of 6 dual level pneumatic thrusters. The thrusters are supplied gas from either the high pressure regulator or the low pressure regulator depending on the position of the various isolation valves. As previously shown in Figure 5-150d of Task 3, each set of six thrusters is capable of providing complete control in all three axes. During orbit transfer, high level thrust is provided by using gas supplied from the high pressure regulator. The low level operation is for backup to the reaction wheel/magnetic torquer on-orbit attitude control system. Either complete set of six thrusters can be isolated in the event of a failed open or leaking

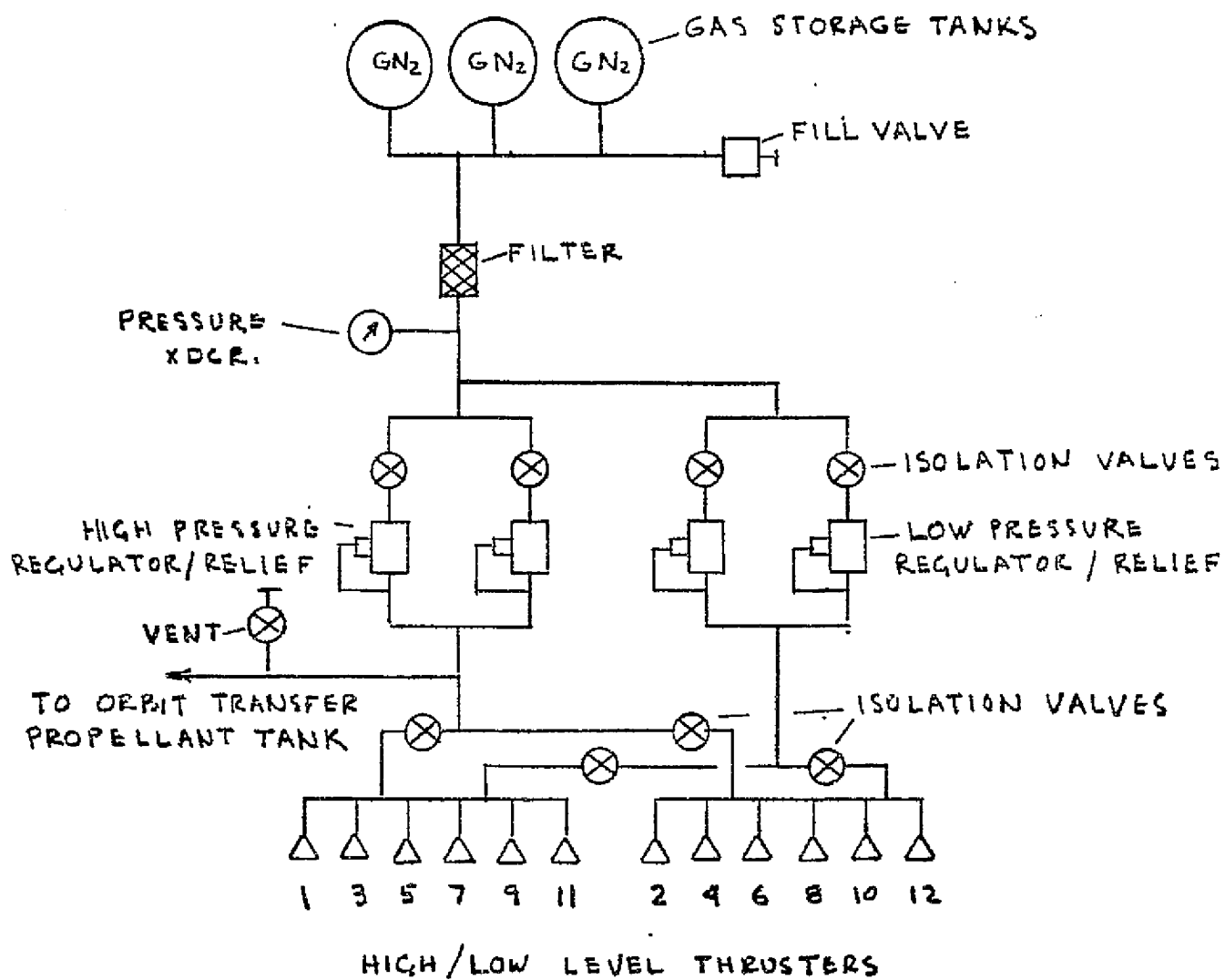


Figure 5-152. RCS Schematic

valve by closing the appropriate isolation valve. Two regulators in parallel are provided for both the high pressure and low pressure sides of the system to eliminate single point failure in the failed closed mode. Each regulator is additionally protected against the failed open mode by a downstream relief valve and an upstream isolation valve. The pressure transducer upstream of the regulators is used to monitor the amount of gas remaining in the tanks and as a means of detecting leakage in any of the components or connections in the system. A single high capacity filter is used to contain contamination from the propellant tanks. The regulators and propellant valves each contain integral filters to trap contamination generated within the system below the main tank filter.

The gas storage requirement, including gas to pressurize the orbit transfer system and a leakage contingency of 4 pounds, is approximately 68 pounds. This capacity is provided by three 16-inch diameter 4000 psia tanks. For systems which do not require orbit transfer, the gas requirements would be substantially reduced from 68 to approximately 10 pounds. In this case a single 12.5 inch 4000 psi tank would be adequate. The gas vent is used for depressurizing the system during operations after the system has been recovered by the Shuttle.

All component parts for this system have been previously qualified for use in similar applications except the tanks. Table 5-72 shows the complete hardware list, with weights, costs, and recommended suppliers.

Table 5-72. Hardware List

Item	Quantity	Unit Cost	Total	Unit Weight	Total	Source
Tanks*	3	27.6	82.8	10.0	30.0	PSI
Fill Valve	1	0.5	0.5	3.9	3.9	TRW
Filter	1	0.5	0.5	2.6	2.6	Wintec
Pressure Transducer	1	0.5	0.5	5.2	5.2	Statham
Isolation Valves	9	0.6	5.4	5.2	46.8	HRM
Regulators	4	1.2	4.8	10.0	40.0	Sterer
Thrusters	12	0.7	8.4	4.5	54.0	Sterer
Lines			5.0		5.0	TRW
			<u>107.9</u>		<u>182.5</u>	
GN <sub>2</sub>			68.0			
			<u>175.9</u>			
Engineering					70.0	
Quality Assurance					<u>17.0</u>	
					269.5	

\*For system not requiring orbit transfer, one tank ~12 lbs at 8.0K would be used in place of three tanks. GN<sub>2</sub> would be 10 lbs.

### 5.3.1.5 Orbit Adjust Design

#### 5.3.1.5.1 Task Description

Review requirements for total impulse, frequency of firing and impulse accuracy. Evaluate incorporating the orbit adjust function into either the orbit transfer or the reaction control system.

#### 5.3.1.5.2 Problem Discussion

For the Titan configuration, it is evident from Task 1 that the orbit adjust function can be performed by the orbit transfer system thrusters by adding approximately 15 pounds of propellant to the orbit transfer propellant (843 pounds). The  $\Delta V$  maneuvers for orbit adjust performed with these thrusters could readily be performed with a predictability of a few inches per second.

### 5.3.2 Propulsion System Design - Thor-Delta

#### 5.3.2.1 Task Description

Prepare system schematics and layouts for an orbit adjust system and reaction control system for the Thor-Delta actuation module. Evaluate one system which separates the two functions for application to missions which may or may not require orbit adjust and one system which combines the two functions to minimize weight, cost, and volume. Determine system mass properties and identify all system component parts.

#### 5.3.2.2 Problem Discussion

The Thor-Delta boosted spacecraft is designed to operate in either a 315 n.mi. circular orbit or a 387 n.mi. circular orbit. The spacecraft weights are 2650 pounds and 2525 pounds, respectively. Orbit adjust  $\Delta V$  for the 315 n.mi. orbit is 250 ft/sec and for the 387 n.mi. orbit, 145 ft/sec. Reaction control system requirements are to provide backup spacecraft control for up to 30 days (667 lb-sec impulse), and impulse for acquisition maneuvers and attitude control during orbit adjust maneuvers (200 lb-sec impulse).

Two systems will be evaluated for performing these functions: the first system will consist of a blowdown pressure-fed monopropellant hydrazine system for performing orbit adjust maneuvers and a separate pneumatic system for performing RCS functions; the second system will combine the orbit adjust and RCS capability into a single system.

#### 5.3.2.3 Analyses and System Descriptions

##### 5.3.2.3.1 Blowdown Pressure-Fed Hydrazine Orbit Adjust with Separate Pneumatic RCS

The worst-case orbit adjust requirements are for the 315 n.mi. orbit. For a spacecraft weight of 2650 pounds and a  $\Delta V$  of 250 ft/sec, the total impulse required is 20,215 lb-sec. At an estimated average specific impulse of 210 sec, the propellant required is 96.3 pounds. Tank volume for storing the hydrazine is 1.54 cubic feet. Assuming a blowdown ratio of 2:1, which was shown to be near optimum in Task 2, the tank volume required is 3.08 cubic feet. Tank diameter is 21.6 inches. Extrapolating

the tank weight from an existing similar size tank results in a tank weight estimate of 10.5 pounds. Allowing 2 pounds for a surface tension screen or a tank diaphragm results in a total tank weight of 12.5 pounds.

For a total propellant weight of 96.3 pounds, it is possible to use a much smaller thruster than was recommended for the Titan system which uses 858 pounds of propellant. There are three advantages to the smaller thrusters: 1) cost is less than half, 2) weight and size are significantly reduced, and 3) the control torque required during orbit adjust maneuvers are proportionately reduced. There are no apparent disadvantages. The TRW MRE-4 is typical of thrusters in the 3- to 5-pound class suitable for this application. This thruster is nominally 4 pound thrust at 600 psi inlet pressure reducing to 2 pounds thrust at approximately 200 psi inlet pressure.

The system schematic for the orbit adjust is shown in Figure 5-153. Table 5-73 lists the components with cost and weight estimates based on information obtained from the recommended source.

The pneumatic RCS, shown in Figure 5-154, is similar to the Titan system configured in Task 4. In this system, however, only one pair of regulators is required because torque for control during orbit adjust have been reduced by one order of magnitude through the use of the lower thrust orbit adjust thrusters. Table 5-74 lists the components with cost and weight estimates obtained as in Table 5-73.

#### 5.3.2.3.2 Combined Orbit Adjust and Reaction Control Systems

Combining the orbit adjust and reaction control systems as shown schematically in Figure 5-155 results in a reduction in the total cost, weight, and volume requirements for the system. If all flights must perform both orbit adjust and reaction control, the combined system is clearly preferable to the two separate systems.

In the combined system, regulated pressurant gas is used to pressurize the hydrazine tank. The pressurant gas is stored with RCS gas in a slightly larger pressurant tank than that used in the separated system.

The tank size for the hydrazine is reduced from 3.08 cubic feet to 1.54 cubic feet and one pressure transducer has been deleted as a result of combining the two systems. The hardware list showing estimated cost and weight is shown in Table 5-75.



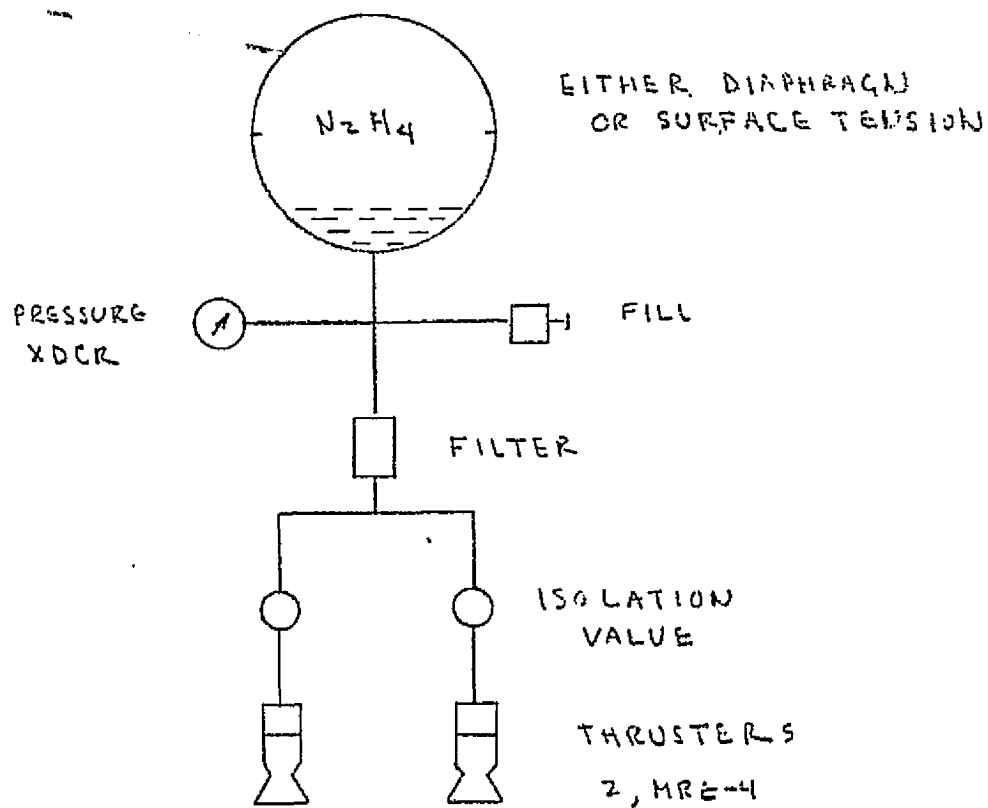


Figure 5-153. Blowdown Orbit Adjust System

Table 5-73. Hardware List - Orbit Adjust -  
Blowdown System

Item	Quantity	Unit Cost	Total	Unit Weight	Total	Source
Tank	1	30.0	30.0	12.5	12.5	PSI
Fill	1	3.9	3.9	0.5	0.5	TRW
Pressure Transducer	1	5.2	5.2	0.5	0.5	Statham
Filter	1	2.6	2.6	0.5	0.5	Wintec
Isolation Valve	2	5.2	10.4	0.5	1.0	HRM
Thrusters	2	12.5	25.0	0.6	1.2	TRW
Lines			3.0		3.0	TRW
			80.1		31.7	
Engineering			50.0			
Quality Assurance			10.0			
			140.1			
GN <sub>2</sub>					3.2	
Propellant					96.3	
					131.2	

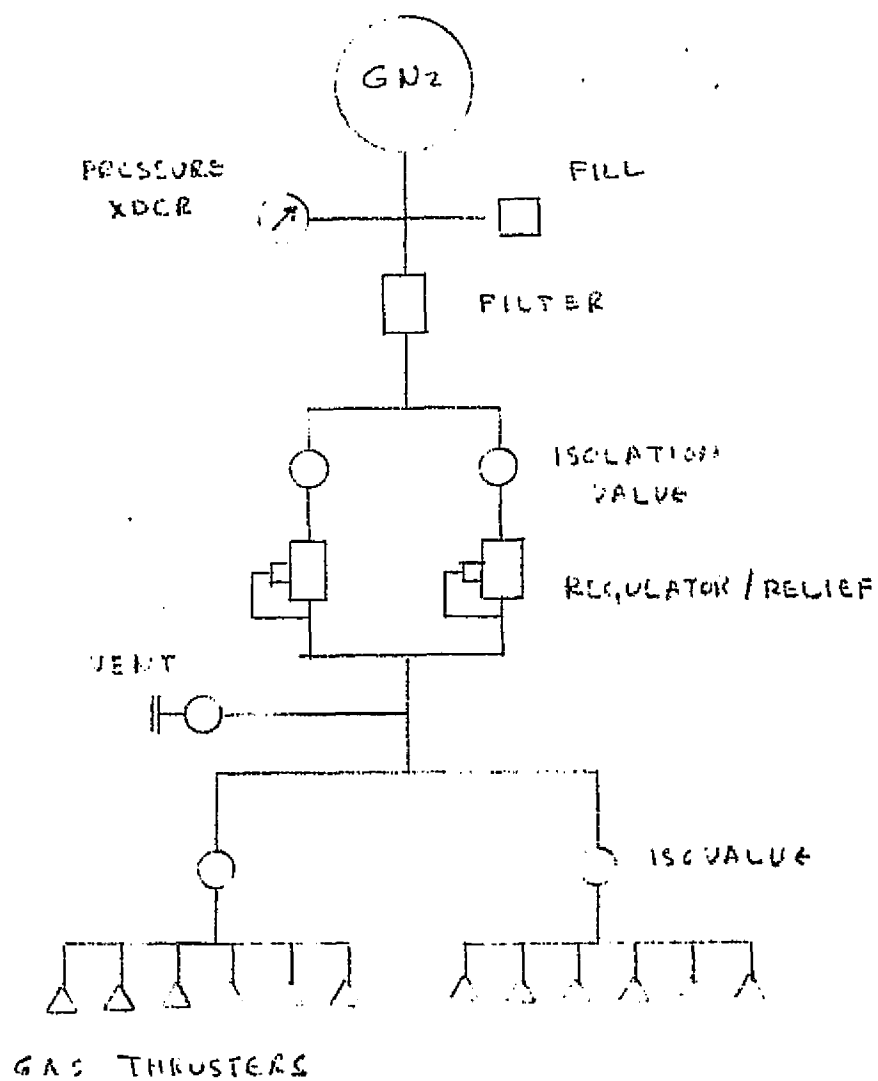


Figure 5-154. Reaction Control System

ORIGINAL PAGE IS  
OF POOR QUALITY

Table 5-74. Hardware List - Reaction Control System

Item	Quantity	Unit Cost	Total	Unit Weight	Total	Source
Tank	1	10.0	10.0	18.0	18.0	PSI
Fill	1	3.9	3.9	0.5	0.5	TRW
Pressure Transducer	1	5.2	5.2	0.5	0.5	Statham
Filter	1	2.6	2.6	0.5	0.5	Wintec
Isolation Valves	4	5.2	20.8	0.6	2.4	HRM
Regulator	2	10.0	20.0	1.2	2.4	Sterer
Vent	1	5.2	5.2	0.6	0.6	HRM
Thrusters	12	4.5	54.0	0.7	8.4	Sterer
Lines			5.0		5.0	TRW
			<u>126.7</u>		<u>38.3</u>	
Engineering			70.0			
Quality Assurance			<u>17.0</u>			
			213.7			
GN <sub>2</sub>					<u>16.3</u>	
					54.6	

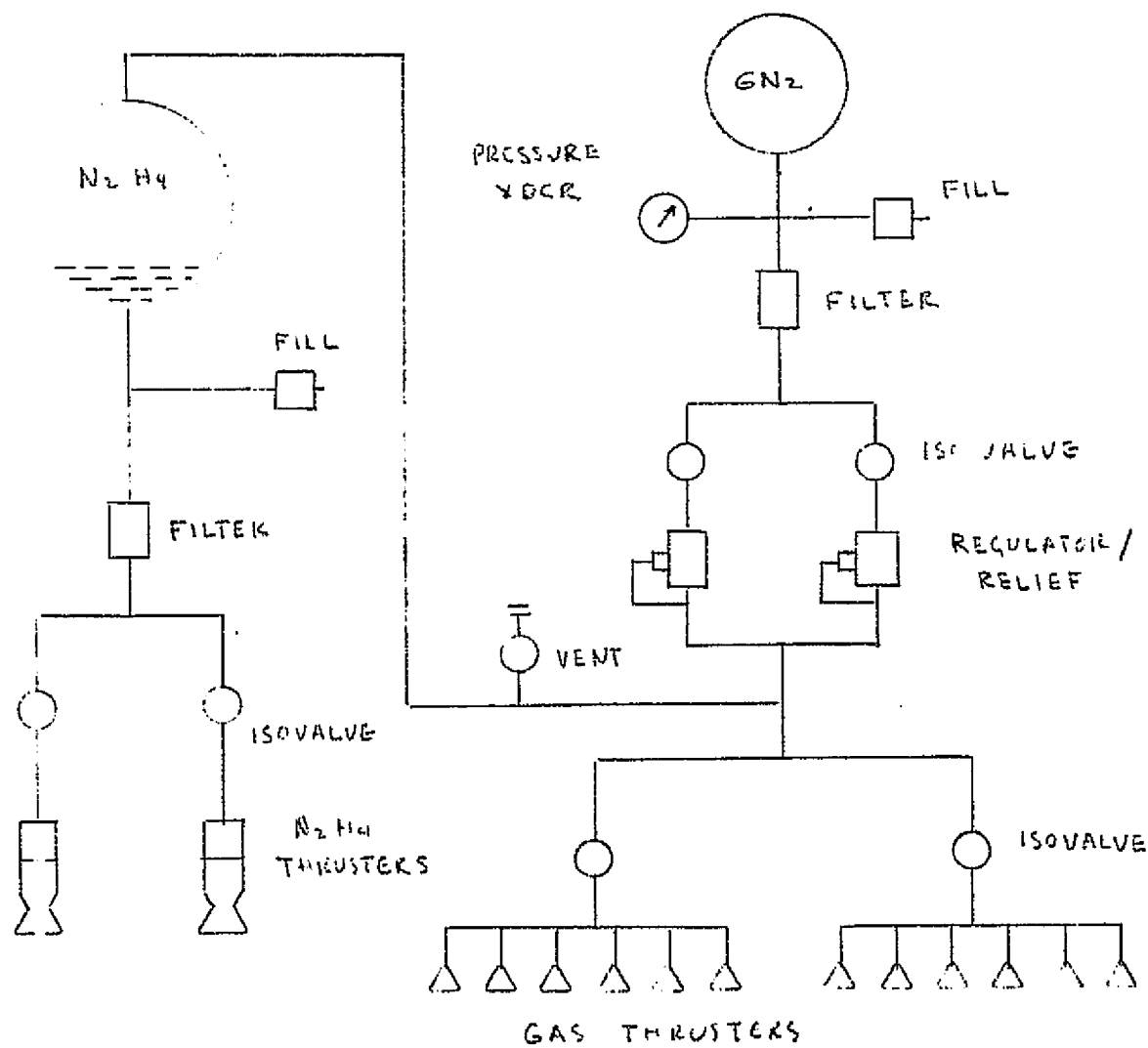


Figure 5-155. Combined Reaction Control Orbit Adjust Systems

Table 5-75. Hardware List - Combined Orbit Adjust and Reaction Control System

Item	Quantity	Unit Cost	Total	Unit Weight	Total	Source
N <sub>2</sub> H <sub>4</sub> Tank	1	20.0	20.0	8.4	8.4	PSI
GN <sub>2</sub> Tank	1	12.0	12.0	22.5	22.5	PSI
Fill	2	3.9	7.8	0.5	1.0	TRW
Pressure Transducer	1	5.2	5.2	0.5	0.5	Statham
Filter	2	2.6	5.2	0.5	1.0	Wintec
Isolation Valves	6	5.2	31.2	0.6	3.6	HRM
Vent	1	5.2	5.2	0.6	0.6	HRM
Regulator	2	10.0	20.0	1.2	2.4	Sterer
N <sub>2</sub> H <sub>4</sub> Thruster	2	12.5	25.0	0.6	1.2	TRW
GN <sub>2</sub> Thrusters	12	4.5	54.0	0.7	8.4	Sterer
Lines			5.0		5.0	TRW
			190.6		54.6	
Engineering			100.0			
Quality Assurance			20.0			
			310.6			
GN <sub>2</sub>					18.7	
N <sub>2</sub> H <sub>4</sub>					96.3	
					169.6	

## 5.4 ELECTRIC POWER AND ELECTRICAL INTEGRATION

### 5.4.1 Power Budgets and Profiles

#### 5.4.1.1 Problem Discussion

The power budget and power profile development was initiated early in the study to enable effective trade studies. The power requirements reflect the spacecraft and payload equipment selected to satisfy the mission requirements. The EOS-A power budget was constrained by the array area that can be accommodated on the Thor-Delta vehicle.

The power profile for on-orbit operation was developed from the knowledge of Central Data Processing Facility (CDPF) locations, an assumption on the Low Cost Ground Station (LCGS) operation and the nominal orbit for EOS-A. The timeline basis for the profile is shown in Figure 5-156.

#### 5.4.1.2 Assumptions

The assumptions made for development of the power budget and power profile were as follows:

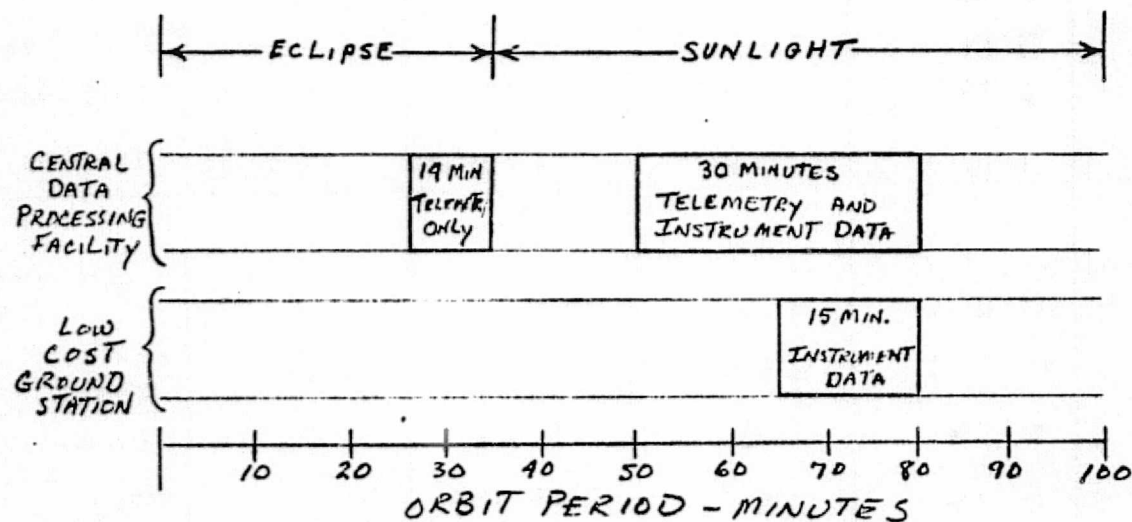
- a) Each module would contain a power converter for all secondary power required by the assemblies comprising that module.
- b) The Data Interface Units would include a self-contained converter.
- c) Instrument power would be supplanted by an equivalent heater when the instruments are off, but losses due to power conversion would not be included.

#### 5.4.1.3 Conclusions

The power budget for the EOS-A mission indicates that an average power of 530 watts is required during eclipse, and 950 watts in sunlight. The detailed breakdown by module is shown in Table 5-76 along with the summary power requirements which provide the basis for solar array and battery sizing calculations.

The impact of later mission power requirements were analyzed using the basic spacecraft subsystems and instrument power.

## OPERATION PER ORBIT



## OPERATION PER DAY

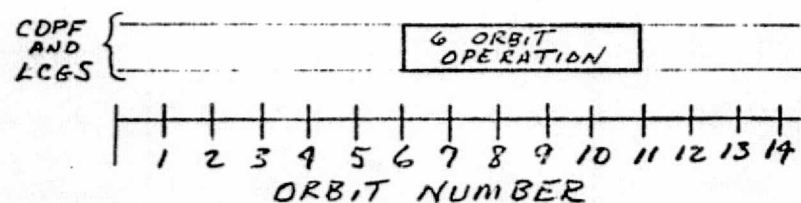


Figure 5-156. Timeline for Power Profile



Table 5-76. Electrical Power Load Requirements  
Summary (power in watts)

MODULE	Mission Phase	ORBIT (INSTRUMENTS OFF)	ORBIT (INSTRUMENTS ON)	ECLIPSE AVERAGE	SUNLIGHT AVERAGE	ORBIT AVERAGE	
ELECTRICAL POWER		15.0	15.0	15.0	15.0	15.0	
SOLAR ARRAY & DRIVE		6.2	6.2	6.2	6.2	6.2	
ATTITUDE DETERMIN.		59.6	59.6	59.6	59.6	59.6	
ACTUATION		50.0	50.0	50.0	50.0	50.0	
COMMAND & DATA HAND.	CDPE/ TLM OFF	46.5 27.5	46.5 27.5	35.1	36.3	35.9	
WIDEBAND COMM	CDPE/ LGS	5.5	25.8 45.8	5.5	31.0	22.1	
THEMATIC MAPPER		70.1	139.1	70.1	102.0	90.8	
HRPI	CDPE/ LGS	88.8	88.8 136.0	88.8	110.6	106.8	
THERMAL		179.0	179.0	179.0	179.0	179.0	
Subtotal		520.7 CDPE 501.7 TLM OFF	644.7 CDPE 727.2 LGS	509.3	589.7	561.6	
Battery Charge Load		—	—	—	332.0	215.8	
Cable Losses		—	—	11.2	19.6	16.7	
Contingency		—	—	50.9	59.0	56.2	
Total		—	—	571.4	1000.3	850.3	

Table 5-76. Power Requirements (ELECTRICAL POWER MODULE)

[illegible]



Table 5-76. Power Requirements (Solar Array and Drive Module)

[illegible]



Table 5-77. Power Requirements (Actuation Module)

[illegible]

Table 5-77. Power Requirements (Communication and Data Handling Module)

[illegible]



Table 5-77. Power Requirements (Wideband Communications Module)

[illegible]

ORIGINAL PAGE IS  
OF POOR QUALITY

Table 5-77. Power Requirements (Thematic Mapper Module)

Unit Name	Number of Units (Total/Operating)	Source *	Voltage (Volts)	Power (Watts)					Duty Cycle		Remarks
				Continuous Load	Intermittent Load	Maximum Steady-State Power	Pulse Load	Peak Power	Inter	Pulse	
OPTICAL ENCODER	1/1	MAIN BUS	28±7VDC	6.5	—	6.5	—	—	—	—	
SCAN DRIVE MOTOR	1/1			7.25	—	7.25	—	—	—	—	ON DURING BOOST
POINTING MIRROR DRIVE & CONTROL	1/1			—	8.0	8.0	—	—	LOW	—	
FOCUS DRIVE AND CONTROL CIRCUITS	1/1			—	3.5	3.5	—	—	LOW	—	
TELEMETRY BUFFERS	1/1			0.3	—	0.3	—	—	—	—	
TEMP MONITORING CIRCUITS	1/1			0.5	—	0.5	—	—	—	—	
CAL AND RETICULE	1/1			1.7	—	1.7	—	—	—	—	
AMPLIFIERS	1/1			29.1	20	49.1	—	—	LOW	—	29.1W AVG.
SCAN DRIVE COMMUTATORS	2/2			4	—	4	—	—	—	—	
PHASE LOCK LOOP	2/2			3	—	3	—	—	—	—	
SIGNAL PROCESSOR	1/1			20	—	20	—	—	—	—	
MOMENTUM COMP. CIRCUITRY	1/1			7.25	—	7.25	—	—	—	—	ON DURING BOOST
ICC CIRCUITRY	1/1			5.0	—	5.0	—	—	—	—	
ICC HEATERS	1/1			0	10	10	—	—	LOW	—	MAINTAIN TOTAL POWER CONSTANT
DATA ACQUIS. SYSTEM	1/1			10	—	10	—	—	—	—	
DIU	1/1			3	—	3	—	—	—	—	

\* PROVIDES OWN CONVERTER



Table 5-77. Power Requirements (HRPI Module)

[illegible]

111

ORIGINAL PAGE IS  
OF POOR QUALITY

## 5.4.2 Battery Studies

### 5.4.2.1 Battery Charge/Discharge Study

The nickel-cadmium secondary battery system is temperature-sensitive with respect to performance and service life. Figure 5-157 shows the relationship between charge-discharge cycle life and depth-of-discharge with battery temperature a parameter. The data obtained from continuing NASA-sponsored testing at NAD-Crane shows that an increase in operating temperature produces a reduction in expected charge-discharge cycle life.

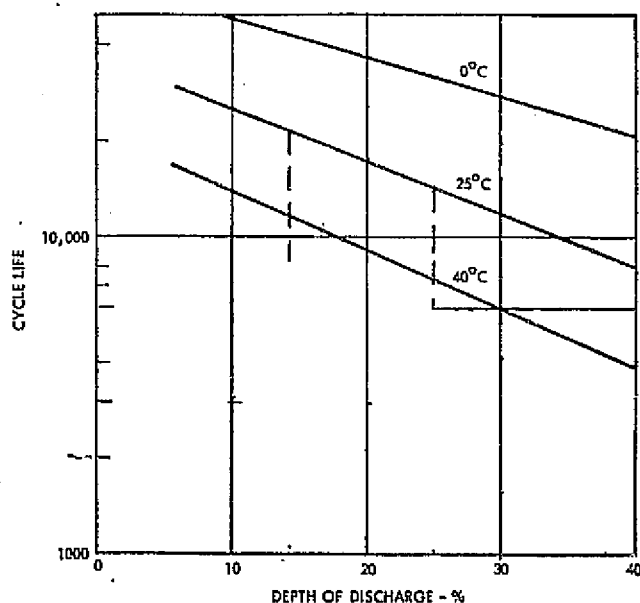


Figure 5-157. Nickel-Cadmium Battery Cycle Life Versus Depth-Of-Discharge and Average Temperature

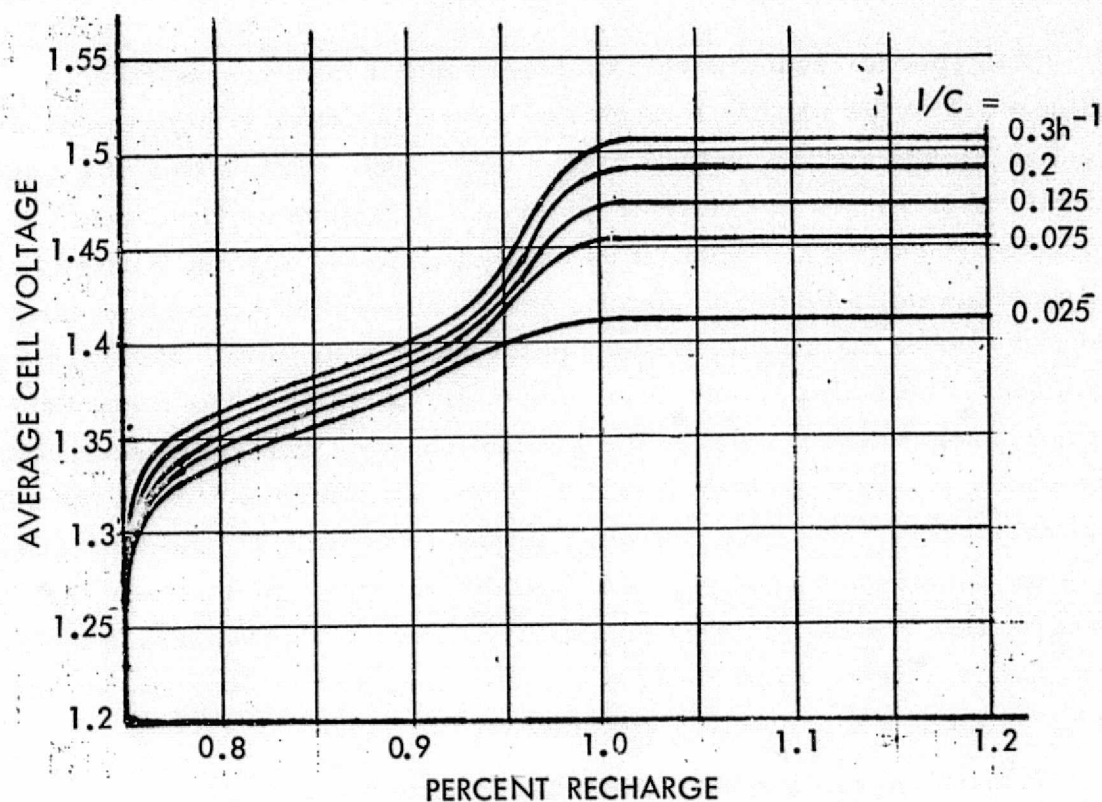
This characteristic behavior is caused by the following processes and conditions. First, it is known that higher temperatures produce an acceleration of the electrochemical side reactions within the cell that are the cause of electrical performance degradations. If the temperatures are too high, organic materials within the cell, e.g., nylon separators, will begin to decompose. Such materials problems are manifested by the appearance of short-circuits within individuals of the cell population.

The second reason is that thermal control becomes extremely difficult due to the battery's electrical characteristics at high temperatures. Figures 5-158a and b show the charge voltage characteristics of a typical nickel-cadmium cell at two temperatures. It is obvious from the characteristics that the imposition of any particular battery voltage limit will produce much higher asymptotic values of overcharge current (and, therefore, overcharge dissipation) in the warmer battery. Under these conditions, the battery tends to be thermally unstable. The high overcharge current also results in the production of oxygen gas at the positive electrodes at a rate greater than the recombination capability of the negative electrodes. The resulting over-pressure could lead to terminal seal leaks or to cell case rupture. To partially compensate for these thermal characteristics and to protect the battery from over-pressure, a temperature-compensated voltage limit is usually incorporated into the battery charge control and protection scheme.

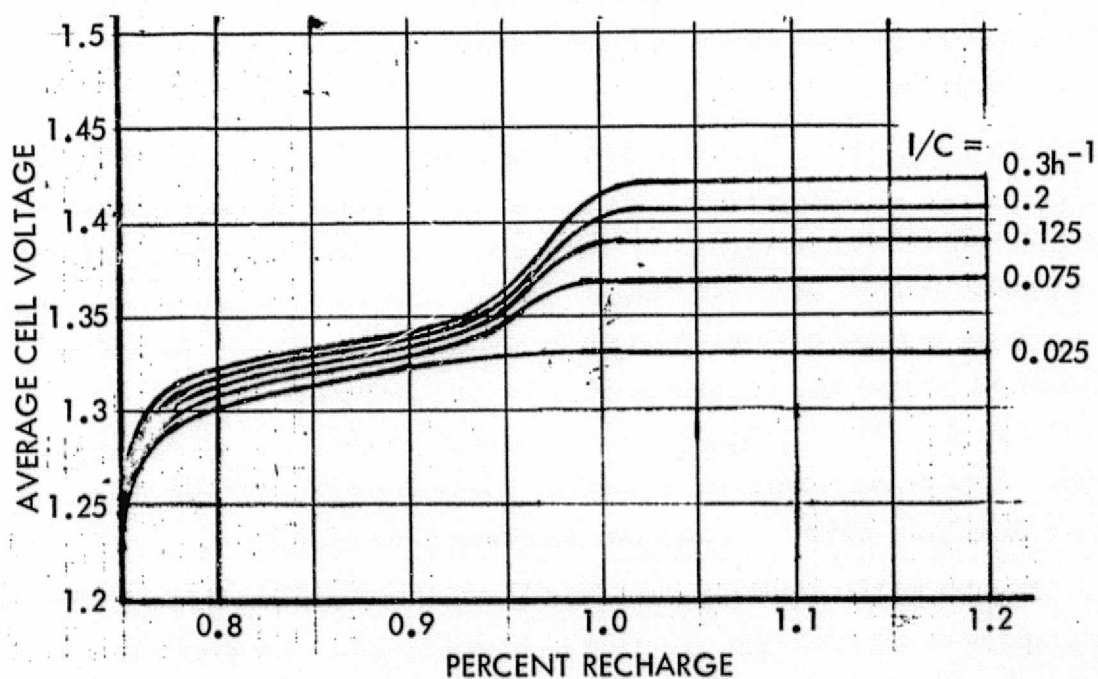
A third reason for the shortening of battery life under high temperature service conditions is that the battery is relatively inefficient when it is warm and, thus, may not become fully recharged on a cycle-by cycle basis. This effect is demonstrated by consideration of Figures 5-159 and 5-160.

Figure 5-159 contains a family of eight battery voltage-temperature limit curves. A similar family was used to control battery charge for the Orbiting Astronomical Observatory satellite series. OAO-2 orbital experience showed that after initial adjustment, the voltage level required to maintain energy balance decreased with mission time. At end-of-mission (4 years) OAO operated at Level 1 (equivalent to EOS-A Level 3 or 4). The voltage limit curves have been lowered below those of OAO-2 to provide improved control range for EOS-A. The levels shown in Figure 5-159 are similar to those used on OSO-6.

Figure 5-160 contains data from OAO development tests which show that the ampere-hour recharge fraction is controlled by changing the voltage limit. For a given temperature the recharge fraction increases as the cell voltage is increased. The ability to select voltage-limit curves by ground command provides the capability to maintain energy balance under widely varying conditions. A related benefit of this procedure is



(a) 20°C Charge Voltage Characteristics



(b) 40°C Charge Voltage Characteristics

Figure 5-158. Typical Nickel-Cadmium Battery Charge Voltage Characteristics versus Percent Recharge and Charge Rate (Normalized Against Capacity, C)



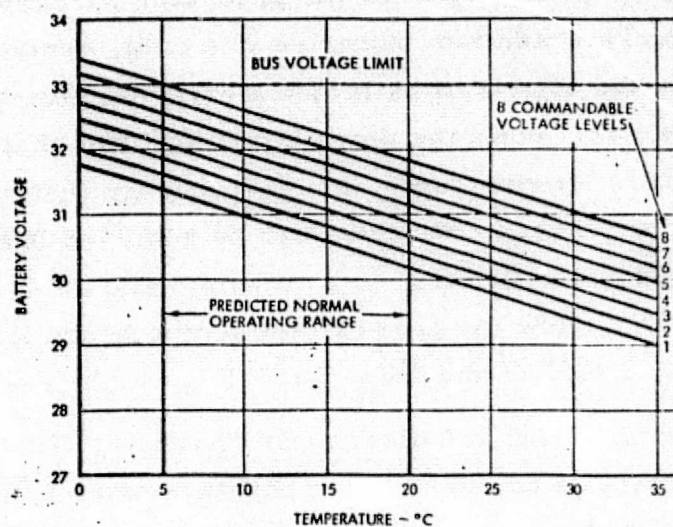


Figure 5-159. EOS-A Battery Voltage-Temperature Limit (BVL) Curves

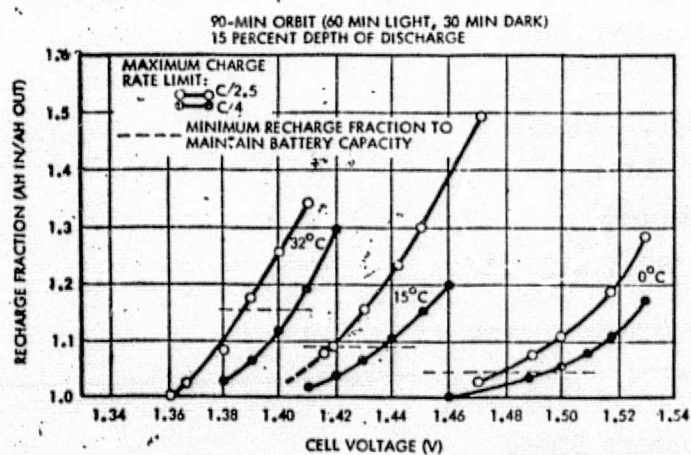


Figure 5-160. Recharge Fraction Control By Commandable Voltage Limits

the capability to reduce battery dissipation, subject to energy balance requirements, by lowering the voltage limit.

Summarizing the points made in the preceding paragraphs; it is desirable to keep nickel-cadmium batteries in a cool, controlled environment to (1) reduce the affects of battery material degradation under temperature stress, (2) avoid the thermal instabilities that occur with higher average battery temperatures, and (3) ensure that recharging is performed efficiently. These objectives can be achieved if average battery temperatures are controlled to be within 0 and 20°C with a range of 5 to 15°C preferred. The average battery temperature for EOS-A will be held between 1.7°C (35°F) and 18.3°C (65°F), which is acceptable.

Table 5-78 summarizes the dissipation characteristics of one EOS-A 40 ampere-hour battery at an average temperature of 15.6°C (60°F). The particular method of battery charge control selected for EOS requires that the temperature gradients between batteries be kept low, e.g., that the average temperature of each battery mounting surface must be held to within  $\pm 1.4^\circ\text{C}$  (2.5°F) of the average of all of the battery mounting surfaces.

Table 5-78. EOS-A Battery Dissipation Summary

EOS-A Battery Parameter	Battery Failures	
	None	One of Two
Depth-of-Discharge per Unfailed Battery, percent	15	30
Average Dissipation, watts		
Discharge (0.58 hr)	36.0	72.0
Charge (0.66 hr)	- 5.2	- 5.2
Overcharge (0.41 hr)	33.7	67.3
Orbit-Average Dissipation, watts	18.9	40.0

#### 5.4.2.2 Battery Design Study

The selection of the parallel charging method for EOS was based on considerations of mission commonality, efficiency and low cost. This configuration has been flight-proven on the Orbiting Astronomical Observatory satellite program. Efficiency is high because at end-of-life the

power system transfers energy directly from the solar array to the battery without a charge control loss. Commonality is enhanced because this charge approach can be adapted to batteries of widely differing size in orbits ranging from low to geostationary altitude. It offers cost advantages because there is less equipment to manufacture and test in comparison to a system that utilizes a charger with each battery. The cost and design tradeoffs are discussed in another appendix, 5.4.4. The trade parameters are reduced hardware costs obtained with the parallel charging method, reduced solar array costs obtained from lower power losses and the cost of battery cell matching.

#### 5.4.2.2.1 Cell Matching Requirement

The cost of cell matching is based on the following rationale. It is usually necessary to over order battery cells by 38 percent to ensure that the cells of one battery are properly matched. Thus, 32 cells would be ordered to enable the selection of 22 plus 2 spare cells. Multiple batteries with different nominal capacity can be used in the same power system with isolated charge control. This is not the case with parallel charging; it is necessary to over order by approximately 50 percent to have a cell population of sufficient size to obtain two matched batteries of 22 plus 2 spare cells each.

#### 5.4.2.2.2 Temperature Effects

The parallel charging scheme proposed for EOS requires that several batteries be charged directly from the solar array until one or both reaches a temperature-compensated voltage limit. Attainment of this charge state is sensed and a regulator is placed in series with the array and the batteries to limit charge voltage to that required by the voltage limit. If the batteries are at different temperatures but are charged at the same voltage -- a necessary condition -- their respective states-of-charge will differ by approximately  $0.3 \text{ \%}/^{\circ}\text{C} / \text{ orbit}$  when measured from an initial condition in which both batteries were at identical states-of-charge. The warmest battery will tend to draw the greatest amount of available charge current. Thus, it would tend to reach the over charge region earlier, resulting in a higher orbit-average dissipation for the higher temperature battery. If the temperature difference between batteries is too great, the warmest battery will tend to become



the only effective battery in the system thereby leading to excessive values of depth-of-discharge, charge and over charge currents.

To mitigate this effect it is necessary to have batteries that are very uniform and similar in temperature and capacity. The temperatures of each battery should not differ by more than  $\pm 2.5^{\circ}\text{F}$  from the average temperature of all of the batteries. This requirement is greatly facilitated if the number of battery assemblies is minimized. Fewer batteries simplify the thermal control problem by reducing the thermal interaction between assemblies and by minimizing "edge effects" that might result with a cluster of smaller batteries within the power module.

#### 5.4.2.2.3 Thermal Control

The requirement for precise battery temperature control is placed upon the thermal control subsystem of the power module. However, this is an interface specification in the sense that the temperature measurement point corresponds to a thermal node located at the battery mounting surface. It is thus important to pay particular attention to the thermal gradients that will naturally exist within the battery assemblies. To place this problem in perspective a test was performed on an unmodified DSP battery. The results are shown in Figure 5-161 which is a plot of the temperature gradients that result as a function of battery dissipation. For EOS-A the orbit-average dissipation is about 19 watts per battery with a peak overcharge dissipation of about 34 watts. The test results show that without thermal shims a gradient of  $5^{\circ}\text{C}$  ( $9^{\circ}\text{F}$ ) will occur. The addition of thermal shims will reduce the gradient from cell top to bottom as shown by the analysis summarized in Figure 5-162. The temperature difference between cells and shims will be less than  $0.1^{\circ}\text{C}$  in the proposed EOS-A packaging. A packaging ratio (package cells to unpackaged cells) of 1.3 has been assumed to account for the additional weight increment. A design requirement for the battery is that the total gradient from the battery mounting surface (power module surface) to the top of the cell be less than  $2.5^{\circ}\text{C}$  ( $4.5^{\circ}\text{F}$ ).

#### 5.4.2.2.4 Battery Capacity

It was noted earlier that the thermal control of the batteries could be simplified by minimizing the number of batteries within the power module. The discussion just presented is based upon the use of a 40 AH

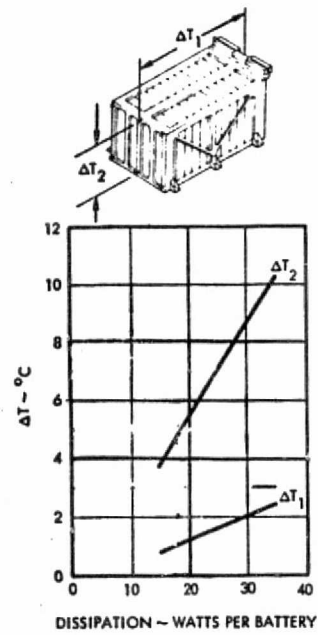


Figure 5-161. Battery Test Thermal Gradients

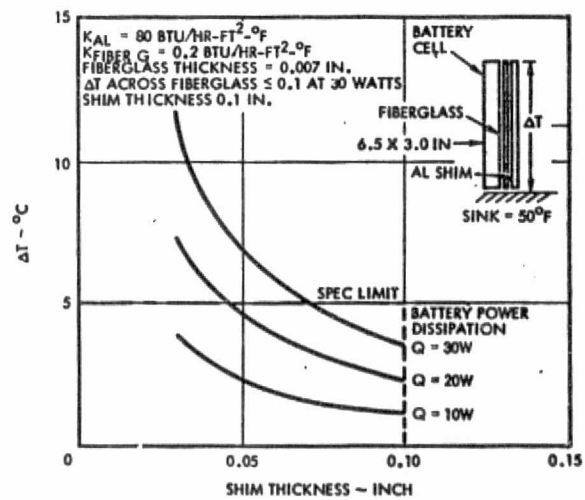


Figure 5-162. Thermal Shim Performance

cell. The selection of a larger cell size for the baseline battery is also consistent with the goal of cost-effectiveness. Although, as a first approximation, the cost of doubling cell capacity from 20 AH to 40 AH may itself double, there is a considerable compensating savings in the elimination of the recurring integration and test costs that would otherwise result if a greater number of lower capacity batteries were substituted for the baseline EDS-A battery configuration. Although the 40 AH cell will require complete and thorough qualification, it is a reasonable extension of current battery technology. This selection for the baseline design is consistent with the concept of accepting increased non-recurring costs in return for a low recurring cost flexible operational system.

The use of one battery cell size for all mission applications is advantageous in that (a) only one battery size need be qualified, (b) only one version of special test equipment and handling fixtures is required, and (3) documentation is minimized. Lower costs accrue from each of these. The size of a nickel-cadmium secondary battery system is determined by

- Discharge voltage (average and minimum)
- Discharge load power (average and peak)
- Number of discharge periods
- Temperature
- Available charge power and energy.

The discharge voltage requirement determines the number of series battery cells. The relationship between cycle life, depth-of-discharge and temperature has been discussed in Section 5.4.2. Charge power or, actually, charge current affects battery size if the charge rate tends to exceed  $C/3$  for extended periods. (Depending upon battery temperature, high current rates increase the possibility of the essentially irreversible generation of hydrogen gas pressure within the cells.) Otherwise, with temperature and depth-of-discharge specified for the satellite design and mission profile, there is a direct relationship between the battery capacity and the solar array increment required for battery recharge. The increment of solar array is greatest for missions in low earth orbits when the percentage of satellite run time is minimal. From the standpoint of the battery charge regulator the total current-handling capacity

of the regulator must be approximately one-third as great in a low orbit than in a geostationary orbit for a comparable level of constant load. Thus, the EOS-A charge and regulator requirements represents a worst-case condition for the range of EOS missions.

#### 5.4.2.2.5 Summary

The EOS-A power module is designed mechanically, thermally and electrically to accommodate four battery assemblies with a combined total capacity of 160 AH.

As defined for EOS-A, the resulting power module has considerable internal design flexibility and will directly satisfy the assumed requirements of the EOS missions in all proposed orbits. The proposed design is preferred to one which utilizes a variable number of small modules each containing battery/regulator units (series charge control technique). Although such a system implies a relaxation of the battery thermal control requirements, it does not eliminate the requirement completely and, otherwise, presents added complexities in the development of a common battery discharge bus as discussed in Section 5.4.3. In addition, the modular charge technique represents an inefficient use of regulating equipment. In conclusion, the use of one module with a variable number of large-capacity (40 AH) batteries is a cost-effective approach for the full range of EOS missions defined at this time.

### 5.4.3 Electrical Power Control Configuration

The design of an electrical power system for the EOS spacecraft must be compatible with missions for which the load characteristics vary over a wide range. Planned future missions will include loads with high peak power and low duty cycle. This type of load has considerable impact on the design of battery discharge regulators. In order to avoid the added cost and complexity of the discharge regulators and to facilitate supplying peak loads with minimum line transients, the batteries will be discharged through diodes or directly to the main bus.

The resulting poor regulation of the power distribution bus must be accommodated by regulators in the user subsystem. This is not regarded as a penalty of this approach since regulation and conversion of user power is a requirement resulting from the aspects of commonality with mission variable load characteristics, individual module power requirements, and the EMC constraints on primary and secondary power grounds.

#### 5.4.3.1 Configuration Study

Supplying peak and eclipse loads by conditioned discharge of more than one battery places a limitation on methods for individual battery charge as illustrated in Figures 5-163a, b, c, and d. For the configuration of Figures 5-163a and b, all solar array power flows through the regulators and the system is penalized due to the power loss in the regulator. In addition, the approach of Figure 5-163a requires each regulator to be capable of handling full array power since the total current may flow from the solar array to the power bus through the circuit which contains the battery with the higher voltage. The use of current limiting, either electronic or by sectioning the array as in Figure 5-163b, could result in failure to regain full charge due to imbalance in battery terminal voltage. The battery with the higher terminal voltage (lower temperature) receives the least charge since a larger portion of the available solar array current would be diverted to the load. The unequal charge currents would tend to increase the imbalance of temperature and terminal voltage between the batteries. The use of shorting relays around the regulators reduce the

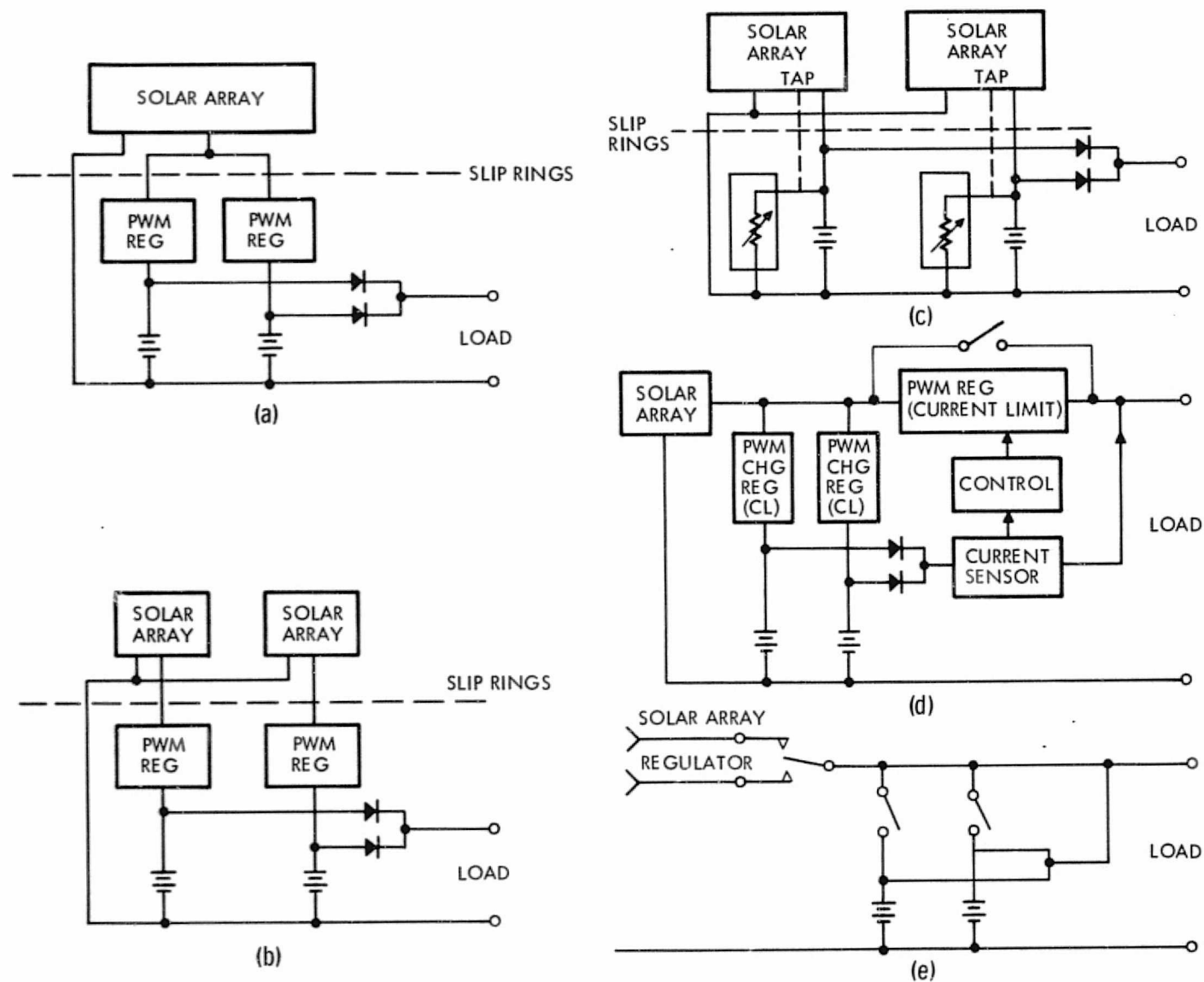


Figure 5-163. Battery Charge/Discharge Conditioning

losses due to regulator efficiency but have a negative effect on the recharge performance of this approach. The shunt charge regulators of Figure 5-163c eliminate the regulator loss but do not improve the recharge capability. Control of battery charge and retaining direct discharge capability may be achieved with the configuration of Figure 5-163d. The line regulator maintains the bus voltage sufficiently high to prevent significant current from flowing from the batteries during normal loads and the recharge of the batteries is completely controlled by the battery charger. During peak loads, full array current will flow through the line regulator and be supplemented with battery current. This system is penalized with the losses in the line regulator and the battery chargers.

A parallel charge approach used on the OAO program is illustrated in Figure 5-163e. The batteries receive their principal recharge current directly from the solar array. Voltage across the load is dependent on battery and load characteristics. When either one of the batteries reach a voltage determined by the control logic, the main bus regulator is switched in to begin taper charge. Since charge rate and the initiation of taper charge is not individually controlled, the effectiveness of this method is dependent on the degree to which the battery characteristics can be matched. The temperature differences between batteries as well as between cells must be held to small values to prevent dispersion of the recharge characteristics. The additional thermal control and increased cost of cell and battery must be charged to this approach. Battery and cell selection are discussed in Section 5.4.2. Thermal control requirements of the power module are described in Section 5.5.1. Table 5-79 gives a comparison of recurring costs between the three configurations.

#### 5.4.3.2 Regulator Configuration

##### 5.4.3.2.1 General Constraints

The selection of battery charge configuration discussed in the previous section does not imply a specific configuration for the main bus regulator. All combinations of shunt and series regulators constitute valid electrical approaches for this system. The factors which must be considered in selecting an optimum approach for the EOS program are:

- Cost. Cost is reflected in the effective use of available power. Any irreducible power loss will increase the required output power of the solar array. For the purposes of this tradeoff study, the cost of power is estimated to be \$600 per watt. The

Table 5-79. Comparative Recurring Cost Estimates for Battery Charge/Discharge Configurations

Charge/Discharge Configurations	Configuration a	Configuration b	Configuration c
Relative hardware power <sup>(1)</sup> requirement	1, 1	1, 0.5, 0.5	1 <sup>(6)</sup>
Estimated number of parts <sup>(2)</sup>	1760	2240	880
Cost of hardware <sup>(3)</sup>	114.5K	146K	57.2K
Power loss	10%	10%	11.5% <sup>(7)</sup>
Cost of power loss <sup>(4)</sup>	60K	60K	9.0K
Additional battery/cell selection	0	0	12.8K
Relative configuration cost	174.5K	206K	79.0K

- Notes:
- (1) Unity (1) is equal to solar array power (1 kw for this model)
  - (2) Based on  $N = 480 + 400P$  for fully redundant power system ( $P$  = power in kw)
  - (3) Estimated \$65/part recurring cost
  - (4) Estimated \$600/watt, solar array recurring cost
  - (5) Additional cost for matching two batteries
  - (6) Hardware represents necessary line regulator
  - (7) Thermal power loss of 1.5 percent included for battery temperature control.



number of parts is a useful cost indicator since on any one program, the nonrecurring and recurring costs tend to be quasi-linear functions of that quantity. The averaged recurring cost used in the previous section was \$65 per part. This factor was selected on the assumption of a minimum cost program.

- Thermal Control. The method of regulation implemented must address the problem of the thermal control of the power module. The battery charging approach requires the temperature range and gradients of the battery assembly to be maintained within narrow limits. Excessive dissipation or extreme fluctuations of dissipation in the power module increase the thermal design problem and limit the maximum power capability of the power system configuration.
- Commonality. The series of planned missions include peak power estimates of as high as 2.6 kw (including housekeeping) and possible average power of 2.0 kw. Assuming a typical lower orbit and ampere-hour recharge ratios of 1.05, this average power could require an average array current capability of 115 amperes. As the load definitions become better defined, it is anticipated that the average power numbers will decrease, but 100 ampere capability at nominal bus voltages appears to be a reasonable estimate of future requirements of the power system. The approach for implementing the power system growth in a manner consistent with the modular approach must be considered in the configuration selection.
- Performance. The constraints as indicated by the model GSFC specification (EOS-410-04) and the Demonstration Model Space Description (EOS-410-05) are used as tentative performance requirements in this study.

#### 5.4.3.2.2 Regulator Control Requirements

Power bus regulation is controlled by battery terminal voltage during eclipse (discharge) and the principal portion of the sunlit period of the orbit. When one battery reaches an approximate full charge condition as indicated by a selected voltage/temperature function, the regulator is activated to limit overcharge. The total range of possible operating conditions is illustrated in Figure 5-164 for a nominal array design.

The requirement on the regulator is to maintain bus (and battery) voltage at the value determined by the selected battery voltage limit switch (BVLS) function of voltage and temperature as illustrated in Figure 5-165. The accuracy with which these characteristics should be maintained by the regulator is not specified at this time. Since the BVLS functions are based on satisfactory laboratory and flight test data, it is reasonable to require the tolerance of the regulator output voltage to be less than half

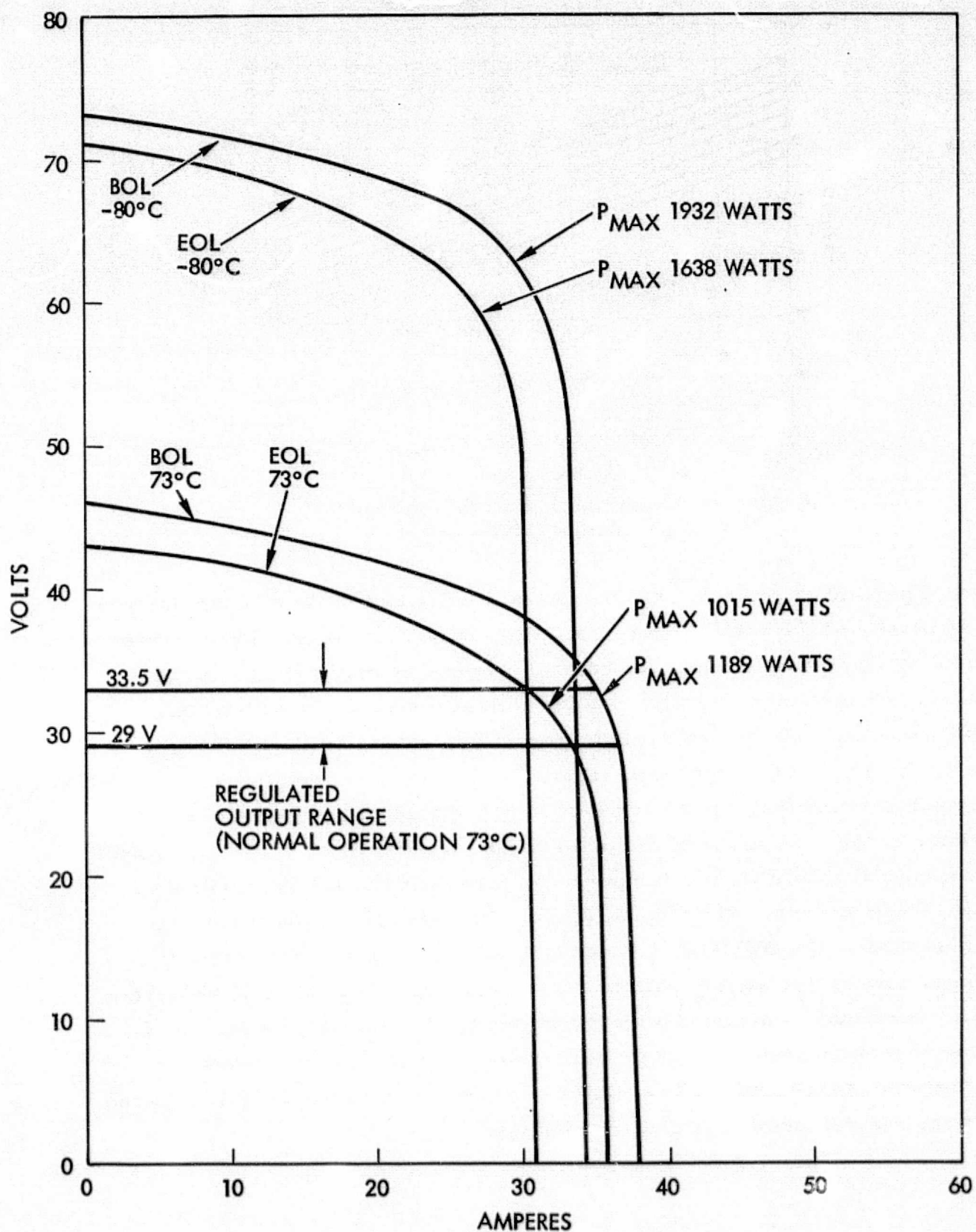


Figure 5-164. Solar Array Characteristics at Temperature Extremes

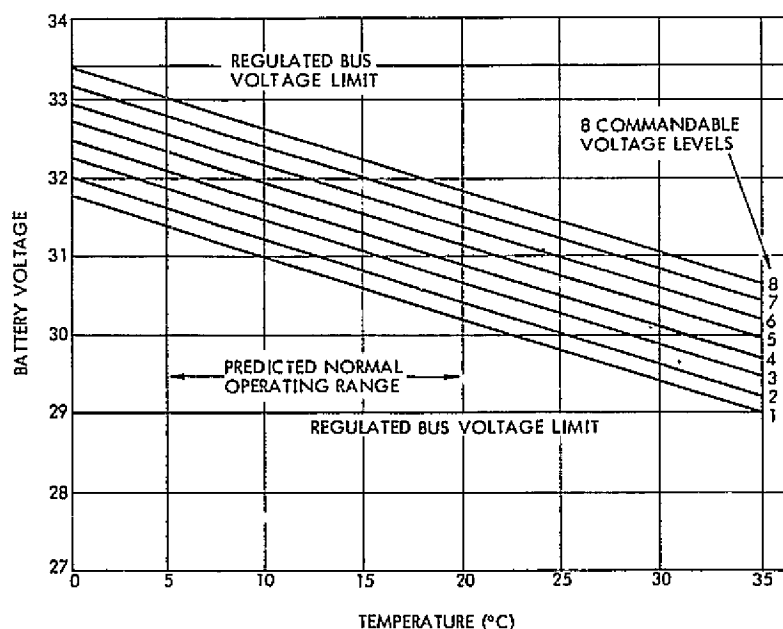


Figure 5-165. Charge Control Voltage/  
Temperature Levels

( $\approx 0.4$  percent) the spacing between characteristics to maintain the desired granularity of the control characteristics. Discussions in literature supplied by GSFC indicate that the control problem is more severe at the higher temperatures and may require voltage regulation with tolerance approaching  $\pm 4$  Mv per cell ( $\approx 0.25$  percent) to enable adequate charge control. The control approach requires combination of voltage and temperature measurements and errors associated with each sensor contribute to the total error of the main regulator. The  $\pm 4$  Mv error translates into approximately  $\pm 1.1^\circ\text{C}$  temperature change on the BVLS characteristic. Since the implementation of this battery control approach permits adjustment of the BVLS level based on observed battery performance rather than actual battery voltage, the critical regulator control requirement is primarily directed at reproducible performance for a period of time consistent with reasonable observation of battery characteristics. A tentative specification of regulator tolerances to implement the required charge control function is provided below:

<u>Output Voltage (E(BVLS))</u> <u>Tolerance (%)</u>	<u>Parameter</u>	<u>Range</u>
±0.2	Temperature	0 to 25°C
±0.2	Load current	15 to 30a
±0.5	Long-term stability	6 months

The regulation over the temperature range should be achievable with a temperature compensated voltage standard. The gain required to maintain load regulation may be reduced by standard line/load compensation techniques. The short-term stability of the temperature sensing circuitry is primarily a function of the characteristics of resistors in the thermistor bridge and associated electronics. Short-term temperature compensation is not expected to present a problem and tolerances of less than 1°C are reasonable. The locations of the voltage standard, temperature and voltage transducer circuitry should be in close proximity to simplify temperature compensation procedures. Further study of the regulation requirements of the EOS power system during the C/D design phase should evaluate the possibility of relaxing regulation requirements since the small tolerances discussed here will tend to impact recurring vehicle cost due to the time required to implement the compensation procedures and tests required to verify performance.

#### 5.4.3.2.3 Candidate Configurations

The fundamental configurations for power regulation consist of series or shunt regulators operating in dissipative or nondissipative switching modes. The regulators are required to provide control of the bus voltage over the voltage range specified by the BVLS functions (29 to 33.5 volts). For the purposes of evaluation, the solar array characteristic given in Table 5-80 will be used and it will be assumed that the array may be divided into arbitrary sections. Twelve slip rings are assumed to be available for use by each regulator configuration.

#### 5.4.3.2.4 Series Dissipative Regulator

The configuration of the regulator is shown in Figure 5-166. The worst-case power dissipation in normal operation occurs for the lowest required output voltage. The maximum dissipation for this model case is calculated

Table 5-80. Solar Array Characteristics

(a)

(b)

SOLAR ARRAY CHARACTERISTICS			RUN 13
AU = 1.0038 FLUENCE ON CELLS = 0.00E+01 E/CM2			
YEAR = 0 THETA = 90 DEG TEMP = 73 DEG C			
N(S) = 98 N(P) = 144 N(T) = 14112			
CELL: 2X4 CM 2 OHM-CM 354 UM THICK			
ISC = 270 MA IPM = 245 MA			
VOC = 589 MV VPM = 476 MV			
154 UM FUSED SILICA COVER			
FLAT ORIENTED			
29.0	36.869	1369.215	
30.0	36.610	1093.285	
31.0	36.287	1124.911	
32.0	35.889	1148.434	
33.0	35.385	1167.735	
34.0	34.758	1181.731	
35.0	33.979	1189.272	PMAX
36.0	33.011	1188.397	
37.0	31.808	1176.915	
38.0	30.314	1161.943	
39.0	28.468	1139.932	
40.0	26.158	1046.314	
41.0	23.302	955.371	
42.0	19.759	823.887	
43.0	15.367	663.731	
44.0	9.323	436.625	
45.0	3.516	154.223	
46.0	.132	1.451	
47.0	.001	.003	

SOLAR ARRAY CHARACTERISTICS			RUN 2
AU = 1.0038 FLUENCE ON CELLS = 3.24E+13 E/CM2			
YEAR = 2 THETA = 90 DEG TEMP = 73 DEG C			
N(S) = 93 N(P) = 144 N(T) = 14112			
CELL: 2X4 CM 2 OHM-CM 354 UM THICK			
ISC = 270 MA IPM = 245 MA			
VOC = 589 MV VPM = 476 MV			
154 UM FUSED SILICA COVER			
FLAT ORIENTED			
29.0	33.549	972.923	
30.0	33.342	991.262	
31.0	32.428	1005.263	
32.0	31.685	1013.911	
33.0	30.773	1015.496	PMAX
34.0	29.661	1008.483	
35.0	28.313	990.939	
36.0	26.676	953.519	
37.0	24.659	813.502	
38.0	22.280	646.631	
39.0	19.358	4754.949	
40.0	15.815	632.533	
41.0	11.521	472.341	
42.0	6.317	265.303	
43.0	1.374	59.039	
44.0	.000	.000	

5-472

ORIGINAL PAGE IS  
OF POOR QUALITY

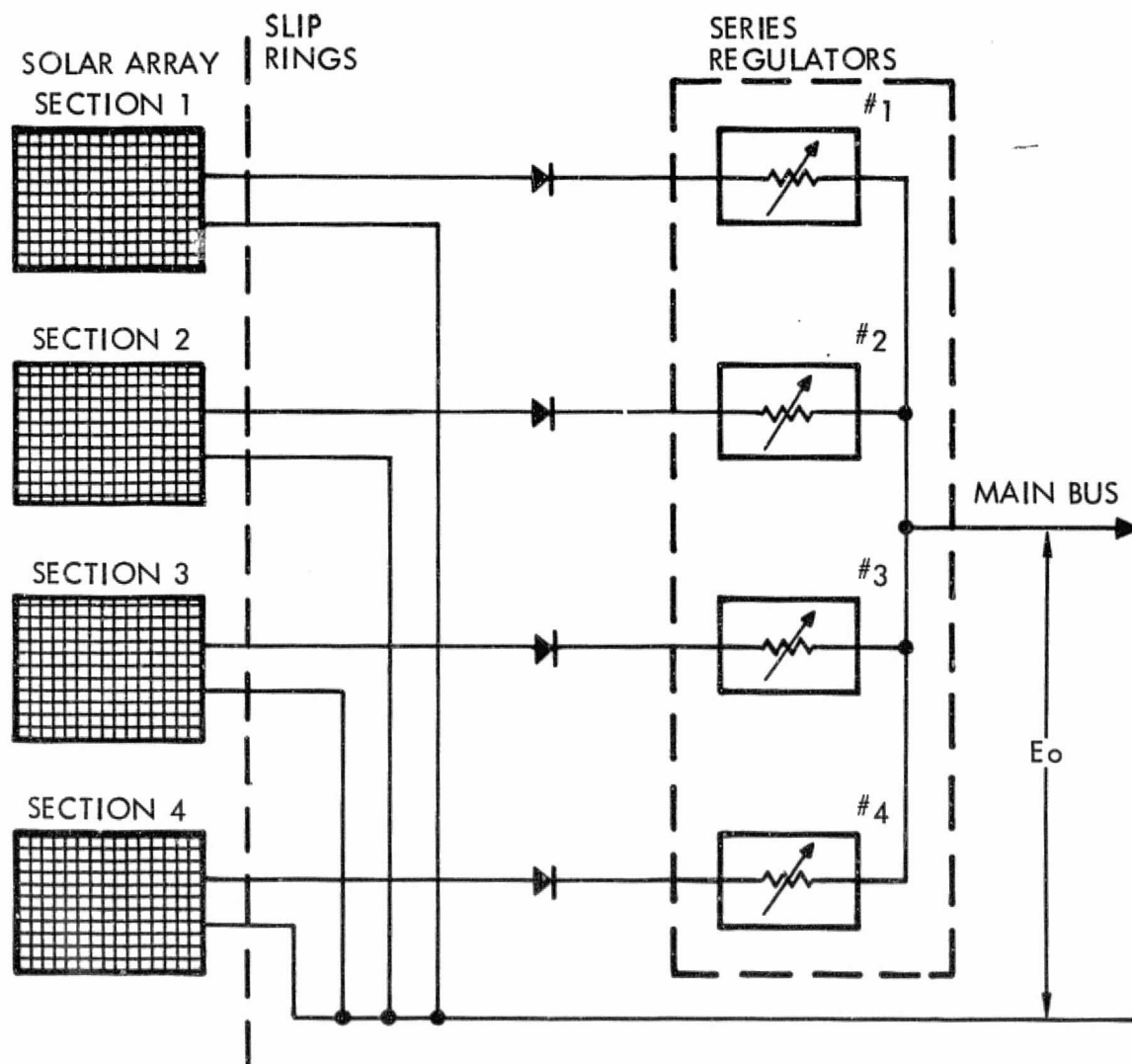
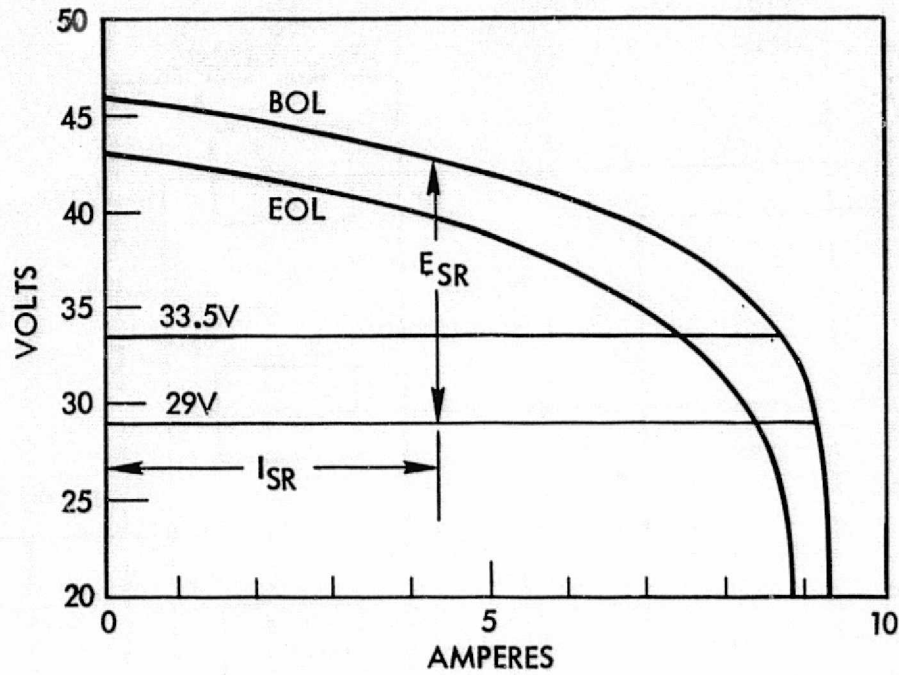
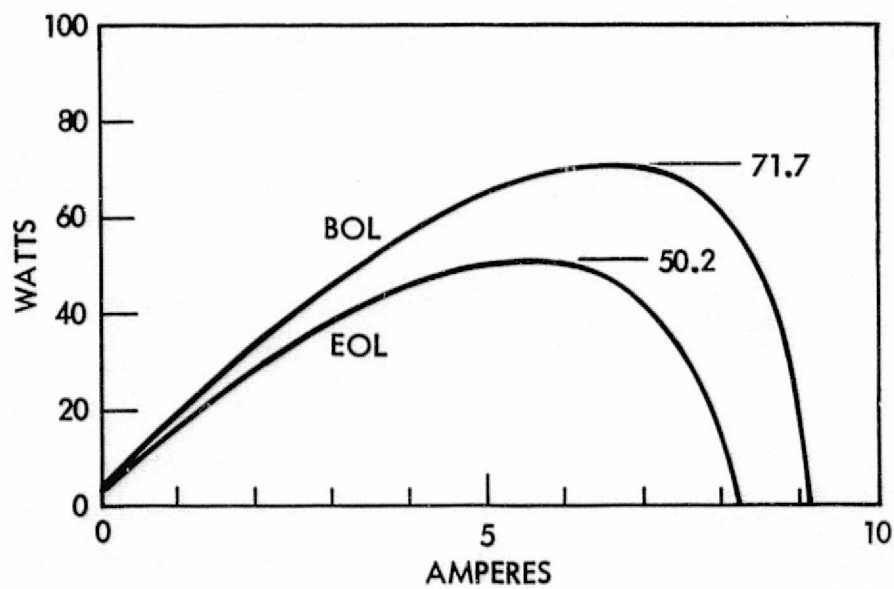


Figure 5-166. Series Dissipative Regulator Configuration for Four-Section Solar Array

from Table 5-80a and is 71.1 watts at 6.0 amperes. It should be noted that if the 12 available slip rings were used, the maximum dissipation in each series element is 47.8 watts (six solar array sections) at the cost of additional parts. Dissipation at saturation is less than 1.0 watt (Solitron SDT 5853). Assuming base drive current is delivered with 10 percent efficiency the maximum dissipation in the power module due to the series regulators is 80.7 and 63.8 watts for the parallel four and six regulators, respectively. The method of calculation and dissipation for all operating points are illustrated in Figure 5-167a, b. It is assumed for all dissipative controls that the parallel control elements are operated in sequence from



a) Series Regulator Operating Points



b) Series Regulator Dissipation

Figure 5-167. Series Regulator Characteristics

saturation to cutoff to minimize maximum power dissipation in the module. A particular advantage of this approach is that the currently available NPN transistors in this design provide a low-dynamic impedance over a wide frequency range due to low emitter resistance and the grounded base configuration. The usual disadvantages of this design are the high array voltage following eclipse and the possibility of a severe negative line transient which could increase transistor dissipation. High array voltages during regulation is an abnormal condition since the regulation system would be fully saturated or shorted subsequent to eclipse in order to provide maximum recharge current to the battery. Lower bus voltages than 29 volts can occur; however, the regulator would be fully saturated and not be overstressed. Assuming a finite possibility of operation at the worst-case array temperatures ( $-80^{\circ}\text{C}$ ) and a bus voltage of 29 volts, the maximum stress a single regulating element must withstand is 44 volts ( $V_{oc} - 29\text{V}$ , BOL) and 258 watts (35 volts, 7.2 amps BOL). The stresses under these circumstances are within state-of-art transistor DC ratings. It is improbable that any single fault could cause a regulator to exceed the maximum of 71.1 watts previously calculated. The failure mode is short circuit which would create an irreducible minimum power output from the array of approximately 292.2 watts at 33.5 volts. Although a definite minimum load has not been established for the mission, it is expected to exceed this value (i.e., 25 percent of maximum power to load). Standard piece part redundancy techniques may be used to eliminate this single-point failure mode.

#### 5.4.3.2.5 Shunt Dissipative Regulator

The shunt dissipative regulator serves as a sink for array output current not required by the battery and load at the operating point determined by battery voltage and temperature. Full shunt regulators are connected between the array output terminal and ground; partial shunt regulators are connected to a tap on the array at a point less than full voltage. The partial shunt is frequently used where it is not desirable to apply full array voltage to the elements of the shunt dissipator.

Either approach is viable in this application, however, the full shunt results in less power dissipation in the power module. A digital shunt control was not considered since required degree of access to the



solar cell panels is not compatible with a gimbaled array and battery/load regulation requirements. The full shunt configuration is illustrated in Figure 5-168 and uses four shunt assemblies. The shunts are operated from saturation to cutoff in sequence so that only one is capable of dissipating significant power at any particular time. When a shunt power control element is in saturation, the power drawn from the associated array section is dissipated in a distributed resistance included in the structure of that section. This requires a separate slip ring for the shunt current. The four-section regulator used in this model requires a total of 12 slip rings. The basic power calculation consists in determining the shunt resistance required for maximum array current at minimum BVLS voltage.

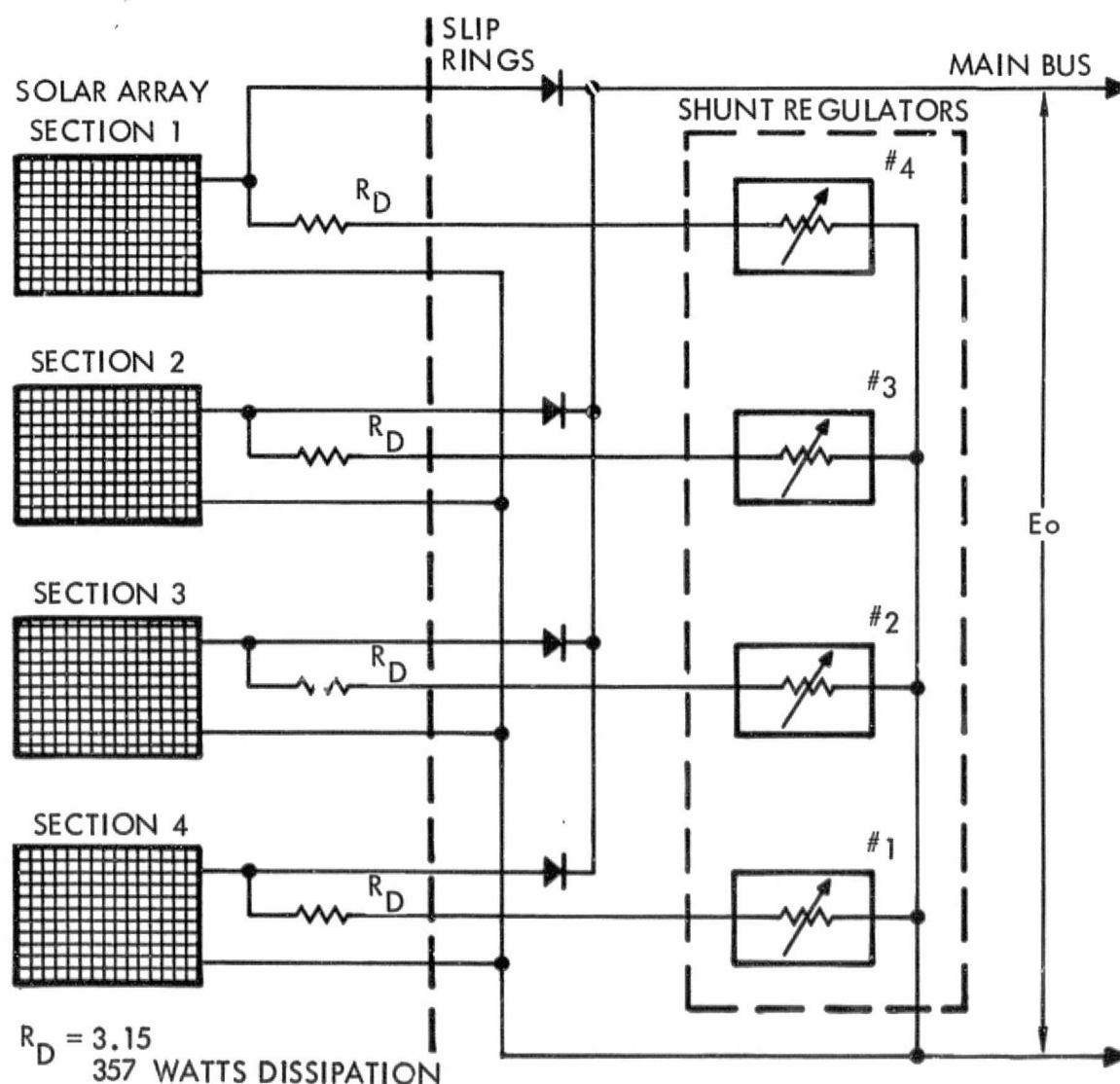


Figure 5-168. Shunt Dissipative Regulator Configuration

As indicated in Figure 5-169, the value of  $R_S = 3.15$  ohms and corresponds to the 29 volt, 9.2 ampere point on the array (BOL). The maximum power in the shunt power control element is determined by the maximum BVLS voltage (33.5 volts) and the resistance of  $R_S$ .

$$P = 1/4(33.5)^2/3.15$$

$$= 89 \text{ watts}$$

The maximum power dissipated in the module under normal conditions is 89 watts plus the dissipation in the remaining shunt elements in the saturated condition.

$$P_{\max} = 89 + 3(3.2) = 98.6 \text{ watts}$$

The shunt dissipative regulator provides excellent performance although the transient response is not as fast as the series regulator due to the grounded emitter configuration.

The failure mode is short circuit which for this design decreases the power system capability by 25 percent. This single-point failure mode may be removed by standard piece-part redundancy.

The sequential control of the shunt regulators is similar to that of the series regulator. Control electronics power ground may be conveniently tied directly to the local signal ground. The shunt regulator must have at least one additional slip ring for each array section controlled. The dissipating resistor (3.15 ohms, 357 watts dissipation) is dispersed over broad areas of the array either as distributed strip resistors or resistance wire contained in the array structure. Both approaches increase the cost of the array about one percent ( $\approx \$2K/\text{section}$ ) and may create further expense in thermal analysis and verification due to the possibility of "hot spots." High temperature ceramic resistors mounted

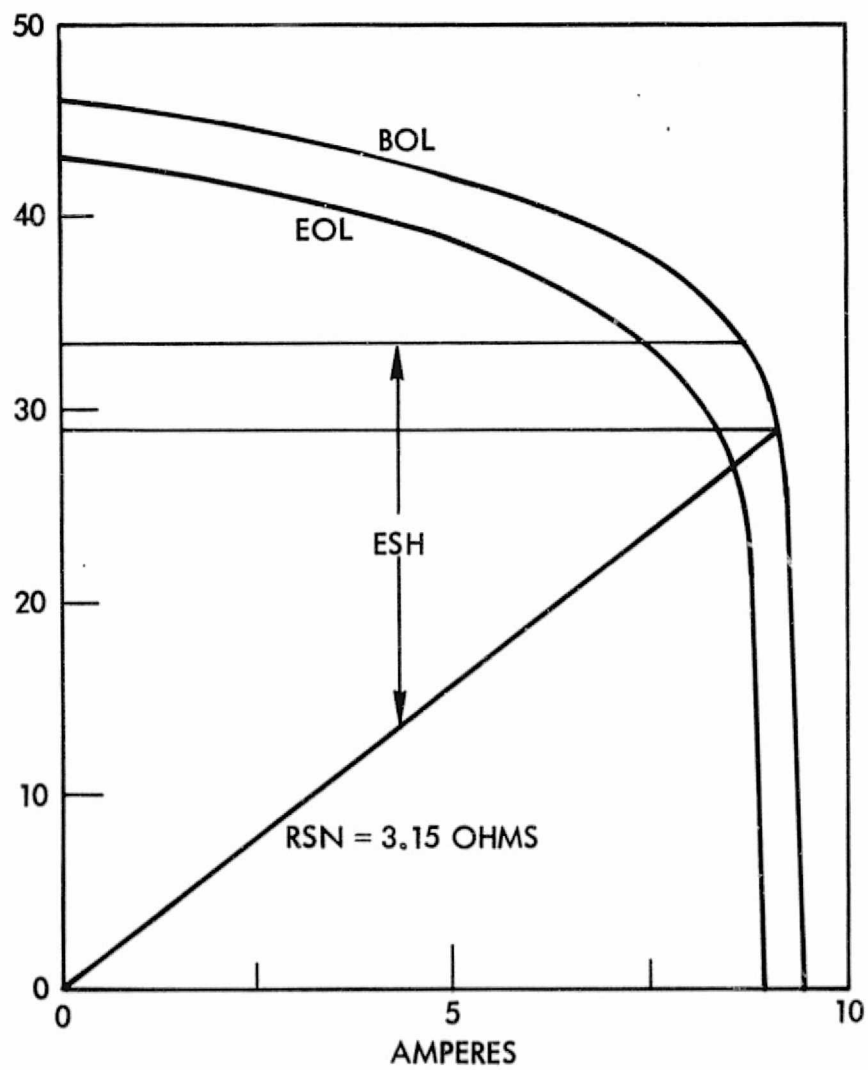


Figure 5-169. Shunt Dissipative Regulator Operating Points

on a radiator may be used instead of array mounted dissipators if a location can be specified which is compatible with Shuttle resupply operations. The dissipation resistors are mission-peculiar and must be available for resupply for every change in solar array power. Use of dispersed dissipation resistors on the array is consistent with commonality constraints and modular concepts.

#### 5.4.3.2.6 PWM Buck Regulator

The PWM buck regulator (Figures 5-170 and -171) or nondissipative regulator has the same general configuration as the series dissipative regulator.

The power control function is performed by chopping input voltage with a solid-state switch and integrating the resulting waveform with the output filter inductance.

The effect is comparable to an autotransformer and with similar low inherent losses. The adjustable transformer effect makes possible the efficient coupling of the maximum power point on the solar array to the regulated output (maximum power tracker). This approach has been applied on the Skylab program with satisfactory results as indicated in Figure 5-172.

Efficiencies of the order of 95 percent have been achieved however, 90 percent is a more conservative average estimate for a regulator with standard design and control features. Losses are due to transistor drive power, ohmic resistance of the saturated switching transistor and filter inductances, hysteresis and eddy currents in the input choke of the output filter, power loss in the diode, and switching losses which are a function of the response characteristics of the switching transistor and diode. A typical efficiency curve is illustrated in Figure 5-173 as a function of rated load. Peak power dissipation will occur at the moment the regulator is switched to initiate battery taper charge. Assuming a 1 kw array, peak dissipation of approximately 95 watts may be expected at that time. As the taper charge decreases, total load approaches 50 percent of full load and dissipation will drop back to approximately 50 watts for the remainder of the sunlit period.

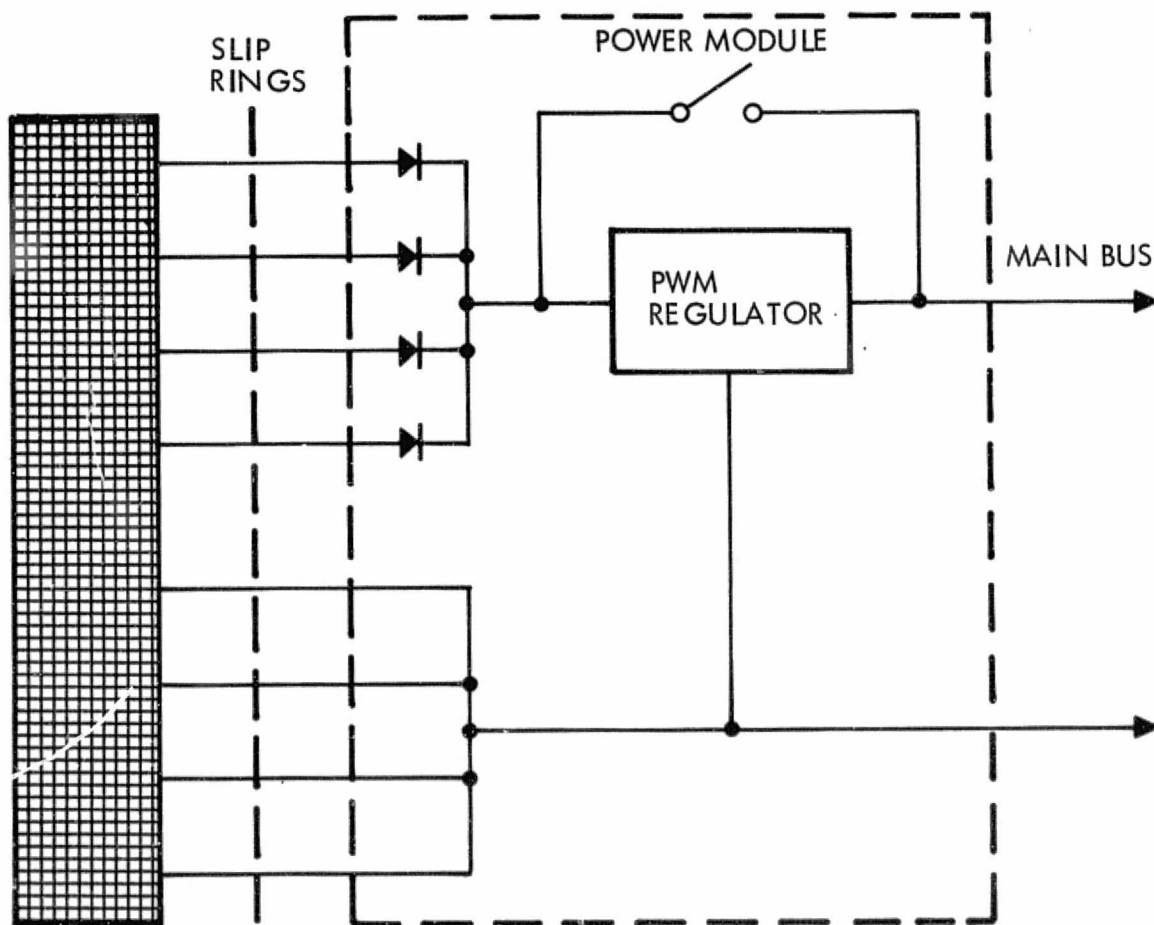


Figure 5-170. PWM Regulator Configuration

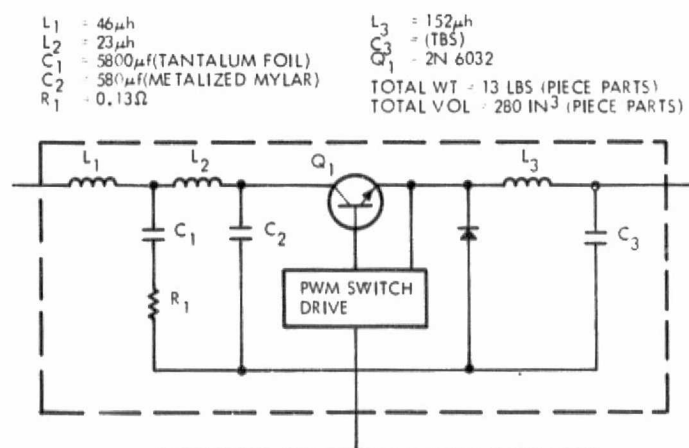


Figure 5-171. 1.0 KW PWM Regulator

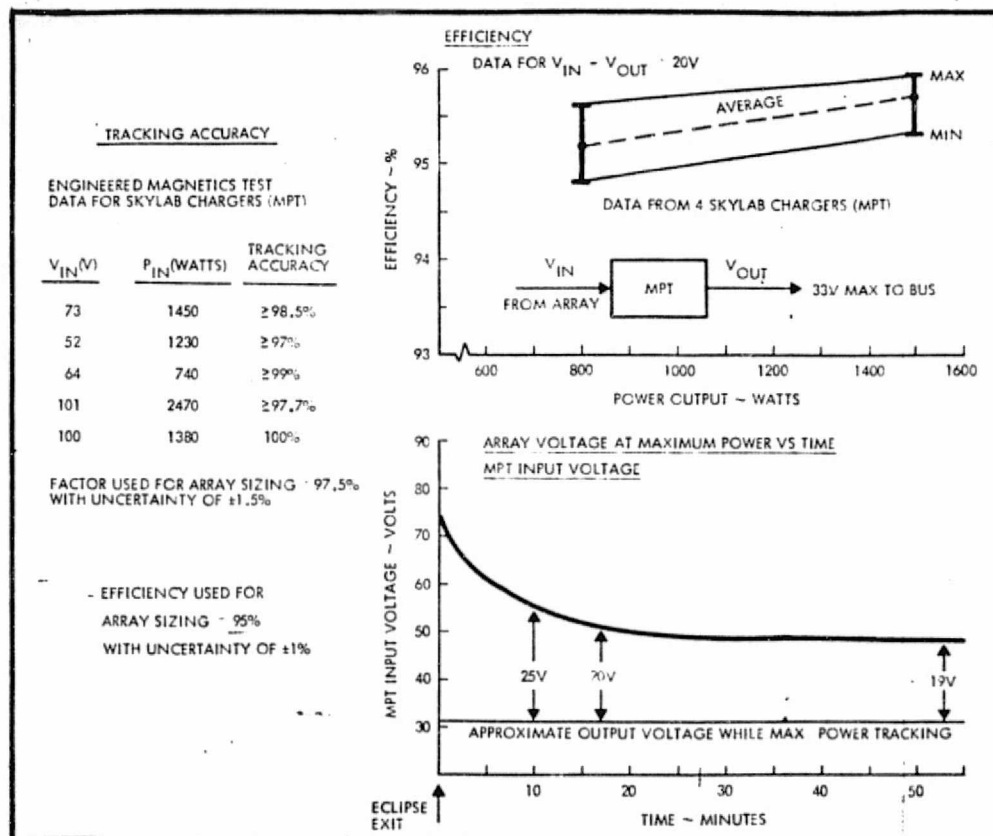


Figure 5-172. PWM Regulator (Maximum Power Tracker) Performance

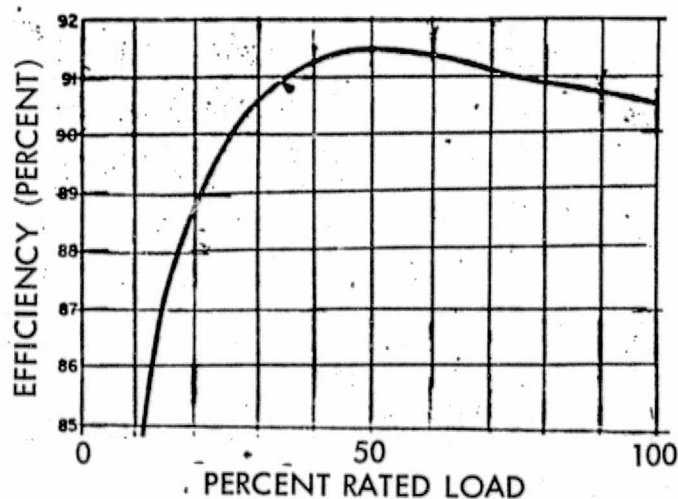


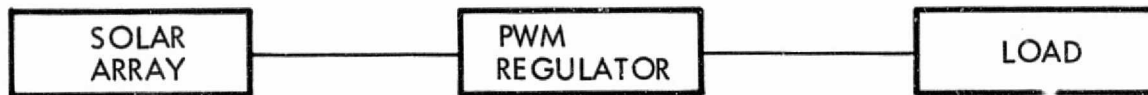
Figure 5-173. PWM Regulator Typical Efficiency

The filter elements shown in Figure 5-170 are essential to the function of the regulator as well as maintaining ripple current within power subsystem and EMI specifications. The input filter design also restricts startup overshoot voltages to approximately 30 percent of steady state values. Calculations are based on an optimized filter design program available at TRW. Transistor Q1 was selected on the basis of switching performance and in the final design may consist of a matched pair operating in parallel to reduce maximum stress and improve reliability.

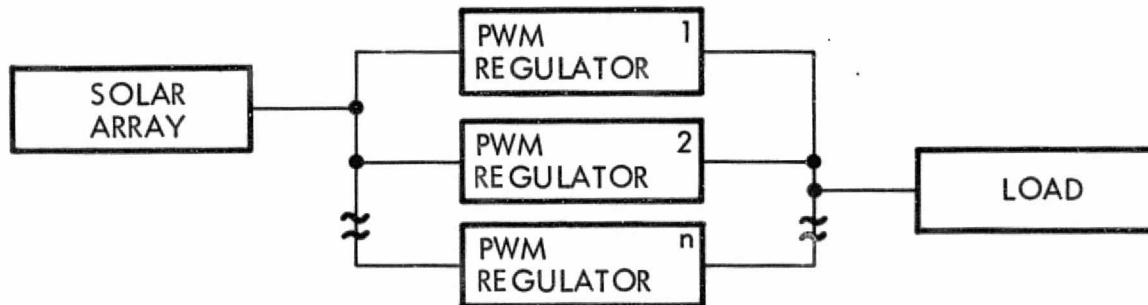
Power capability may be increased by paralleling regulators or splitting the load. Designing a regulator to service all missions (Figure 5-174a) would tend to inflict unnecessary cost and weight penalties on the more numerous low power (1 kw) missions. The parallel PWM regulator configuration (Figure 5-174b) has demonstrated performance on the Skylab mission. This configuration requires an approach for stabilizing the system with an arbitrary number of regulators and necessitates the use of common mode balance and control.

Splitting the load (Figure 5-174c) and supplying power to each section with a solar array/regulator/battery combination is a more modular configuration. Reliability of the system is increased by providing power to the housekeeping functions from all buses through isolation diodes. Batteries for each load section receive more individual control enhancing life and reducing the cost of battery matching. Some penalty must be exacted for the difficulty of matching the capability of each power subsystem to a subset of load requirements. Splitting the array and sequencing regulators to the common bus provides the most flexible system as complex load switching is avoided and there is no problem of coupled instability. The maximum dissipation would consist of the maximum dissipation of one regulator since all others would be shorted out or cutoff. Splitting the 1.0 kw array into four equal sections comparable to the dissipative configurations would result in a reduction of the power dissipation in the power module to approximately 25 watts. This power dissipation decrease is obtained without the use of additional slip rings. It should be noted that peak power tracking cannot be implemented with a sequenced system.

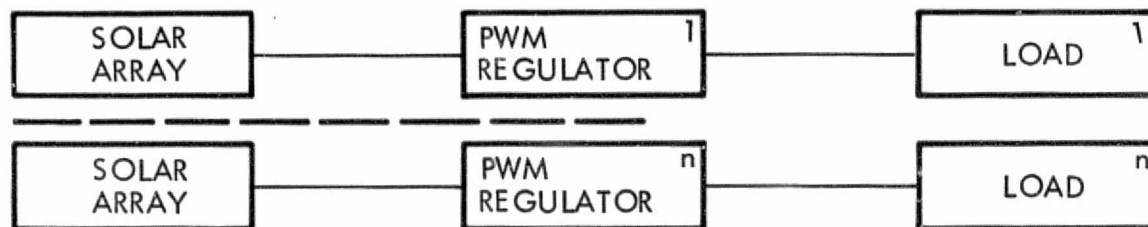
Failure modes for the PWM regulator normally occur as shorted transistor switches and filter capacitors. A shorted transistor switch



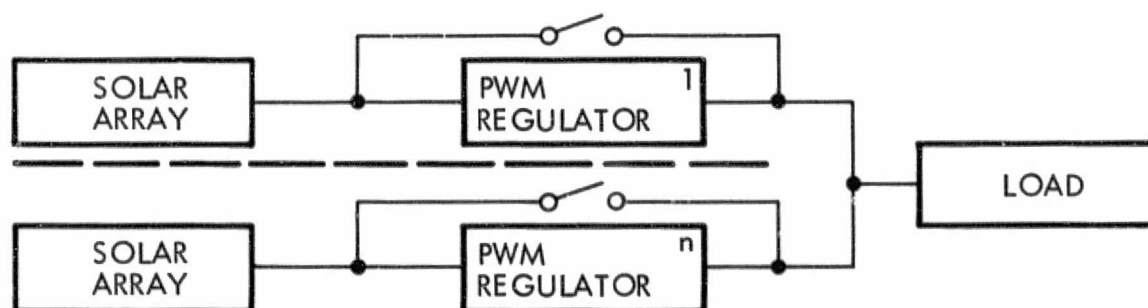
(a) HIGH POWER REGULATOR



(b) PARALLEL REGULATORS



(c) PARALLEL SUBSYSTEMS SPLIT LOAD



(d) SPLIT ARRAY SEQUENCED REGULATORS

Figure 5-174. PWM Regulator Configurations



would prevent taper charge in configurations 5-174a, b and c but would not be a catastrophic failure in 12d. The output capacitor of the input filter ( $C_2$ ) is particularly vulnerable to damage due to the high AC currents flowing in this element. A failure in this capacitor would short the main bus to ground. Failures in the PWM are removed by fault sensing (over-current, undervoltage,  $E(\text{input})/E(\text{output}) \neq I(\text{output})/I(\text{input}) \pm 10$  percent) and power switching. Piece part redundancy may be utilized as shown in Figure 5-175. Redundancy is also implemented by switching at the black box level. Advantage may be derived from configurations 5-174b, c, and d since one for one black box redundancy is not required. One standby redundant regulator can serve as backup for more than one active regulator.

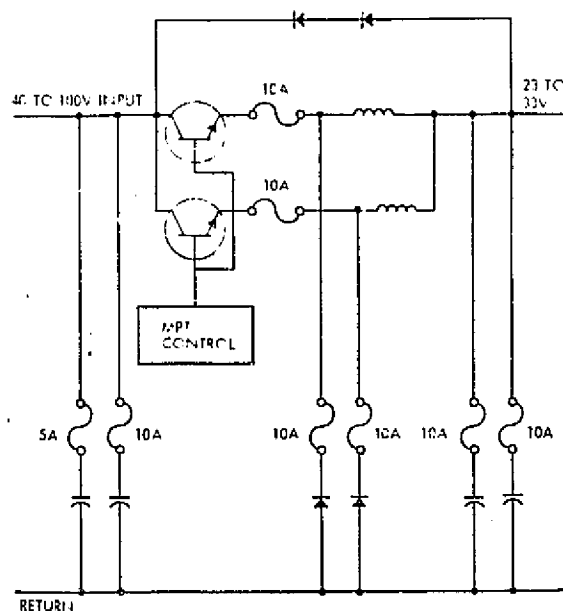


Figure 5-175. Simplified Power Module Diagram Showing Piece Part Redundancy and Fusing

#### 5.4.3.2.7 Maximum Power Tracking

The pulse width modulated regulator may be used to implement tracking of the maximum power point on the solar array. This is particularly useful if the temperature of the solar array has broad excursions for significant periods of time. Two conditions exist among the planned EOS mission profiles where power savings may be achieved with this feature. These conditions occur in the short period following eclipse and in the non-sun synchronous orbits with a single degree-of-freedom solar array gimbal.

The temperature on the array decreases to approximately  $-80^{\circ}\text{C}$  during the 35-minute eclipse period. The power available from the array at this temperature with full illumination is equal to 1,932 watts at BOL and 1,638 watts at EOL. It is expected that the temperature will increase to the steady-state value ( $\approx 73^{\circ}\text{C}$ ) with approximately a 12-minute time constant. The EOL characteristic behavior is illustrated in Figure 5-176. The total area under the curve represents approximately a seven percent increase in available power. However, due to the assumed 90 percent efficiency of the regulator, the area between the regulator loss curve and the curve for the high resistivity cells represents the true power improvement and this is approximately three percent.

For the case of the non-sun synchronous orbit, with a single degree-of-freedom solar array drive and a fixed hinge angle, it is necessary to operate the solar array at large angles of incidence. Associated with these angles are lower array temperatures and maximum power points at voltages in excess of the nominal.

Figure 5-177 is a plot of power available at the maximum power point relative to the power available at a voltage which represents the maximum power point for normal sun incidence. Assuming 90 percent efficiency for the regulator, the array must be at an angle of 45 degrees with respect to the sun before any power gain is achieved by the use of a maximum power tracker (MPT).

Figure 5-178 illustrates the power required from the array to supply power to the battery and load relative to the power required by the load for a range of angles between the orbit polar axis (observatory pitch axis) and the local sun vector. If it is assumed that the solar array can be

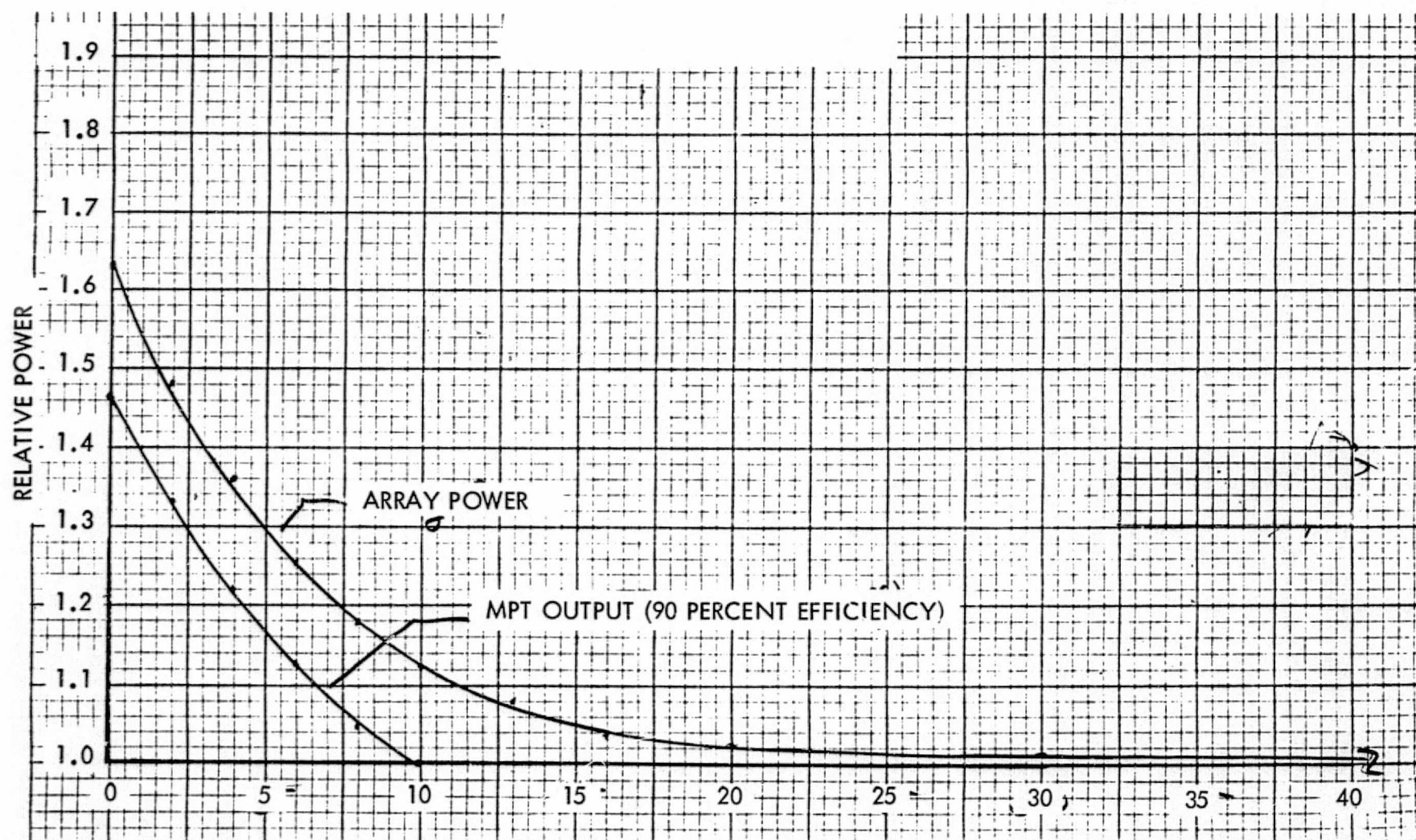


Figure 5-176. Solar Array Maximum Power Versus Time from Eclipse

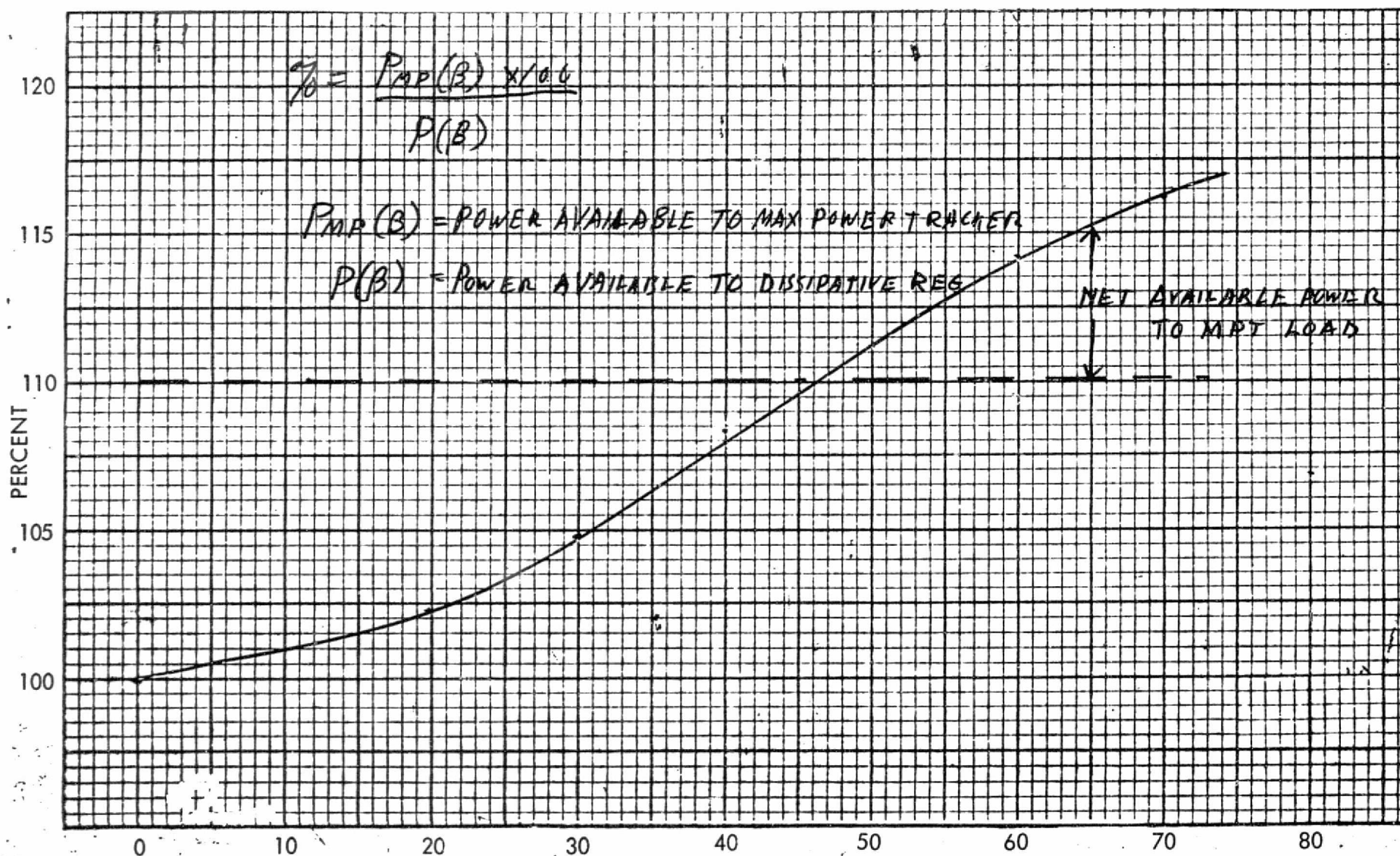


Figure 5-177. Solar Angle of Incidence

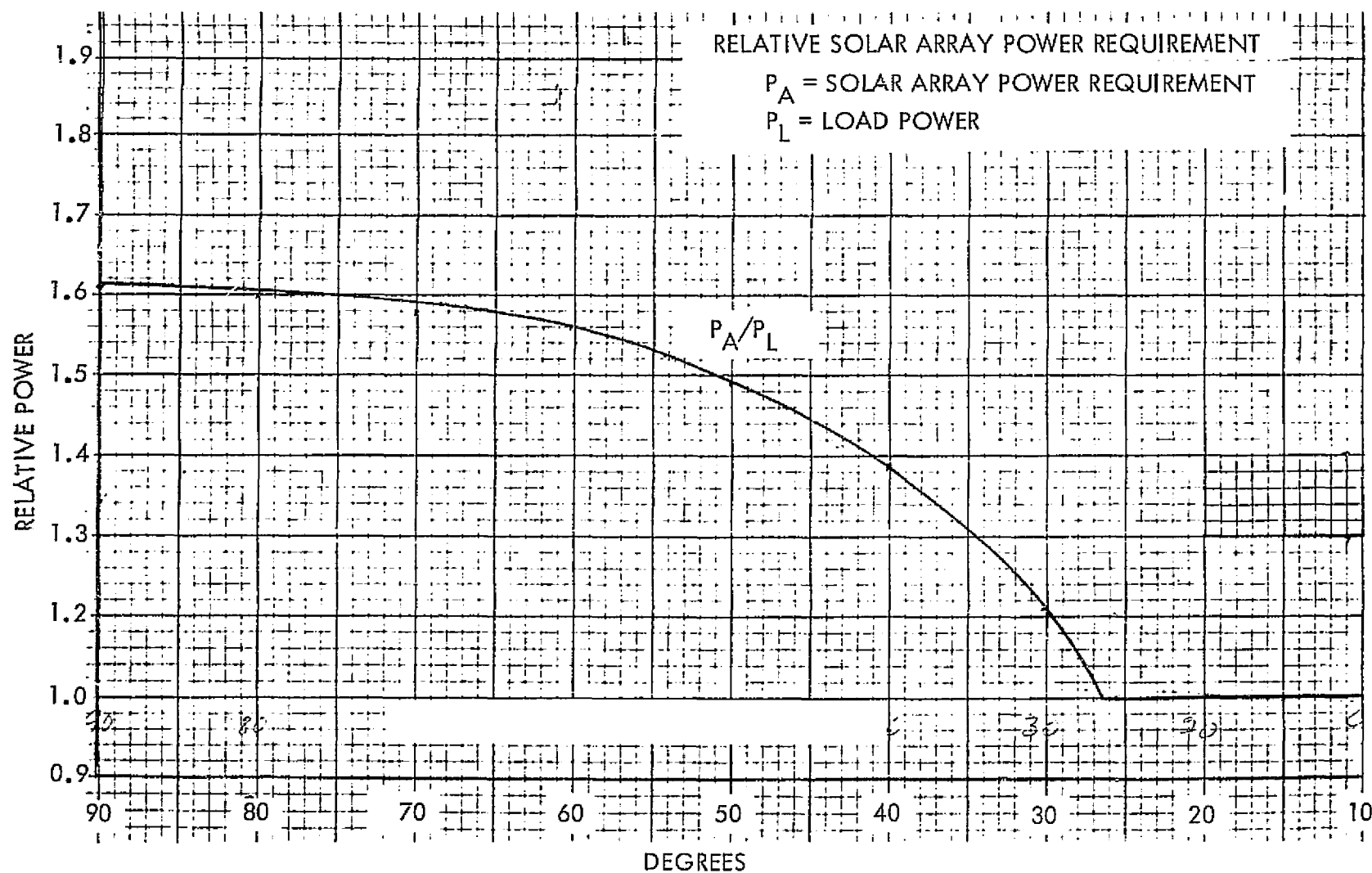


Figure 5-178. Orbit Axis/Sun Angle

maneuvered to arbitrary orientations, the maximum array power required occurs at  $\beta = 90$  degrees (high-noon orbit) and is equal to  $1.61 P_L$  ( $P_L$  is nominal load power). If single-axis control of the array orientation is considered and a 32-degree fixed hinge is added to the array boom, the nominal array power required to supply the observatory loads by the Direct Energy Transfer (DET) approach is illustrated by the solid curve in Figure 5-179. This configuration takes advantage of the decreased power demand at small  $\beta$  angles. The array size, which would provide power for a non-sun synchronous vehicle, is equal to the highest value along the solid curve ( $P_A/P_L = 1.90$ ). The percentage increase over the array requirements of Figure 5-175 is:

$$\Delta\% = \frac{1.90 - 1.61}{1.61} \times 100$$

$$= 18\%$$

The angle of solar incidence ( $\alpha$ ) on the array is given by,

$$\alpha = |58 - \beta|$$

$$\left. \begin{array}{l} \alpha \geq 45^\circ \\ \beta \leq 13^\circ \end{array} \right\} \begin{array}{l} \text{Conditions for MPT} \\ \text{power gain} \end{array}$$

The power advantage of the use of the maximum power tracker is illustrated by the dashed line of Figure 5-176. Readjusting the hinge angle to optimize a design would not provide significant savings ( $\approx 1.0$  percent) in solar array sizing due to the large slope of the curves in the vicinity of  $\beta = 0$ .

This analysis has assumed that the maximum power tracking function is implemented by the on-board computer with no additional power loss due to the MPT circuitry (efficiency = 90 percent). The results do not indicate a significant advantage for this approach. It must be noted, however, that it has also been assumed that power must be delivered to the battery and load at the highest BVLS voltage (33.5 volts). In actual practice an MPT would be used throughout the charge regime with cell voltage moving from 1.40 to approximately 1.45 volts. This represents



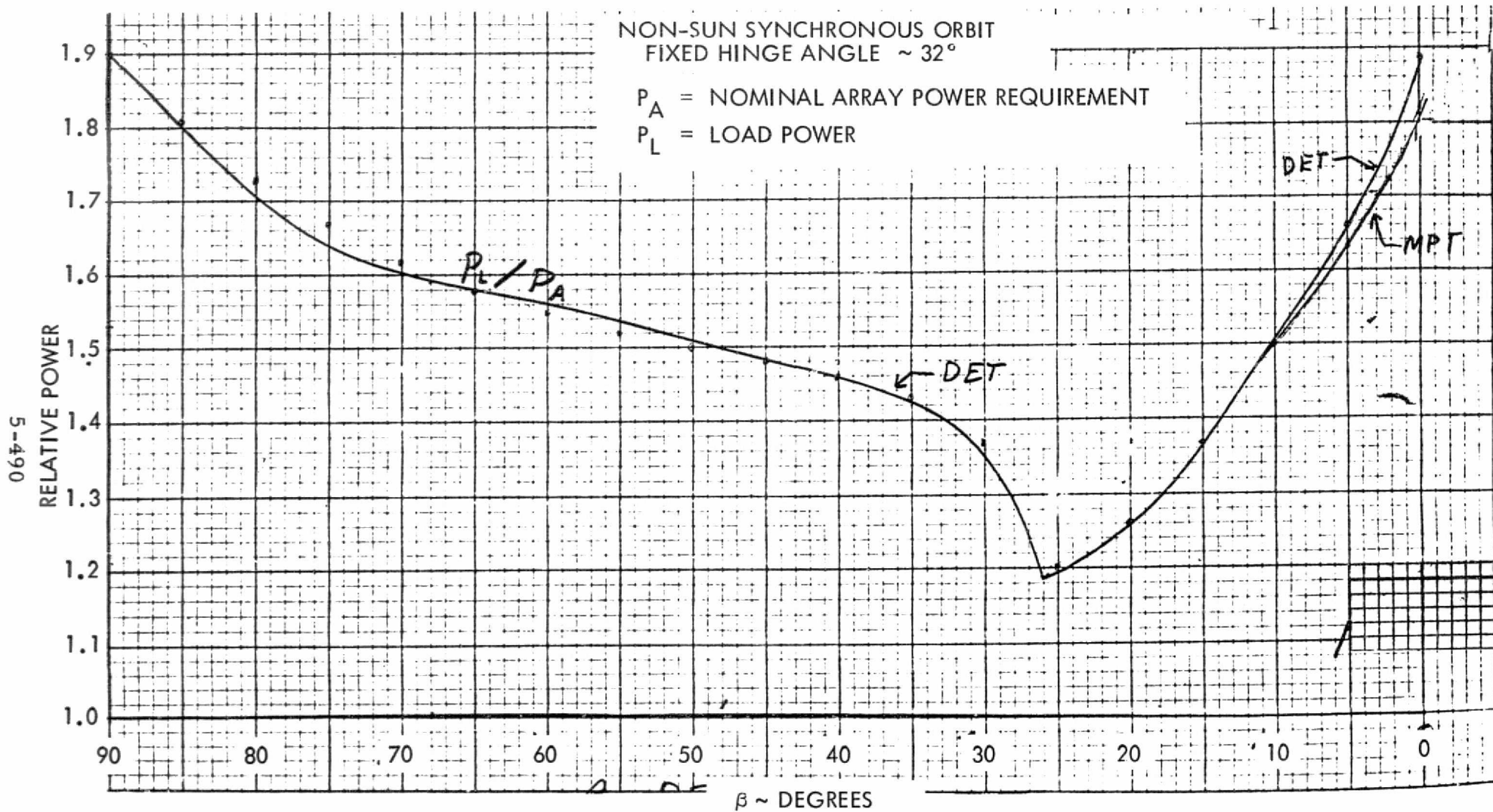


Figure 5-179. Orbit Axis/Sun Angle

a mean voltage which is approximately 95 percent of the expected maximum voltage at which the load must be powered. Factoring this into the previous analysis, the improvement obtained by the MPT under normal operating conditions is

$$\text{Eclipse } \Delta = 3\% + 5\%$$

$$= 8\%$$

$$\text{Non-sun-synchronous } \Delta = 1\% + 5\%$$

$$= 6\%$$

It is emphasized that this is expected performance improvement based on nominal battery performance and does not include the tolerance indicated by the full range of BVLS curves.

#### 5.4.3.3 Summary

Comparison of the power system configurations primarily involve tradeoffs on the regulator since the battery, load, solar array, and control interfaces (Figure 5-180) remain the same for each approach. The output impedance requirement must be met by the combination of regulator and battery. Each regulator will include the battery and load in parallel in the feedback control loop. With the exception of random resistive heater loads, all loads will use PWM regulator/converters. Consequently, the input filter of these devices is the primary dynamic load interface. The effective network that the main bus regulator will see is illustrated in Figure 5-181.

The two 40 amp-hr batteries are modelled as RL circuits based on measurements of battery dynamic impedance (Batteries for Space Power Systems, NASA SP-172, Figure 4-16 and 4-17, page 93). This is a simplified model of battery impedance but adequate for the purposes of this discussion. The load filter shown is a standard low-surge/overshoot design for a 200-watt PWM regulator/converter. The dynamic impedance presented to the regulator is primarily that of the battery and will have a corner frequency at about 4 kHz. This load impedance presents no unusual design problems to any of the three configurations considered.

The dynamic impedance presented by the battery may be modified with an RC circuit to maintain low-resistive dynamic impedance over the full range to meet the output impedance requirement. It should be noted



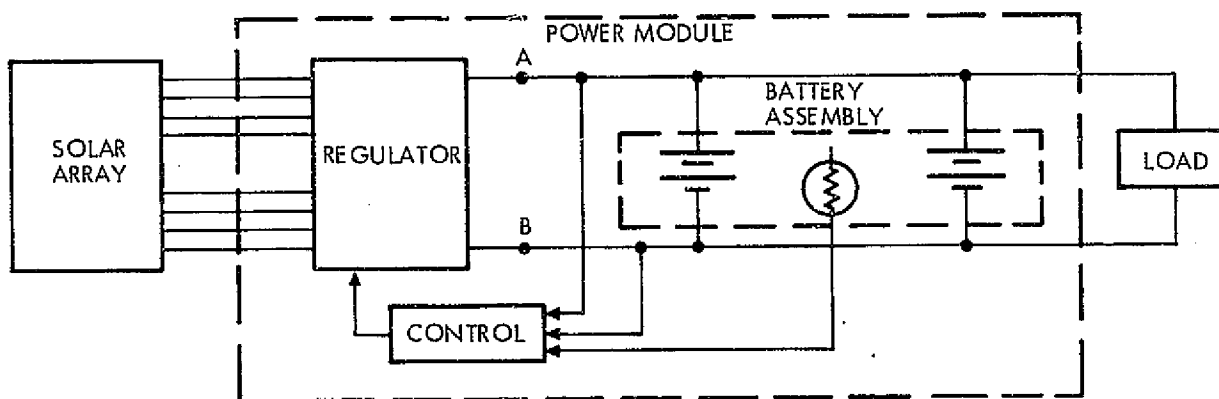


Figure 5-180. Regulator Interfaces

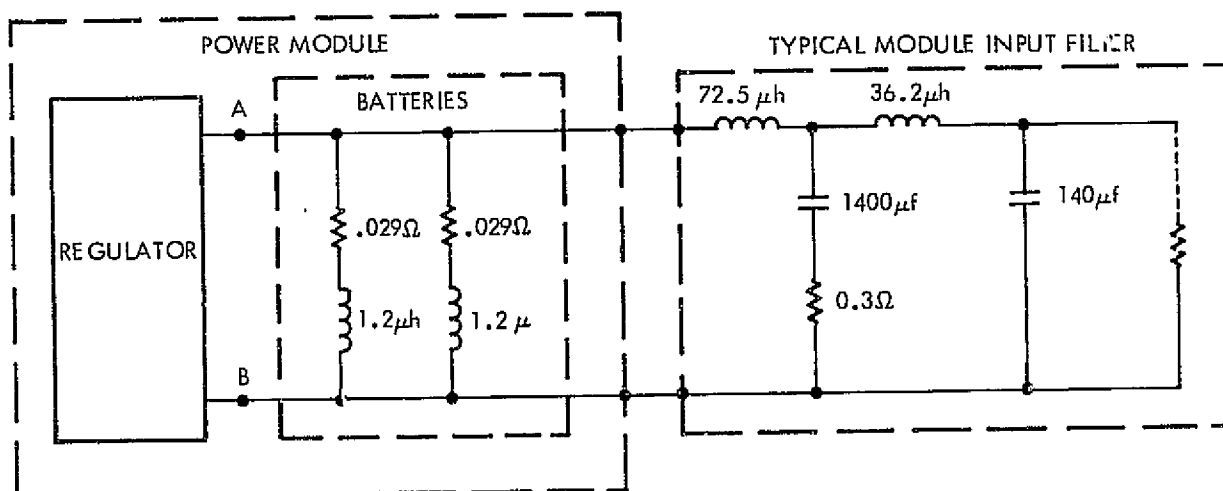


Figure 5-181. Regulator Dynamic Load

that the final design must include a complete analysis of the battery impedance and bus regulator output filters to detect possible resonance conditions.

All considered power control configurations may be implemented for the EOS missions without impacting solar array power requirements. Due to the maximum power tracking capability of the PWM regulator, it may be possible to decrease the size of the array slightly but this is not considered a significant factor. All configurations have been successfully applied to aerospace missions and the question of design feasibility is not pertinent to this study. Furthermore, the cost of the basic regulating

hardware is considered approximately equal for each design since this parameter is primarily dependent on the required control features and redundancy rather than the regulator configuration.

The series dissipative regulator provides low dissipation in the power module and excellent dynamic impedance characteristics with minimum modifications to the solar array configuration. However, the possible implementation of this approach on the present concept of EOS must be deferred until more rigorous analysis can be performed of solar array minimum temperatures with associated high voltages over the full range of missions. Furthermore from the more general considerations of commonality it is not considered desirable to incorporate a regulator design which is sensitive to variations in solar array design.

The shunt dissipative regulator provides excellent performance and may be designed to regulate any arbitrary range of power. It is necessary with this design to provide a radiating surface for power dissipation outside the power module. From the standpoint of commonality and resupply aspects, the ideal location for dissipating the excess power is the solar array structure. Increasing power will also require a mission peculiar slip ring assembly. This factor in addition to the cost impact of solar array structure modifications and associated thermal analysis and test required, detract from the obvious advantages of this approach.

The PWM regulator is capable of regulating large amounts of power with a single unit without modifications to the solar array or the gimbal slip rings. Power dissipation is approximately equivalent to the shunt dissipative system assuming conservative efficiency coefficients. If the sectioned array and slip rings necessary for the dissipative approaches are used, the dissipation of the PWM regulator is significantly reduced. Maximum power tracking capability will probably provide margins of 6 percent or better for all low orbit missions, however this is based on expected battery operating points and does not reduce the required size of the array. Based on these considerations, the PWM regulator is considered the preferred approach.

#### 5.4.4 On-Board Computer (OBC) Power Management

The use of the OBC for power supervision and control provides potential capability for improving performance and extending the useful life of the EOS Observatory. More elaborate monitoring of diagnostic data would detect undesirable trends in performance and enable early re-configuration of operational modes which may otherwise lead to fault conditions. Commonality would be enhanced since any modification of control functions required by future missions may be easily implemented by the OBC. Observatory modularity is reduced due to the increased complexity of the data interface and the probability that power control functions would be programmed by hardwire devices (ROM) rather than by electronically stored data. The value of the use of OBC functions is diminished by the critical nature of power control functions as is illustrated in the following sections.

##### 5.4.4.1 Control Functions

###### 5.4.4.1.1 Power Switching

The block diagram of the power module (Figure 5-182) includes the power disconnect assembly. Operation of these breakers contain hazards that could lead to catastrophic failure such as:

- Opening both spacecraft buses would result in loss of the Observatory.
- Closing any breaker on a short in the harness could result in catastrophic failure due to contacts welding.

The only noncritical function remaining is opening the payload buses. These buses are opened during fault conditions or if battery charge falls below a critical level. Since the latter may occur in conjunction with a computer failure, removing this function from the power module is not desirable.

###### 5.4.4.1.2 Battery Charge Control

Battery state of health is a basic concern of the power system. The observable parameters are battery and cell voltage, current, and temperature. Battery parameters are measured and used for the automated

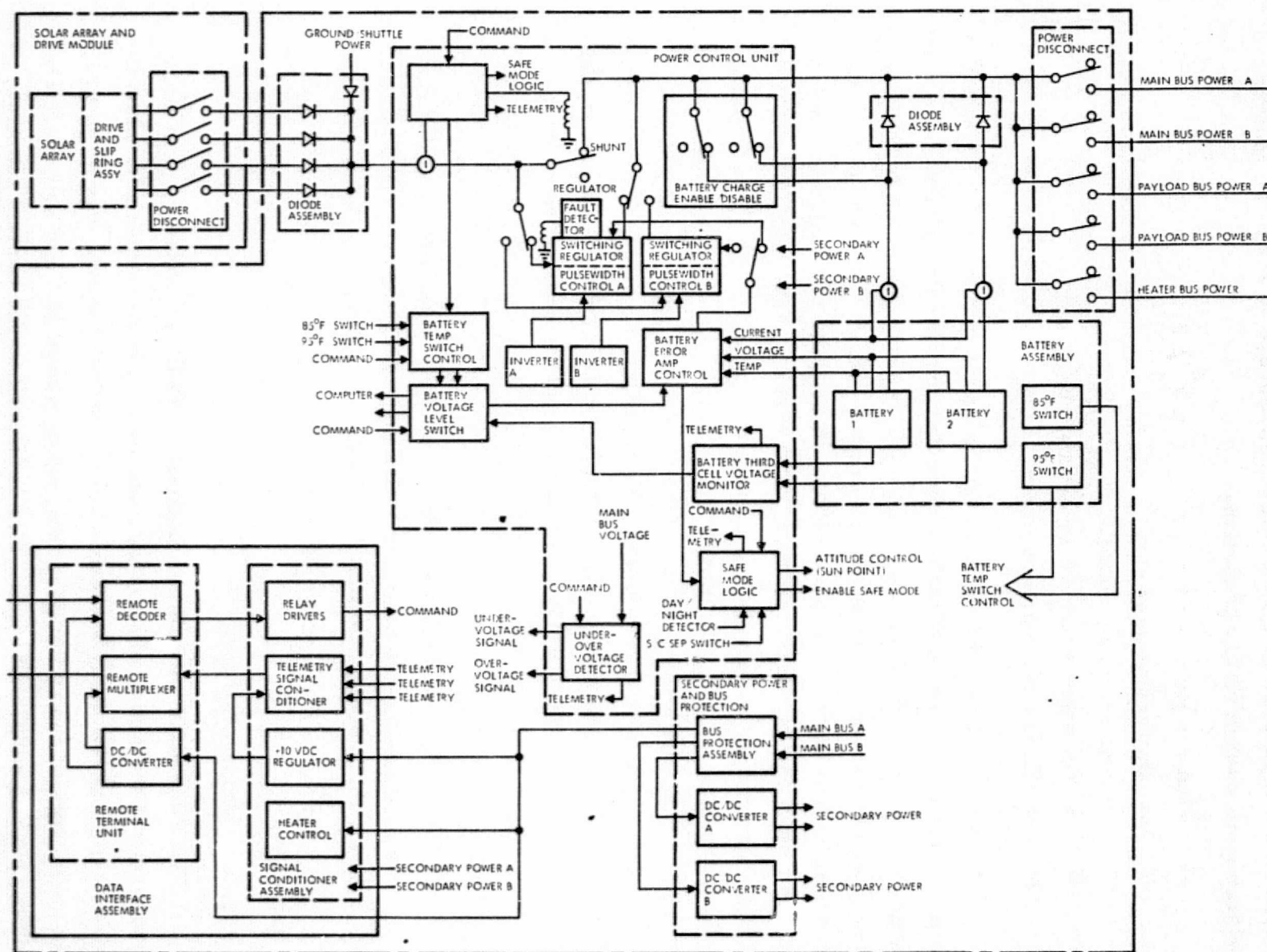


Figure 5-182. Electrical Power Module Block Diagram

regulation function that controls battery charge. This control adds the output of the temperature and voltage transducers to form the battery voltage limit switch (BVLS) function:

$$K_n \quad AV + BT \quad n = 1, 2, \dots 8$$

V = Battery voltage

T = Battery temperature

$K_n$  = Constant selected by ground command

A, B, = Characteristic constants.

When the battery voltage and temperature cause the BVLS function to become an equality, a threshold detector operates to activate the regulator and maintain the equality. The OBC could be inserted in the control loop and perform the addition, comparison, and threshold detection function. The output would be a bilevel to activate the regulator and an analog signal for regulator control. For a fully redundant system, this would remove approximately 150 piece parts and replace them with three A/D converters, three D/A converters, buffer registers and associated circuitry. The modification would result in a net reduction of 75 to 100 piece parts. Failure of the charge control would not result in immediate failure of power system such as a complete loss of charge or catastrophic overheating. However, ground operated override control would be required within a few orbits and would effectively eliminate the net reduction of piece parts.

This rationale would apply to all functions presently incorporated in the power module. On this basis it is concluded that the OBC participation in Power Module operation be limited to additional control features that can improve performance but are not essential and diagnostic monitoring data.

#### 5.4.4.1.3 Maximum Power Tracking

The pulsewidth modulated regulator (PWM) is capable, with additional control features, of supplying optimum power coupling between the solar array and the main bus loads. The control method may be based on measurements of array temperature, open circuit voltage and short circuit current of additional solar cells dedicated to the control function, and the dynamic resistance of the solar array. The last method is preferred and involves modifying the operating point on the array until

voltage and current variations have the desired ratio. The measurements may be based on current and voltage variations induced by: a) ambient load changes or deliberately induced by b) decreasing the attenuation of the PWM input filter or c) providing an AC test signal with additional circuitry in the solar array and drive module. Implementation with either b) or c) is preferred since performance is more predictable. Based on the solar array resistance calculated from the current and voltage variations, the OBC would supply an analog signal to the PWM for pulse width control. The failure mode for this method would be detected by battery discharge during the sunlit portion of the orbit due to the low PWM duty cycle, or by battery overheating due to taper charge mode failure. Either failure mode may be removed by simple fault detection circuitry or ground command. The necessary computer sampling rate depends on the degree of signal conditioning in the power module and would vary between twice the frequency of the test signal and that required to give sufficient speed to track the movement of the maximum power point ( $\approx 1$  Hz).

#### 5.4.4.2 Diagnostic Functions

##### 5.4.4.2.1 Battery

Battery voltage, current, and temperature are measured and telemetered as well as used for automated control as described above. Cell voltage and temperature could be used as an indicator of impending cell failure but is only of academic interest since no controls are provided to avert the failure. Actual failure of a cell is indicated by battery temperature, voltage and current.

State of charge is a significant parameter since optimum battery performance requires a narrow range of overcharge to be reached after each cycle. Accurate measurement of this parameter would provide ground control with useful data for updating the battery charge mode before variations of the less sensitive terminal voltage parameter indicate reconfiguration is necessary. State of charge is not directly observable but may be measured by integrating battery current over each orbit period. The rate of change of battery current indicates that an interval between samples of 15 seconds or less is adequate with a measurement accuracy of  $\pm 1$  percent.

#### 5.4.4.2.2 Regulator Performance

The design performance of the PWM regulator may deteriorate due to part degradation or extreme load conditions. Fault sensors which detect catastrophic failure do not normally measure regulator performance quality which is primarily indicated by efficiency. Automated fault detectors which provide this capability involve a considerable number of parts and may actually create a reliability hazard. Regulator performance may be determined with the OBC by calculating the input and output voltage current products. Measurements obtained at approximately 2-minute intervals would provide a characterization of regulation efficiency over approximately half the control range. During the period prior to regulator operation, the regulator is shorted out and the result of the measurement (100 percent) will serve as a check on the performance of the calculation.

#### 5.4.4.2.3 Module Temperature

Temperature measurements performed on each black box chassis, PWM switching, transistor heat sink, and the batteries would provide a thermal profile of the power module. This may be used to signal a warning to ground control that thermal balance is deteriorating and provide a data base for reconfiguration of operation and loads. The sampling interval required would be on the order of minutes.

#### 5.4.4.3 Summary

None of the above implementations of the OBC are essential to the operation of EOS. Maximum power tracking provides added power margin but is not considered a required capability. The diagnostics may provide reduction in ground control surveillance at the cost of additional signal conditioning and cost in the power module. The potential reduction in operating cost appears to be minimal. Since the purpose of the EOS mission is functional, rather than experimental, and all of the essential housekeeping approaches have been flight tested, it is not recommended that the OBC be used for power control and supervision.

#### 5.4.5 Power Module Electrical Design

The function of the electric power module is to provide main bus distribution control and regulation as required by the batteries. These functions are illustrated in the simplified block diagram of Figure 5-183. Raw power is conducted from the array through slip rings and relays in the solar array and drive module to power module on four twisted pairs. Electrical isolation of the raw power buses is maintained in the power module with power diodes to protect against single point catastrophic failure due to short circuits in the structure raw power harness. The power relays in the solar array and drive module may be operated open only by hardwire command from the ground or Shuttle umbilical. The breakers in the power module may be operated open by similar commands as well as by overload fault conditions. Protection is provided against disconnecting both spacecraft buses except by explicit hardwire command from the Shuttle or launch umbilical.

##### 5.4.5.1 Power Module Operation

The functions of the electric power module are illustrated in the functional block diagram of Figure 5-184. The primary function of the regulator is to maintain charge control on the battery as indicated by the selected

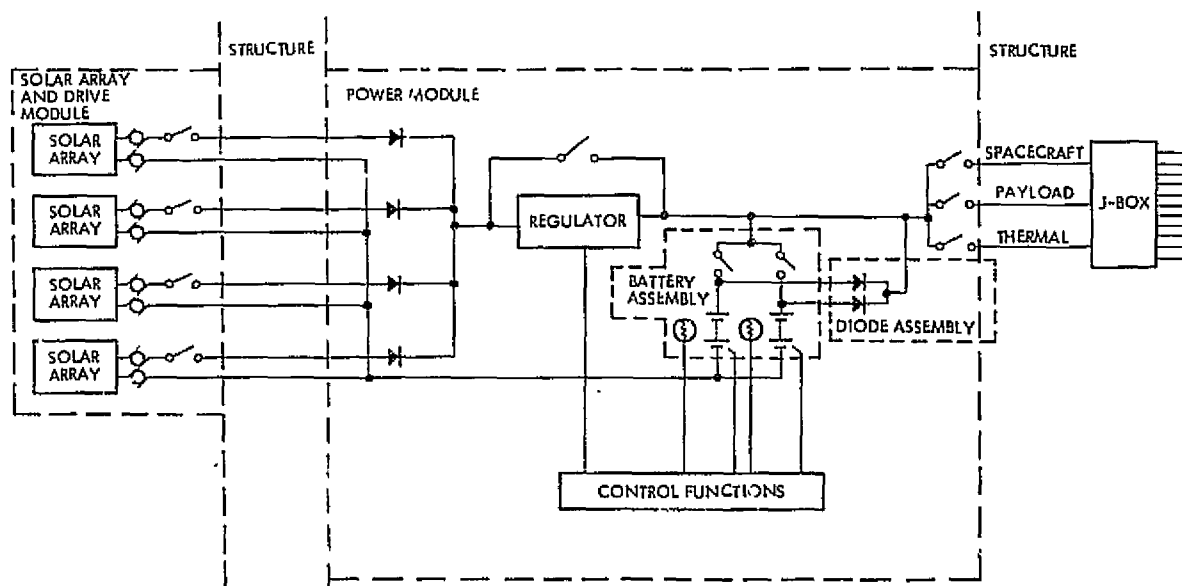


Figure 5-183. Power Module and Interface Block Diagram



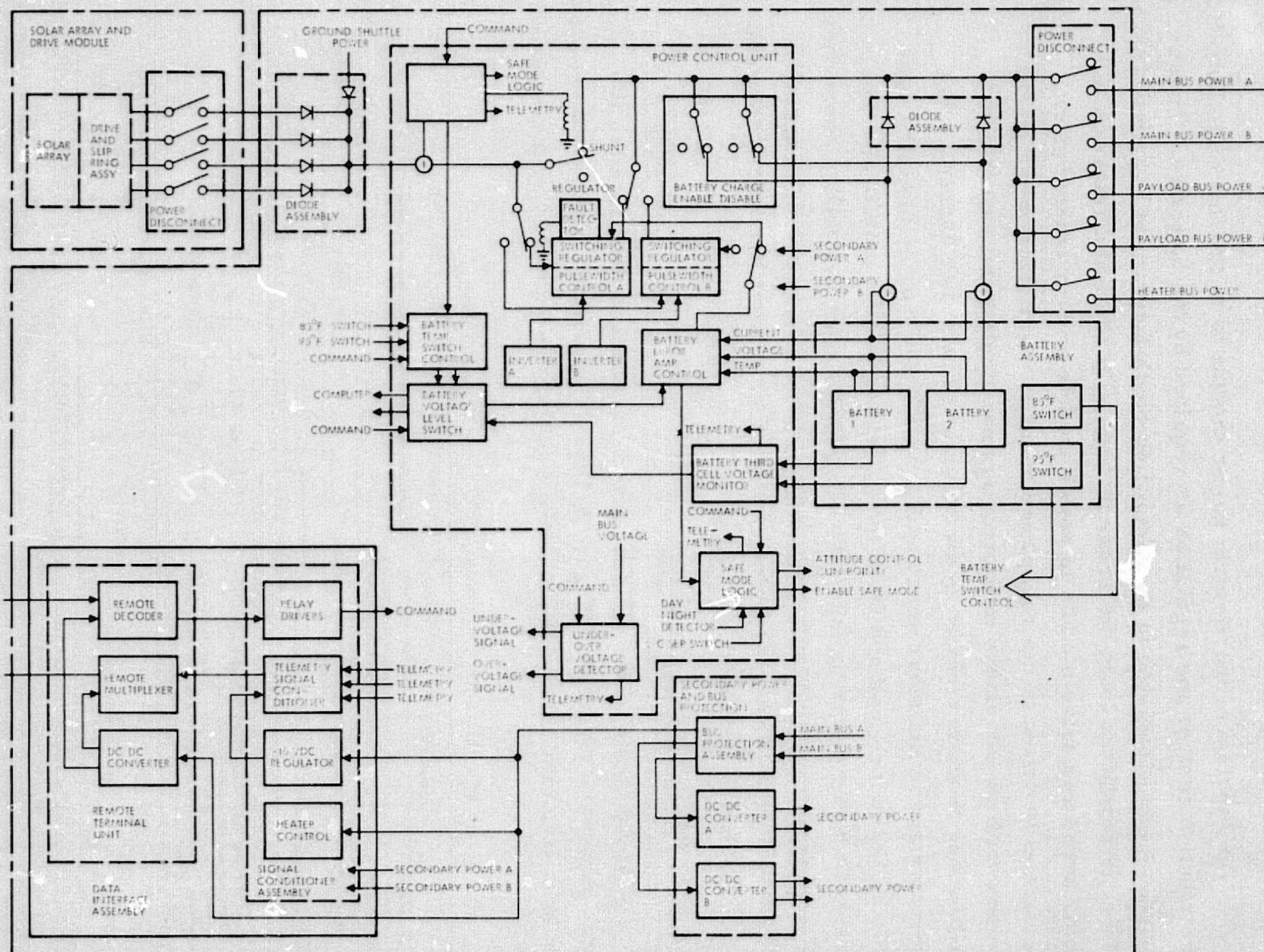


Figure 5-184. Electrical Power Module Block Diagram

battery voltage level switch (BVLS). The normal sequence of operation consists of three battery charge/discharge regimes: 1) battery discharge to load during eclipse, 2) a shunt charge mode in which the solar array provides raw power for battery charging and spacecraft loads, and 3) regulated control of the main bus voltage as required by the BVLS (Figure 5-185) characteristic to enable battery taper charge. During each phase of operation the battery characteristics determine the main bus voltage. The nominal main bus regulation is  $28 \pm 7$  volts; however, the excursions of the bus will not go below 26 volts on discharge (15 percent DOD) with the battery charge/discharge enable switches closed, or above 33.5 volts (see Figure 5-185) during normal operation.

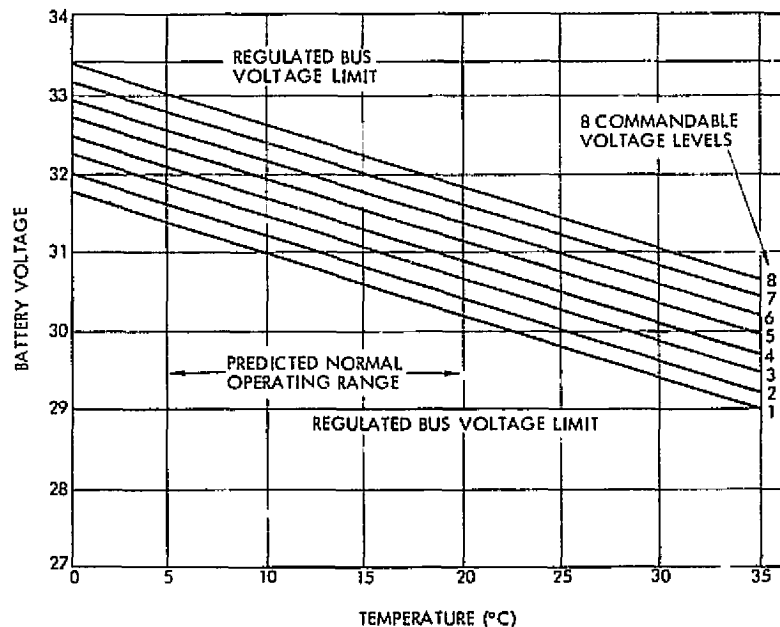


Figure 5-185. Battery Voltage Limit Curves

The battery charge/discharge enable switches allow the batteries to be removed from the bus by ground command or due to fault sensing. A shorted cell in one battery would produce overheating on charge and possible rupture of the battery cells. Under these conditions it is necessary to operate on one battery or charge the batteries separately. The diodes insure that the main bus is never without available stored energy regardless of the state of the charge/discharge enable switches.

#### 5.4.5.2 Battery Charge Control

The battery charge control senses battery temperature and battery voltage. These signals are combined to implement the error control signal for the regulator.

$$C = E_n - AT + BV$$

$$C = \text{Error voltage}$$

$$E_n = \text{Selected BVLS reference } (n = 1, 2, \dots 8)$$

$$T = \text{Battery temperature}$$

$$V = \text{Battery voltage}$$

$$A, B = \text{BVLS function constants.}$$

Eight BVLS levels are available for selection to allow for variation in battery characteristics and aging effects. These levels are selected by ground command based on observed battery performance. The accuracy with which this control should be maintained is approximately

$$E (\text{BVLS}) \pm 0.25\% \quad \text{Short-term}$$

$$E (\text{BVLS}) \pm 0.5\% \quad \text{Long-term (6 months)}$$

These tolerances are based on the discussion of Section 5.4.3.

A more detailed description of switching and control functions is contained in the following paragraphs.

#### 5.4.5.3 Detailed Description

##### 5.4.5.3.1 Battery Voltage Level Switch

A functional block diagram of the battery voltage level switch is provided in Figure 5-186. Three individually controlled latching relays are used to insert or bypass the three resistors in series with a reference voltage supplied to the battery error amplifier control circuits. By individual control of each relay, eight separate control currents can be selected to control battery charge voltage. Provisions are included to control each relay by ground command, onboard computer, as required by the battery thermal switch control functions, or as determined by the battery third electrode cell voltage detector circuit.

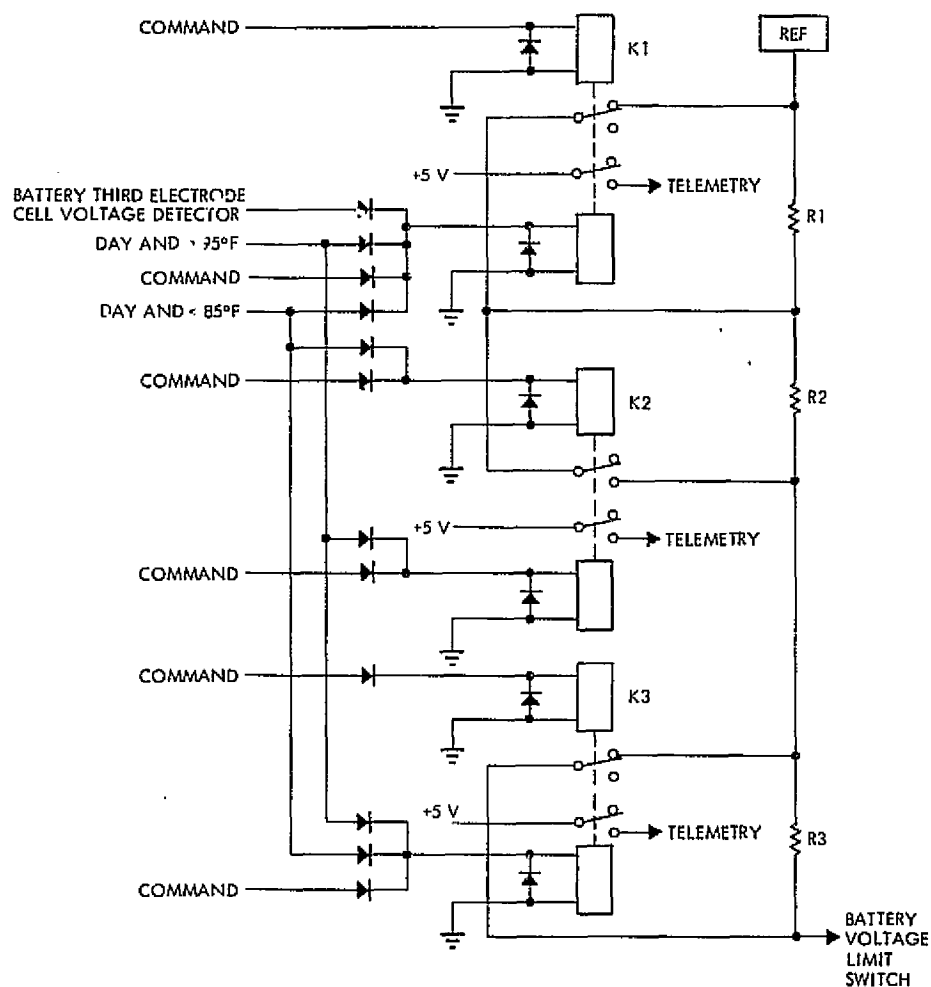


Figure 5-186. Battery Voltage Limit Switch

#### 5.4.5.3.2 Battery Thermal Switch Control and Day/Night Detection

A functional block diagram of the battery thermal switch control functions and the day/night detection circuits is provided in Figure 5-187. During the daylight portion of the orbit, the solar array provides power to the spacecraft and array current is sensed enabling the relay driver to energize relay K1. A reference voltage is supplied through the energized contacts of relay K1 to relay K2. When relay K2 is not energized, this reference voltage places the battery voltage level switch to the nominal battery voltage setting. When relay K2 is energized, the reference voltage places the battery voltage level switch to the minimum battery voltage setting. During the eclipse portion of the orbit, relay K1 is not energized. The reference signal supplied through the de-energized contacts of relay K1 is distributed to control the regulator shunt relay in the

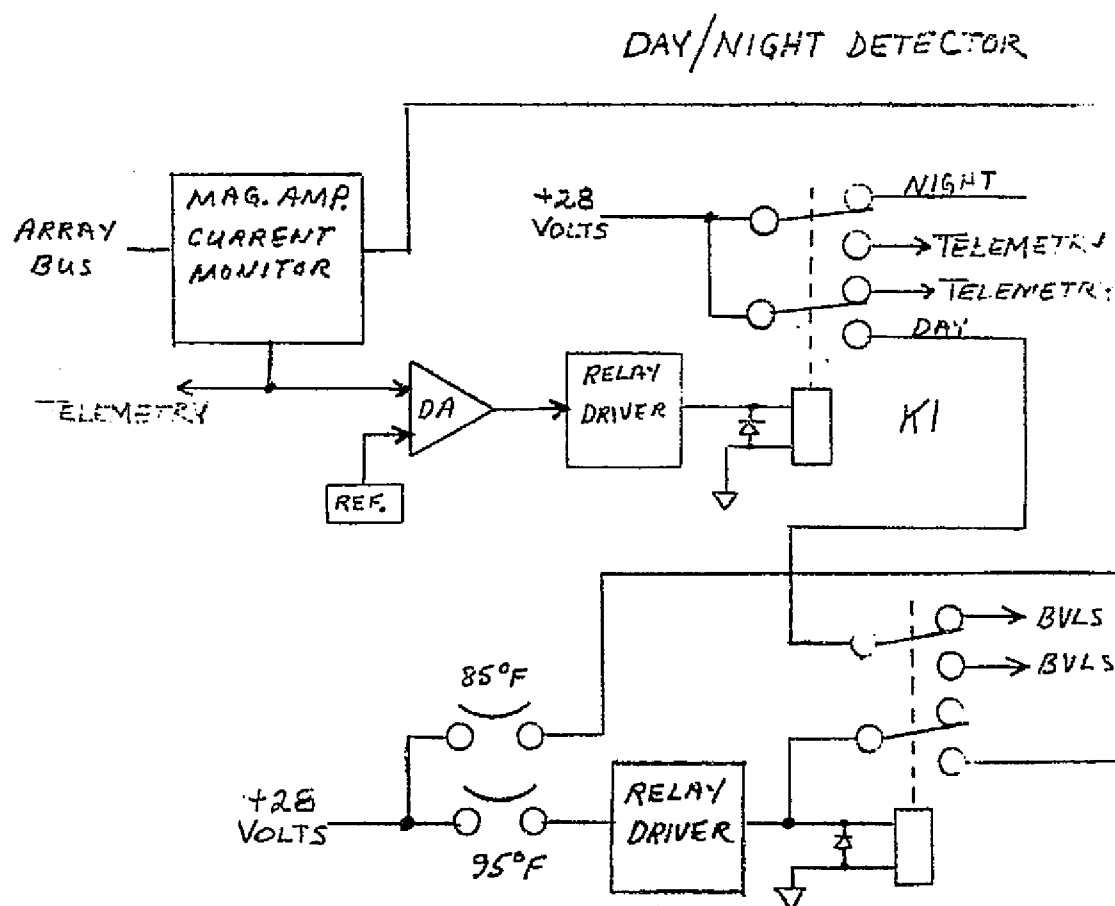


Figure 5-187. Battery Thermal Switches

PCU to the shorting position. This signal is also distributed to the attitude control safe mode logic circuit in the PCU to start the eclipse counter and to set the state of the battery voltage limit flip/flop.

Relay K2 is controlled by the 85 and 95°F battery thermal switches. When the battery assembly temperature increases above 85°F, this 28 volts is applied to the energized contacts of relay K2. As battery assembly temperature increases above 95°F, relay K2 is energized by the relay driver and latched up through the 85°F thermal switch. K2 will now remain energized until the battery assembly temperature becomes less than 85°F.

#### 5.4.5.3.3 Power Regulator Unit Select and Fault Isolation

A functional block diagram of the power regulator unit selection and fault isolation circuits is provided in Figure 5-188. Relay K1 provides a bypass function on switching buck regulators by shunting the solar array

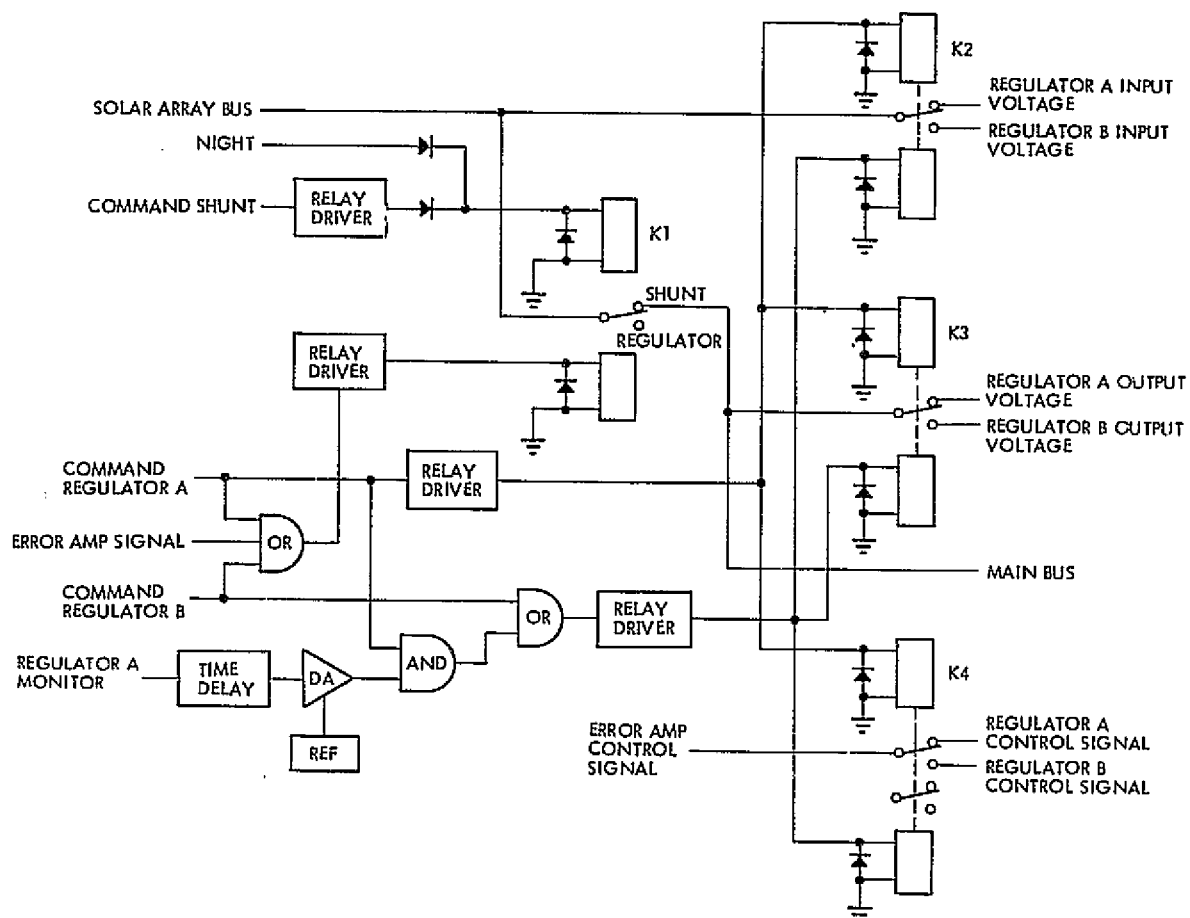


Figure 5-188. Power Regulator Unit Select and Fault Isolation

current directly to the main bus loads and the batteries. Relays K2, K3, and K4 provide selection of the redundant regulator units. Ground command control is provided for these four relays in addition to the night detection control of relay K1 to the shunt position, and the battery error amplifier control of relay K1 to the regulator position.

#### 5.4.5.3.4 Battery Charge Enable/Disable

The battery charge enable/disable functions are shown in Figure 5-189. Relays K1 and K2 are individually controlled by ground command to enable or disable battery charging. For normal battery operation, relays K1 and K2 will remain in the battery charge enable position. In this position, the batteries are connected directly to the main power bus discharging directly to the main bus during eclipse conditions and recharging in parallel during the sunlit portion of the orbit. If a battery exhibits abnormal operation, the corresponding relay can be commanded to the charge disable position removing the battery charging current. In this position, the battery is connected to the main bus through a series diode to provide the capacity remaining in this battery to the electrical loads if required. By monitoring battery telemetry, ground commands can be initiated to control individual battery charging functions depending on the cause of the abnormal battery operation.

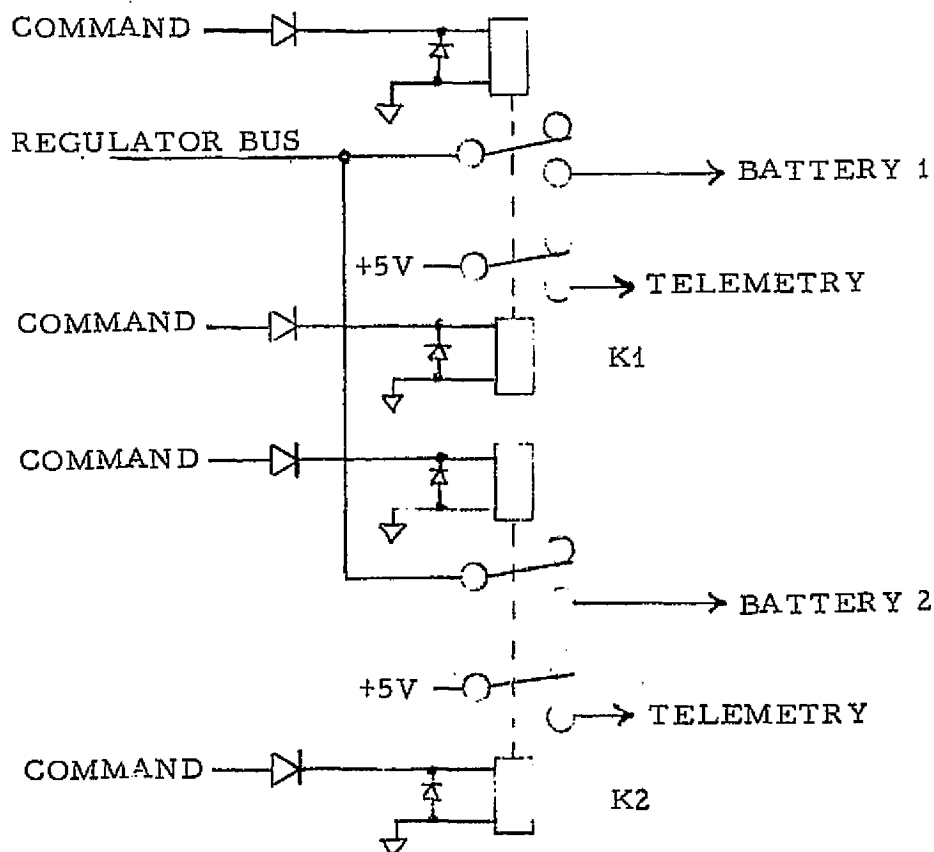


Figure 5-189. Battery Charge Enable/Disable

#### 5.4.5.3.5 Under/Overvoltage Detection

The under/over voltage detection circuit is shown in Figure 5-190. The main bus voltage is applied to two operational amplifier circuits U1 and U2. U1 provides a buffered signal to place the spacecraft in the safe mode when the main bus voltage decreases to less than 23.0 VDC. U2 provides a buffered signal to the attitude control module that results in placing the observatory in a sun bathing orientation. Non-critical loads are disconnected to maximize the vehicle survivability. Relay K1 provides ground command override control of the over/under voltage functions.

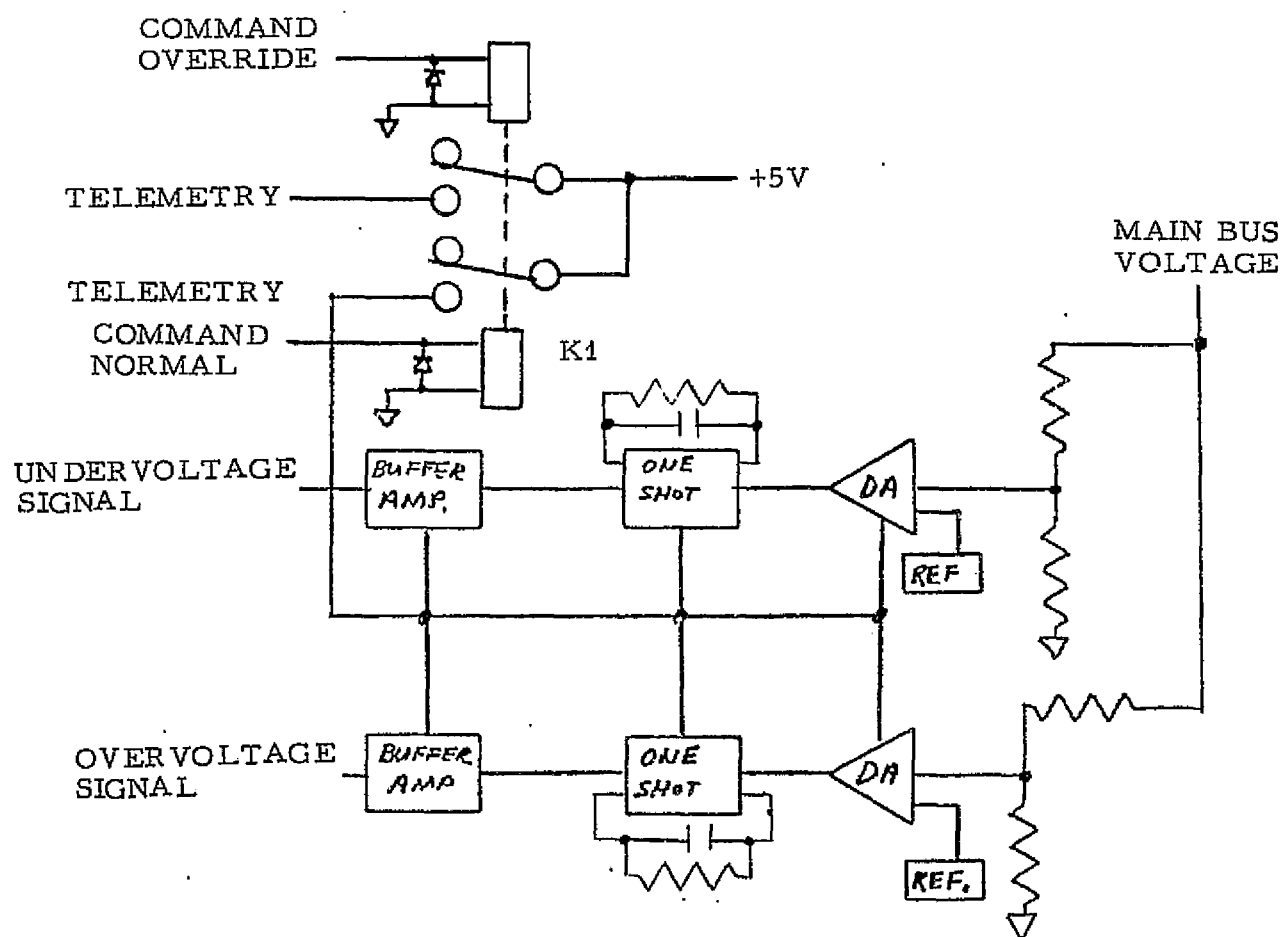


Figure 5-190. Under/Over Voltage Detection Circuit



#### 5.4.5.3.6 Attitude Control Safe Mode Logic

The attitude control safe mode logic block diagram is shown in Figure 5-191. These circuits are required to enable the attitude determination module safe mode functions. This logic is provided to sense anomalous sun pointing by monitoring power module functions. This logic is activated if either of two conditions occur:

- 1) Loss of solar array current for a period exceeding the maximum eclipse time.
- 2) Two consecutive sun light periods without the batteries reaching the voltage limit (BVLS).

The attitude control safe mode logic receives a signal from the day/night detector and starts a 45-minute timer. If the condition persists for 45 minutes and the logic circuit is enabled, the attitude control module safe mode functions will be enabled. If the day/night detector senses solar array current, the 45-minute timer will be reset.

When the spacecraft enters eclipse, a signal from the day/night detector will set the state of the battery voltage limit sense circuit and also start the two stage eclipse counter circuit. If the batteries fail to attain sufficient charge as indicated by failure to reach the battery voltage limit for two eclipse periods, the attitude control module safe mode functions will be enabled. If the batteries reach full charge, the battery voltage limit circuit will reset the logic and the eclipse counter. The eclipse counter can also be reset by ground command.

#### 5.4.5.3.7 Maximum Power Tracking

The evaluation of the effectiveness of the Maximum Power Tracking (MPT) function has not demonstrated that a significant power gain can be achieved (see Section 5.4.3). However, the presence of the computer makes it possible to implement this function with minimum circuitry in the power module. The approach would consist of measuring the dynamic impedance of the solar array and driving the pulse width control until the measured value corresponded with a preselected value. If there were continuous variations in load current, it would suffice to measure the array voltage and current to determine impedance. However, with the range of missions considered, it is not desirable to configure the system with

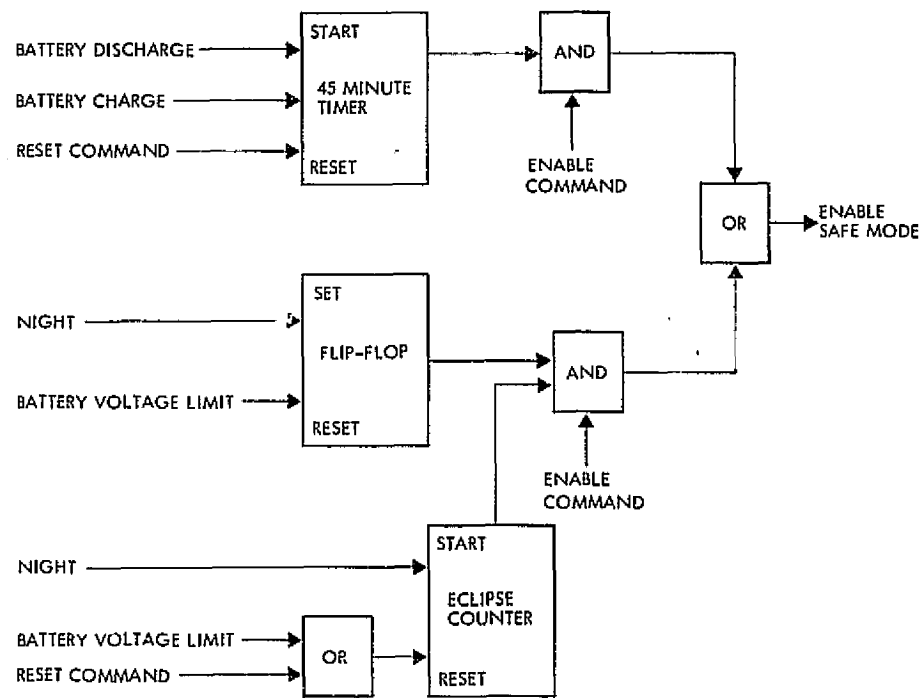
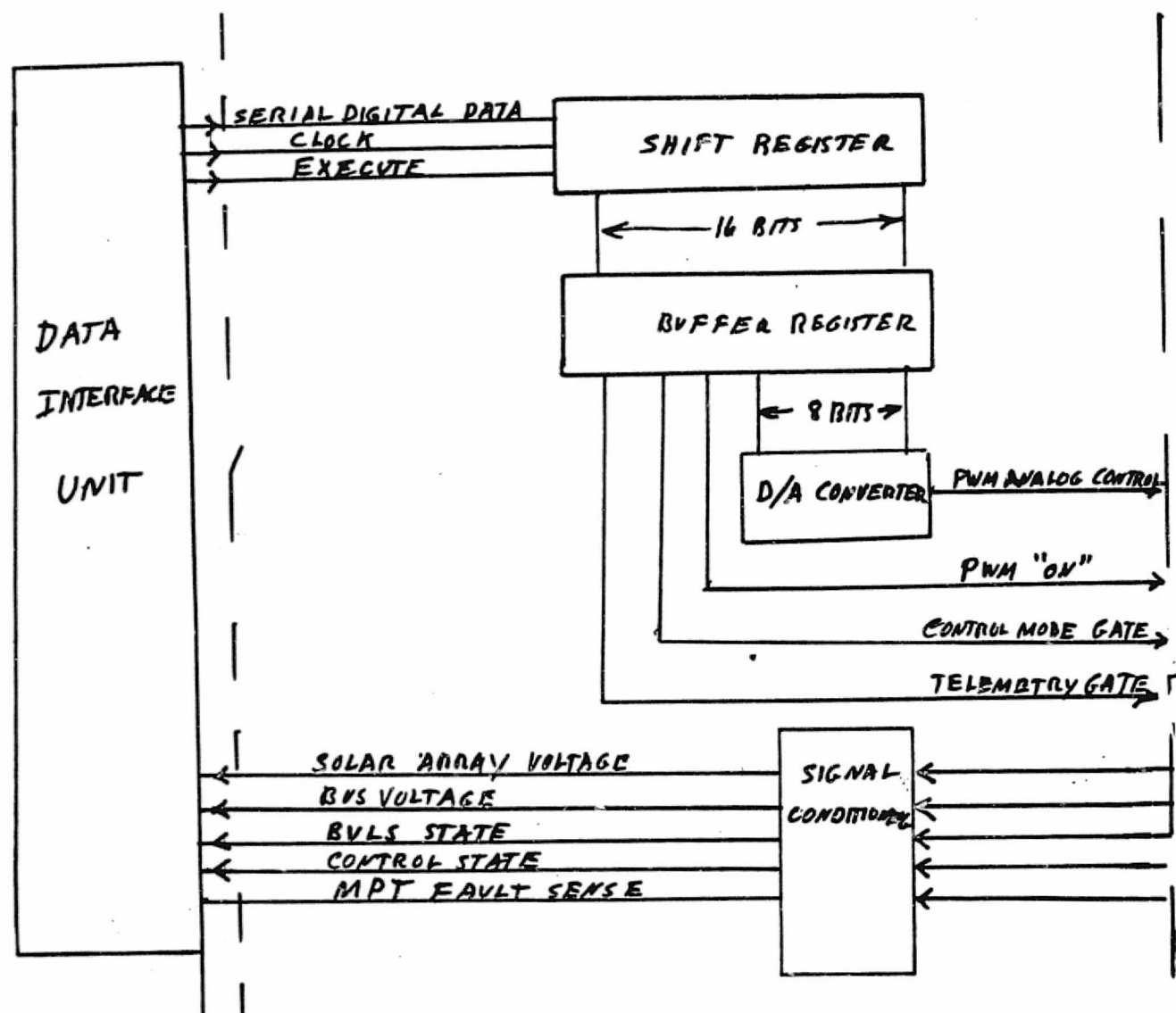


Figure 5-191. Attitude Control Safe Mode Logic

respect to the load characteristic. Consequently, it is necessary to generate a current test signal with predictable characteristics which will be applied to the solar array. Comparison of the solar array voltage variations and the current test signal provide sufficient information to develop an MPT control signal. The implementation of this signal is not defined at this time. The presence of the signal in the solar array bus may require an exception to be made to the EMI specification. As a result the definition of the detailed design is deferred until further evaluation of the total approach is performed.

The implementation of MPT requires the normal Pulse Width Modulator regulator (PWM) control to be supplanted by the computer. The functions required are illustrated in Figure 5-192. The remote decoder provides a 16-bit serial digital signal for conversion to analog signals; an 8-bit signal is considered adequate for PWM analog control. In addition, signals are required to (a) activate the PWM at a time when it would normally be off, (b) enable the MPT control mode, and (c) enable telemetry circuits associated with the MPT. The computer requires



PCU

Figure 5-192. Maximum Power Tracker Control Interface

solar array voltage and main bus voltage to measure pulse width. The BVLS state would signal termination of MPT and return to normal regulator control to maintain the battery voltage/temperature requirements. Failure of the MPT control would be sensed by detection of battery discharge or battery overheating. In addition to establishing the MPT control mode, it is desirable to modify the PWM control. The present feedback concept utilizes multiple control loops. The dominant control is derived from the BVLS circuitry which outputs an analog signal. The PWM control modifies the duty cycle of the solid state switch to provide an output current proportional to the input error signal. This approach is advantageous when paralleling regulators but is not desirable when the desired operating point is the solar array maximum power point since it represents a null in the secondary feedback characteristic. The solar array voltage at the input to the PWM is a preferred source of error signal during maximum power tracking since this is a monotonic function of pulse width when providing power to a bus stabilized by a battery.

#### 5.4.5.3.8 Battery Third Electrode Voltage Detector

The battery third electrode voltage detector functional diagram is presented in Figure 5-193. The third electrode cell voltage of each battery is monitored continuously. This voltage is amplified and compared with a reference voltage by the operational amplifier circuit U1 or U2. If the third electrode cell voltage of either battery increases beyond the preset reference, an output signal enables the relay driver circuit and places the battery voltage level switch to the lowest position.

#### 5.4.5.3.9 Secondary Power and Bus Protection Assembly

The secondary power and bus protection assembly provides the fault isolation components necessary to protect the spacecraft main power buses from load faults occurring within the electrical power module. The DC/DC converters necessary to generate the secondary power required by the power module equipment is included on this assembly.

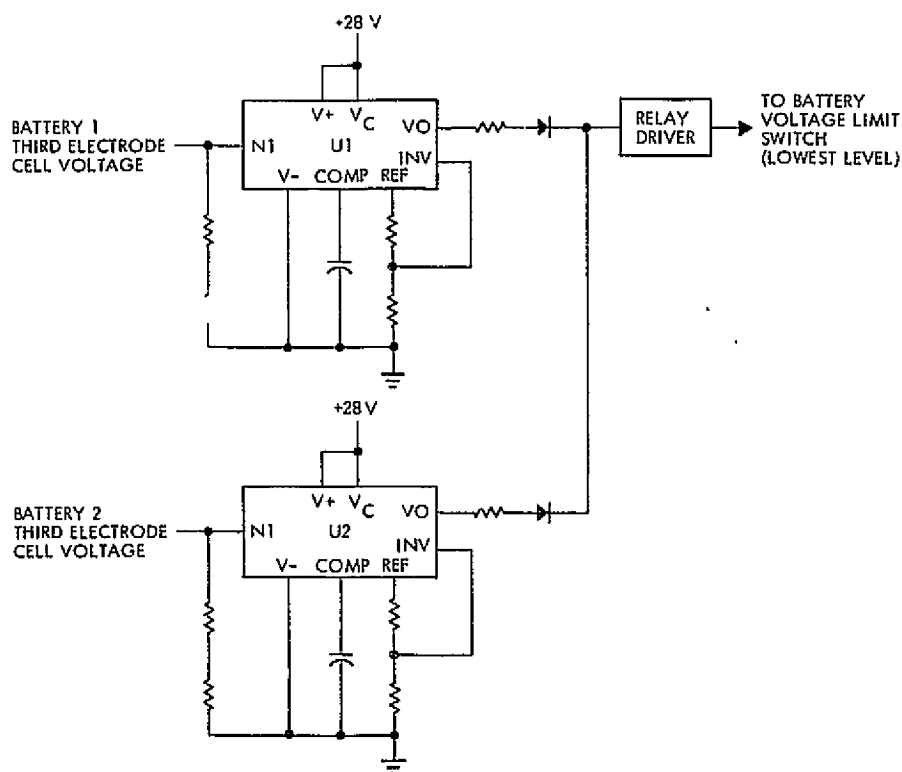


Figure 5-193. Battery Third Electrode Cell Voltage Detector

A functional block diagram of the bus protection assembly is provided in Figure 5-194. Power is supplied from main power bus A and main power bus B. These buses are connected together through series isolation diodes in the bus protection assembly. Power is distributed to each load through a fuse paralleled by a fuse and series diode fault isolation configuration. As long as both fuses are functional, the fuse with the diode in series will not conduct. Should the primary fuse fail, the fuse/diode path will carry the load current. The heater power bus is also supplied to the bus protection assembly and distributed to each heater load with the fuse protection configuration described above.

#### 5.4.5.3.10 Power Converters

Redundant DC/DC power converters are provided to supply the secondary power required by the Electrical Power Module. The block diagram of the converter is provided in Figure 5-195 and depicts the basic circuitry functions.

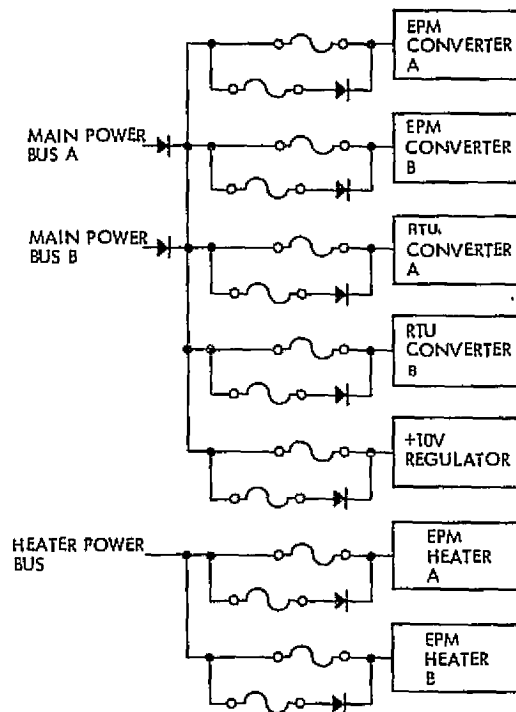


Figure 5-194. Electrical Power Module Bus Protection Assembly

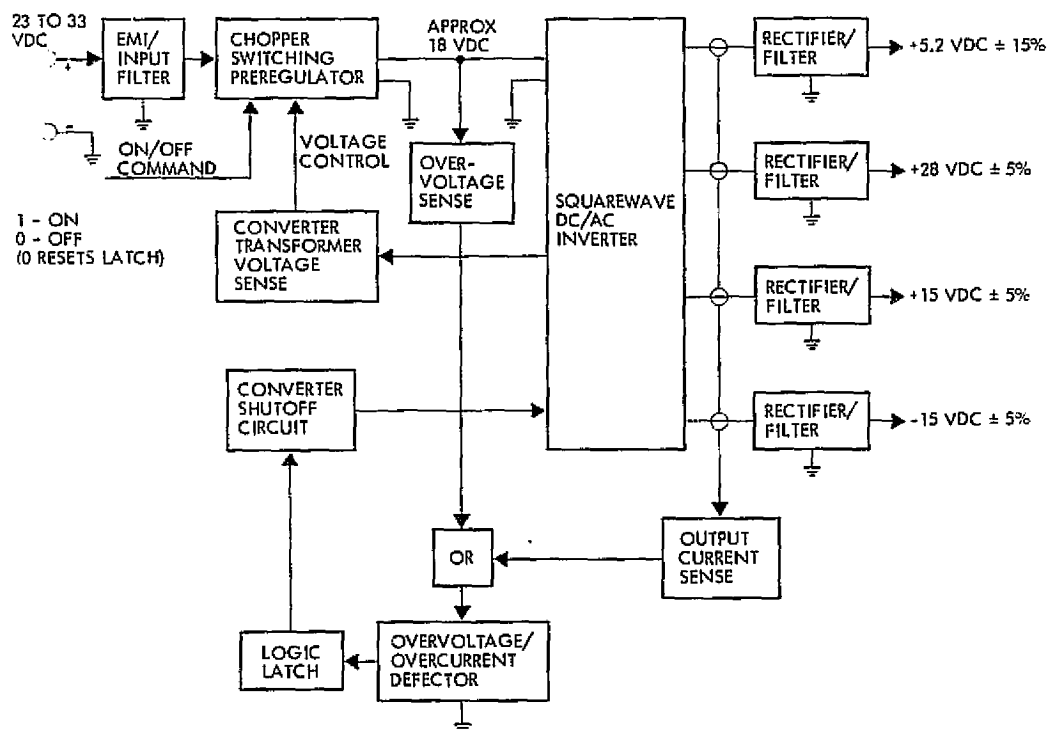


Figure 5-195. Secondary Power Converter

Relatively wide output load variations necessitate using the pre-regulator/squarewave inverter approach to meet the output voltage regulation requirements and to ensure minimum noise coupling between outputs during load transients. The preregulator output, approximately 18 VDC, serves as the power source for the multiple output squarewave inverter. Rectifier-filters on each inverter transformer output provide DC outputs with a common ungrounded return. Output voltage regulation is accomplished by sensing the magnetic flux in the inverter transformer and using the resultant voltage to control the preregulator output. The switching regulator uses a two-loop feedback (AC and DC) control circuit technique to obtain optimum dynamic output regulation.

Converter output overcurrent and overvoltage protection are provided by sensing each output load with a current transformer and "or" gating these outputs with an overvoltage sense signal into a detector which terminates power transistor switching when activated. A logic latch is used to prevent converter on/off oscillation during a sustained overload or overvoltage. The converter on/off command is an "1" or "0" state command with its return common to the input power return. During the "1" state command the converter is on unless the overload/overvoltage latch has been tripped. If so, the command state must be returned to 0 and then to 1 again to re-energize the converter. The squarewave inverter, rather than the preregulator, must be shut off during a potential overvoltage condition since shorting of the preregulator pass element could cause an unprotected output overvoltage.

#### 5.4.5.3.11 Diode Assembly

A diode assembly is provided in the module for powering the spacecraft main power bus during ground testing and also from the Shuttle during refurbishment or release of a new spacecraft. The solar array bus is connected to the main bus through diodes to provide protection against short circuits in the unregulated power bus. In addition, diodes connect the batteries to the main bus to ensure that battery discharge power is always available to the loads.

#### 5.4.5.3.12 Power Disconnect Assembly

The power disconnect assembly contains circuitry necessary to remove all input and output power from the module, and to automatically open individual lines in the event of a fault. Circuitry consists of relays that are controlled by external commands and that also automatically open the contacts in the event excess current is flowing in the circuit. Each relay is a hermetically sealed magnetic latching relay with two sets of contacts. The main set of contacts (single pole, double throw, double break) rated at 50 amps and auxiliary contacts (single pole, double throw) rated at 5 amps.

#### 5.4.5.3.13 Batter Assembly

Two batteries are contained in the EOS-A power module. Their physical and performance characteristics are summarized in Table 5-81.

An EOS-A battery is constructed in the following way: The battery cells are clamped in two rows of 11 between aluminum end-plates. The compression preload compensates for normal pressures within the cells. L-shaped thermal shims placed between the cells conduct heat to the battery baseplate. Each cell is electrically insulated from thermal and structural members. A packaging ratio of 1.3 (packaged/unpackaged cells) provides a sufficient weight allowance to enable thermal gradients within the battery to be summarized.

Each battery is equipped with one cell that contains a third electrode for the generation of a signal proportional to cell pressure. Each battery pack also contains three thermal control circuits which provide a temperature signal for BVL charge control and signals for the high temperature BVL switches (85 and 95°F). The signal conditioning required for the



temperature and pressure signals is performed within each battery assembly on printed circuit boards. Each battery contains two electrical connections; one is used for the monitoring of individual cell voltages during ground test sequences while the other contains all flight harness functions.

Table 5-81. EOS-A Battery Characteristics

Total battery system capacity, Ah	80
Battery cell capacity, Ah	40
Batteries per spacecraft, no.	2
Cells per battery, no.	22
Maximum depth-of-discharge, percent	15.2
Total delivered energy, Wh	333.3
Weight per battery, eb	104.5
Total battery weight, eb	209.0

The average temperature of each battery mounting surface will be maintained within the range of 1.7°C (35°F) to 18.3°C (65°F). The average temperature of each battery mounting surface will be within  $\pm 1.4^\circ\text{C}$  ( $\pm 2.5^\circ\text{F}$ ) of the average of all of the battery mounting surfaces.

#### 5.4.5.3.14 Data Interface Units

The data interface unit is described in detail in Section 6.1, Communication and Data Handling Module.

#### 5.4.5.4 Future Mission Adequacy

##### 5.4.5.4.1 Battery Capability

The design of the power module is constrained by the capabilities of the batteries. Parallel battery charge/discharge performance is possible only if the temperature range indicated in Figure 5-185 is maintained and thermal gradients between cells and batteries are held to small values. There is considerable interdependency between battery power dissipation, battery temperature and recharge capability. All of these factors are reflected in allowable depth of discharge and life. Table 5-82 indicates peak and average dissipation for the EOS-A design. Figure 5-196 demonstrates the effect of temperature and depth of discharge on battery life assuming thermal gradients are maintained within acceptable bounds. Future

missions which require higher power will also require more available stored energy. This increased requirement will be served by increasing the ampere-hour capability of the power system. Thermal analysis indicates that power dissipation may be increased by a factor of four without violating the constraints on allowable temperature range. Size and weight may be traded against time in orbit by increasing the depth of discharge. Operation at higher altitudes with decreased frequency of discharge permit greater DOD without penalties on battery and power system life. The largest power requirements in foreseeable missions are approximately 3 kw (solar array) or a factor of three over present capability. From this basis it may be assumed that the EOS-A design will provide sufficient capability for future missions.

#### 5.4.5.4.2 Power Regulation Capability

Power regulation capabilities and concepts for high power regulation have been reviewed and are adequate to perform all required functions on future missions. The configurations and approaches for these missions are discussed in Section 5.4.3.

Table 5-82. Battery Power Dissipation

Summary, 60°F	DOD	
	15%	30%
<u>Orbit Average Dissipation</u>	18.9 w	40.0 w
<u>Approximate Period</u>		
0.58 h avg. discharge	36. w	72. w
0.66 h avg. charge	- 5.2 w	- 5.2 w
0.41 h avg. overcharge	33.7 w	67.3 w
<u>Peak Dissipation</u>		
Discharge	35.8 w	71.6 w
Charge	-10.3 w	-10.3 w
Overcharge	67.9 w	135.7 w

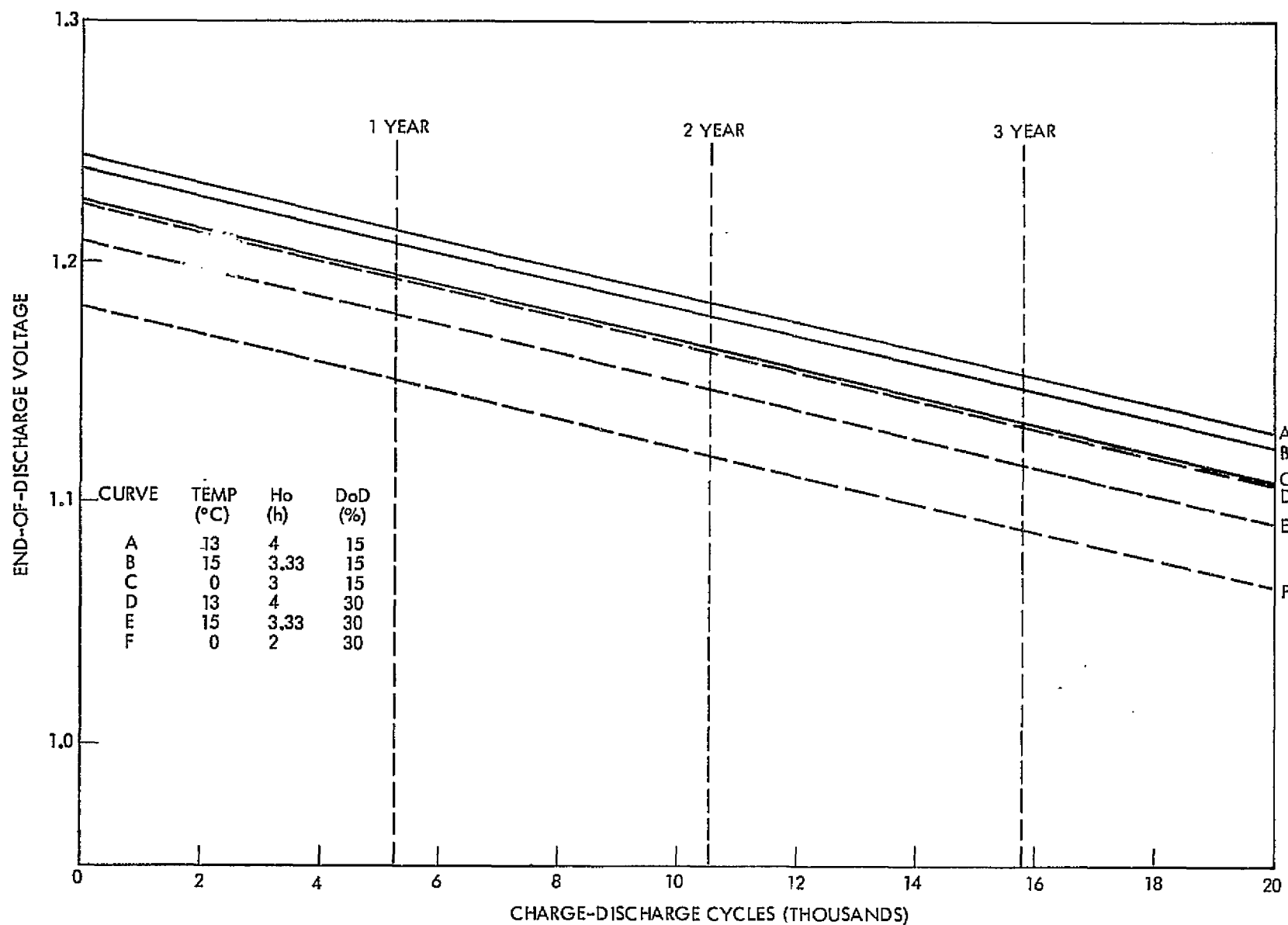


Figure 5-196. Effect of Temperature and Depth of Discharge on Battery Life

#### 5.4.6 Solar Array Design

##### 5.4.6.1 Solar Array Electrical Design

A solar cell array is subject to the following degradations during its service life in the space environment:

- Changes to the light transmission properties of coverglass and coverglass adhesive materials
- Radiation damage to exposed semiconductor surfaces produced by low-energy proton fluences
- Reduction in electrical output due to stresses induced in the interconnection system by repetitive thermal cycling
- Radiation damage due to solar flare protons
- Radiation damage due to trapped orbital electrons and protons.

The first two degradations are insensitive to orbital altitude. They are a function of material characteristics and design configuration. As such, they are predictable and are always reflected in the array design and sizing procedures. The last three degradations are orbit-dependent.

We first consider the thermal cycling environment. As orbit altitude increases the annual number of thermal cycles experienced by the array is reduced from roughly 5000 to 90. Concurrent with the altitude increase there is a decrease in the eclipse-exit temperature of the array from the range of  $-60$  to  $-80^{\circ}\text{C}$  to the range of  $-160$  to  $190^{\circ}\text{C}$ . Improper selection of solar cell interconnect material, configuration or joining process will result in interconnect failures for any particular combination of number of cycles and minimum array temperature. The degradation or failure mechanism is a form of low-cycle low-temperature fatigue failure. However, proper design of the interconnection system for the particular mission profile will ensure that the degradation is held to (typically) 2 percent of power at the end of the mission period.

The baseline EOS design is not dependent upon a particular solar cell interconnection system provided that it has been qualified for a 2-year mission in a 717 km (387 n mi) circular orbit. Interconnect materials such as copper, silver, Kovar, molybdenum, and Invar are reasonable candidates provided that they possess the proper metallurgical

properties and have been prepared for soldering. (Welding is under development as a technique for solar cell interconnection. However, until more test and flight experience is obtained, and solar array fabricators have developed production capability with this technique, it is reasonable to retain solder joining as a baseline for cost evaluations and comparisons.) At higher altitudes (colder temperatures), or particularly with longer missions, the candidate materials are reduced to Kovar, molybdenum, and Invar with the latter material being the most promising from both technical and cost viewpoints.

No significant cost tradeoff exists between interconnect systems with the possible exception of one that utilizes plated molybdenum. It is to be emphasized, however, that qualification of an array design for a low-altitude mission does not confer immediate qualification of the same design for the geostationary orbit. Hence, there are dollar savings to be obtained if an all-mission array is developed and qualified.

Solar flares, when they occur, produce significant fluences at geostationary altitude and account for a large portion of the radiation damage at that altitude. Figure 5-197 shows the variation of predicted total equivalent 1-Mev fluence resulting from solar flares as a function of calendar year. At lower altitudes, the effect of solar flares is considerably reduced by the shielding provided by the magnetosphere. At altitudes below 1853 km (1000 nautical miles) solar flare activity can be ignored for the purpose of preliminary design.

Solar cells are always protected from excessive radiation damage by glass filters made of either fused silica or Corning microsheet. The thickness selected depends upon the fluence that the array is exposed to in orbit which is, in turn, a function of orbit altitude and inclination. Figure 5-198 describes this relationship for selected altitudes and coverglass thickness. Table 5-83 contains a summary of the results of the radiation analyses performed for the EOS mission series.

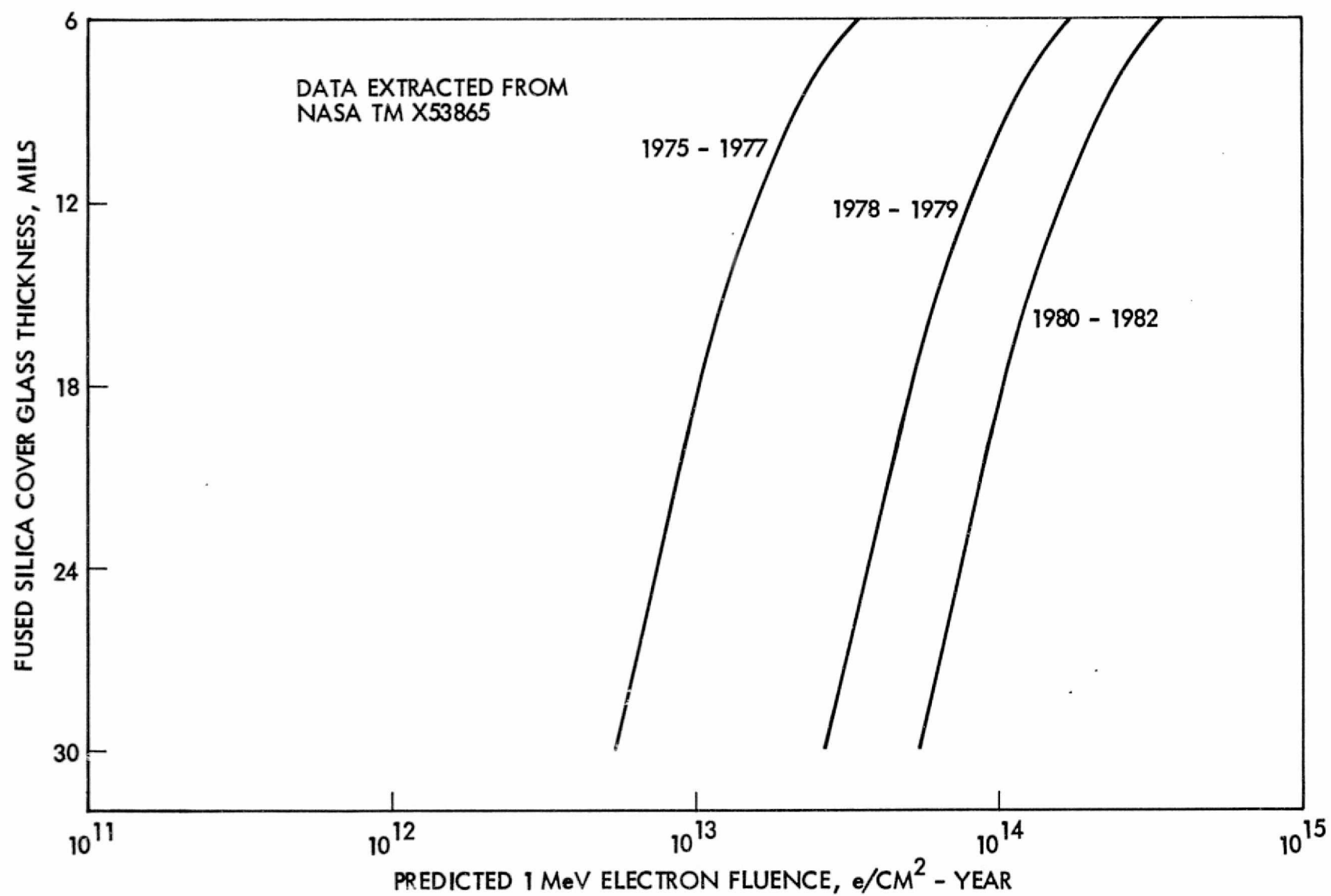


Figure 5-197. Predicted Equivalent 1 MeV Electron Fluence for Solar Flare Protons

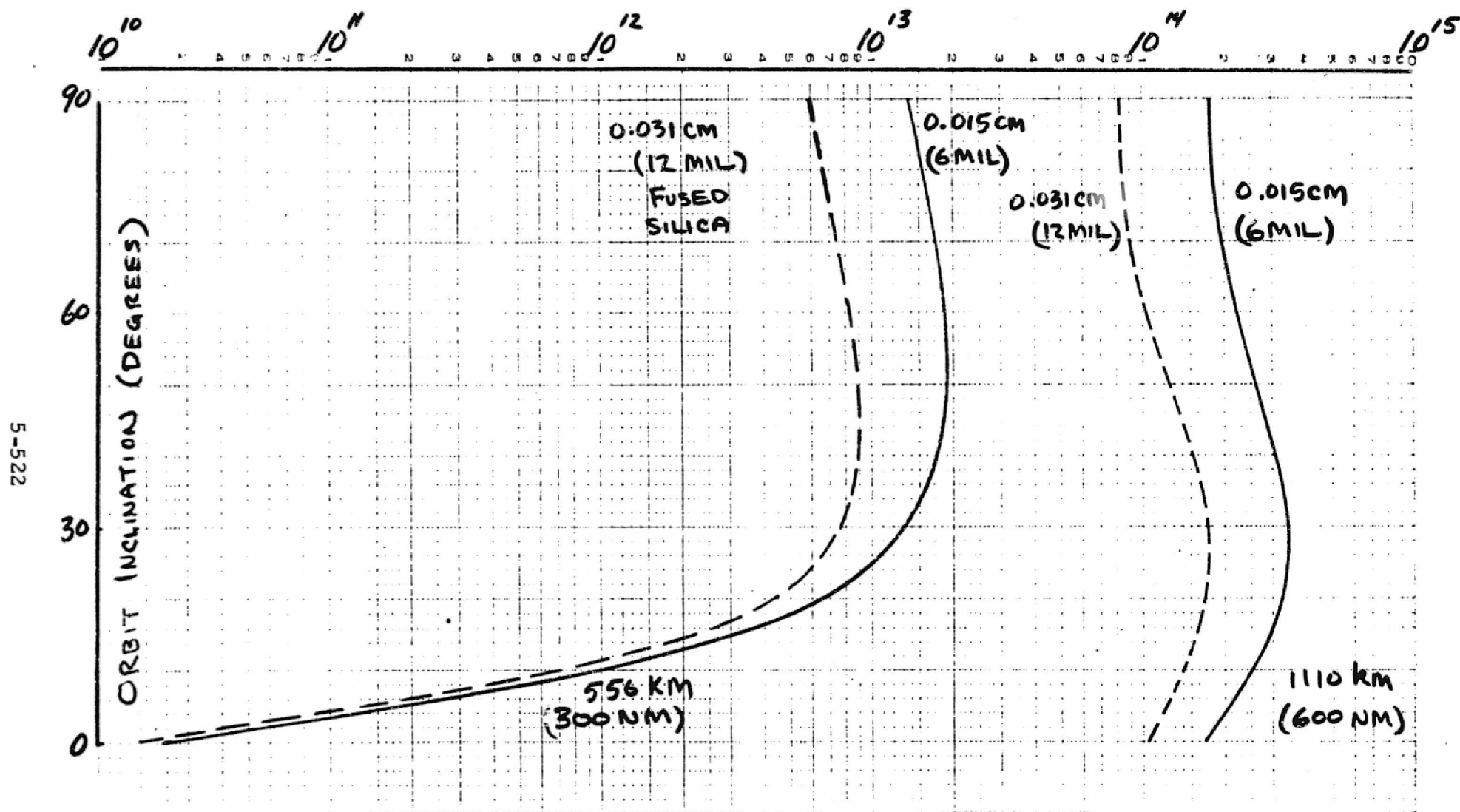


Figure 5-198. Annual Equivalent 1-MeV Electron Fluence for  $P_{max}$  Due to Trapped Electrons and Protons ( $e/cm^2$ )

Table 5-83. Radiation Analysis Summary

Altitude (n mi) (km)		Coverglass Thickness ( $\times 10^{-3}$ inch) (cm)		Annual 1-Mev Equivalent Trapped Particle Fluence ( $e/cm^2$ )	
				i = 60 deg	i = 90 deg
300	556	6	0.015	1.85E13	1.38E13
600	1110	6	0.015	2.40E14	1.75E14
800	1480	6	0.015	1.79E15	1.48E15
300	556	12	0.031	8.35E12	6.00E12
600	1110	12	0.031	1.02E14	8.35E13
800	1480	12	0.031	8.01E14	6.67E14
1000	1853	12	0.031	2.49E15	1.88E15
1500	2780	20	0.050	4.10E15	3.38E15

The baseline EOS-A solar array uses 0.015 cm (0.006 inch) thick covers attached to a 0.036 cm (0.014 inch) thick N on P silicon solar cell. The coverglass thickness is consistent with the radiation environment of the low-altitude orbit. The result is a low-weight design that is compatible with the Thor-Delta mission although not as cost-effective as an array that uses covers of greater thickness. The relationship between unit cost and thickness of covers and solar cells is shown in Figure 5-199.

The absolute power output that can be obtained from a solar cell is a function of its base resistivity and thickness. An increase in the resistivity decreases the power output but increases the radiation resistance of the solar cell. A reduction of the thickness of the solar cell reduces the power output but also results in less radiation degradation. A low base resistivity cell (1 to 3 ohm-cm) has been selected for EOS-A. However, missions in higher orbits would benefit from the radiation resistance provided by the high base resistivity cell.

In summary, a solar array has been designed which will meet the requirements of the EOS-A mission assuming either a Thor-Delta or Titan launch vehicle. The design is not optimized for the entire range of



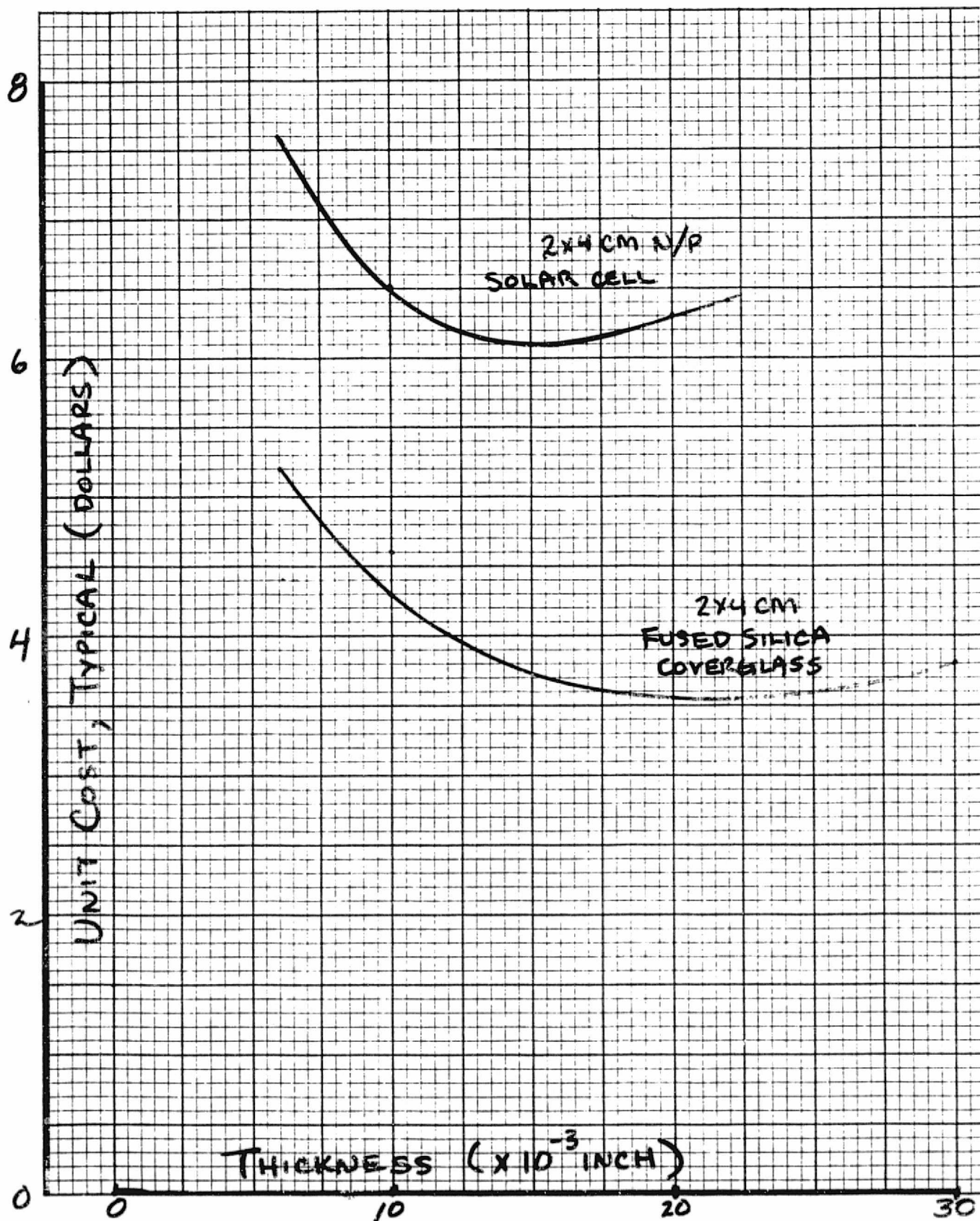


Figure 5-199. Cell and Cover Costs

anticipated EOS missions. An all-mission cost-effective design is feasible and would require:

- 0.05 cm (0.020 inch) thick covers
- 7 to 13 ohm-cm base resistivity solar cells
- Qualified interconnection system.

#### 5.4.6.2 Solar Array Drive and Electronics

##### 5.4.6.2.1 Requirements

In addition to the usual requirements imposed by usage in a spacecraft environment, (e.g. low weight, high reliability, withstand launch loads, low cost, etc.), the solar array drive must meet many requirements peculiar to a specific spacecraft application. The particular need of EOS is for a drive design that will be compatible with the high order of pointing accuracy required for the spacecraft scientific payload in addition to the usual requirements. Since the solar array drive links the inertia of the rotating solar array to the inertia of the spacecraft, dynamic analyses of this coupling imposes transverse and torsional stiffness requirements on the solar array drive. Also the power and array drive module being mission-dependent impose the need to vary the output shaft rate for the various orbits. The actual design approach for the solar array drive is affected by all the above needs. There is at present, two basic approaches available for design. One approach is to use a continuous drive and the other is to use a step drive. There are numerous variations possible in these two methods and many of the variations have been made to meet the requirements of different spacecrafts. It is evident that many requirements will conflict and tradeoffs must be made and evaluated. The solar array being canted at an angle with the axis of rotation of the drive mechanism creates a relationship between the variation in rate of array drive and the payload pointing accuracy that must be investigated. The mass center of the solar array generates a circle of about 15 inch diameter during one complete revolution of the drive. A rate variation in the solar array drive shaft introduces an error in pointing, principally about the roll axis and to a lesser amount about the pitch and yaw axes. Therefore, the geometry relating the solar array to the

spacecraft establishes a requirement that the drive rate be either continuous or that the step size be sufficiently small so that the pointing error contribution of the array drive is acceptable.

The inertia of the typical solar array imposes additional requirements on the drive mechanism because of the dynamic coupling with the spacecraft. Typically, this results in the need for a high transverse and torsional stiffness of the drive, which in turn leads to the preloading of ball bearings that support the solar array boom. For EOS the transverse stiffness must be  $1 \times 10^6$  in-lb/rad minimum and a torsional stiffness of  $1 \times 10^5$  in-lb/rad. Although the state of the art in the design of digital control systems and the development of this type of hardware has advanced markedly in recent years, the advantages of a continuous drive for this application will be examined first along with its limitations.

#### 5.4.6.2.2 Continuous Drive

The design of a continuous drive has many possible combinations; the drive may be direct or geared, the motor may be AC or DC, and the motor may be brush or brushless. While a direct continuous drive does not use any gearing, the effects of friction torque variation in the ball bearings is seen directly at the motor and requires a closed-loop servo system to minimize variations in the output shaft rate. Friction torque spikes, however, are a real possibility in preloaded ball bearings and must be taken into account in the design of the control system. The Bendix Corporation has developed a solar array drive of the direct type using a multi-pole two-phase brushless synchronous motor. The design was produced as a backup for the Nimbus solar array drive. It is understood that "stick-slip" and overshoot have been observed on that particular drive mechanism and while it may be of an acceptable level for the Nimbus program, quantitative data would have to be examined to determine its acceptability for EOS. For the Nimbus program, the motor driving frequency was extremely low (on the order of several minutes per cycle). It is also reported that inaccuracies of the waveshape introduced some stepping action that could be reduced by additional design of the wave synthesizer electronics. The drive uses 8 watts and has a sun sensor on the output shaft for position feedback in a closed-loop servo system.

It would appear that the one principle limitation of a continuous direct drive is the cogging effect of friction torque spikes in the ball bearings.

The Nimbus solar array drive (produced by TRW) that has been flown is of the geared continuous drive type. This drive uses a two phase 400-cycle servomotor with an integral gearhead driving a "wabble" type gear reducer via one spur gear pass — the overall gear ratio being 23,760 to 1. This drive also uses about 8 watts and has a sun sensor on the output shaft for position feedback in a closed-loop servo system. This particular drive does not meet the necessary transverse stiffness requirement for EOS.

#### 5.4.6.2.3 Step Drive

The usual approach in a step drive is to insert a gear reduction between the drive motor and the solar array because of the rather large step angle of the motor and the relatively large array inertia. Numerous stepper motors are available with step angles ranging from 90 degrees down to 1.8 degrees. In the FLTSATCOM project the drive motor is a 1.8 degree-stepper motor with a 100:1 gear reducer producing a step angle of 0.018 degree at the solar array. For the developed COMSAT drive, the step angle at the output is 0.0375 degree. Regardless of the stepper motor used, the load receives a rotational impulse. The magnitude of this impulse can be reduced by increasing the gear ratio and/or reducing the step size of the drive motor. There is a realistic limit using this approach that is determined by the availability of stepper motors and gear reducers with the appropriate characteristics. Since high torsional stiffness is required, the size and quantity of gearing is affected. A large gear ratio using conventional spur gearing would have a relatively low torsional stiffness when weight and size are minimized. One reasonable approach for the gear reducer is the harmonic drive. This device has a relatively large gear ratio in a single pass and a reasonably high-spring constant.

#### 5.4.6.2.4 EOS Array Drive and Electronics Design Selection (Figures 5-200 and -201)

Table 5-84 compares the characteristics of three continuous drives and two stepper drives with the principal requirements of EOS. The selected solar array drive design uses the TRW developed COMSAT drive mechanical design with the motor being operated synchronously with sine wave excitation rather than in a stepping mode. This design approach provides the advantages of high stiffness and continuous drive to minimize spacecraft altitude perturbations.



Figure 5-200. TRW COMSAT Solar Array Drive

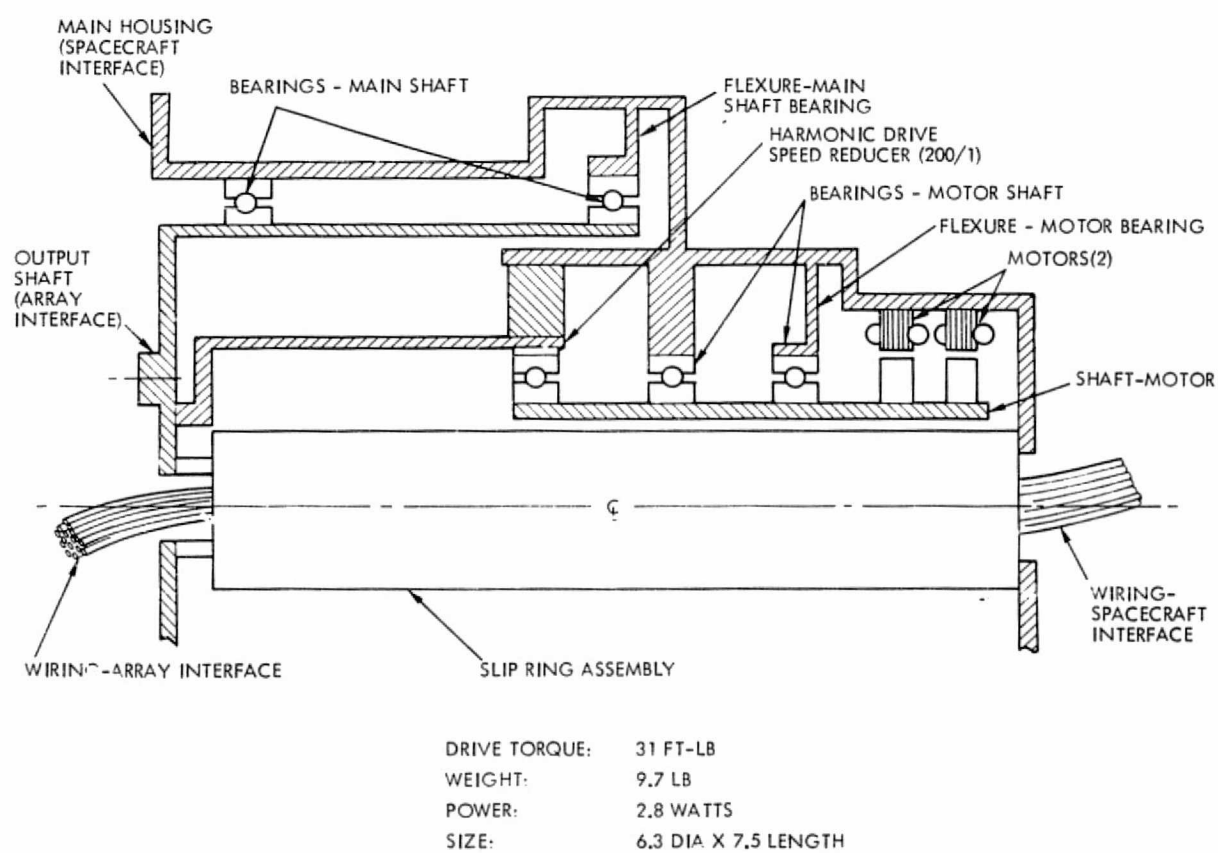


Figure 5-201. Solar Array Drive Schematic

Table 5-84. Comparison of Solar Array Drive Characteristics

		Continuous			Step	
		Geared	Direct		FLTSATCOM	COMSAT
	Required	Nimbus	Bendix	169		
Torsional stiffness	$1 \times 10^5$ in-lb	$3 \times 10^5$	No information	(1)	$1.9 \times 10^4$	$2.16 \times 10^5$
Transverse stiffness	$1 \times 10^6$ in-lb	$5 \times 10^5$	No information	(1)	$2 \times 10^5$	$1 \times 10^6$
Angular rate or Angular step-size	0.06 deg/sec 0.002 deg	0.06 deg/sec See Note 3	0.06 deg/sec with "Stick-slip"	0.25 deg/sec	0.018 deg	0.06 deg/sec or 0.0375 deg (2)
Power w (max)		8	8	12	5	9
Control method		Closed loop	Closed loop	Closed loop	Open loop	Open loop
Weight (lb)		25 includes electronics	No information	11	15.5	9.7
Motor type		2-phase servo 400 cycle	2-phase Hyst Sync Brushless	DC torque brush type	1.8 deg stepper permanent magnet.	7.5 deg-stepper permanent magnet

- (1) This design is for a "through" shaft to drive two solar arrays.  
 (2) Sine wave excitation.  
 (3) Subject to angular accelerations.

The present COMSAT drive uses a redundant 24-pole DC stepper motor that develops 65-in-oz. holding torque with a 7.5-degree displacement step to an energizing voltage step input. Using a 200:1 gear ratio the output shaft rotation per step is  $7.5/200 = 0.0375$  degree. The COMSAT drive motor can be driven in a continuous mode by supplying its windings with sine (cosine) excitation instead of square pulses. The present motor will be modified to minimize its detent torque in order to run efficiently in a continuous mode. A torque margin of 3.5 can be provided at a motor power dissipation of 2.8 watts (continuous).

The motor rotor is supported by ball bearings that are preloaded by use of a flexure that contains one of the ball bearings. The motor drives a harmonic drive which has a gear ratio of 200:1. This gear reducer produces the rotation of the output shaft. This shaft is also supported by ball bearings that are preloaded using a flexure in the same manner as that noted above. The slip ring assembly is a self-contained bearing mounted unit, and the ring and brush materials are those delineated by Poly-Scientific (Division of Littor Products Inc.) in specifications numbers 39 and 383. Nominally, the composition of the brushes is 12 percent  $\text{MoS}_2$  (3 percent graphite and 85 percent silver) and the rings are made of coin silver. The flight slip ring assemblies will contain four pairs of power circuits rated at 10 amperes each. Additional 7-signal circuits define the total electrical signal transfer capability. The reliability feature of parallel combinations of rings is enhanced by two brush/ring design. Solid lubricant is used for the bearings and the balls are separated by nylon retainers. The unit is designed with small radii rings in order to minimize friction. The slip ring assembly is located inside the hollow output shaft. The ring member of the assembly is driven by the output shaft by means of two pins pressed into the outboard flange of the slip ring assembly. The housing of the slip ring assembly is attached to the solar array drive assembly housing by means of a large diameter flange at its inboard end.

Two redundant single-turn potentiometers for position readout are mounted on the stationary side of the slip ring enclosure. Anti-backlash

gears on the potentiometer shafts are geared off the slip ring shaft with 1:1 ratio. The potentiometers contain a conductive plastic resistive element, which is lightly coated with NPT-4 for lubrication.

The solar array drive assembly design uses two flexural suspension systems, as noted above; one supports the output shaft and the other suspends the motor rotor. These two suspensions are decoupled by virtue of the stiffness properties of the harmonic gear train and the self-centering characteristics of the Oldham coupling through which the motor rotor motion is induced to the output drive shaft.

The implementation of the bearing suspensions uses two radial contact bearings which support the shafts in conjunction with a diaphragm type flexure. All bearings are slip fitted (0.0005 inch maximum clearance on the diameter) to allow convenience in assembly and to offset the bearing's diametral clearance reductions due to the temperature gradients across the bearings. The outboard bearings (bearings not associated with the preload flexures) provide the axial, and in part, the lateral stiffness and bear the burden of cyclic axial loads. The inboard bearings are preloaded via a diaphragm flexure characterized by a low-axial and relatively high-radial stiffness. The bearing preload is accomplished by securing both bearings against the shaft shoulder. The preload is a function of the diaphragm axial spring rate and the initial displacement increment between the shaft shoulder and the inner races of both bearings. This increment is accomplished by placing a shim between the solar array drive assembly housing inboard-flange and the flexing end of the flexure element prior to its securement (clamping) to the structure of the flange.

Functionally, the output shaft suspension provides the structural integrity and reacts to the loads and environment imposed by the payload interface. This shaft suspension dominates the transverse rotational and axial stiffness of the solar array drive assembly but the torsional stiffness by virtue of the assembly configuration is essentially a function of the flexspline element component of the harmonic drive.

#### a. Materials

The entire supporting structure of the COMSAT solar array drive assembly is made of 6061-T6 aluminum alloy. The bearings are made of



440C corrosion resistant steel and the balls are separated by retainers made of Nylasint 64HV, a sintered porous nylon. A fluid lubricant is used for these ball bearings. The harmonic drive uses a flexspline made of type 321 corrosion resistant stainless steel meshing with its circular spline made of 17-4 PH corrosion resistant stainless steel.

b. Lubrication

Except for the slip ring assembly, which uses a dry lubrication scheme, all other solar array drive assembly components will be lubricated with NPT-4 manufactured by the Bray Oil Company. The oil will be first used in conjunction with activities prior to assembly. Hence, the precleaned bearings, their retainers, pertinent housing, and shaft surfaces will be lubricated. The harmonic drive splines will be lubricated with NPT-4 carried in lithium stearate binder. The latter was adapted to mitigate the potential danger of surface damage of the splines by introducing higher viscosity lubricant. A light coat of this grease will be also inserted in the grooves of the labyrinth seals to deter the lighter oil molecules from escape, especially during the initial phases of operation in space. The oil is stored in several replenishment reservoirs (Nylasint). The reservoirs are sized as follows. The weight of oil loss is estimated by

$$W_L = fQAt = 0.916 \text{ gram}$$

where:

$W_L$  = Quantity of oil loss, gram

$f$  = Attenuation factor . 0.174

$Q$  = Evaporation rate -  $0.6 \times 10^{-4} \text{ gm/cm}^2/\text{hr}$  (at  $70^\circ\text{F}$ )

$A$  = Duct area =  $0.446 \text{ cm}^2$

$t$  = Operational time = 87,600 hr

The corresponding volume of the oil loss is

$$V_L = W_L/\gamma = 0.916/0.951 = 0.963 \text{ cm}^3$$

Although the porosity of the chosen Nylasint formulation is 50 percent, the effective retention (including oil loss due to venting) is taken as 25 percent. Hence, the necessary volume of the replenishment reservoirs is

$$V_R = V_L / 0.25 = 3.85 \text{ cm}^3 = 0.235 \text{ in.}^3$$

Since the present design has reservoir capacity of  $9.52 \text{ in.}^3$ , the estimated life of the lubricant is

$$L_L = \frac{(9.52)_{10}}{0.235} = 405 \text{ years}$$

### c. Drive Electronics (Continuous Drive)

Figure 5-202 shows the mechanization of the solar array drive electronics. In this arrangement, sine and cosine voltages are applied to the corresponding windings of the solar array stepping motor in a manner to cause the motor to rotate at a constant rate as determined by a ground command. The step motor is essentially operated as a synchronous AC motor where rotational rate is controlled by the excitation frequency applied to its windings. The variable frequency AC voltages are generated by dividing a high-frequency clock signal by a variable modulo frequency divider that may be programmed by ground command. The resultant clock output frequency is then applied to an 8-bit binary counter that forms the address inputs to a pair of read-only memories (ROM) which, in turn, generates 256 sequential 8-bit words. Each 8-bit word forms the magnitude and sign value of either the sine or cosine output as a function of the solar array drive motor equivalent rotational angle. The output of each ROM is D/A converted and applied to a power amplifier to drive the two-phase motor windings.

This arrangement, while less efficient from a power standpoint than a step drive, offers a method of solar array drive that can be precisely synchronized with any orbit rate without causing excessive spacecraft attitude perturbations. The operation is essentially equivalent to a brushless DC motor without the attendant complexity of electrical commutation and proportional control of the power amplifiers. Two-array drive electronics assemblies are used, one for each of the redundant solar array drive motors.

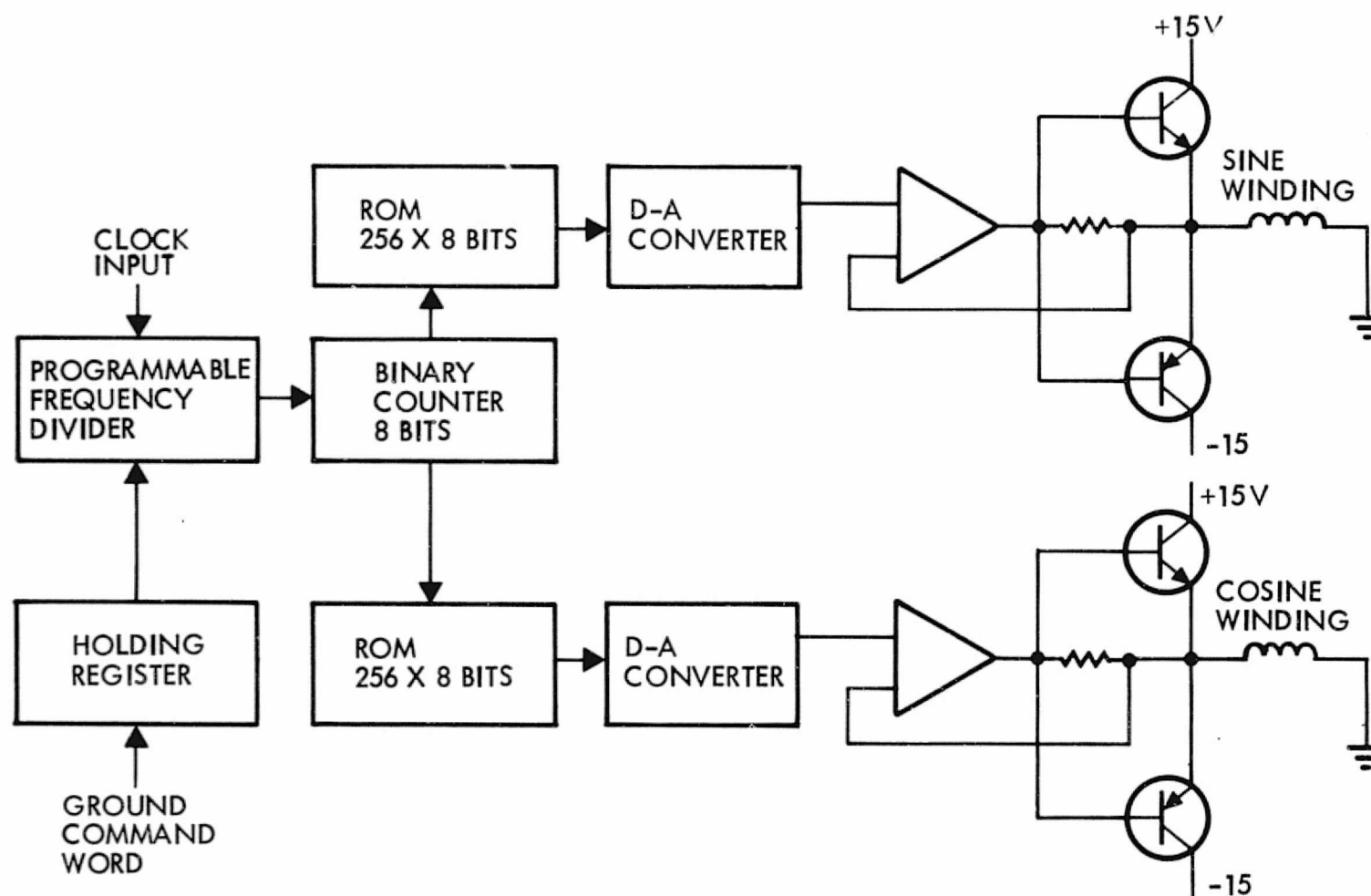


Figure 5-202. Solar Array Drive Electronics

## 5.5 THERMAL CONTROL

### 5.5.1 Active Thermal Control

#### 5.5.1.1 Problem Discussion

System heater power requirements and duty cycle for active thermal control require thermal power characteristics of each sensor, of each module and of both payload and subsystem structures. In turn these individual units are dependent upon the power profile, including the activation points in orbit. System heater power requirements are generated from the module thermal design study (Section 5.5.3), from the structure thermal design study (Section 5.4.4), and from updated sensor requirements.

Computer mechanism of thermal control law concerns the use of an on-board computer to process measured thermal data, utilize the processed data in accordance with a specified algorithm, and output commands that control the active units of a thermal system. It should be noted that computer-control represents only one of several heater-control methods examined in the structure thermal control design study presented in Section 5.5.4.

#### 5.5.1.2 System Heater Power Requirements

A system heater power profile require timewise power characteristics of each component. This information is not available and usually is not deterministic; it was necessary to separate the heater power requirement as continuous or arbitrary cycling.

##### 5.5.1.2.1 Module Heater Power Requirements

Module heater power requirements are dependent upon many factors with the need to control attachment point temperature being a significant consideration. Since attachment point temperature is governed by overall module thermal design, the degree of assurance in maintaining control is governed by heater power requirements with higher the risk lower the power.

Module heater power requirements based on very small risk are summarized in Table 5-85. These requirements are governed by the following design requirements:

1) Radiator sizing,

- Reference orbit (11:00 am node/sun phase, sun-synchronous, near-earth)
- Orbit-average conditions
- Nominal environment ( $2\sigma$  cold condition is simultaneously satisfied)
- No non-deterministic heat leaks
- Effective emittance,  $\epsilon^*$ , of multilayer insulation = 0.005
- Radiator temperature,  $T = 70^\circ\text{F}$
- Orbital average temperature,  $T = 70^\circ\text{F} \pm 10^\circ\text{F}$ , maintained with very high probability

2) Heater Power sizing,

- Estimated non-deterministic heat leaks
- Heat loss through multilayer insulation based on  $\epsilon^* = 0.01$
- Module temperature,  $T = 60^\circ\text{F}$

Note if a higher risk in maintaining an orbital average temperature of  $70^\circ\text{F} \pm 10^\circ\text{F}$  is taken by using an  $\epsilon^* = 0.01$ , the required module heater power requirements may be reduced substantially (refer to Table 5-85).

If an orbital average temperature of  $70^\circ\text{F} \pm 10^\circ\text{F}$  is to be maintained for all near-earth orbits, approximately 18 watts of additional heater power is required with the 6 a.m. orbit representing this condition.

#### 5.5.1.2.2 Structure Heater Power Requirements

Structure heater power requirements are dependent upon many factors including temperature, sun angles and multilayer insulation characteristics. Effect of these factors on heater requirements is displayed in Section 5.5.4, Figure 5-203. Effective emittance  $\epsilon^*$ , and average structural temperature

Table 5-85. Module/Structure Heater Power Requirements

Module/Structure	Radi- ator Area (ft <sup>2</sup> )	Reference Orbit - Small Risk Orbit Average Heater Power (Watts)					Ref. Orbit Higher Risk (watts)	Max. Power	6 a.m. Orbit (watts)
		Nominal Conditions (No heat leaks)	Heat (2) Loss thru MLI	Other Heat Leaks	Heater Power Req'mts	Duty Cycle			
Module									
Wideband Comm.	2.32	0	8.2	6	14.2	(3)	6	Twice orbit avg. power require- ments.	18.2
Attitude Determination	1.93	0	4.7	3	7.7	(3)	3.0		12.7
Command & Data Handling	2.49	0	4.7	3	7.7	(3)	3.0		24.9
Electrical Power	4.0	16.2	4.7	3	23.9	Orbital	19.2		18.2
Actuation (including Pro- pulsion)	1.82	8.6	8.4	5.5	22.5	Orbital	17.8		1.3
Solar Array & Drive	.21	0	.3	1.0	1.3	(3)	1.3		
Total Module Power					77.3		50.3		93.5
Structure (4) (Payload & subsystem)		( Structural members uniformly heated)			64		50		64
Total (Module/Structure)					141.3		100.3		157.5

(1) Radiator area sizing based on effective emittance,  $\epsilon^*$ , of MLI = .005 & no heat leaks

(2) Heat loss through MLI based on  $\epsilon^* = .01$  &  $T_{\text{module}} = 60^\circ\text{F}$

(3) Will not be activated if heat loss and leak estimates are accurate

(4) Average structural temperature is  $\cong 70^\circ\text{F}$

COMPUTER CONTROLLED HEATER SYSTEM CAN OPTIMIZE USAGE OF AVAILABLE POWER AND PROVIDE FINE TEMPERATURE CONTROL

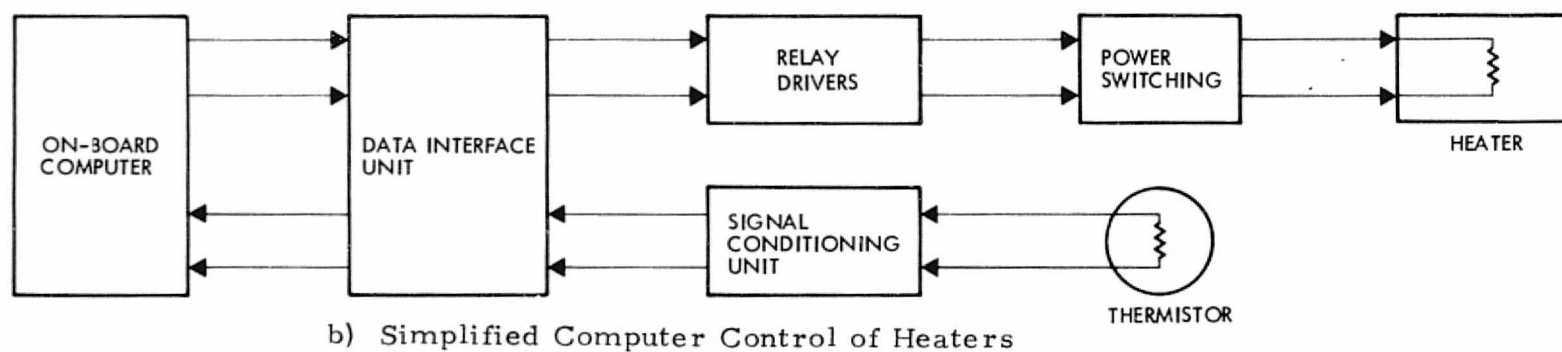
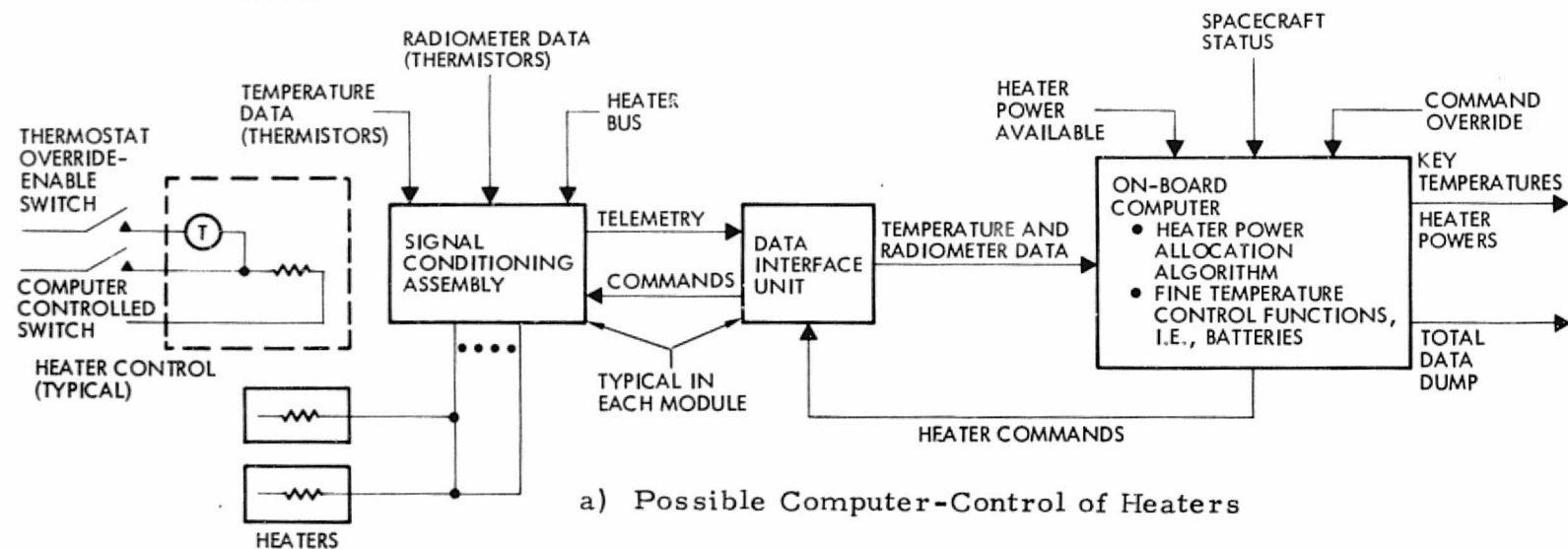


Figure 5-203. Computer-Control Methods of Heaters

are two of the more important factors. If structural members were heated uniformly, heater power requirements are 64 watts for an average temperature of 70°F, for an MLI effective emittance,  $\epsilon^*$ , of .01, and for the reference orbit.

#### 5.5.1.2.3 Sensor Heater Power Requirements

Mechanical and thermal characteristics of sensors as specified by manufacturers are indicated in Table 5-86. Included in this table are heater power requirements.

#### 5.5.1.3 Computer-Controlled Heaters

Heater circuits represent active elements of the structure thermal control system with number and location dependent upon the power-control method. Computer-control is one of many methods including thermostats, electronic switching, and ground command that were evaluated. The present task examines computer-control as a serious contender because of the availability of an on-board computer.

##### 5.5.1.3.1 Characteristics

Advantages of computer-control include:

- Considerable flexibility provided by in-flight adjustment of:
  - Power level
  - Temperature level set point
  - Temperature swing set points
  - Sampling rate of measurements
- Allocation of power
  - Degree of sophistication dependent upon specified requirements
- Temperature averaging of several sensor locations
- Accurate temperature set points
- Very small temperature deadband
- Fast response
- Large growth potential



Table 5-86. Specific Manufacturers Mechanical and Thermal Parameters with New Design Comments

INSTRUMENT	MANUFACTURER	WEIGHT (LBS)	SIZE	ELECTRONICS POWER (WATTS) (ORBIT AVERAGE)	ESTIMATED HEATER POWER (WATTS) (1)	ACTIVE THERMAL CONTROL?	ESTIMATED +Z FACE VIEW PORT SIZE (FT <sup>2</sup> )	MLI QUALITY, $\epsilon^*$ (2)	INSTRUMENT/ SPACECRAFT THERMAL RESISTANCE (°C/W) (3)
THEMATIC MAPPER	HUGHES	360 TO 450	36 IN. DIAMETER x 84 IN. LONG MAXIMUM ENVELOPE	55	---	NOT STATED	8.2	NOT STATED	---
	TE	590		110	6	YES	8.2	0.03	---
	HONEYWELL	600		183	50	YES	8.2	0.002	NOT STATED
HRPI	WESTINGHOUSE	553		102	19	YES	9.0	0.03 (ESTIMATED)	HIGH
SAR	(WESTINGHOUSE GOODYEAR)	200 TO 400	13 TO 27 FT ANTENNA	165	---	NO	---	0.03 (ESTIMATED)	NOT STATED
PMMR	OPERATIONS RESEARCH	150	75 FT <sup>3</sup>	70	---	NO	---	NOT STATED	NOT STATED

INSTRUMENT	MANUFACTURER	MANUFACTURERS PLANNED LOCATION AND SIZE (FT <sup>2</sup> ) OF HEAT DISSIPATOR SURFACES (4)		AREA ON +Z SURFACE REQUIRED TO DISSIPATE ELECTRONICS POWER AT 70°F (FT <sup>2</sup> )	SUFFICIENT RADIATING AREA AVAILABLE ON +Z SURFACE?	SPECIAL THERMAL FEATURES
		LOCATION	SIZE			
THEMATIC MAPPER	HUGHES	NOT SPECIFIED	NOT SPECIFIED	3.9	YES	ALL CONTAIN RADIATIVE LOW TEMPERATURE DETECTOR COOLER WHICH REQUIRES A CUTOFF ON THE -Z, +Y AREA OF THE SPACECRAFT STRUCTURE.
	TE	-Z, +Y	5.0	7.9	YES	
	HONEYWELL	-Z, +Y	5.7	13.1	YES	
HRPI	WESTINGHOUSE	-Z, +Y	5.0	7.3	YES	USES HEAT PIPE BETWEEN SCAN MOTORS AND RADIATOR DETECTOR CONTROLLED 0.5°C
SAR	(WESTINGHOUSE GOODYEAR)	NOT SPECIFIED	3.5 (AT 158°F)	6.4 (AT 158°F)	YES	USES HEAT PIPES, STEARIC ACID TO SMOOTH POWER PULSE.
PMMR	OPERATIONS RESEARCH	NOT SPECIFIED	NOT SPECIFIED	5.0	YES	

- (1) Heater power estimates by sensor manufacturers are incomplete
- (2) TRW interface guidelines assumes an  $\epsilon^* = .02$  or better
- (3) Interface resistance between sensor and structure will be provided in the attachment fitting; the resistance will be  $\geq 5$  °F-HR/BTU
- (4) Radiators located on the -Z face must be moved either to the +Z or +Y face

ORIGINAL PAGE IS  
OF POOR QUALITY

Disadvantages of computer-control include:

- Reliability dependent upon computer reliability
- Requires data interface unit (DIU), signal condition unit, relay drivers, and power switches (mechanical or electronic)
- Cost generally higher than other control methods.

#### 5.5.1.3.2 Computer Mechanization of Thermal Control Law

Use of computer for heater control can range from a simple ON-OFF command to the processing of a relatively sophisticated optimum power allocation algorithm. A flow chart of how a computer with a high degree of sophistication could be used to allocate available power and provide fine temperature control is illustrated in Figure 1a. With this scheme, temperature as well as heat flow measurements are necessary and cost can be expected to be high. Heater power allocations as well as temperature control can be based on general heat balance equations with dynamic programming used for optimum power allocation.

#### General Heat Balance Equations

$$C_i \frac{dT_i}{dt} = Q_i(t) - \sum_{j=1}^M [G_{ij} (T_i - T_j) + T A_i F_{ij} (T_i^4 - T_j^4)] \quad i = 1, 2, \dots$$

where:

- $C_i$  = thermal capacity of  $i$ th node
- $T_i$  = temperature of the  $i$ th node
- $T_j$  = temperature of nodes connected to  $T_i$
- $G_{ij}$  = linear conductance
- $F_{ij}$  = script F from node  $i$  to node  $j$
- $Q_i(t)$  = sum of internal heat generation and external heating on  $i$ th node

Use of Equation (1) in the computer-control method represents an extreme measure that does not appear necessary for the EOS TCS. It does, however, provide clues on how a reasonable computer-control of heaters should operate with the degree of sophistication dependent upon the requirements. In general, measurements should be limited and equations decoupled, if used.

Since sensing of measurements are much more rapid than dynamics of nodal thermal response, measurements in conjunction with the on-board computer, may be used for real-time temperature extrapolation which would be used to estimate activation of power turn-on or off of each heater circuit. In turn, real-time estimate of present and near-future total heater power needs would be available.

Algorithm for the on-board computer can be rather sophisticated as indicated before, but for a cost effective computer use, it appears realistic to minimize sophistication of optimum power allocation and to emphasize computer adjustment capabilities. These adjustments which can be ground-commanded include:

- Temperature set points
- Allowable temperature excursion
- Power level
- Sensing interval
- Power slicing to prevent thermal dynamics

A simple power allocation algorithm could consist of power allocation based on priorities with each heater circuit having a pre-flight established priority.

A schematic of a reasonable computer-control scheme that allows considerable flexibility but with only reasonable cost is shown in Figure 5-203b.

#### 5.5.1.4 Summary

Computer-control of heaters provides considerable flexibility, growth potential and margin. It provides a means of accommodating inherent thermal design uncertainties by providing for in-flight adjustment of pertinent heater control parameters.

### 5.5.2 Modular Thermal Design Validation

Modularity design concept allows the separation of the EOS thermal control system (TCS) into a structure TCS and a module TCS with module/structure interface as interacting constraints. Details of the module thermal design and of the structure thermal design are reported in Section 5.5.3 and Section 5.5.4, respectively. This task summarizes and reviews the detailed studies for the validation of modular design concept and for the generation of interface specifications.

#### 5.5.2.1 Problem Discussion

##### 5.5.2.1.1 General Modular Thermal Design Requirements/Goals

General requirements have guided the thermal control design. These requirements pertain to both Thor-Delta and Titan L/V payloads but with the exception that Thor-Delta modules/sensors need not be re-supplied. Many requirements are not subsystem compatible; for example mechanical interfaces must satisfy thermal isolation but yet provide structural integrity.

General requirements and goals are:

- Thermally decouple modules/sensors from payload/subsystem structures
  - to allow independent module thermal design
  - to permit module interchangeability
  - to prevent significant module impact on structural thermal distortion
  - to allow orbit module replacement
- Provide design flexibility and growth margin
  - to accommodate wide range of experiments
  - to accommodate various near-earth missions
- Limit structural temperature gradient and fluctuations
  - to preserve structural alignment by satisfying thermal distortion pointing allocation

- Provide for module replacement in orbit (for Titan L/V but not for Thor-Delta)
  - to permit module replacement via shuttle
- Minimum total program cost but with reasonable risk factors

#### 5.5.2.1.2 Modularity Study Approach

Modularity requires that individual module thermal design be essentially independent. Since mechanical interfaces are not ideal, a major design consideration is the allowable impact of these interface interactions on the structure and module thermal design. In turn, interface interactions must be translated to specifications. Methods then must be established to validate modular constraints. Validation includes both analytical and test methods.

#### 5.5.2.2 Review of Structure and Module Thermal Design Analysis and Trades

##### 5.5.2.2.1 Structure Thermal Design

Thermal design consists of structural frame sandwiched with multilayer insulation, several independently controlled heaters, and thermal isolation at the attachment interfaces. Effects of performance parameters were evaluated by exercising a multi-node ( $\sim 200$  nodes) math-model. Various trades involving range of thermal element property values, types of heater circuits, and costs were made. Central to all these trades was accommodation of structure thermoelastic deformation with impact of interface heat flow being a major consideration. A range of interface heat flow levels was evaluated with the results indicating that one-watt per attachment point being a reasonable allowance from structural thermal distortion considerations. This relatively high allowable interface flow is due to rate of temperature change attenuation by thermal inertia.

##### 5.5.2.2.2 Module Thermal Design

Each module has its own independent thermal control system consisting of multilayer insulation blankets over all surfaces, except for those used as radiators. The radiator area is silvered Teflon and thermostatically-controlled heaters are used to limit module temperature excursions as well as to provide for inherent design uncertainties.

Impact of one-watt per attachment point on module thermal design is a maximum four-watt perturbation that is readily accommodated by a slightly higher module temperature or an increase in heater power requirements.

#### 5.5.2.2.3 Module/Structure Interface Heat Flow Control

Limitation of interface heat flow to one-watt per attachment point is obtained by a combination of mechanical coupling thermal isolation design and temperature gradient control. If the structure and module temperatures near the attachment are permitted to swing  $\pm 10^{\circ}\text{F}$ , then the interface resistance must be  $\geq 5.9^{\circ}\text{F-Hr/BTU}$  under the worst temperature difference conditions. This interface resistance is readily obtained by using reasonable mechanical isolation consisting of low conductance material and minimal contact area; thermal control design was based on slightly relaxed value of  $\geq 5^{\circ}\text{F-Hr/BTU}$ . An attachment thermal design to achieve the required interface resistance is illustrated in Figure 5-204.

Detailed examination of a typical module thermal response indicates that the module temperature swings at the radiator are attenuated considerably by the capacity-resistance effects between the radiator and attachment; this results in attachment temperature excursions significantly less than  $\pm 10^{\circ}\text{F}$ .

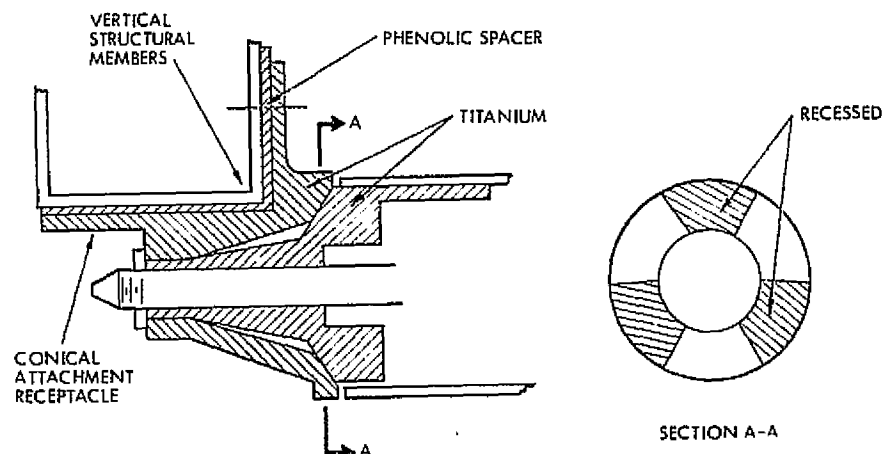


Figure 5-204. Module Attachment Fitting Design for Thermal Isolation

#### 5.5.2.3 Attainment of Thermal Interface Requirements

Allowance of less than 1-watt heat flow per attachment for the TRW modular thermal design is readily achieved using a combination of reasonable interface resistance and temperature gradient control. Since the radiator temperature variations are considerably attenuated at the attachment, the interface heat flow can be expected to be significantly less than 1-watt per attachment point.

#### 5.5.2.4 Modularity Guidelines

Modularity is based on the concept that each module/sensor is thermally decoupled from the structure and from each other. This modular concept is achieved with imposition of only minimal constraints on the modular, structure and attachment thermal design by defining an interface heat flow that can be readily accommodated.

In the discussion to follow the interface constraints have been separated as structure and module/sensor with the responsibility of meeting these requirements belonging to the contractor who furnishes these components.

##### 5.5.2.4.1 Structure

###### a. Static Frame Temperature at Attachment Point

Structure TCS must provide static frame temperature control at attachment point of:  $70^{\circ}\text{F} \pm 10^{\circ}\text{F}$ .

###### b. Dynamic Frame Temperature Response

Structure TCS must limit structural thermal dynamics due to external environment and/or limit heater induced thermal transients to be significantly less than interface heat flow transients.

###### c. Conductive Thermal Isolation at Attachment Points

Each module attachment fitting thermal resistance must be  $>5 \text{ Hr-}^{\circ}\text{F}/\text{BTU}$ .

d. Thermal Insulation Between Module and Structure

The effective emittance,  $\epsilon^*$ , of the thermal radiation insulation barrier between module and structure must be:  $\leq .02$ .

e. Electrical Power for Heaters

Total orbit-average power for structure  $\leq 75$  watts  
Total peak power  $\leq 150$  watts.

5.5.2.4.2 Module

The module thermal design must satisfy the following requirements:

- (1) The subsystem module shall be capable of operation when the heat sink temperature is  $\pm 20^\circ\text{F}$  greater than worst-case predicted operating temperatures. Heat sink is defined as the structure or panel to which the electronic black boxes and other module equipment is mounted. These will be termed the heat sink qualification temperatures.
- (2) The subsystem module shall be designed so that the nominal set point temperature\* of the heat sink is  $70^\circ\text{F}$  with electrical heaters off.
- (3) Electrical heaters shall be incorporated to maintain the orbit-average temperature at the module attachment locations above  $60^\circ\text{F}$  with the response approximating more closely sine pulse over one orbital period than a step-input pulse.
- (4) All module heat dissipation shall be radiated to space from the outboard facing panel.
- (5) The surfaces of the module, except for the panel radiator areas, shall be thermally insulated with multilayer insulation, such that the effective emissivity,  $\epsilon^*$  is:  $\leq .01$ .

5.5.2.5 Validation

5.5.2.5.1 Thermal Resistance of Module/Structure Attachment Fitting

Thermal resistance ( $\geq 5^\circ\text{F-Hr/BTU}$ ) to be verified by T/V test and analysis.

\*Set point temperature is the orbit-average temperature of the heat sink based on nominal environments and nominal operating duty cycles, i.e., the time-average temperature of a 1-node model of the module.



#### 5.5.2.5.2 Effective Emittance of Multilayer Insulation Blanket

Effective emittance ( $\leq .01$ ) for the external insulation blanket is to be verified by a T/V test and analysis.

#### 5.5.2.5.3 Module Thermal Design

Module thermal design to be validated by module T/V test and analytical correlation.

#### 5.5.2.5.4 Structure Thermal Design

Structure thermal design to be validated by prototype T/V test and analytical correlation.

### 5.5.3 Thermal Design of Modules

Objective of this task was to select a thermal design for each subsystem module that meets design requirements, after evaluating and comparing various candidate methods. For example, it was necessary to determine electrical power requirements for heaters in the modules, to establish allowable heat flow through the mechanical attachments, and to evaluate various parameters that affect thermal performance of subsystem modules. Since the treatment of all modules (except the Power System Module) is very similar, the discussion has been consolidated here for thermal design areas noted below:

- Wideband Communications
- Attitude Determination
- Command and Data Handling
- Power System
- Actuation (including propulsion)

This presentation consists of:

- (1) Assessment of EOS-A thermal environmental conditions for module thermal design
- (2) Identification of critical temperature limits
- (3) Evaluation and comparison of thermal control methods, and
- (4) Discussion of the selected thermal design, performance.

#### 5.5.3.1 Problem Discussion

The modular concept requires that the individual module thermal designs essentially be independent of the module/structure interface; however, the module must be capable of limited heat flow at these attachment interfaces. In this discussion, it is assumed that the necessary thermal isolation between the module and structure will be provided in the attachment fittings. A reasonably high thermal resistance ( $R > 5 \text{ hr-}^\circ\text{F/BTU}$ ) at each attachment fitting is considered necessary. It is further assumed that the spacecraft structure adjacent to the fitting will be maintained at temperature levels necessary to meet interface heat flow constraints.

In the evaluation of each module, a thermal design was formulated, based on the environments associated with the 11:00 a.m. node/sun phase Reference Orbit. Impact on this reference orbit design, in terms of wider operating temperatures or use of extra heater power, was assessed for the range of 6:00 a.m. to 6:00 p.m. node/sun phase orbits.

#### 5.5.3.2 Thermal Method and Design Trades

##### 5.5.3.2.1 Thermal Method Trades

Prior to selecting a preferred thermal design for each module, the following candidate methods were considered:

- Louvers
- Variable-conductance heat pipes (cold gas control)
- Passive thermal control with contingency heaters (that turn on if module reaches the minimum allowable equipment operating temperature)
- Basically passive thermal control, with thermostatically-controlled heaters to minimize temperature difference across interface fittings, i.e., to maintain the module above  $60^\circ\text{F}$  at all times.

Louvers and Variable-Conductance Heat Pipes (VCHP) are similar functionally because both automatically adjust the effective radiator area to provide close temperature control over a wide range of external heating environments and variations in internal power dissipation. Louvers were eliminated from consideration because experience at TRW has shown that VCHPs are more efficient thermally and considerably less expensive than louvers.

A heat pipe system becomes attractive when its cost is offset by cost savings resulting from reduction of heater power required for a thermostatically controlled heater system. The recurring cost of each VCHP is about \$3000; this must be compared to the cost of electrical power at about \$400 per watt (orbit-average). A complete heat pipe system, including redundancy, will cost about \$10,000 per module; this means that necessary cost savings requires a power reduction of at least 25 watts. A heat pipe system was considered for the Power Subsystem Module, because of very stringent battery temperature requirements and because of large variations in battery and other equipment heat dissipation. Variations in heat dissipation are due to state of charge, operating duty cycles, time in sunlight, etc. It is shown in a later section that the orbit-average heater power is 16 watts for this module, using thermostatically-controlled heaters to maintain the batteries at temperatures between 30 and 55°F. Thus, the electrical power penalty was not sufficient to offset the cost and other complexities associated with heat pipes. Heat pipes for the baseline design are not a cost-effective solution, but could become a viable candidate if the electrical power subsystem were to grow significantly for future missions.

#### 5.5.3.2.2 Design Trades

Design trade involved the selection of module orbit-average temperature, or set-point temperature based on a passive heat balance, and the selection of cold module temperature before heater turn-on. A set-point temperature of 70°F was chosen, which corresponds to the orbit average temperature of the spacecraft structure. This means, for nominal conditions,

the average heat flow across the interface fittings will be zero. The heater turn-on temperature of 60°F was selected to minimize heat leaks from the spacecraft structure because of structure thermal distortion requirements. Module heater power requirements are determined for a minimal risk design and for a design with a higher risk; this will be discussed in a subsequent section.

### 5.5.3.3 Module Design and Analysis

#### 5.5.3.3.1 Design Considerations

Reference orbit for this study was the 11:00 a.m. node/sun phase with an altitude of 914 km, but node/sun phase from 6:00 a.m. to noon were also considered; for noon to 6:00 p.m. node/sun phases, a 180° S/C yaw turn is assumed. Normal operating duty cycle during an orbit consisted of three 12-minute operations of sensor and communications and data handling modules. Power dissipation within each module is summarized in Table 5-87. Most of the electronic equipment is capable of operating at temperatures from 20 to 120°F; exceptions are the batteries, which are to be operated between 30 and 55°F and hydrazine which must be held above 40°F.

#### 5.5.3.3.2 Orbit Heating Conditions

Transient and orbit-average heat inputs to each module were calculated for four different node/sun phase from twilight (6:00 a.m.) to noon, as illustrated in Figure 5-205. Low  $\alpha_s/\epsilon$  coatings are used on radiators to minimize variations in solar and albedo heating. Table 5-88 presents orbit-average absorbed heating for each surface for each of four orbits. As noted on the table, these heat inputs are based on  $\alpha_s = 0.12$  and  $\epsilon = 0.80$ .

#### 5.5.3.3.3 Modules of Similar Characteristics

Design approach and resulting performance of all modules, except for the Electrical Power Module, are very similar. Each module is completely enclosed by multi-layer insulation (MLI) blankets, except for those areas on the outside used for radiators, as illustrated in Figure 5-206. Each module is thermally isolated from the spacecraft structure by high thermal

Table 5-87. Heat Dissipation by Module Equipment

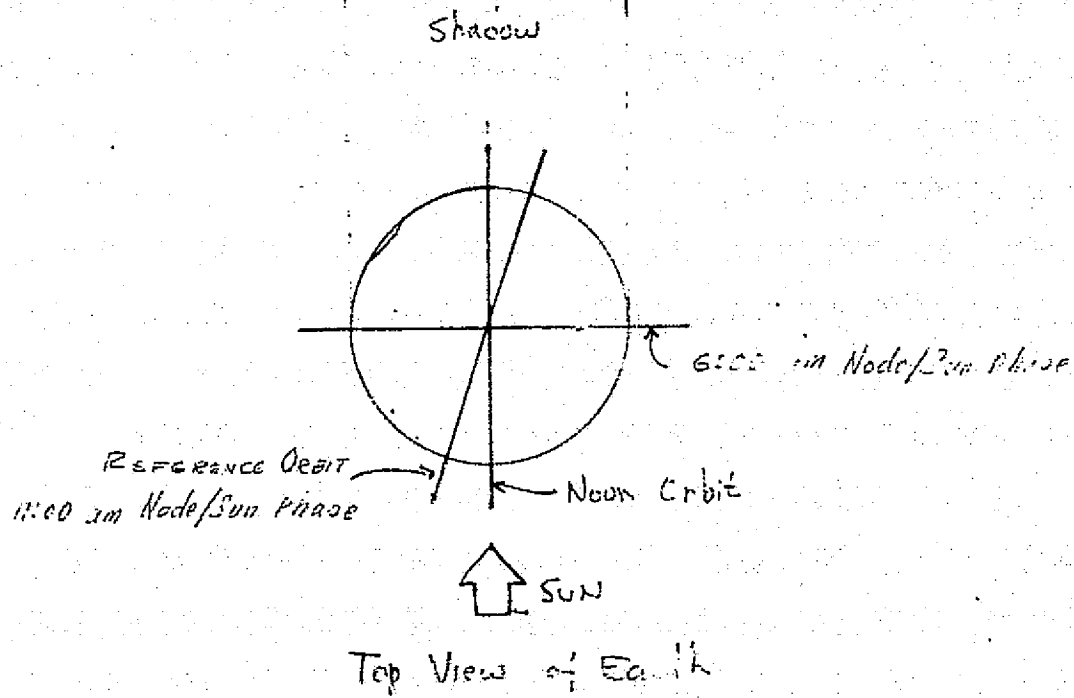
Module	Heat Dissipation (watts)			
	Continuous	Intermittent	Maximum Load	Orbit-Average
Wideband Communications	25.5	73.1	98.6	47.4
Attitude Determination	49.1	27.6	76.7	57.4
COMMUNICATIONS AND DATA HANDLING	38.8	6.5	45.3	40.1
Electrical Power System	--	187.1 <sup>△</sup>	187.1	77.7
Actuation System	45.0	31.2	76.2	48.1
Solar Array and Drive	5.0	19.8	24.8	5.9

<sup>△</sup> See Figure 1 for heat dissipation versus time of batteries, PCU and other equipment in the power module.

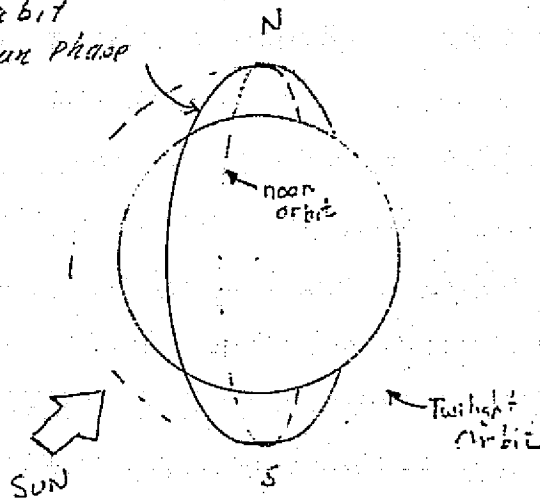
Table 5-88. Absorbed External Heating by Module Radiators

Module and Location	Heat Source	Orbit-Average Absorbed Heat Inputs (BTU/ft <sup>2</sup> -hr) <sup>△</sup>			
		6:00 a.m. Twilight Orbit	9:30 a.m. Orbit	10:30 a.m. Orbit	12 noon Orbit
<ul style="list-style-type: none"> <li>+Z-Side (Facing earth)</li> <li>• Wideband Communications</li> <li>• Communications &amp; Data Handling</li> </ul>	Solar Albedo Earth Total	0 0.58 <u>46.4</u> 46.98	3.44 2.97 <u>46.4</u> 52.81	2.46 3.86 <u>46.4</u> 52.72	2.35 4.17 <u>46.4</u> 52.92
<ul style="list-style-type: none"> <li>-Z-Side (Facing away from earth)</li> <li>• Attitude Determination Module</li> <li>• Solar Array &amp; Drive Module</li> </ul>	Solar Albedo Earth Total	0 0 <u>0</u> 0	11.9 0 <u>0</u> 11.9	15.55 0 <u>0</u> 15.55	16.8 0 <u>0</u> 16.8
<ul style="list-style-type: none"> <li>+Y-Side (Anti-sun side)</li> <li>• Electrical Power Module</li> </ul>	Solar Albedo Earth Total	0 0 <u>12.54</u> 12.54	0 0.68 <u>12.54</u> 13.22	0 1.02 <u>12.54</u> 13.56	0 1.2 <u>12.54</u> 13.74
<ul style="list-style-type: none"> <li>-Y-Side (Sun side)</li> <li>• Actuation Module</li> </ul>	Solar Albedo Earth Total	53.2 0.5 <u>12.5</u> 66.2	27.8 0.9 <u>12.5</u> 41.2	13.7 1.1 <u>12.5</u> 27.3	0 1.1 <u>12.5</u> 13.6

<sup>△</sup> Orbit Average Heat Inputs based on: Solar Constant = 430 BTU/ft<sup>2</sup>-hr  
 Albedo = 0.36  
 Earth Radiation = 68.8 BTU/ft<sup>2</sup>-hr  
 Radiator:  $\alpha_s = 0.12$   
 $\epsilon = 0.80$



Reference Orbit  
11:00 am Node/Sun Phase

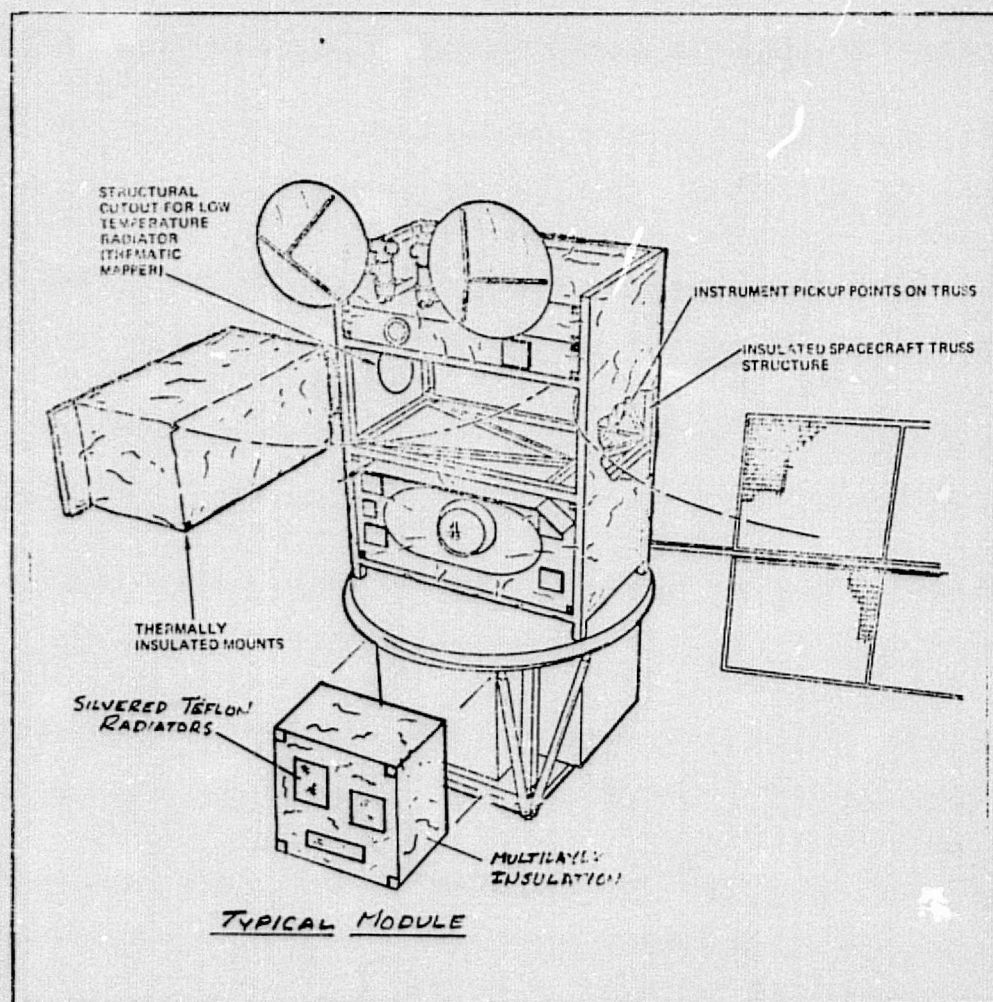


- Orbit Altitude : 385 nmi
- Inclination = 98.4°

Figure 5-205. Definition of Orbits

ORIGINAL PAGE IS  
OF POOR QUALITY





MODULES	LOCATION	RADIATOR AREA (FT <sup>2</sup> )
W/B DATA MODULE	+Z	2.32
ATTITUDE DETERMINATION MODULE	-Z	1.93
ACTUATION MODULE (INCLUDING PROPULSION)	-Y	1.82
COMMAND & DATA HANDLING MODULE	+Z	2.49
ELECTRICAL POWER MODULE	+Y	4.0
SOLAR ARRAY DRIVE	-Z	0.0

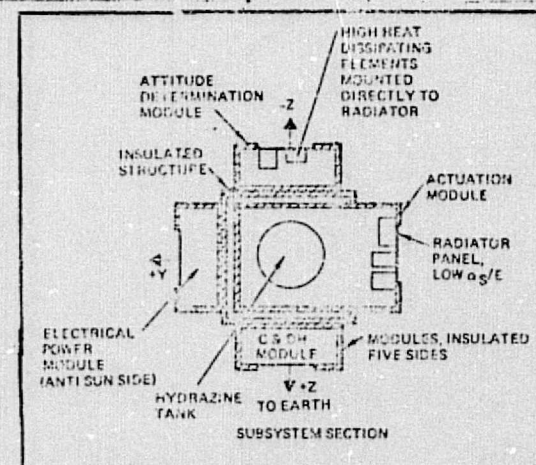


Figure 5-206. Description of Modules Thermal Design

resistance mechanical attachments which are discussed in Section 5.5.1. The radiators will be covered with a low  $\alpha_s/\epsilon$  material such as quartz second-surface mirror or silvered Teflon.

a. Radiator Sizing

Size of each module radiator area was selected to maintain the equipment platform at 70°F, considering the 11:00 a.m. reference orbit and the orbit-average heat dissipation of the electronic equipment. Radiator areas, summarized in Figure 5-206, assume no heat exchange with the spacecraft structure (which also has an average temperature of 70°F), and nominal heat losses through the insulation blankets with  $\epsilon^*$  of .005.

With the radiator area sized, calculations were then made to determine transient variations of the equipment platform temperature, due to time variations in the external heating environment and to equipment operating duty cycles. Temperature history at a typical location on the equipment platform for each subsystem module is shown in Figures 5-207 to -211. Weight of module structure and internal equipment is also noted on these figures.

Typical platform temperature oscillations are  $\pm 3^\circ\text{F}$  about the orbit-average temperature. Time wise temperature swings are small because external heating variations are tempered by the low  $\alpha_s/\epsilon$  of the radiators, the short operating duty cycles, and the large mass in each module. Local areas of each equipment platform are expected to have larger temperature excursions because of the presence of a heat dissipating electronic black box, but average temperature swing of the equipment platform is expected to be small.

b. Thermostatic-Heaters and Power Requirements

In order to maintain alignment stability of the spacecraft structure, temperature gradients and temperature variations of the space structure must be well controlled. The design approach was to minimize module/structure interface heat flow by using high thermal resistance mechanical attachments and by controlling spacecraft structure and subsystem module temperature



- Location 1 + 2 SIDE (FACING EARTH)
- WEIGHT
  - 500 LBS
  - 500 LBS
- Radiant Heat: 2.42 m<sup>2</sup>
- Temperature: 54 m<sup>2</sup>

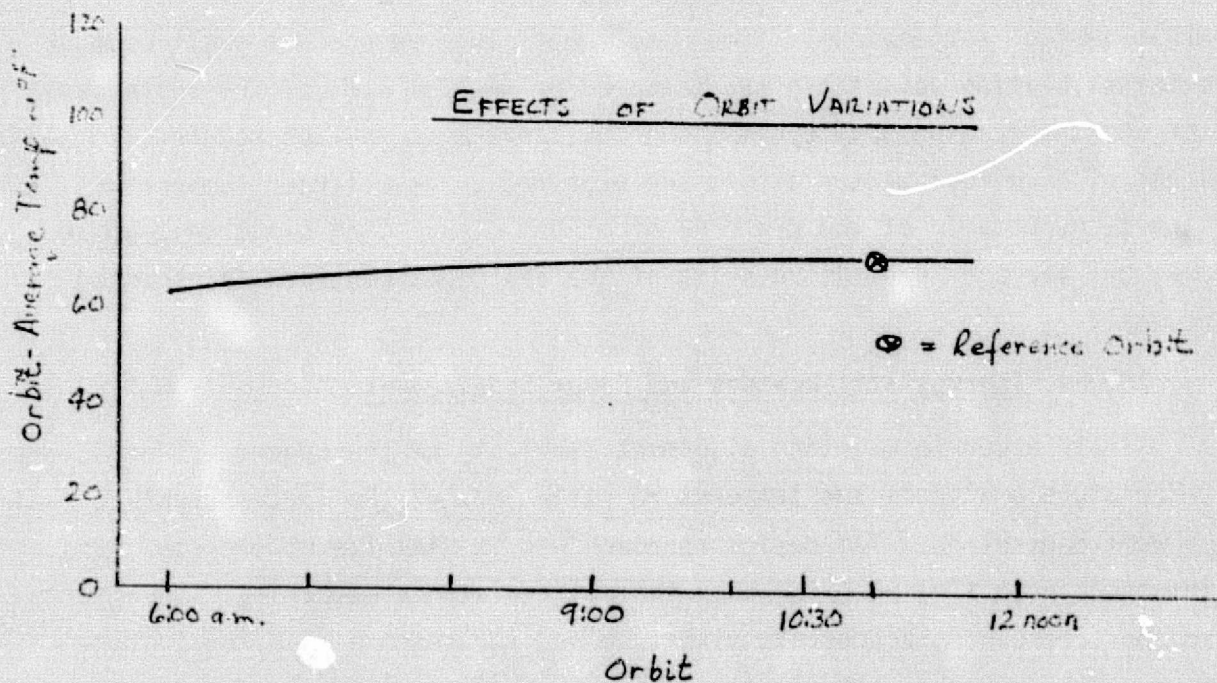
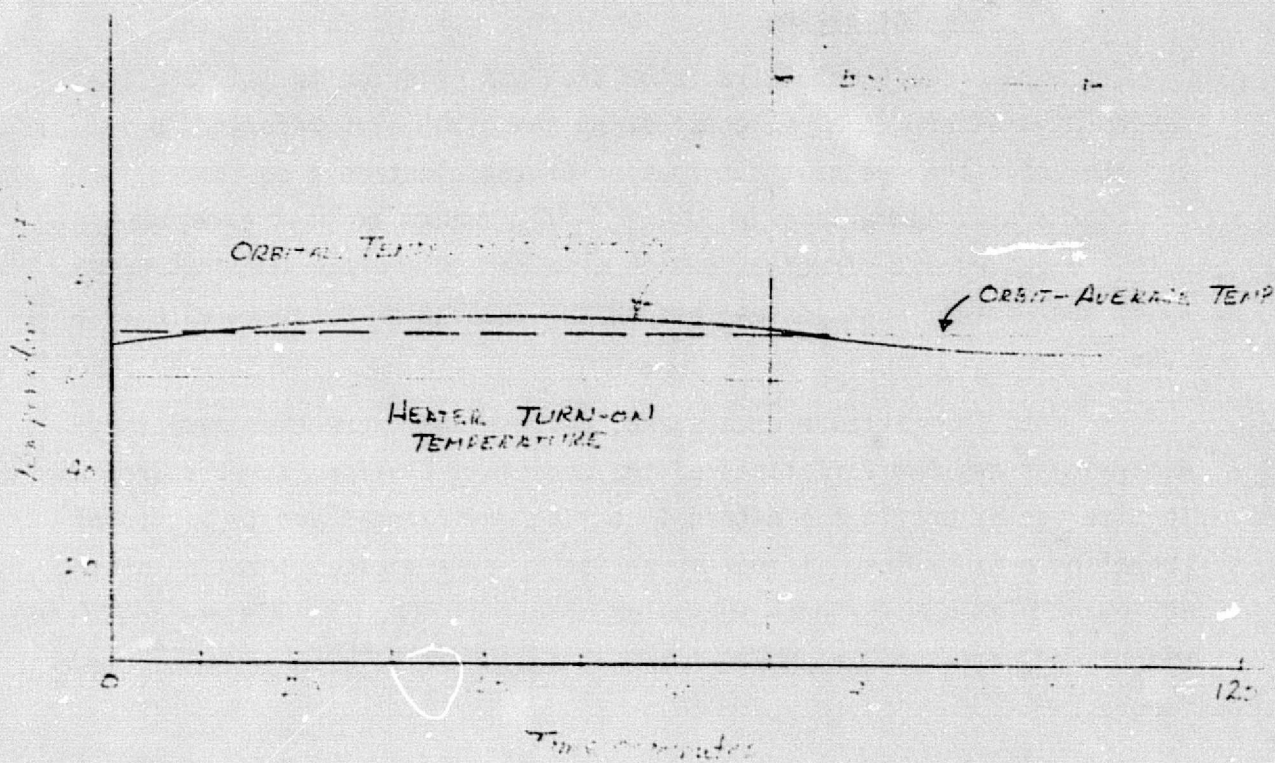
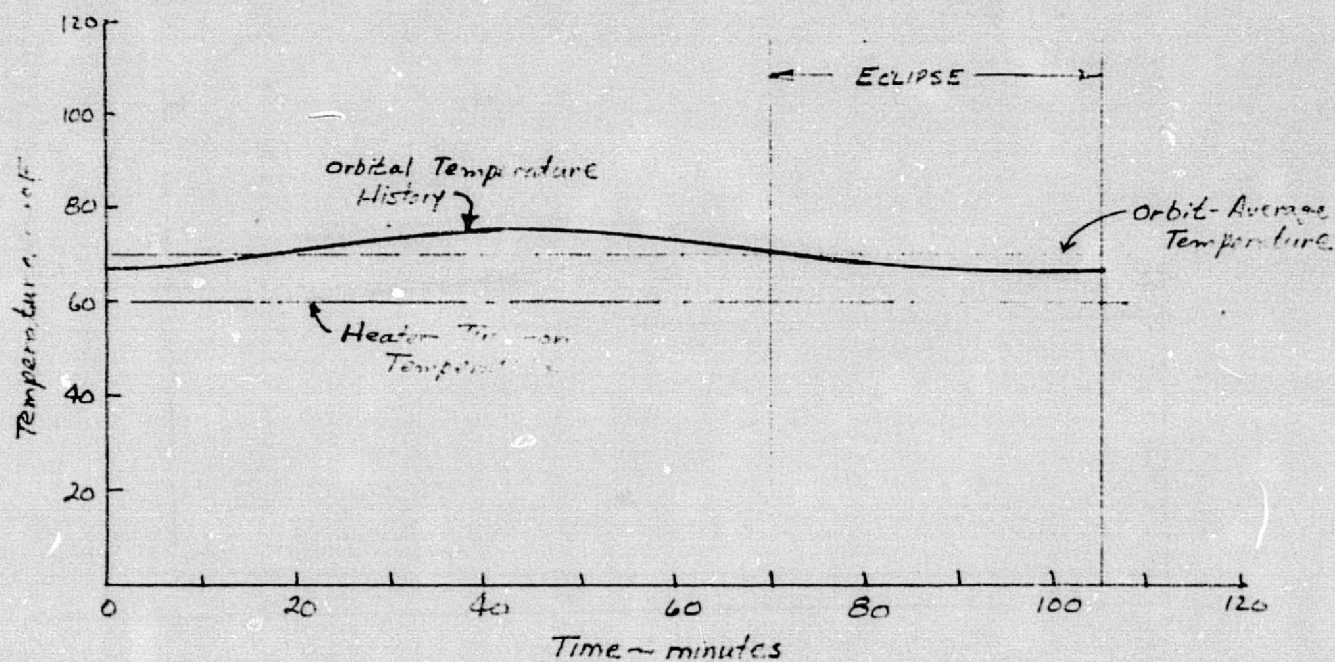


Figure 5-207. Thermal Behavior of Communications and Data Handling Module

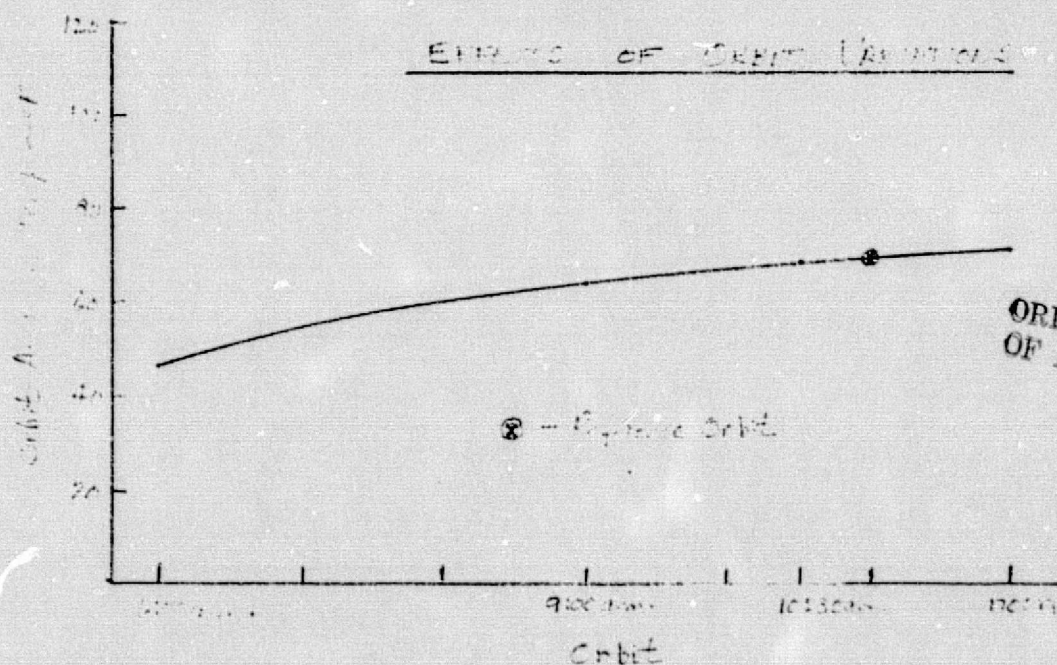


- Location: -Z side (facing away from Earth)
- Weight:
  - Structure 87 lb
  - Electronics 93 lb
- Radiator Area: 1.73 ft<sup>2</sup>
- Insulation Area: 54 ft<sup>2</sup>

### EQUIPMENT OPERATING TEMPERATURE HISTORY



### ERRORS OF ORBIT CALCULATIONS



ORIGINAL PAGE IS  
OF POOR QUALITY

Figure 5-208. Thermal Behavior of the Attitude Determination Module



# Actuation Sequence

# Propulsion Sequence

• Location

-Y side (Long Axis)

-X side (Opp. to Long Axis)

• Weight

• Mass

92

180

• Volume

93.5

107 (cc)

• Launch Area

1.82 sq ft

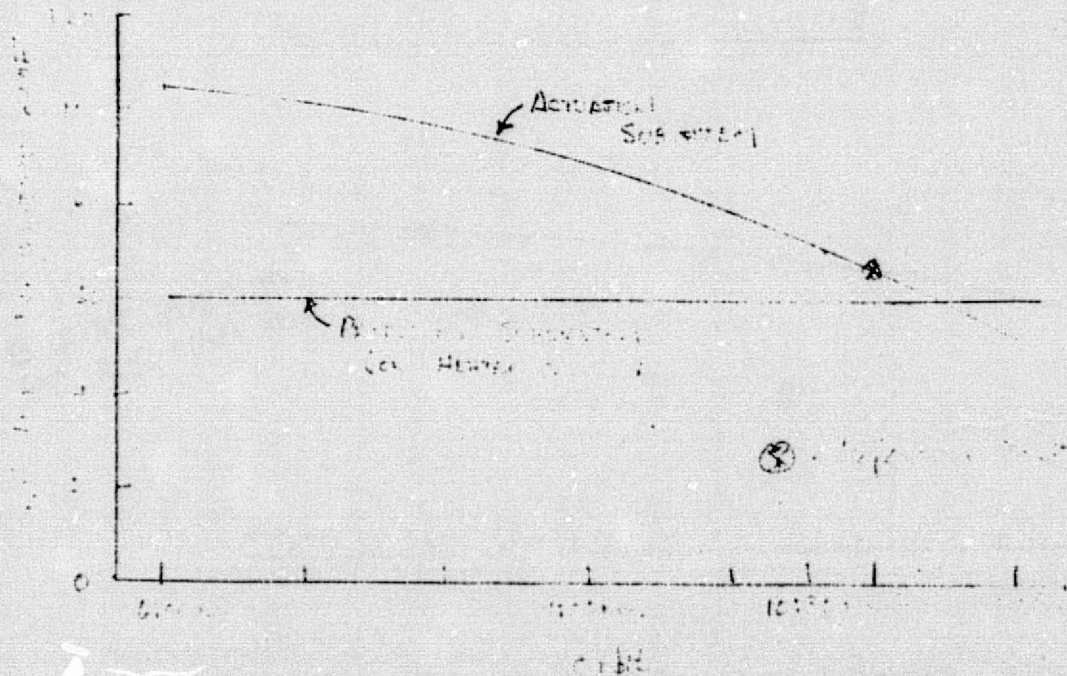
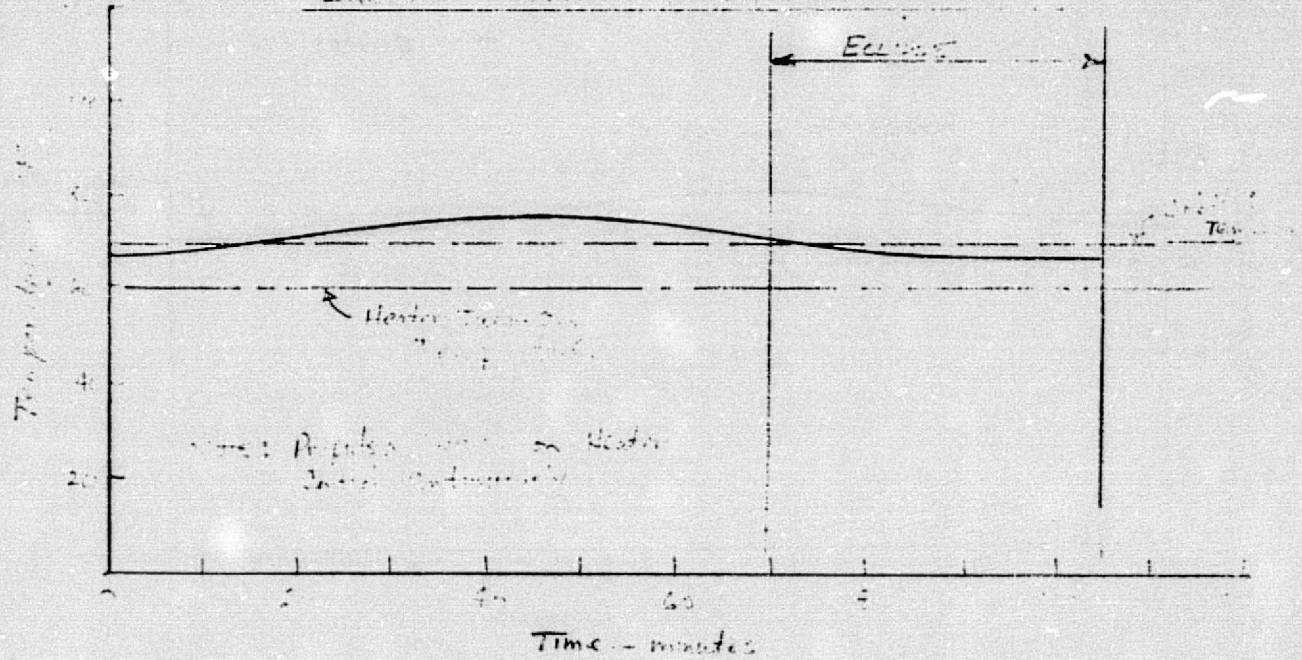
3.00

• Inertia

52 sq ft

2.14

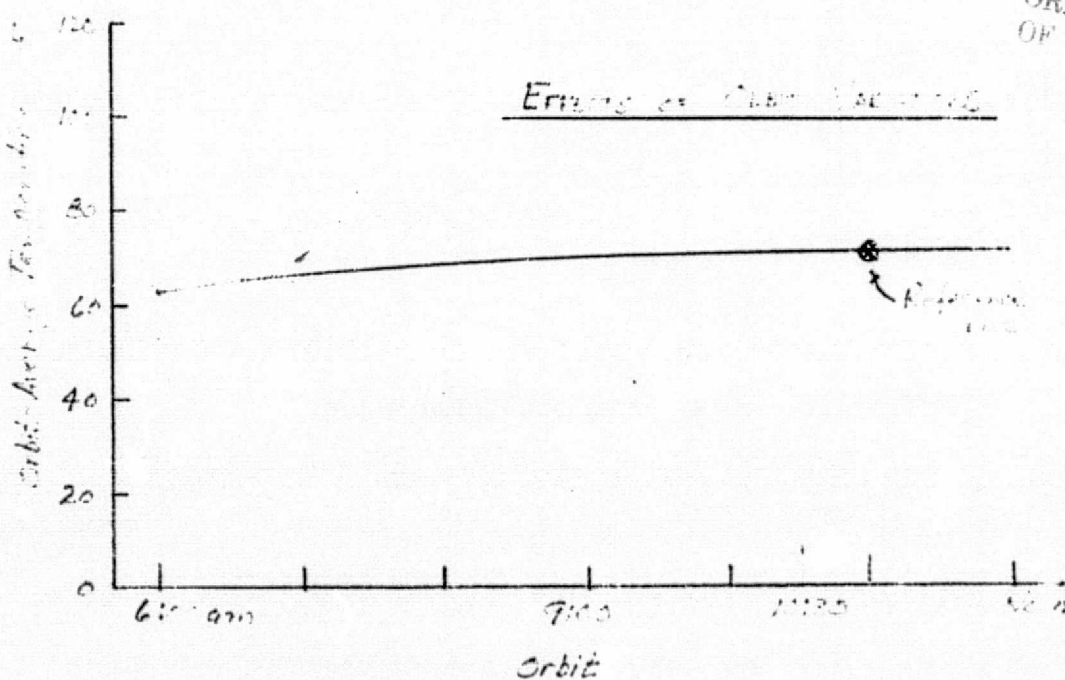
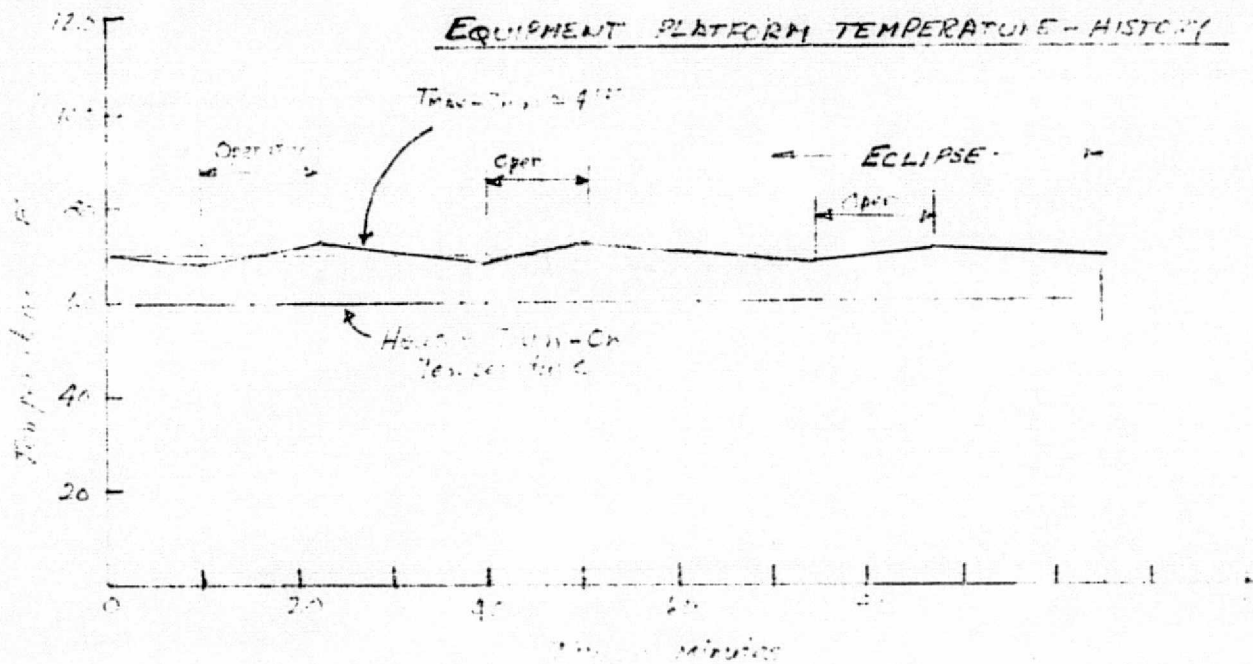
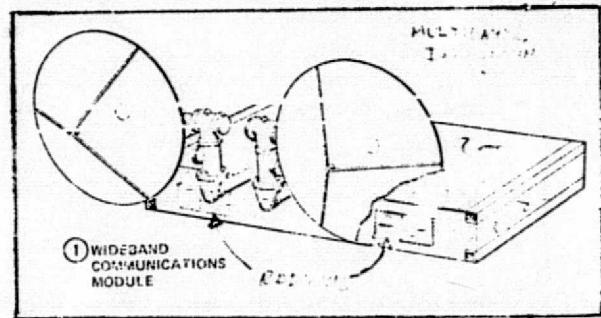
## Equilibrium Temperature vs. Time



ORIGINAL PAGE 5  
OF POOR QUALITY

Figure 5-209. Thermal Behavior of Actuation (including Propulsion) Module

- Location : +Z side (facing Earth)
- Weight
  - Electronic Boxes 99.8 lb
  - Structure 151 lb
- Radiator Area : 2.32 ft<sup>2</sup>
- Insulation Area : 46 ft<sup>2</sup>



ORIGINAL PAGE 13  
OF POOR QUALITY

Figure 5-210. Thermal Behavior of the Wideband Data Communications Module



• LOCATION: RADIATORS FACE +Y DIRECTION  
(ANTI-SUN SIDE)

- WEIGHT :
- RADIATOR AREA: 0.21  $\text{m}^2$
- INSULATION AREA: 7  $\text{ft}^2$
- CONTINUOUS POWER: 5.0 watts
- ORBIT-AVERAGE POWER: 5.9 watts

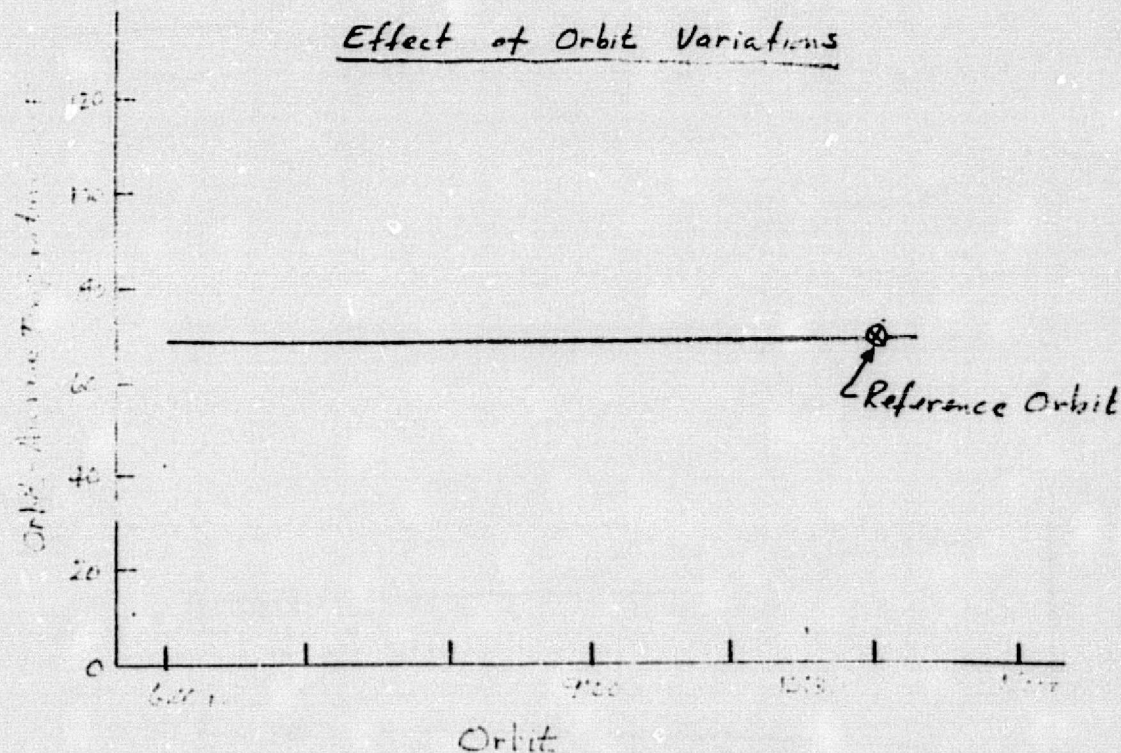
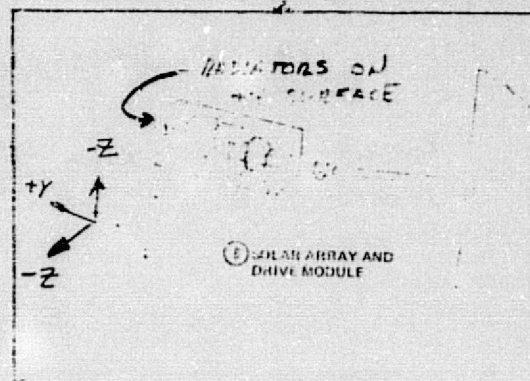


Figure 5-211. Solar Array and Drive Module

excursions. This control is achieved by the use of thermostatically-controlled heaters on modules and computer-control on structure. In this study, heaters for subsystem modules have been located on the equipment platform. The activation temperature is 60°F and the turn-off temperature is about 70°F.

Under nominal conditions that include the 11:00 a.m. reference orbit, nominal external heating and nominal operating duty cycles, heaters in five of seven modules will not be active. Only the electrical power module (to be detailed in a later section) and the actuation module require heater power under nominal conditions. Heater power in the actuation module is required to offset heat leaks through large areas of insulation around the hydrazine and nitrogen tanks. Other modules will require heater power only if a "cold condition" is encountered on-orbit. The cold condition was determined by considering predictable variations in duty cycles and heating environments, and parameter uncertainties in thermal properties, heating environments, insulation leaks, etc. This type of analysis yields  $2\sigma$  worst variations in module temperature as a result of including effects of  $2\sigma$  uncertainties. For most modules, the  $2\sigma$  uncertainty in module temperature level was less than  $\pm 10^\circ\text{F}$ , i.e., the analysis indicates there is a 95 percent probability that the modules average temperature on-orbit will be within  $\pm 10^\circ\text{F}$  of the desired  $70^\circ\text{F}$  nominal.

This uncertainty analysis indicates that there is a low probability that the modules will reach the 60°F turn-on temperature, and, if it is reached, the heater operating duty cycle will be quite low. Table 3 lists calculated (orbit-average) heater power usage for nominal and worst case conditions. This table shows that additional heater power required to maintain modules above 60°F is reasonable for a small risk design and thus represents a reasonable approach for limiting module temperature swings as part of the overall method to minimize alignment errors.

#### 5.5.3.3.4 Electrical Power Module

Thermal design for the Electrical Power Module must be tailored to accommodate the peculiarities of the batteries. Batteries, unlike the other electrical equipment, must be operated at a lower temperature level and within a smaller temperature range to enhance their operating lifetime. A



Table 5-89. Subsystem Module Heater Power Requirements, Reference Orbit

Module	Radiator Area (ft <sup>2</sup> ) <sup>1</sup>	Orbit-Average Heater Power Usage (watts)			Power Sensitivity $\Delta T/\Delta P$ °F/Watt
		Nominal Conditions	Nom. Envir. Zero Duty Cycle	2 $\sigma$ Cold Case <sup>2</sup> Nom. Duty Cycle	
Wideband Communications	2.32	0	19.8	14.2	1.8
Attitude Determination	1.93	0	6.3	7.7	2.2
Command & Data Handling	2.49	0	4.3	7.7	1.7
Electrical Power System	4.0	16.2	16.2	23.9	1.1
Actuation System	1.82	8.6	14.7	22.5	2.3
Solar Array and Drive	0.36	0	0.9	1.3	11.9
Total	--	24.8	--	77.3	--

1 Radiator sizing based on effective emittance,  $\epsilon^*$ , of MLI = .005 & no heat leaks;

2 Heat leaks through MLI based on  $\epsilon^* = .01$  &  $T_{\text{Module}} = 60^\circ\text{F}$

battery temperature range between 30 and 55°F is desired. Remainder of the electrical power module will operate with a mean temperature of 70°F. To accommodate this difference in platform temperature, batteries will be grouped together on a portion of the platform which is thermally isolated from the remainder of the platform and form the module structure as illustrated in Figure 5-212.

- A phenolic fiberglass splice will conductively isolate the battery area of the equipment platform from the other equipment.
- Phenolic washers will isolate the battery platform from the module structure.
- A single-layer radiation shield made of aluminized Mylar will radiatively decouple the batteries from the surroundings.

Oversized radiators will be employed to assure that the batteries do not exceed 55°F, even if their heat dissipation is 50 percent larger than expected. The heater power penalty for the extra radiator area is 8 watts per battery (on an orbit-average basis). Thermostatically-controlled heaters will maintain the batteries above 30°F during periods of low heat dissipation.

Another requirement on the power system thermal design is that the temperature of the two batteries be nearly identical. To accommodate this requirement, the batteries are located contiguous and with a doubler on the equipment platform under the batteries to increase the thermal conductance. A 0.150-inch thick doubler was chosen based on results which are summarized in Figure 5-213. This figure presents data from steady-state analyses which evaluated temperature differences between batteries for various platform thicknesses and heat dissipations. Although the batteries are expected to have nearly identical power dissipation, power differences of 10 and 20 watts were selected to study their effect: A power difference of 10 watts was used to size the doubler thickness even though a 5-watt difference may be more reasonable.

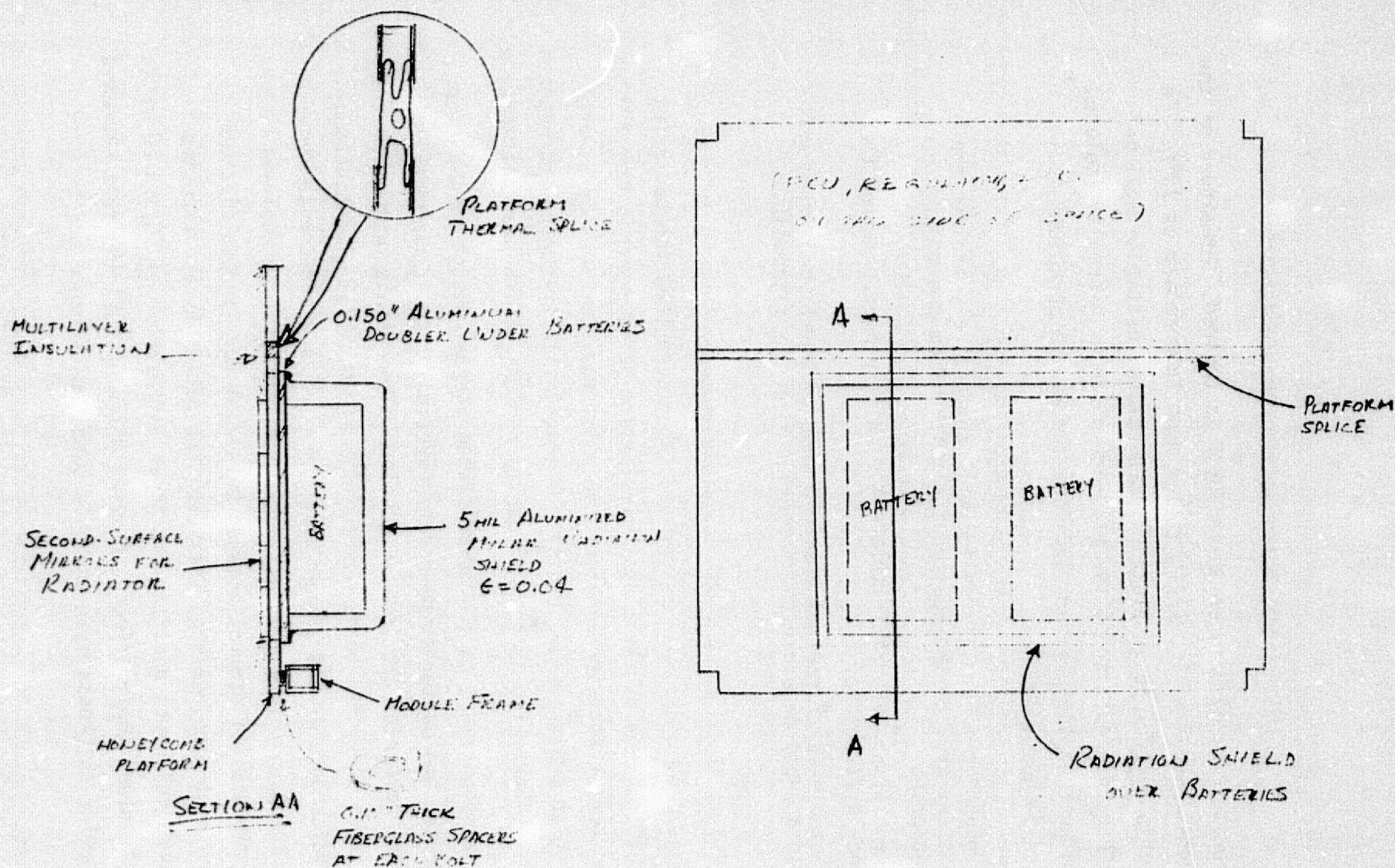


Figure 5-212. Thermal Design of Power System Module



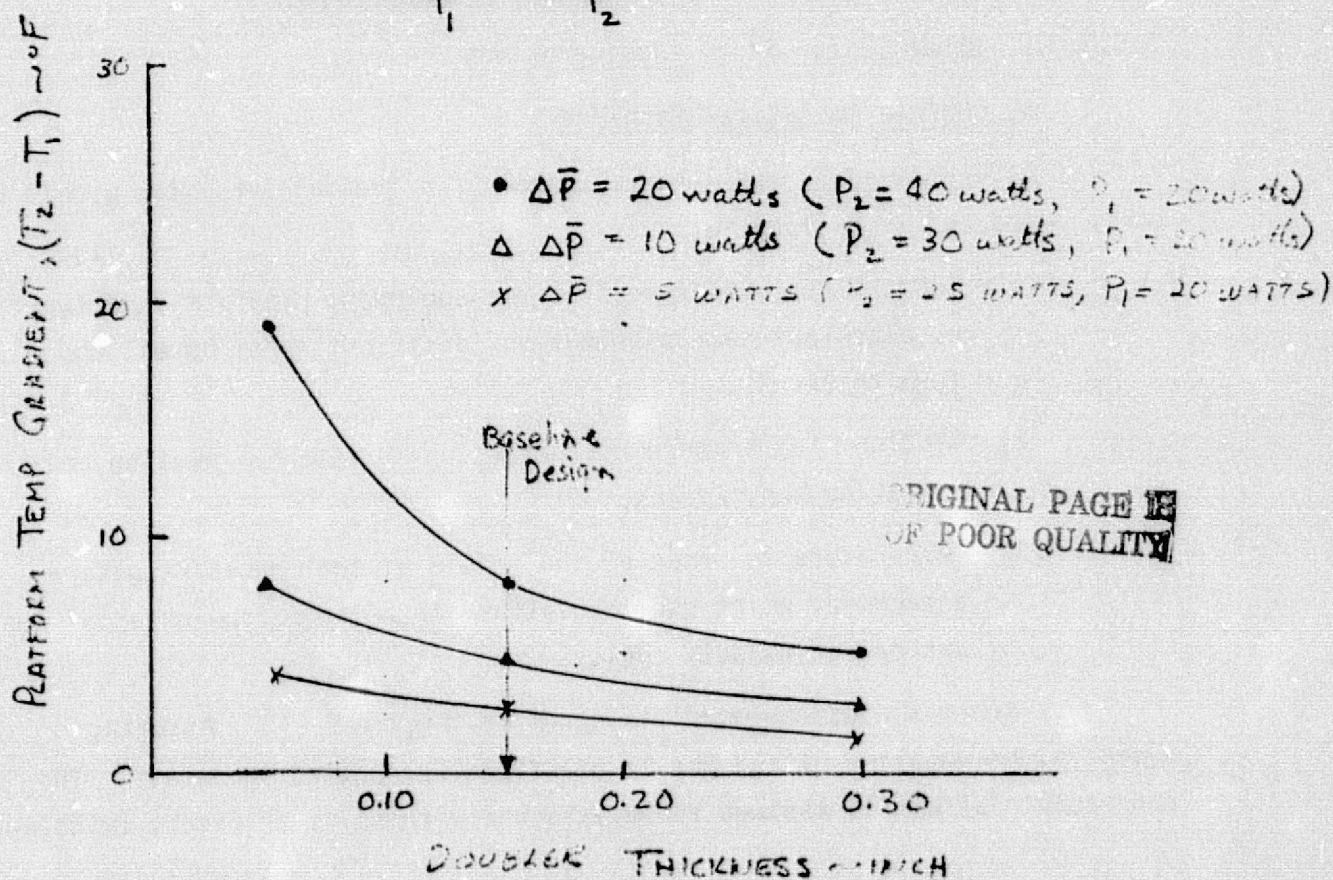
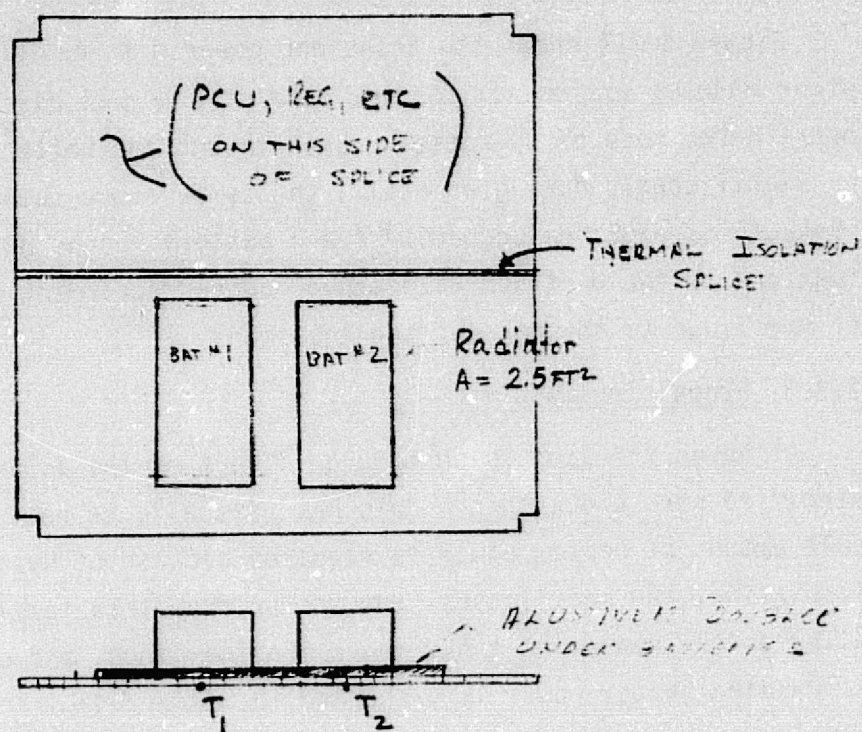


Figure 5-213. Platform Thickness Requirements to Maintain Small Temperature Difference Between Batteries

Figure 5-214 shows the transient power dissipation of a battery and other modules equipment, for the case of a normal discharge, charge and over-charge mode of operation. Even though the battery power dissipation varies significantly during an orbit, the temperature swing is less than  $\pm 5^{\circ}\text{F}$  because of high heat capacity (each battery weighs 82 lbs). Temperature fluctuations of the platform with other mounted equipment also will be rather small due to the mass of the equipment.

#### 5.5.3.3.5 Propulsion Module

Although the propulsion module is part of the actuation module, it is identified here since this module has virtually no heat dissipation. A sizeable amount of heater power is required because of heat leaks through the insulation, and heat losses from the primary thrusters. Heaters will be installed on the hydrazing tank, the hydrazine lines, and on the thrusters. The calculated heater power is presented in Table 5-89.

#### 5.5.3.3.6 Other Design Study Considerations

##### a. Module Analytical Math-Model

A 58-node analytical thermal model of a typical subsystem module was constructed and exercised to study:

- (1) Temperature differences in the equipment platform as a function of black box heat dissipation, distribution of boxes, and platform thickness.
- (2) Platform temperature histories due to external heating and operating duty cycles.
- (3) Temperature response of the module at the module/structure attachment point due to platform transients from external heating and operating duty cycles.

A schematic of the model is shown in Figure 5-215. Assuming symmetry, one-quarter of the module platform was modeled in detail. The honeycomb platform is assumed to be attached with bolts or rivets (with an



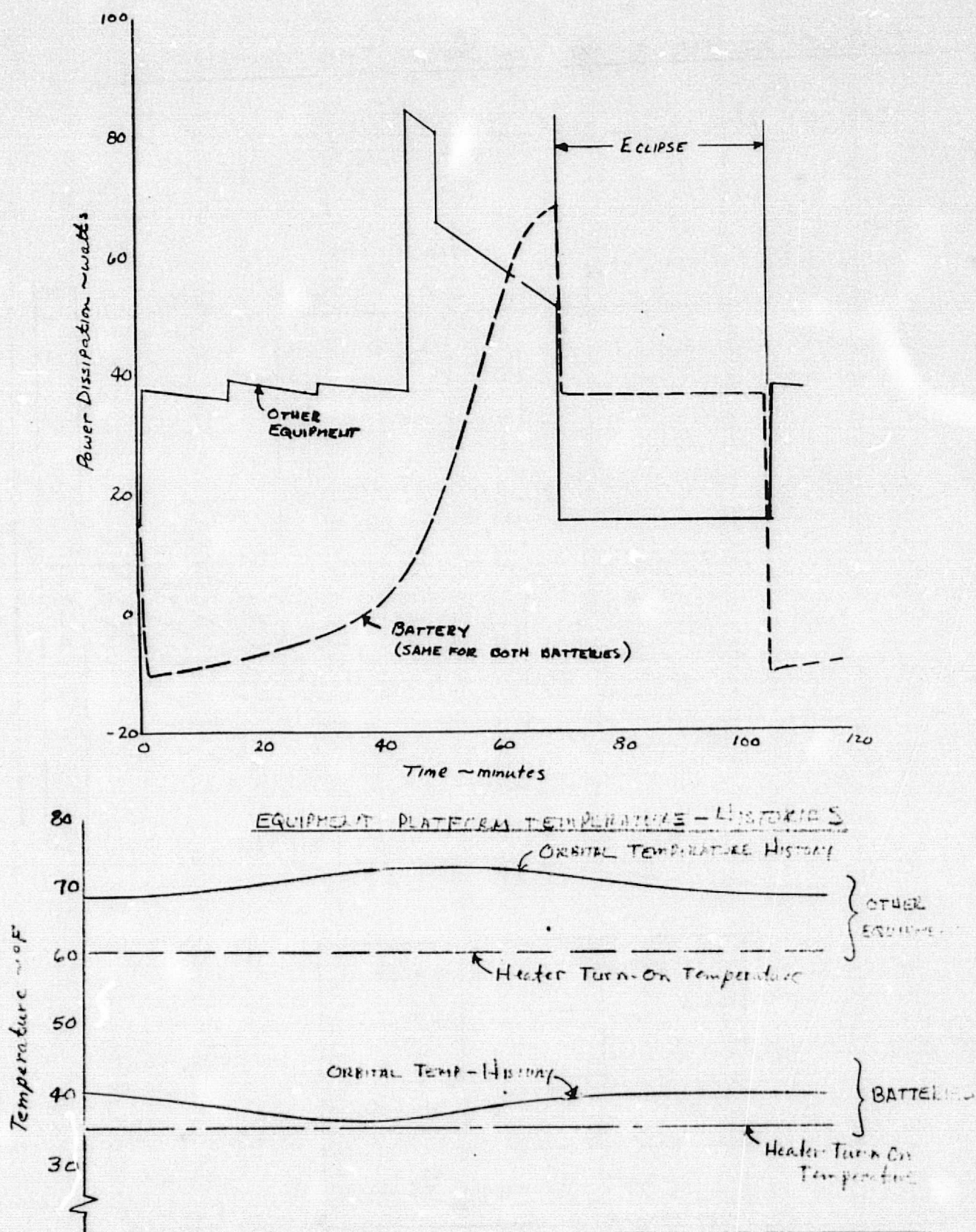


Figure 5-214. Heat Dissipation by Batteries and Electrical Power Subsystem Equipment





interface conductance ( $h_j$ ) of 10 BTU/ft<sup>2</sup>-hr or better). An arbitrary but realistic distribution of black boxes and heat dissipation (typical of real equipment) was used. Radiator areas were distributed on the platform to maintain an average temperature of 70°F and to minimize temperature gradients across the platform.

Attachment Temperature Characteristics: Transient analyses indicated that temperature fluctuations of the equipment platform are attenuated significantly before reaching the module to spacecraft attachment interface. A 10°F oscillation of the platform diminishes to less than 1°F at the attachment interface. Thus, the spacecraft structure will be relatively unaffected by dynamic changes including external heating environment and equipment operating duty cycles.

Platform Temperature Characteristics: A study of platform thickness requirements was made to determine typical temperature variations across the face of an equipment platform. Honeycomb platforms with inside face sheets of 0.012 and 0.024-inch were considered, and typical black boxes, ranging in heat dissipation from 2 to 8 watts were distributed on the platform, as shown in Figure 5-215. In general, the module radiator was adjacent to the heat dissipating black boxes.

Steady state temperatures for a typical case are indicated in Figure 5-215. The results indicate that the tubular frame around the edge of the platform adds appreciable conductance. Temperature variations in the platform are quite small except where the radiator is offset from the black box. Detailed analyses were not performed for each module because of lack of information on the platform layouts, black box sizes and heat dissipation. Extra weight has been set aside in the weight budget for use in localized doubler on the platforms to increase lateral conductance as required.

#### b. Effect of Deviations from Reference Orbit

The baseline thermal design is tailored to maintain each subsystem module at 70°F when the vehicle is in the 11:00 a.m. node/sun phase reference orbit. If the reference orbit spacecraft is to be operated in other orbits, such as the 6:00 a.m. twilight orbit or the 12:00 noon orbit, or in mode where the orbit plane regresses from the noon to the twilight orbit, then there is some penalty in heater power usage, unless the design is altered.



The baseline thermal design is adequate for any orbit from twilight to noon, provided that extra heater power is available. The table below indicates that an additional 16.2 watts (orbit-average) is needed to maintain all modules above 60°F in the 6:00 a.m. node/sun phase which has the lowest external heating environments.

<u>Module</u>	<u>Extra Heater Power for 6:00 a.m. twilight orbit</u>
Wideband Communications	4.0 watts
Comm. & Data Handling	5.0
Attitude Determination	10.5
Power Module	1.0
Actuation Module	-4.3
Propulsion	0
Solar Array Drive	<u>0</u>
Total	16.2 watts

c. Assessments of Uncertainties on Module Temperature Level

The subsystem modules are designed to operate at 70°F by a passive heat balance between the heat dissipated by the electronic units, and the heat rejected by the radiators. The on-orbit temperature level may deviate from desired 70°F due to the effects of uncertainties in the heating environments and in the spacecraft thermal properties.

This section presents an estimate of parameter uncertainty effects on the average module temperature and estimates additional heater power requirements to compensate for uncertainties. This analysis evaluates average temperature uncertainty due to parametry uncertainty, including the solar constant, the albedo, the emittance of the radiator, and the insulation effective emittance,  $\epsilon^*$ . The communication and data handling module was evaluated as a typical subsystem module. Table 5-90 shows the terms that were considered in the analysis, the estimated  $2\sigma$  variation of each and how each contributes to the total uncertainty of the module temperature level. This method of uncertainty analysis, which was developed by Camack and Edwards\*

---

\* W. G. Camack and D. K. Edwards, "Effect of Surface Thermal-Radiation Characteristics on the Temperature-Control Problem in Satellites", from First Symposium, Surface Effects on Spacecraft Materials, 12 May 1959.

Table 5-90. Uncertainty Analysis of the Orbit-Average Temperature of the Command and Data Handling Module

Parameter	Nominal Value	Estimated 2 $\sigma$ Variation	$\Delta T$ °F
• Solar Constant $\triangle$	430 Btu/ft <sup>2</sup> -hr	$\pm 2.5\%$	$\pm 0.1$
• Albedo	0.36	$\pm 0.05$	$\pm 5.7$
• Earth IR	68.8 Btu/ft <sup>2</sup> -hr	$\pm 5.4$	$\pm 5.7$
• Radiator Emittance	0.80	$\pm 0.04$	$\pm 3.4$
• Radiator Absorptance	0.12	$\pm 0.02$	$\pm 0.6$
• Equipment Heat Dissipation	40.1 watts	$\pm 5\%$	$\pm 3.4$
• Insulation $\epsilon^*$	0.005	$\pm 0.003$	$\pm 4.1$
RSS Total			$\pm 8.5$

$\triangle$  In addition,  $\pm 3.4\%$  seasonal variations contributed  $\pm 0.2^\circ\text{F}$  variation in temperature

shows that  $2\sigma$  uncertainty in each of the contributing sources can be estimated. Then, by definition, there is a 95 percent probability that the variation in the module's on-orbit temperature should be within the  $\pm 10^\circ\text{F}$  of our predicted temperatures.

It can be seen that the most significant sources of uncertainty are the radiator's emittance, the total power dissipation in the module, and the  $\epsilon^*$  of the insulation (its thermal conductance).

Using the power sensitivity value of  $1.7^\circ\text{F}/\text{watt}$  as tabulated in Table 3 for the command and data handling module, the additional heater power required because of the uncertainty is 5.0 watts.

#### d. Heater Power Savings Versus Risk

The radiator area for the baseline thermal design was based on a best estimate of insulation conductance ( $\epsilon^* = 0.005$ ) and on the assumption there are no miscellaneous heat leaks. This approach will result in a conservative area for the radiators and the need for heater power for cold case conditions. However, the possibility of the modules operating too warm is very remote because there undoubtedly will be heat leaks that cannot be identified a priori in the analysis. This approach leads to a small risk design and prevents underestimation of heater power requirements. A less conservative design approach reduces heater power requirements but at a higher risk. This approach bases the module radiator area on a larger heat loss through the thermal insulation ( $\epsilon^* = 0.01$ ) and in turn may yield module temperatures higher than desired under a  $2\sigma$  worst hot condition. Using an  $\epsilon^*$  of 0.01 rather than 0.005 reduces the radiator area for most of the modules by about 10% since the insulation heat losses increase about 5 watts. Figure 5-216 presents the results of this evaluation. It shows that if the module has no heat leaks except for the insulation ( $Q_L = 0$ ), and experiences a  $2\sigma$  worst case of uncertainties (heating environments, surface properties, insulation  $\epsilon^*$ , etc.), the orbit-average temperature of the module could be  $82^\circ\text{F}$ , or  $12^\circ\text{F}$  above the design condition. When orbital transients are considered, local areas of the platform will be operating at about  $90^\circ\text{F}$ . However, if heat leaks do occur, the peak orbit-average temperature is reduced about  $2^\circ\text{F}$  per watt leaked. Thus, it is unlikely that the orbit-average temperature would exceed  $80^\circ\text{F}$ .

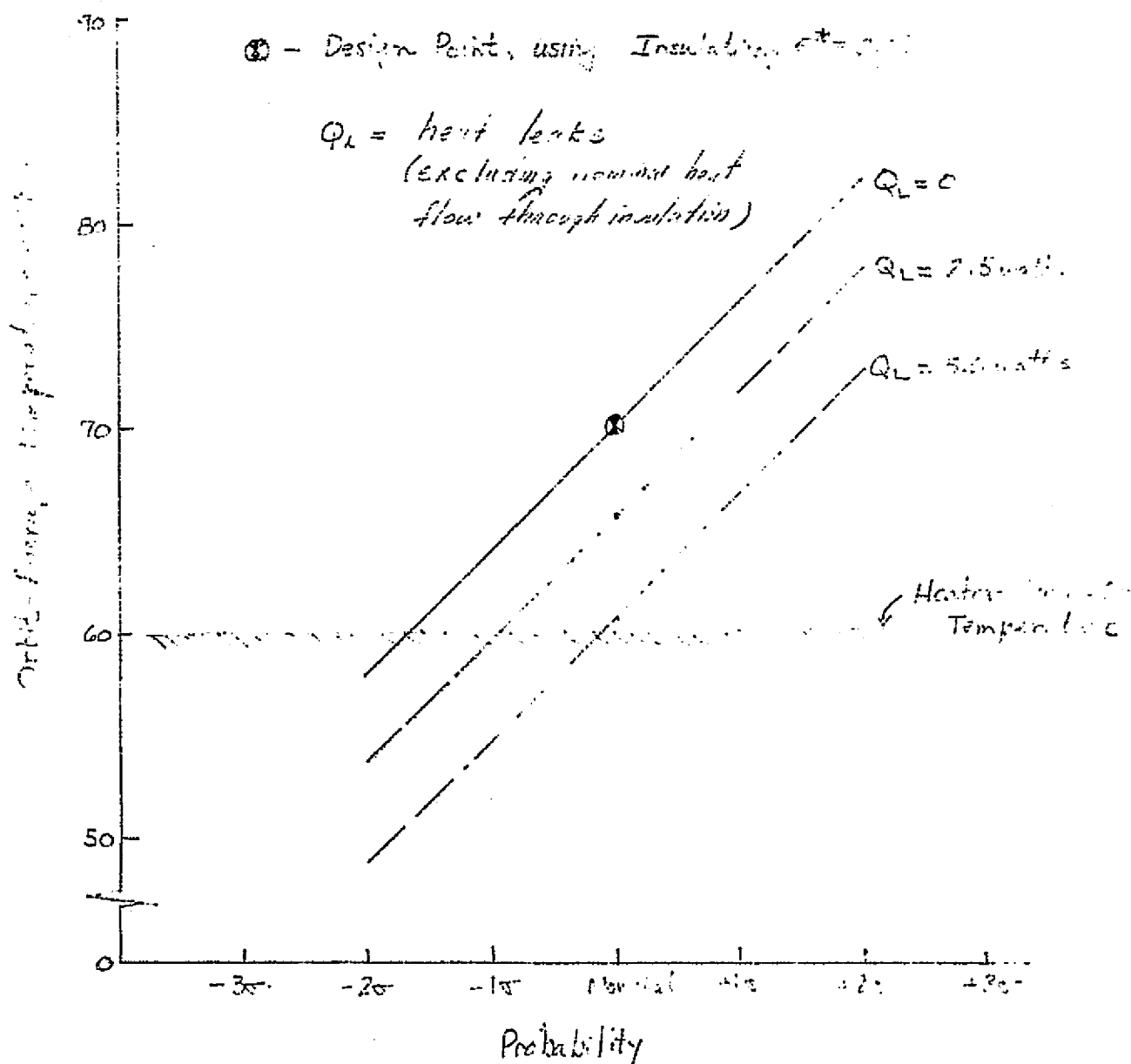


Figure 5-216. Orbit-Average Temperature of a Typical Subsystem Module for Nominal and Worst-Case Conditions

The following orbit-average heater power savings, for the 2σ cold case conditions, would be realized by this design approach:

<u>Module</u>	<u>Orbit-Average Heater Power Savings*</u>
Wideband Communications Module	8.2 watts
Attitude Determination	4.7
Command and Data Handling	4.7
Electrical Power System	4.7
Actuation System	4.7
Total	<hr/> 27.0 watts

e. Thermal Growth Potential

Thermal growth potential as defined pertain to the capability of accommodating subsystem growth including higher power dissipation and the capability to perform satisfactorily in other orbits other than the 11:00 node/sun phase Reference Orbit.

Accommodation of Subsystem Growth: In general, growth of equipment in a subsystem module will result in only a small direct thermal impact because only simple tailoring of the radiator area is required. In other words as a subsystem heat dissipation increases, the thermal design can be readily modified by enlargement of the radiator area to reject this additional heat. This represents a simple change. However, the need for additional electrical power to accommodate off-nominal conditions must be considered. No extra heater power is needed for nominal or hot conditions. The magnitude of heater power for cold conditions will increase in direct proportion to the increase in heat dissipation by the electronic equipment in the module.

Sufficient surface area is available for radiator enlargement. The largest radiator of the Reference Orbit design is located on the electrical power module and occupies only 25 percent of the available surface area.

The electrical power module may present a special problem if the number of batteries is increased from two in the baseline design to three or

four. Since the batteries must be maintained within a close temperature tolerance it may be necessary to add simple heat pipes to the equipment platform to provide adequate lateral conduction.

Accommodation of Other Orbits: The baseline thermal design is tailored to maintain the subsystem module at 70°F when the vehicle is in the 11:00 a.m. Reference Orbit. If the spacecraft is to be operated in other orbits, such as the 6:00 a.m. twilight orbit or the 12:00 noon orbit, or in a mode where the orbit plane regresses from the noon to the twilight orbit, then there will be either a design cost penalty or performance degradation. Performance degradation means to establish a passive thermal design and permit the module to operate over a wider temperature range due to the changing external environment. The change in orbit-average temperature varies from about 8°F for the command and data-handling subsystem to about 40°F for the actuation subsystem as indicated in Figures 5-207 to -211. Design cost penalty is associated with a solution to maintain a constant orbit-average temperature for various orbits by using added thermal control devices, such as variable-control heat pipes, louvers, or thermostatically controlled heaters. An examination of this problem eliminated heat pipes and louvers because the cost would be too high. The lowest-cost method of maintaining nearly constant operating temperatures would be to use thermostatically controlled heaters. An additional 16 watts (orbit-average) of electrical power would be needed to maintain the subsystem modules at a constant operating temperature regardless of the orbit plane as indicated in Section 4.6.2.

#### 5.5.3.4 Comparison of Titan and Thor/Delta Thermal Design Configurations

Thermal designs and analyses have been predicated on the subsystem module configuration associated with the Titan launch vehicle. A comparison of the Thor/Delta configuration to the Titan is presented in Figure 5-216. Only the attitude determination module has an identical orientation for both vehicle launches.

The module thermal designs for the Thor/Delta were based on the modularity concept of thermal independence. This means that:

- (1) Each subsystem module is conductively isolated from the spacecraft frame by high resistance mechanical attachments; and
- (2) Each subsystem module is radiatively insulated from the structural frame.

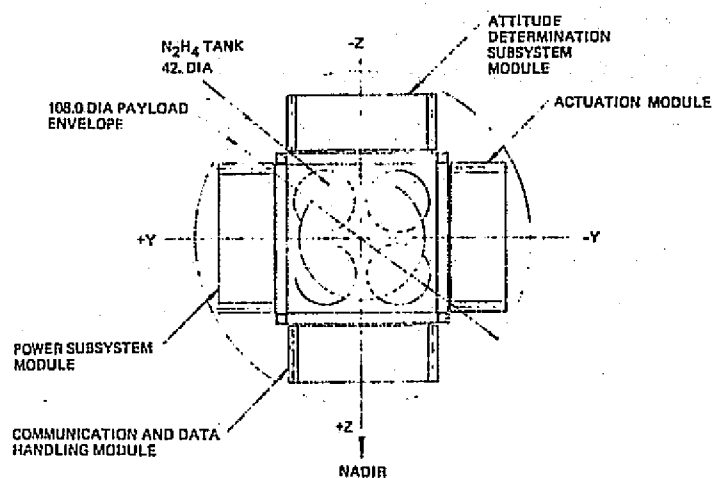
A comparison of absorbed external heat inputs for the 11:00 a.m. Reference Orbit and required radiator areas are presented in Figure 5-217. These results show that the command and data-handling module requires less radiator area, whereas the power system module requires about 20 percent more radiator area for the Thor/Delta configuration.

If the Thor/Delta configuration is to be flown on the 6:00 a.m. twilight orbit as well as the 11:00 orbit, then additional radiator area is required for the command and data-handling module, as the solar heating increases significantly. The changes in heat inputs to the other modules for various orbits is not appreciable, and does not require modifications to the radiator areas.

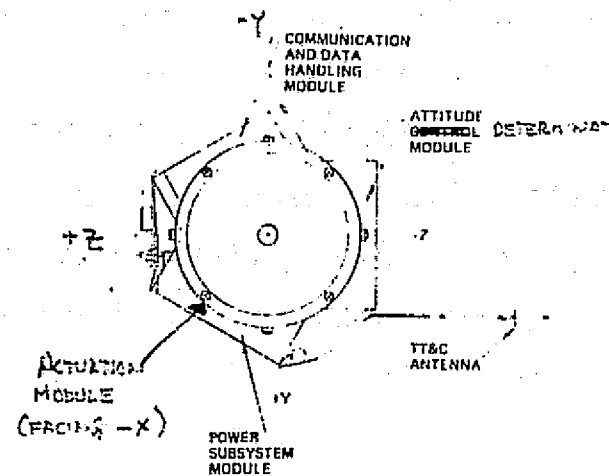
A major mission difference between Titan and Thor/Delta L/V that impacts the thermal design configurations is the resupply requirement for Titan and not for Thor/Delta. For the Thor/Delta, the thermal insulation can be custom fitted; this means that heat leak uncertainty for Thor/Delta is less than for Titan.

#### 5.5.3.5 Summary

A basically passive thermal design approach has been used to maintain subsystem modules (including the wideband communications module) at satisfactory operating temperatures. Heater power is required, however, to maintain the batteries within very narrow operating temperature/limits and to maintain the propulsion system above 40°F. All modules are equipped with thermostatically-controlled heaters to prevent module temperatures lower than 60°F in the event of a worst-case cold environment; this lower temperature control is provided to limit interface heat flow from the structure.



TITAN SUBSYSTEM CONFIGURATION  
(VIEWED FROM +X DIRECTION)



TITAN-DELTA CONFIGURATION  
(VIEWED FROM -X DIRECTION)

Subsystem Module	Orbit - Average Absorbed Heating $\Delta$ (BTU/(ft <sup>2</sup> -hr))		Radiator Area $\Delta$	
	Titan	Titan-Delta	Titan	Titan-Delta
Communication & Data Handling	52.4	41.1	2.47 m <sup>2</sup>	1.85 m <sup>2</sup>
Actuation System	27.3	21.5	1.82	1.83
Attitude Determination	15.6	15.6	1.93	1.73
Power System	13.6	28.2	4.0	4.87

$\Delta$  For Titan and Titan-Delta

Figure 5-217. Comparison of Launch Vehicles on Subsystem Modules Thermal Design

ORIGINAL PAGE IS  
OF POOR QUALITY



Uncertainty analyses indicate that the maximum orbit-average temperature will not exceed 80°F (on a  $2\sigma$  worst-case basis); this means that the maximum orbit-average temperature excursion of the module at the spacecraft fitting will not exceed  $\pm 10^\circ\text{F}$  above the nominal set point temperature of 70°F. This narrow module temperature swing with controlled structure temperatures and a reasonably high thermal resistance attachment fittings will limit heat flow at each module/structure attachment to less than one watt.

The baseline thermal design can readily accommodate the considered near-earth orbits with only a slight increase in heater power requirements if baseline control is maintained.

#### 5.5.4 Structure Thermal Design

Structure thermal control system (TCS) must limit structural temperature gradient and fluctuations to preserve structural alignment by satisfying thermal distortion pointing allocation. A TCS that not only meets these requirements but also meets other constraints including minimum cost at reasonable risk has required examination of various insulation and heater control methods, assessment of module/structure interactions, and generation of structural temperature maps. Selection of the preferred design was based on a comparison of relative cost, performance, margin and growth potential.

##### 5.5.4.1 Problem Discussion

Structure provides support for modules and sensors with the attachment method particularly significant in structural temperature control because of thermoelastic pointing requirements. Thermal distortion pointing allocation has both an uncertainty allocation of 30 arc secs between in-orbit calibration points and a rate of change allocation not to exceed 0.01 degrees/hour. These highly accurate pointing requirements of instruments coupled with the long distance between instrument and attitude determination module requires a dimensionally stable structure. The periodic in-orbit pointing calibration suggests that appreciable deterministic temperature gradients are permissible thus the structure temperature distribution uncertainties and fluctuations must be limited between orbital calibration points. Dynamic thermal distortion requirements impacts allowable rate of structural temperature change. The structural alignment requirement must be compatible with other considerations including:

#### Control Methods

- High efficiency multilayer insulation to temper natural (external) and radiative (internal) environments
- Module/structure thermal interface control with mechanical and temperature gradient control
- Heater circuits to control temperature level, distribution and fluctuations
- Effective emittance (or equivalent conductance) range
- Interface
  - Resistance range
  - Temperature gradient range
- Number and placement of heaters
- Type of heater control
  - Thermostatic
  - Computer
  - Electronic switching
  - Ground command
- Temperature level

Each module and sensor is attached to the spacecraft structure with four fittings, one at each corner of the inboard side. A design objective is restriction of this interface heat flow to a reasonable level of less than 1 watt per attachment point. This goal is achieved by controlling structure/module temperatures with heaters and by mechanical design of attachment fittings to provide a reasonably high resistance. Design goal is a resistance of  $> 10 \text{ Hr-}^\circ\text{F/BTU}$  but spacecraft thermal control system is based on a value of  $5 \text{ Hr-}^\circ\text{F/BTU}$ , which can be attained with use of titanium fittings, minimal contact area, and fiberglass isolation as discussed in Section 5.5.2 and illustrated in Figure 5-218.

Fluctuation of the module temperature near the attachment fitting is tempered considerably by the time constant effect between the attachment and radiator with the result that temperature swing and rate of change at the attachment point is small.

#### 5.5.4.2 Physical and Thermal Characteristics used in Math-Model

- Structural Members (Aluminum)
  - Conductivity =  $100 \text{ Btu/hr-ft-}^\circ\text{F}$
  - Density =  $0.1 \text{ lb/in}^3$
  - Specific Heat =  $0.2 \text{ Btu/lb-}^\circ\text{F}$

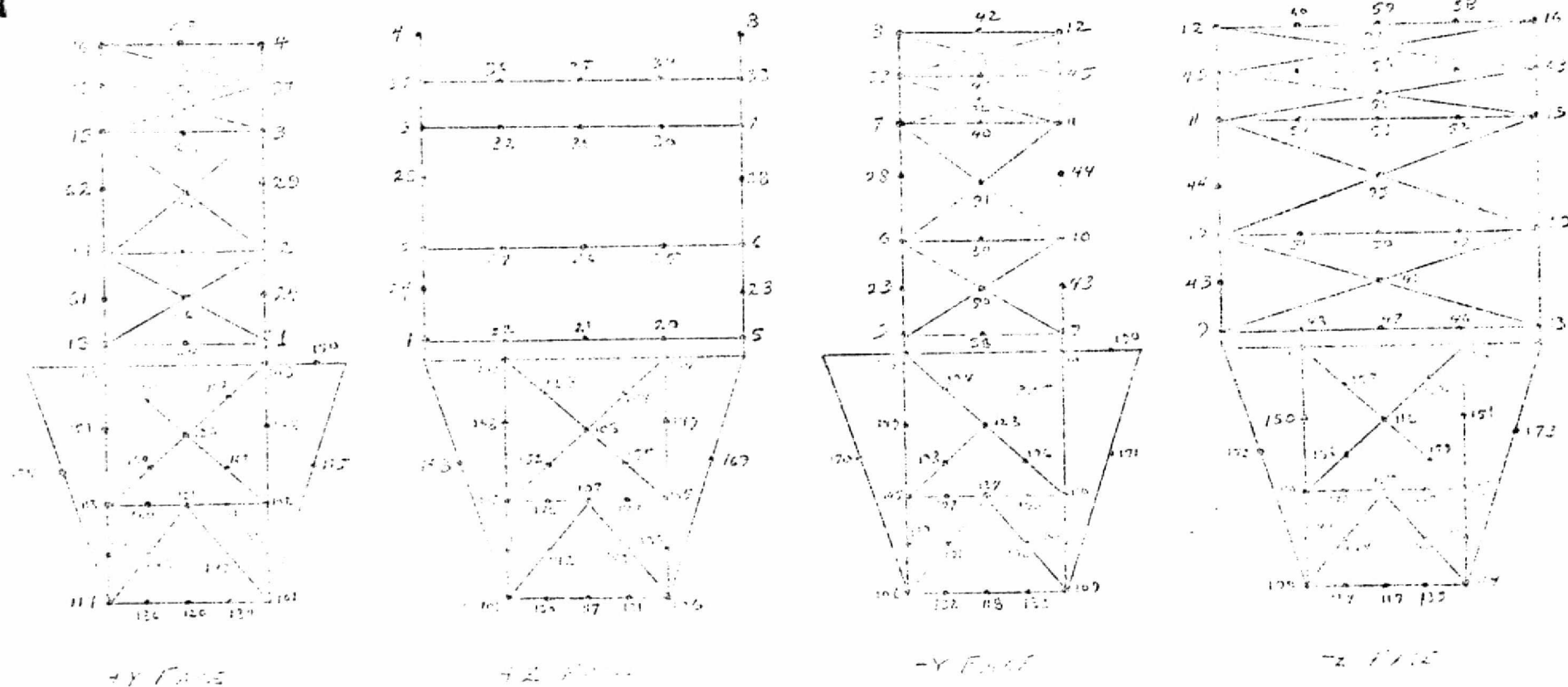


Figure 5-218. EOS Structure Thermal Math-Model Showing Nodalization and Node Numbers

- Multi-Layer Insulation (> 20 layers 1/4-mil aluminized Mylar)
  - Effective Emittance ( $\epsilon^*$ ) = 0.01
  - Density = 0.1 lb/ft<sup>2</sup>
  - Specific Heat = 0.3 Btu/lb-°F
- Outer Layer of Multilayer Insulation
  - (a) Silvered Teflon
    - Emittance = 0.78
    - Solar Absorptivity = 0.08 (initial)  
0.13 (degraded)
  - (b) Aluminized Kapton
    - Emittance = 0.80
    - Solar Absorbtivity = 0.4 (initial)  
0.50 (degraded)
- Environmental Characteristics
  - Solar Constant = 416 to 443 Btu/hr-ft<sup>2</sup>
  - Albedo = 0.3
  - Effective Earth Temperature = 458°R
  - Orbit Altitude = 386 nmi
  - Node to Sunline Phases = 6 am to 6 pm
- Module Interfaces
  - Maximum Conductance Per Mount Point = 0.2 Btu/hr-°F
  - Module Attachment Temperature = 70 ± 10°F (Sinusoidal variation)

- (1) Accommodation of Environmental Conditions for the following Orbits.
  - Circular, sun-synchronous  
Altitude (h) = 300 - 900 nmi (with corresponding inclination range from 97.7° to 103.1°)
  - Node/sun phasing from 6 am to 6 pm
  - Reference orbit (h = 386 nmi, i = 98.4° and 11am phasing of node to sun line)
- (2) Provision for module/structure isolation as required by the mechanical/temperature method used by TCS.
  - Isolation specifics are discussed in Section 5.5.2
- (3) Satisfaction of 3-year mission life performance of thermal control elements (coatings, insulation, heaters, etc.).
- (4) Provision for design flexibility and growth margin.
- (5) Provision for module replacement in orbit (for Titan L/V but not for Thor/Delta).
- (6) Minimum total program cost but with reasonable risk factors.

Accommodation of alignment requirements is a coupled structural-thermal consideration involving a number of interacting factors affecting performance. Important factors with variability considerations consist of:

- |  |   |
|--|---|
| <p>(1) Performance Factors</p> <ul style="list-style-type: none"> <li>• External Environment               <ul style="list-style-type: none"> <li>- Solar</li> <li>- Albedo (earth reflected solar)</li> <li>- Earth emission</li> </ul> </li> <li>• Induced Environment               <ul style="list-style-type: none"> <li>- Module/structure interface</li> <li>- Payload structure/transition ring interface</li> <li>- Heat leaks</li> </ul> </li> </ul> | <p>Variability Considerations</p> <ul style="list-style-type: none"> <li>• Orbit               <ul style="list-style-type: none"> <li>- Altitude</li> <li>- Node/sun phasing</li> </ul> </li> <li>• Interface               <ul style="list-style-type: none"> <li>- Conductive interface resistance</li> <li>- Temperature gradient across interface</li> <li>- Radiative interchange</li> </ul> </li> </ul> |
| <p>(2) Control Parameters</p> <ul style="list-style-type: none"> <li>• Temperature level</li> <li>• Temperature distribution</li> <li>• Temperature fluctuations</li> </ul>  |   |

#### 5.5.4.3 Analysis and Trades

##### 5.5.4.3.1 General Consideration

Analysis of various thermal control designs was conducted by exercising a multi-node model of the structure. This model as shown schematically in Figure 5-218 has approximately 200 nodes. Timewise temperature maps generated for various conditions and thermal designs were used for thermal distortion evaluation. Since in-flight pointing calibration will be conducted, deterministic thermal distortions will be accommodated by biasing. This means that only the uncertainty and dynamic pointing between calibration points need to be considered; periodicity of calibration has not been specified since it is a variable dependent upon many factors (refer to Appendix A, Section 5.2.7) but a reasonable maximum period is twenty-four hours with shorter periods of say once per orbit being more nominal.

Structure temperature changes from a calibration point are due to: (1) changes in the external environment; (2) changes in module/sensor temperatures; and (3) perturbations induced by a structure heater system.

##### 5.5.4.3.2 Design Characteristics and Trades

Basically, the thermal design approach consisted of attenuating external heating effects, of minimizing module/structure interface heat flow, and of controlling structure temperature level.

###### a. External Environment Attenuation and Effects

Structure temperature variations induced by the external environment is attenuated significantly by insulating the structure with multi-layer insulation (> 20 layers, 1/4 mil Mylar). The outside layer is aluminized Kapton (silvered Teflon was also studied as an outside layer). Since the modules are to be re-supplied for the Titan configuration, the inside surface of the structure is also insulated; for the Thor/Delta configuration, the inner structure insulation blanket is not necessary.

### Structure Time Constant

Effect of the external environment on an insulated structure can be readily evaluated from the structural time constant with external heating as the excitation (refer to Figure 5-219). This time constant is expressed as:

$$\tau = \frac{(WC_p)_s}{\epsilon^* \sigma (T_s^2 + T_I^2) (T_s + T_I) A_{Is}} \quad (1)$$

where:

$\epsilon^*$  = Effective emittance of insulation

$A_{Is}$  = Effective radiative area between structure and outer insulation layer

$(WC_p)_s$  = Thermal capacity of structure element

$T_s$  = Structure temperature

$T_I$  = Outer insulation temperature

For,

$$\epsilon^* = .01$$

$$T_s = 530^\circ R$$

$$T_I = 360^\circ R$$

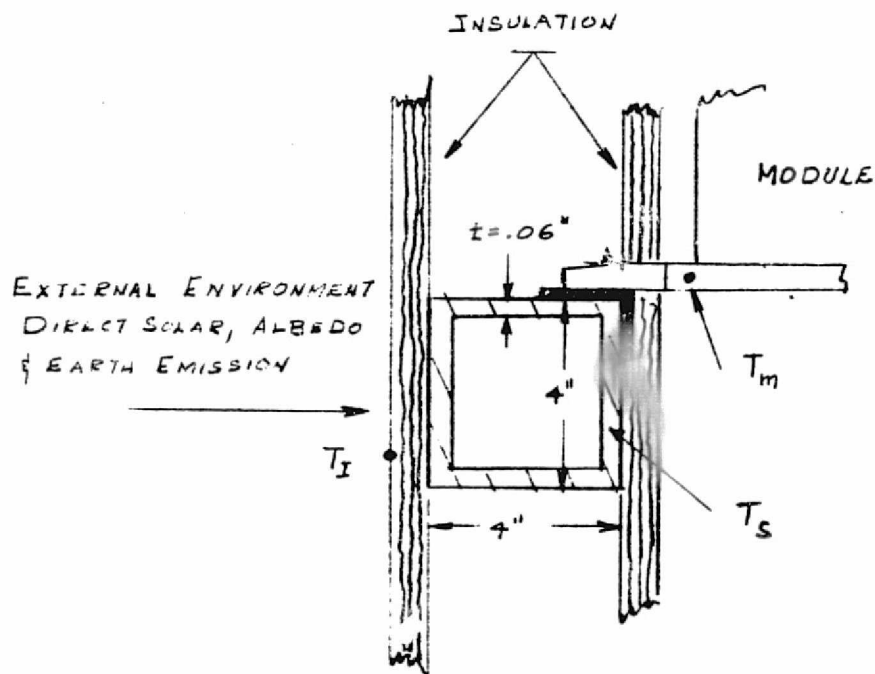
$$A_{Is} = \frac{8}{12} \times L \quad (L = 1 \text{ ft})$$

$$W = 1.15 \text{ lb}$$

$$C_p = 0.2 \text{ BTU/lb } ^\circ F$$

$$\tau = 55 \text{ hr}$$





$T_s$  = TEMPERATURE OF STRUCTURE

$T_m$  = TEMPERATURE OF MODULE AT ATTACHMENT

$T_I$  = TEMPERATURE OF OUTER INSULATION LAYER

Figure 5-219. Module/Structure/Insulation Math-Model for Time-Constant Evaluation

Since the orbital period (<2 hours) is much less than the structure time constant, effect of orbital heating variations are significantly attenuated and thus may be replaced with orbital average inputs.

#### Insulation Characteristics and Heater Power Requirements

Insulation characteristics of the structure are important from the standpoint of heater power requirements to maintain a specified temperature level. For a uniformly heated structure (payload, subsystem and transition ring), the heater power requirement as function of average structure temperature is displayed in Figure 5-220. These results used, an effective MLI emittance,  $\epsilon^*$ , of 0.01 which represents a reasonably attainable value based on past TRW experiences; heater power requirements are a direct function of  $\epsilon^*$ . Note that the outside insulation characteristics has appreciable impact on the heater power required to maintain a specified temperature. Silvered Teflon outer layer provides more structural distribution uniformity than aluminized Kapton but is not particularly important since the deterministic gradients may be biased-out by in-flight calibration. Node to sun line phase from 6 a.m. to 6 p.m. has little effect on the heater power requirements.

#### b. Module/Structure Interface

Importance of module/structure interface heat flow can be gauged from the structure time constant with the interface as the excitation. This time constant is expressed as:

$$\tau = \frac{(WC_p)_s}{G_{SM}}$$

where:

$G_{SM}$  = Module/structure interface conductance

for, structural element length = 2 ft

$$G_{SM} = 0.2 \frac{\text{BTU}}{\text{Hr} \cdot ^\circ\text{F}} \quad (G_{SM} = \frac{1}{R_{SM}})$$

$$\tau = 2.3 \text{ Hours}$$

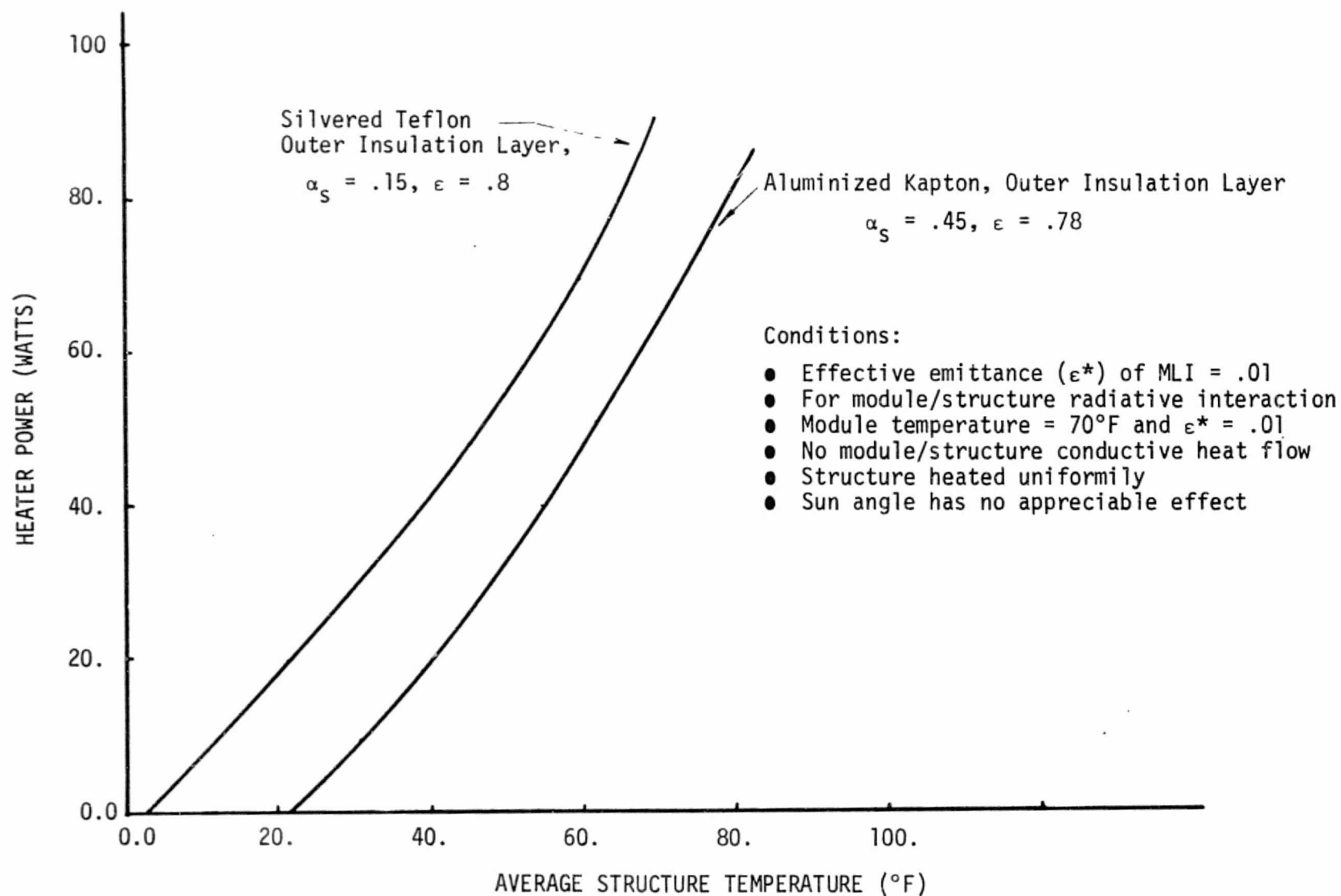


Figure 5-220. EOS Structure Heater Power Requirements

This means that variations in interface heat flow is important since the structure will react to this heat flow.

Each module and sensor is attached to the spacecraft structure with four fittings, one at each corner of the inboard side. A design objective is restriction of this interface heat flow to a reasonable level of less than 1 watt per attachment point. This goal is achieved by controlling structure/module temperatures with heaters and by mechanical design of attachment fittings to provide a reasonably high resistance. Design goal is a resistance of  $> 10 \text{ Hr} - ^\circ\text{F}/\text{BTU}$  but spacecraft thermal control system is based on a value of  $5 \text{ Hr} - ^\circ\text{F}/\text{BTU}$ , which can be attained with the use of titanium fittings, minimal contact area, and fiberglass isolation as discussed in Appendix A, Section 5.5.2.

Fluctuation of module temperature is attenuated considerably by the time constant effect between attachment and radiator with the result that temperature swing and rate of change at the attachment point is small. Details are reported in Appendix A, Section 5.5.3. For evaluating the impact of heat flow on the structure, a sinusoidal approximation of the module temperature fluctuation was used.

#### c. Control of Structure Temperature Level and Distribution

Control of structure temperature was centered on the use of independently controlled heater circuits with the structure sandwiched with multi-layer insulation. Since initial study results indicated that heater circuits can induce significant structural thermal transients relative to those by either the external environment or the module/structure interface heat flow, a number of control methods were examined to minimize or eliminate these thermal transients but at a reasonable cost. Heater placement and number were also part of the investigation. Heater-induced thermal transients can be minimized by reducing the temperature control "dead-band" or eliminated by having constant power heater circuits. The temperature "dead-band" can be reduced by using either computer-control or electronic switching. A constant power heater circuit requires either voltage regulation or computer-control with electronic switching since the bus voltage swings from 26 to 32 volts. Various control methods with design characteristics and performance characteristics are summarized in Table 5-91. These performance characteristics for comparative purposes are expressed in terms of a temperature rate change. Thermoelastic distortion results indicated a degree of correlation with average temperature of vertical members. Alignment due to structure-thermal

Table 5-91. Summary of Structure Heater Control Methods and Design Characteristics

CONTROL METHODS	DESIGN CHARACTERISTICS
1. Power Requirements	<ul style="list-style-type: none"> <li>64 watts to maintain orbital average temperature of 70°F (Refer to Figure 2).</li> </ul>
2. Number of Circuits	<ul style="list-style-type: none"> <li>Variable, from 9 to 36 circuits depending upon control methods.</li> </ul>
3. Control Methods	
3.1 No Heaters	<p>Performance</p> <ul style="list-style-type: none"> <li>Not satisfactory (temperature transient = 8.0°F/hr)</li> </ul> <p>Comments</p> <ul style="list-style-type: none"> <li>Large uncertainty and risk</li> <li>No positive control with temperature level governed by natural and induced environments</li> <li>Interface heat flow much greater than the desired one-watt per attachment</li> </ul>
3.2 Temperature-Controlled	
(1) Thermostatic	<p>Performance</p> <ul style="list-style-type: none"> <li>9 circuits: Marginal (temperature transient = 16°F/hr)</li> <li>36 circuits: Satisfactory (temperature transient = 4°F/hr)</li> </ul> <p>Comments</p> <ul style="list-style-type: none"> <li>Pre-flight temperature setting</li> <li>Heater-induced thermal transients</li> <li>No in-flight adjustments</li> <li>Reasonable risk for 36-circuit design</li> </ul>
<ul style="list-style-type: none"> <li>9 circuits</li> <li>36 circuits</li> <li>Cost, \$1K/circuit</li> <li>Dead-Band = 10°F (minimum)</li> </ul>	
(2) Computer (with auxiliary units)	<p>Performance</p> <ul style="list-style-type: none"> <li>Not studied but expected to be satisfactory</li> </ul> <p>Comments</p> <ul style="list-style-type: none"> <li>Some heater-induced transients</li> <li>Has in-flight adjustment of temperature setting, "Dead-Band" width, etc capability</li> <li>Number of circuits, nine</li> <li>Reasonable risk</li> </ul>
<ul style="list-style-type: none"> <li>Used in on-off thermostatic sense</li> <li>Cost, function of number of circuits (For 9 circuits, = \$40K)</li> </ul>	

Table 5-91. Summary of Structure Heater Control Methods and Design Characteristics (Continued)

CONTROL METHODS	DESIGN CHARACTERISTICS
<p>3.3 Power Level Control</p> <p>(1) Unregulated</p> <ul style="list-style-type: none"> <li>● Pre-flight power setting</li> <li>● Cost, &lt; \$10K (9 circuits)</li> </ul> <p>(2) Regulated</p> <ul style="list-style-type: none"> <li>● Pre-flight power setting</li> <li>● Cost, &gt; \$50K (9 circuits)</li> </ul> <p>(3) Computer with Electronic Switching</p> <ul style="list-style-type: none"> <li>● Power slicing method prevents heater induced transients</li> <li>● Cost, = \$40K (9 circuits)</li> </ul>	<p>Performance</p> <ul style="list-style-type: none"> <li>● Not studied but expected to be unsatisfactory</li> </ul> <p>Comments</p> <ul style="list-style-type: none"> <li>● In-flight power level variation of 50 percent due to swinging bus voltage of 26 to 32 volts</li> </ul> <p>Performance</p> <ul style="list-style-type: none"> <li>● Satisfactory (temperature transient = 4.5°F/hr)</li> </ul> <p>Comments</p> <ul style="list-style-type: none"> <li>● No heater-induced thermal transients</li> <li>● Number of circuits, nine</li> <li>● No in-flight adjustment</li> <li>● Reasonable risk</li> </ul> <p>Performance</p> <ul style="list-style-type: none"> <li>● Satisfactory (temperature transient = 4.5°F/hr)</li> </ul> <p>Comments</p> <ul style="list-style-type: none"> <li>● Software (simple or sophisticated)</li> <li>● Small risk</li> <li>● In-flight adjustment of power level, temperature, level, etc</li> <li>● Number of circuits, nine</li> </ul>

considerations were discussed previously. A description of these heater control methods follows:

(1) No Heaters on Structure

This method requires no additional cost but the structure temperature is dependent upon the insulation characteristics, the external environment and interface heat flow. With silvered Teflon as the insulation outer surface, the structure orbital average operating temperature would be approximately 0 °F. With an aluminized Kapton outer surface, the structure temperature is about 20 °F. These low structure temperatures allows considerably more module/structure heat flow than the desired one-watt per attachment point, which negates the modularity concept.

The average temperature rate change of a vertical member is about 8 °F/hr, which is higher than other methods but appears to be within the allowable distortion limits. However, high uncertainty and risk, no positive control, and particularly excessive module/structure interface heat flow are factors that makes a no-heater system unacceptable.

(2) Temperature-Control

Temperature-controlled heaters typically have ON-OFF elements such as thermostats which have minimal "dead-band" range from 6 to 10 °F. This "dead band" which generates heater-induced thermal transients can be minimized or eliminated by using other methods such as electric switching and computer control. If thermostats are used, "dead-band" effects can be tempered by using a large number of independent heater circuits. Unless the number of heater circuits can be eliminated, electronic switching and computer-control are considerably more expensive than thermostatically controlled heaters because of the need for auxiliary units such as signal conditioning and relay drivers.

Thermostatically-controlled heaters are examined here; electronic-switching and computer control are discussed in the following section since these methods are used more effectively as power-level controller. Since cost is a function of the number of circuits, both 9 and 36 independent heater circuits were studied. The nine-circuit design had one on each corner member of the payload and subsystem structures and one circuit on the transition ring. With a "dead band" of 10 °F, the temperature change of vertical members were excessive.

With 36 independent heater circuits, the rate change of structure temperatures were much lower and satisfactory from a distortion standpoint; the lower temperature rate change is due to the averaging effect of the large number of circuits. This performance is achieved with a cost penalty. The thermostatic-control method provides positive control within the framework of pre-flight temperature setting.

### (3) Power-Level Control

For ON-OFF heater control methods, with appreciable "dead band", heater-induced transients cannot be sufficiently tempered unless a large number of circuits are used. An alternative to On-Off temperature control is power level control. The simplest is the unregulated method but the heater induced transients caused by 50 percent power variation because of swinging bus voltage, nominally from 26 to 32 volts, are unacceptable.

A combination computer-control with electronic switching appears to offer a cost-effective way of maintaining a constant power level. The constant power is maintained by power slicing; this means that the ON-OFF switching is very rapid relative to the thermal time constant and electronic switching is required from a reliability standpoint. A schematic of this method is illustrated in Figure 5-221.



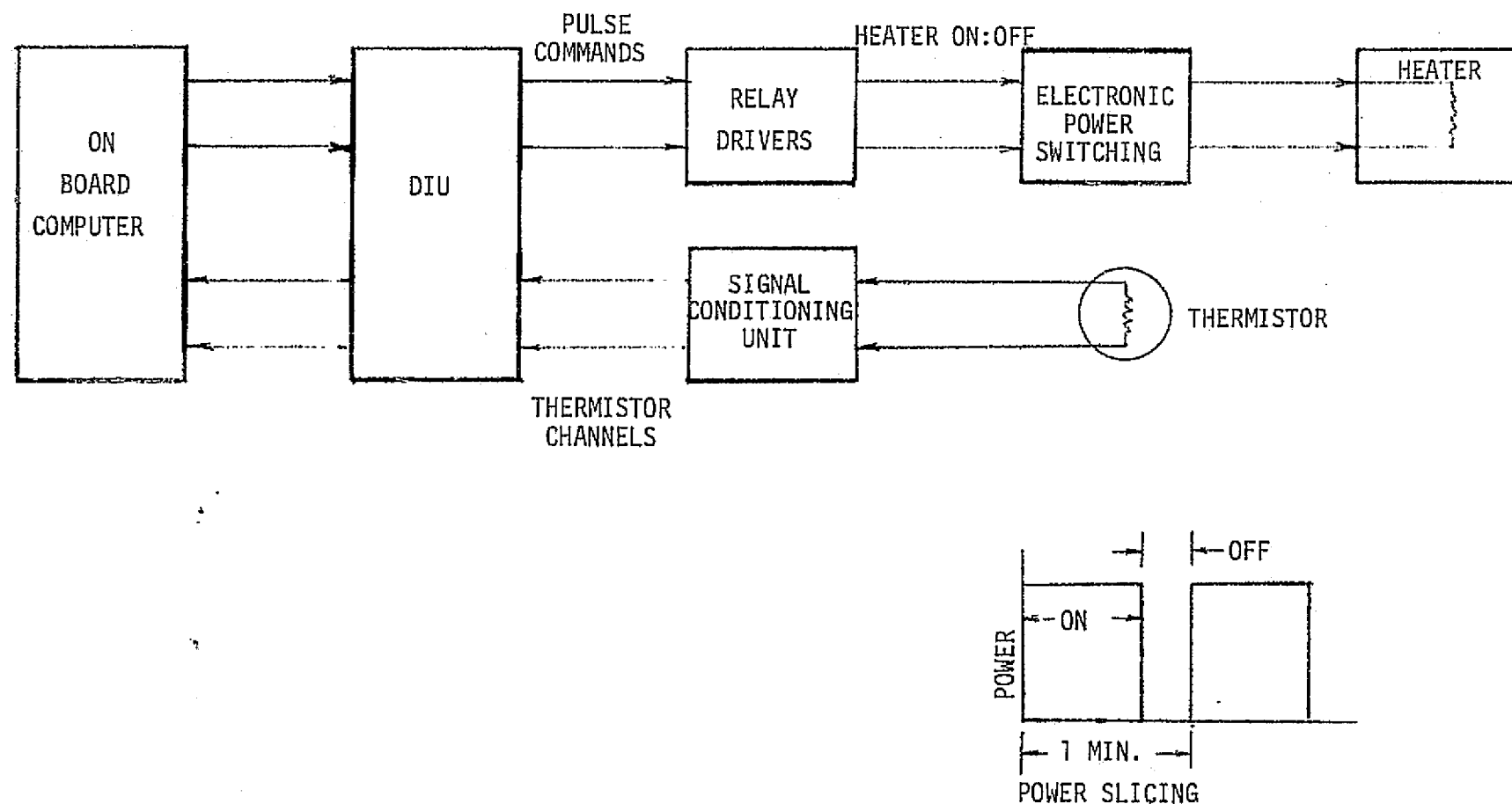


Figure 5-221. Schematic of Computer/Electronic Switching Power Level Control of Heater Circuits

With a constant power level, the change in structure temperature is due primarily to the module/structure interface heat flow with a sinusoidal approximation; this temperature rate change is about the same as the 36-circuit thermostat design.

#### 5.5.4.3.3 Structure Temperature Display - Constant Power Level Control

##### a. Nominal Conditions

Structure temperature transients are displayed in Figure 5-222 for two vertical members of the payload structure. Note that a  $\pm 10^{\circ}\text{F}$  module temperature swing at the attachment points induces a  $\pm 1.5^{\circ}\text{F}$  temperature variation in the structure. In general, the module temperature variations at the attachment will be much less than  $\pm 10^{\circ}\text{F}$ . Note that the required power level for this case is 55 watts since the average structure temperature is about  $65^{\circ}\text{F}$ .

A structure temperature map corresponding to the time point 0.0 hr of Figure 5-222 is displayed in Figure 5-223.

##### b. Heater Failure Condition

It is of particular interest to examine a heater failure condition; if a heater on the payload were to fail, the response of vertical members using the ensuing period is shown in Figure 5-224. These results indicate a gradual temperature decay of the vertical member to a lower quasi-steady condition. Since the larger temperature gradient can be biased-out by calibration, alignment difficulties would not be anticipated.

#### 5.5.4.4 Titan and Thor/Delta Structure Thermal Designs

Basically, thermal design of the Titan and Thor/Delta configurations are the same except for details since modularity has been applied to both. Design differences are due to: (1) the resupply requirement for Titan and not for Thor/Delta; and (2) the square-shaped Titan subsystem structure versus the triangular Thor/Delta subsystem structure.

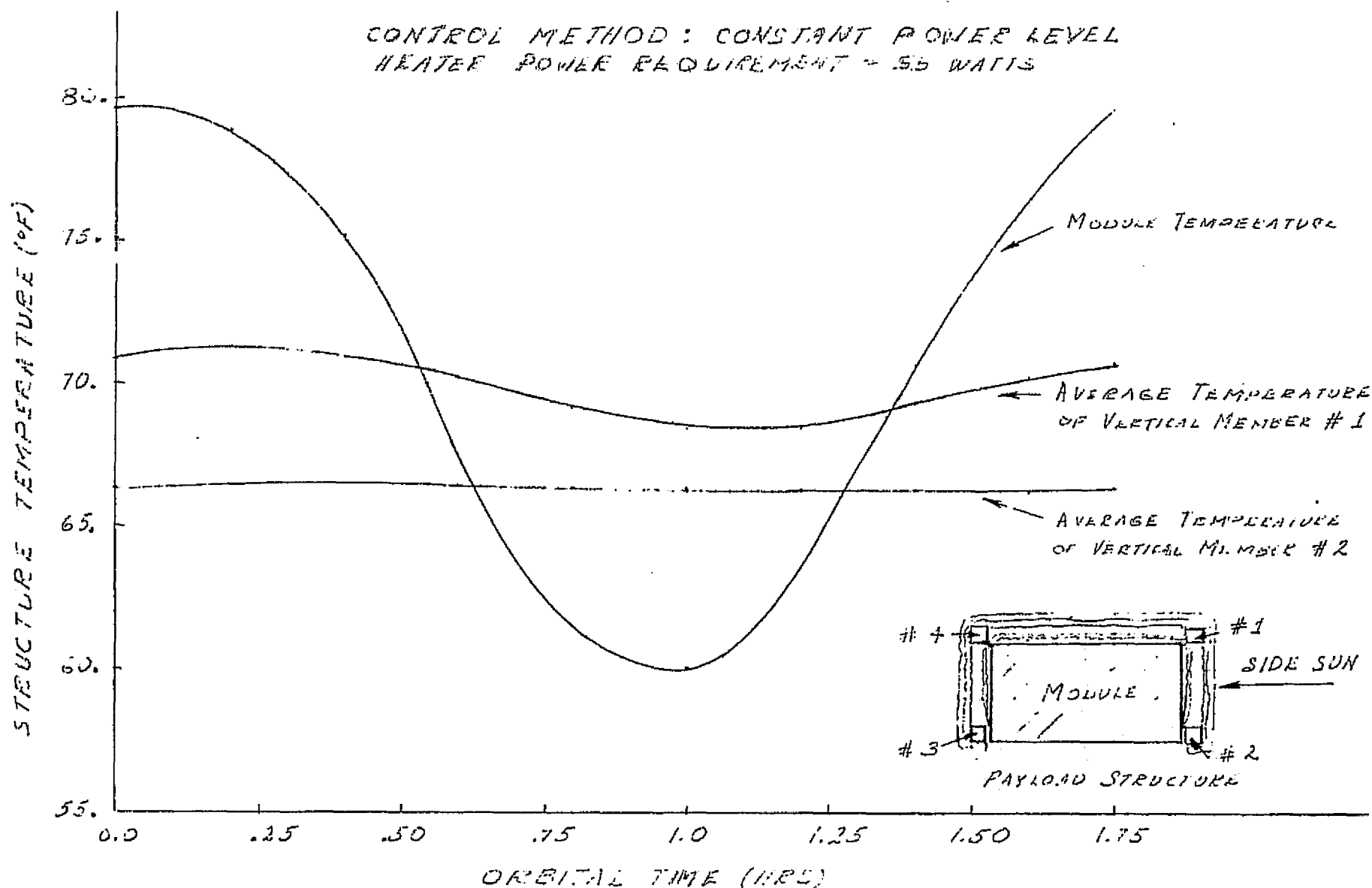
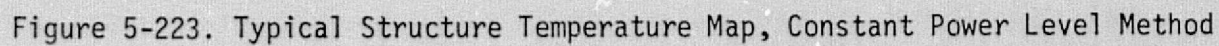


Figure 5-222. Structure Response to Module Temperature Variations

5-599



C-5

STRUCTURE TEMPERATURE (°F)

5-600

CONTROL METHOD: CONSTANT POWER LEVEL  
HEATER POWER REQUIREMENT = 64 WATTS  
MODULE TEMPERATURE VARIATION  $70 \pm 10^\circ\text{F}$

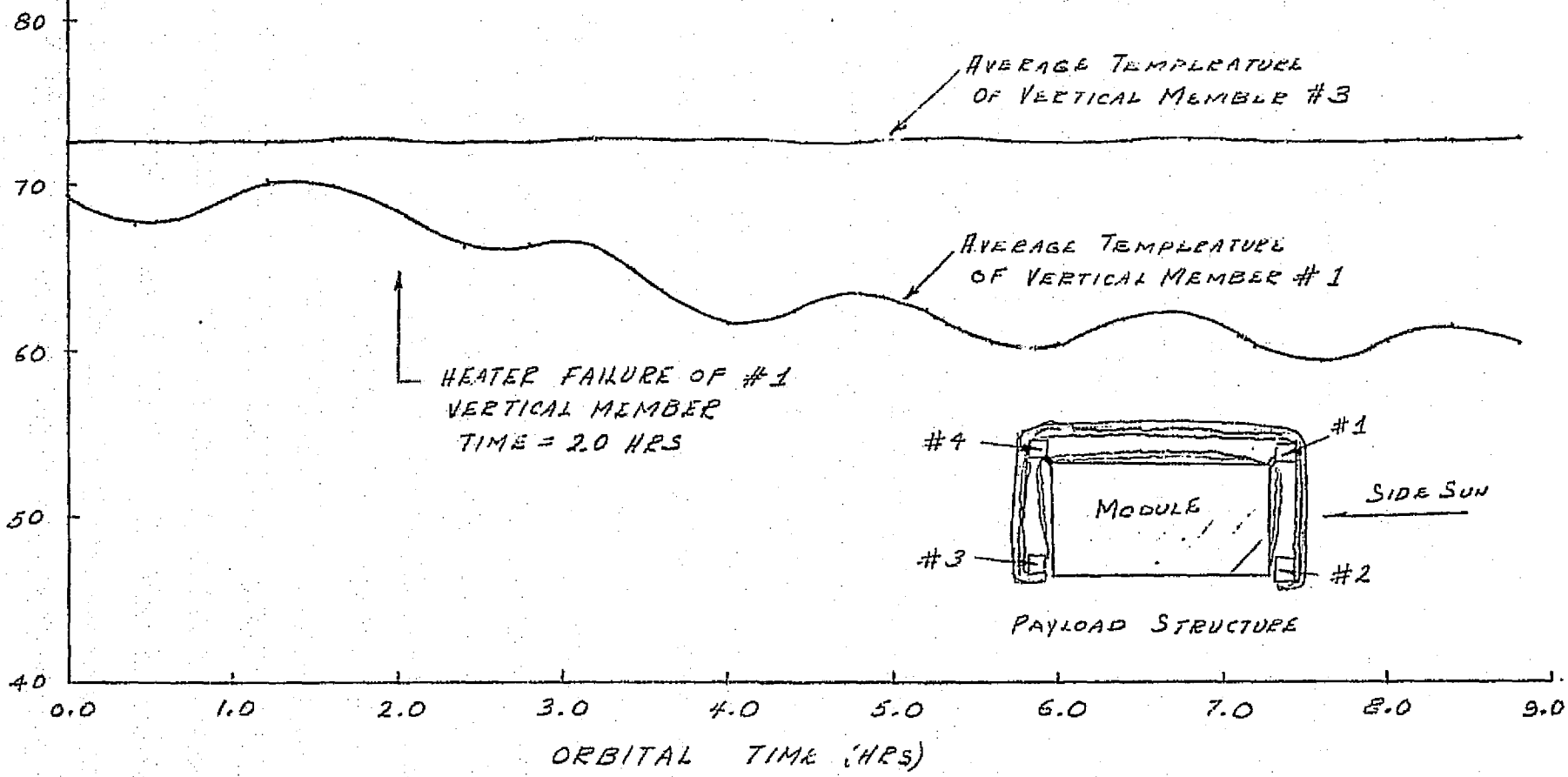


Figure 5-224. Effect of Heater Failure on Structure Temperature

Both configurations will employ computer-controlled heaters on structure which is blanketed with multilayer insulation. Since the Thor/Delta configuration need to be resupplied and thus the insulation custom installed, heat leak uncertainty should be significantly less than the Titan configuration.

#### 5.5.4.5 Summary

The results of this study indicate the following:

- (1) For an insulated structure, orbital average external heat input can be used since the time constant of the structure to external inputs is approximately 30 orbit periods;
- (2) A structure without heaters allows a strong module/structure interaction that negates the modularity concept;
- (3) Temperature-controlled heaters system with large "dead band" such as thermostats induce significant temperature transients that can be tempered satisfactorily only with a large number of circuits;
- (4) Power level controlled heater eliminates heater induced thermal transients and provides effective control with only 9 heater circuits.
- (5) Approximately 64 watts of structure heater power is required to maintain an average structure temperature of 70 °F.

#### 5.5.4.6 Recommendation

A power level controlled heater system consisting of computer control with electronic switching is recommended.

## 5.5.5 Impact of Sun-Orbit Geometry

### 5.5.5.1 Task Description

The TRW point designs are based on a specific orbit but accommodates a range of orbits that correlates with various land resources missions (LRM). Impact on the module and instrument point thermal design for the various mission are examined.

### 5.5.5.2 Mission Modes and Characteristics

#### TRW Point Design

- Altitude = 386 nmi
- Inclination = 98.4°
- Node/sun phasing = 11 am phasing of node to sunline

#### Orbits Accommodated by TRW Design

- Altitude range, 300-900 nmi
- Circular, sun synchronous with a corresponding inclination range from 97.7° to 103.1°
- Node/sun phasing from 6am to 6pm (arbitrary)

#### Future Orbits

- Geosynchronous, sun angle assumed to vary  $\pm 23.5^\circ$  from X-Z plane

#### Mission Modes

- Launch
- Transfer orbit
- Shuttle replenishing

### 5.5.5.3 Study Approach

Impact of various orbits on the modular thermal design can be represented in a number of ways but the rejection capacity of radiators on the S/C faces offers a concise and clear display. Thermal properties of second surface mirrors (SSM) on radiators were used for this evaluation.

Impact of non-orbital mission modes was evaluated in a general sense because these modes are usually of short duration and serious impacts can be generally controlled by mission mode constraints.

#### 5.5.5.4 Study Results

##### 5.5.5.4.1 Orbital Mode

- Node/sun phasing effects on the radiator heat rejection capability on various S/C faces are indicated in Table 5-92. It should be noted that radiators are located on all faces except the +X faces. These results show that the heat rejection capability increases on all faces at various node/sun phase from the 11:00 am reference orbit except for the significant reduction on the -Y face. The actuation module radiator is located on this -Y face.

Variability in the heat rejection capability results in heater power penalty if the 11:00 am reference orbit - average temperatures are to be maintained; the heater power penalty for the various modules are discussed in Section 5.5.3.

Orbit effects significantly affects module location interchangeability even if other subsystem constraints may be satisfied. Subsystem module location interchangeability trade-study is presented in Section 5.5.3.

- Altitude effects on the radiator heat rejection capability is insignificant on some faces and appreciable on others. Again variation in the heat rejection capability will result in heater power penalty if the 11:00 am reference orbit - average temperatures are to be maintained.
- Geo-synchronous effects on the heat rejection capability are significant as indicated in Table 5-92 since the sun is incident on all faces for a thermally long period. Sun is incident normal to all faces except for the shallow angles ( $\pm 23.5^\circ$  from plane of Y-faces) on the +Y faces.
- Sun angle effects on radiator coolers and sensor optics must be considered from a shading/protection standpoint.

##### 5.5.5.4.2 Non-Orbital Modes

- Ascent effects are controlled by fairing ejection time and are not considered to be significant.
- End-of-ascent to near earth orbit effects are typically not significant if the duration is short. However, incident sun on the optics must be given due consideration.



Table 5-92. Effect of Node/Sun Phase and Altitude on Heat Rejection Capability of Module Radiators

NODE/SUN PHASE  SURFACES	EFFECT OF NODE/SUN PHASING*					ALTITUDE 300nm   900nm 10:30 AM		GEO-SYNC. ***
	6 AM	7:30 AM	9 AM	10:30 AM	12 AM	Q REJECTION (WATTS/FT <sup>2</sup> )**		
+Z	17.9	15.1	15.8	15.9	15.9	15	18.3	12.2
-Z	32	31.7	27.3	25.9	25.5	25.9	25.9	12.2
+Y	30	27.9	27.8	27.7	27.6	27.3	28.3	22.6
-Y	8.1	9.7	17.5	22.6	27.6	22.2	23.2	22.6
+X	28	25.5	24	22.4	23	22.9	28.9	12.2

\* Altitude 386 nmi

\*\* Coating (Second Surface Mirror),  $\alpha = .15$ ,  $\epsilon = .8$  and orbital average environmental input,  $T = 70^\circ\text{F}$

\*\*\* Sun Angle,  $\pm 23.5^\circ$  from Z -X plane

Special Note: In Section 5.5.3,  $\alpha = .12$  and  $\epsilon = .80$  (for silvered Teflon) was used for the radiator. Since the intent of this study was to show relative differences, the results are sufficiently accurate.

- Transfer orbit(s) to geo-synchronous orbit effects can be appreciable, particularly cold conditions unless sufficient heater power is available because of the long transfer orbit period. Incident sun angle effects must also be given due consideration.
- Shuttle retrieval effects can be particularly significant because of disruption of S/C and module power. Need for S/C and module power is dependent upon the sun angle, the allowable non-operational module and structure temperatures, and the length of the retrieval time. During retrieval, a cold problem is anticipated unless power is provided in the modules. An indication of the module cool-down rate is displayed in Figure 5-225.
- Shuttle door open effects can be expected to yield a hot problem with a module in the shuttle if the open door is sun illuminated.
- Re-entry effects on the overall module temperature will raise the average module temperature about 20°F with lighter weight components such as insulation and solar array temperatures changing more.

#### 5.5.5.5 Summary

Impact of near-earth orbits on the module thermal design is variability in radiator heat rejection capability. This variability results in heater power penalty and impacts module location interchangeability.

Geo-synchronous orbit significantly impacts module thermal design with the result that each module thermal design must be individually re-examined.

Non-orbital mission modes can impact the module thermal design but requires mission mode specifics to ascertain the problems and solution methods.

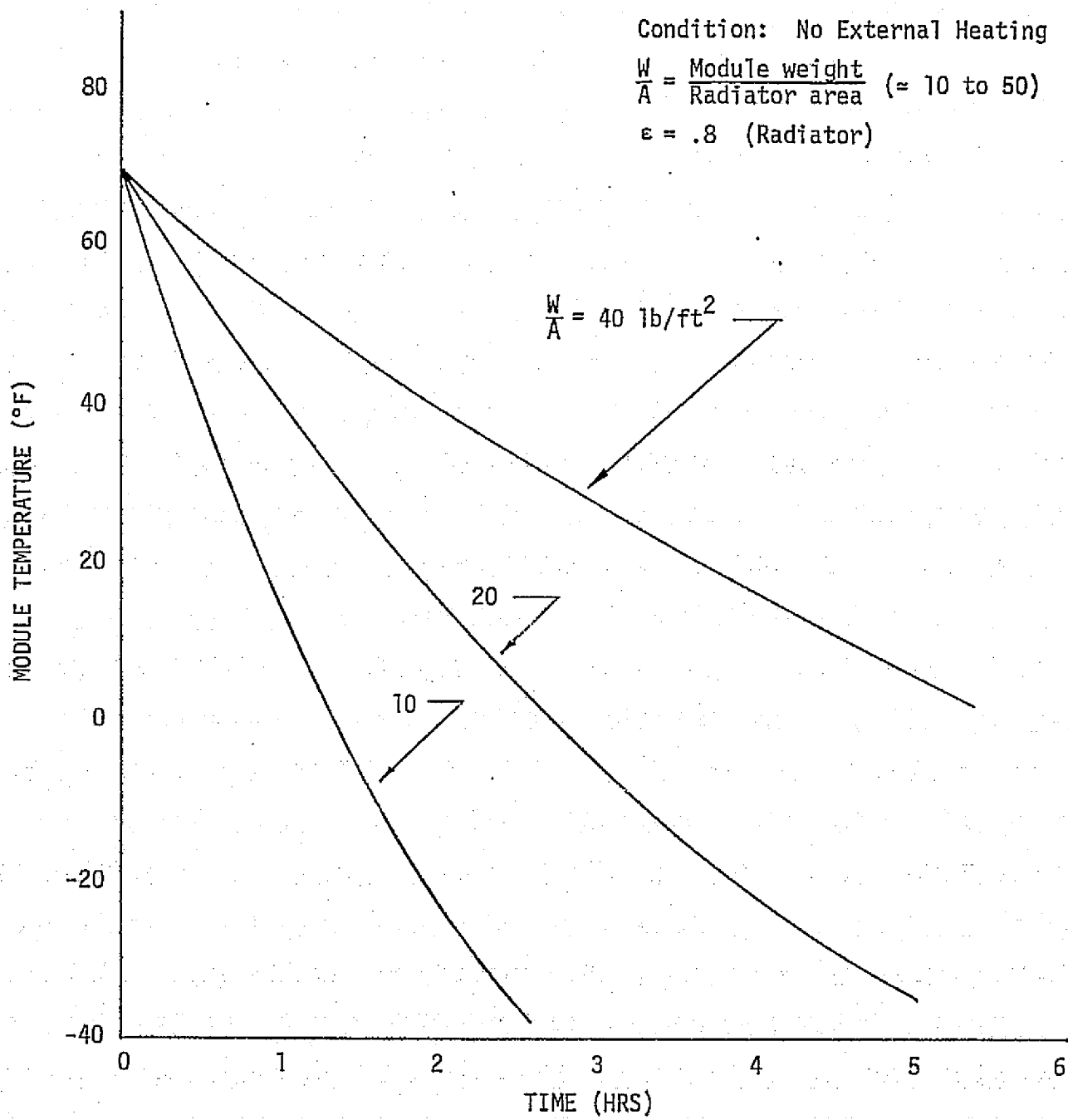


Figure 5-225. Cooldown of Isothermal Module

### 5.5.6 General Information Used in Thermal Design, Analysis and Trades

#### 5.5.6.1 Orbit Characteristics

TCS is designed for the reference orbit but accommodates a range of near-earth orbits.

##### Reference Orbit Characteristics

- Altitude (h) = 386 nmi
- Inclination =  $98.4^\circ$
- 11 am phasing of node to sun line

##### Near-Earth Orbit Characteristics Accommodated by TCS

- Altitude (h) = 300 - 900 nmi
- Corresponding inclination =  $97.7^\circ$  to  $103.1^\circ$
- Node/sun phasing = 6 am to 6 pm

##### Geostationary (Future Missions)

#### 5.5.6.2 Environmental Requirements

TCS must meet various environmental requirements corresponding to mission modes (including interfaces).

##### Pre-Launch

- Surrounding air temperature extremes, typically  $25^\circ\text{F}$  to  $100^\circ\text{F}$
- Incident solar, typically  $360 \text{ Btu/hr-ft}^2$

##### Launch/Ascent

- Fairing temperature governed by aerodynamic heating which is dependent upon trajectory
- Fairing jettison time must accommodate TCS requirements

##### Transfer Orbit

- Range of sun-angle, typically
- Range of eclipse duration
- Solar albedo, near earth
- Earth emission, near earth

#### On-Orbit

- Solar intensity,  $S$   
 $S = 416 - 442 \text{ Btu/hr-ft}^2$  (Analysis utilized  $442 \text{ Btu/hr-ft}^2$ )
- Solar albedo,  $\rho_s$   
 $\rho_s = .3$  used in analysis
- Earth emission,  $q_e$   
 $q_e = 75.5 \text{ Btu/hr-ft}^2$  (used in analysis)

#### 5.5.6.3 Thermal Properties

Thermal properties are listed in Table 5-93.

Table 5-93. List of Thermal Properties  
and PMP Specifications

Item	Absorptance* (Initial)	Absorptance <sup>α</sup> (Degraded)	Emittance* (Hemispherical)	TRW Specifications
Second Surface Mirrors, silvered	0.07	0.14	0.78	SP7168(S)11 MT3-68-2 PR4-41-1
3M Velvet Black Paint	0.98	0.98	0.90	MT6-8 PR5-13
Black Cat-a-Lac Paint	0.97	0.97	0.86	MT6-9 PR5-2
S-13G LO White Paint	0.22	0.50	0.88	PR5-25-1-2
Aluminized Kapton, 3-mil	0.44	0.50	0.78	MT3-14, Type 2
2-mil	0.39	0.45	0.74	
Aluminized Kapton 3-mil, temperature degraded	0.44	0.68	0.78	MT3-14, Type 2
Vacuum Deposited Aluminum	0.11	0.11	0.04	PR6-11
5-mil Silverized Teflon Tape	0.08	0.21	0.8	C125741-1
3-mil clear Kapton painted with DC92007 White Paint (Kapton side)	0.48	0.65	0.86	MT3-14, Type 2 MT6-7
TRW Aluminum silicone paint	0.25	0.25	0.28	MT6-11-1 PR5-29-1
MLI BLANKET	Conductance K/1 = BTU/hr-ft <sup>2</sup>			
12 layers	.012			
15 layers	.008			
24 layers	.003			

\* Based on nominal values

<sup>α</sup> 5-4r equivalent sun, synchrnous orbit; for near-earth, degraded values would be less

## 5.6 STRUCTURE

### 5.6.1 Modal Analysis

Modal analyses were performed on both the Titan and Thor-Delta versions of EOS-A. Model sizes are as follows:

	<u>Titan</u>	<u>Thor-Delta</u>
No. of Joints	87	58
No. of Members	192	129
No. of Plates	0	38
No. of Modes <50 hz	8	6
Weight (lb)	5000	2532

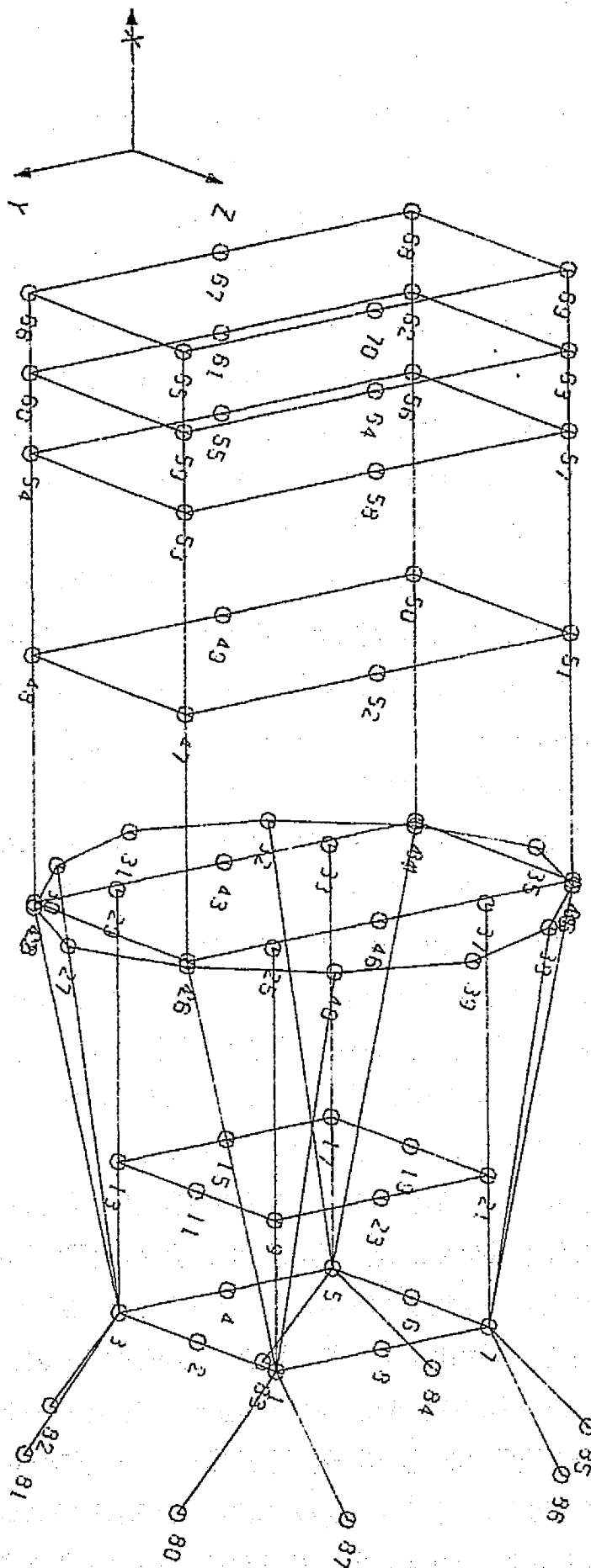
These models include only primary structure and, hence, ignore flexibility of the solar arrays, antennas, and modules. Since modes above 50 hz can be ignored in loads analysis, it is a design goal to keep module frequencies above this value. This may prove difficult for some payload modules having heavy instruments and requiring thermal isolation. However, evaluation of this aspect is beyond the scope of this study. Current plans are to tie the solar array to the payload structure during boost, thereby stiffening it to frequencies above 50 hz.

The conclusions of the modal analyses are that, with either version of EOS-A, there are only a few primary structural modes below 50 hz and that, with the exception of the torsion mode, all modes can be excited readily by sinusoidal base excitation in one of three axes. Thus each sinusoidal sweep will probably excite only 3 or 4 modes in the 5 to 50 hz range, permitting accurate frequency identification.

Plots of the dynamic models and mode shapes are presented on the following pages.

EOS-A MODE SHAPES  
TITAN VERSION





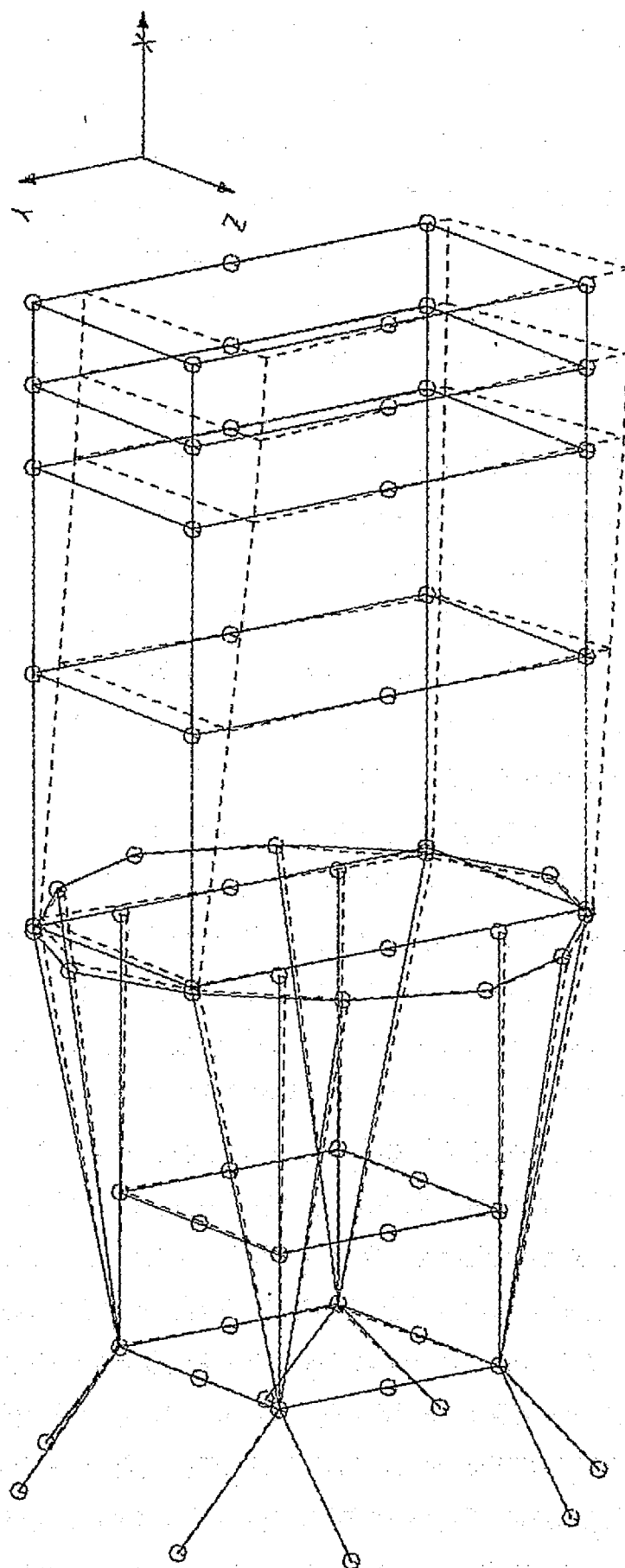
EOS-A

Titan  
Version

Dynamic  
Model

(Diagonal  
Braces  
Removed)

5000 lb.  
Refurbishable

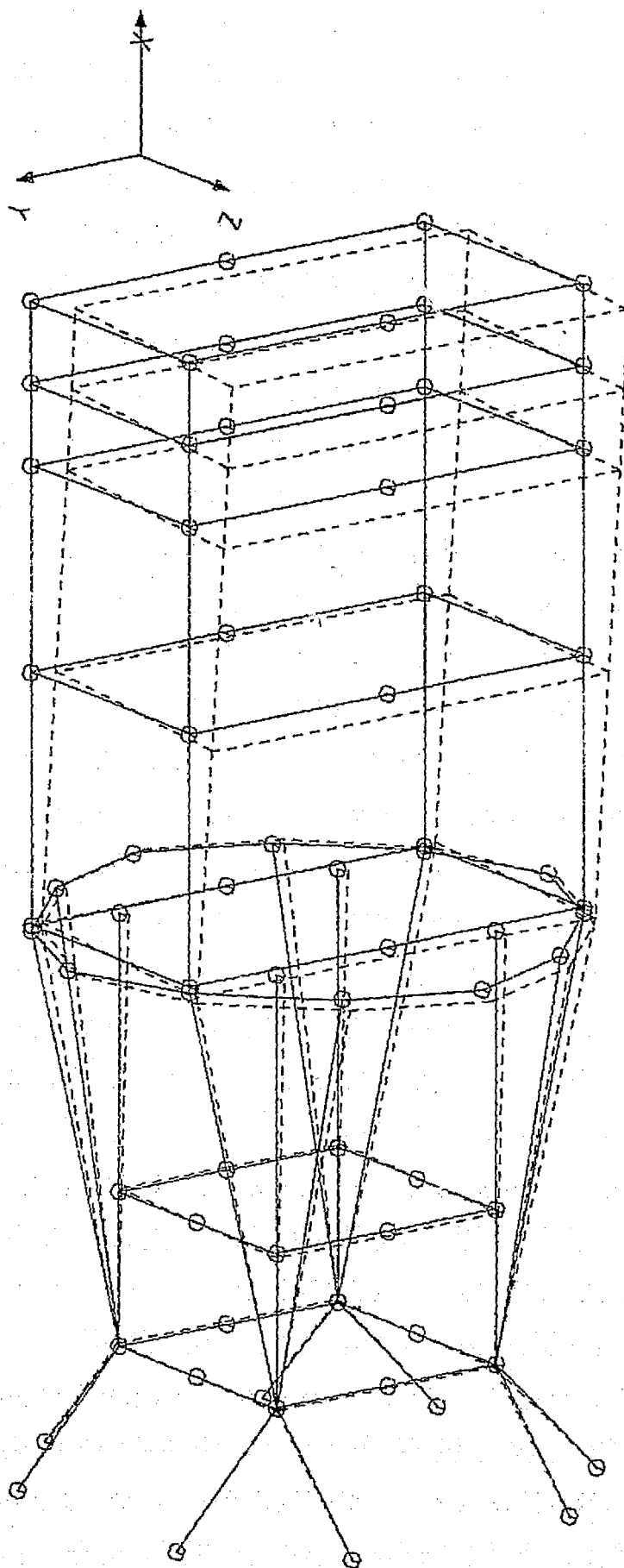


EOS-A

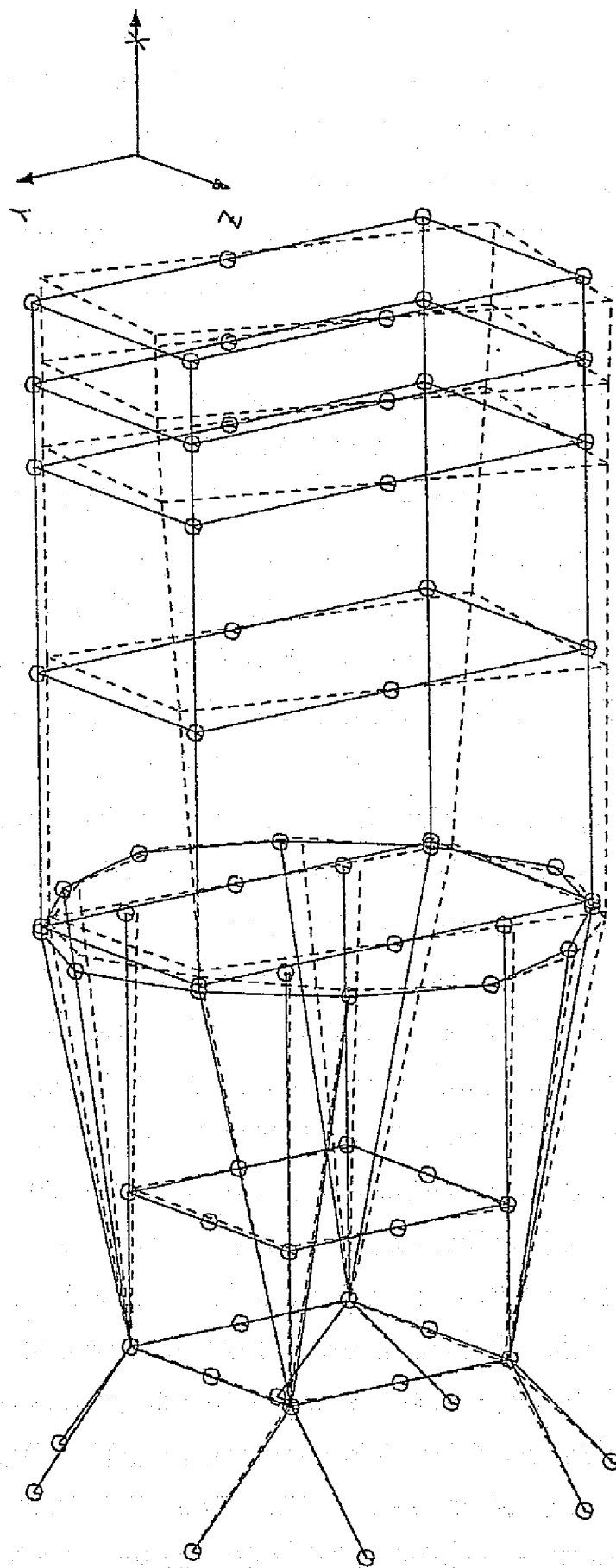
Titan  
Version

Mode 1

7.2 Hz



EOS-A  
Titan  
Version  
Mode 2  
9.1 Hz

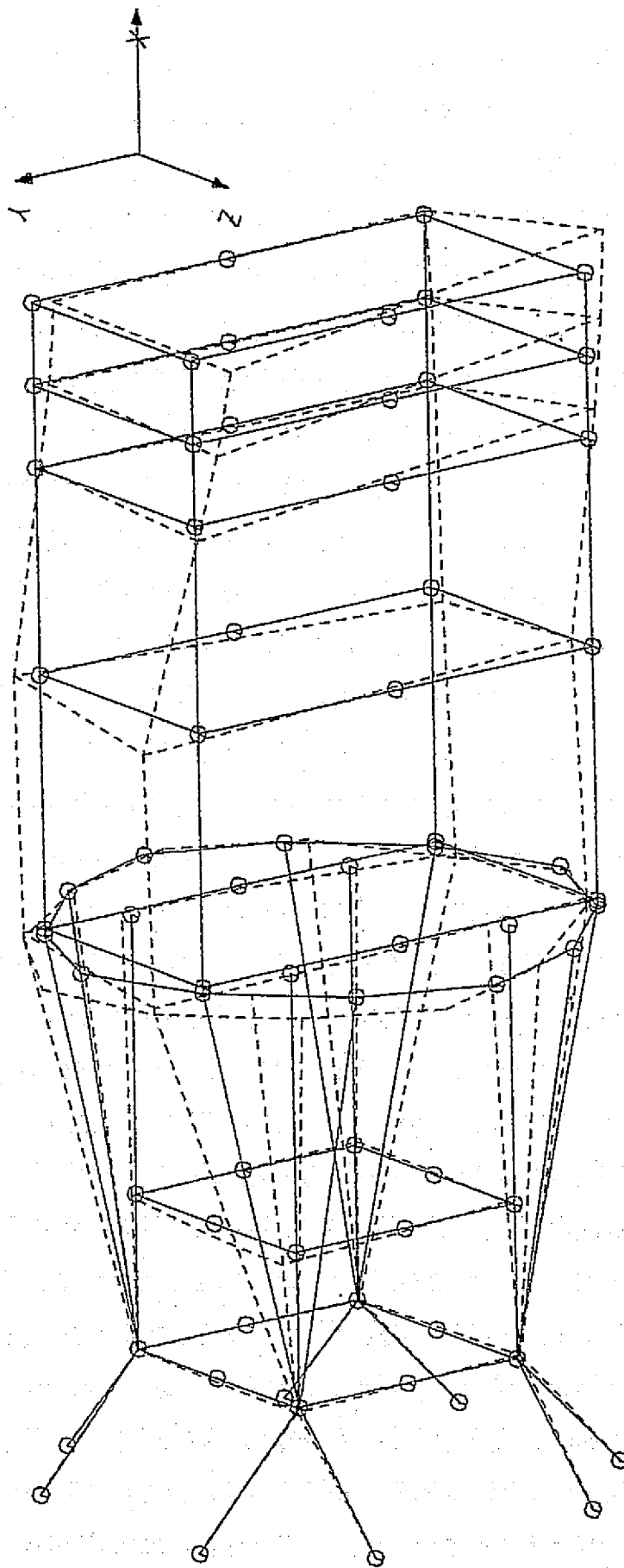


EOS-A

Titan  
Version

Mode 3

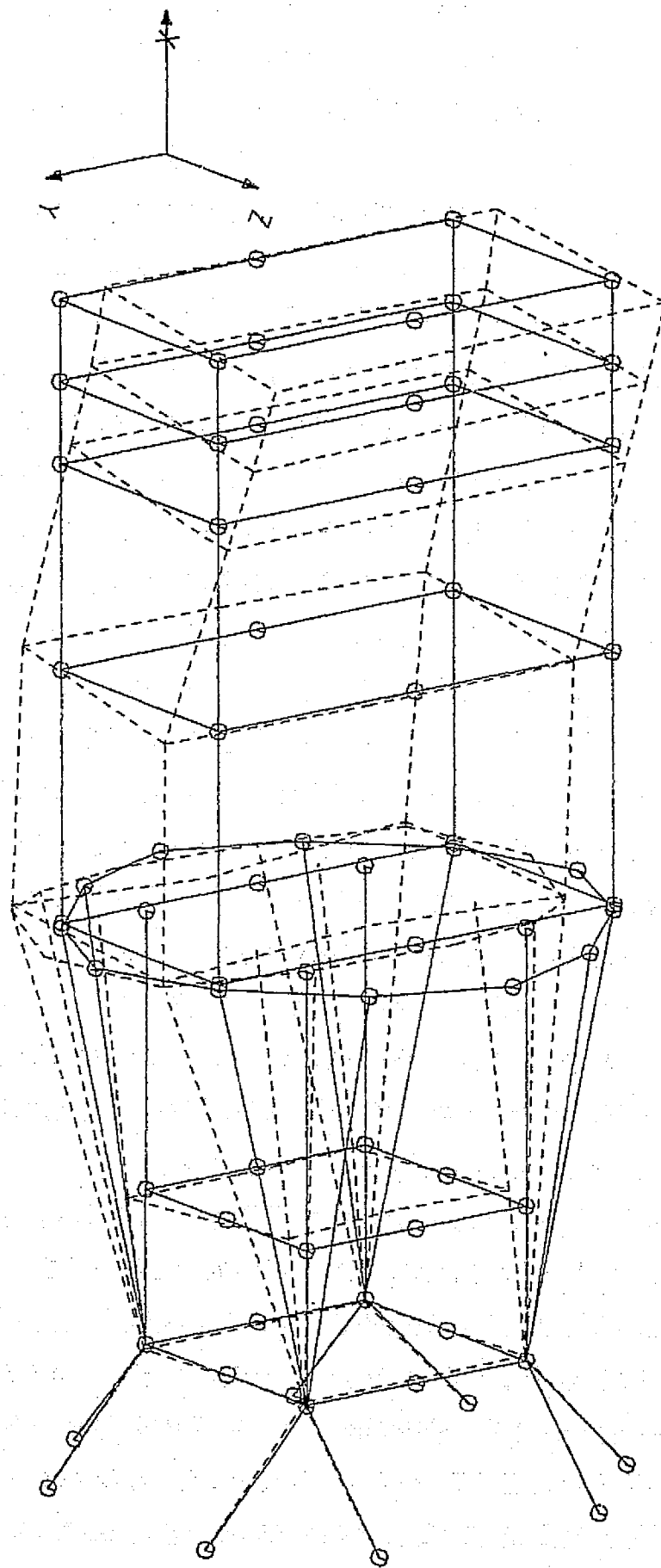
12.6 Hz



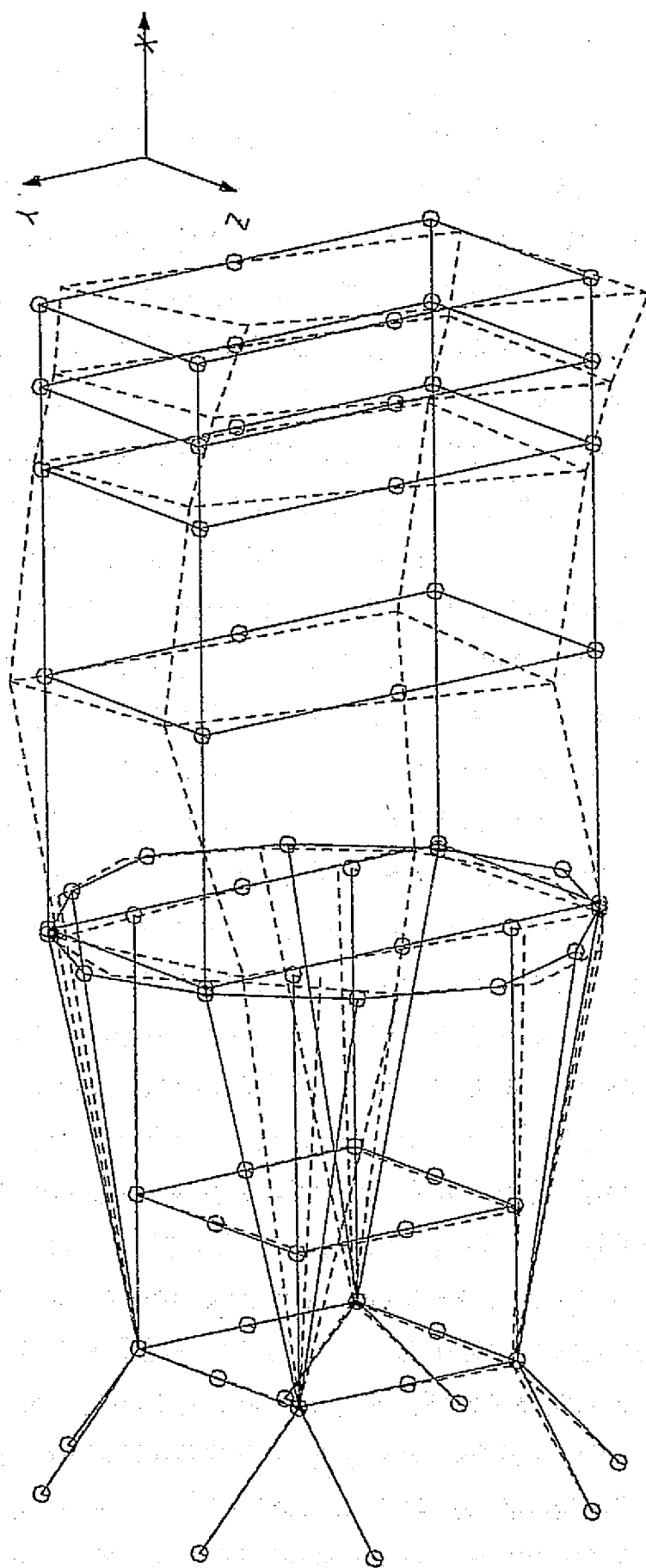
EOS-A

Titan  
Version

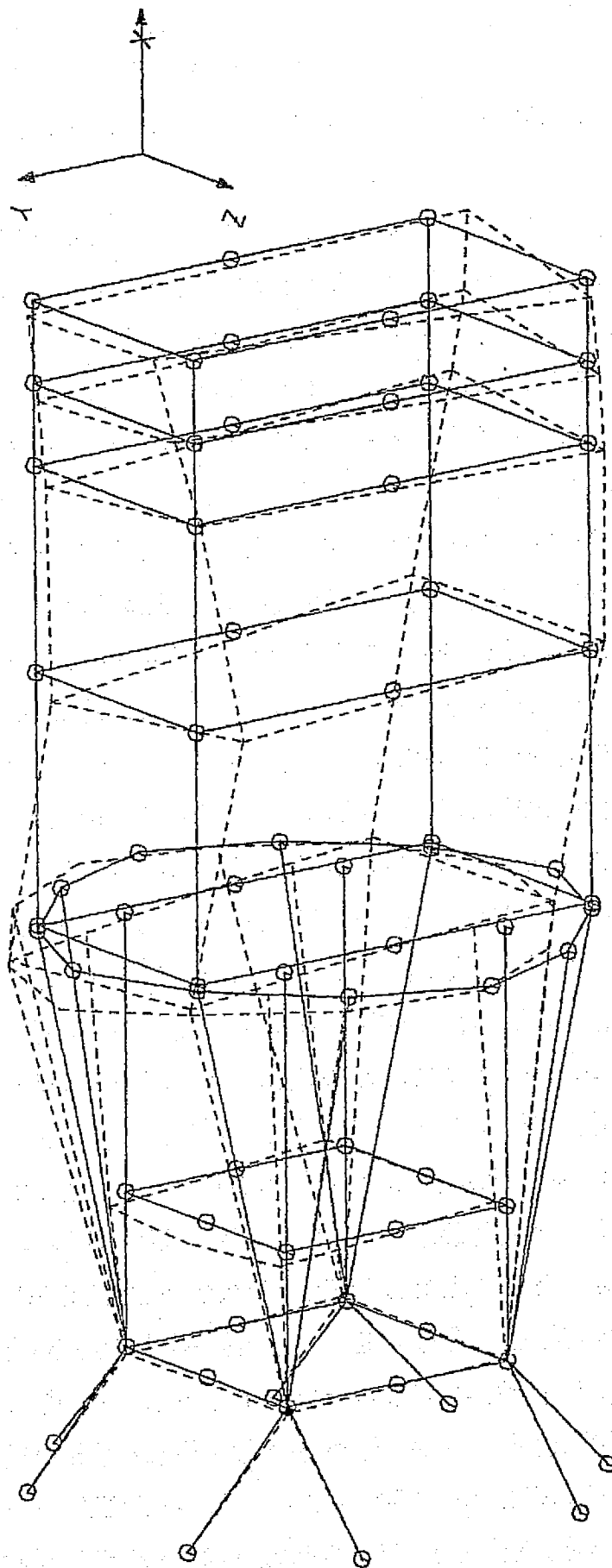
Mode 4  
27.5 Hz



EOS-A  
Titan  
Version  
Mode 5  
30.7 Hz



EOS-A  
Titan  
Version  
Mode 6  
36.9 Hz

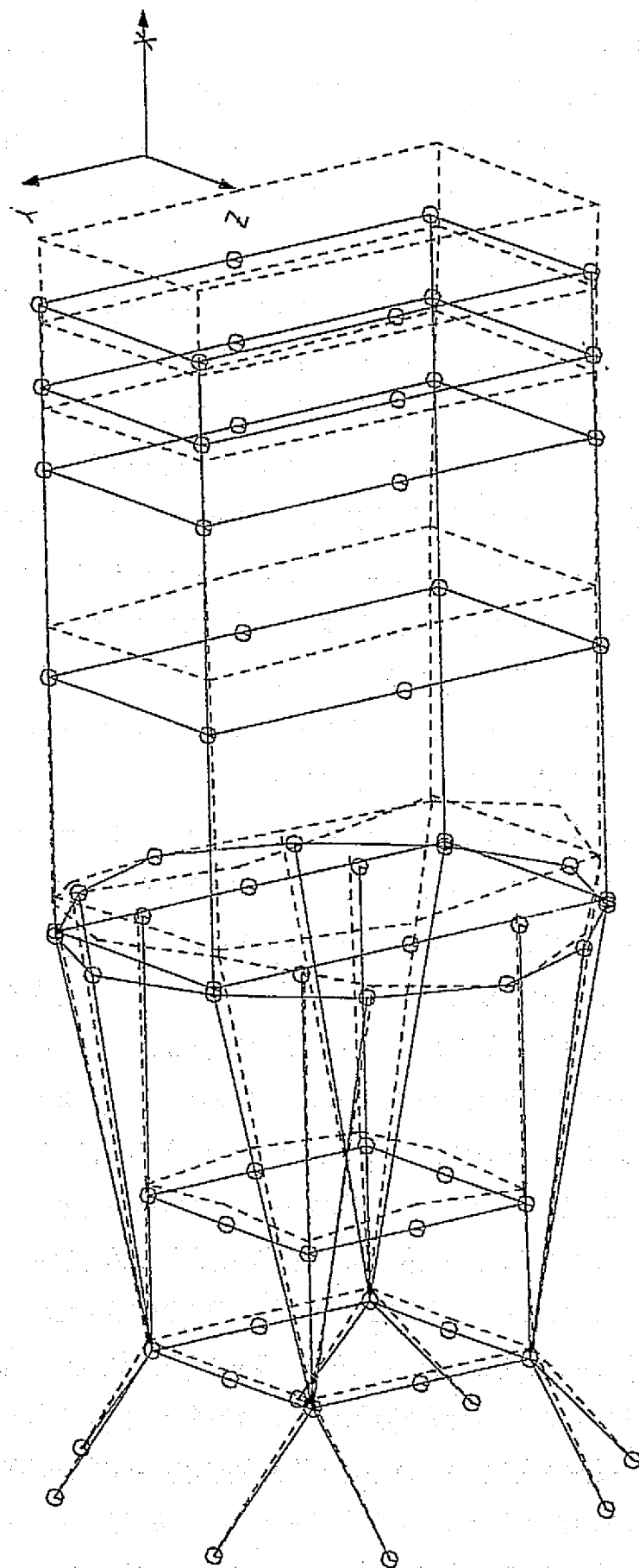


EOS-A

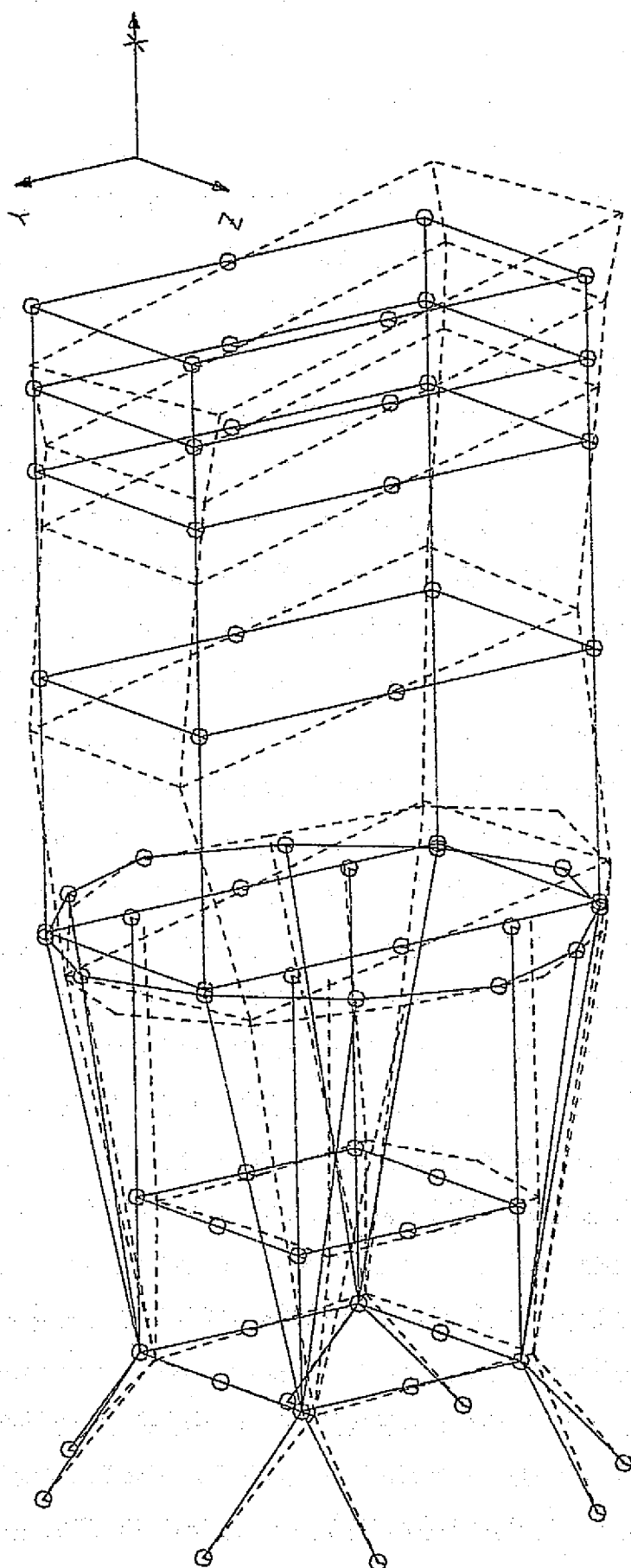
Titan  
Version

Mode 7  
39.1 Hz





EOS-A  
Titan  
Version  
Mode 8  
41.7 Hz



EOS-A

Titan  
Version

Mode 9  
50.7 Hz

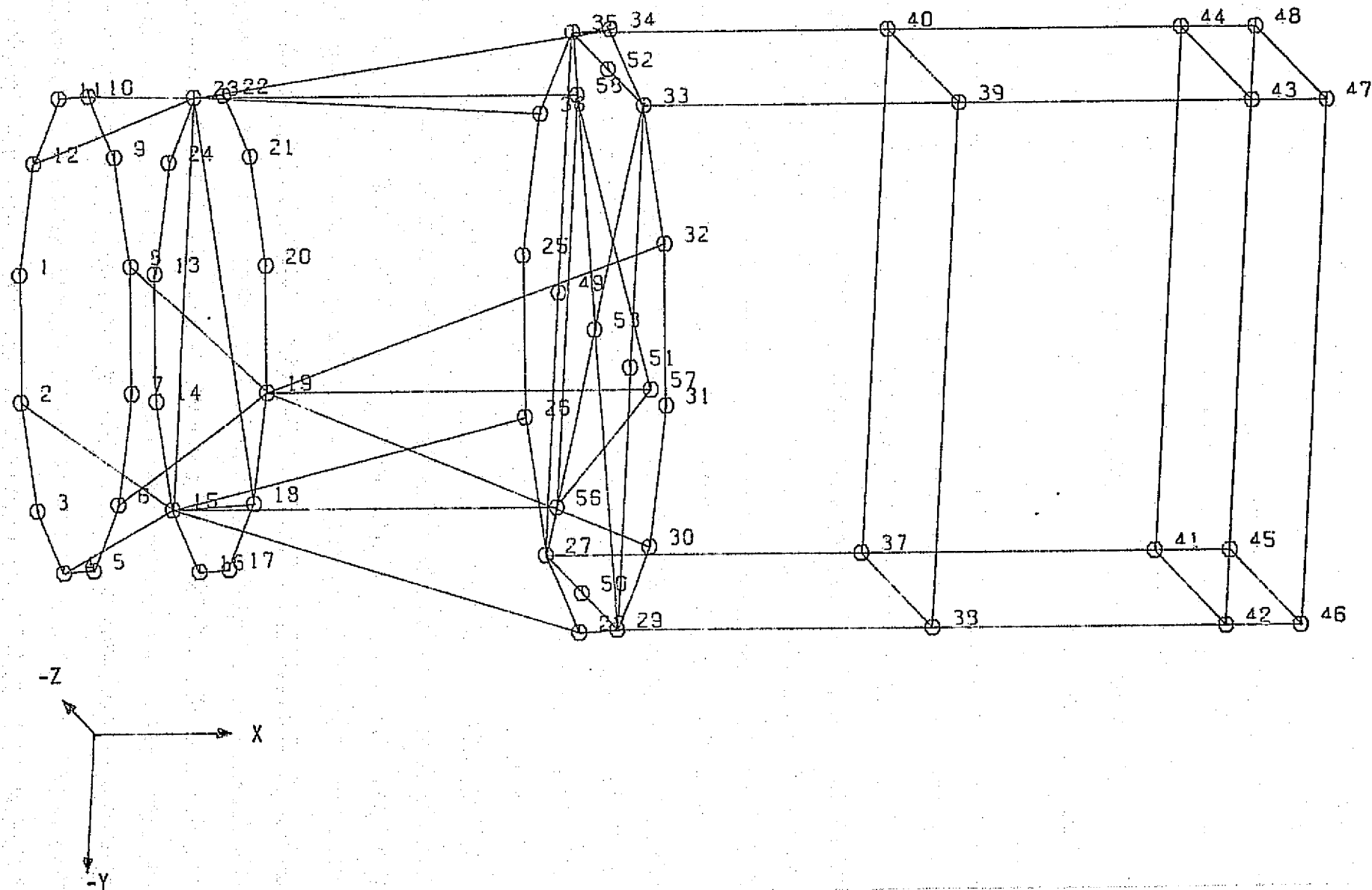
EOS-MODE SHAPES  
THOR/DELTA VERSION

# EOS-A DELTA VERSION

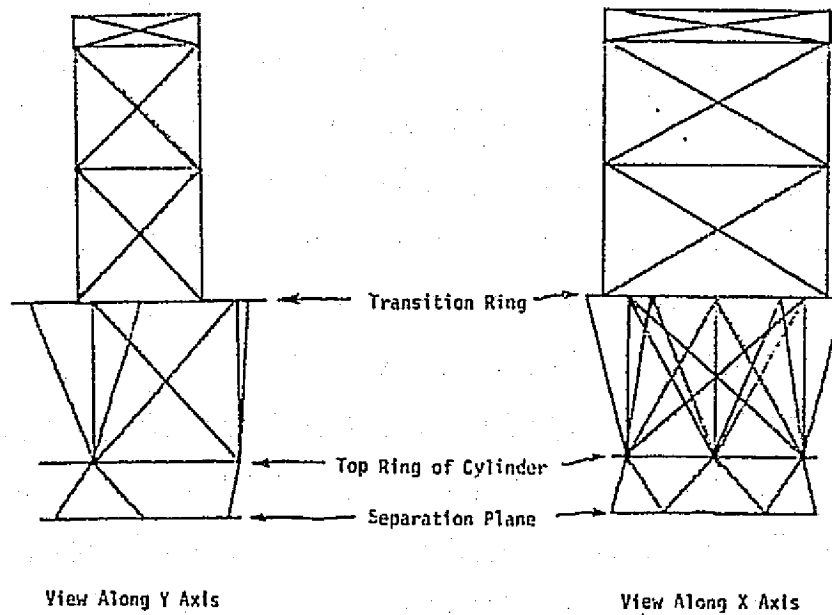
(Diagonal Braces and Plate Elements not shown)

2532 1b Non-serviceable

5-623

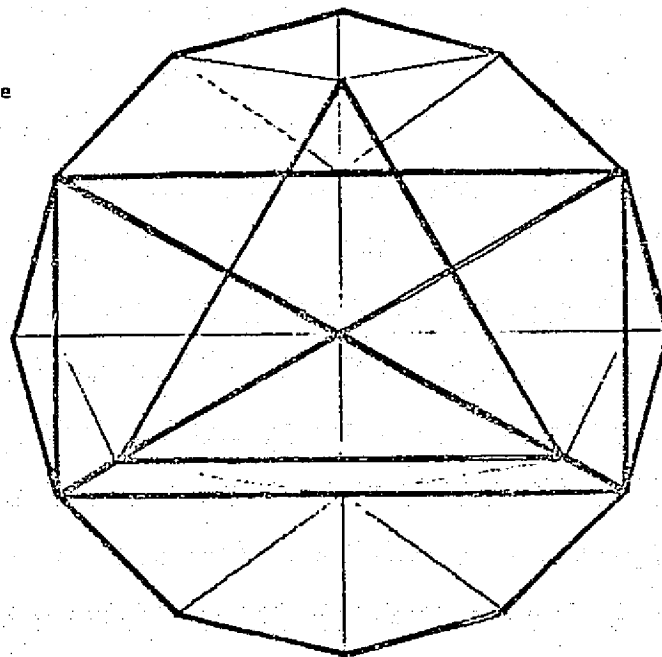


EOS-A THOR-DELTA VERSION  
STRUCTURAL MEMBERS ONLY



DETAILS OF PLANE OF TRANSITION RING

— Members  
— Edges of Plate Elements



EOS-A DELTA VERSION

MODE NO. 1

FREQUENCY

9.620 HZ

5-625

A 3D wireframe model of a rectangular structure, possibly a building or a container, with internal bracing. The structure is defined by a rectangular prism with additional internal members. Nodes are represented by small circles, and lines represent the structural members. The model is shown in a perspective view, with the front face on the left and the back face on the right. The structure appears to be a rectangular prism with a complex internal bracing system, including diagonal members and cross-bracing. The nodes are distributed throughout the structure, with a higher density of nodes in the central and front regions.

A 3D coordinate system diagram with axes labeled X, Y, and Z. The X-axis is horizontal and points to the right. The Y-axis is vertical and points downwards. The Z-axis is diagonal and points towards the upper left. The origin is at the intersection of the three axes.

EOS-A DELTA VERSION

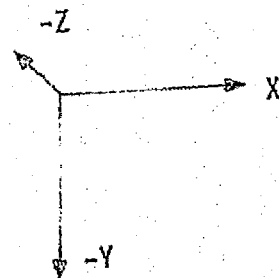
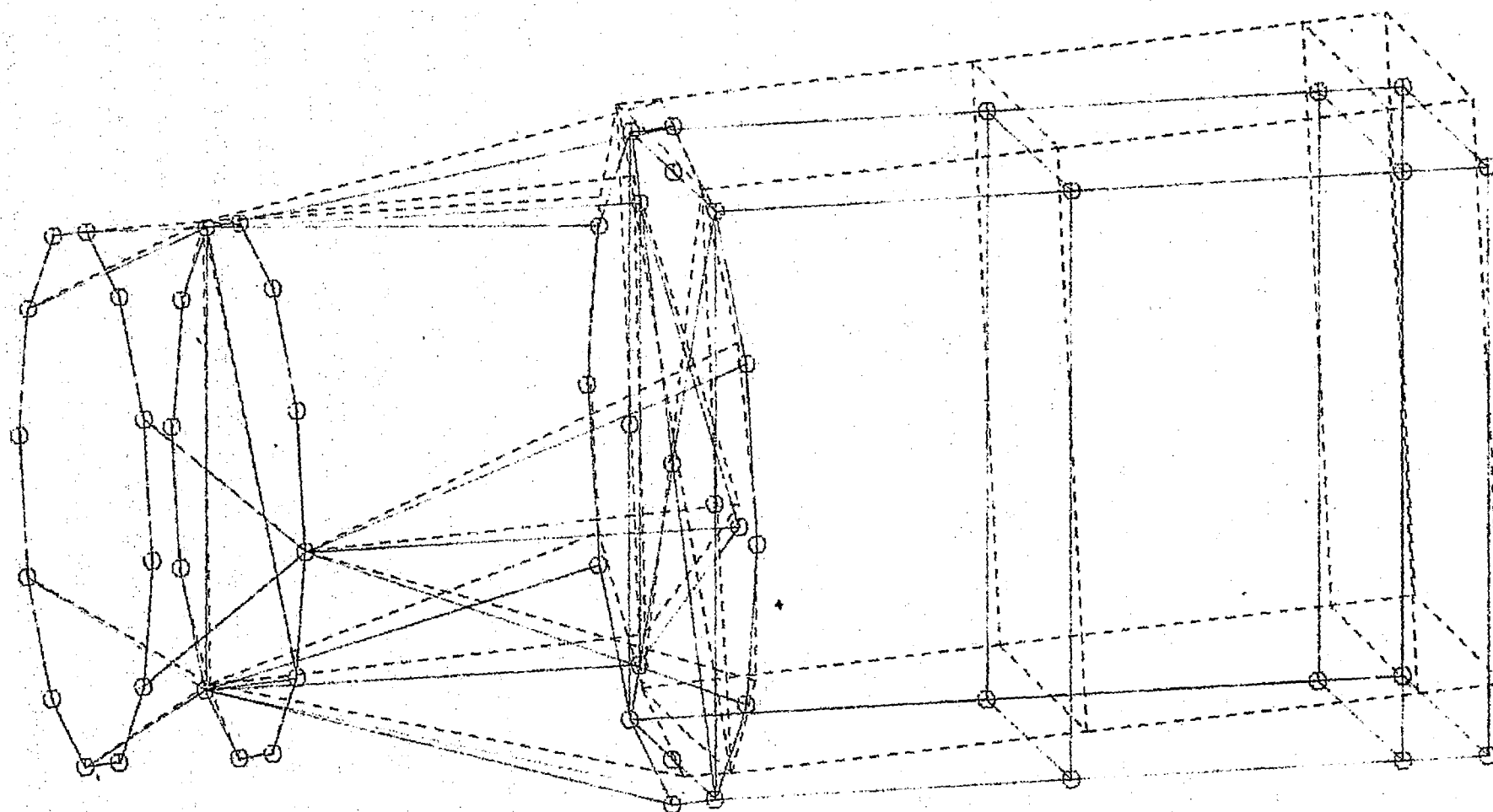
MODE NO

2

FREQUENCY

13.209 HZ

5-626



EOS-A DELTA VERSION

MODE NO. 3

FREQUENCY 16.214 HZ

5-627

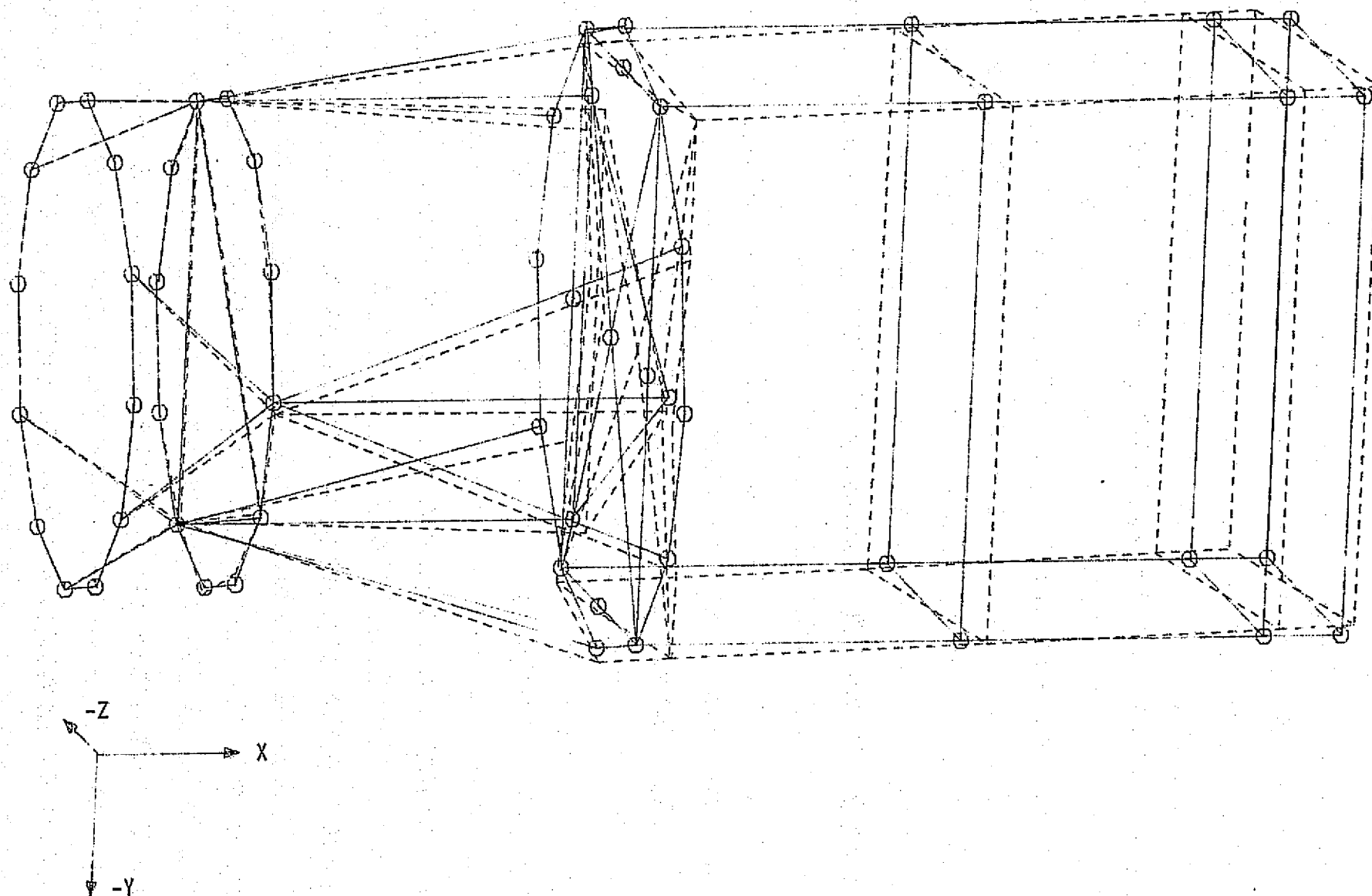


EOS-A DELTA VERSION

MODE NO. 4

FREQUENCY 25.025 HZ

5-628

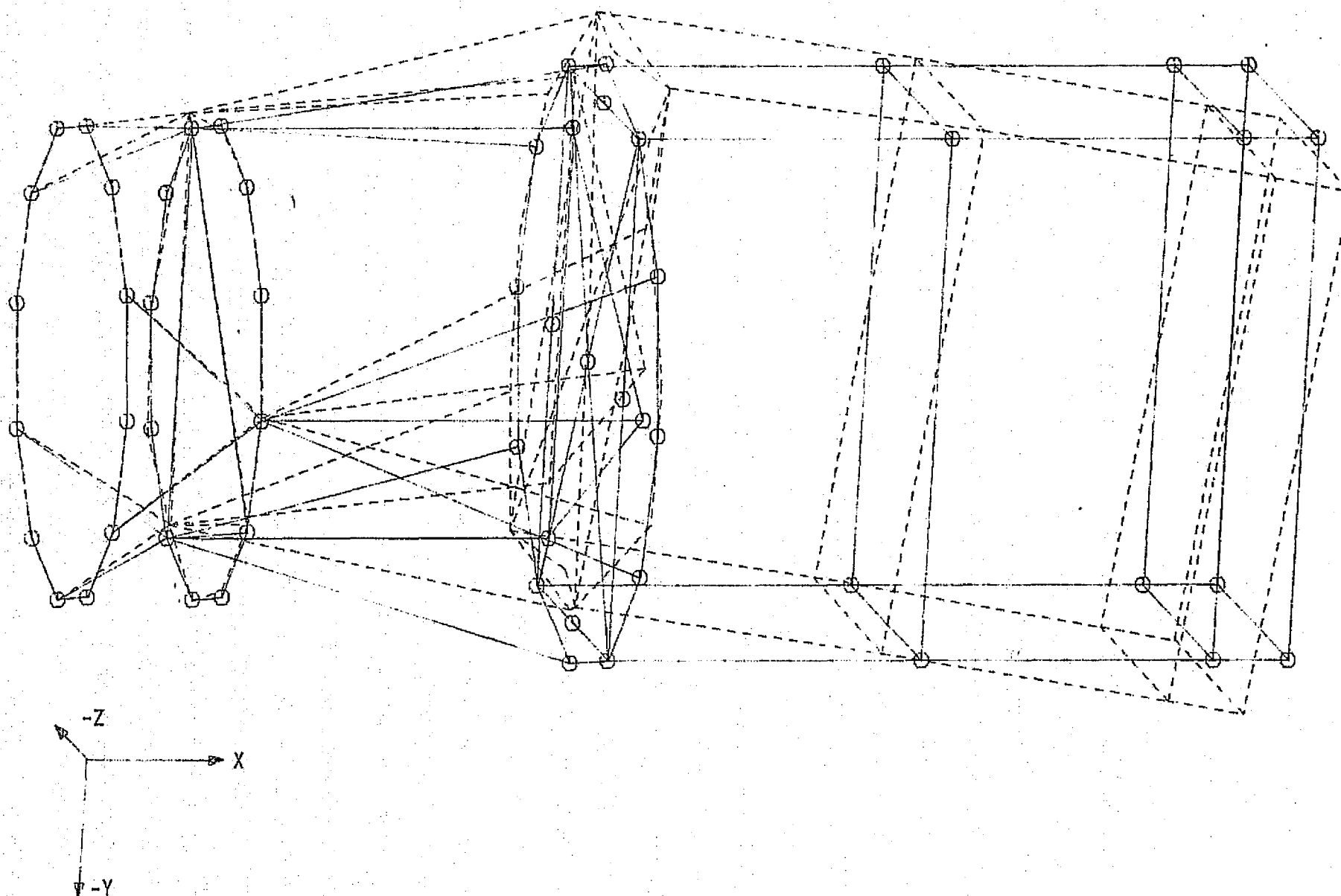


LOS-A DELTA VERSION

MODE NO. 5

FREQUENCY 37.185 HZ

5-629

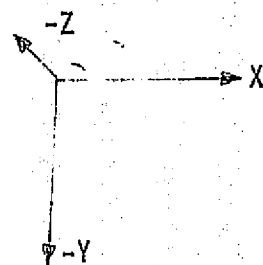
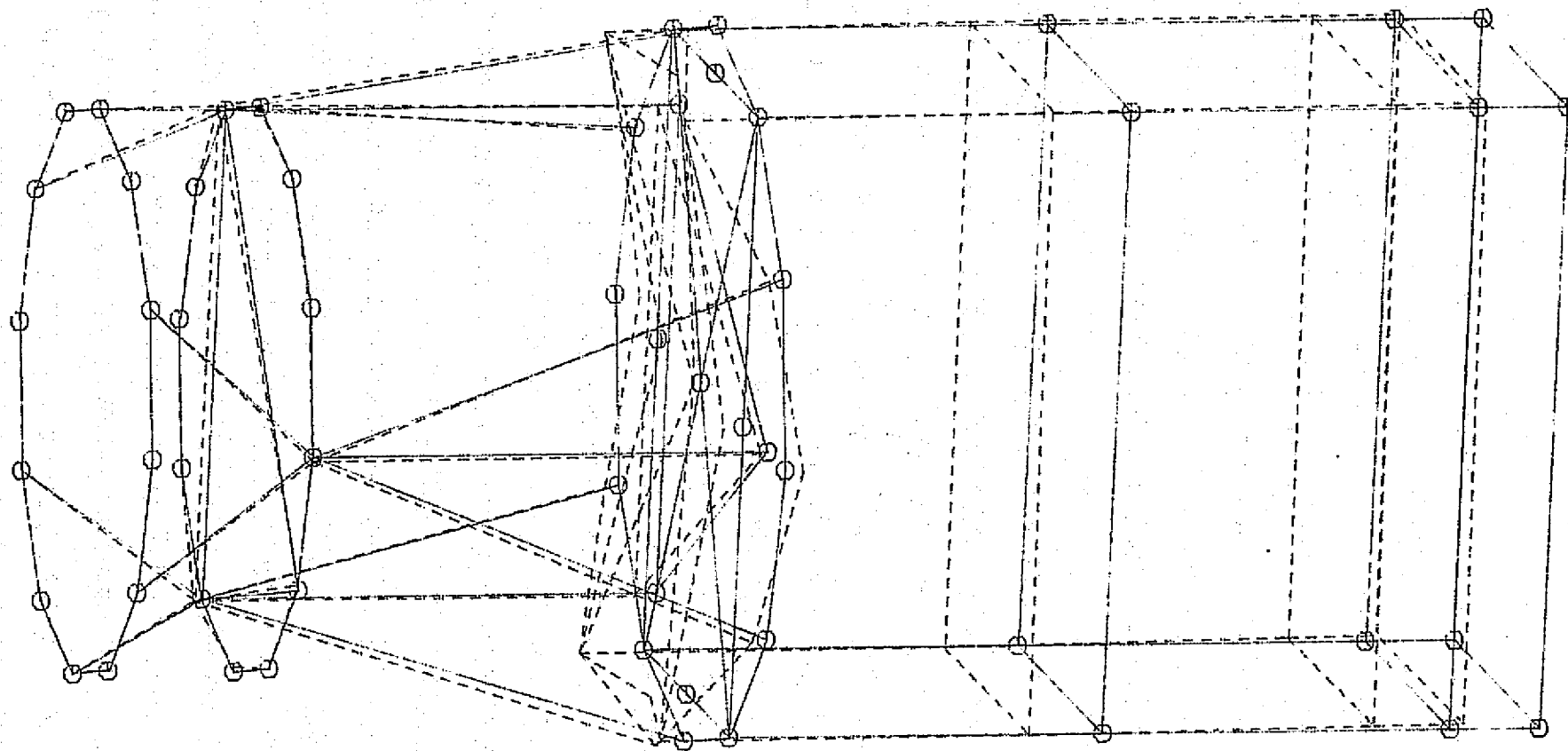


EOS-A DELTA VERSION

MODE NO. 6

FREQUENCY 39 800 HZ

5-630

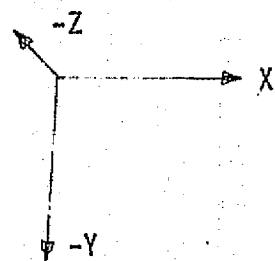
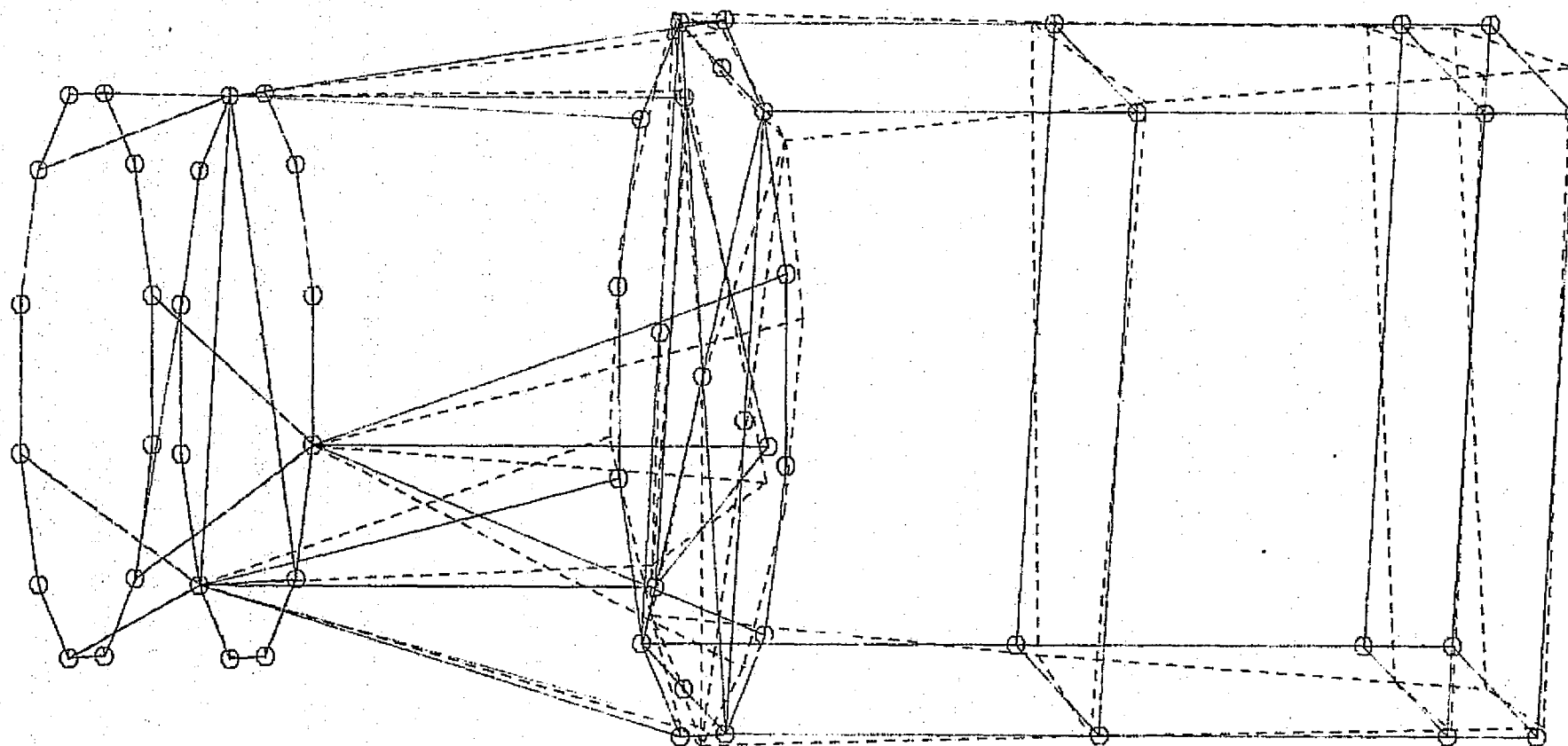


EOS-A DELTA VERSION

MODE NO. 7

FREQUENCY 61.326 HZ

5-631



## 5.6.2 Stress and Distortion Analyses

The calculations performed to provide the summary data in Sections 6.8 and 6.9 of this report are included here as a matter of documented reference material. Two sets of calculations are included:

- 1) Margin of safety calculations for the stress analysis and;
- 2) Distortion calculations and plots for the pointing accuracy check (thermal/structural) in Section 6.9.

### 5.6.2.1 Stress Analyses

Stress analyses of both the Titan and Thor-Delta observatory configurations were performed using the analytical models shown in Section 6.8. The Static Structural Analysis Program (SSAP) computes directly the stresses in various members and plates. The maximum stress in each major structural member type was taken from the computer output and checked against the critical allowable stress for that member configuration. (Axial load plus lateral load in two mutually perpendicular directions were considered and the more critical used.) The first eight pages of the attached computations show the maximum stresses, the member and joint in the analytical model at which they occurred, the computation of the allowable stress, and the computed margin of safety. Each observatory configuration is separated into the spacecraft and payload sections in agreement with the separation between Section 6.8 and 6.9 in the report.

The last two pages of computations are similar except that they are for the power module. This module and therefore these computations are considered representative for all the spacecraft modules. Since the power module is the heaviest, the analysis should be conservative for all other modules.

PREPARED

*H. J. Dean* *4/28/74*

REPORT NO.

PAGE 1

CHECKED

MODEL

*FEOS-A TITAN*

**STRESS ALLOWABLES & MARGINS  
OF SAFETY**

CRITICAL STRESSES :

COLUMN ALLOWABLE

S/C LONGERONS 49, 52, 55, 58 L = 54" <sup>12</sup>

4 X 4 X .125 SQ. TUBES

$$P_{cr} = \frac{\pi^2 EI}{L^2} = \frac{\pi^2 (14.7 \times 10^6) (4.27)}{(54)^2} = 176370 \text{ LB}$$

$$F_{cr} = \frac{P_{cr}}{A} = \frac{176370}{1.94} = 90912 \text{ PSI (NO CRITICAL IN A COLUMN)}$$

CHECK LOCAL CRACKING

$$b/t = \frac{4.0}{.125} = 32 \quad F_{cc} = 23000 \text{ PSI (6061-T6 AL AL)}$$

MEMBER 55, JT 17, LOAD CASE 8

$$f = 5907$$

$$M.S. = \frac{23000}{5907} - 1 = \underline{\underline{2.88}}$$

LOWER BOX 33, 36, 39, 42, 45, 48, 27, 30

SECTION 1 MEMBERS 1 - 60

MEMBER 16, JT 13, LOAD CASE 8 LONGERON

$$f_{max} = 16488 \text{ PSI}$$

$$M.S. = \frac{23000}{16488} - 1 = \underline{\underline{0.39}}$$

TRANSITION RING - MEMBERS 61 - 72

MEMBER 63, JT 28, LOAD CASE 8

$$f = 6044 \text{ PSI}$$

$$M.S. = \frac{23000}{6044} - 1 = \underline{\underline{2.80}}$$

ORIGINAL PAGE IS  
OF POOR QUALITY

PREPARED

W. J. Dean

6/30/74

REPORT NO.

PAGE 2

CHECKED

MODEL

EOS-A TITAN

**MARGINS OF SAFETY**
**CROSS DIAGONALS :**

 MEMBERS: 14, 15, 17, 18, 20, 21, 23 & 24 LOWER  
 50, 51, 53, 54, 56, 57, 59, & 60

**LOWER DIAGONALS :**

MEMBER 23, JT 9 LOAD CASE 7

$$f_{max} = 7334 \text{ psi}$$

$$F_{cr} = 23000 \text{ psi}$$

$$M.S. = \frac{23000}{7334} - 1 = \underline{\underline{2.14}}$$

**UPPER DIAGONALS :**

NOT CRITICAL RELATIVE TO LOWER DIAGONALS

**HORIZONTAL FRAME MEMBERS :**

1-8, 27, 30, 33, 36, 39, 42, 45, 48

MEMBER 33, JT. 15, LOAD CASE 8

$$f_{max} = 13262 \text{ psi}$$

$$F_{cr} = 23000 \text{ psi}$$

$$M.S. = \frac{23000}{13262} - 1 = \underline{\underline{0.73}}$$

**OUTRIGGER STRUTS :**

MEMBER NOS. 161, 162, 163, 164, 165, 166, 167, 168

$$b/t = \frac{3.0}{.12} = 25; F_{cr} = 27000 \text{ psi} \quad (6061-T6 AL AL)$$

MEMBER 165, JT 34, LOAD CASE 7

$$f_{max} = 12343 \text{ psi}$$

$$F_{cr} = 27000 \text{ psi}$$

$$M.S. = \frac{27000}{12343} - 1 = \underline{\underline{1.19}}$$

PREPARED

*H. J. Dean*

6/30/74

REPORT NO.

PAGE 3

CHECKED

MODEL *FOS-A TITAN*

MARGINS OF SAFETY

## TITAN PAYLOAD STRUCTURE

### PRIMARY LONGERONS

LOWER MEMBERS 87-90

MEMBER 89, JT 34, LOAD CASE 8

$$f_{MAX} = 21479 \text{ psi}$$

$$F_{CR} = 27000 \text{ psi} (6061-T6)$$

$$M.S. = \frac{27000}{21479} - 1 = \underline{\underline{0.26}}$$

### HORIZONTAL FRAME MEMBERS

LOWER MEMBERS 101-105

MEMBER 121, JT. 51, LOAD CASE 7

$$f_{MAX} = 2868 \text{ psi}$$

$$F_{CR} = 27000 \text{ psi}$$

$$M.S. = \frac{27000}{2868} - 1 = \underline{\underline{8.40}}$$

### CROSS DIAGONALS (VERTICAL PLANES)

95-100, 111-116, 127-132, 149-154

MEMBER 96, JT. 42, LOAD CASE 8

$$f_{MAX} = 4234 \text{ psi}$$

$$F_{CR} = 27000 \text{ psi}$$

$$M.S. = \frac{27000}{4234} - 1 = \underline{\underline{5.38}}$$

### HORIZONTAL CROSS BRACES

MEMBERS 177-183

MEMBER 177, JT. 44, LOAD CASE 7

$$f_{MAX} = 2403 \text{ psi}$$

$$F_{CR} = 27000 \text{ psi}$$

$$M.S. = \frac{27000}{2403} - 1 = \underline{\underline{10.24}}$$

ORIGINAL PAGE IS  
OF POOR QUALITY



PREPARED

*A. J. Dean*

6/30/74

REPORT NO.

PAGE 4

CHECKED

MODEL

FOS-A THOR DELTA

MARGINS OF SAFETY

S/C LONGERONS : 3" X 3" SQ. TUBE ;  $t = 0.11$  in.

$$b/t = \frac{3.0}{.11} = 27$$

$$F_{CR} = 25000 \text{ psi}$$

MEMBERS : 91, 92, & 93

MEMBER 93, JT. 58, LOAD CASE 4

$$f_{MAX} = 11845 \text{ psi}$$

$$M.S. = \frac{25000}{11845} - 1 = \underline{\underline{1.11}}$$

S/C CROSS BRACES : 2" X 3" TUBE :  $t = 0.050$  in.

$$b/t = \frac{3.0}{.05} = 60$$

$$F_{CR} = 17500 \text{ psi}$$

MEMBERS : 94 - 99

MEMBER 95, JT. 97, LOAD CASE 5

$$f_{MAX} = 8904 \text{ psi}$$

$$M.S. = \frac{17500}{8904} - 1 = \underline{\underline{0.96}}$$

LOWER CLOSE-OUT FRAME :  $\Delta$  2" X 3" X 0.136" RECT. TUBE

$$b/t = \frac{3.0}{.136} = 22$$

$$F_{CR} = 27500 \text{ psi}$$

MEMBERS 127 - 129

CHECK CRITICAL COLUMN STRESS FOR  $L = 60.8$  in.

$$F_{COR} = \frac{\pi^2 EI}{AL^2} = \frac{\pi^2 (10.7 \times 10^6) (.41)}{(1.36) (60)^2} = 8844 \text{ psi}$$

MEMBER 129, JT. 15, LOAD CASE 4

$$f_{MAX} = 2985 \text{ psi}$$

$$M.S. = \frac{8844}{2985} - 1 = \underline{\underline{1.96}}$$

PREPARED J. J. Dean 6/30/74

REPORT NO.

PAGE 5

CHECKED

MARGINS OF SAFETY

MODEL EOS-A THUR DELTA

UPPER CLOSURE-OUT FRAME : MEMBERS: 124-126, L = 54 IN.

$$F_{COL} = \frac{\pi^2 EI}{AL^2} = \frac{\pi^2 (10.7 \times 10^9) (.41)}{(1.36) (54)^2} = 10918 \text{ psi}$$

MEMBER 124, JT. 57, LOAD CASE 5

$$f_{MAX} = 4025 \text{ psi}$$

$$M.S. = \frac{10918}{4025} - 1 = \underline{\underline{1.71}}$$

LOWER SKIRT RING :

MEMBERS: 67-78

$$F_{CR} = F_{CY} = 35000 \text{ psi}$$

MEMBER 71, JT. 6, LOAD CASE 5

$$f_{MAX} = 4710 \text{ psi}$$

$$M.S. = \frac{35000}{4710} - 1 = \underline{\underline{6.43}}$$

UPPER SKIRT RING: MEMBERS 79-90

$$b/t = \frac{1.0}{.089} = 11.2$$

$$F_{CR} = 21000 \text{ psi} \text{ CRIPPLING ALLOWABLE}$$

MEMBER 84, JT. 18; LOAD CASE 5

$$f_{MAX} = 16686 \text{ psi}$$

$$M.S. = \frac{21000}{16686} - 1 = \underline{\underline{0.26}}$$

TRANSITION RING MEMBERS 55-66

$$F_{CR} = F_{CY} = 35000 \text{ psi}$$

MEMBER 59, JT. 29, LOAD CASE 5

$$f_{MAX} = 15445 \text{ psi}$$

$$M.S. = \frac{35000}{15445} - 1 = \underline{\underline{1.27}}$$

ORIGINAL PAGE IS  
OF POOR QUALITY

PREPARED H. J. Dean 6/30/74

REPORT NO.

PAGE 6

CHECKED

MODEL EOS-A THOR DELTA

MARGINS OF SAFETY

S/C OUTRIGGERS MEMBERS 7-12

$$F_{CR} = \frac{\pi^2 EI}{AL^2} = \frac{\pi^2 (10.7 \times 10^6) (0.4)}{(1.8) (54.9)} = 17519 \text{ psi}$$

$$F_{CR} = 17519 \text{ psi}$$

MEMBER 8, JT. 15, LOAD CASE 5

$$f_{MAX} = 8647 \text{ psi}$$

$$M.S. = \frac{17519}{8647} - 1 = \underline{\underline{1.03}}$$

FRAME AT TRANSITION RING - MEMBERS 13-24

$$b/t = \frac{3.0}{.11} = 27$$

$$F_{CR} = 26000 \text{ psi}$$

MEMBER 13, JT 50, LOAD CASE 5

$$f_{MAX} = 11295 \text{ psi}$$

$$M.S. = \frac{26000}{11295} - 1 = \underline{\underline{1.30}}$$

SKIRT DIAGONALS MEMBERS 1-6

$$b/t = \frac{2.0}{.17} = 12$$

$$F_{CR} = 34000 \text{ psi}$$

MEMBER 2, JT 15, LOAD CASE 5

$$f_{MAX} = 8739 \text{ psi}$$

$$M.S. = \frac{34000}{8739} - 1 = \underline{\underline{2.89}}$$

AFT SKIRT MEMBERS - PLATES 1-12

PLATE 6, JT. 7, LOAD CASE 5, BUCKLING CRITICAL

$$f_{MAX} = 17907 \text{ psi}; \text{ ASSUME STIFFENERS ON } 8'' \text{ CENTERS}$$

$$\sqrt{K_c} \text{ FOR } \frac{L^2}{Rt} = \frac{48^2}{(1.5)(.06)} = 171 \leq \sqrt{K_c} = 6; \quad b/\sqrt{K_c} = \frac{8}{.06(6)} = 22.2$$

$$F_{CR} = 19500 \text{ psi} \quad 2024-T3 \text{ AL AL} \quad M.S. = \frac{19500}{17907} - 1 = \underline{\underline{0.09}}$$

PREPARED W. J. Dean

6/30/74

REPORT NO.

PAGE 7

CHECKED

MARGINS OF SAFETY

MODEL EOS-A THOR DELTA

PLATFORM - TRANSITION PLANE PLATES 13-33

SANDWICH PLATE 16, LOAD CASE 5

$$f_{MAX} = 638 + 8942 = 9580 \text{ psi}$$

CHECK INTRA-CELL BUCKLING

$$S = 0.188 \text{ in. } t_F = 0.05$$

$$S/t_F = \frac{0.188}{0.05} = 3.76 \text{ NOT CRITICAL}$$

$$F_{cx} = F_{cy} = 36000 \text{ psi}$$

CHECK WRINKLING

$$S/t_{cw} = \frac{0.188}{0.001} = 188$$

$$F_{cw}/n = 50000 \text{ psi}$$

$$F_{cy}/F_{cw}/n = \frac{36000}{50000} = 0.72$$

$$F_{cw}/F_{cy} = 0.95$$

$$\therefore F_{cw} = 0.95 (36000) = 34200 \text{ psi}$$

$$M.S. = \frac{34200}{9580} - 1 = \underline{\underline{2.57}}$$

ORIGINAL PAGE IS  
OF POOR QUALITY

PREPARED

*St. J. Klean*

*6/30/74*

REPORT NO.

PAGE 8

CHECKED

MODEL *EOS-A THOR DELTA*

**MARGINS OF SAFETY**

**PAYLOAD SECTION OF THOR-DELTA CONFIGURATION**

LONGERONS: MEMBERS 43-54

$$b/t = \frac{3.0}{.083} = 36$$

$$F_{CR} = 22500 \text{ psi}$$

MEMBER 43, JT. 27, LOAD CASE 4

$$f_{MAX} = 14670 \text{ psi}$$

$$M.S. = \frac{22500}{14670} - 1 = \underline{\underline{0.53}}$$

**CROSS BRACES - VERTICAL PLATE**

MEMBERS 100-123

$$b/t = \frac{3.0}{.06} = 50$$

$$F_{CR} = 20000 \text{ psi}$$

MEMBER 100, JT. 27 LOAD CASE 4

$$f_{MAX} = 9546 \text{ psi}$$

$$M.S. = \frac{20000}{9546} - 1 = \underline{\underline{1.10}}$$

**HORIZONTAL FRAMES MEMBERS 25-28, 31-34, 37-40**

$$b/t = \frac{3.0}{.04} = 75$$

$$F_{CR} = 12500 \text{ psi}$$

MEMBER 25, JT. 38, LOAD CASE 5

$$f_{MAX} = 2272 \text{ psi}$$

$$M.S. = \frac{12500}{2272} - 1 = \underline{\underline{4.50}}$$

**HORIZONTAL CROSS BRACES: MEMBERS 29, 30, 35, 36, 41 & 42**

$$b/t = \frac{3.0}{.021} = 143$$

$$F_{CR} = 5000 \text{ psi}$$

MEMBER 29, JT. 37, LOAD CASE 4

$$f_{MAX} = 1642 \text{ psi}$$

$$M.S. = \frac{5000}{1642} - 1 = \underline{\underline{1.04}}$$

PREPARED H. J. Dean 7/1/74

REPORT NO.

PAGE 9

CHECKED \_\_\_\_\_

MODEL EOS-A TITAN

MARGINS OF SAFETY

POWER MODULE

CORNER POSTS MEMBERS 45-49

$$b/t = \frac{3.75}{.125} = 30$$

$$F_{cr} = 25000 \text{ psi}$$

MEMBER 48, JT. 12, LOAD CASE 4

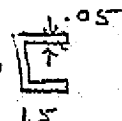
$$f_{max} = 2094 \text{ psi}$$

$$M.S. = \frac{25000}{2094} - 1 = \underline{\underline{10.94}}$$

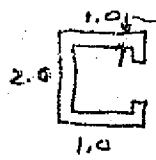
NC FRAME MEMBERS

CRITICAL MEMBER 3, JT. 3, LOAD CASE 5

$$f_{max} = 60973 \text{ psi}$$

NOMINAL FRAME CHANNEL  IS NOT ADEQUATE

MAKE SECTION WITH LIP AS FOLLOWS

  $b = (1.0 - 0.12) = 0.88 \text{ in}$   $t = 0.06 \text{ in}$   
 $b/t = \frac{.88}{.06} = 14.7$  NO EDGE FREE

$$F_{cr} = 65000 \text{ psi} \text{ FOR } 7075\text{-T6 ALAL}$$

$$M.S. = \frac{65000}{60973} - 1 = \underline{\underline{0.07}}$$

DIAGONAL FRAME MEMBERS: MEMBERS 62-69

MEMBER 62, JT 25, LOAD CASE 4

$$f_{max} = 14699 \text{ psi}$$

$$b/t = \frac{1.0}{.06} = 16.7 \text{ ASSUME NO LIP}$$

$$F_{cr} = 16000 \text{ psi}$$

$$M.S. = \frac{16000}{14699} - 1 = \underline{\underline{0.09}}$$

PREPARED W. J. Dean 7/1/74

REPORT NO.

 PAGE 10

CHECKED \_\_\_\_\_

**MARGINS OF SAFETY**

 MODEL EOS-A TITAN
**POWER MODULE CONT'D.**

SANDWICH RADIATOR PANEL

$$\text{LET } S = 1/4" ; t_r = 0.030"$$

CHECK INTRACELL BUCKLING

$$S/t_r = \frac{0.25}{0.030} = 8.3 \quad \text{NOT CRIT}$$

$$F_{ci} = F_{cy}$$

CHECK WRINKLING

$$S = 1/4" ; t_c = 0.0007"$$

$$S/t_c = \frac{0.25}{0.0007} = 357$$

$$F_{cw}/n_2 = .43 \sqrt[3]{E_c' E_c' E_F}$$

$$F_{cw}/n_2 = .43 \sqrt[3]{(17 \times 10^3)(6.4 \times 10^3)(10 \times 10^6)}$$

$$F_{cw}/n_2 = 0.43 (10.3 \times 10^4) = 44226 \text{ psi}$$

$$F_{cy}/F_{cw}/n_2 = \frac{36000}{44226} = 0.81$$

$$F_{cw}/F_{cy} = 0.9$$

$$F_{cw} = 0.9(36000) = 32400 \text{ psi}$$

PLATE 22, LOAD CASE 4

$$J_{MAX} = 3164 + 1991 = 5155 \text{ psi} \quad \begin{matrix} \text{(ASSUME MEMBRANE} \\ \text{BENDING MOO FOR} \\ \text{CONSERVATISM)} \end{matrix}$$

$$M.S. = \frac{32400}{5155} - 1 = \underline{\underline{5.28}}$$

SHEAR WEBS:

 NOT CRITICAL BY COMPARISON WITH ABOVE ( $t_F = 0.05$ )

#### 5.6.2.2 Distortion Analysis

Using the analytical model of the Titan baseline configuration, temperature distributions at three different orbit times were imposed on the observatory and the resulting distortions were computed again using SSAP.

To determine the effective pointing error or uncertainty of an experiment relative to the attitude determination module, four corner points of each module were used to effectively describe a plane (this involved averaging rotations and/or displacements relative to a given plane). The spacecraft corners were joints 13, 17 (lower) and 29, 33 at transition ring. Thematic mapper joints were 42,44 (lower) and 48,50 (upper). HRPI joints were 48,50 (lower) and 54, 56 (upper).

Each pair of points were plotted to exaggerated scales as shown in the following pages and from these plots the average pitch and roll angle of each module could be computed. With the three time sequenced sets of data the rate of change was computed assuming a sinusoidal function as shown in Figure 1 (attached and in the text, Section 6.9). The individual times (20.8, 21.4, and 22.2 hours) shown on the computation sheets relate to specific computer runs and have been converted to a single orbit cycle time in Figure 1.

Two pages of plots are shown for each time. The first is a plot of each horizontal plane as it moves in the Y-Z plane in the Z direction (+Z = NADIR). Using the average values of these Z displacements, the pitch and roll slopes of the individual modules can be computed. The second page of each set shows the pitch angle relative to zero for each module. The relative value of pitch angle is then computed and shown on this second page.

The total results are shown in Figure 1 and summarized in the report in Section 6.9.



PREPARED

*H. J. Dean*

*4/27/74*

REPORT NO.

PAGE

*1*

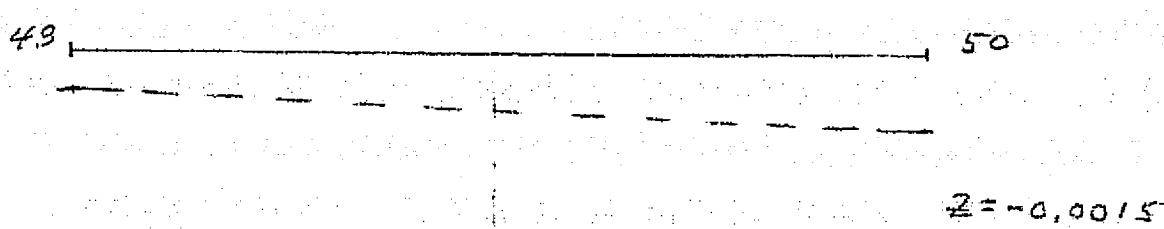
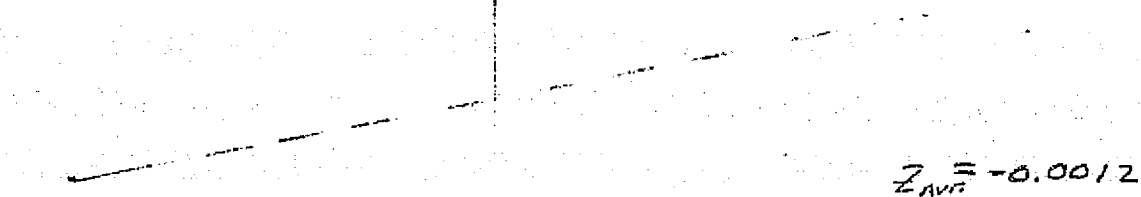
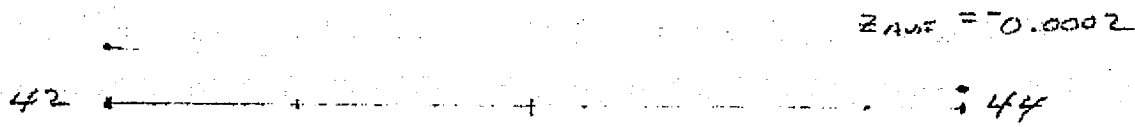
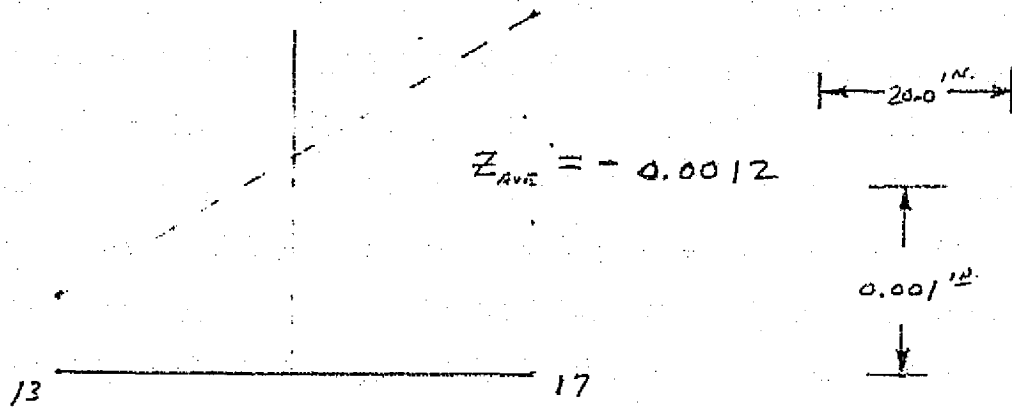
CHECKED

*DISTORTION ANALYSIS*

MODEL

*EOS-A TITAN*

*TIME = 20.8 Hrs.*



PREPARED

*H. J. Dean*

6/27/74

REPORT NO.

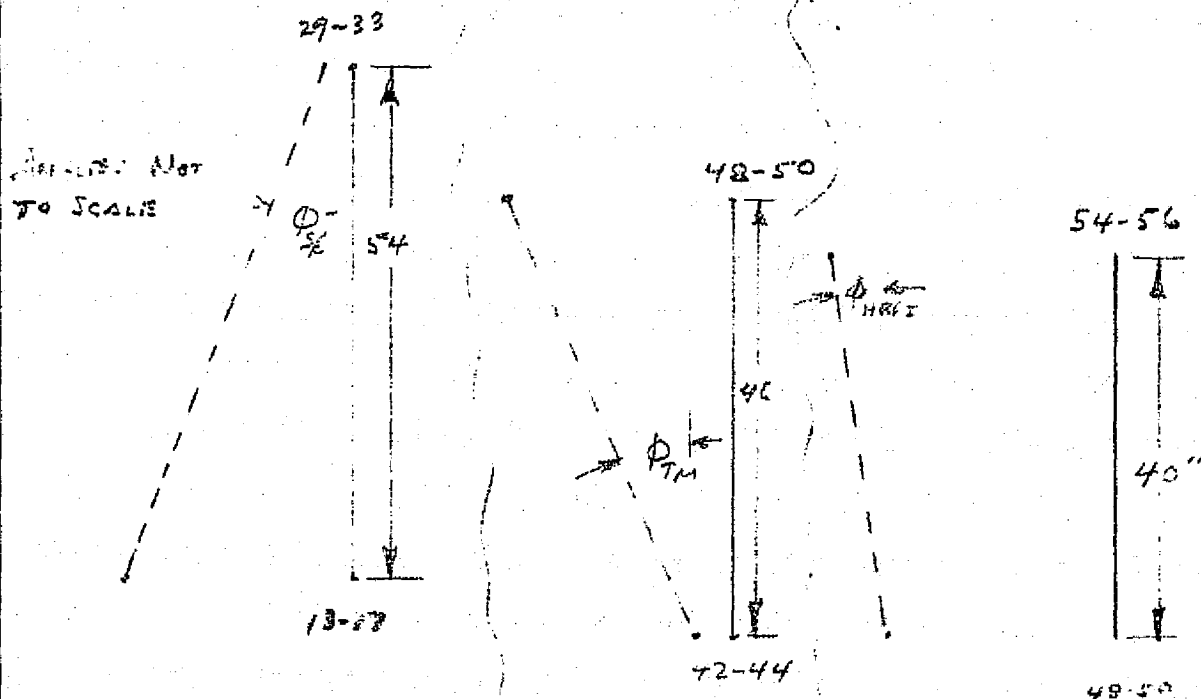
PAGE 2

CHECKED

MODEL *EOS-A TITAN*

# *DISTORTION ANALYSIS*

*SLOPES @ TIME = 20.8 HRS.*



PITCH ANGLE

$$\phi_{S/C} = 4.0 \text{ arc sec}$$

$$\phi_{TM} = 4.5 \text{ arc sec.}$$

$$\phi_{HRPT} = 1.5 \text{ arc sec}$$

RELATIVE ANGLE BETWEEN S/C ATTITUDES DETERMINATION  
MODULE AND EXPERIMENTS:

$$\phi_{S/C, TM} = 4.0 + 4.5 = 8.5 \text{ arc. sec.}$$

$$\phi_{S/C, HRPT} = 4.0 + 1.5 = 5.5 \text{ arc sec.}$$

ORIGINAL PAGE IS  
OF POOR QUALITY

PREPARED

*M. J. Dean*

*6/27/74*

REPORT NO.

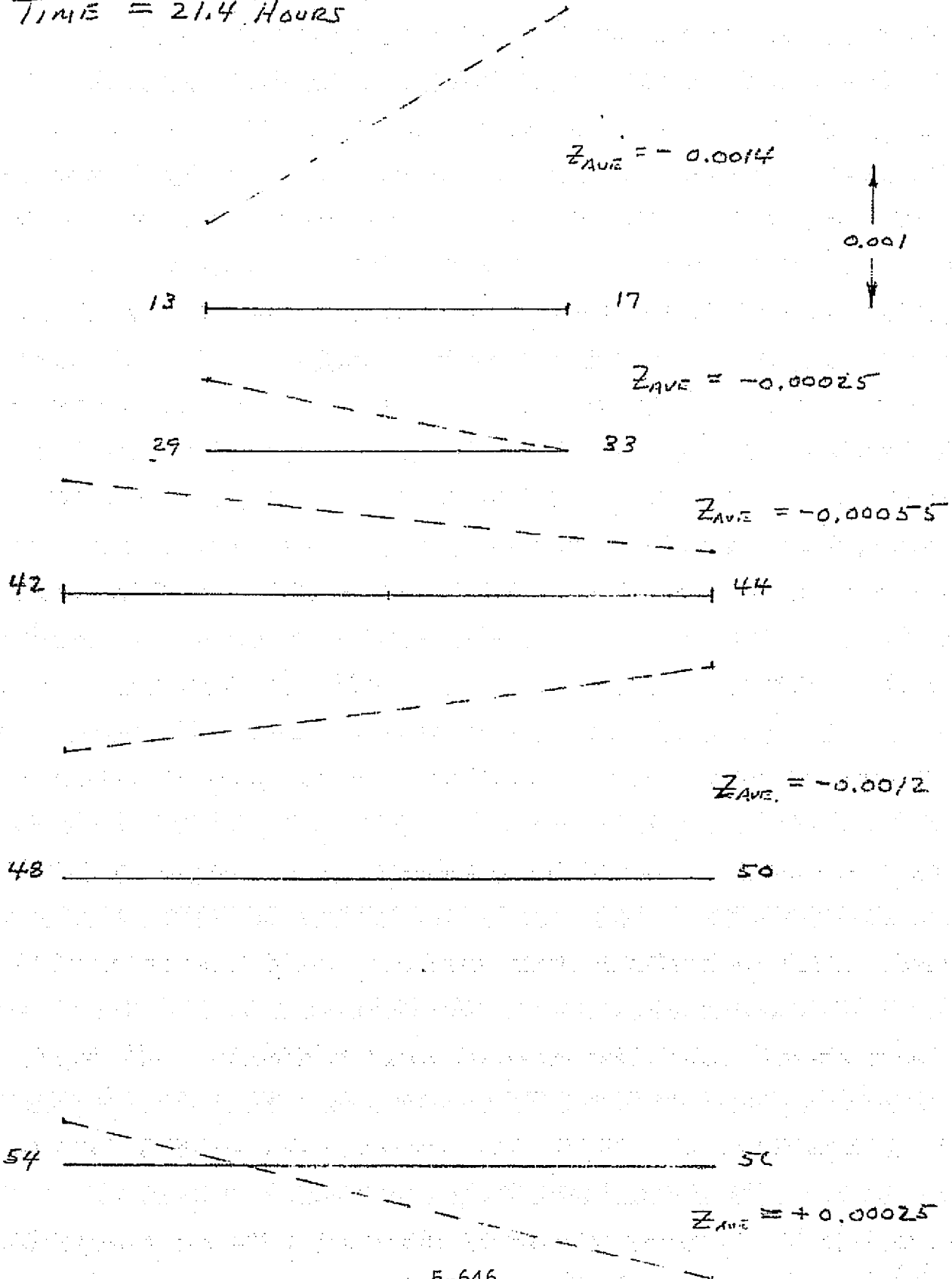
PAGE **3**

CHECKED

MODEL *EOSA TITAN*

*DISTORTION ANALYSIS*

*TIME = 21.4 HOURS*



PREPARED W. J. Dean

6/27/74

REPORT NO.

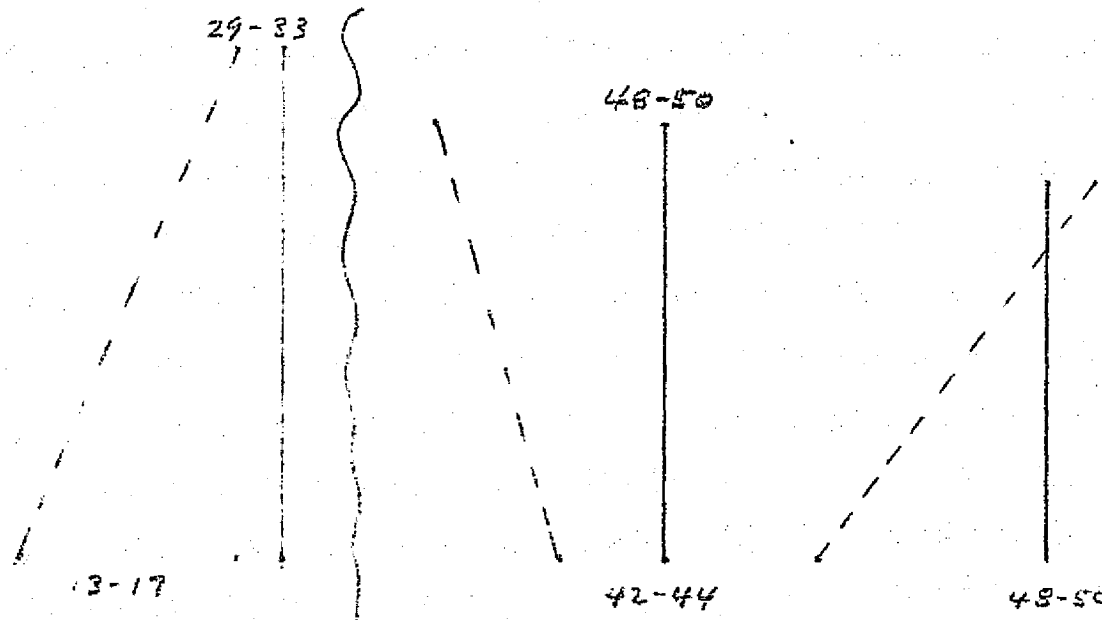
PAGE 4

CHECKED \_\_\_\_\_

MODEL EOS-A TITAN

# DISTORTION ANALYSIS

SLOPES @ TIME = 21.4 HOURS



PITCH ANGLES

$$\phi_{S/C} = 4.4 \text{ arc sec.}$$

$$\phi_{TM} = 2.9 \text{ arc sec.}$$

$$\phi_{HREP} = -7.5 \text{ arc sec.}$$

RELATIVE ANGLE BETWEEN S/C ATTITUDE DETERMINATION  
MODULE AND EXPERIMENTS :

$$\phi_{S/C, TM} = 4.4 + 2.9 = 7.3 \text{ arc sec.}$$

$$\phi_{S/C, HREP} = 4.4 - 7.5 = 3.1 \text{ arc sec.}$$

ORIGINAL PAGE IS  
OF POOR QUALITY

PREPARED

*H. J. Dean*

*6/27/74*

REPORT NO.

PAGE *5*

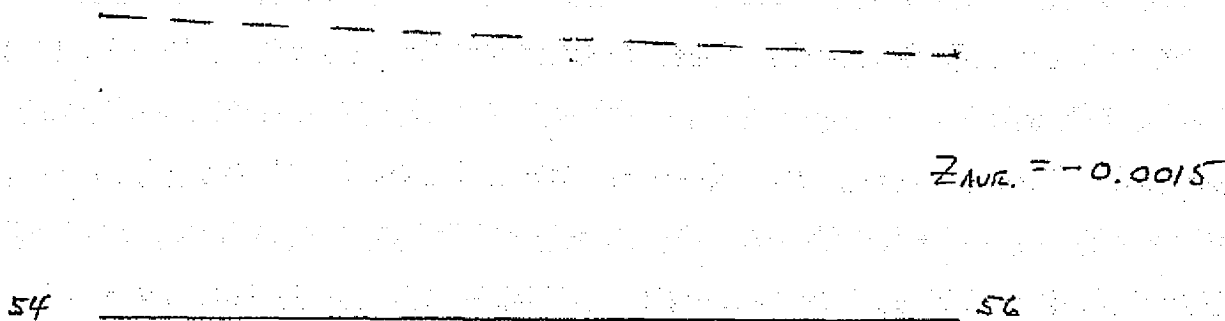
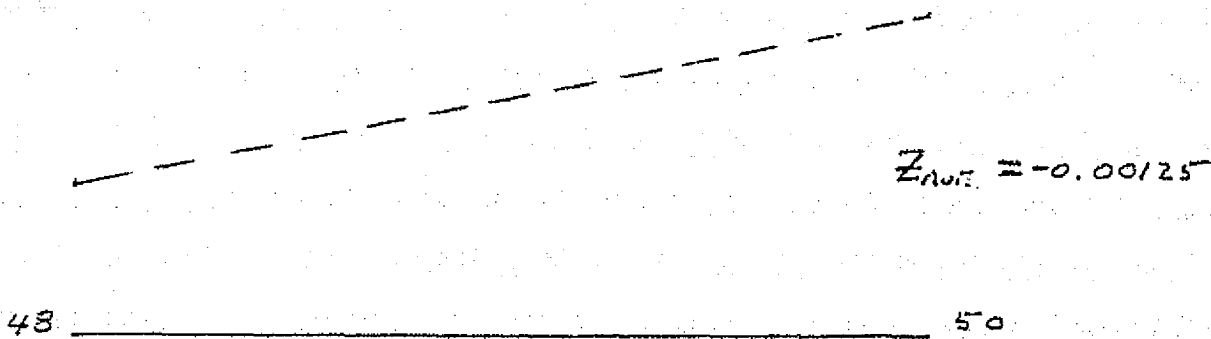
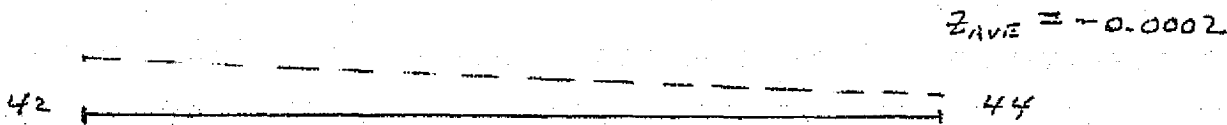
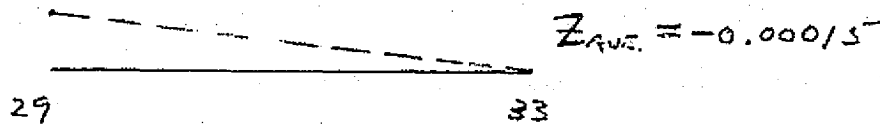
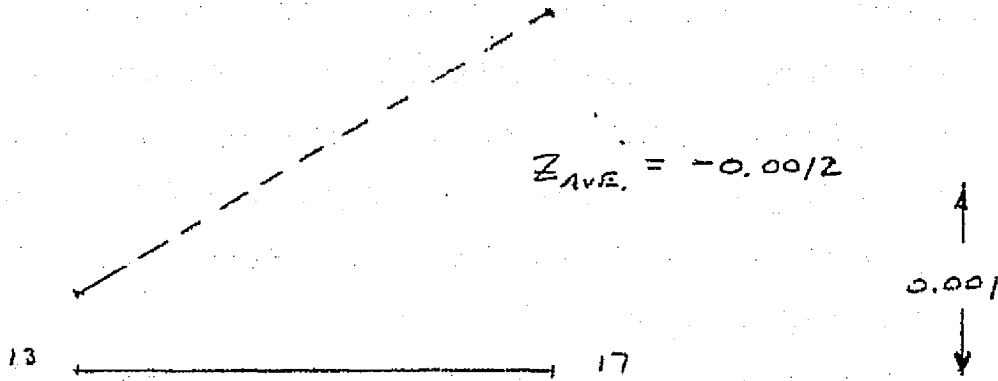
CHECKED

MODEL

*EOS-A TITAN*

# *Distortion Analysis*

*TIME = 22.2 HOURS*



PREPARED St. G. Dean

6/27/74

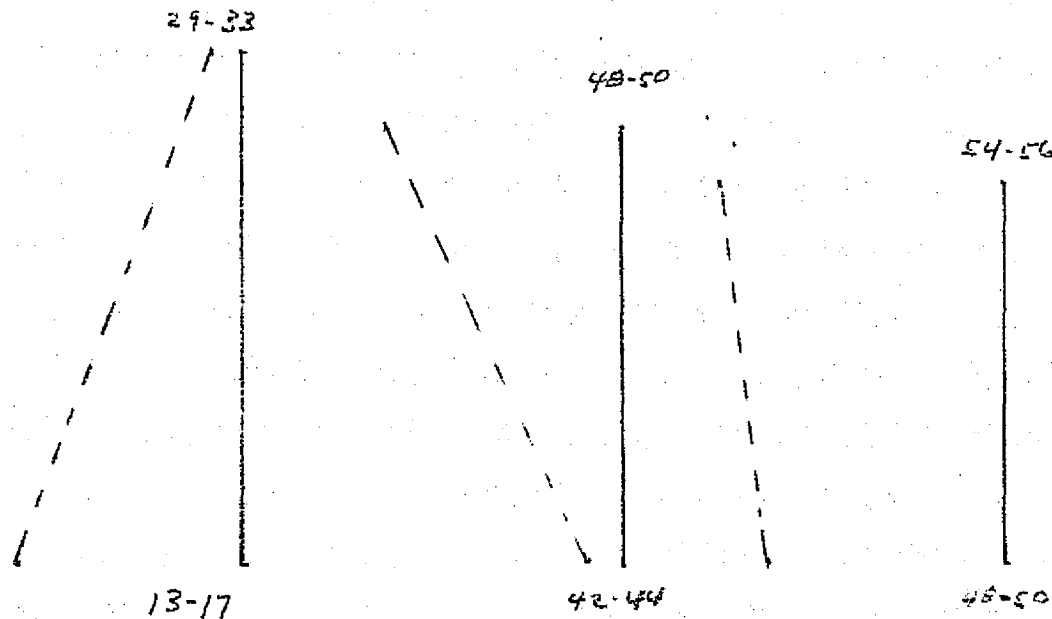
REPORT NO.

PAGE 6

CHECKED \_\_\_\_\_

MODEL EOS-A TITAN

**DISTORTION ANALYSIS**



PITCH ANGLES :

$$\phi_{S/C} = 4.0 \text{ arc sec.}$$

$$\phi_{TM} = 4.7 \text{ arc sec.}$$

$$\phi_{HAPS} = 1.3 \text{ arc sec.}$$

RELATIVE ANGLE BETWEEN S/C ATTITUDE DETERMINATION  
MODULE AND EXPERIMENTS :

$$\phi_{S/C, TM} = 4.0 + 4.7 = 8.7 \text{ arc sec.}$$

$$\phi_{S/C, HAPS} = 4.0 + 1.3 = 5.3 \text{ arc sec.}$$

PREPARED

*W. J. Dean*

*4/28/74*

REPORT NO.

PAGE

*7*

CHECKED

MODEL

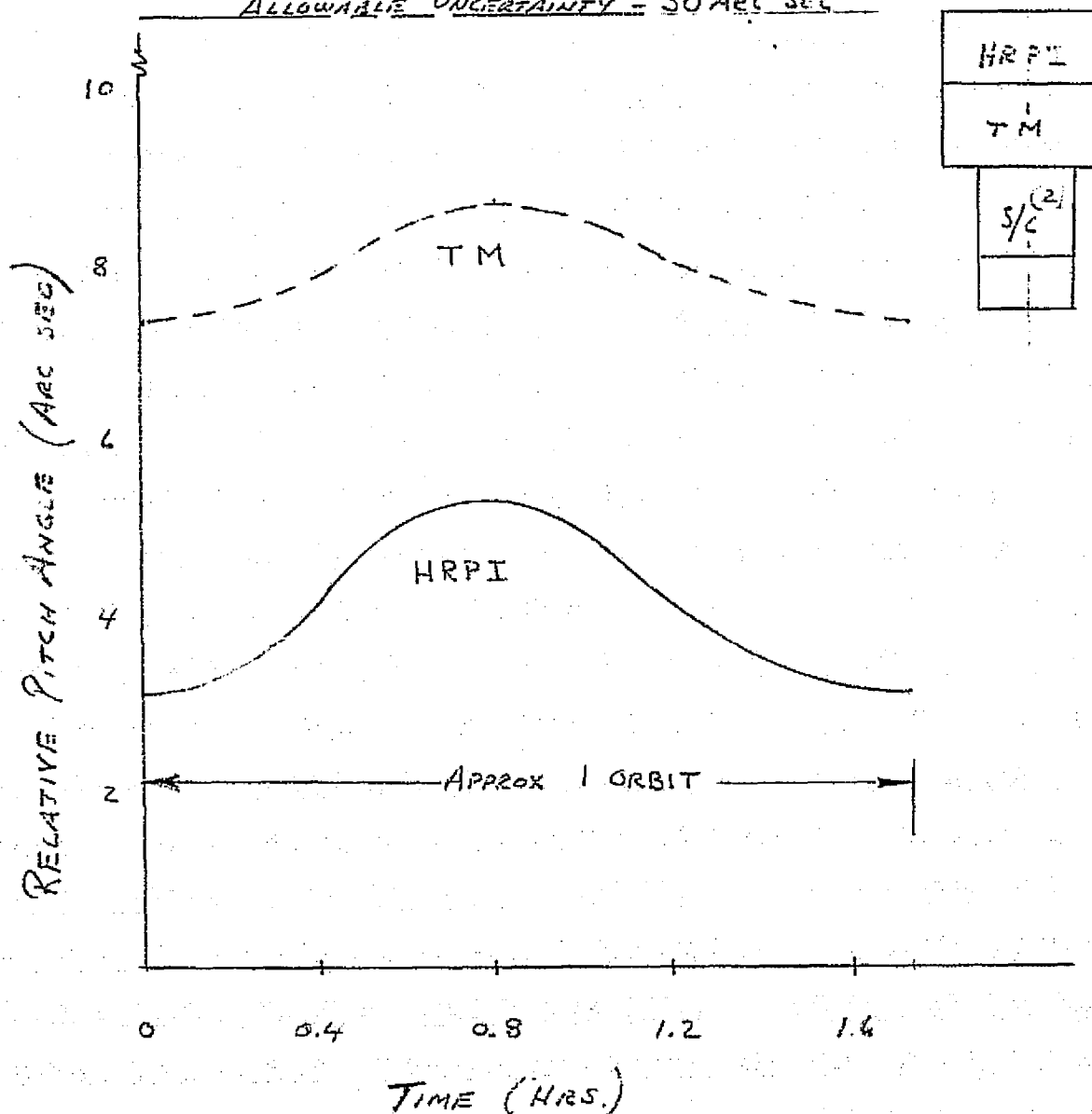
*EOS-A TITAN*

# *DISTORTION ANALYSIS*

*FIGURE 6.9-1. PITCH ANGLE UNCERTAINTY (1)*

*REF APPENDIX A, SECTION 5.5.4 FOR TEMPERATURE DISTRIBUTIONS.*

*ALLOWABLE UNCERTAINTY = 30 ARC SEC*



*DRIFT RATE (MAX) FOR TM = 3.0 ARC SEC/HR*

*DRIFT RATE (MAX) FOR HRPI = 7.7 ARC SEC/HR*

*(1) ROLL ANGLE UNCERTAINTY MAXIMUM = 2.6 ARC SEC*

*(2) S/C - SPACECRAFT (LOCATION OF ATTITUDE DETERMINATION MODULE USED AS BASELINE ATTITUDE REFERENCE)*

## 6. OBSERVATORY INTEGRATION AND TEST

### 6.1 TEST PLAN AND TEST-COST REDUCTION

"The AMS objective for testing is to achieve an optimum balance between maximizing reliability and minimizing cost." "An implicit AMS test goal is thus to minimize requirements for system level environmental tests." These two statements provide the basic guidelines for determination of the EOS test program.

The basic problem is to determine the necessary departure from conventional observatory test programs which is dictated by the modular design approach. Once this has been done, the program is to be optimized from cost, schedule and benefit standpoints. The result should be an approach to testing which gets "the most for your money" while providing the required confidence level for observatory performance verification.

The modular design approach for EOS provides a minimum number of standardized interfaces and the isolation required to prevent interaction at the system level. After this has been verified and margins determined, the test program should be evaluated for possible reduction or elimination of tests. Each of the following test types should be considered.

- Environmental tests
- EMI and EMS measurements
- Functional performance tests

The theme behind testing the modular observatory is interface verification. Of course, internal functional performance determination is important, but conventional designs and hardware are planned for these components. The major advancement is in design and control of the module interfaces, and therefore, the test program needs to be structured in this direction.

The fundamental test concepts planned for "The Advanced Modular Spacecraft" in EOS-L-140 is to be evaluated for technical validity and



cost effectiveness. This approach is to be coupled with the specific EOS design and previous observatory test histories to produce the lowest-cost test program consistent with the required confidence levels for EOS.

#### 6.1.1 Assumptions

The following factors are assumed for this problem:

- The test program must provide, as a minimum, the same level of confidence achieved on present conventional test programs.
- There are no differences in design between qualification and operational modules.
- Both the qualification and operational modules are fabricated by the same manufacturer with the same processes and inspection methods.

#### 6.1.2 Analysis and Tradeoffs

The conventional test plan, today, emphasizes testing at the component (unit) and all-up observatory levels. Limited (or no) testing exists at the subsystem level. The test plan for the Advanced Modular Spacecraft calls for a revision to this approach consistent with the new modular design concepts. That is; extensive testing is performed at the subsystem module level and testing is to be reduced at the all-up observatory.

If we assume that the same degree of testing is required to achieve the same level of confidence, the number of environmental test hours is lowered on the order of 50 percent. The ability to take advantage of the reduced test time is dependent upon: (1) developing adequate test methods for verification of module interfaces (electrical, mechanical and thermal); (2) reducing the number of failures and retest at the module level. The key to reduction in observatory-level tests lies in the module interface verifications. The key to qualification and acceptance testing at the module level lies in limiting the number of component failures which cause module repair and retest.

Cost advantages could be realized for the EOS-A baseline if the role of the integrating contractor would be expanded to include both module and

observatory integration and testing. The following factors support this approach:

- If an observatory is the end item to be delivered and launched, it is believed that performance verification should be at that level. Given this concept, the module-level functional and environmental tests can be reduced with small program risk.
- The EGSE system test set plus two simulators could support the I&T program. Therefore, the module test sets could be eliminated (Section 6.3).
- Module failures at the observatory level could be repaired by component replacement at the integration and test facility. This would negate the necessity to ship failed modules to another contractor and incur the associated schedule delays. Also, the spares concept would be lowest-cost.

### 6.1.3 Conclusions

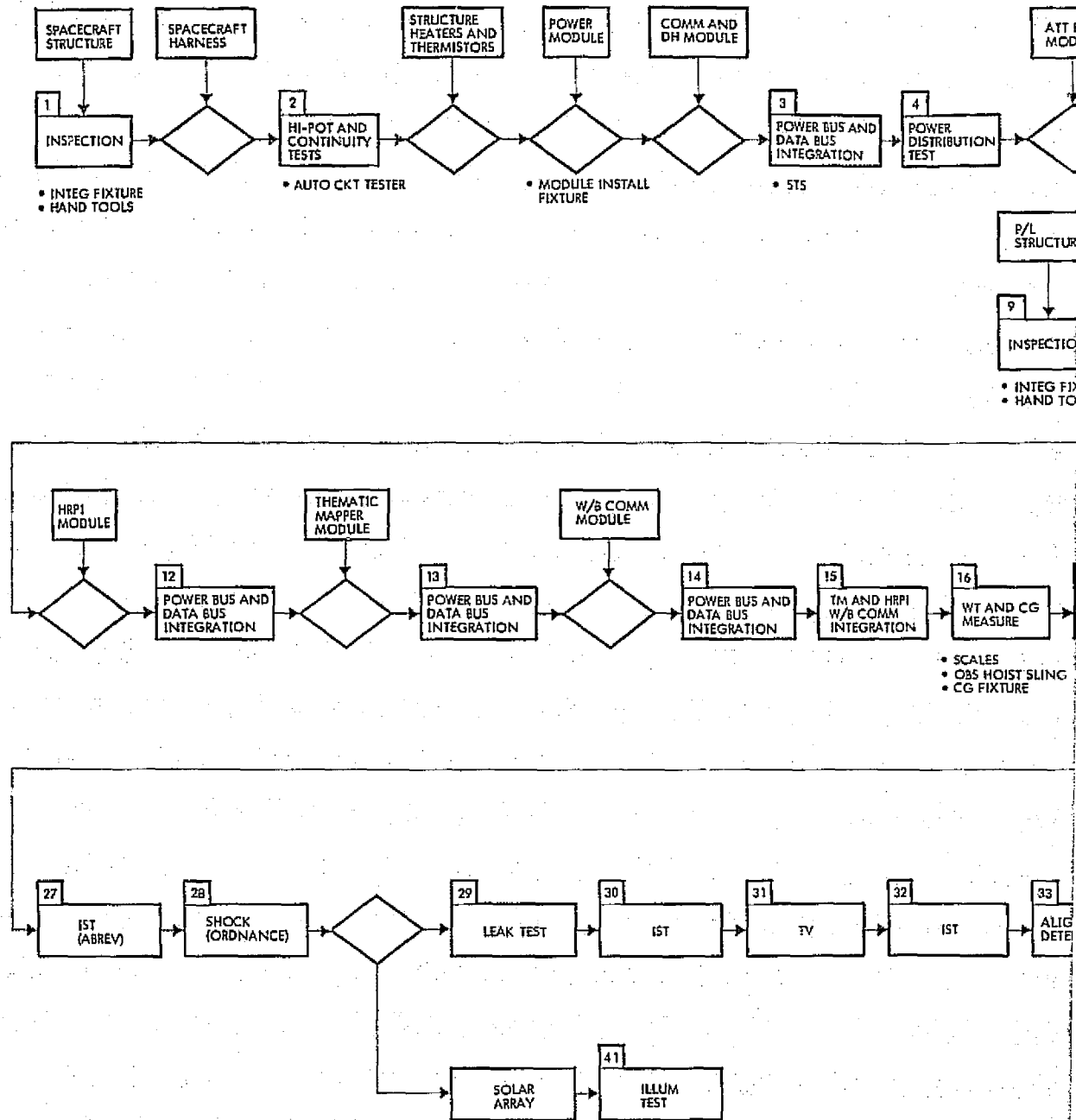
#### 6.1.3.1 Qualification

The qualification test matrix is shown in Table 6-1, and the pilot model observatory integration and test sequence is given in Figure 6-1 and Table 6-2. One component of each type, each module and the all-up observatory should be subjected to the environmental and performance tests shown. The emphasis must be placed upon characterizing each module interface characteristics — thermal, mechanical and electrical performance. Specific comments regarding the proposed qualification testing:

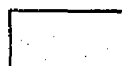
- The only shock testing should be an ordnance firing simulation with a complete observatory.
- Acceleration tests are not required.
- Electromagnetic Compatibility (EMC) tests at the observatory level should be limited to noise measurements at the module test connectors. That, coupled with an integrated system test, should reveal all mutual electromagnetic compatibility problems.
- No spacecraft electrical bench tests separate from the observatory should be required.
- Mass properties can be limited to measurement of weight and center of gravity.
- No static tests are required because of the increased factor of safety for the structure.







LEGEND:



TEST



INSTALLATION OR REMOVAL

NOTE: EQUIPMENT LISTED UNDER FIRST EVENT USED

PRECEDING PAGE

ORIGINAL PAGE IS  
OF POOR QUALITY

FOLDOUT PAGE

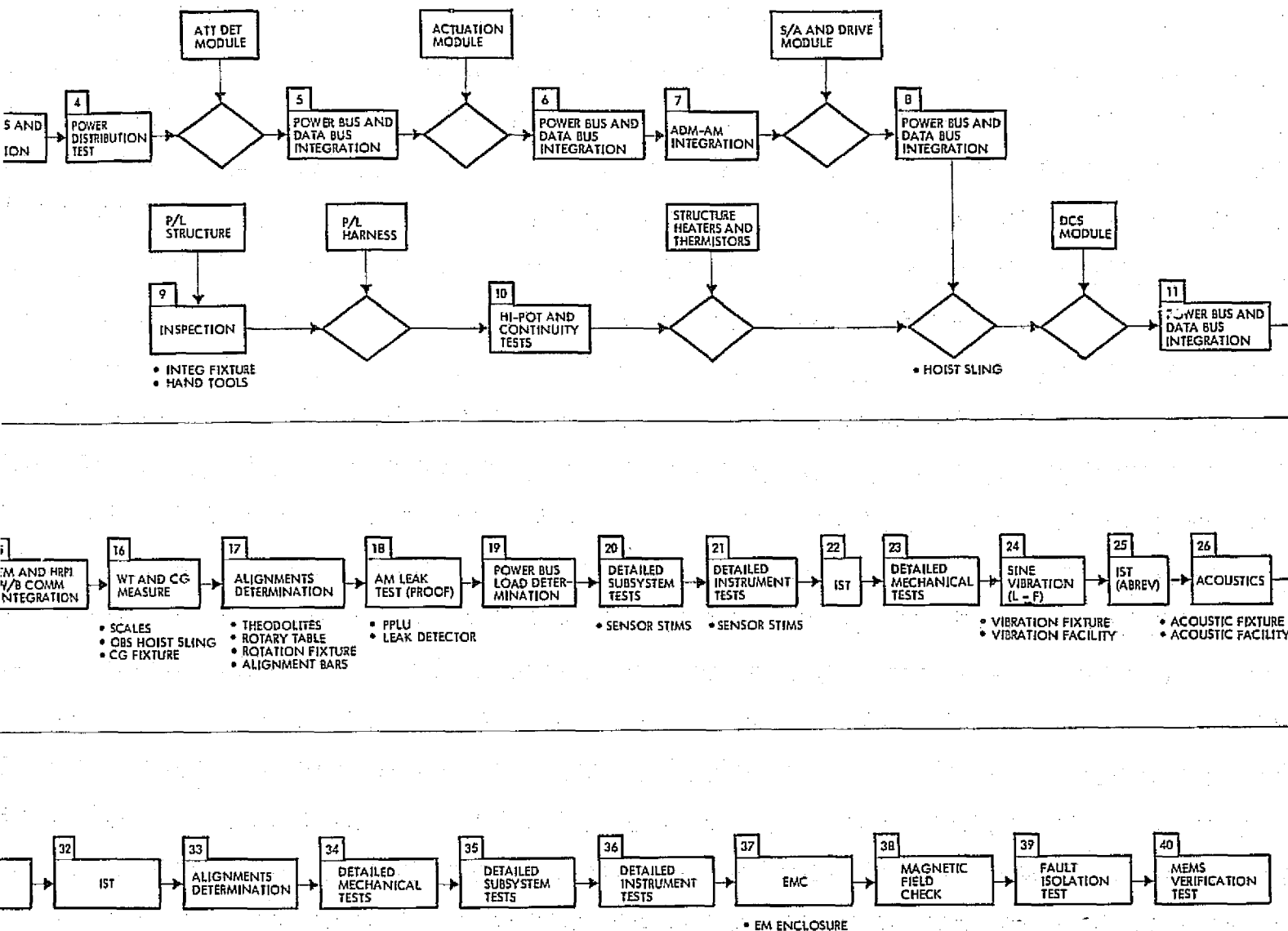


Figure 6-1. EOS-A, I&T Sequence for Qualification

PRECEDING PAGE BLANK NOT FILMED

OLD COPY

Table 6-2. EOS-A Assembly, Integration, and Test for Qualification

No.	Event	Description
1	Inspection	Determine dimensional locations of module attachment interfaces and alignment references.
2	Hi-pot and continuity test	Determine cable harness insulation breakdown and wiring continuity.
3	Power bus and data bus integration	Determine module power demand and voltage level at the user terminals. Determine functional response to each command used by the module. Measure command control signal characteristics. Determine the telemetry control signal characteristics and data outputs for each measurement by the module.
4	Power distribution test	Measure voltage level at each power bus/module interface cable harness connector.
5	Same as 3	Same as 3
6	Same as 3	Same as 3
7	Attitude-actuation modules integration	Simulate sensor outputs and measure characteristics of signals transmitted from the attitude determination module to the actuation module.
8	Same as 3	Same as 3
9	Same as 1	Same as 1
10	Same as 2	Same as 2
11	Same as 3	Same as 3
12	Same as 3	Same as 3
13	Same as 3	Same as 3
14	Same as 3	Same as 3
15	TM and HRPI-Wide Band communications modules integration	Simulate sensor outputs and measure characteristics of data signals from the TM and HRPI modules and transmission from the wide band communications module.
16	Weight and CG measurement	Measure observatory weight and center of gravity.
17	Alignments determination	Determine orientation of attitude sensors (sun sensors, star tracker, magnetometer and gyros), actuation units (thrusters, magnetic torquers and reaction wheels), antennas and instrument sensors (TM and HRPI).
18	Actuation module leak test	Load actuation propellant to proof pressure and measure leak rate.
19	Power bus load determination	Determine the primary power demand for each commanded configuration planned for the mission which creates a unique power condition.
20	Detailed subsystem tests	Measure sensitivity and acquisition frequency of each command receiver. Verify power bus protection functions. Check magnetometer and gyro outputs in Earth's field. Stimulate each attitude sensor and measure output. Measure ranging time delay. Measure downlink spurious.
21	Detailed instrument tests	Stimulate each instrument sensor and verify data output and calibration.
22	Integrated System Test (IST)	Determine baseline system functional performance over a simulated mission profile. Test primary and redundant components and backup modes of operation. Verify all commands and telemetry planned for the mission. Verify OBC memory contents. Measure downlink power output, mod index, frequency and bit rate. Simulate each attitude sensor and measure actuation response. Measure primary power demand and regulated output voltage. Measure firing current for each ordnance circuit. Verify operation of each instrument with simulated sensor outputs. Verify battery and charge control circuits operation.
23	Detailed mechanical tests	Deploy each appendage and measure force and time to latch up. Measure friction torque in solar array drive.
24	Sine vibration test	Vibrate the observatory to qualification levels in 3-axes with low-frequency sine waves. The observatory is in launch configuration, mechanically and electrically. Monitor telemetry data continuously via the RF downlink.
25	IST (abbreviated)	Determine system functional operation via the command and telemetry links. Test primary and redundant components with a reduced (from 23) number of measurements.
26	Acoustics test	Acoustically excite the observatory to qualification levels while in the flight configuration with all equipment operating. Monitor telemetry data continuously via the RF downlink.
27	IST (abbreviated)	Same as 25
28	Shock test	Simulate observatory separation shock by energizing the ordnance devices.
29	Leak test	Load actuation propellant to flight pressure and measure leak rate.
30	IST	Same as 22
31	Thermal vacuum	Measure observatory performance during exposure to a qualification thermal vacuum environment. High and low thermal extremes are introduced at orbital vacuum, and functional performance measured after stabilization. The performance measurements include: (1) IST, (2) temperature levels and thermal control operation, (3) attitude sensor aliveness and (4) instrument sensor aliveness.
32	IST	Same as 22
33	Alignments determination	Same as 17
34	Detailed mechanical tests	Same as 23
35	Detailed subsystem tests	Same as 20
36	Detailed instrument tests	Same as 21
37	Electromagnetic compatibility test	Measure noise levels on critical signals within each module and interface signals between modules. Verify margins.
38	Magnetic field check	Measure level of magnetic field at the magnetometer with the observatory operating at maximum dc power.
39	Fault isolation test	Introduce faults to each power bus protection circuit and verify observatory response.
40	MEM's verification test	Verify the capability and repeatability of module insertion and retraction for Shuttle refurbishment.
41	Solar array illumination test	Illuminate solar array and measure E-I characteristics.

#### 6.1.3.2 Acceptance

The acceptance test matrix is shown in Table 6-3, and the flight EOS integration and test sequence is given in Table 6-4 and Figure 6-2. Each component, module, and Observatory should be subjected to the environmental and performance tests shown.

Specific comments regarding acceptance testing:

- An electromagnetic interference and susceptibility test for modules does not seem warranted for workmanship verification.
- A separate spacecraft-level preintegration functional test is not cost effective.
- A "burn-in" test is recommended at the module level for refurbish items and at the all-up level for a launch of a complete observatory. This will serve two basic purposes: (1) a low-cost thermal test and (2) discovery of infant failures.

#### 6.1.3.3 Launch Operations

Table 6-5 and Figure 6-3 show the major steps for the launch site operations.



**FOLDOUT**

[illegible]

Tanks				X	X															
Pressure Regulator	X		X		X	X														
Electric Power Module	X	X		X*																X
Power Regulator	X		X		X															
PCU	X		X		X															
Diode Box	X		X		X															
Battery	X		X		X															
Power Conditioner	X		X		X															
Data Interface Unit	X		X		X															
Solar Array and Drive Module	X	X		X*				X				X					X		X	X
Solar Panels	X		X		X															
Drive/Slip Ring Assy	X		X		X															
Drive/Readout Elect.	X		X		X															
Deploy/Restow Drive	X		X		X													X		
Power Conditioner	X		X		X															
Data Interface Unit	X		X		X															
Temp. Control/Sig. Cond.	X		X		X															
Ordnance Control	X		X		X															
Structure Subsystem												X					X			
Mechanisms	X										X									
Ordnance								X												
Thermal Subsystem																				
Insulation											X									
Heaters	X																			
Temp. Sensors											X									
Electrical Cable Harness	X					X														
Spacecraft											X									
W/B Comm Module	X	X		X*									X	X	X	X				X
Antennas			X		X								X	X						
Gimbals	X		X		X								X							
Drive and Drive Elect	X		X		X															
X-Band Xntrs	X		X		X															
Antenna Folding Drives	X		X		X														X	
Mod and Input Selector	X		X		X															
TM Speed Buffer	X		X		X															
Data Interface Unit	X		X		X															
Power Conditioner	X		X		X															
Thematic Mapper Module	X	X	X		X									X	X					
Mapper	X														X					
Multiplexer Encoder	X		X		X															
Data Interface Unit	X		X		X															
Power Conditioner	X		X		X															
HRPI Module	X	X	X		X									X	X					
HRPI	X														X					
Multiplexer Encoder	X		X		X															
Data Interface Unit	X		X		X															
Power Conditioner	X		X		X															
DCS Module	X	X		X*									X	X	X					X*
S-Band Antenna	X		X		X								X							
UHF Antenna	X		X		X								X							
Transponder	X		X		X															
Power Conditioner	X		X		X															
Observatory**	X	X		X		X		X		X					X	X				X

NOTES: \* If refurbish items.  
\*\* If launched as complete observatory.

Table 6-4. EOS-A Assembly, Integration, and Test for Acceptance

No.	Event	Description
1	Inspection	Same as Q1
2	Hi-pot and continuity test	Same as Q2
3	TV outgas	Thermal vacuum soak of structure and harness for outgassing.
4	Inspection	Same as 1
5	Hi-pot and continuity test	Same as 2
6	TV outgas	Same as 3
7	Module alignment checks	Check orientation of each module to verify mechanical mating with the structure.
8	Integrated System Test (IST)	Same as Q23
9	Acoustics	Acoustically excite the observatory to acceptance levels while in the flight configuration with all equipment operating. Monitor telemetry data via the RF downlink.
10	IST	Same as 8
11	Detailed subsystem tests	Same as Q21
12	Same as Q22	Same as Q22
13	Burn-in	Operate the observatory continuously for 15 days. A simulated mission profile will be run with temperature cycling via primary power demand and heater current variations.
14	Alignments determination	Same as Q18
15	Leak test	Same as Q30
16	Mechanical T-O Verification	Measure torque as a function of angle throughout deployment arc for each appendage and over 360 degrees rotation of solar array drive.
17	Solar array illumination test	Same as Q42
18	Shipment	Load observatory into its shipping container.

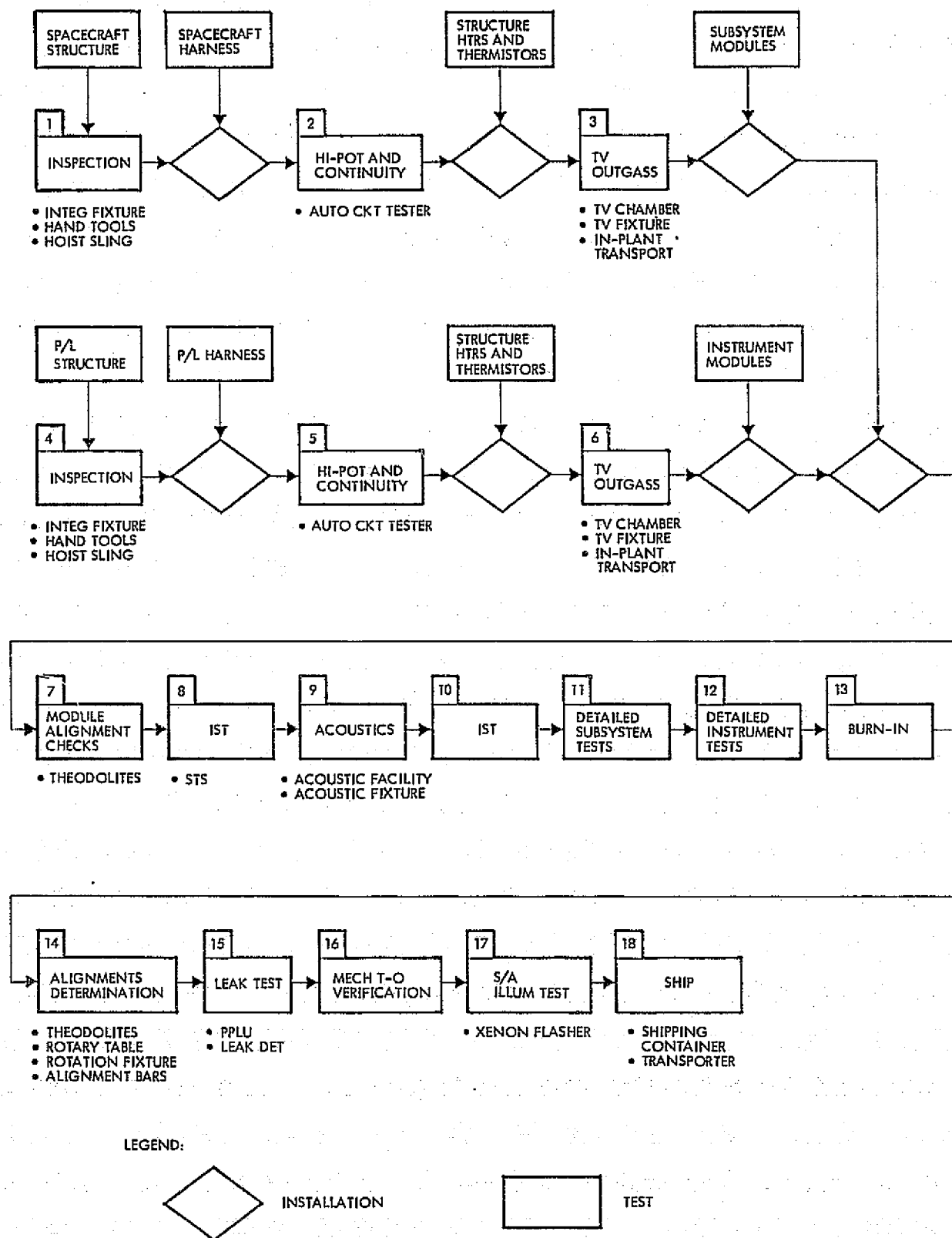


Figure 6-2. Assembly, Integration, and Test Sequence for Acceptance

Table 6-5. EOS-A Launch Operations

No.	Event	Description
1.	Receiving Inspection	Visual inspection of the complete observatory for shipping damage. Examine instrumentation records for excessive transportation environmental conditions.
2.	Transport to Pad	Load shipping container onto a vehicle and transport the observatory to the launch pad.
3.	Mate with LV	Hoist observatory and mate (mechanically and electrically) with the launch vehicle.
4.	On-Stand Functional Check-Out	Verify electrical interconnections to the blockhouse and RF communications for commands and telemetry.
5.	Combined Launch Vehicle Tests	Perform tests to verify launch vehicle and observatory compatibility.
6.	Integrated System Test	Functional checkout of all modes of operation planned for the mission. Performance measurements of all electrical components.
7.	Countdown Preps	Load propellant and pressurant. Initiate red tag item removal and inspection.
8.	Countdown	Complete red tag item operations. Perform final ordnance checks. Command observatory into the launch configuration and monitor status. Remove external power and verify operation of batteries.

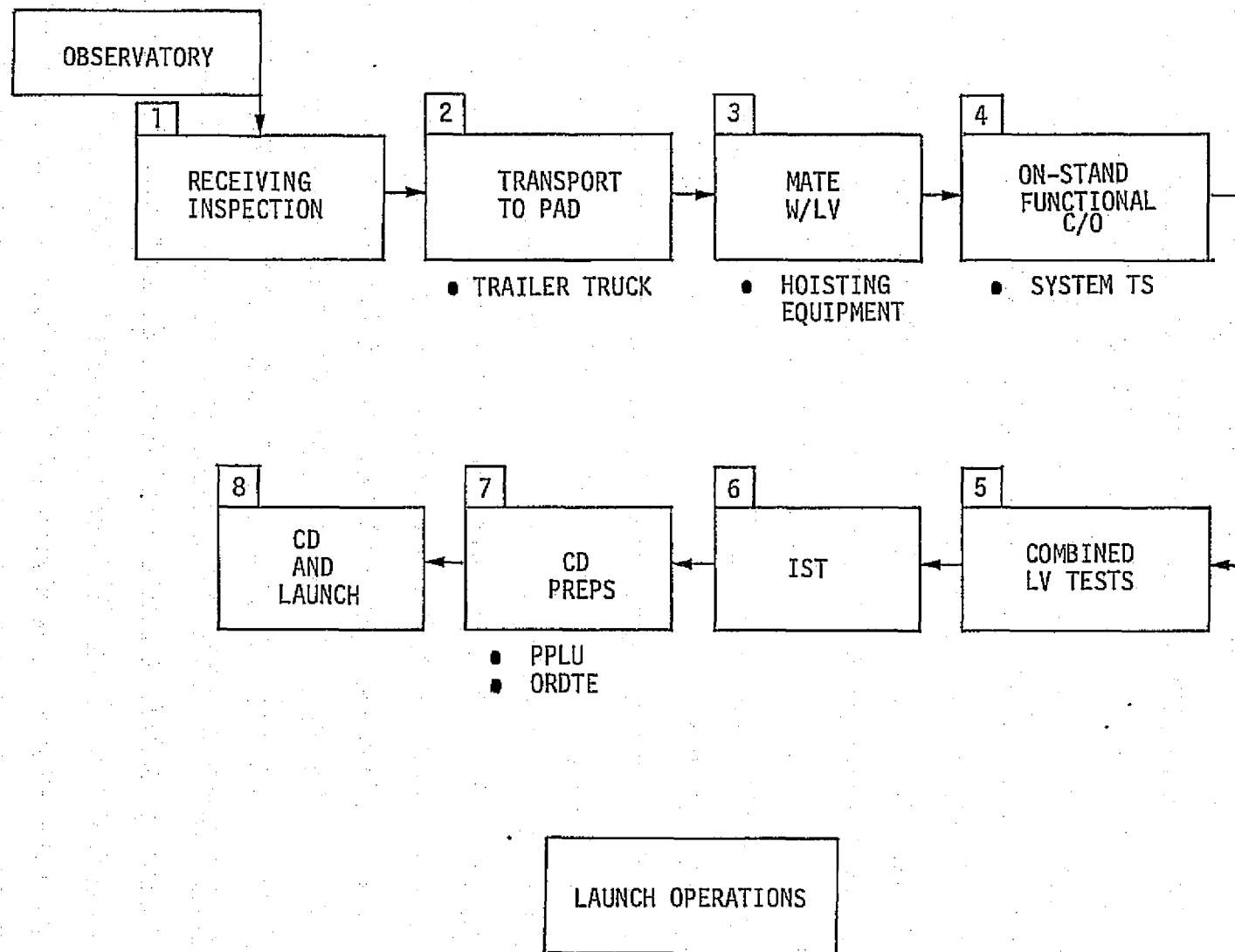


Figure 6-3. Major Steps for Launch Site Operations

## 6.2 LOW-COST TEST DESIGNS

There are certain design characteristics which should be considered for cost impact upon the system test program. Included are:

- Testability provisions — Tests can be simplified or conducted more efficiently if built-in features are incorporated to permit verification by test.
- Accessibility provisions — Observatory integration and failure troubleshooting can be achieved more simply and rapidly if easy access is provided to modules, components and cable harness connectors.
- Design margins — Test requirements can be reduced in scope or tests even eliminated if a design margin exceeds that value considered safe.

### 6.2.1 Assumptions

- Each module provides test connector(s)
- An umbilical connector is provided for launch operations.

### 6.2.2 Analysis and Tradeoffs

#### 6.2.2.1 Testability

Testability provisions are primarily required to stimulate and measure response of the observatory for determination of system performance. These features can be provided via the command/telemetry links and/or hardline test points. The ability to program the OBC for any desired command sequence and telemetry format could greatly simplify hardline requirements.

For system test operations, maximum use should be made of the mission telemetry and commands to provide the necessary monitoring and stimulus. However, module test point hardlines should be provided as required to permit verification of spacecraft system performance, isolation of failures to a replaceable component and enable rapid, efficient test operations. The hardlines should be dictated by the following considerations:

- To supplement telemetry for reasons of unavailability or low sampling rate.
- To supplement command inputs for reasons of unavailability or time constraints.
- To simulate sensor outputs when physical stimulation is not feasible or cannot produce the output characteristics required.
- To prevent breaking electrical interconnections for test.
- To provide EMI measurements.
- If the number of test points becomes excessive from space, weight or cost standpoints, the priority for selection should be in the following order:
  - 1) Required for system performance verification
  - 2) Needed to permit testing of redundancies
  - 3) Useful for failure isolation to a replaceable component

Other testability provisions arise out of the requirements to service the modules and observatory. This servicing is generally required both in-plant and for launch operations.

#### 6.2.2.2 Accessibility

Accessibility provisions (or lack of) can have a significant impact upon integration and test costs. If modules can be installed in any order, schedule constraints are reduced and integration activities can be much more flexible. What level of repair should be handled at the observatory integration test contractor's facility? First of all, spares supply would be much lower cost at the component (black box) level than at the module level. Secondly, it would not be cost-effective to require a module to be returned to the vendor for a component replacement.

#### 6.2.2.3 Design Margins

The following structural design factors of safety are used:

Limit load = maximum expected flight load

Design yield =  $1.5 \times$  limit

Design ultimate =  $1.88 \times$  limit



The above factors represent a 50 percent increase over the conventional design criteria.

### 6.2.3 Conclusions

#### 6.2.3.1 Testability

The following design criteria should apply to test points and connectors:

- All test connectors shall be accessible after a complete assembly of the spacecraft.
- All test points shall be isolated so that grounding the signal shall not cause damage. The isolation circuit selected shall consider the EAGE load/source impedance including cable resistance/capacitance.
- All test connectors shall be female.

The following is a minimum list of testability provisions which are required after complete observatory assembly and after mating with the launch vehicle:

- Command input which does not require acquisition of the RF uplink — This shall apply to all commands for the observatory. This shall be provided both via the module test connector and the umbilical.
- Telemetry output which does not require acquisition of the RF downlink — This shall be provided both via the module test connector and the umbilical.
- An external power input to charge each battery at maximum and trickle charge rates with the observatory deenergized. Battery temperature monitoring shall be provided via hardline test points.
- A deep discharge of each battery for reconditioning with the observatory deenergized.
- Control and monitoring of the actuation valves with the observatory deenergized.
  - Open/close control of each valve
  - Open/close status of each valve
  - Tank temperature monitor

- Measurement of RF power output from each transmitter — The monitor point shall be as near as possible to the antenna input.
- Simulation of the LV-observatory separation switch actuation.
- Simulation of each AVCS sensor output and monitoring each thruster firing signal.
- An external power input to simulate the solar array output — This shall be provided both via the module test connector and the umbilical.
- Verification of parallel redundant elements.
- Propellant and pressurant loading provisions.
- Ordnance bridge wire resistance and firing current measurements.
- Direct memory access to the OBC for loading and readout.

#### 6.2.3.2 Accessibility

The following accessibility provisions are required:

- Insertion of a break-out T-connector between the module and cable harness connectors for interface signal measurements.
- Disassembly of the module structure and thermal insulation to replace a faulty component without requiring retest at the module level.
- Installation or removal of any module and component without requiring removal of other equipment.

#### 6.2.3.3 Design Margins

- Because of the increased safety factors for the structure, static tests can be eliminated.

### 6.3 GROUND SUPPORT EQUIPMENT

The EOS philosophy requires integration and test of modular subsystems in addition to complete satellite. This will require sophisticated module test sets (MTS's) in addition to the system test set (STS) which will tend to cause a significant increase beyond the conventional program cost for support equipment. There is a great deal of commonality in the functional requirements for the MTS's and the STS, and this produces the following approaches for implementing the EOS support equipment.

#### Approach I. Conventional Approach.

Each module contractor would design and fabricate the MTS while the observatory integrating contractor independently designs and fabricates the STS.

#### Approach II. MTS Designs Utilized in the STS.

This differs from Approach I in that the integrating contractor would utilize the MTS designs as appropriate in the STS.

#### Approach III. MTS Hardware Utilized in STS.

The MTS hardware would be used in the STS.

These three approaches are discussed in greater detail below.

#### 6.3.1 Assumptions

In order to make an ROM cost for the three approaches, some assumptions are required:

- 1) Independent contractors are used for each module I&T and the observatory I&T.
- 2) The STS and MTS did not include instrument support equipment.
- 3) A common design will be used for all data and power bus simulators.

#### 6.3.2 Analysis and Tradeoffs

The EOS modular philosophy will require sophisticated Module Test Sets (MTS's) for module-level testing and a System Test Set (STS) for

system-level testing. This leads to the following approaches for the EGSE design and implementation:

Approach I. Conventional Approach.

The module contractors independently design and build the MTS's and the integrating contractor designs and builds the STS in the conventional manner. This permits the MTS contractors and the integrating contractor to proceed with their individual support equipment as they see fit and they are not required to coordinate the support equipment requirements or schedules with other contractors on the program. This provides lower support equipment cost for each MTS contractor but it increases the total program cost due to duplication of designs and hardware.

Approach II. Utilize MTS Designs in the STS.

The module contractors independently design and build the MTS's and the integrating contractor utilizes the MTS designs as appropriate in the STS. This permits the MTS contractors to proceed with their individual support equipment as they see fit and they are not required to coordinate the support equipment requirements or schedules with other contractors on the program.

The MTS contractors would be required to provide design information to the integrating contractor for possible use in the STS. This provides lower support equipment cost for each MTS and decreases the STS design cost, but it requires expenditure for duplication of hardware.

Approach III. Utilize MTS Hardware in the STS.

The module contractors design and build the MTS's for use at both module-level and system-level testing. After completion of module test at the module contractors, the MTS's are delivered along with the modules to the integrating contractor and are used at that facility for satellite integration and system test. The MTS's then are shipped to the launch site to support launch operations.

This approach offers some cost savings for the overall program; however, the following constraints are necessary:

- 1) The MTS functional requirements would be generated and reviewed by several separate organizations; i. e., one or more module contractors, the integration contractor, and NASA. Therefore, the MTS design could not proceed until agreement was reached on all module-level and system-level testing and the associated MTS requirements.

A formal change control system, chaired by NASA, would be required. All organizations would be required to review and approve all changes in EGSE requirements or designs prior to their incorporation into the equipment.

The additional coordination and controls would create schedule and cost impact for the MTS.

- 2) The MTS would have to be designed for operation at several facilities, i. e., the Module Contractor, the Integrating Contractor, and the launch site. While not a major concern, this would require additional coordination and possible changes in design standards for one or more of the organizations. There would be added cost for the additional coordination.
- 3) Formal manuals would be required for each MTS to enable the integrating contractor to operate them properly. This would impact the cost for the MTS.

### 6.3.3 Conclusions

The ROM cost estimates for the three approaches are provided below.

<u>Approach</u>	<u>Cost (\$000)</u>		
	<u>I</u>	<u>II</u>	<u>III</u>
<u>Module Test Sets</u>			
Communication and Data Handling	1,462	1,462	1,809
Attitude Determination	756	756	993
Actuation	473	473	665
Wideband Communications	1,388	1,388	1,738
Electric Power	765	765	997
Solar Array and Drive	<u>507</u>	<u>507</u>	<u>669</u>
Subtotal*	5,351	5,351	6,871
<u>System Test Set</u>			
System Test Set	3,989	2,295	1,231

\*Data bus simulators comprise approximately 40% of this subtotal.

## 7. GROUND DATA PROCESSING SYSTEM

### 7.1 CONTROL CENTER SYSTEM ANALYSIS AND DESIGN

#### 7.1.1 Problem Discussion

The EOS control center must be designed to provide continuous control of EOS missions. The design must be cost effective, must be modularly expandable to support dual EOS operations, and must provide an acceptable level of on-going operational support after singular failures of mission critical equipments.

The baseline concept was designed to be modularly expandable to a system that would support simultaneous dual operations. The detailed designs for each of these concepts are shown in Figures 7-1 and 7-2.

In the multiops design, the Sigma 5 was removed from an off line back up mode and used solely for mission scheduling or mission support operations which permitted simultaneous, noninterfering real time and off line operations.

Although common memory modules are shown for the two processors, the desired hardware/software configuration is not currently available from Xerox. It is however highly probable that such a configuration will be available on a schedule that would support a 1979 EOS flight.

Three existing ERTS consoles were included in the baseline design. In the expanded capability design, two ERTS Evaluation consoles were added. These were to be modified for a full command capability. The M&O console was also to be modified to support all of the equipments of the multiops configuration.

#### 7.1.2 Assumptions

As a first step in establishing the system design of an EOS control center, two operational models were derived.

Model A represented EOS operations in 1980.

Model B represented operations in 1985. Conservative assumptions were used in the definition of both models.

Maximum payload operations and telemetry and tracking readouts were assumed for all stations.

US MULTIPURPOSE (3)

Day	4 Combined Payload Passes/Day
Nite	2-1 Band TM Passes/Day
Other	6 Telemetry Passes/Day

US LOW COST (4)

Day	1 Thematic Mapper Pass/Day (20 mbit)
-----	--------------------------------------

FOREIGN REGIONAL (2)

Day	4 Combined Payload Passes/Day
Nite	2-1 Band TM Passes/Day

FOREIGN LOW COST (5)

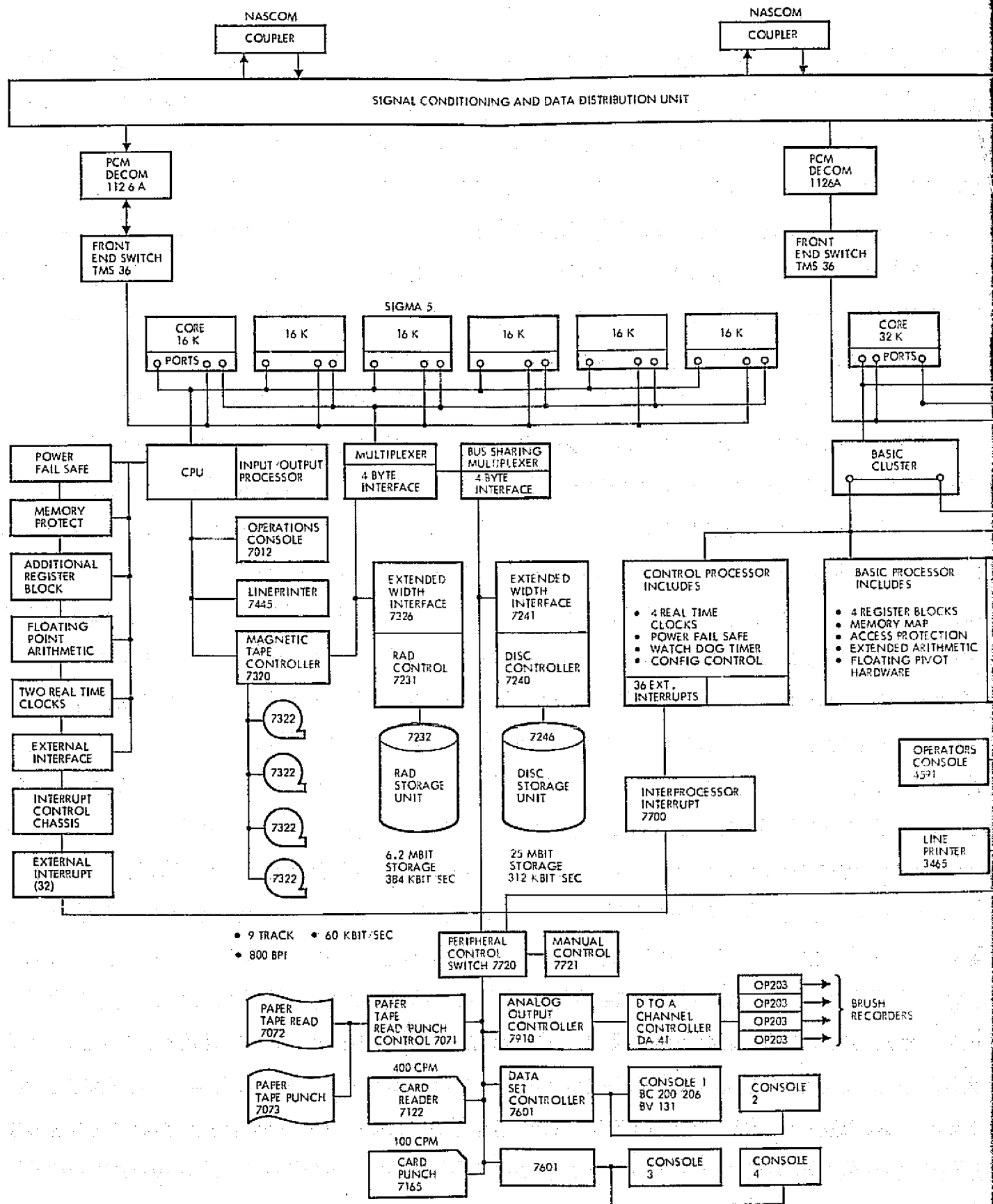
2 Thematic Mapper Passes/Day

REGIONAL & MULTIPURPOSE DAY PASSES

5 HRPI Targets/Pass

Certain other realistic assumptions were made either in support of model operations or in the actual design definition of the control center.

- Spacecraft payload recorders would not be used. All payloads would be read in real time to line of sight ground stations.
- On board telemetry data recorders would not be used.
- DCS data would not be received by EOS ground stations.
- Antenna pointing angles would be generated by the onboard processor.
- Spacecraft power and equipment life would not be considered as normal constraints on payload operation.
- Command sequences would be generated on the ground and uplinked as required.
- Either real time or stored program commands could be used over the US.
- Low cost stations would receive only thematic mapper data (20 mbits).





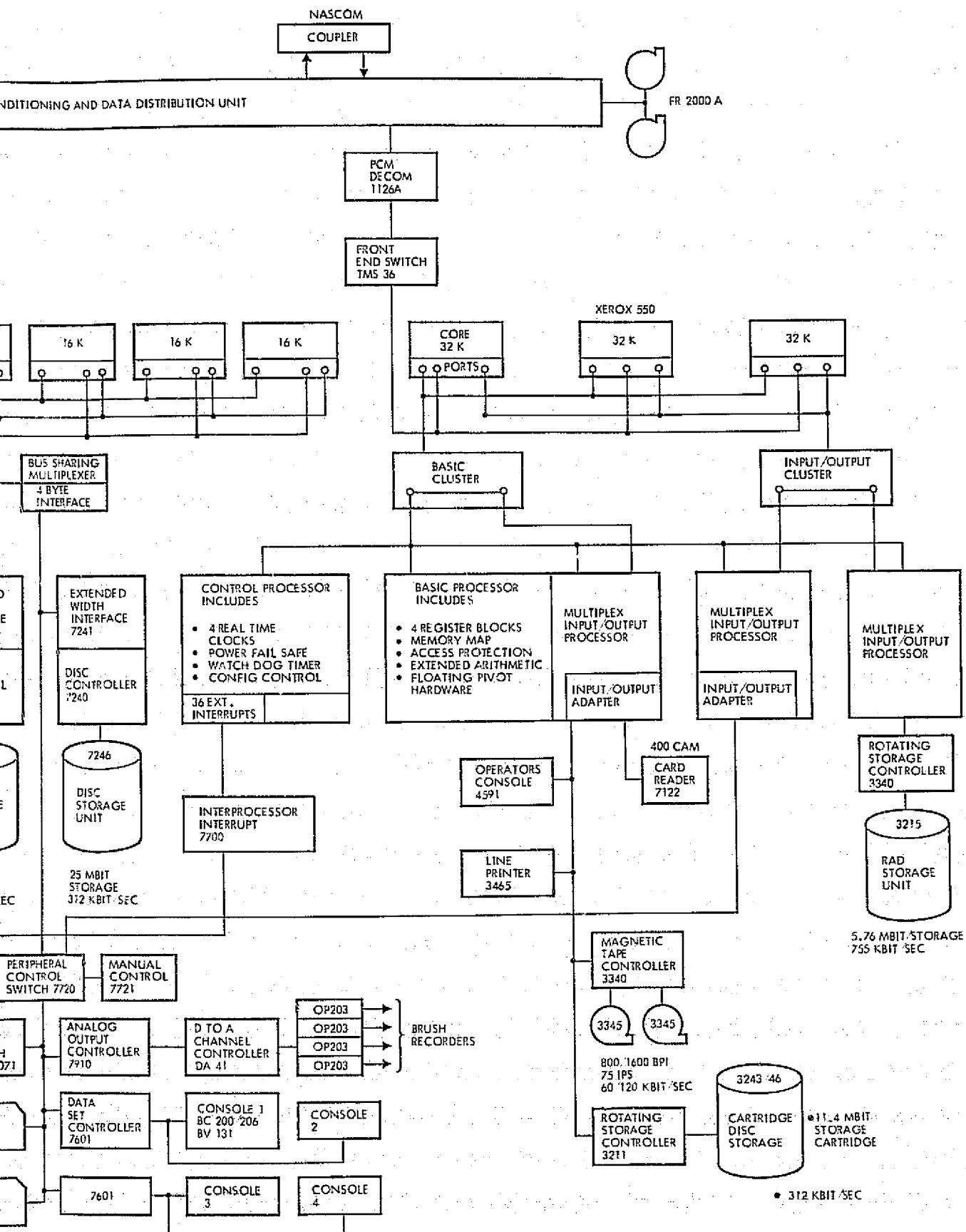
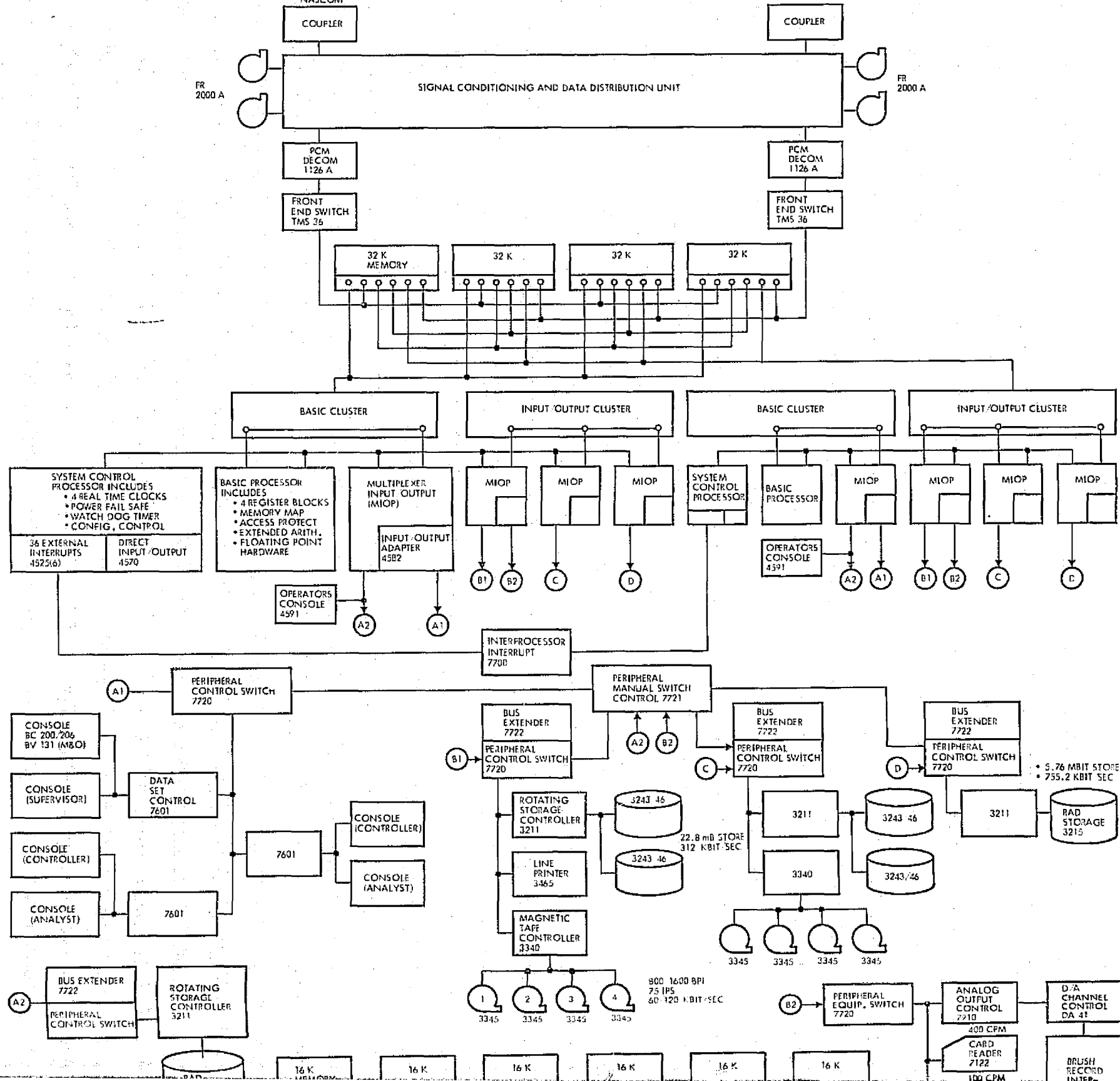


Figure 7-1. EOS Control Center Design Concept



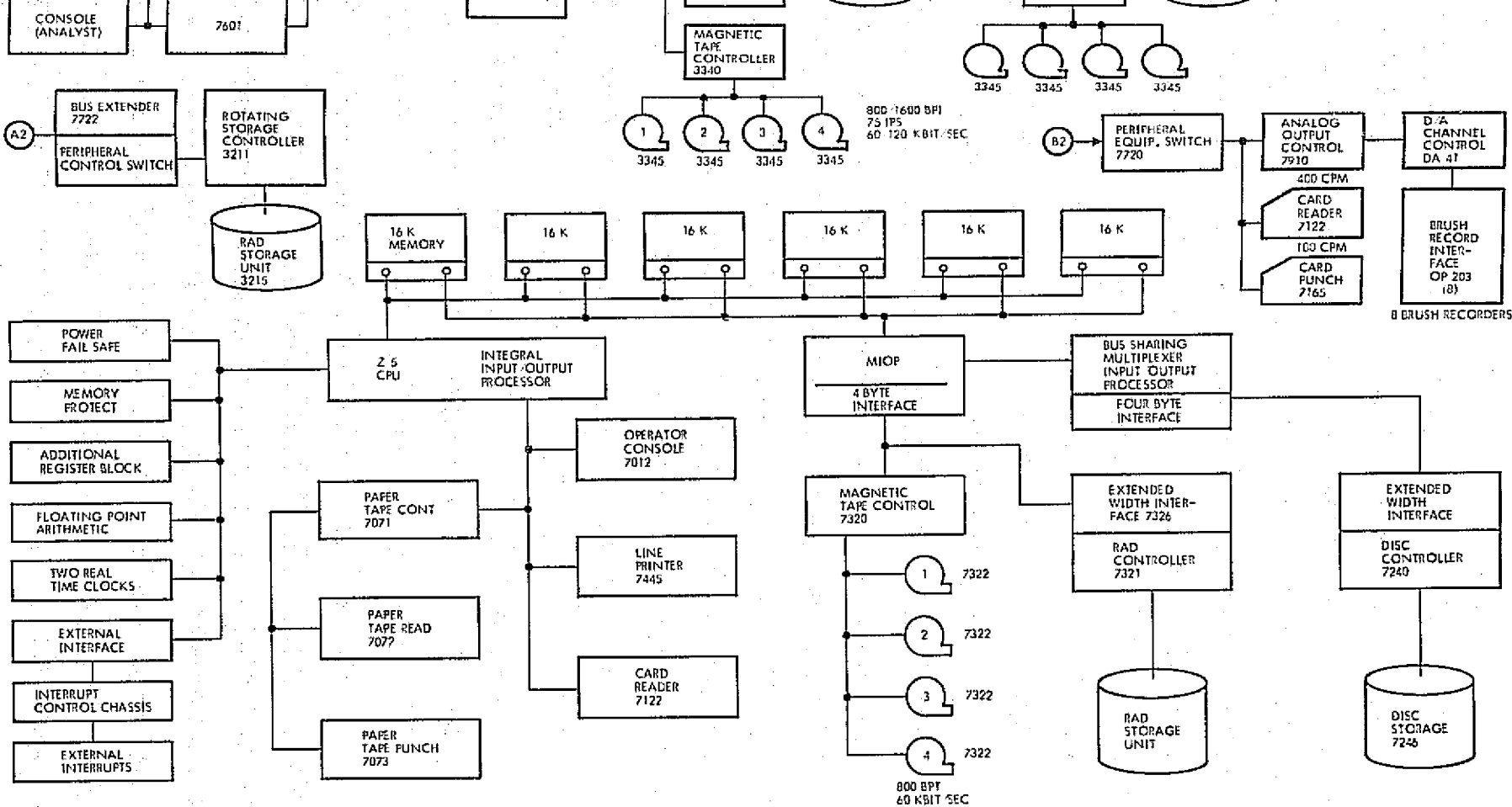


Figure 7-2.

EOS Control Center Multiple  
Operations Design Concept

- The baseline design concept should provide for redundancy of critical hardware.
- The baseline design concept would not include TDRS operations. TDRS implications were to be treated separately.
- Spacecraft downlink telemetry rate would not exceed the capacity of the NASCOM real time link from Alaska existing in 1979.

### 7.1.3 Analysis and Tradeoffs

Before we initiated any analytical efforts or trade studies, we made a general comparison of the EOS configuration and operational concept with that of ERTS to permit early identification of and concentration on the most important factors.

BASELINE EOS vs ERTS	EOS IMPLICATIONS
EOS will have not tape recorders and payload operations will not be power limited.	The mission scheduling and command generation functions will be somewhat simpler with the removal of the tape recorder constraints. The overall system reliability will improve but if out of sight anomalies occur in the spacecraft, limit checked stored data may not completely support evaluation efforts.
EOS will have a pointable payload	If HRPI is used to its full potential which includes multi-target (and (multi-angle) pointing on each US pass to extend the scope of the TM and potentially compensate for cloud cover, <u>MISSION SCHEDULING &amp; COMMAND GENERATION ARE GOING TO BECOME MUCH MORE COMPLEX.</u>
EOS wide band antennas will require pointing information.	Antenna pointing angles will be generated by the onboard processor and will require only time and station identification from ground command accompanied by a periodic state vector update to the spacecraft.

BASELINE EOS vs ERTS	EOS IMPLICATIONS
EOS will service multiple user stations both in US and foreign.	<u>Mission scheduling</u> will undoubtedly become more and more <u>complex</u> with an increase in the number of stations. As currently planned low cost ground stations will only receive thematic mapper output which greatly reduces the scheduling complexity as HRPI will only be scheduled for use in line of sight of US ground stations or foreign regional stations.
EOS will not read out DCS data to EOS ground stations.	DCS tapes will not have to be processed by the Control Center or Data Processing Facility.

We then derived the basic functional requirements for the EOS control center, using ERTS as a general model (Figure 7-3).

The principal interfaces between the control center and outside activities identified in Figure 7-4 were expanded to include a listing of the data requirements of the interfaces.

Having established functional requirements and interfaces for the EOS control center, timelines were then derived as a basis for determining the loading on both equipments and personnel. These timelines were based on normal operations with margins inserted for abnormal or failure modes.

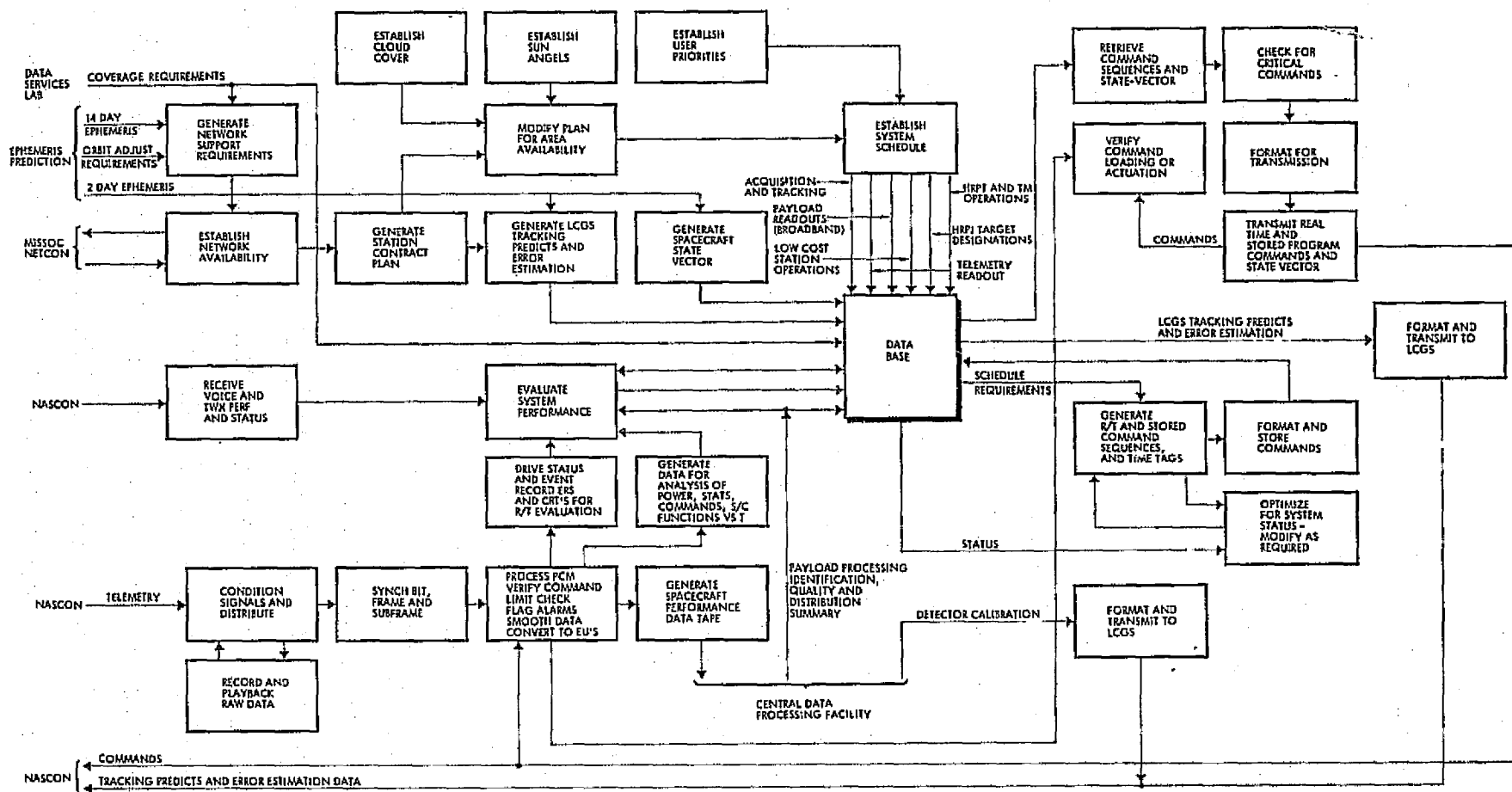


Figure 7-3. EOS Control Center Functional Requirements

NASA		EOS CONTROL CENTER
Orbit Prediction Group	14 day ephemeris forecast with in track accuracy of 700 meters →	
	Orbit adjust burn times as required →	
Data Services Lab	Payload operation requirements daily as received and screened →	
NOA	Weather forecast next 24 hours all target areas — next 12 hours and 6 hours North America →	
NETCON	STDN availability for EOS support next 14 days and next 24 hours →	
NASCOM	Communications, Command and data flow as currently available. →	
	LCGS tracking predicts error estimation and detector cal. →	
CDPF	Spacecraft performance data tape every 24 hours →	
CDPF	Payload quality every 24 hours →	
	Detector calibrations for LCGS →	
	Timing-32 bit serial binary time plus 42 bit parallel GMT - 1 MHz continuous clock signal →	
VARIOUS	Utilities, material, facilities →	

Figure 7-4. EOS Control Center Interface Definition

	PASS	12 HOURS	24 HOURS	2 WEEKS
• Generate network support requirements				X
• Establish network availability				X
• Generate station contact plan				X
• Modify plan for sun angles and weather			X	
• Modify plan for user priorities			X	
• Establish system schedule			X	
• Generate and transmit LCGS tracking predicts.			X	
• Generate and transmit LCGS error estimation			X	
• Generate and transmit state vector			X	
• Generate command seq. & store			X	
• Generate and trans. detector cal.			X	
• Retrieve commands		X		
• Check for critical commands		X		
• Format for transmission		X		
• Transmit		X		
• Verify loading or activation	X	X		
• Distribute real time telemetry data	X			
• Record raw data	X			
• Process PCM	X			
• Drive real time displays	X			
• Conduct real time performance evaluation	X			
• Generate and display data for evaluation			X	
• Evaluation system performance and report			X	
• Generate input tape for CDPF			X	
• Maintenance			X	



In the baseline system, the entire daylight North American operation stored program could be uploaded on the last seaward pass to the East before land coverage was required. On the reference day, this would have been on pass 13. The commands for payload operations outside the US could be uploaded on pass 3. This spaced out potential on line peak activities as indicated.

Figure 7-5 suggested that the cyclic nature of the EOS coverage was such that the mission planning and command generation efforts of the control center could be done at either 12 or 24 hour intervals.

When we further superimposed approximations of the principal real time control requirements, it seemed desirable to select a 24 hour mission scheduling and command generation cycle to limit potential ground processor conflict that could occur when the principal US real time support missions and the foreign mission scheduling and command generation missions were superimposed. If TDRS were operational it might ultimately prove desirable to implement a 12 hour cycle or even an eight hour cycle (see Figure 7-6).

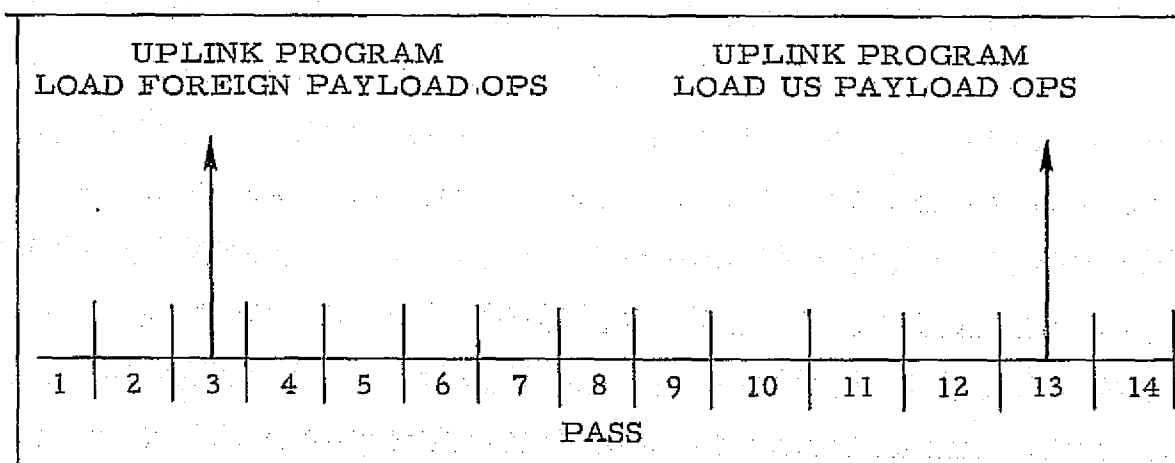


Figure 7-5. Potential Peak Command Activities

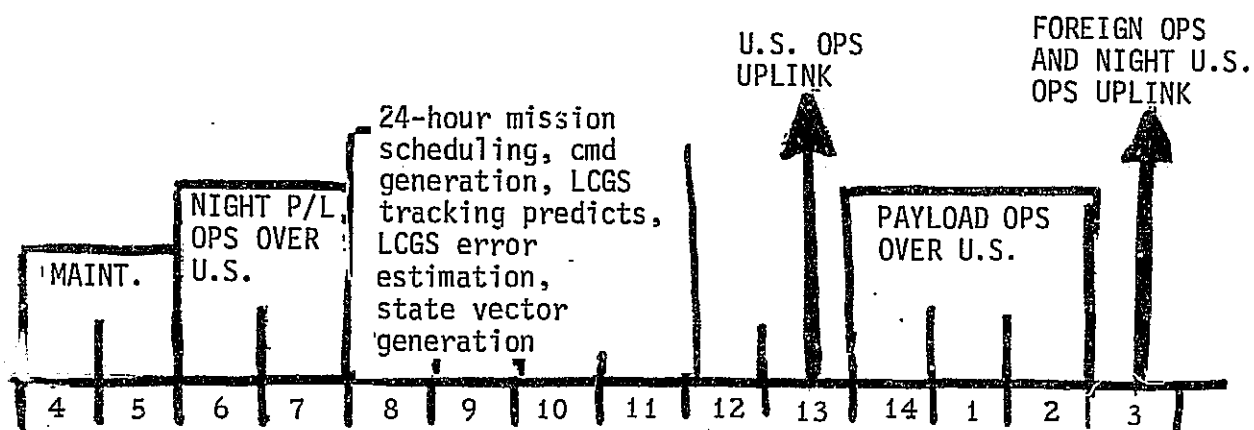


Figure 7-6. 24 Hour Control Center Timeline

An expansion of a typical cycle was made which included all control station off line functions (except maintenance) and extended through one real time daylight pass over North America (Figure 7-7).

This 24 hour mission planning cycle appeared desirable from both a machine usage and personnel manning viewpoint based on the forecasted workload for EOS-A. In areas outside North America, 24 hour weather forecasts were used which did not optimize HRPI scheduling. As more and more ground stations are built and as control station personnel become more experienced in rescheduling complex missions, the 24 hour cycle can be reduced to 12 hours, 8 hours, or over North America, to consecutive passes. The principal effect of shorter scheduling cycles will not be in hardware/software but in the requirement for multiple shift manning in mission scheduling and operations support.

In establishing a Low Cost Ground Station design, we believed it mandatory to reduce ground station costs wherever possible to encourage the broadest type of potential user participation in direct EOS payload readout. The approach taken was to drive LCGS antennas with accurate ephemeris information rather than require these stations to have auto

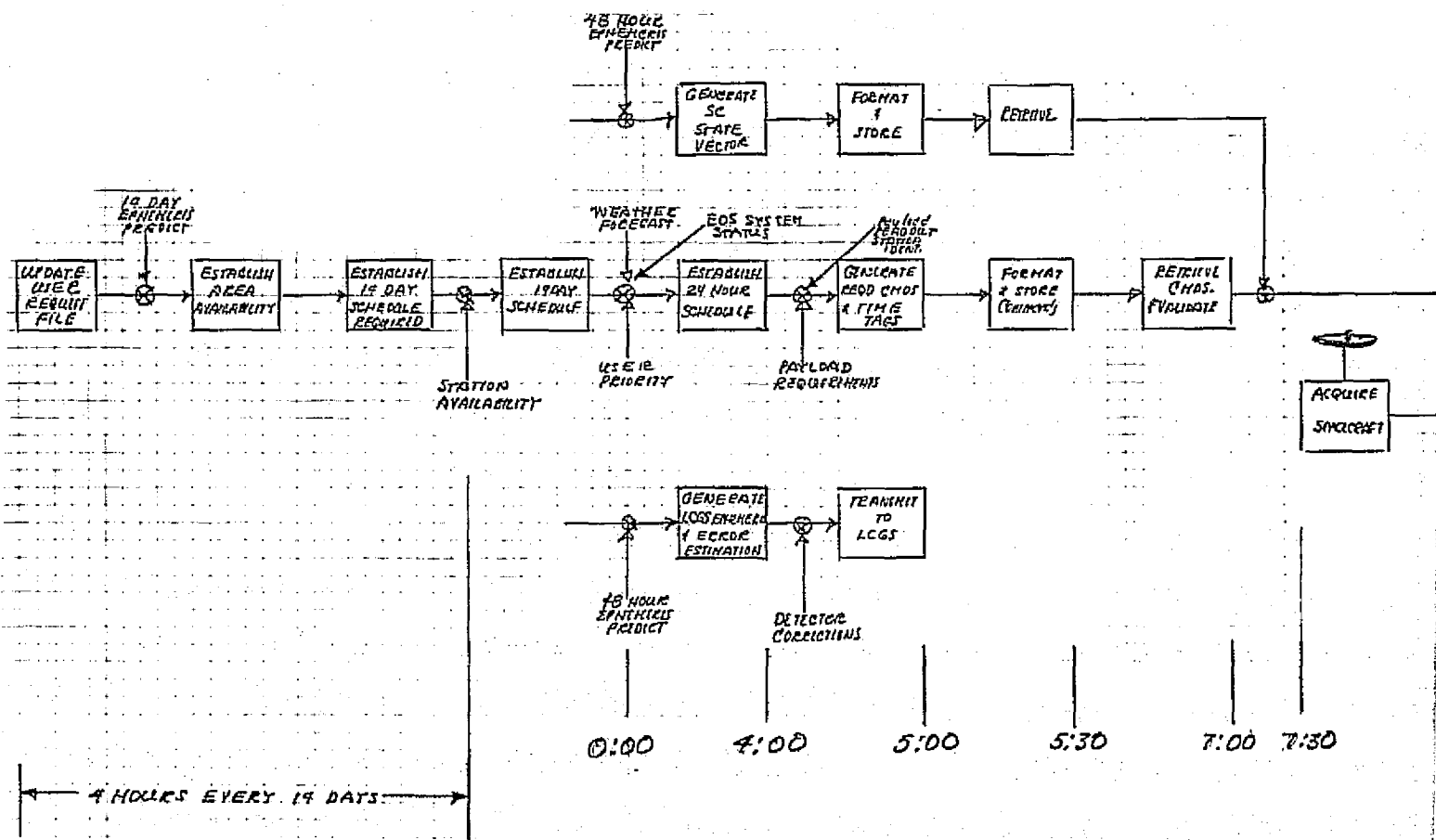
track receivers and antennas capable of the required accuracy. This resulted in a requirement for generation of these accurate tracking predicts and error estimation in the EOS control center and the transmission of the data to the Low Cost Ground Stations. It was planned to use these same low speed communication links to send detector calibration data for use at the LCGS. If the 14-day orbit prediction can achieve an in track accuracy of 700m, then a majority of this data can go by mail. Our trade studies, using worst case estimates, indicated that our overall approach was cost effective if more than two or three low cost ground stations existed.

Assuming a 24 hour cycle, our basic timeline analysis showed that we had predicted 8 hours of work in an available 10 hours. The margin of 2 hours of unscheduled time was a reserve to permit rescheduling if errors were detected in the command load or to accommodate changes in the forecasted weather or in system status.

In our timeline analysis, we allocated a lengthy span to mission planning, scheduling and command generation although at the same time stating that most of the process would be automated. Our span reflected the introduction of the High Resolution Pointable Imager (HRPI).

The optimum use of HRPI had an almost order of magnitude effect on scheduling complexity. Looking at EOS operations over a particular region of the US, thematic mapper coverage on two consecutive days appears generally as shown in Figure 7-8. The scheduling model for the thematic mapper operation is quite simple. If the target is in the shaded area, it can be mapped subject to constraints of weather, sun angle and an available ground station. Relative priority does not routinely enter into the model.

The targets that HRPI can potentially cover lie in the shaded areas shown in Figure 7-9 for the same orbits.



FOLDBOUT FRAME /

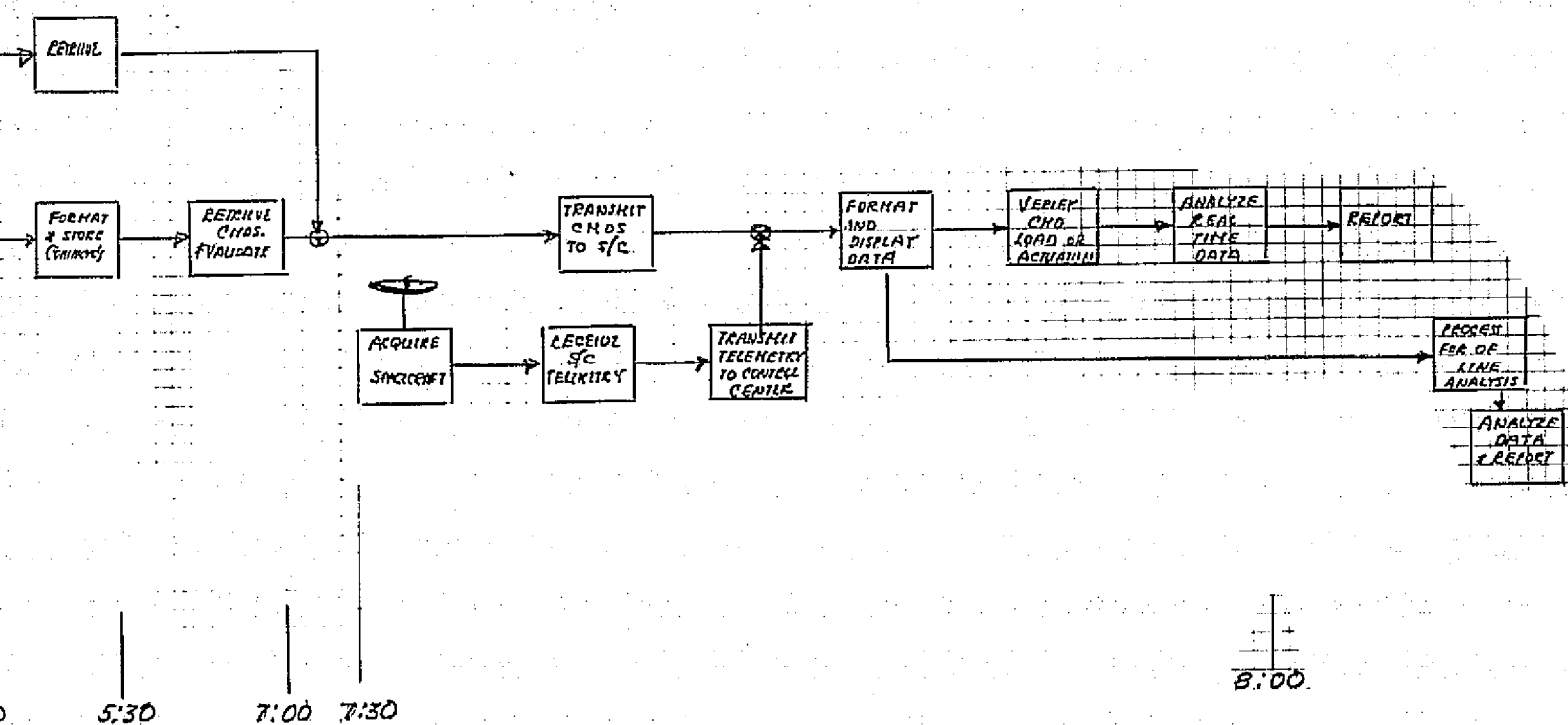


Figure 7-7. Expanded Timeline for EOS Control Center

ORIGINAL PAGE IS  
OF POOR QUALITY

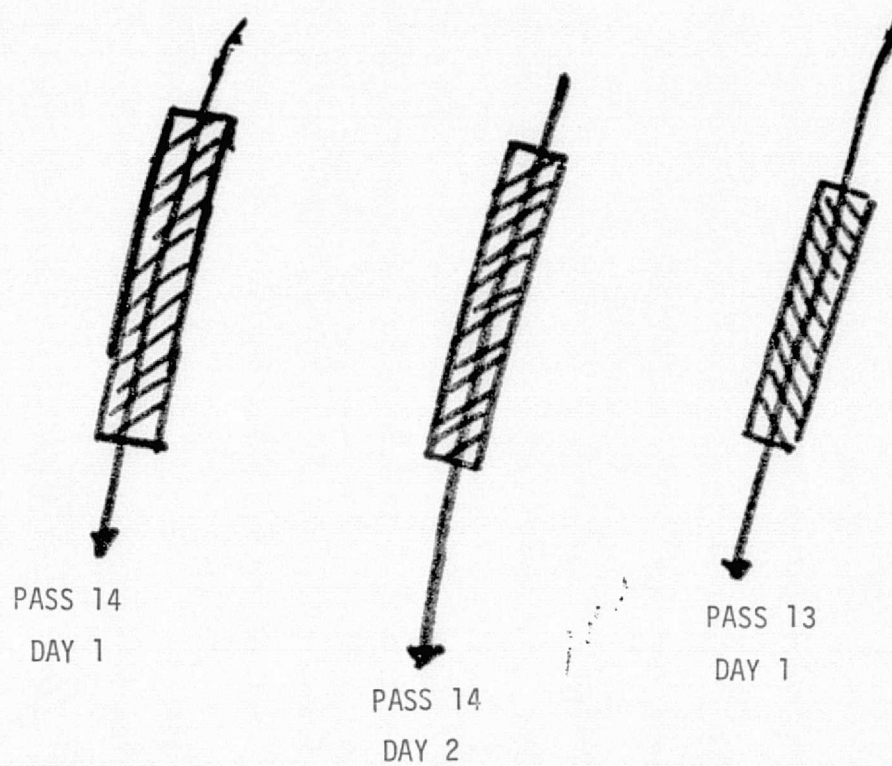


Figure 7-8. Representative Thematic Mapper Coverage

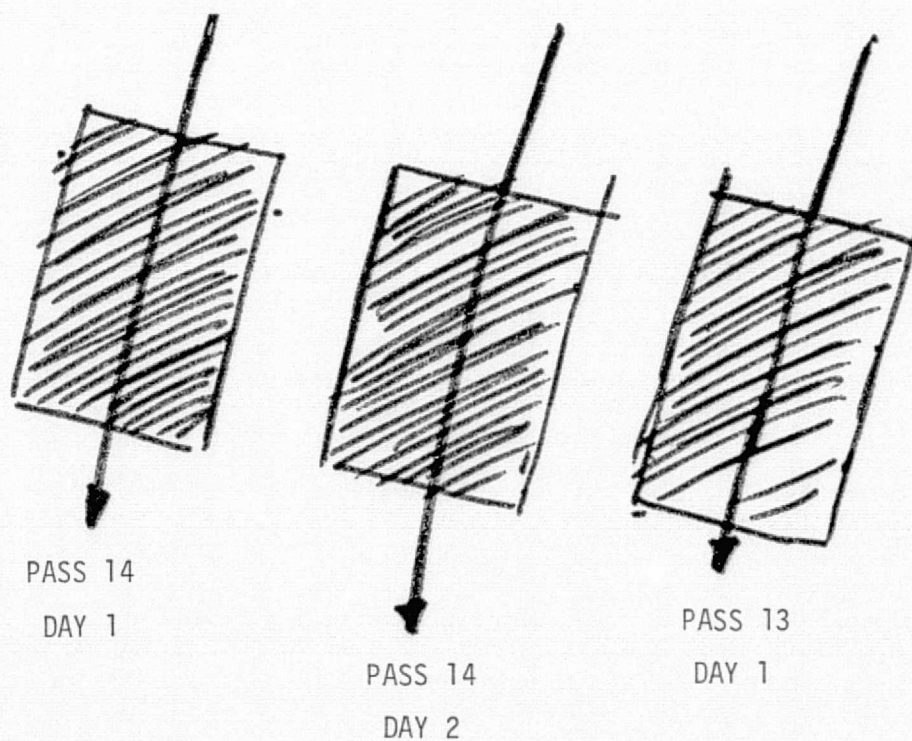


Figure 7-9. Potential HRPI Targets

With its lesser swathwidth, the HRPI obviously can not cover the area that the thematic mapper can but it can potentially map targets far outside the thematic mappers range and can cover them at far shorter intervals.

From a scheduling point of view, HRPI introduces choice of target and with the choice, priority considerations and perhaps even variable priorities. To produce an optimum HRPI schedule, assuming a heavy load of user requirements, it may eventually be necessary to optimize over some significant number of advance days and reiterate on a daily basis.

Our efforts to this point had not considered the implications or impact of TDRS. Without TDRS, the potential real time command and readout of EOS was approximately 170 minutes per day. A fully operational TDRS results in a potential real time operation of 24 hours per day. The land mass viewing time over North America is only about 15 percent of the possible land mass viewing areas of interest in the world.

A fully operational TDRS then offers a potential increase of real time land mass viewing of

$$\frac{85}{15} \approx 6$$

and of telemetry and command functions of

$$\frac{24}{3} \approx 8$$

Obviously the design impact would not be a factor of 6 or 8, but it would be significant. Our control center design concept assumed a mission planning through execution time of 24 hours. An operational TDRS could dictate a cycle time of 8 hours which in itself would strongly support a requirement for separate systems for real time support and mission planning and scheduling.

But more significantly,

- If data is available in near real time someone will specify the ability to look at it in near real time.
- If real time commands can be sent at virtually any time, someone will specify the ability to send them in real time.

It then seemed far more cost effective to establish a control center design concept that was not sized to the potential of TDRS operations but could presumably support these operations if TDRS become operational. Based on the rather limited data available from the ERTS Milestone 2 document, we attempted to follow the ERTS software design very closely. The greatest changes occurred in the scheduling area where the optimum use of the HRPI required an approach that was completely different from that of ERTS.

A basic two-pass method was proposed for mission scheduling. The first pass results in an isolation of all the targets which could possibly be accessed by the HRPI or the thematic mapper on a given rev. The second pass accomplishes the detailed payload event scheduling by applying payload operations constraints to the targets isolated in the first pass and selecting from among them the optimal path for the sensors. Additionally, during this pass, X-band antenna operations will be defined to allow the accomplishment real-time payload data transmission to the ground station required to receive the data from a given target.

#### 7.1.4 Conclusions

The requirements for EOS could be translated into a variety of equipment configurations. With the relative costs of hardware and software, cost effective design dictated that we attempt to maximize the use of ERTS software. Our design concept then very closely followed the ERTS design modified as required by the EOS mission and the availability of cheaper, faster, more reliable hardware.

The principal features of the EOS design concept were:

- No preprocessors
- Software programmable PCM decoders
- A more powerful main processor



- Use of existing Sigma 5 as a back up on line processor and for mission scheduling, LCGS tracking predicts, LCGS state vector computation, and formatting of LCGS error estimates
- Redundant discs and RADS
- Maximum cross switching of processors and peripherals
- A paper tape generation capability for LCGS antenna angles
- Software mods or additions
- More sophisticated scheduling
- Faster real time processing
- LCGS tracking predictions
- LCGS error estimation
- Spacecraft state vector generation.

While certain of the subroutines developed for the 14-Day Cycle Station Scheduling program appeared applicable to the Swath Sort (first pass) routine, the Sensor Planning (second pass) routine must be built from scratch. TRW has developed a prototype program which will somewhat reduce the necessary design problem for the Sensor Planning routine, but a total programming task must be contemplated in its development.

When we eliminated the Sigma 3 processors, a redesign of all of the comm processing, and some of the display functions, was necessary as the ERTS programs had been written in assembly language which would not run on either the Sigma 5 or 550.

Command generation software for EOS will bear substantial similarity to the command generation software currently utilized in ERTS. The ERTS philosophy of using prestored command sequences appears to provide minimum risk and a high degree of command generation effectiveness for EOS. The only basic differences in the command generation software for ERTS and for EOS, center around the initial interface between EOS event files and the command sequence generation program, and any EOS software requirements as associated with changes in the command transmission equipment and/or the onboard command system. For the purposes of this analysis, no changes have been assumed in either of these hardware areas.

Performance evaluation for EOS parallels the telemetry processing as currently being performed for ERTS. No modification of substantive processing requirements has been assumed, i. e., no new computational routines will be required.

The real-time telemetry processing software and the off-line telemetry processing software currently in use on ERTS appear to be directly usable on EOS with but minor "front-end" modifications.

## 7.2 SOFTWARE SIZING

### 7.2.1 Problem Discussion

As the ERTS A and EOS-A Missions are very similar, the most cost effective approach to EOS-A software design seemed to be to make a maximum use of ERTS software, designing all additions or modifications so that minimum changes would be required to support future missions.

Our general allocation of functions has been very similar to ERTS.

- Mission scheduling
- Command generation, verification and validation
- Comm Processing
- Real time or on-line support
- Off-line processing for analysis and reporting

### 7.2.2 Assumptions

Initial station schedule for EOS support will be done on a 14-day predict basis. The cycle length, i.e., 14 days, is, of course, flexible and the frequency with which the scheduling is performed may be tailored to fit the operations requirements for the EOS system. The results of the 14-Day Cycle Station Scheduling process will be the production of EOS stations operations support schedules for STDN stations and for each required low cost ground station or foreign regional station. Such schedules will reflect thematic mapper-only, HRPI-only, and combined thematic mapper/HRPI operations. The output of this process could also include 14-day payload requirements satisfaction data, if this feature appears to offer results that warrant its development.

Our operational concept was that EOS payload operations scheduling would be performed, off-line, on 24-hour cycles. The output of this process would be the detailed events to be accomplished by the system over said period. Additionally included would be the spacecraft X-band antenna targets and times for that same period.

TRW studies have shown that optimal target selection can be made for thematic mappers and HRPI operations, as measured against user requirements, within the time periods available for off-line processing during

pass periods that do not involve payload operations. If worldwide real time EOS operations occur with the advent of TDRS; with the proliferation of foreign regional stations; or even with multiple EOS type missions, sufficient flexibility and growth capability are inherent in our design approach to permit mission scheduling on a continuous, rather than a cyclic, basis.

### 7.2.3 Analyses and Tradeoffs

Of the ERTS routines which currently appear in use for mission scheduling, only NODTM (6.5K) appears able to be usable directly in EOS operations. The STAT. CONT routine (7.6K) can probably be used to a great extent if low cost ground station location data can be readily added to the station data base. If not, modification will have to be made to add the same and the routine size could increase as much as 25 percent. This estimate assumes that as in the ERTS practice, the Station Contact Prediction Tape will be available as input to the STAT.CONT routine.

It is estimated that the Swath Sort routine will require 25K to 30K words of memory and that the Sensor Planning routine will require 10K words. None of the current software utilized in ERTS Systems scheduling appears to be applicable to the 24-hour Payload Scheduling function.

The 24-hour Payload Scheduling function will be run independently of the Command Generation function. Payload schedules can then be analyzed and, if necessary, modified by current weather inputs prior to the detailed translation of payload events into command sequences.

Rather than area availability determination as currently performed in ERTS scheduling, EOS will require that target availability be estimated as based upon the user request file (target deck) and the potential requirements for thematic mapper and HRPI sensor operations. An initial estimate for the size of the routine for such a function varies between 25K to 30K words of memory. If the size grows much beyond that point, multipass computer operations are feasible for reducing core residency requirements with minimum performance penalty. For a user request file of 15,000 targets, probably a maximum growth consideration, it is estimated that 60K words of data will be used by this routine. There is, of course, no requirement that this total data set be resident at any given time because the set can

easily be preprocessed on the basis only of latitude and longitude with full data only being input for those targets which have consideration on a given rev.

Minor support programs necessary to complete the 14-day Cycle Station Scheduling procedure will at most add another 15K words to overall requirements.

It is estimated that the total core requirement for this procedure will be substantially the same as, if not slightly less than the utilization now extant for the Mission Planning function in ERTS.

The COMCOM routine (27.5 memory) is used by ERTS to translate activity schedules into command sequences. This particular routine will require substantial modification or replacement in order to satisfy the interface requirements between EOS events and command sequences. The addition of HRPI and X-band antenna events require substantially more complicated command sequences and generate new software requirements. While the exact size of the new routine cannot be precisely estimated at this time, it appears reasonable that the new module will have a 10 percent to 20 percent greater core requirement than COMCOR. At the command level the COMCOR replacement routine will be utilized to identify conflicts in command loads (messages) in a way that will allow manual resolution by the operator.

The balance of the ERTS command generation software appears usable "as is" for EOS assuming that the ERTS design is such that modest increases in requirements can be accommodated without complete program redesign.

Comm processing and real time processing appear to be adequate as is although the Sigma 3 routines will have to be recoded for Sigma 5/550 use and the call routines of the executive modified as required. Minor changes in the PCM processing software will be required to handle the different formats and rates but only minimal increase over ERTS program lengths or files is visualized.

Off-line processing for evaluation will cause the existing software, with again minor changes to reflect the different spacecraft measurement

parameters of EOS. Again no significant increase in ERTS program or file size is envisioned.

#### 7.2.4 Conclusions

Only minimal growth in program lengths and files is envisioned for EOS-A over ERTS in every routine except mission planning.

Mission planning software will have to reflect the impact of optimum scheduling on the HRPI and the potential inclusion of large numbers of either low cost or regional stations.

Our hardware design concept has allowed for this growth with adequate margin and flexibility to accommodate the unforeseen requirements of future missions.

### 7.3 CONTROL CENTER SUPPORT TO LOW-COST GROUND STATION

#### 7.3.1 Problem Discussion

Low cost ground stations capable of receiving only the restricted or compressed thematic mapper output and regional stations capable of receiving both the TM output and the high resolution pointable imager output could conceivably exist virtually anywhere in the world and in any number if it became in the best interest of organizations or governments to build or buy them. It is important that we at least bound the one time and recurring impacts of these stations on EOS control center design and operations.

#### 7.3.2 Assumptions

Those previously made in 7.1, Control Center System Analysis and Design.

The onboard processor can support normal spacecraft functions and simultaneously generate pointing angles for both wide band antennas.

Accurate antenna pointing predictions and error estimations must be generated and transmitted to low cost ground stations for each pass.

The thematic mapper, and all required spacecraft functions, will be routinely on for all North American daylight passes.

#### 7.3.3 Analysis and Tradeoffs

The first low cost ground station that exists to receive, process and evaluate EOS payload data has an impact on EOS system design and operations. In general terms, additional stations merely increase the workload to some point where their numbers may force a system redesign. In support of our analysis effort, we categorized by:

- North American Low Cost Stations
- Foreign Low Cost Stations
- Foreign Regional Stations (receive both Thematic Mapper and HRPI)

The impact of these stations was further studied in terms of the first low cost station, and the one hundredth low cost station, both in North America and in foreign countries.

Our basic studies in Section 7.1, Control Center System Analysis and Design showed that the impact of a low cost station in North America was in:

Mission Planning. Essentially no impact as mission planning and scheduling software had to be created to support the basic EOS missions and low cost station requests constitute a simple subset of this software.

Spacecraft. Very minimum impact as onboard software had to be created for the basic EOS missions to generate the pointing angles for the wide band antennas. A low cost ground station merely required the introduction of an additional set of station coordinates into onboard processor memory.

Mission Support. The cost effective LCGS design created a requirement for generation and transmission of accurate LCGS tracking predicts, error estimations, and detector calibrations from the EOS Control Center.

Commands. A single LCGS, assuming the operator was only interested in local geography, required coverage on a maximum of perhaps two passes in seventeen days which required a total of six commands in seventeen days.

In a 17 day cycle over North America, with 100 low cost stations requesting coverage of 200 areas, on a random basis there would be 6 areas to be mapped on each pass.

Mission Planning. The problem is no more complex than for one low cost station requiring essentially only more memory and processor time. With the slight probability of readout station conflict over antenna pointing, some priority assignment could be required.

Spacecraft. Requires the storage of some extra number of station coordinates depending on the memory loading concept (at most 24 words).

Mission Support. Requires the generation and transmission of 12 station predict tapes and error estimations daily as well as detector calibrations as generated.

Commands. A days operation would require the generation, validation, transmission and verification of 36 extra commands.



The impact of adding foreign low cost stations is somewhat different than that of North American stations because the payload and related transmitter functions are not routinely turned on in these areas. There are approximately ten daylight land mass passes potentially involving foreign stations. While the impact on Mission Planning and Spacecraft is no different than that of North American stations, it may be much more difficult to transmit antenna predicts. Although the quality of international communications may improve to a point where foreign low cost stations can be readily reached, it cannot conservatively be assumed that this will happen during the EOS lifetime. It appears more likely that 14 day ephemeris predictions will become sufficiently accurate that accurate tracking predictions can be provided most stations by airmail, eliminating a need for direct phone or teletype communications in most instances.

Certainly a considerable number of commands may be required for foreign stations operations. If again we assumed one hundred foreign low cost stations randomly distributed and each requesting coverage of 2 areas in each coverage cycle, the command load per pass is approximately 30, and per day, 300.

Foreign regional stations pose a very significant problem because of their HRPI requirements. Between two and three such stations would double the mission planning and command load of EOS Control Center.

#### 7.3.4 Conclusions

Any added stations have the obvious effect on spacecraft power, array life, and perhaps individual module life. In addition to those effects, the impact on EOS design and operations is matrixed below.

	North American Low Cost Stations	Foreign Low Cost Stations	Foreign Regional Stations
Mission Planning	Slight	Slight	Very significant due to HRPI operations
Mission Support	Slight with some impact on orbit prediction group and CDPF	Considerable communication burden for track- ing predict, error estimation and detector calibrations	Slight but will have to send general schedules and detector calibration
Spacecraft	Slight	Slight with minor increase in memory required	Slight with minor increase in memory
Commands	Slight	Considerable if a number of stations exist, well dispersed in longitude.	Very significant. If over 3 stations exist, may require a radical change in OPS concept.

## 7.4 CONTROL CENTER MAN-MACHINE INTERFACES

### 7.4.1 Problem Discussion

The principal functions of the EOS control center can be categorized as

- Mission Planning and Scheduling
- Command generation, validation, transmission and verification
- Low Cost Ground Station tracking predicts and error estimation generation and transmission
- Spacecraft state vector generation, transmission and verification
- On-line performance evaluation
- Off-line performance evaluation
- Control center configuration control
- Ground system maintenance
- Reporting.

A cost effective design requires that these functions be allocated to man and machine in a manner that optimizes life cycle costing and that this interface, as well as all of the internal and external interfaces of the system, be clearly established.

### 7.4.2 Assumptions

The same as the assumptions of Section 7.1, Control Center System Analysis and Design.

### 7.4.3 Analysis and Tradeoffs

We have divided these functions into on-line or real-time functions and non real-time. On-line interreaction with a processor or the data base is complex, costly, and rarely efficient. Limiting this on-line activity results in those desirable system characteristics such as simplicity, shorter development spans, reliability, maintainability, and reduced one time and recurring costs. It has a further benefit in that it is difficult to accurately size and time a complex on-line interrupt driven system. By deliberately specifying a portion of the load to be in an off-line batch processing mode, we both limited the potential system peak loads and the system complexity.

## REAL-TIME

## NON REAL-TIME

Command Transmission

Command Verification

On-Line Evaluation

Control Center Configuration Control

Mission Planning

Mission Scheduling

Command Generation

Command Validation

Off-Line Evaluation

Maintenance

Reporting

LCGS tracking predicts an error estimation

Spacecraft state vector generation and transmission.

The non real-time functions would be heavily supported by software and hardware and the man-machine interface would be the standard one involving card punches and readers, typewriter keyboard inputs, and high and low speed printer outputs.

The on-line or real-time functions are those whose execution in real-time are either mandatory, or at least extremely important to mission success, and the man-machine interface for these functions is assumed to exist in control and display consoles.

In more detail, these on-line functions are:

- Monitor control center equipment status.
- Establish control center equipment configurations in both routine and failure modes
- Monitor EOS system status
- Maintain awareness of NASCOM and STADN status in EOS support
- Validate reasonableness of all commands before transmitting to spacecraft.
- Format commands for transmission
- Transmit stored program and real-time commands
- Verify storage or actuation of commands
- Make near real-time evaluation of spacecraft performance.

We did not attempt to prejudge whether certain commands should be stored program or real-time. As we had assumed that spacecraft recorders would not be used, it appeared that stored programs could be used almost exclusively. This required that the command controller(s) only monitor real-time passes to ensure that commands were being executed, overriding if circumstances seemed to warrant it.

This command controller requires real-time displays that clearly present the command sequences that are to be executed and data to show whether or not they were executed at the correct time. The complexity of the controllers job is directly related to how well this latter requirement is satisfied by the processing and display system. If the controller must seek out and interpret data in some time consuming manner, then his work is easily doubled or trebled.

With effective hardware and software support, our experience has been that one controller is optimum for the baseline type EOS mission as multiple controllers merely complicate communications. If payloads are flown in later missions that require some type of real time decision-making or very flexible mission scheduling, then separate vehicle and payload controllers would be required.

While some degree of failure mode analysis and corrective action is inherent in the spacecraft design, provisions could not be made for all potential failure modes. It is rare to encounter a significant spacecraft failure that is both detected and cured or compensated for in real time but it has been our experience that they do occur and that the fast reaction diagnostic and command capability should exist on-line.

A comparison between Johnson Spacecraft Center's Manned Spacecraft Operations and ERTS operations indicates that a certain degree of arbitrariness exists as to the proper degree of support that should be provided to operations in real time. We chose to be guided by the rather lean, but apparently effective, general support philosophy of ERTS and take a position that only one on-line spacecraft analyst was required (as differentiated from the possible requirement for multiple off-line technical analysts).

The two positions, controller and analyst, could exist in a single console or in separate consoles if effective eye and voice contact was readily maintained.

To provide for training, operational flexibility and critical equipment redundancy, controller and analyst consoles should be identical. No attempt has been made to design the consoles but certain minimum design criteria should be met.

Consoles should each have:

- Independent access to all real time data on at least two independently selectable CRT's
- Status lights or equivalent discrete markers for critical events
- Ability to construct, edit and execute any vehicle command either with time tags or in real time
- Ability to select, without construction, and execute, a small number of critical real time commands
- Voice communications with multipurpose station controller and OCC support personnel
- Ability to designate a particular display for attention by another console operator
- Time displays.

The minimum requirement for a command controller and on-line evaluator can be fairly readily established for normal operations. There is a requirement for another position in the control center - that of an on-line supervisor. This position is not easy to define in single satellite operations because for normal operations, he need not be on-line.

When spacecraft anomalies occur, however, an on-line supervisor is essential to direct operations and buffer between management and operators and analysts. To that end, a third console is proposed for a supervisor, identical with those of the command controller and on-line evaluator except that a spacecraft command function need not be provided. This supervisor will coordinate the activities of both halves of the center when a multi-operation capability is achieved.

A fourth on-line hardware supported function that we have not discussed is one of monitoring and controlling the operation of the various equipment in the control center. This is considered to be a single position charged with:

- Monitoring all of the control center equipment performance
- Selecting equipment configurations

- Effecting limited trouble shooting (individual equipment level)
- Scheduling emergency maintenance
- Effecting processor mode selection.

The importance of this position varies directly with the degree of flexibility and redundancy in the control center design. If a configuration is to finally evolve, capable of supporting dual operations and having equipments that could be selectively switched to either operations, then this would be a complex, demanding function. If this flexibility does not exist, then the position is more one of monitoring and simple trouble shooting.

The function should be supported with a console having the necessary CRT's; diagnostic scope and lights and alarms necessary to monitor and trouble shoot. It should have control of all peripheral equipment switches. It should be designed to be readily expandable to a dual control center configuration.

#### 7.4.4 Conclusions

Personnel involved in non real-time functions do not require system or mission peculiar hardware but can use standard computer peripherals.

Four on-line positions have been identified, each requiring a console:

- Command controller
- On-line evaluator
- On-line supervisor
- On-line control center equipment monitor and configuration controller.

## 7.5 USE OF ERTS CONTROL CENTER

### 7.5.1 Problem Discussion

The very close similarity between the operational requirements of EOS-A and ERTS indicates that almost all of the ERTS Control Center hardware, and much of the ERTS software, should be usable for EOS-A.

Further, the operation of EOS-A with its high resolution pointable imager, introduces mission scheduling and command generation problems that appear to be at least as complex as those of follow on missions. If our conceptual design is adequate for EOS-A, it will probably be adequate for follow on missions with mission-peculiar software modifications.

### 7.5.2 Assumptions

The single mission and multiple mission hardware concepts as delineated in Section 7.1, Control Center System Analysis and Design.

All facility modes are accomplished permitting processors and critical devices to be co-located as required to eliminate excessively long cabling runs.

### 7.5.3 Analysis and Tradeoffs

There appeared to be no cost effective alternative to making maximum use of existing software. This in turn dictated the use of Xerox hardware assuming that upward compatible hardware existed. Maximum use was made of existing ERTS hardware consistent with producing a design concept that must remain valid for at least 15 years.



#### 7.5.4 Conclusions

In our initial phase design concept, the following equipments were required to replace a supplement existing ERTS Control Center equipment.

XEROX MODEL NO.	QUANTITY	DESCRIPTION
8275	1	4-Byte Interface
8264	6	Port Expansion
7236	1	Extended Width Interface
8261	1	8K Memory
8262	1	8K Memory Addition
4501	1	Xerox 550
4525	2	External Interrupts
4561	2	16K Memory, 2 Ports
4562	3	16K Memory Increment
4570	1	Direct I/O Interface
4580	1	I/O Cluster
4581	2	MIOP
4582	1	I/O Adapter
4591	1	KSR 35 Keyboard Printer
4566	4	Two Port Memory Expansion
3340	1	Mag Tape Controller
3345	2	Add On Tape Drive
3465	1	Line Printer
3211	2	Rotating Storage Cont.
3215	1	RAD Storage Unit
3243	2	Cartridge Disc Drive
3246	2	Disc Cartridge
7071	1	Paper Tape Control
7072	1	Paper Tape Reader
7073	1	Paper Tape Punch
1126A	2	PCM Decom
TMS36	2	Switch

In the second phase design concept which was to support multi-satellite operations, additional equipments were required as follows:

XEROX MODEL NO.	QUANTITY	DESCRIPTION
4501	1	Xerox 550 CPU
4525	2	Ext Interrupts
4561	1	16K Memory (2) Ports
4562	1	16K Memory Incr.
4570	1	Direct I/O Interface
4580	1	I/O Cluster
4581	3	MIOP
4582	1	I/O Adapter
4591	1	KSR 35 Keyboard Print
4566	4	Two Port Memory Exp.
3340	1	Mag Tape Controller
3345	6	Add On Tape Drive
3211	2	Rotating Storage Unit
3215	1	RAD Storage Units
3243	2	Cartridge Disc Drives
3246	2	Cartridge Discs
7720	2	Peripheral Switch
7722	4	Bus Extender
OP203	5	Interface to Recorders
FR2000A	2	Analog Recorders
	4	8 Channel Brush Recorders and Amplifiers
	1	Event Recorder

## 7.6 NON-ORTHOGONAL SCAN IMPACT

A candidate EOS Thematic Mapper (TM) concept involves a mirror scan mechanism which describes a circular arc with the detector IFOV's on the surface of the earth. This results in a substantial across-scan skew between the sensor scan lines and usual map projections, considerably more than can reasonably be expected to be handled in high-speed random-access memory. Two approaches exist for handling of this problem: linearization of the sensor scan lines prior to image correction processing; or processing and output of the data in conical scan coordinates.

### 7.6.1 Conical Scan Linearization

The conical scan TM describes a  $\pm 24^\circ$  arc on either side of the sensor ground track to cover the required 185KM ground swath width as shown in Figure 7-10. At a 30M pixel spacing along track, a  $24^\circ$  arc subtends 655 orthogonal scan lines, or 32E6 pixels for the six primary bands (5.4E6/band) at 8492 pixels per scan line. Thus the brute force scan linearization buffer requirement is over 32MB.

A theoretical minimum of 10E6 pixels would suffice if the sensor arc trailed the spacecraft, still far in excess of computer core addressability and requiring prodigious feats of skill in software pixel shuffling. Further reductions are possible by tilting the scan rotation axis to put the sensor arc through the spacecraft nadir, but only at the expense of other primary advantages of the conical scan concept (i. e., constant reflection exit angle, etc.). Consequently, the use of rotating memory is necessitated.

A compromise between software difficulty and linearization buffer storage and bandwidth divides the sensor swath into 16 subswath segments of 512 samples each. The swath segments are buffered in core to optimize transfer efficiency to the disk. The swaths are stored on the disk in such a format that on retrieval an entire linearized scan

can be accessed within one disk rotation by jumping between surfaces (record heads) within the same cylinder (record head array position). Only one segment is buffered in core at any time for all six bands, the unformatted segments being swapped on and off a second swapping disk. Core required is 1.2 MB. Throughput is highly limited by disk bandwidth and swapping times. Considerable CPU interaction is required, consequently a separate processor with multi-port memory arranged as a very large virtual memory is required in addition to parallel high speed disks to achieve required throughputs.

Scan linearization further requires pixel interpolation along track, since linearized output scan lines will seldom coincide with any of the conical input scan lines. This interpolation is separate from and in addition to any interpolation required for geometric correction (ref. Section 7.9). Nearest-neighbor (zero-order interpolation) will result in unacceptable discontinuities in linearized scan lines, consequently a higher order interpolation process is required. This interpolation is performed in place by special purpose hardware through special control units connected to independent memory ports. Throughput capacity of the system is under 25TM scenes per 16 hour work shift.

An alternative scan linearization concept entails transposition of the scan lines (i. e., interchange of rows and columns) on a scene by scene basis. Then the conical scan rectification becomes an along scan position shift, easily handled at the same time as geometric correction. The process of transposition, however, is as formidable as brute force linearization, requiring mass bulk (disk) storage, multiple passes through the data, and large core buffers. Parallel disks with multiple heads per cylinder are required to achieve tractable data throughputs due to highly limited disk transfer efficiency. Processing time and costs are expected to equal or exceed those of brute-force linearization.

#### 7.6.2 Conical Coordinate System Processing

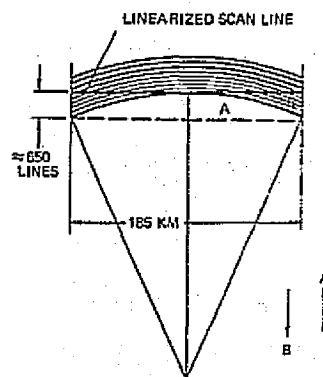
In light of the expense and limited throughput of the above TM input formatting schemes, consideration of a system where images are processed and output in conical scan coordinates is indicated. The

sensor data is geometrically corrected in a conical scan coordinate system (without scan linearization) and output to digital tape or to a film recorder designed expressly for the conical scan coordinates, i. e., lays the image on film in conical arc scan lines. Data correction proceeds much the same as for linear scans, with distortion on an array of points calculated precisely and distortion at all other points calculated via bilinear interpolation of the array of points (ref Section 7.9).

Difficulties arise in interpretation of the resulting data, since lineal distance and areal extent calculations are complex functions of directions in the image. Difficulties also arise in calculation of the geometric distortion. A metric is difficult to define since the along-scan and along-track axes are not orthogonal, presenting difficulties in unambiguous definition of distortion displacements. Piecewise-bilinear interpolation results in discontinuities of geometry at block boundaries since boundaries cannot be defined along orthogonal axes. Approximations must be made.

The sensor aperture rotates relative to the scan direction, resulting in variable resolution across the image. This is not a problem for film products, but can degrade change detection performance with images from spacecraft passes with displaced ground tracks. Section 7.9 discusses the applicability of aperture correction for the conical scan sensor.

In summary, because of limited throughput, high technical risk, and high cost for input reformatting, it is recommended that conical scan sensor scans not be linearized, but processed in conical scan coordinates, with the attendant slight performance degradation and difficulty of image interpretation. More to the point: unless there are numerous overt advantages to conical scan sensors over lineal scan, the data processing impact of scan linearization dictates that lineal-scan sensor be utilized in the EOS system.



CONICAL SCAN LINEARIZATION REFORMATTING

Figure 7-10. Conical Scan Ground Swath

## 7.7 APPLICABILITY OF ERTS EQUIPMENT TO CDPF

The ERTS program utilizes equipment in the NDPF which is directly transferable to the EOS CDPF. Use of the ERTS equipment further decreases the bottom-line EOS program cost. The attached table indicates the ERTS NDPF equipment which would be usable at the EOS IOC date. The list of equipment was abstracted from the 1 March 1974 revision of the "NASA Support Plan, Earth Resources Technology Satellite A and B", pages 4310.16-4310.21.

An item is said to be applicable if it could be used in the 35 scenes/day (CONUS only) EOS-A design envisioned by TRW. Reliability/age/maintenance costs/etc. were not of issue. Estimate of direct replacement costs (ROM) for each applicable subsystem are broken out below:

a)	Support Services - Central Computer System	\$517K
	(Sigma 5 peripherals -- \$361K)	
b)	Photo Processing Subsystem	691K
c)	Support Services Subsystem	1K
d)	User Service	53K
e)	Quality Assurance Subsystem	125K
f)	Digital Processing Subsystem	300K

TOTAL	\$1,577K
-------	----------

Subsystem and ComponentsQuantityAPPLICABLE EQUIPMENT:

## SUPPORT SERVICES — CENTRAL COMPUTER SYSTEM

Sigma 5 CPU and 84K of Memory with 3 MIOPS*	1
Keyboard/Printer	1
Card Punch	1
Card Reader	1
Line Printer	1
RAD Controller and Storage	2
Accessory Cabinet	1
Disc Controller	1
49 MB Disc	1
24 MB Disc	1
7-Track Tape Controller	1
7-Track Tape Drive	2
Keyboard/Display MOD II	2
Remote Keyboard/Printer	3
9-Track Tape Controller	3
9-Track Tape Drive (60 kc)	6
9-Track Tape Drive (120 kc)	4
Communications Controller/Timer	1
I/O Processor	1
Keypunch (029)	2
Keypunch (129)	1

## PHOTO PROCESSING SUBSYSTEM

Model 1811 Color Film Processor for Color Negative	1
Versamat 11C-M B/W Processor	6
Color Composite Printer	1
EN-70 Enlarger	2
Colorado Strip Printer	1
Log E Mark III	2
Log E Mark II	6
Model 1119, Studio Printer	1
Color Paper Processor, Model 20	1
Omega Pro-Lab D-6 B/W Enlarger	1
V-184 Color Enlarger	1
Color Processor Model 30 for Single Color Prints	1
GA 204 Temperature Control Sink and Water Recirculation	1
Vibration Isolation Table for S and R Enlarger	2
Film Drying Cabinet, Model 2	1
Versa Rack Washer 54102A	2
Freezer	1
Tacky Roll Film Cleaner TR-127-2	1
Chem Mix Room (Tanks, Plumbing Mixers)	-
Microfilm Processor, LM-SN/P	1
Recron Microfilm Duplicator, 35C	1

\* Might be used in CC should a larger machine be required for the CDPF.



Subsystem and ComponentsQuantity

## PHOTO PROCESSING SUBSYSTEM (cont)

Recordak Micro-File Machine, MRD 2/30	1
Model 1576 Sensitometer	2
Model 1155 QC Light Table	4
MacBeth Densitometer RD 400 D	2
MacBeth Densitometer TD-102	2
Model 820 Digital Photometer	1
Miscellaneous Small QC Equipment	-
MacBeth Densitometer TD-504	2
MacBeth Densitometer TD-404	1
ECP-70 Printer	2
CCP Punch	1

## SUPPORT SERVICE SUBSYSTEM

70 MM Viewers	2
Browse File Equipment (Microfilm Viewers, etc.)	-
Diebold Tub File No. 62204	1
Miscellaneous Furniture (Shelves, Cabinets, Work Benches, Lockers)	-
Miscellaneous Furniture, Shelves, Cabinets, Benches, and Other GSA Equipment	-

## USERS SERVICE

Densitometer (MacBeth TD-504)	1
Density Slicer (Spacial Data 703)	1
I <sup>2</sup> S Additive Color Viewer (International Imaging Systems)	1
Multispectral Viewer (Spectral Data)	1
Light Tables (70 mm) (Richards Corp)	5
ProofLite Light Table	4
Vanguard Monitor Analyzer	1
Variscan Mark II	1
"400" Page Search Reader	2
Varityper Headliner	1
COR 7DI Microfilm Header	1
Diebold Power File	1
19-Hole Paper Punch	1
IBM Selectric Mag Card	1
XDS Terminals	2
Modified Light Table with Magnifying Lens	1

## QUALITY ASSURANCE SUBSYSTEM

Mann Data Logger	1
Mann Comparator	1
Joyce Lobel Microdensitometer	1
Tech/Ops Isodensitracer	1
P.D.S. Microdensitometer	1
Light Table	1
Itec Microfilm Viewer/Printer	1
Color Analysis View Box	1
500 3M Reader Printer	1

<u>Subsystem and Components</u>	<u>Quantity</u>
QUALITY ASSURANCE SUBSYSTEM (cont)	
MacBeth TD-504	1
Power Rewinds — Neumade	1
Sartorius Metric Scales	1
Mettler Scales	1
Richards Light Table	1
Mcor-701 Microfilm Viewer	1
May-o-Matic Drafting Table w/ Drafting Arms	1
Hamilton Drafting Table	1
Precision-Ground Granet Block	1
Set Precision Right Angles	1
Hewlett-Packard Model 10 Calculator	1
Standard Inductor	5
Super Gage B and L	1
Potentiometer Leeds and Northrup	1
Corning Model 12 PH Meter	1
DIGITAL PROCESSING SUBSYSTEM	
Control Computer	
Central Processor and Memory (Sigma 3)	1
Keyboard Printer	1
9-Track Tape Controller	2
9-Track Tape Drive (120 kc)	4
9-Track Tape Drive (60 kc)	1
<u>NON-APPLICABLE EQUIPMENT:</u>	
DIGITAL PROCESSING SUBSYSTEM	
HDDTR	2
HDDTR Control	1
Signal Transfer Matrix Console	1
Cabling	1
Application Software*	1
INITIAL IMAGE GENERATING SUBSYSTEM	
MSS VTR	1
MSS VTR Controller	1
RBV VTR	1
RBV VTR Controller	1
EBR	1
EBR Controller	1
HDDTR	1
HDDTR Controller	1
CCIU	1
Cabling	1
Application Software	1

\*May be applicable

Subsystem and Components

Quantity

INITIAL IMAGE GENERATING SUBSYSTEM (cont)

Control Computer	1
Central Processor and Memory (Sigma 3)	1
Keyboard Printer	1
9-Track Tape Controller	1
9-Track Tape Drive (60 kc)	3

## 7.8 CDPF SOFTWARE FUNCTIONS

### 7.8.1 CDPF

Software functions are identified for EOS, requirements are analyzed, and the applicability of existing ERTS software is examined.

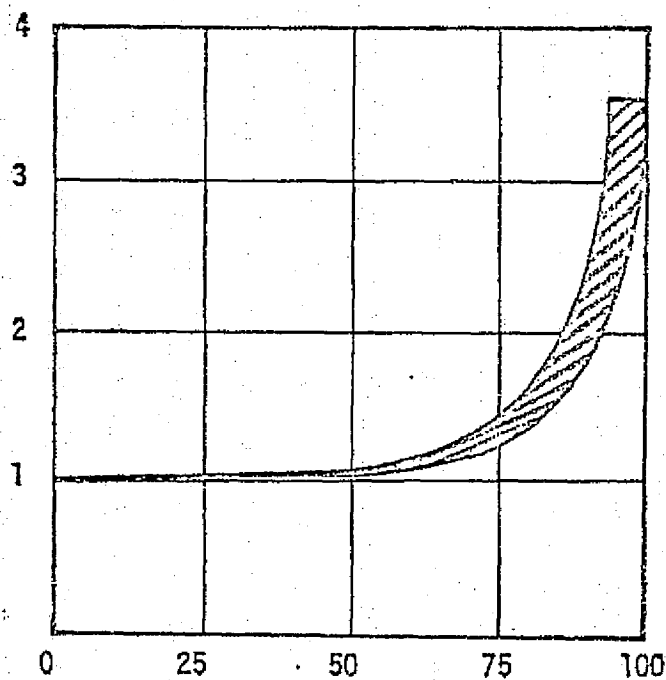
### 7.8.2 Problem Discussion and Assumptions

Basically this is a task to define and size the CDPF software. Once the software requirements are established, hardware configurations can be specified, and hardware costs determined. The reason for approaching the CDPF hardware configuration in this manner is that there are striking cost implications associated with the sizing. This is particularly true if the computer(s) is so selected that almost all of its resources are used by the application/software situated thereon. Note in particular Figure 7-11. This figure shows software development costs rising dramatically as either the memory capacity or the machine throughput limits are approached. The figure strongly suggests that for a relatively small increase in hardware cost, a major savings in software cost may be realized. Such a savings would occur if the machine were significantly larger than needed to handle the problem for which the machine was selected. To realize the potential savings in selecting an oversized computer, it is necessary to exercise good control in management over the software so that a Parkinsonian effect does not predominate over the effect shown in the figure.

In line with this concept, and given the existence of developed ERTS software which reflects many of required EOS functions, the ERTS NASA Data Processing Facility (NDPF) system was used as a baseline from which the EOS software configuration was established. As envisioned, most of the major functions of the present NDPF are retained, but are augmented/modified as required to meet EOS requirements. In connection with this decision, a requirement was levied to first consider utilization of the existing XDS Sigma 5 (augmented as needed) and then upward software compatible XDS machines if the Sigma 5 can not do the task.

The subsequent discussion is divided into two parts: the first provides a brief overview of the total NDPF including hardware and software; and the second reviews the EOS requirements in more depth.

RELATIVE  
COST  
PER  
INSTRUCTION



SPEED AND MEMORY UTILIZATION

Software development costs vary as the throughput limit of the machine is approached. Minimum software development cost is incurred if design point is near 50% of computer capacity.

Figure 7-11. Software Development Costs

### 7.8.3 Analysis

#### 7.8.3.1 Overview of the Goddard NDPF (Abstracted from References 5, 8, and 9)

The NDPF processes and stores all ERTS sensor data and disseminates large quantities of this data to users in the form of film imagery, computer compatible tapes and Data Collection System (DCS) tapes, cards, and listings. Figure 7-12 illustrates the flow of data through the NDPF and its relationship to the various subsystems required to accomplish the cited tasks.

Figure 7-16 and the related discussion, summarizes the intervening figures, tables, and text which provides detailed discussion of the ERTS NDPF computer and its software. Figure 7-16 may be contrasted with Figure 7-19 in Section 7.8.3.2, which summarizes the EOS CDPF system.

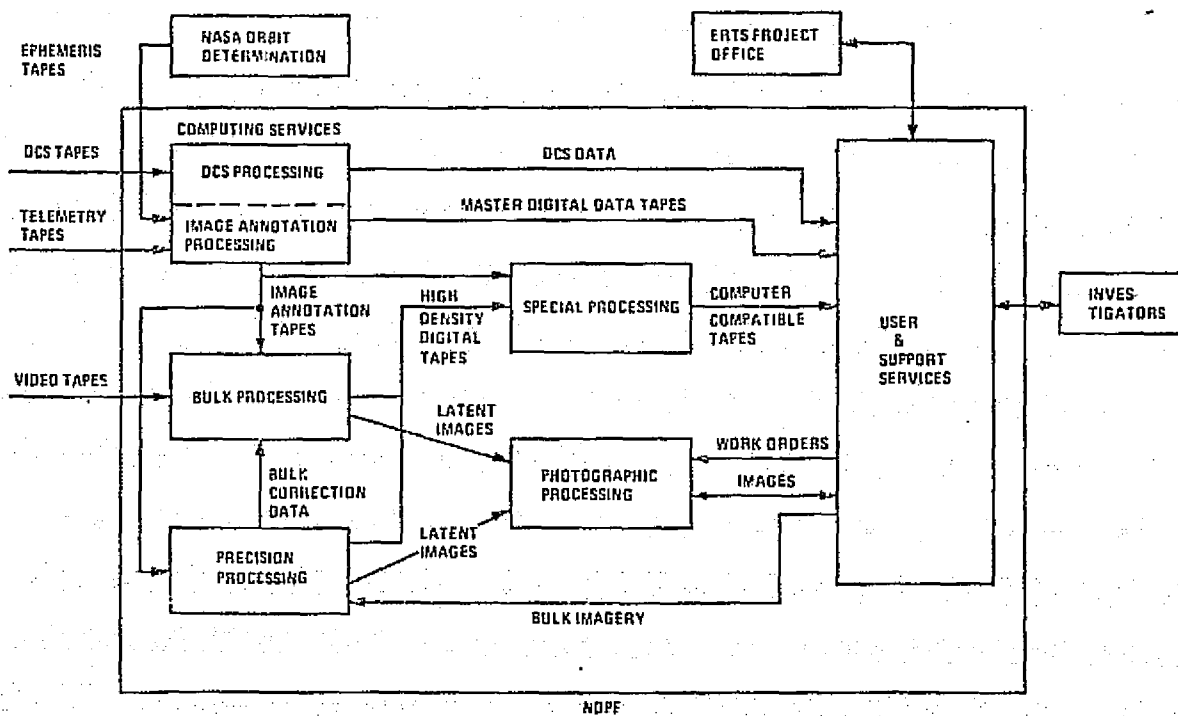


Figure 7-12. NDPF Subsystems

The subsystem at Goddard performs the following major operations:

1. Generation of master digital data tapes (MDDT) containing the basic data required for image annotation tape (IAT) production. This data includes: spacecraft attitude, sensor performance and ephemeris information extracted from the spacecraft performance data tape (SPDT) and best fit ephemeris tape (BFET) supplied by the Operations Control Center (OCC) and Orbit Determination Group (ODG), respectively.
2. Generation of IATs containing data used in the image processing element of the DPF for image location, annotation, and correction. A daily image annotation tape (DIAT) containing individual IATs for each day's operation is also produced and used for archival storage.
3. Data collection system (DCS) information processing and generation of user products (cards, listings, tapes).
4. Copying of computer compatible tapes (CCT) containing digital imagery data.
5. Generation of internal work orders used in scheduling and controlling MDDT, IAT, DCS, CCT, and user product processing and production.
6. Internal production accounting and reporting, quality control, etc.

All these functions are performed on a single XDS Sigma 5 computer having an 84K memory\* together with 3 disk drive units and 10 tape drive units. A configurational overview of the hardware is given in Figure 7-13. (See also author's memo on applicability of ERTS CDPF equipment.) Operating personnel consists of 7 persons working 3-2-2-per shift.

---

\* 1K = 1024 words of 32 bits each.

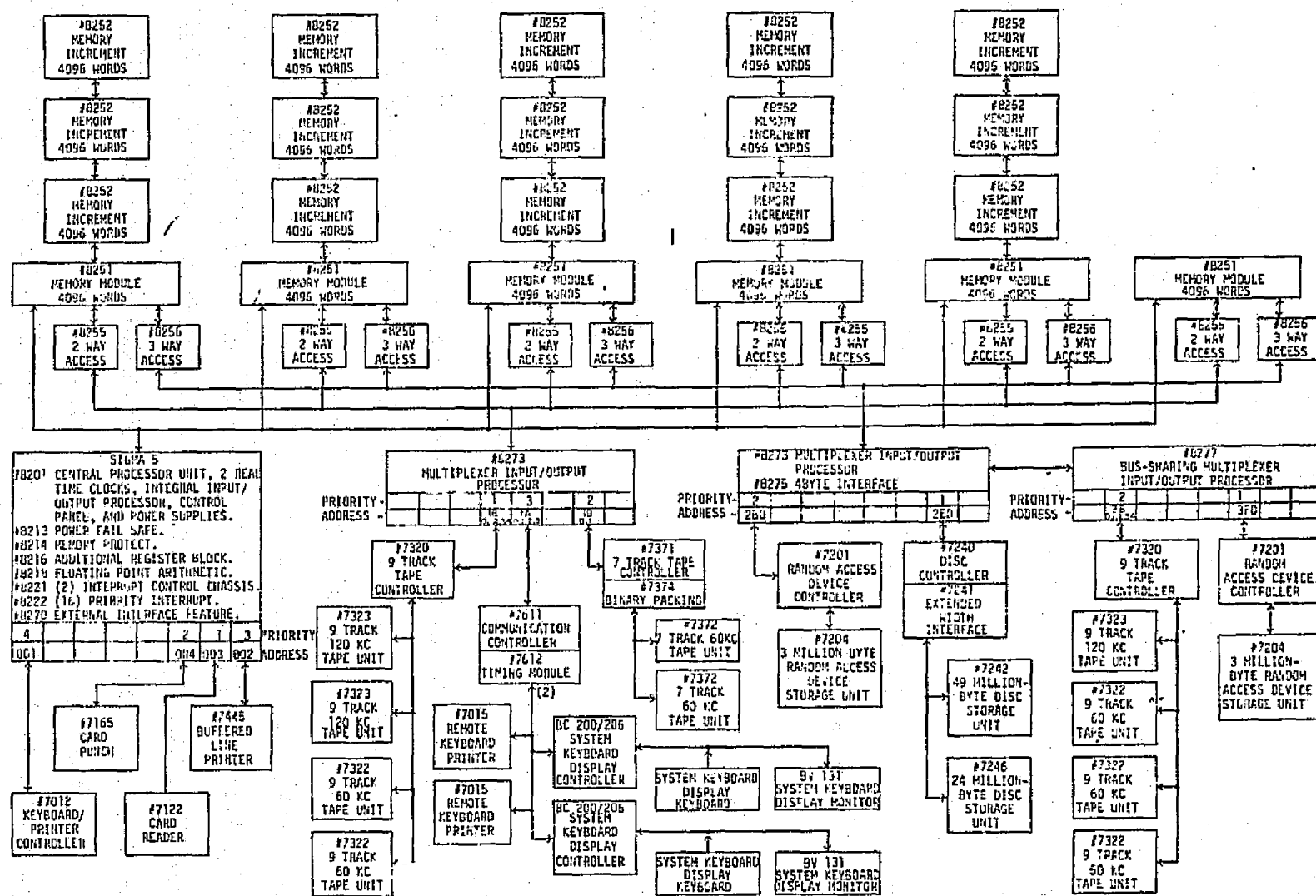


Figure 7-13. Overview of the XDS Sigma 5 System Configuration



The NDPF software is divided into two basic subsystems: 1) an information subsystem, and 2) a computational subsystem. The first deals primarily with data storage and retrieval, production control, management reporting, and services to users. The second deals with the computations, editing, and formatting required for production of master digital data tapes, image annotation tapes, and data collection system products.

The information subsystem itself is divided into nine basic load modules. These and their major functions are summarized in Table 7-1. Similarly, the computational subsystem consists of the five load modules outlined in Table 7-2.

From an external functional point of view, the NDPF operates as a set of activities processed by an ERTS monitor. These activities correspond to subroutines comprising the various load modules as outlined in Table 7-3 and -4. The ERTS monitor utilizes the command language module and the XDS software to read, interpret, and respond to control cards, or interactive commands controlling execution of these activities.

Two modes of operation can be controlled through the ERTS monitor; batch processing (BPM) and interactive processing (BTM). Batch processing runs in the background environment of memory (around 44K allocated), and interactive processing in the "time sharing" environment (around 20K allocated) as shown in Figure 7-14. The remaining core is allocated to systems software.

Figure 7-15 illustrates the flow of data and how activities are used in the BPM and BTM environments. Note that the systems software is stored on disc and activities are called into memory only as needed.

The "data base" shown in Figure 7-15 consists of some 23 separate data files stored on disk. These files, including granules of allocated storage are summarized in Table 7-5. Access to the files is accomplished through the maintenance module activities (Table 7-1).

Table 7-1. Load Modules Comprising Existing  
NDPF Software (Information Subsystem)

LOAD MODULE	MAJOR FUNCTION
Command Language	Interfaces XDS System Software and Application Modules
File Maintenance	Accesses and Updates Data Base Files
Query Support	Provides Current Production and Available Imagery Reports
Retrieval Support	Determines Available Imagery Corresponding to User Requirements
Input Module	Indicates Availability of Input Tapes, Keeps Track of Prepared Image Data and User Request Information
Production Control	Produces Work Orders For All Production Work, and Shipping Orders for Finished Products
Catalog Material	Produces Standard and Image Descriptor Catalogs
Management Report	Produces Management Reports Including Current Processing, Historical Statistics, Image Generation Summaries
Utility Module	Creates and Saves ERTS Data Base and System Files

Table 7-2. Load Modules Comprising Existing  
NDPF Software (Computational Subsystem)

LOAD MODULE	MAJOR FUNCTION
Master Digital Data Generation	Produces Master Digital Data Records for Use in Image Annotation Processing
Image Annotation Generation	Produces Image Annotation Data Records for Use in Image Processing
Data Collection System	Processes DCS Platform Data and Produces DCS User Products
Photographic Quality Control	Provides Interactive Support to Photographic Facility for Computing Gammas, Film Speeds, etc.
Digital Product Preparation	Copies Computer Compatible Tapes (CCT) Containing Digital Imagery Data

Table 7-3. Information Subsystem Major Activities

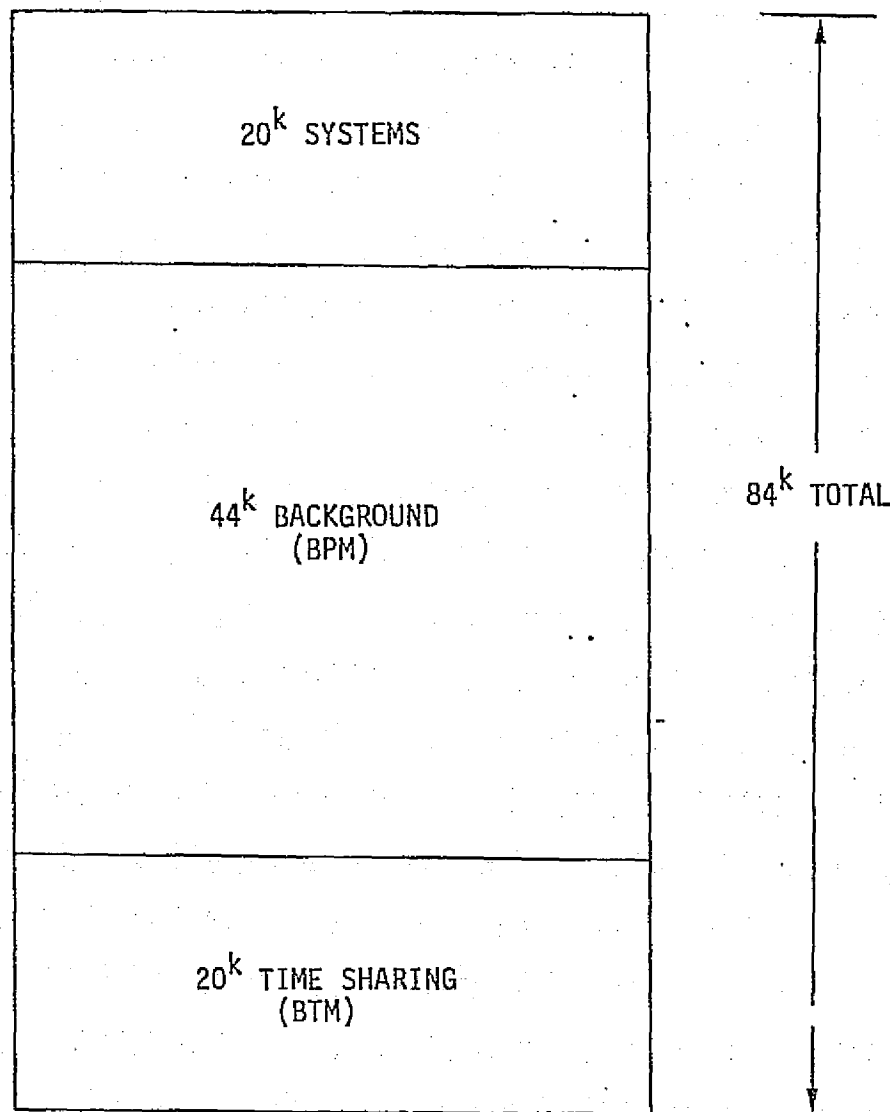
MODULE	ACTIVITY	CORE REQ'D.	DESCRIPTION
Input Module	IADRES	19 <sup>k</sup>	Input user address entries
	IADTAK	21.5 <sup>k</sup>	Take entries out of annotation data file
	IASSES	16.9 <sup>k</sup>	Input image assessment data
	ICALUP	17.9 <sup>k</sup>	Remote batch call
	IMGDSC	20.5 <sup>k</sup>	Input image descriptors
	IPRCMP	18.9 <sup>k</sup>	Terminate work orders
	IRECED	24.5 <sup>k</sup>	Input data received entries
	IREQES	25 <sup>k</sup>	Input data request entries
	IROLLN	35.8 <sup>k</sup>	Input roll number
	ISATCV	23 <sup>k</sup>	Input satellite coverage entries
	ISHPED	25 <sup>k</sup>	Input data shipped entries
	ISTDOR	22.5 <sup>k</sup>	Input standing order entries
	ITEST	25 <sup>k</sup>	Test of best generation inputs
Product Control	PETBPR	17.9 <sup>k</sup>	Produce estimated bulk production report
	PROBAT	25.6 <sup>k</sup>	Produce bulk annotation tape work orders
	PROIMG	19.4 <sup>k</sup>	Produce image generation work orders
	PROWDR	29 <sup>k</sup>	Produce data request work orders
	PROWUP	29 <sup>k</sup>	Produce user profile work orders

Table 7-3. Information Subsystem Major Activities (Continued)

MODULE	ACTIVITY	CORE REQ'D.	DESCRIPTION
Management Report	LIMGEN	16.4 <sup>k</sup>	Produce image generation report
	LHDSHU	14.8 <sup>k</sup>	Produce historic data shipped to users
	LHRSTT	15.4 <sup>k</sup>	Produce historic request statistics
	LPHTIN	13.8 <sup>k</sup>	Produce photographic inventory
	LPROFL	14.3 <sup>k</sup>	List user profiles
	LSTUSR	21 <sup>k</sup>	Produce status by user report
Utility Module	UINITL	8.7 <sup>k</sup>	Initial files
	ULISTF	9.7 <sup>k</sup>	List files
	USAVEF	14.3 <sup>k</sup>	Save files
	URESTF	10.2 <sup>k</sup>	Restore files
	UMODIF	8.2 <sup>k</sup>	Modify file words
Catalog Material	CABCAT	23 <sup>k</sup>	Produce standard catalog
	CMICRO	35 <sup>k</sup>	Produce microfilm work orders
	CMONTG	18.4 <sup>k</sup>	Produce catalog montage listing
	CSHCAB	12.3 <sup>k</sup>	Produce shipping labels

Table 7-4. Computational Subsystem Major Activities

MODULE	ACTIVITY	CORE REQ'D.	DESCRIPTION
Master Digital Data Generation	WIMDDG	26.1 <sup>k</sup>	Runs master digital data file generation
Image Annotation Generation	AIBIAT	38.4 <sup>k</sup>	Produce bulk image annotation tapes
	AIPIAT	24.1 <sup>k</sup>	Produce precision image annotation tapes
	AISIAT	24.1 <sup>k</sup>	Produce special image annotation tapes
Data Collection System Processing	DPROCS	23 <sup>k</sup>	DCS processing and generation of DCS user products
	DDDUMP	Total	Daily DCS dump
Photographic Quality Control	YPHOTO	-----	Photographic quality control support
Digital Product Preparation	TAPBAK	-----	Copy CCT in background



\*1<sup>k</sup> = 1024 words of 32 bits each.

Figure 7-14. Present NDPE Sigma 5 Core Utilization (BPM/BTM XDS Operating System)

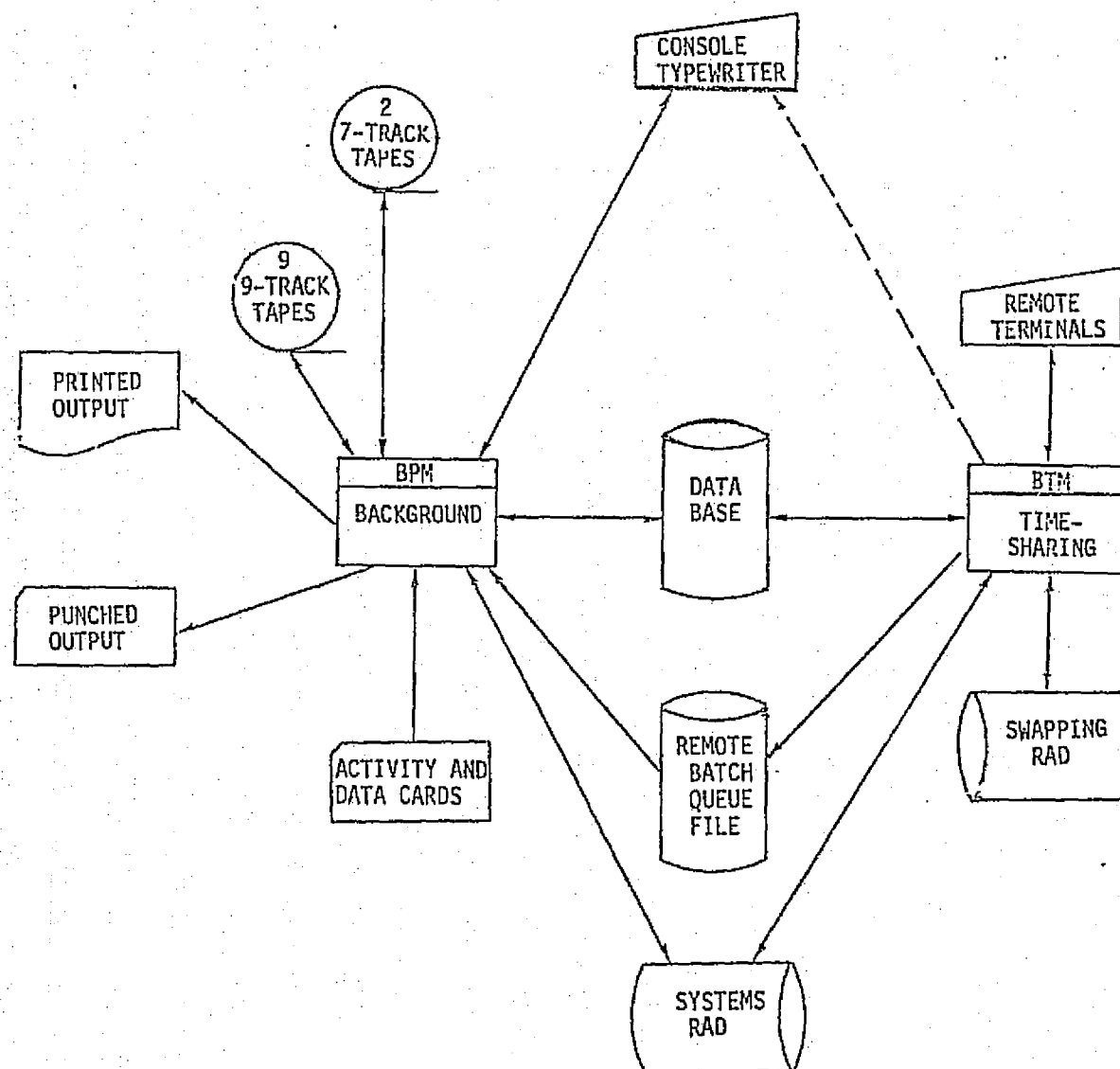


Figure 7-15. Flow of Data in the BPM/ BTM Environment



Table 7-5. Present DSC Data Base Disk Allocation

FILE NAME	DESCRIPTION	GRANULES*
FADF	Active Data File	2500
FADR	User Address File	102
FCAL	Calibration Values	3
FCMF	Catalog Maintenance	16
FCOV	Satellite Coverage	600
FDPR	Delayed Print	512
FHST	Historical Statistics	870
FIAD	Annotation Data	396
FIAT	Image Annotation Tape	1280
FIMG	Main Image	6000
FMDD	Master Digital Data	3840
FMST	Master Index Granule	1
FPID	Platform ID	2
FPRE	User Profile	1040
FPSE	Swath File	600
FREC	Data Received	12
FREQ	Data Request	674
FRIM	Rejected Image	134
FROL	Archival Roll	269
FSCR	Scratch File	256
FSRF	Standing Request	50
FWRK	Work Order	768
SORT	Temporary Work	3
		19928 TOTAL

\* 1 granule = 512 words of 32 bits each.

### Summary of ERTS NDPF System Overview

Figure 7-16 summarizes the NDPF system discussed on the previous pages. All functions shown in Figure 7-16 are performed on a single XDS Sigma 5 computer having 85K ( $1^k = 1024$  32-bit words) memory together with 3 disk drive units and 10 tape drive units. Operating personnel consists of 7 persons working 3-2-2 per shift. Figure 7-16 also shows the Sigma 5 core utilization. The total ERTS disc data base at the NDPF requires 10.2M words (32 bits per word). The system software is stored on disc and is called into memory as needed. It is understood that approximately 80 percent of the ERTS software operates under BPM control and 20 percent of the ERTS software operates under BTM control. The specification of Sigma 5 throughput for MSS-RBV imagery is 86 scenes/week, maximum, of digital product, and 860 scenes/week, maximum, of film product (Reference 13).

#### 7.8.3.2 CDPF Software Functions, Interfaces, and Requirements

This section summarizes the key requirements for the EOS Central Data Processing Facility (CDPF) software. Figure 7-17 shows the functional CDPF elements and the interfaces to the rest of the Ground Data Handling System (GDHS).

##### 7.8.3.2.1 User and Operational Requirements

Because of the diverse applications and the ever-growing user community, the EOS GDHS must process, generate, and disseminate high quality products efficiently and in a cost-effective manner. Consequently, the GDHS data generation functions must be:

- User oriented
- Capable of speedy and efficient data access
- Standardized and modularized
- Flexible
- Capable of accommodating EOS program growth.

It is expected that NASA will retain responsibility for, and control of, all system-induced errors associated with the output data from the payload. That is, NASA will have responsibility and control for error control and/or error measurement-correction of:

ORIGINAL PAGE IS  
OF POOR QUALITY

7-59

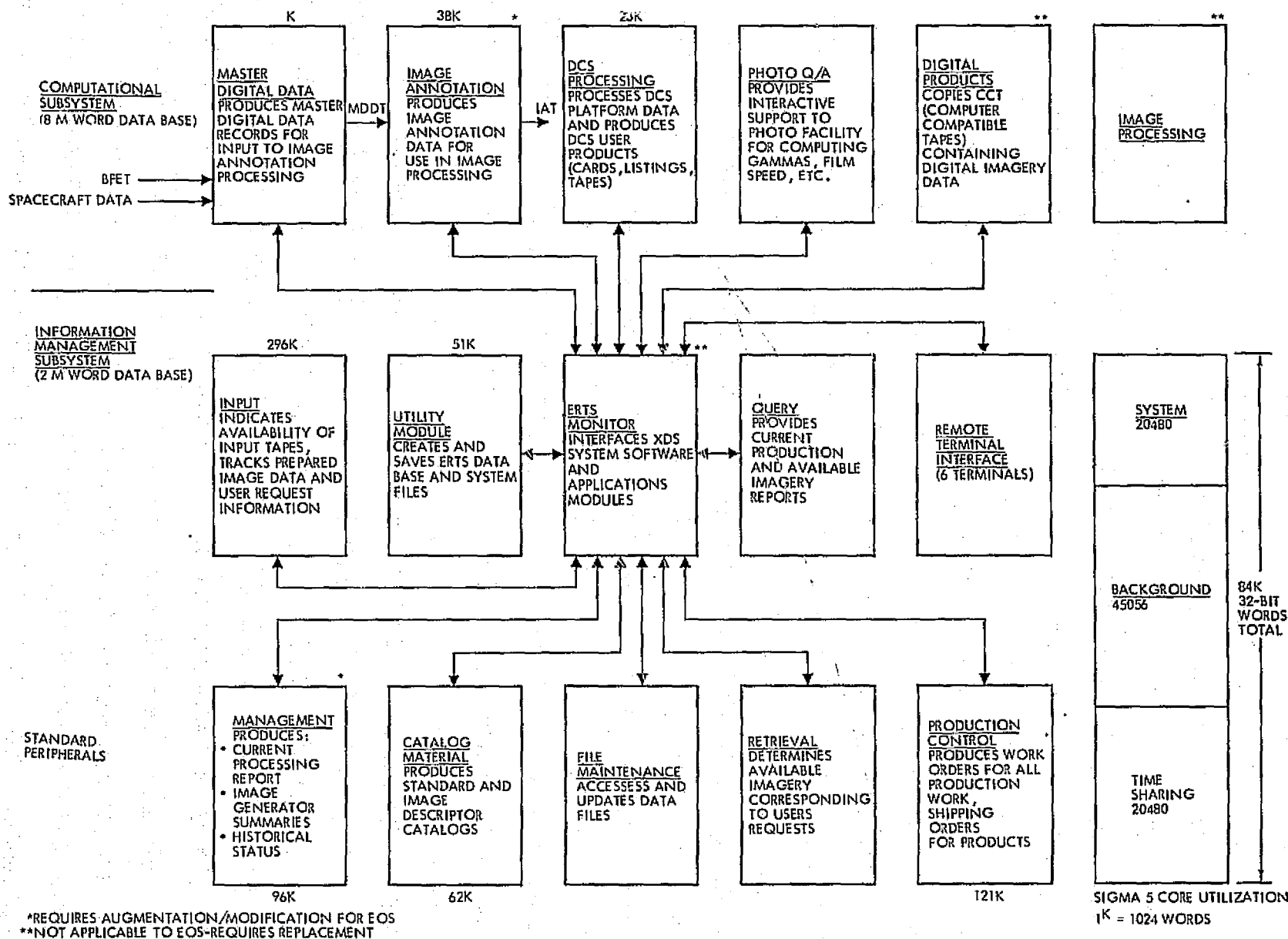


Figure 7-16. NDPF System Overview

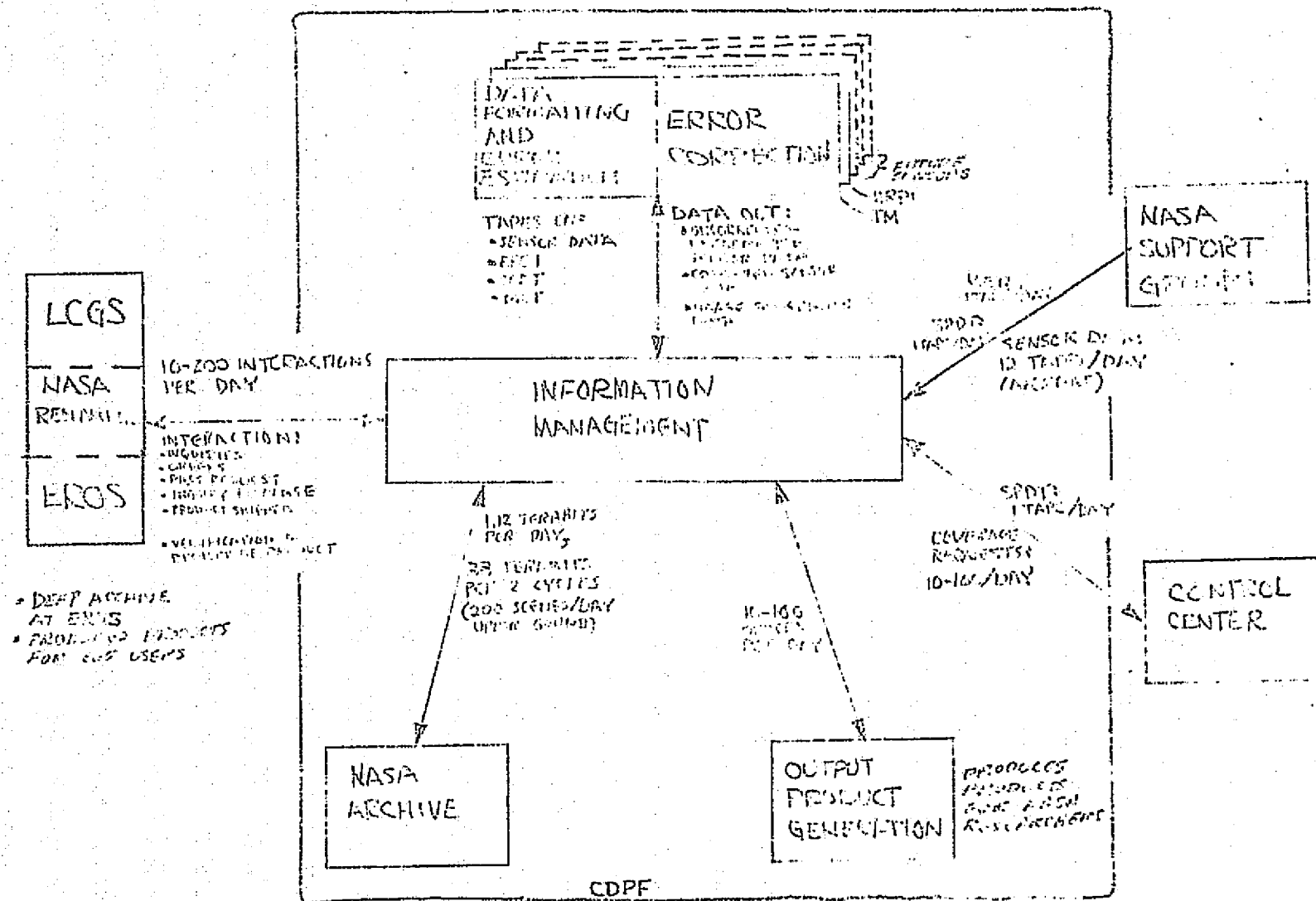


Figure 7-17. CDPF Functional Interfaces

- Spacecraft and payload functions
- Ground data capturing functions
- System error correction functions.

To make the system responsive to the majority of users as to types of end products and as to ease and speed of product availability, EROS (Department of the Interior) will have the responsibility to generate and disseminate the primary end products (film, computer compatible tape; high density digital tapes, and the necessary associated documentation) from data that has been corrected for system-induced errors by the CDPF. EROS will also be supplied uncorrected imagery data supplemented with the necessary correction parameters to remove system induced errors. This uncorrected data set will be used for deep archiving of EOS data.

A short term archive (90 days) will be maintained at the CDPF. The CDPF will also maintain the capability to create primary end products for a small number of NASA researchers (principle investigators).

In order to provide the data base from which the primary end products are created for both NASA researchers and EROS users, the CDPF must be designed as a flexible, standardized, and modularized system capable of accommodating EOS program growth. Figure 8 charts TRW's estimates of the EOS program growth curves. The baseline CDPF software was sized to handle the indicated "nominal" growth. Figure 7-18 was derived from considerations presented in Reference 16 and two servicing cases. The servicing cases postulated are:

Case A: (Baseline). U.S. coverage only from EOS-A type missions; downlink data rates -- 200 to 700 MB/sec; sensors -- TM/HRPI, HRPI/PI/SAR; primary end product generation for a maximum of 10-100 NASA researchers (maximum of 20 working days timeliness); EROS master data tapes in a maximum of 10 working days. Data from non-EOS-A type missions are processed by other groups/agencies. Provision for servicing 20-100 LCGS.

Case B: U.S. coverage only from EOS-A, B, C type missions; downlink data rates -- 50 to 700 MB/sec; typical sensors -- TM, HRPI, PI, SAR; PMMR, AAS, SSTIR, CRMS, PMS, GMS, WPS, VTS, VHRR, SLT; primary

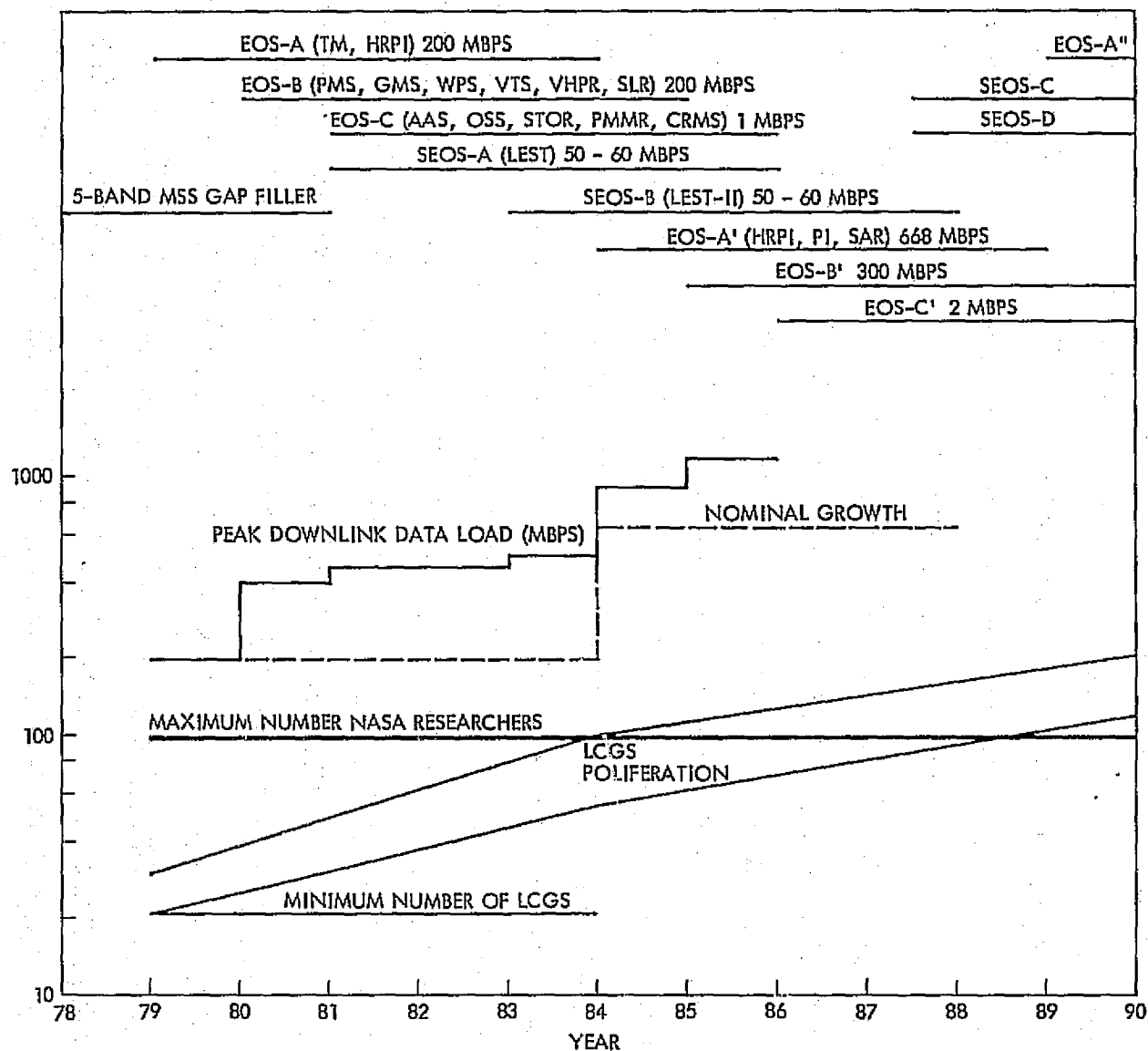


Figure 7-18. EOS Growth Projection

end product generation for a maximum of 10-100 NASA researchers (maximum of 20 working day timeliness); EROS and other agencies master data tapes in a maximum of 10 working days; servicing of 20-100 LCGS. SMM, SEOS, and SEASAT will not be supported by the CDPF.

Imagery throughput considered is 50 scenes/day and 200 scenes/day total input from all sensors.

There will be a first generation 241 mm black and white film product for each scene processed. Second and third generation film products will be produced as required to support NASA researchers with an estimated volume of 20 copies of 100 scenes per day.

LCGS proliferation data in Figure 7-18 may be conservative. LCGS proliferation impacts CDPF design as it is the CDPF which services the LCGS. Typical services include:

- Interface between LCGS and CC to process pass requests; processed requests are handed over to the CC to schedule pass assignments. The CC is structured to handle generation of, and distribution of LCGS pass assignments possibly using computer data link technology. Pass requests must be received by the CDPF one cycle prior to desired pass date.
- Provide data to initialize LCGS data correction process. Data will be disseminated by U.S. mail.
- Schedule LCGS operation support
  - Siting
  - Equipment calibration
  - Equipment changes required by second generation spacecraft
- Provide requested technical information within NASA scope.

DCS considerations have no impact on the CDPF due to TRW's "bent-pipe" approach and, consequently, are not considered here.

#### 7.8.3.2.2 EOS Baseline Software

EOS software functions mirror those of ERTS except for image processing. This is reflected in Figure 7-19 which depicts the CDPF system overview (of Figure 7-16). Figure 7-19 summarizes the software descriptions presented on subsequent pages and shows the CDPF instruction and data base deltas over the NDPF numbers given in Figure 7-16. Table 7-6 per-

COMPUTATIONAL  
SUBSYSTEM  
(4 MWORD DATA BASE)  
(1 MWORDS)

INFORMATION MANAGEMENT  
SUBSYSTEM  
(3 MWORDS)  
(3 MWORDS)

7-64

ORIGINAL PAGE IS  
OF POOR QUALITY

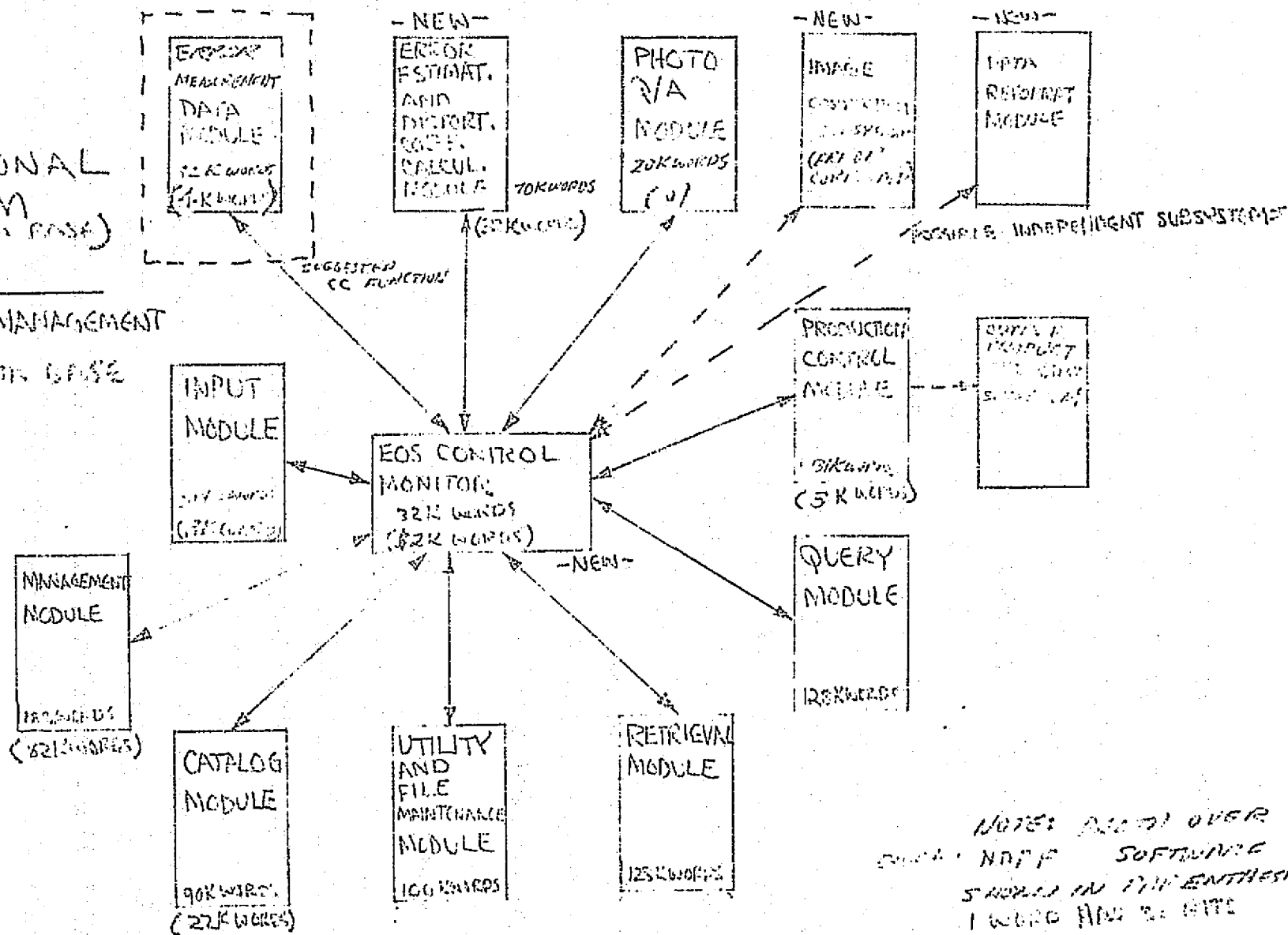


Table 7-19. CDPF System Overview



Table 7-6. ERTS/EOS Software Comparison

SOFTWARE MODULE	EOS SOFTWARE					ERTS COUNTERPART					MODULE NAME
	TOTAL MODULE SIZE	LARGEST ROUTINE SIZE	EXECUTION TIME * (SEC)	EXECUTION RATE	SOURCE **	TOTAL MODULE SIZE	LARGEST ROUTINE SIZE	EXECUTION TIME (SEC)	EXECUTION RATE	SOURCE **	
ERROR MEASUREMENT DATA	32K	32K	1800	1/DAY	E,8,9	26K	26K	1630	1/DAY	8,9	MASTER DIGITAL DATA
ERROR ESTIMATION MODULE	70K	38K	91	1/SCENE	E,8,9	38K	38K	15	1/SCENE	8,9	IMAGE ANIMATION
PHOTO Q/A MODULE	20K	20K	2	1/FILM	E,8					8	PHOTO Q/A
PRODUCTION CONTROL MODULE	131K	32K	10	6/DAY	E,3,8	128K	29K			8	PRODUCT CONTROL
QUERY MODULE	128K	20K	3	100/DAY	E,6,8,9					8	QUERY
RETRIEVAL MODULE	123K	20K	5	200/DAY	E,6,8,9					8	RETRIEVAL
UTILITY AND FILE MAINTENANCE	100K	20K	1/2	1K/DAY	E,8,17	52K	14K			8	UTILITY
CATALOG MODULE	90K	38K	2000 (MAX)	1/DAY	E,8	68K	35K			8	CATALOG
MANAGEMENT MODULE	180K	32K	900 (MAX)	1/DAY	E,3,8	98K	21K			8	MANAGEMENT
INPUT MODULE	304K	36K	2 (MAX)	250/DAY	E,3,8	297K	36K			8	INPUT
EOS MONITOR	32K	32K	1/10	20K/DAY	E,3,7,10,11	20K	20K			8	ERTS MONITOR

\* INCLUDES 15% OVERHEAD

\*\* NUMBER INDICATES REFERENCE NO.; E INDICATE ENGINEERING ESTIMATE

ORIGINAL PAGE IS  
OF POOR QUALITY

mits a side-by-side comparison of the NDPF and CDPF software functions. The subsequent descriptions are designed to accommodate the nominal growth curve of Figure 7-18, and 120 users (total) interfacing with the CDPF (includes NASA researchers, EROS, and LCGS). It is further assumed for this sizing study that the worst case "video" volume is 200 scenes/day and that all users interface with the CDPF each day but that only 70 percent of the total users require all CDPF products per day. The computational software descriptions come first followed by the system and information management summaries. The summary forms contain the following information:

- Function name
- Descriptive comments
- Derivation or references from which the software was obtained (Cited reference 19 provides detailed breakdowns of the major modules).
- Limitations
- Previous usage of software
- Functions/routines called by this function
- Input and output lists
- Algorithm structure
- Memory size in units of 32-bit words (instructions plus invariant data base)
- Execution time and rate
- Desired language characteristics

Figure 7-20 indicates the general process flow for the CDPF image processing function, while Figure 7-20 depicts a typical production timeline.

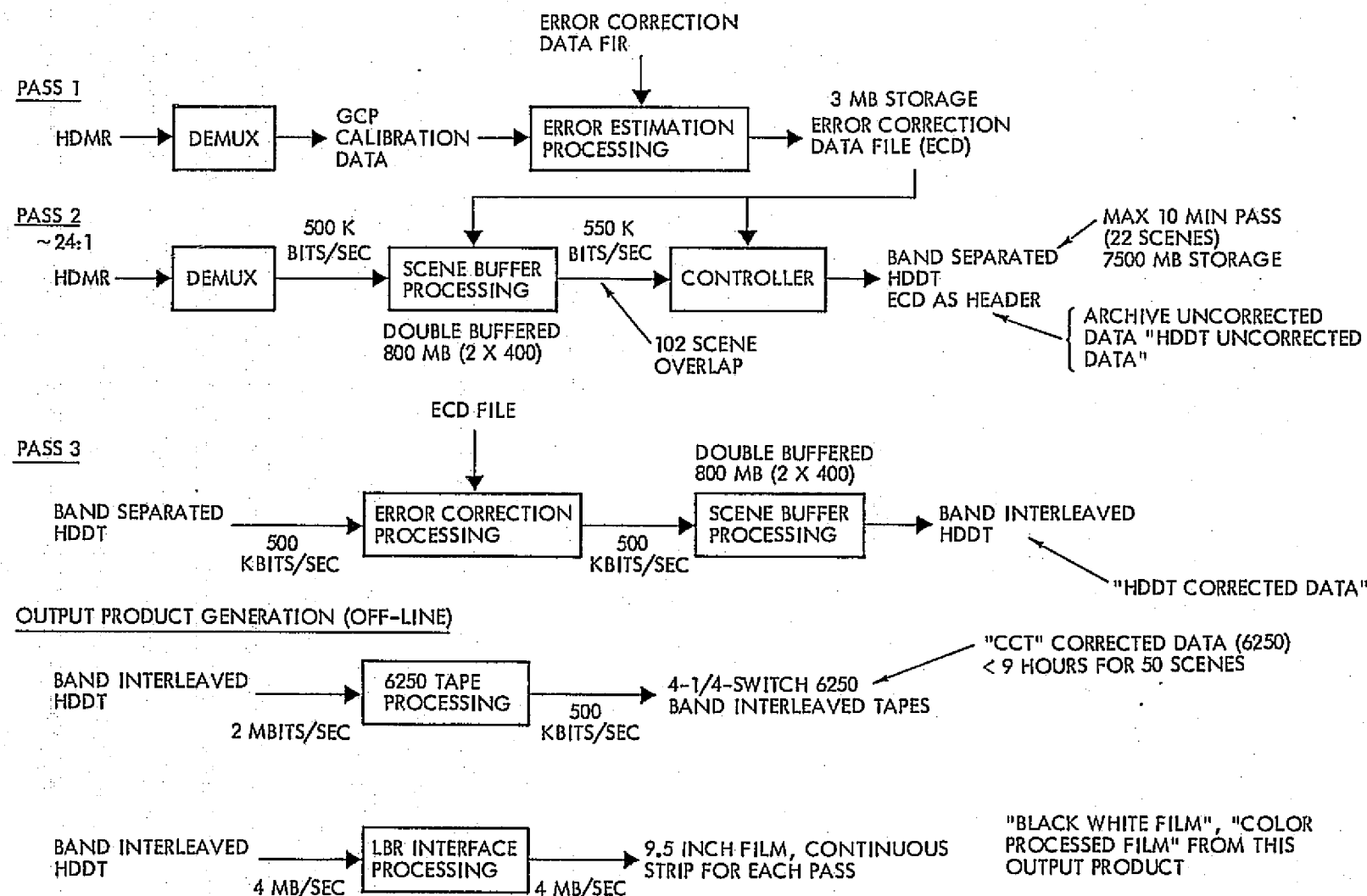


Figure 7-20. CDPF Image Processing Function  
(Quotes Indicate Item is an Output Product)

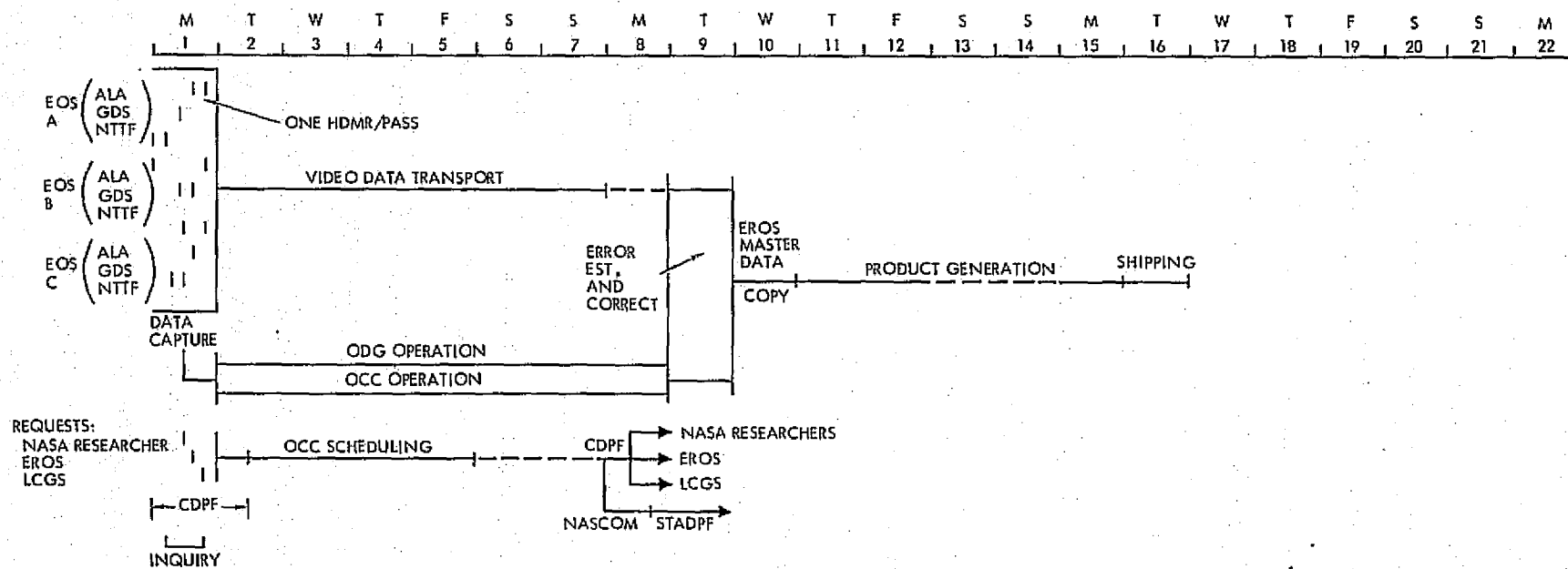


Figure 7-21a. Production Timeline

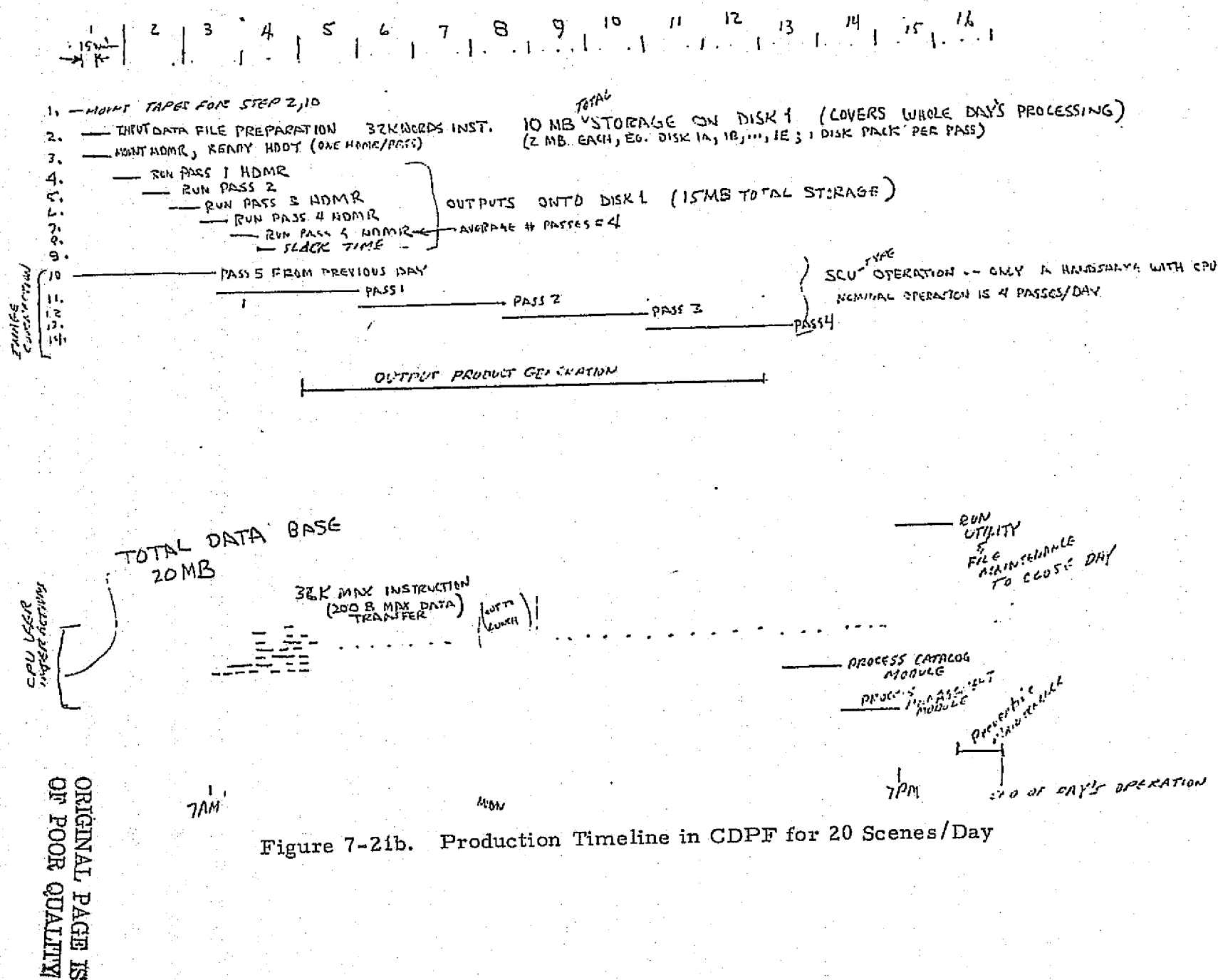


Figure 7-21b. Production Timeline in CDPF for 20 Scenes/Day

## SOFTWARE MODULE SUMMARY

NAME: Error Measurement Data Module

DESCRIPTION: Extract data from BFET, S/C Performance Data Tape (SPDT), and Meteorology Tapes to create Error Correction Data (ECD) File by merging of data; HRPI calibration data may be on SPDT.

REFERENCES: 8, 9

LIMITATIONS: This function might reside on CC off-line computer

PREVIOUS USAGE: Similar in function and scope to NDPF Master Digital Data Module located on Sigma 5.

FUNCTIONS/ROUTINES CALLED: Utility Module, System Module, File Maintenance Module

INPUT: BFET, S/C Performance Data, MET data

OUTPUT: Error Correction Data file onto disc pack (2 MB)

ALGORITHM STRUCTURE: ☒ Straight Line ☐ Iterative  
☐ Mult. Branches ☐ Table Driven

MEMORY SIZE (32 bit words): 32K

Execute Time: 30 min

Execute Rate: 1/day

### DESIRED LANGUAGE CHARACTERISTICS:

- |  |   |
|--|---|
| <input checked="" type="checkbox"/> List Processing                                | <input type="checkbox"/> Bit Manipulation                             |
| <input checked="" type="checkbox"/> Logical Statements                             | <input checked="" type="checkbox"/> Machine Language I/O              |
| <input type="checkbox"/> Real-Time Control   | <input type="checkbox"/> Fixed-Float Conversions                      |
| <input checked="" type="checkbox"/> Data File Management                           | <input type="checkbox"/> Explicit Control of Registers and Indicators |
| <input type="checkbox"/> Interrupt Masking and Handling                            | <input type="checkbox"/> Direct Control of Indexing Facilities        |
| <input type="checkbox"/> Common Memory   | <input type="checkbox"/> Indirect Addressing                          |
| <input type="checkbox"/> Message Skeletons   | <input type="checkbox"/> Double Precision                             |
| <input type="checkbox"/> Vector/Matrix Operations                                  | <input type="checkbox"/> Byte Addressing                              |
| <input checked="" type="checkbox"/> Algebraic Operations (Boolean, Exponent, etc.) | <input type="checkbox"/> _____  |
| <input type="checkbox"/> Floating Point Operations                                 |   |

## SOFTWARE MODULE SUMMARY

NAME: Error Estimation Module

DESCRIPTION: Process ECD file together with ground truth data to obtain distortion coefficients for Error Correction Process; annotation data generated; calibration data formatted; ground truth file maintenance; updates catalog data base.

REFERENCES: 8, 9

LIMITATIONS:

PREVIOUS USAGE: Annotation function exists at NDPF, a resident function on TRW's ERTS Data Processing System.

FUNCTIONS/ROUTINES CALLED:

System Module, Utility and File Maintenance Modules

INPUT: ECD File; Ground Truth Data from reformatter

OUTPUT: ECD File (5 MB)

ALGORITHM STRUCTURE: ☒ Straight Line ☐ Iterative  
☐ Mult. Branches ☐ Table Driven

MEMORY SIZE (32 bit words): 70K

Execute Time: 91 sec

Execute Rate: 1/scene

DESIRED LANGUAGE CHARACTERISTICS:

- |  |   |
|--|---|
| <input checked="" type="checkbox"/> List Processing                                | <input type="checkbox"/> Bit Manipulation                             |
| <input checked="" type="checkbox"/> Logical Statements                             | <input checked="" type="checkbox"/> Machine Language I/O              |
| <input type="checkbox"/> Real-Time Control   | <input checked="" type="checkbox"/> Fixed-Float Conversions           |
| <input checked="" type="checkbox"/> Data File Management                           | <input type="checkbox"/> Explicit Control of Registers and Indicators |
| <input type="checkbox"/> Interrupt Masking and Handling                            | <input type="checkbox"/> Direct Control of Indexing Facilities        |
| <input checked="" type="checkbox"/> Common Memory                                  | <input type="checkbox"/> Indirect Addressing                          |
| <input type="checkbox"/> Message Skeletons   | <input type="checkbox"/> Double Precision                             |
| <input checked="" type="checkbox"/> Vector/Matrix Operations                       | <input checked="" type="checkbox"/> Byte Addressing                   |
| <input checked="" type="checkbox"/> Algebraic Operations (Boolean, Exponent, etc.) | <input type="checkbox"/> _____  |
| <input checked="" type="checkbox"/> Floating Point Operations                      |   |

## SOFTWARE MODULE SUMMARY

NAME: Photo Q/A Module

DESCRIPTION: Provides interactive support to photographic product facility for computing film speeds, gammas, etc. Provides data quality information for management report.

REFERENCES: 8, 19

LIMITATIONS:

PREVIOUS USAGE: Existing routine at NDPF

FUNCTIONS/ROUTINES CALLED: System Module, File Maintenance, Input Module

INPUT: Photo parameters

OUTPUT: Photo parameters, update to Q/C data base

ALGORITHM STRUCTURE: ☒ Straight Line ☐ Iterative  
☐ Mult. Branches ☐ Table Driven

MEMORY SIZE (32 bit words): 20K

Execute Time: 2

Execute Rate: 1/film image (est. maximum)

### DESIRED LANGUAGE CHARACTERISTICS:

- |  |   |
|--|---|
| <input checked="" type="checkbox"/> List Processing                                | <input type="checkbox"/> Bit Manipulation                             |
| <input checked="" type="checkbox"/> Logical Statements                             | <input checked="" type="checkbox"/> Machine Language I/O              |
| <input type="checkbox"/> Real-Time Control   | <input checked="" type="checkbox"/> Fixed-Float Conversions           |
| <input type="checkbox"/> Data File Management                                      | <input type="checkbox"/> Explicit Control of Registers and Indicators |
| <input type="checkbox"/> Interrupt Masking and Handling                            | <input type="checkbox"/> Direct Control of Indexing Facilities        |
| <input type="checkbox"/> Common Memory   | <input type="checkbox"/> Indirect Addressing                          |
| <input type="checkbox"/> Message Skeletons   | <input type="checkbox"/> Double Precision                             |
| <input type="checkbox"/> Vector/Matrix Operations                                  | <input type="checkbox"/> Byte Addressing                              |
| <input checked="" type="checkbox"/> Algebraic Operations (Boolean, Exponent, etc.) | <input type="checkbox"/> _____  |
| <input checked="" type="checkbox"/> Floating Point Operations                      |   |



## SOFTWARE MODULE SUMMARY

NAME: Production Control Module

DESCRIPTION: Produces estimated daily master data production report; produces work orders for master data generation, image generation, and digital product generation; produces shipping documents and lists.

REFERENCES: 3, 8, 19

LIMITATIONS:

PREVIOUS USAGE: Similar function exists at NDPF

FUNCTIONS/ROUTINES CALLED: System Module, Utility and File Maintenance

INPUT: Schedule job orders

OUTPUT: Work orders and shipping documents

ALGORITHM STRUCTURE: ☒ Straight Line ☐ Iterative  
☐ Mult. Branches ☐ Table Driven

MEMORY SIZE (32 bit words): 131K

Execute Time: 10 sec

Execute Rate: 6/day (est. maximum)

DESIRED LANGUAGE CHARACTERISTICS:

- |   |   |
|---|---|
| <input checked="" type="checkbox"/> List Processing                     | <input checked="" type="checkbox"/> Bit Manipulation                  |
| <input checked="" type="checkbox"/> Logical Statements                  | <input checked="" type="checkbox"/> Machine Language I/O              |
| <input type="checkbox"/> Real-Time Control                              | <input type="checkbox"/> Fixed-Float Conversions                      |
| <input checked="" type="checkbox"/> Data File Management                | <input type="checkbox"/> Explicit Control of Registers and Indicators |
| <input type="checkbox"/> Interrupt Masking and Handling                 | <input type="checkbox"/> Direct Control of Indexing Facilities        |
| <input checked="" type="checkbox"/> Common Memory                       | <input type="checkbox"/> Indirect Addressing                          |
| <input checked="" type="checkbox"/> Message Skeletons                   | <input type="checkbox"/> Double Precision                             |
| <input type="checkbox"/> Vector/Matrix Operations                       | <input type="checkbox"/> Byte Addressing                              |
| <input type="checkbox"/> Algebraic Operations (Boolean, Exponent, etc.) | <input type="checkbox"/> _____  |
| <input type="checkbox"/> Floating Point Operations                      |   |

## SOFTWARE MODULE SUMMARY

NAME: Query Module

DESCRIPTION:

Provides available imagery reports to browse facility user/management.

REFERENCES: 3, 4, 6, 8, 18, 19

LIMITATIONS:

PREVIOUS USAGE: Similar function at NDPF

FUNCTIONS/ROUTINES CALLED: System Module, File Maintenance,  
Input Module

INPUT: User query

OUTPUT: Inquiry response — Figure 7-22.

ALGORITHM STRUCTURE: ☒ Straight Line ☐ Iterative  
☐ Mult. Branches ☐ Table Driven

MEMORY SIZE (32 bit words): 128K

Execute Time: 3 sec

Execute Rate: 200/day

DESIRED LANGUAGE CHARACTERISTICS:

- |   |   |
|---|---|
| <input checked="" type="checkbox"/> List Processing                     | <input type="checkbox"/> Bit Manipulation                             |
| <input checked="" type="checkbox"/> Logical Statements                  | <input checked="" type="checkbox"/> Machine Language I/O              |
| <input type="checkbox"/> Real-Time Control                              | <input type="checkbox"/> Fixed-Float Conversions                      |
| <input checked="" type="checkbox"/> Data File Management                | <input type="checkbox"/> Explicit Control of Registers and Indicators |
| <input checked="" type="checkbox"/> Interrupt Masking and Handling      | <input type="checkbox"/> Direct Control of Indexing Facilities        |
| <input type="checkbox"/> Common Memory                                  | <input type="checkbox"/> Indirect Addressing                          |
| <input checked="" type="checkbox"/> Message Skeletons                   | <input type="checkbox"/> Double Precision                             |
| <input type="checkbox"/> Vector/Matrix Operations                       | <input type="checkbox"/> Byte Addressing                              |
| <input type="checkbox"/> Algebraic Operations (Boolean, Exponent, etc.) | <input type="checkbox"/> _____  |
| <input type="checkbox"/> Floating Point Operations                      |   |

Observation ID	Orbit No.	Station ID	Ephemeris Type	Data Quality	Scene Center Geographic Area		Time	Cloud Cover	Products	
					Lat	Lon			HRPI	TM
1000-00001	0001	G	R	G	121.55	36.21	1600	10	FFFX	CCHCCCC

↑ Mission  
 1 = A  
 2 = B  
 3 = C

↑ Receiving  
 Site  
 G = Goldstone  
 F = Fairbanks  
 N = NTTF, Goddard

R = Refined  
 P = Predicted

↑ Percent  
 Cloud  
 Cover

↓  
 H = HDDT available  
 F = Film products  
 available  
 C = CCT available  
 X = All products  
 available

G = Good  
 F = Fair  
 P = Poor

Figure 7-22. Query Response

## SOFTWARE MODULE SUMMARY

NAME: Retrieval Module

DESCRIPTION: Identifies available imagery by browse facility user's descriptor input.

REFERENCES: 3, 4, 6, 8, 18, 19

LIMITATIONS:

PREVIOUS USAGE: Similar function exists at NDPF

FUNCTIONS/ROUTINES CALLED: System Module, File Maintenance, Input Module

INPUT: User query

OUTPUT: Inquiry Response — Figure 7-23

ALGORITHM STRUCTURE: ☒ Straight Line ☐ Iterative  
☐ Mult. Branches ☐ Table Driven

MEMORY SIZE (32 bit words): 128K

Execute Time: 5 sec

Execute Rate: 200/day

### DESIRED LANGUAGE CHARACTERISTICS:

- |   |   |
|---|---|
| <input checked="" type="checkbox"/> List Processing                     | <input type="checkbox"/> Bit Manipulation                             |
| <input checked="" type="checkbox"/> Logical Statements                  | <input checked="" type="checkbox"/> Machine Language I/O              |
| <input type="checkbox"/> Real-Time Control                              | <input type="checkbox"/> Fixed-Float Conversions                      |
| <input checked="" type="checkbox"/> Data File Management                | <input type="checkbox"/> Explicit Control of Registers and Indicators |
| <input checked="" type="checkbox"/> Interrupt Masking and Handling      | <input type="checkbox"/> Direct Control of Indexing Facilities        |
| <input type="checkbox"/> Common Memory                                  | <input type="checkbox"/> Indirect Addressing                          |
| <input checked="" type="checkbox"/> Message Skeletons                   | <input type="checkbox"/> Double Precision                             |
| <input type="checkbox"/> Vector/Matrix Operations                       | <input type="checkbox"/> Byte Addressing                              |
| <input type="checkbox"/> Algebraic Operations (Boolean, Exponent, etc.) | <input type="checkbox"/> _____  |
| <input type="checkbox"/> Floating Point Operations                      |   |

OBSERVATION ID 1018-05453

Orbit Number:	0196	Subsat Point (long):	-80.83
Total Cloud Cover:	10	Subsat Point (lat):	41.83
Station	Goldstone	Picture Center (long):	-80.84
Ephemeris Type:	R	Picture Center (lat):	541.79
Altitude:	492.32	Sun Elevation:	33.70
Heading:	36.38	Sun Azimuth:	40.62
Track:	48.32		
Microfilm Roll:	4179		
Position in Roll:	0591		

SENSOR QUALITY

HRPI				TM						
1	2	3	4	1	2	3	4	5	6	7
G	G	G	G	G	G	G	G	G	P	P

Image Descriptors: Forestry Rivers  
Number of Products Present: 13

Product:	P-CL	Band Indicator:	11111111010
Date Produced:	09/15/81	Last Request Date:	09/15/81
Product:	CCT	Band Indicator:	01100000011
Data Produced:	09/15/81	Last Request Date:	09/15/81

Figure 7-23. Retrieval Processing —  
Display Image Output

## SOFTWARE MODULE SUMMARY

NAME: Utility and File Maintenance

### DESCRIPTION:

Utility software creates and saves disc data files; file maintenance software access and updates disc data files

REFERENCES: 8, 17, 19

### LIMITATIONS:

PREVIOUS USAGE: Typical system routines -- Functions currently present at NDPF.

FUNCTIONS/ROUTINES CALLED: System Module

INPUT:

OUTPUT:

ALGORITHM STRUCTURE: ☒ Straight Line ☐ Iterative  
☐ Mult. Branches ☐ Table Driven

MEMORY SIZE (32 bit words): 100K

Execute Time: 1/2 sec

Execute Rate: 1K/day

### DESIRED LANGUAGE CHARACTERISTICS:

- |   |   |
|---|---|
| <input type="checkbox"/> List Processing                                | <input type="checkbox"/> Bit Manipulation                             |
| <input type="checkbox"/> Logical Statements                             | <input type="checkbox"/> Machine Language I/O                         |
| <input type="checkbox"/> Real-Time Control                              | <input type="checkbox"/> Fixed-Float Conversions                      |
| <input checked="" type="checkbox"/> Data File Management                | <input type="checkbox"/> Explicit Control of Registers and Indicators |
| <input checked="" type="checkbox"/> Interrupt Masking and Handling      | <input type="checkbox"/> Direct Control of Indexing Facilities        |
| <input checked="" type="checkbox"/> Common Memory                       | <input type="checkbox"/> Indirect Addressing                          |
| <input type="checkbox"/> Message Skeletons                              | <input type="checkbox"/> Double Precision                             |
| <input type="checkbox"/> Vector/Matrix Operations                       | <input type="checkbox"/> Byte Addressing                              |
| <input type="checkbox"/> Algebraic Operations (Boolean, Exponent, etc.) | <input type="checkbox"/> _____  |
| <input type="checkbox"/> Floating Point Operations                      |   |

## SOFTWARE MODULE SUMMARY

NAME: Catalog Module

### DESCRIPTION:

Produces catalog masters; produces microfilm work orders; produces catalog montage master listing.

REFERENCES: 4, 8, 13, 19

LIMITATIONS: Needs to be modified to reflect EOS mission payload

PREVIOUS USAGE: Currently exists at NDPF

FUNCTIONS/ROUTINES CALLED: System Module, Utility and File Maintenance Module, Input Module

INPUT:

OUTPUT: See Figure 7-14 showing sample catalog page

ALGORITHM STRUCTURE: ☒ Straight Line ☐ Iterative  
☐ Mult. Branches ☐ Table Driven

MEMORY SIZE (32 bit words): 90K

Execute Time: 2000 sec (est. maximum)

Execute Rate: 1/day

### DESIRED LANGUAGE CHARACTERISTICS:

- |   |   |
|---|---|
| <input checked="" type="checkbox"/> List Processing                     | <input type="checkbox"/> Bit Manipulation                             |
| <input checked="" type="checkbox"/> Logical Statements                  | <input checked="" type="checkbox"/> Machine Language I/O              |
| <input type="checkbox"/> Real-Time Control                              | <input type="checkbox"/> Fixed-Float Conversions                      |
| <input checked="" type="checkbox"/> Data File Management                | <input type="checkbox"/> Explicit Control of Registers and Indicators |
| <input type="checkbox"/> Interrupt Masking and Handling                 | <input type="checkbox"/> Direct Control of Indexing Facilities        |
| <input type="checkbox"/> Common Memory                                  | <input type="checkbox"/> Indirect Addressing                          |
| <input checked="" type="checkbox"/> Message Skeletons                   | <input type="checkbox"/> Double Precision                             |
| <input type="checkbox"/> Vector/Matrix Operations                       | <input type="checkbox"/> Byte Addressing                              |
| <input type="checkbox"/> Algebraic Operations (Boolean, Exponent, etc.) | <input type="checkbox"/> _____  |
| <input type="checkbox"/> Floating Point Operations                      |   |

Observation ID	Microfilm Roll No. Position in Roll		Date	Cloud Cover	Image Center		Sun Ele.	Sun Azi.	Data Quality	
	HRPI	TM			Lat	Long			HARI	TM
1000-00001	00001/0001	00002/0001	08/01/81	70	25.64N	99.35W	53.5	127.1	GGGG	GGGGGGG

Available Product Types

Digital		Film	
HDDT	CCT	B	C
X	X	X	X

Figure 7-14. Sample Catalog Format



## SOFTWARE MODULE SUMMARY

NAME: Management Report

DESCRIPTION: Produces image generation report; produces historic shipping list; produces historic request statistics; produces photographic inventory; produces data quality statistics; provides user profiles; produces status-by-user reports; customer reaction statistics compiled; rework analysis module; LCGS pass request list.

REFERENCES: 3, 4, 6, 7, 8, 13, 19

LIMITATIONS:

PREVIOUS USAGE: Similar function exists at NDPF

FUNCTIONS/ROUTINES CALLED: System Module, Utility and File Maintenance, Input Module

INPUT: Report code number to retrieve desired data

OUTPUT: Desired reports (off-line)

ALGORITHM STRUCTURE: ☒ Straight Line ☐ Iterative  
☐ Mult. Branches ☐ Table Driven

MEMORY SIZE (32 bit words): 180K

Execute Time: 900 (est. maximum)

Execute Rate: 1/day

DESIRED LANGUAGE CHARACTERISTICS:

- |   |   |
|---|---|
| <input checked="" type="checkbox"/> List Processing                     | <input type="checkbox"/> Bit Manipulation                             |
| <input checked="" type="checkbox"/> Logical Statements                  | <input checked="" type="checkbox"/> Machine Language I/O              |
| <input type="checkbox"/> Real-Time Control                              | <input type="checkbox"/> Fixed-Float Conversions                      |
| <input checked="" type="checkbox"/> Data File Management                | <input type="checkbox"/> Explicit Control of Registers and Indicators |
| <input type="checkbox"/> Interrupt Masking and Handling                 | <input type="checkbox"/> Direct Control of Indexing Facilities        |
| <input checked="" type="checkbox"/> Common Memory                       | <input type="checkbox"/> Indirect Addressing                          |
| <input checked="" type="checkbox"/> Message Skeletons                   | <input type="checkbox"/> Double Precision                             |
| <input type="checkbox"/> Vector/Matrix Operations                       | <input type="checkbox"/> Byte Addressing                              |
| <input type="checkbox"/> Algebraic Operations (Boolean, Exponent, etc.) | <input type="checkbox"/> _____  |
| <input type="checkbox"/> Floating Point Operations                      |   |

## SOFTWARE MODULE SUMMARY

NAME: Input Module

DESCRIPTION: General man/machine interface: inputs user address entries, image assessment data, image descriptors, data received entries, data request entries, pass request entries, roll number entries, satellite coverage entries, data shipped entries, standing order entries; terminate work orders entries; remote batch call; delete entries.

REFERENCES: 3, 4, 6, 12, 17, 19

LIMITATIONS:

PREVIOUS USAGE: Similar function exists at NDPF

FUNCTIONS/ROUTINES CALLED: Order staging, order scheduling, etc.  
(see Ref. 19); all major modules defined herein.

INPUT:

OUTPUT:

ALGORITHM STRUCTURE: ☐ Straight Line ☐ Iterative  
                                  ☒ Mult. Branches ☐ Table Driven

MEMORY SIZE (32 bit words): 304K

Execute Time: 2 sec (est. maximum)

Execute Rate: 250/day

DESIRED LANGUAGE CHARACTERISTICS:

- |   |  |
|---|--|
| <input checked="" type="checkbox"/> List Processing                     | <input type="checkbox"/> Bit Manipulation  |
| <input checked="" type="checkbox"/> Logical Statements                  | <input checked="" type="checkbox"/> Machine Language I/O                         |
| <input type="checkbox"/> Real-Time Control                              | <input type="checkbox"/> Fixed-Float Conversions                                 |
| <input checked="" type="checkbox"/> Data File Management                | <input checked="" type="checkbox"/> Explicit Control of Registers and Indicators |
| <input checked="" type="checkbox"/> Interrupt Masking and Handling      | <input checked="" type="checkbox"/> Direct Control of Indexing Facilities        |
| <input checked="" type="checkbox"/> Common Memory                       | <input checked="" type="checkbox"/> Indirect Addressing                          |
| <input checked="" type="checkbox"/> Message Skeletons                   | <input type="checkbox"/> Double Precision  |
| <input type="checkbox"/> Vector/Matrix Operations                       | <input checked="" type="checkbox"/> Byte Addressing                              |
| <input type="checkbox"/> Algebraic Operations (Boolean, Exponent, etc.) | <input type="checkbox"/> _____   |
| <input type="checkbox"/> Floating Point Operations                      |  |

## SOFTWARE MODULE SUMMARY

NAME: EOS Monitor

DESCRIPTION: The collection of system functions which control, monitor, and interface all other modules -- manages the computer resource. Possible Xerox operating system is CP-V.

REFERENCES: 3, 10, 11, 12, 14, 17, 19

LIMITATIONS: CP-V utilizes only CAL-1; certain transferable ERTS  
BTM routines will require modification

PREVIOUS USAGE: New software

FUNCTIONS/ROUTINES CALLED:

INPUT:

OUTPUT:

ALGORITHM STRUCTURE: ☐ Straight Line ☐ Iterative  
☐ Mult. Branches ☒ Table Driven

MEMORY SIZE (32 bit words): 32K

Execute Time: 1/10 sec (est. maximum)

Execute Rate: 20K/day (estimated)

DESIRED LANGUAGE CHARACTERISTICS:

- |  |  |
|--|--|
| <input checked="" type="checkbox"/> List Processing                                | <input checked="" type="checkbox"/> Bit Manipulation   |
| <input checked="" type="checkbox"/> Logical Statements                             | <input checked="" type="checkbox"/> Machine Language I/O   |
| <input checked="" type="checkbox"/> Real-Time Control                              | <input checked="" type="checkbox"/> Fixed-Float Conversions                                      |
| <input checked="" type="checkbox"/> Data File Management                           | <input checked="" type="checkbox"/> Explicit Control of Registers and Indicators                 |
| <input checked="" type="checkbox"/> Interrupt Masking and Handling                 | <input checked="" type="checkbox"/> Direct Control of Indexing Facilities                        |
| <input checked="" type="checkbox"/> Common Memory                                  | <input checked="" type="checkbox"/> Indirect Addressing  |
| <input checked="" type="checkbox"/> Message Skeletons                              | <input checked="" type="checkbox"/> Double Precision   |
| <input type="checkbox"/> Vector/Matrix Operations                                  | <input checked="" type="checkbox"/> Byte Addressing  |
| <input checked="" type="checkbox"/> Algebraic Operations (Boolean, Exponent, etc.) | <input checked="" type="checkbox"/> <u>Scheduling, Queue Management, Memory Management, etc.</u> |
| <input type="checkbox"/> Floating Point Operations                                 |  |

## REFERENCES

1. NASA/GSFC RFP No. 5-66203-202, "Earth Observatory Satellite System Definition Study," 17 January 1974
2. NASA/GSFC Document EOS-410-07, "The Earth Observatory Satellite (EOS), A System Concept," 4 September 1974
3. Department of Interior Pre-RFP Document, "Computer System at EROS Data Center," 13 February 1974
4. IBM Report EOS-L-68, "EOS Attitude Control/Ground System Study," IBM Federal Systems Division, 26 September 1973
5. NASA/GSFC Document 71SD4249, "Data Users Handbook, Earth Resources Technology Satellite."
6. TRW Document, "GIM (Generalized Information Management) System Summary"
7. TRW Document 4811.50-126, "Functional Description of the Glendale Police Department Real-Time Data Capture Subsystem," 16 June 1972
8. General Research Corp. Document WGRC 73-3273, "Image Data Processing System Requirements Study, Vol. 1, Analysis," T. Honikman, et. al., October 1973
9. General Electric Document 71SD5216, "Earth Resources Technology Satellite, Image Annotation Processing (IAP) Software Description," 1 October 1971
10. IBM Document, CD No. 16-955-2168, "Critical Design Review, CONUS Ground Station Software," January 1972
11. TRW Proposal 17563.000, "Proposal for Real Time Operations, Dispatch, and Scheduling (RODS) System," December 1970
12. General Electric Document, "Milestone 2 ERTS Data Processing System Description and Process Flow," 12 August 1971
13. NASA Document, "NASA Support Plan, Earth Resources Technology Satellite A and B," revised, 1 March 1974
14. TRW Report 18718.000, "Data Management System Control Study," February 1972
15. TRW Proposal No. 22296.000, "Earth Observatory Satellite System Definition Study (EOS), Part 2," 18 February 1974
16. TRW IOC EOS-52, "Mission Model (EOS, SEOS, SEASAT, SMM, 5-Band MSS)", P. E. Romo, 20 May 1974

17. Xerox Corporation, "Xerox Control Program - Five (CP-V), System Management Reference Manual," 90-16-74F, March 1964
18. Xerox Corporation, "Xerox Data Management System (DMS) Reference Manual," 90-17-38B, March 1973
19. Unpublished notes, "Preliminary Examination of EOS CDPF Software Functions (Excluding Image Processing)," D. McKinnon, April 1974
20. GE CDRL document No. 212, "Earth Resources Technology Satellite Ground System Equipment and Software Summary," 29 September 1971.

## 7.9 IMAGE PROCESSING ALGORITHMS

Ultimate performance and throughput of the EOS system is determined by the effectiveness of the image correction subsystem. Absolute error control is neither possible nor cost-effective, with radiometric and geometric errors inherent in the sensor data. In addition, error magnitudes are imperfectly known, and sensor design constraints dictate sampling strategies and formats incompatible with user requirements. Effectiveness of the image correction subsystem depends upon usage of sufficiently sophisticated algorithms that performance of the sensor is not degraded and of sufficiently clever hardware realizations that the extreme data rates of EOS can be handled within reasonable work schedules and cost constraints. This report reviews data quality, format, and throughput requirements; discusses the required (and preferred) algorithms for reformatting, error calculation and correction; presents an operational correction procedure; and presents a hardware realization of the algorithms capable of exceeding the throughput needs at high accuracy.

### 7.9.1 Image Data Quality Requirements

The end data product of the EOS system is a sampled estimate of the irradiance profile of the earth surface in several spectral bands, suitable for recognition and measurement of terrain makeup and comparison of this makeup with itself over periods of time. The quality of the EOS end-product is a measure of its utility to these functions and is theoretically limited only by the characteristics of the sensor. Quality can be subdivided into six generic classes:

- 1) Resolution or system gain at high-spatial frequencies relative to system gain at lower frequencies
- 2) Internal geometric accuracy or uniformity (linearity) of scale within each image
- 3) Geodetic control or absolute location accuracy of each terrain feature

- 4) Photometric accuracy or absolute intensity measurement accuracy at each terrain sample and relative intensity accuracies between spectral bands
- 5) Signal-to-noise ratio or effects of intensity errors uncorrelated from terrain sample to terrain sample including quantization errors
- 6) Timeliness or delay between receipt of terrain samples and availability of the end-product to the user.

In each of these areas, all-digital handling of the sensor data is imperative. Analog techniques, i. e., those employing intermediate film copy or other hard copy image generation, introduce intolerable quality degradation in all respects. Use of sufficiently high-order image processing algorithms can retain the resolution capability of the sampled sensor or even enhance it; in some sense, at the expense of signal-to-noise ratio. Precision attitude control to within arc-seconds can give internal geometric consistency within fractions of a picture element with minimal image processing. In this case, processing need only correct for calibratable sensor distortions, earth curvature, and spacecraft altitude above the terrain. Alternatively, attitude control to better than 0.1 degree with attitude determination to within arc-seconds can, with appropriate digital ground processing, give comparable results at a slight cost in throughput and internal correction processor buffer storage. Lower altitude determination accuracy requires use of ground control point locations to preserve internal consistency.

Given an internally-consistent image, geodetic control can be obtained to within a fraction of a picture element via use of an adequate number of ground control points. The number of ground control points required depends on tracking accuracy and the attitude estimate stability. For purpose of change discrimination and cartography, it is desirable that the terrain radiance profile be sampled on a uniform, predetermined, repeatable grid. Given sufficient internal consistency and geodetic control, the radiance samples from the sensor can be used to construct an estimate of the original continuous radiance profile, which can then be resampled at the desired locations. The accuracy of this process affects geometric accuracy, resolution, and photometric accuracy of the end-product.

Photometric accuracy also includes calibration of the sensor detectors. Calibration source accuracy and sensor linearity affect the accuracy, and sensor linearity and the number of individual detectors in the sensor impact processing speed. Signal-to-noise ratio of the data communications link and bulk storage devices determine bit error rates, which can be considered as image noise. Sensor and calibration quantization and digital processing errors contribute image noise that can be minimized via proper tradeoffs with processing time.

Each of these criteria of data quality is in reality affected by several other facets of the data handling system. In the case of resolution, the basic resolution of the sensor can be degraded by insufficient sampling rate or low-order image correction algorithms in the ground data handling system. Internal geometric accuracy is affected by the spacecraft attitude control and residual errors in the ground processing due to inadequate attitude estimation accuracy, lack of sensor calibration data, or to low-order correction algorithms. Geodetic control is affected by spacecraft ephemeris and sensor boresighting errors uncorrected by the ground processing. Photometric accuracy depends on sensor calibration sources, atmospheric degradation of the reflected intensities, and accuracy of the ground processing. Signal-to-noise ratio is measured by the statistics of errors in photometric intensity, which are uncorrelated from pixel-to-pixel, including data communications subsystem performance, quantization errors, and ground processing errors due to sample aliasing. Timeliness is affected primarily by the ground processing.

In summary, the important error sources contributing to internal consistency errors include:

- Spacecraft altitude above the terrain
- Mapper nonlinearities
- Pointing imager viewing aspect
- Earth curvature and rotation
- Mapper scan line count and detector commutation delays
- Attitude rates, if any, during imaging
- Ephemeris error rates



- Rotation to desired map projection
- Commutation skew.

Geodetic control error sources include:

- Ephemeris errors
- Framing errors
- Residual ACS bias errors
- Spectral misalignment, if any
- Sensor boresighting errors and pointing
- Ground control point location errors.

Photometric, noise, and resolution error sources include:

- Sensor dwell time variations
- Quantization
- Calibration accuracy
- Atmospheric attenuation and reflectance
- Sampling aperture and smear
- Optics resolution
- Downlink bit errors
- Bulk bit errors
- Aliasing due to insufficient sampling rate.

A seventh measure of EOS end product utility is the output data format. The EOS sensors scan multiple lines simultaneously in several bands due to physical limitations on detector dwell time. However, output photographic products require line-sequential pixel-ordered data in band-separated format for usage of high-speed film recorders. Simultaneously, spectral classification users require line-sequential pixel-ordered data in band-interleaved format to allow loading of all bands of a given pixel location with tractable memory buffer requirements and throughput. The reformatting process, especially converting line parallel or pixel-scrambled data to line-sequential, pixel-ordered data and converting

between band-separated and band-interleaved data formats, requires substantial-size high-speed memory buffers, and as such represents the primary throughput bottleneck in the form of rotating memory devices. Conversion from conical scan formats to linear scan is a particularly difficult problem at high rates within realistic core memories and is discussed further in Section 7.6.

The user community of EOS data can be exemplified by Table 1. Spectral classification users require maximum relative radiometric accuracy between bands with moderate to low geometric and geodetic accuracy requirements. Change detection users require extremely precise relative geometric accuracy between successive spacecraft passes over the same area, together with high resolution, although relatively unrelated to geodetic accuracy. Registration errors exceeding  $1/4$  pixel can be shown empirically to significantly degrade change detection performance. Cartographic users require high geodetic accuracy, but not to the relative accuracy requirements of the registration users. All users require resolution compatible with the capability of the sensors. Photographic output products are significantly less sensitive to residual image errors than computer-compatible tape products, since digital techniques are capable of extracting image information content which is not readily apparent in visual inspection of film complement.

Output products from the CDPF should perform corrections common to all users, with special processing of digital products such as spectral classification or MTF compensation, left to the individual users. Thus, radiometric calibration and geometric corrections are performed by the CDPF. Multiple passes through successive correction algorithms results in greater residual error than a single-pass through a composite algorithm. Consequently, since geometric correction for at least scan nonlinearities, sensor commutation skew, and earth rotation skew are necessary for geodetic users and more precise corrections are required for temporal registration users, all data is corrected to the accuracy required by the latter.

#### 7.9.2 Geometric Correction and Temporal Registration

Both geometric (geodetic) correction and temporal registration can be discussed in three steps: 1) distortion estimation, 2) distortion

Table 7-7. User Data Quality Requirements

EOS - A THEMATIC MAPPER AND HRM DATA USER OUTPUT PRODUCT REQUIREMENTS

END USE OF DATA PRODUCT	RESOLUTION REQUIREMENT	GEOMETRIC PRECISION	GEODETIC CONTROL	SPECTRAL REGISTRATION	RADIOMETRIC FIDELITY	PRINCIPAL OUTPUT MEDIA	SPECIAL PROCESSING	TAPE (2) FORMAT
SPECTRAL SIGNATURE CLASSIFICATION	MODERATE-HIGH (10 - 30 M)	LOW	LOW	HIGH (~0.1 PIXEL)	HIGH	FILM/DIGITAL TAPE		BAND INTERLEAVED
CHANGE DETECTION	MODERATE-HIGH (10 TO 30 M)	VERY HIGH (~1/4 PIXEL)	MODERATE-LOW	LOW	MODERATE	FILM/DIGITAL TAPE	INTENSITY NORMALIZATION/REGISTRATION	BAND SEPARATED
MAPPING	MODERATE-HIGH (1 TO 2 PIXELS)	HIGH NATIONAL MAP (1) ACCURACY STANDARDS	HIGH NATIONAL MAP (1) ACCURACY STANDARDS	LOW	LOW	FILM	GCP'S	BAND SEPARATED
MENSURATION	MODERATE-HIGH (1 TO 2 PIXELS)	HIGH (~1 PIXEL)	MODERATE-LOW	LOW	LOW	FILM/DIGITAL TAPE		BAND SEPARATED
TERRAIN PATTERNS	MODERATE-HIGH	MODERATE-LOW	MODERATE-LOW	LOW	MODERATE	FILM		BAND SEPARATED

(1) DEPENDS ON SCALE

(2) SOME USERS MAY REQUEST BAND INTERLEAVED OR SEPARATED TAPE FORMATS INDEPENDENT OF END USE OF PRODUCT

modelling, and 3) distortion removal. For geometric or geodetic correction, the distortion function is measured relative to some map projection such as Universal Transverse Mercator (UTM) or Space Oblique Mercator (SOM). For temporal registration, the distortion function is measured relative to a reference image from a previous spacecraft pass over the same scene.

#### 7.9.2.1 Distortion Estimation

Sources contributing to image distortion are discussed above. Relative magnitudes of error contributions are discussed in Section 5.2.5. Geometric correction can be performed without reference to scene content with accuracies required for temporal registration except for the combined effects of residual ACS errors, sensor alignment errors, and ephemeris measurement errors. The remaining sources are adequately calibrated and/or measured. To satisfy registration and geodetic accuracy requirements features from the scene itself, called control points (CP), must be located and compared with their expected locations, thus giving measurements of scene distortion at several discrete points within the scene. These measurements are then incorporated with a priori calibration and other measurement data in a recursive estimator to solve for the best (minimum mean-squared error, unbiased) estimate of the combined effects of attitude angles and rates and ephemeris measurement errors. The complete process by which CP libraries are built up is discussed in Section 7.9.4.

The recursive filter can be summarized as

$$\hat{x}_{k+1} = \Phi_k \hat{x}_k + A_{k+1} (y_{k+1} - \hat{y}_{k+1})$$

where  $\hat{x}_k$  is an estimate based on  $k$  control points of the error sources  $x$  contributing to the image distortion (i.e., the composite effects of unknown alignments, rates, and others),  $y_k$  is the distortion measurement at CP number  $k$ ,  $\hat{y}_{k+1}$  is the optimal estimate of the distortion at CP number  $k+1$  based on the first  $k$  CP's, and  $A_{k+1}$  is the optimal gain matrix defined recursively by

$$S_{k+1} = \Phi_{k+1} P_k \Phi_{k+1}^T + Q_{k+1}$$

$$A_{k+1} = S_{k+1} M_{k+1}^T \left[ M_{k+1} S_{k+1} M_{k+1}^T + R_{k+1} \right]^{-1}$$

$$P_{k+1} = \left[ I - A_{k+1} M_{k+1} \right] S_{k+1}$$

Here,  $M_{k+1}$  is the distortion measurement sensitivity to the error source vector  $\underline{x}$ ,  $R_{k+1}$  is the covariance of statistical errors in error source propagation over time, and  $Q_{k+1}$  is the covariance of the CP point measurement uncertainty.  $P_{k+1}$  is the estimate  $\hat{\underline{x}}_{k+1}$  uncertainty covariance and  $\Phi_{k+1}$  is the state transition matrix defining the dynamic behavior of the error sources. The quantity  $\underline{y}_{k+1} - \hat{\underline{y}}_{k+1} = \underline{y}_{k+1} - M_{k+1} \hat{\underline{x}}_k$  is the measurement residual prior to incorporation of the measurement into the distortion source estimate. The covariance of the residual,  $M_{k+1} S_{k+1} M_{k+1}^T + R_{k+1}$ , can be used to edit out obviously bad CP location measurements via reasonableness checks.

Only the composite effect of the various geometric error sources is of importance to the distortion estimation process, thus a fairly low-order state vector will suffice for the EOS estimator. Computer time requirements for a 10-element state and up to 5 CP's per scene is less than 20 msec/scene. Core requirements are minimal, less than 3000 words.

The primary advantages of the recursive distortion estimation procedure include invariance of the algorithm with differing numbers of CP's, incorporation of all other distortion measurement data (a priori data) with the CP locations in the estimate, the residual edit capability, and the intermediate distortion estimates which reduce the problem of finding later CP's to negligible proportions (1 to 2 pixel a priori uncertainty). The details of the estimator are discussed in Section 5.2.5.

### 7.9.2.2 Distortion Modelling

As a result of CP measurements, the magnitude of distortion due to residual alignment, attitude, and ephemeris errors can be reduced to the order of the knowledge of CP locations with a small number of CP's per pass (reference Section 5.2.5). Thus, the precise location of every pixel could be calculated from this data via calculation of the line-of-sight of the appropriate detector cell at the appropriate scan angle and its intercept with the desired map projection of the earth's surface. However, this would be an extremely time consuming operation. A much faster approach to the calculation of the image warp at each pixel involves calculation of the precise warp on a matrix of  $N \times M$  points within the image, called pseudo-reseau points. The warp at all other pixels is then determined by bilinear interpolation of the surrounding pseudo-reseau points. Degradation in geometric accuracy is determined by the spacing of the pseudo-reseau points. For ERTS-A images, an array of 81 points ( $9 \times 9$ ) is sufficient to ensure a worst-case modelling error of  $1/3$  pixel throughout the scene when using the bilinear model. The number of pseudo-reseau points can be increased by an order of magnitude with negligible impact on processing time.

The distortion at each pixel can then be calculated recursively using only one addition per pixel, after the appropriate initialization.

$$u(x, y) = x + \delta x(x, y)$$

$$v(x, y) = y + \delta y(x, y)$$

$$\delta x(x + 1, y) = \delta x(x, y) + c_0(y)$$

$$\delta y(x + 1, y) = \delta y(x, y) + c_1(y)$$

where  $u, v$  are the input (distorted) image coordinates corresponding to the precision reference coordinate  $x, y$ , and  $\delta x, \delta y$  are the distortions in the  $x$  and  $y$  axes at the same location. The initial conditions are

$$\delta x(0, y) = d_0(y)$$

$$\delta y(0, y) = d_1(y)$$

The  $c_0$ ,  $c_1$ ,  $d_0$ , and  $d_1$  are constant for a given line ( $y$ ) and related to the bilinear interpolation coefficients for the corresponding piecewise bilinear block by

$$d_0(y+1) = d_0(y) + a_2, \quad d_0(0) = a_0$$

$$d_1(y+1) = d_1(y) + b_2, \quad d_1(0) = b_0$$

$$c_0(y+1) = c_0(y) + a_3, \quad c_0(0) = a_1$$

$$c_1(y+1) = c_1(y) + b_3, \quad c_1(0) = b_1$$

where  $a_i$ ,  $b_i$  are the interpolation coefficients defined by

$$\delta x(x, y) = a_0 + a_1x + a_2y + a_3xy$$

$$\delta y(x, y) = b_0 + b_1x + b_2y + b_3xy$$

The  $a_i$ ,  $b_i$  are calculated from the distortion at the four surrounding pseudo-reseau points by substitution in the above equation and solution of the resulting eight simultaneous equations. Thus, at each position  $x$  along a scan line  $y$  in the precision reference coordinate system, the corresponding location  $u$ ,  $v$  in the distorted input image coordinate system can be calculated by a simple addition to the  $u$ ,  $v$  for the previous position. The actual calculation of the distortions  $\delta x$ ,  $\delta y$  is done in the image correction processor using the  $a_i$ ,  $b_i$  coefficients.

By referencing position  $x$ ,  $y$  within a given piecewise-bilinear block with respect to the upper left corner (first pixel, first line) of the block, the distortion coefficients are solved for by:

$$a_0 = \delta x(0, 0)$$

$$a_1 = [\delta x(x_m, 0) - a_0]/x_m$$

$$a_2 = [\delta x(0, y_m) - a_0]/y_m$$

$$a_3 = [\delta x(x_m, y_m) - a_0 - a_1 x_m - a_2 y_m]/(x_m y_m)$$

where  $x_m$ ,  $y_m$  are the last pixel and line in the block. A similar set of equations exists for the  $b_i$ 's in terms of  $\delta y$ . The  $\delta x(a, b)$  are the distortions at the pseudo-reseau points at  $a, b$ .

To avoid discontinuities in the corrected image geometry at the boundaries between adjacent piecewise-bilinear interpolation blocks, it is necessary that the pseudo-reseau points be taken on a regular grid in the output precision  $x, y$  coordinate system, i. e., arrayed along constant  $x$  and constant  $y$  lines. The distortion estimate from the recursive estimator allows direct calculation of pseudo-reseau point distortions on a regular grid in the input distorted  $u, v$  coordinate system. These latter distortions are used to initialize an iterative process that converges to the distortion values on the desired (rectified) output precision regular pseudo-reseau grid.

In practice, the distortion correction process first corrects for distortion along constant input lines, resulting in an intermediate coordinate system whose columns (constant- $y$  direction) coincide with the desired output precision reference coordinate system. Then the intermediate system is corrected for distortion across scan resulting in the precision reference coordinate system. This two-pass correction process can produce identical geometric corrections to those achievable by a single-pass (two dimensions at once) process. However, the two-pass approach is substantially faster, more flexible, and allows correction of individual sensor scan lines for commutation-time-difference skew (time delay between sampling of detectors or position stagger between detectors) and for sensor-scan-related distortions such as mirror scan nonlinearity.



The distortion coefficient calculation process, including pseudo-reseau grid calculation and rectification, is approximately 10 sec per scene, depending on the convergence criterion used in the rectification. This process thus accounts for a major portion of the half-hour estimated for the entire distortion estimation process.

An important alternative to the above distortion modelling procedure is to characterize the distortion as a high-order two-dimensional global polynomial, e.g., fifth-order:

$$\delta x(x, y) = \sum_{j=0}^N \sum_{k=0}^{N-j} a_{jk} x^k y^j$$

with a similar equation for  $\delta y(x, y)$ , and  $N$  is the order of the polynomial. The disadvantages of this approach include: modelling errors in excess of registration accuracy requirements for tractable size  $N$ ; limited applicability of a set of coefficients to more than one scene and the corresponding susceptibility to partial cloud cover; a greatly increased requirement for number of control points; difficulty in incorporating auxiliary data such as attitude measurements, alignments, and geometric calibration data; and potential discontinuities at the boundaries between successive scenes.

#### 7.9.2.3 Radiometric Calibration

Measurements of detector and amplifier response (gain) at several points on the response curve are transmitted to the ground station for each detector using the mirror scan retrace time on the downlink. The most flexible method of radiometric correction is table lookup, using the uncalibrated pixel value as the table address and the corresponding calibrated value as the table entry. A different table is required for each detector making this approach difficult for the HRPI sensor with its 19,000 detectors, but tractable for the TM and its 100 detectors. The table entries can trace any desired nonlinear correction curve, including de-log-compression, and is consequently the preferred approach for the TM. The table entries are calculated by curve-fitting the transmitted calibration points.

For the HRPI, point-slope (linear) calibration is performed by multiplying the pixel intensity by an appropriate gain and adding a constant. The gain and constant are determined from least-squares fit of the transmitted calibration points. The table is updated only once per spacecraft pass due to the stability of the HRPI detectors and the time required to store the correction coefficients.

The radiometric correction of each pixel is performed by special-purpose hardware in the image correction processor. Radiometric correction is performed prior to geometric correction since the correction coefficients are detector-specific. Table generation for the TM is performed twice per pass for each detector and requires less than 0.5 second per update for all detectors. HRPI correction coefficient generation requires 10 sec per pass. The actual correction time is included in the time required for geometric correction.

#### 7.9.2.4 Distortion Correction

The distortion model derived above allows removal of the calculated geometric distortion by determining, at each sample point in the precision reference coordinate system, the location of the corresponding point in the distorted input coordinate system. Thus, the intensity at each sample point in the precision reference grid can be calculated as a function of the sample intensities in the distorted coordinate grid received from the sensor. In general, the distorted grid location corresponding to the desired precision reference location will seldom coincide with any of the locations of the sensor samples. Thus, the problem of geometric distortion removal becomes the problem of determining what intensity the sensor would have seen had it happened to be sampling with the appropriate sampler phase and scan line orientation to have sampled at the desired location.

If the sensor were to be sampled at an infinite rate with infinitely-closely-spaced lines, a two-dimensional continuous intensity surface corresponding to the continuous reflectance of the earth's surface would be generated. This measured intensity surface would include the spatial-frequency-limiting effects of the sensor optics and field stop and the amplifier filters.

$$g(\underline{x}(t)) = \int_0^\infty h(\tau) [\psi(\underline{x}(t - \tau)) + n(t - \tau)] d\tau$$

$$\psi(\underline{x}) = \int_{\underline{X}} \gamma(\underline{z}) f(\underline{x} - \underline{z}) d\mathbf{z}$$

where  $g(\underline{x}(t))$  is the detector amplifier output at scan position  $\underline{x}(t)$  (a two-dimensional vector: along- and across-scan components) at time  $t$ ,  $h(t)$  is the amplifier impulse response,  $n(t)$  is the amplifier noise process,  $\gamma(\underline{x})$  is the sensor aperture function (composite of optics, field stop, and detector size), and  $f(\underline{x})$  is the scene intensity at position  $\underline{x}$ . The spectrum of the amplifier output is thus

$$S_g(\underline{\omega}) = \left| H(j\underline{\omega}^T \underline{l}_v) \right|^2 \left\{ \left| \Gamma(j\underline{\omega}) \right|^2 S_f(\underline{\omega}) + \sigma_n^2 \right\}$$

where  $\underline{\omega}$  is the two-dimensional spatial frequency,  $v$  is the scan velocity,  $\underline{l}$  is a unit vector along the scan direction,  $H$  is the Fourier transform of  $h$ ,  $\Gamma$  is the transform of  $\gamma$ ,  $\sigma_n^2$  is the amplifier noise variance, and  $S_f(\underline{\omega})$  is the input scene spectrum.

Typical forms of  $\Gamma$  and  $H$  (square apertures and integrate-dump or Butterworth filters) providesubstantial high-frequency smoothing, which, when combined with the spectral content of the original scene, guarantees a considerable degree of smoothness to the two-dimensional continuous intensity surface. It is precisely this fact which allows determination of the proper sampling rate such that minimal (or at least reasonable) aliasing occurs, yet reasonable data rates are incurred. The impact of sensor sampling rate is discussed further in Section 5.2.5.

If the continuous intensity surface is now sampled at a rate exceeding twice the highest spatial frequency in the intensity surface, the entire surface

can theoretically be reconstructed from the samples. Shannon's sampling theorem extended to two dimensions guarantees that the intensity at any point in the continuous surface can be calculated precisely by weighting the sample values by the appropriate function of their distances from the desired location and adding them together, i. e.,

$$g(\underline{x}) = \sum_{\underline{u}_k} g(\underline{u}_k) R(\underline{x} - \underline{u}_k)$$

where  $R(\underline{x})$  is the interpolation kernel shown in Figure 7-25a (two-dimensional sinc, or  $\sin(x)/2$ , function). Thus, the continuous surface samples obtained with any given sampler phasing can be calculated from the samples obtained from a different sampler phasing. I. e., the intensity value the sensor would have seen had it sampled at the desired location can be calculated from the actual received samples. This is called the "resampling" or "image-reconstruction" process. The problem of change detection becomes a comparison of samples of the continuous surface at different times with independent sampler phases, requiring resampling of at least one of the two scenes (sample sets). Geometric correction involves resampling at locations on a selected map reference system grid.

The difficulty with the above approach to calculating the appropriate intensity at each precision reference grid point is that each of these points is a function of a very large number of input samples (the significance of the interpolation kernel decreases as  $\frac{1}{(2k+1)\pi}$  where  $k$  is the number of picture elements of separation. Significant contributions are obtained from pixels over 30 pixels away from the desired location. Thus, each output point is a function of over 1000 input points, presenting considerable difficulty with high-speed implementation. Some compromise is indicated in performance to achieve realistic throughput rates. The compromise is further justified by original scene spatial frequency content in excess of half the sample rate, resulting in aliasing noise, and amplifier and quantization noise, all of which limit reconstruction accuracy.

The fastest and least accurate method of image resampling is to find the nearest sensor sample location to the desired precision reference location and use its intensity as the desired precision sample value. This

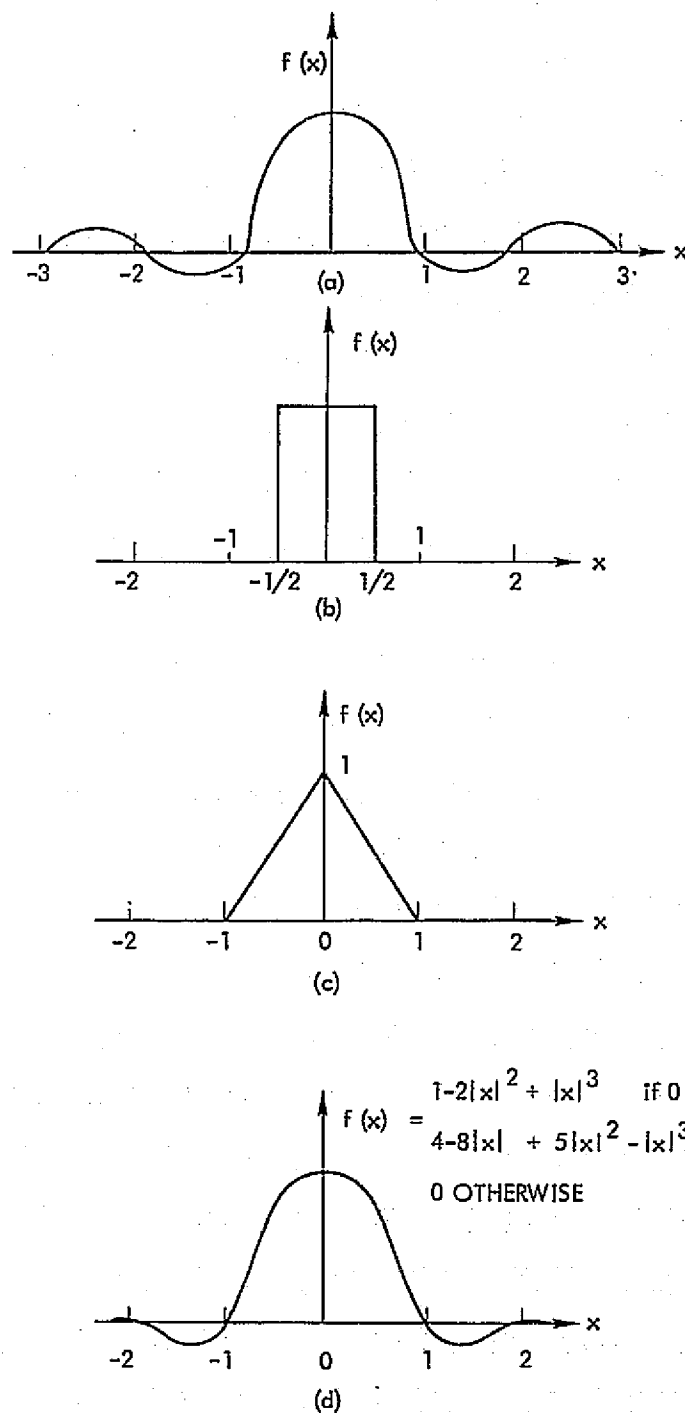


Figure 7-25. Three Interpolation Kernels

The three kernels correspond to a) six x/x interpolation, b) nearest neighbor interpolation, c) bilinear interpolation, and d) TRW's Cubic Convolution Process.

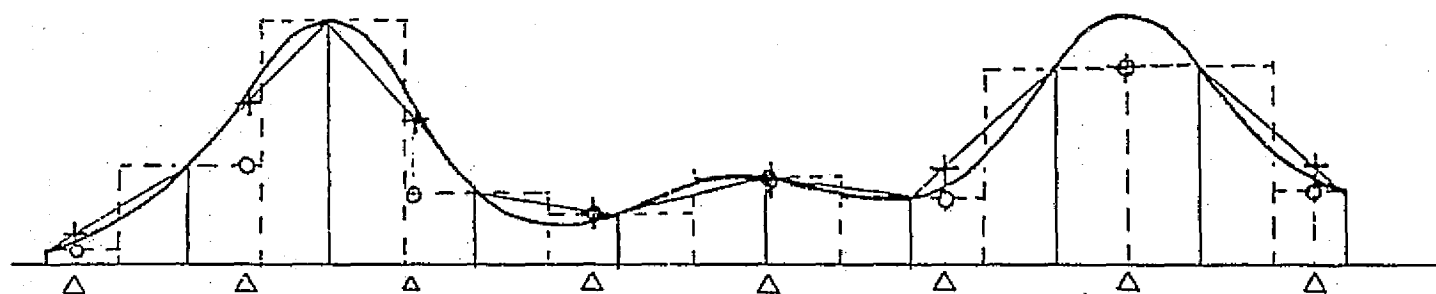
is called nearest-neighbor (NN) resampling and requires loading only one input sample per output sample and no interpolation operations. The NN resampling can further be implemented by shifting whole blocks of pixels at once from the input to the output scene for distortion functions with only slight scale changes, hence the alternative name block-shift. The effective interpolation kernel for NN resampling is:

$$R(x, y) = 1, \quad |x| < \frac{1}{2} \quad \text{and} \quad |y| < \frac{1}{2}$$

$$= 0, \quad \text{elsewhere}$$

The disadvantages of NN resampling are not immediately apparent upon visual inspection of a photo copy of a corrected scene. Indeed, almost all the exact sample intensities in the distorted scene are present in the corrected scene, albeit each with a position error of up to 1/2 pixel in the x, y directions caused by the NN process. These  $< \frac{1}{2}$  pixel position errors are not easily visible in photo copy because they are highly correlated from pixel-to-pixel. They grow (or decrease) linearly with scan position until they would exceed  $\pm \frac{1}{2}$ , when an input pixel is skipped (or replicated) in the output image. The missing or replicated pixels are not apparent unless they coincide with lineal structure in the scene. However, a major portion of the EOS system utility lies in the all-digital handling of the data as opposed to film product dependence. In performing temporal registration, the  $< \frac{1}{2}$  pixel NN errors are uncorrelated between the reference scene and the registered (comparison) scene, resulting in relative position errors of up to one pixel in each direction. These relative position errors can significantly degrade change detection performance resulting in change detected images with broad error bands running through them.

The operation of NN resampling can be further demonstrated by Figure 7-26. The vertical axis of the curve represents intensity and the horizontal axis the along- (or across-) scan position. The smooth heavy curve represents the sensor-degraded image, i. e.; what the sensor would see if it had an infinite-sampling rate. Solid vertical lines are samples the sensor would detect with one particular sampler phase. The curve is



- $\Delta$  - OUTPUT SAMPLE TIMES
- $\circ$  - NEAREST NEIGHBOR SAMPLES
- $+$  - BILINEAR INTERPOLATION SAMPLES

Figure 7-26. Nearest Neighbor and Bilinear Interpolation in One Dimension

guaranteed a degree of smoothness with respect to the sample spacing by the above discussion of spatial frequency content and by the astuteness of the sensor designers in selecting the sensor sampling rate above the Nyquist rate. The locations designated by triangles represent either output locations on the desired map grid or sample locations taken on a later spacecraft pass. NN reconstruction of the image at the output locations results in the intensity samples marked with 0's, i.e., in each case, the intensity value of the nearest input sample. It can be seen that NN reconstruction is equivalent to estimating the original continuous curve with a staircase waveform (dotted lines) going through the input (received) samples. For this example, the third input sample from the left is completely ignored. The position errors of up to 1/2 pixel are apparent.

A considerably more accurate, though more time-consuming, approach to resampling is bilinear interpolation (BI) of the four input (distorted grid) sample intensities surrounding the desired location. The corresponding interpolation function is

$$R(x, y) = (1 - |x|) \cdot (1 - |y|) \quad \text{for } |x|, |y| < 1$$

$$= 0, \quad \text{elsewhere}$$

shown in Figure 7-25c for one dimension. In Figure 7-26, this corresponds to straight-line interpolation of the input samples for the desired location intensities, resulting in those values marked by "+". Considerably greater intensity accuracy is achieved and the discontinuities in NN caused by pixel skipping and replication do not occur for BI. However, BI resampling causes noticeable resolution degradation in the reconstructed (corrected) image. The mechanism of this degradation can be demonstrated at the second output point from the right in the curve of Figure 7-26, where a peak in the continuous curve is truncated by linear interpolation of samples which straddle the peak. The cost of BI in terms of processing time is substantial in software mechanizations since every output pixel is a function of four input samples (and the relative sample phase).

A much more accurate image reconstruction scheme is TRW's cubic convolution (CC) process. Each output pixel intensity is calculated from



16 surrounding input pixel intensities. The corresponding interpolation kernel is

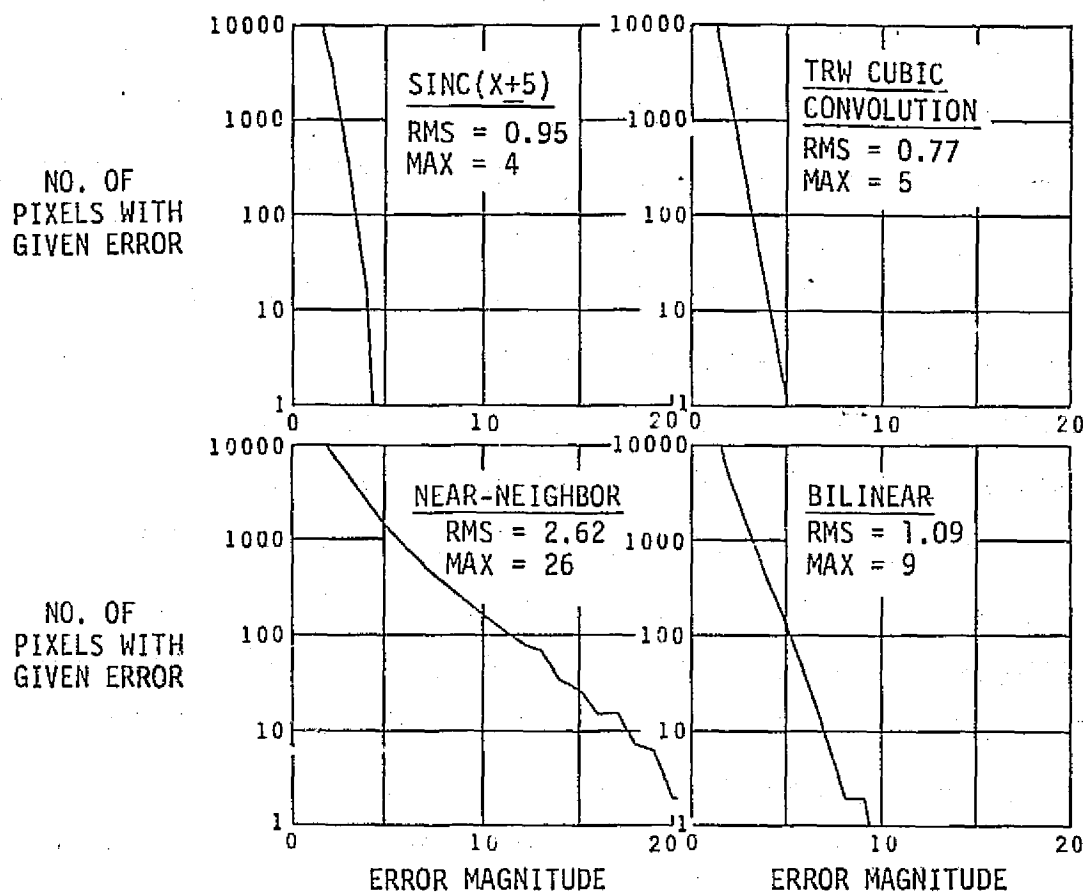
$$R(x, y) = f(x)f(y)$$

where

$$\begin{aligned} f(x) &= 1 - 2|x|^2 + |x|^3, & 0 \leq |x| \leq 1 \\ &= 4 - 8|x| + 5|x|^2 - |x|^3, & 1 \leq |x| \leq 2 \\ &= 0 & \text{otherwise} \end{aligned}$$

shown in Figure 7-25d for one dimension. The CC interpolation kernel is continuous in both value and slope and represents a closer approximation to the sinc function kernel. The interpolation curve generated by this process follows the intensity curve of Figure 7-26 within a few percent

It should be noted that, in regions of approximately constant intensity (fields, water, etc.), all three interpolation processes will give the same answer. It is only at regions of intensity change (spatial information content) that NN and BI processes commit their errors. A comparison of the precision of CC with other reconstruction schemes is shown in Figure 7-27. An image segment from band 5 of the ERTS MSS was selected and resampled 1/2 pixel shifted in the along-scan direction by a 900-point sinc function interpolator, i. e., each resampled point was calculated from 900 surrounding original samples. This same process was performed by NN (1 point), BI (4 points), CC (16 points), and a 100-point truncated sine function. The results were differenced with the 900-point algorithm result and histograms of the differences were plotted. The image segment contained 49,600 pixels. NN gives a very large number of high-intensity differences with a maximum error of 26 (out of 0 to 63 range) for this example. The NN difference image looks like the spatial derivative of the original image, with significant errors at high-spatial frequencies. BI has substantially lower maximum and RMS error with all errors occurring at locations with high spatial-frequency content (roads and field boundaries). The CC process, however, gives the lowest RMS error of all four



(INTENSITY RANGE IS 0 - 63)

Figure 7-27. Resampling Errors

approximations, including the significantly more complex 100-point truncated sinc function. The truncated sinc function difference image contains echoes of high-intensity lineal structure (roads) at  $\pm 5$  pixels on either side of the feature location. These echoes are non-existent in the CC image. These error statistics are indicative of the change detection errors that would occur if the scene did not change between successive spacecraft passes and all other error sources were exactly the same on both passes with the exception of a 30-m lateral shift in orbital ground track.

Registered ERTS scenes of Baltimore (1062-15190-5 and 1080-15192-5) using TRW cubic convolution and NN geometric distortion removal are shown in Figures 7-28 and -29. The residual clutter errors inherent in the NN process are apparent.

Spatial frequency analyses, based upon the power density spectra for processed ERTS data, have also been performed. Figure 7-30 was chosen as a typical image detail (scene 1062-15190-5), 100 lines  $\times$  128 pixels in the corrected image. This detail shows the intersection of I83 (Jones Falls Expressway) and I695 (Baltimore Beltway), and is reproduced from line printer output.\* Using a fast Fourier transform algorithm, line power density spectra were obtained for the detail and then averaged (spectral component by spectral component) over all 100 lines. This was done in turn for nearest-neighbor, bilinear, and TRW's cubic convolution process. To eliminate leakage, due to a large DC component, the mean was removed, padding zeros were added to the data, and a hamming window (cosine taper at the image edges) was employed.

The results are plotted as a function of  $\omega$  (rad/meter) in Figure 7-31. The low frequency contents of three resampled images are very nearly the same. However, that corresponding to the TRW cubic convolution process contains more high frequency components than bilinear resampled images. This is an expected result due to the smoothing nature of bilinear interpolation. The nearest-neighbor processed image is not greatly different from the TRW cubic convolution (bear in mind, the small relative power at the highest spatial frequencies).

---

\*A dot matrix three dots on a side permits use of 10 gray levels for each pixel.



Figure 7-28. TRW Cubic Convolution Processed Image Detail



Figure 7-29. Nearest Neighbor Processed Image Detail

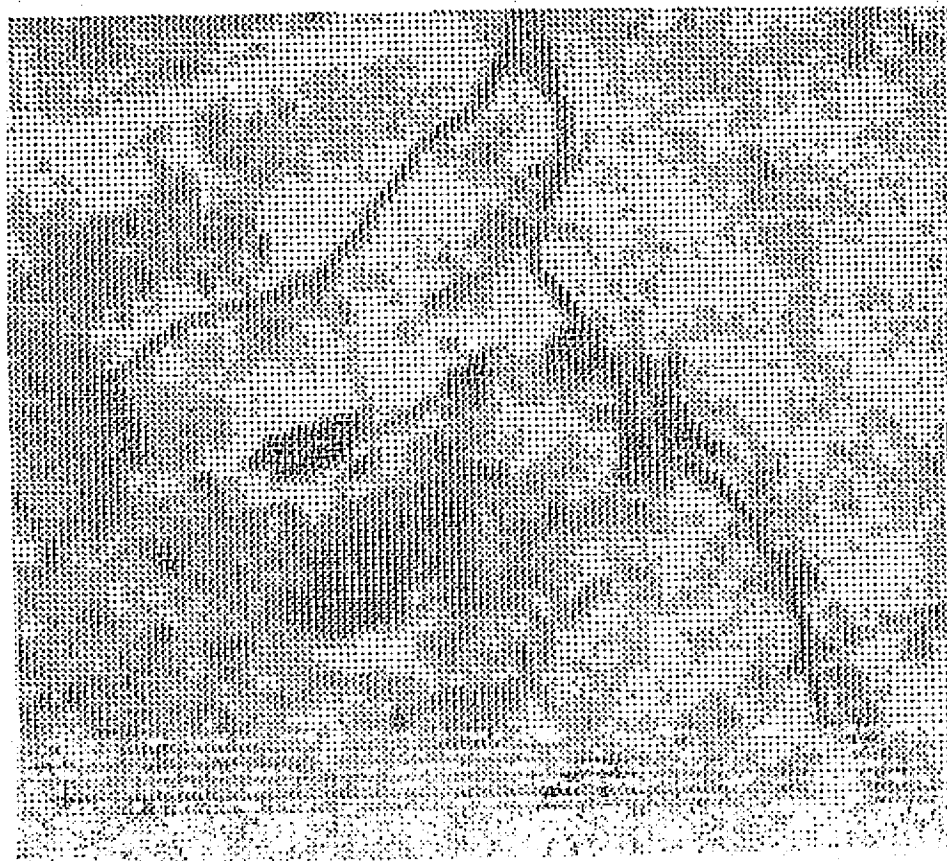


Figure 7-30. Detail of Precision Processed 1062-15190-5

This line-printer output shows the Intersection of I83 and I695,  
resulting from TRW Cubic Convolution Processing

ORIGINAL PAGE IS  
OF POOR QUALITY

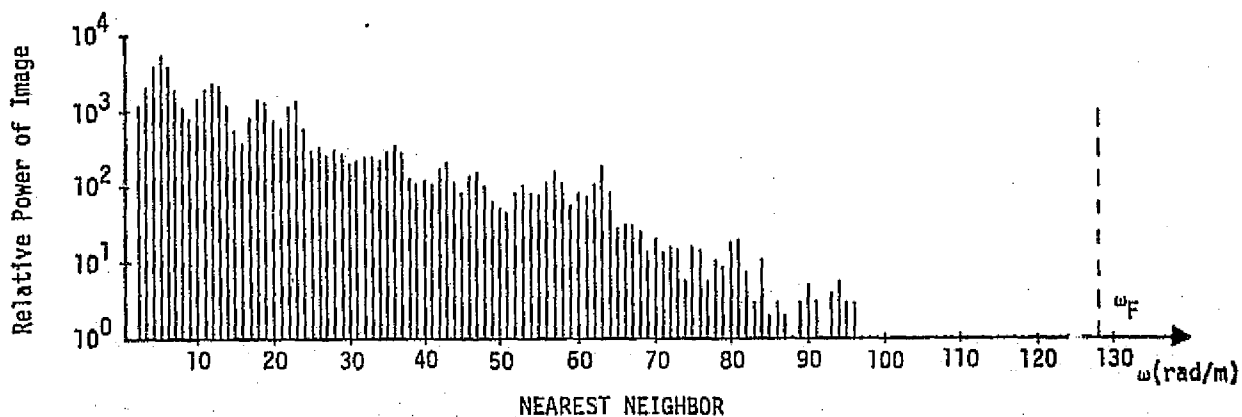
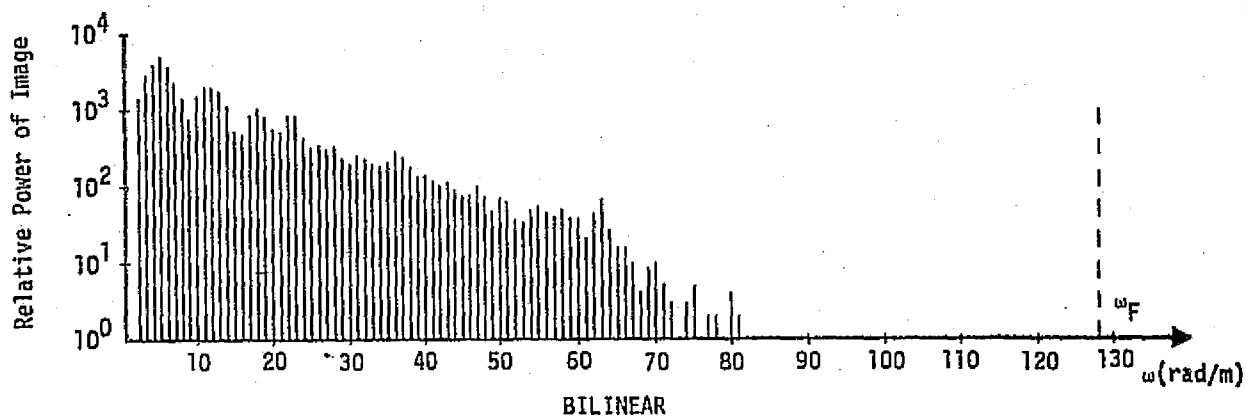
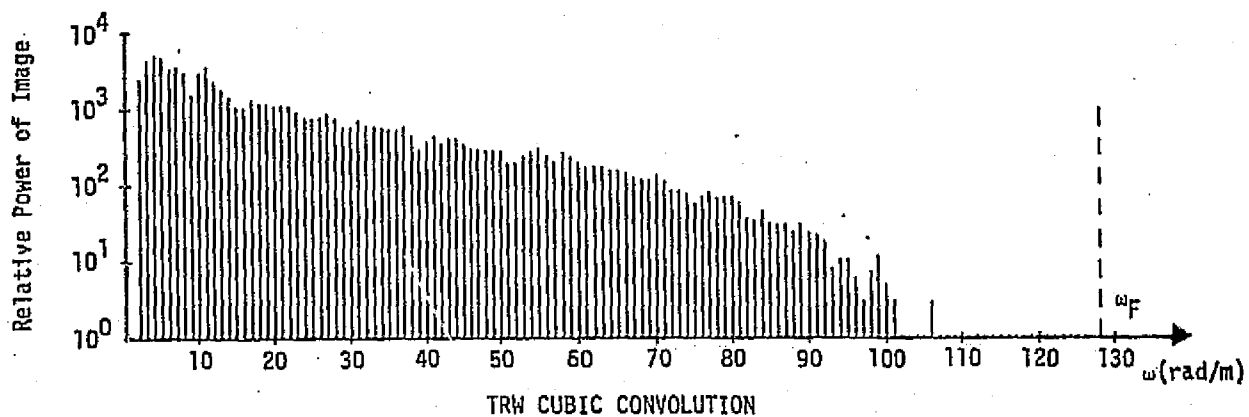


Figure 7-31. Power Spectral Density: Average for 100 Lines

The folding frequency is denoted by  $\omega_F$ , and the frequency interval  $\Delta\omega = \frac{2\pi}{256 \times 57}$  radian/meter

Another way of comparing the three resampling techniques is to generate three images shifted one-half pixel for the scene of Figure 7-32 (bulk data) by the use of nearest-neighbor, bilinear, and TRW cubic convolution process, respectively. The power density spectra of the three shifted images were computed by again averaging over 100 lines. Results, plotted in Figure 7-33, show that the power density spectrum of nearest-neighbor resampled images is indistinguishable from the power spectrum of the original bulk image since a linear shift of half pixel by means of nearest-neighbor resampling should preserve the image samples and thus the statistics. The bilinear resampled image suffers the loss of high-frequency components because of the smoothing effect of bilinear reconstruction. The power density spectrum corresponding to TRW's cubic convolution process has essentially the same spatial frequency content as the nearest-neighbor resampled image; however, the high frequency components are not degraded as is the case for bilinear interpolation.

The cost of the CC reconstruction in terms of processing time requirements is significant if attempted completely in software. TRW's current version requires approximately 80  $\mu$ sec per pixel on a PDP-11/45 in assembly language. This is adequate for occasional processing loads, such as in the low-cost ground stations. However, in a production environment for EOS it is grossly inadequate, requiring 400 minutes per TM scene (all bands). Even if highly-parallel general processors are available, the number of operations required per pixel represents a strong limitation on throughput.



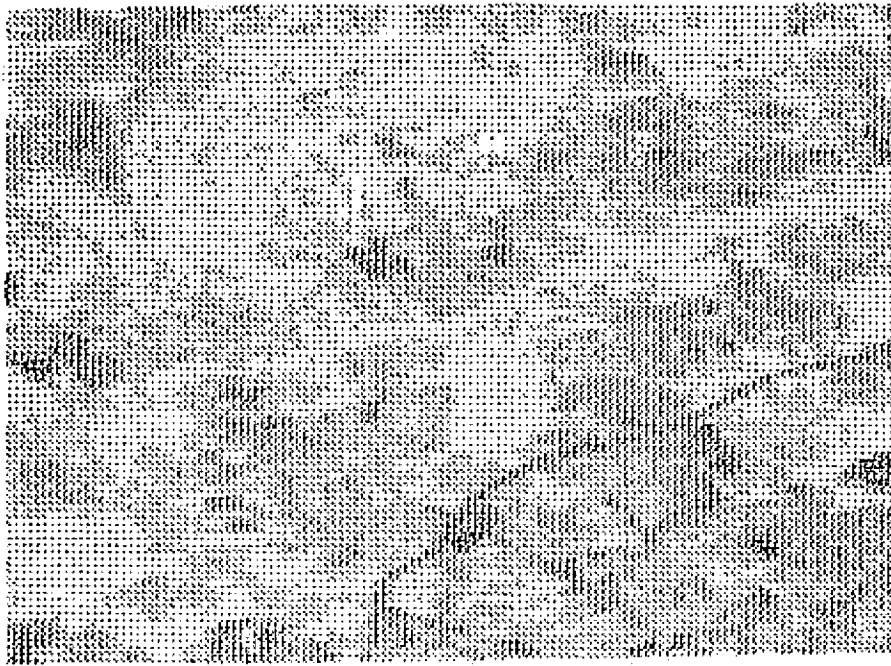


Figure 7-32. Second Detail of Precision Processed 1062-15190-5

ORIGINAL PAGE IS  
OF POOR QUALITY



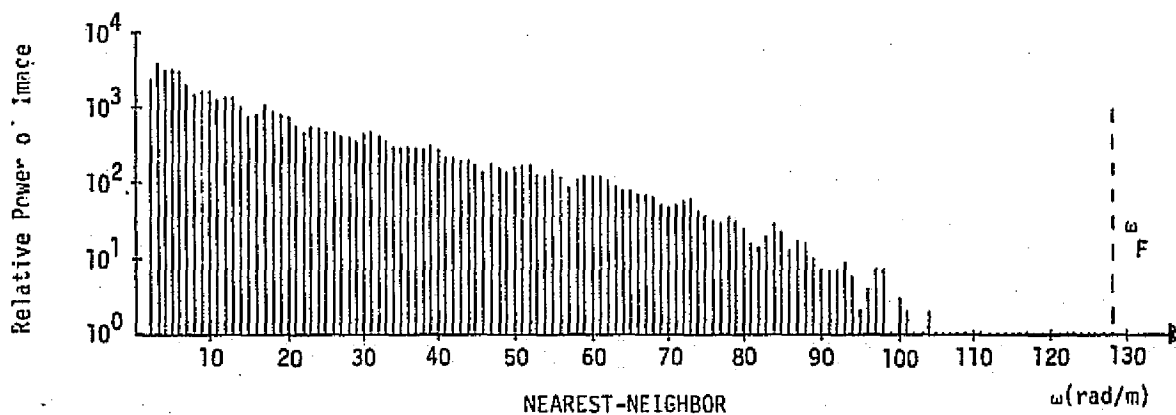
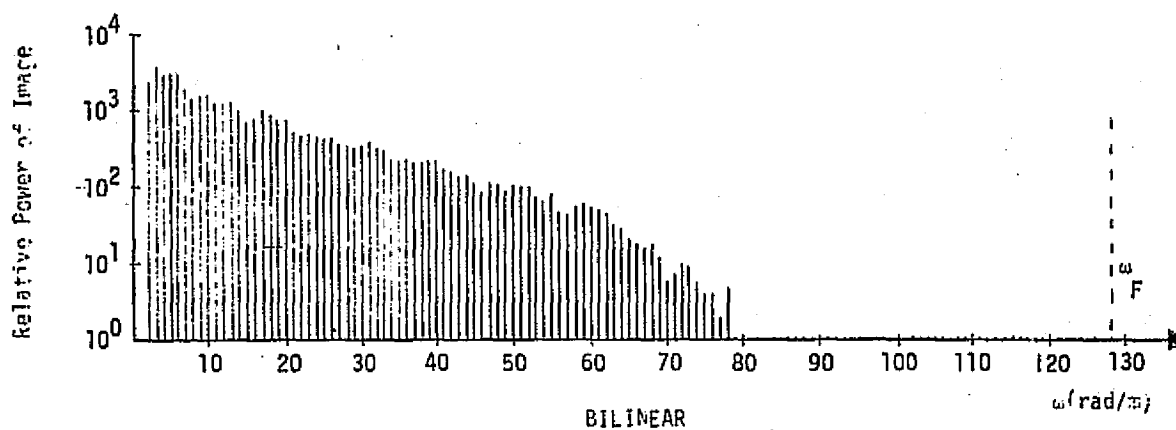
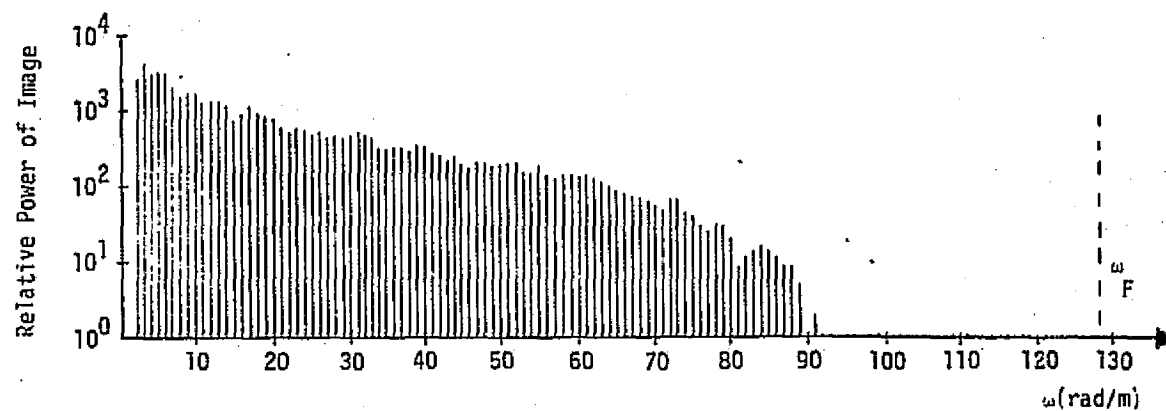


Figure 7-33. Power Spectral Density of Image Shifted One-Half Pixel: Averaged for 100 Lines

The folding frequency is denoted by  $\omega_F$ , and the frequency interval  $\Delta\omega = \frac{2\pi}{256 \times 57}$  radian/meter

### 7.9.3 Image Correction Implementation for High Throughput

Fortunately, the form of the CC reconstruction process is highly amenable to hard-wiring in integrated circuits with an interface to a general-purpose computer for initialization and control. TRW has an operating prototype of such a hard-wired algorithm (called CCI-cubic convolution interpolator) which processes approximately three pixels per  $\mu$ sec, representing a throughput increase of over two orders of magnitude. Throughput limitations are thus only the data bus and buffer storage bandwidth capability for nonprocessor-involvement data transfers. This allows correction of all bands of a TM scene in under 2 minutes, given sufficient general-processor bandwidth. The general processor need only initialize the recursive distortion calculator in the hardware and designate the starting and stopping addresses in the input/output buffers to the CCI hardware interface. These calculations are non-time-critical and performed in FORTRAN software modules.

The CCI special-purpose hardware approach to image correction uses three hardware modules: an along-scan image corrector; an across-scan-skew buffer; and an across-scan image error corrector. The along-scan corrector removes errors aligned along sensor scan lines and the across-scan corrector removes those normal to the scan lines. The along-scan corrector also includes a random-access memory for automatic radiometric calibration of each pixel as it enters the hardware, thus removing the radiometric correction task from the general purpose processor. The general-purpose processor merely passes down previously calculated correction coefficients.

The across-scan-skew buffer stores a sufficient number of along-line-corrected scan lines to subtend an entire precision reference scan line under conditions of worst-case scan rotation between the distorted and corrected grids. If the TM bands for EOS are processed one at a time (band-separated processing), the storage requirements are modest (82 kbit for  $\pm 0.05$  degree maximum rotation) and within the address space capability of several minicomputers (e.g., PDP-11/45). If the TM bands are processed simultaneously (band-interleaved processing), an across-scan buffer is required for each band, although bandwidth requirements allow time sharing of the along- and across-scan correction hardware

between the bands on a line-interleaved basis. The across-scan skew buffer can be implemented in core memory or in hardwired shift registers. The hardwired shift register approach is by far the fastest. Throughput in excess of input/output formatting-disk transfer rate capacity can be achieved by using dual-ported or independent-bank core memories. Detailed sizing and timing analysis for the EOS system are presented in Section 7.11, System Synthesis.

#### 7.9.4 Temporal Registration Process and RCP Library Maintenance

Since temporal registration legislates the most stringent requirements on geometric correction, the entire process of achieving this goal deserves analysis. The accuracies demanded by registration necessitate utilization of registration control points, which in turn must be entered into the system, with capability for later editing, updating, and/or removal. This process is called registration control point (RCP) library maintenance.

RCP library maintenance includes incorporation of new RCP's both with and without geodetic location information, and selective deletion and editing of old RCP's. As successive passes are made over a given site, greater and greater precision is possible with respect to geodetic accuracy, due to RSS'ing of errors. Thus, it is possible to recorrect the geometry of an image on a given spacecraft pass by using information gained on later passes to achieve greater geodetic accuracy. The locations of geodetic control points can thus be known more and more accurately as time progresses. However, change detection and other temporal registration uses require that once the geodesy of a given scene is defined, it must remain invariant. That is, regardless of the geodetic accuracy of a given scene, data from successive passes of the spacecraft must be registered to it precisely. The relative geometry between the two scenes is far more important to these uses than the absolute geodetic accuracy.

Fortunately, sufficient geodetic accuracy can be achieved given geodetic control points on a single-spacecraft pass to satisfy geodetic accuracy requirements. The geometric correction process then entails correction of the first pass of a scene with sufficient geodetic control to the maximum possible geodetic accuracy. Successive passes are then registered to the geometry of this reference scene. This process is shown in more detail in Figure 7-34. Provision is made for partial cloud cover in the reference scene by distinguishing between registration control points (RCP's), and geodetic control points (GCP's).

The locations of GCP's are determined by reference to maps and are specified in earth-centered earth-fixed coordinates or in some (equivalent) map projection such as universal transverse mercator (UTM). Accuracy of GCP location is limited by knowledge of their exact coordinates, inadequate specification of the exact point to which the coordinates apply, and the accuracy of correlating the actual digitized image with the map representation. The locations of RCP's are specified by precision-corrected reference image coordinates. Image segments are extracted from the reference scene at the RCP location and stored in the control point library (CPL) for automatic location of the RCP in comparison scenes from later spacecraft passes. Accuracy of the RCP location is limited only by the correlation process used, since the location of the RCP in the reference scene is precisely specified. The geodetic location of the RCP is irrelevant at this point. Geodetic control points can be used later as RCP's by extracting an image segment at the GCP location from the reference scene and storing it in the CPL. The locations stored with these GCP's are the updated locations in the precision reference coordinate system rather than the a priori map-derived locations. GCP's are weighted according to their relative confidence in determining the precision reference coordinate system, seldom better than  $\pm 1$  pixel. RCP's are weighted considerably greater, corresponding to the accuracy of the location correlation process (e.g.,  $\pm 1/8$  pixel).

Use of a recursive distortion estimator (e.g., Kalman-filter) allows editing of detected locations for obvious errors based on comparison with the expected location and the a priori variance of the expectation (residual standard deviation). The distortion estimator incorporates the location

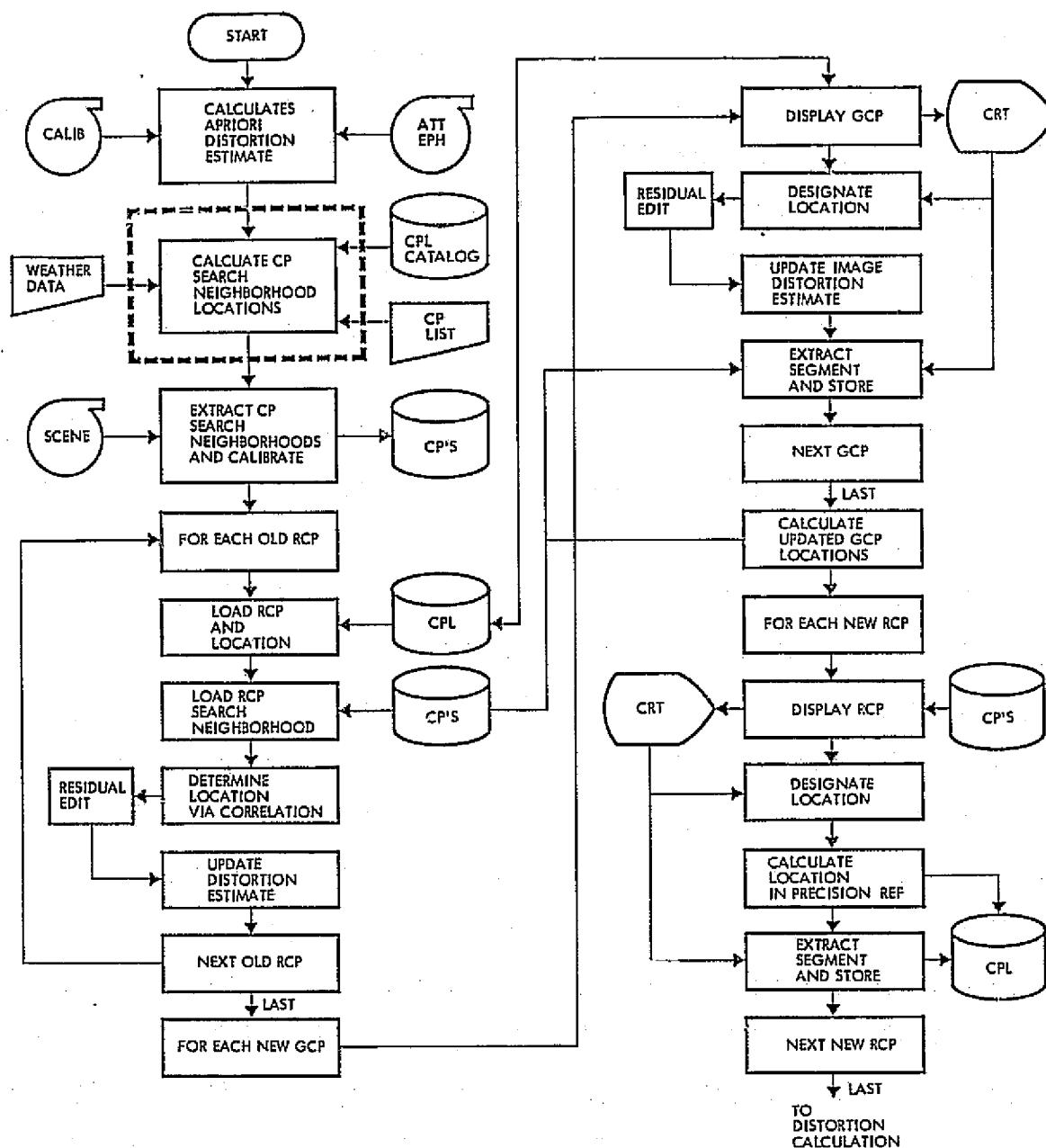


Figure 7-34. Temporal Registration Process and Control Point Library Maintenance

confidence weighting of each CP, forcing the estimate to closely align RCP's at some expense to the GCP locations. Since the RCP's are incorporated into the system only after the geodetic accuracy of the corresponding reference scene is established, the requirements of both cartographic and change detection users are satisfied.

GCP's are located and designated manually using an interactive CRT with track-ball and cursor. By definition, GCP's are defined by map images and coordinates and are not as yet stored as digitized image segments in the CPL. To increase the accuracy of the GCP location, the GCP search neighborhood is expanded in size ("zoomed") using TRW cubic convolution for interpolation of the search neighborhood intensity samples. Coordinates and appearance of the GCP's are established by the operator prior to a distortion estimation pass. Desired GCP's are entered in the CP list.

RCP's, which already exist in the CPL, are correlated automatically with the corresponding RCP search neighborhoods to determine their locations. The RCP's are preprocessed to minimize sensitivity to average intensity, contrast, and, in some cases, possible contrast inversion. The location process includes a search using an optimization of the sequential similarity detection algorithm and a precision location to a small fraction of a pixel using a modified correlation technique. The search process is required only for the first usable CP in a scene, since later CP's are then located to within a few pixels by the recursive distortion estimator. The preprocessing, search, and correlation algorithms are discussed in more detail in Section 7.10.

RCP's which have not as yet been entered into the CPL are designated manually and extracted. Their locations in the precision coordinate system are calculated by the distortion estimator, and they are stored in the CPL. Designation accuracy is relatively unimportant since the locations are automatically determined relative to the RCP segment stored in the CPL.

Performance of the registration process is optimized if the scene used for defining the precision reference coordinate system has sufficiently low cloud coverage to find all required GCP's. Then maximal geodetic accuracy is assured in the precision reference frame. However, several

spacecraft passes over a given scene may be required before this lack of cloud cover is achieved. The above process allows for geodetic correction based on partial GCP availability with later updates with additional GCP's for increased geodetic accuracy in previously cloud-covered regions. Registration accuracy in previously cloud-free areas is assured by the relative weighting of the RCP locations.

Sensitivity to cloud cover is further reduced by incorporating GCP's from an entire spacecraft take in the distortion estimates for scenes covered by the take. Estimation of distortion on this basis also minimizes image discontinuities at the junction between successive scenes such as may occur if distortion in the two scenes is estimated independently. The number of CP's required versus accuracy is discussed in more detail in Section 5.2.5.

#### 7.9.5 Special Processing

Several possible areas of digital image processing fall under the topic of special processing. As discussed earlier, that processing which is common to all users is most cost-effectively performed by the central data processing facility (CDPF), with user-specific processing left to the specific users. Thus, radiometric and geometric correction is performed by the CDPF, whereas spectral classification, color density slicing, factor analysis, and others are not. Some processing tasks fall on the dividing line between these classes and deserve special discussion. These include MTF compensation (correction for sensor and amplifier aperture degradation of high-spatial frequencies), aperture correction (correction for varying aperture shape with scan position to achieve position-invariant resolution), scale expansion (zoom by pixel relocation or interpolation), special map projection coordinates, and nonstandard gamma corrections (nonlinear calibration). It is noted that temporal registration (i.e., overlaying of scenes from successive spacecraft passes over the same area) is explicitly not included under the category of special processing, since it is a by-product of and generated simultaneous with geometric correction (if implemented correctly, as above).

If a large number of users require a specific processing output, it is more cost effective for the central facility to generate that product than for each user to generate it individually. Similarly, if a product can

be generated by a modification of a standard procedure, accuracy will be improved by minimization of the number of passes through the data. I. e., nonstandard map projections generated at the same time as geometric correction by modification of the correction coefficients will have less residual aliasing, interpolation, and quantization-induced errors than if the standard-map projection product were warped a second time by the user to produce the nonstandard product. On the other hand, the throughput capability of the central processing facility is directly related to the number of different products per scene which must be generated, as well as the number of scenes which must be processed.

High-spatial-frequency content of the received imagery is reduced by the combined effects of the optics aperture and field stop, the physical size and shape of the detector cell, and the presampling amplifier filters. Indeed, the amplifier filters are incorporated to minimize scene frequency content above half the sampling rate (Nyquist rate), since frequencies greater than this result in image reconstruction errors (aliasing) and cannot be regenerated unambiguously from the samples. Realizable anti-aliasing filters will also reduce some of the higher-frequency content below the Nyquist rate. Knowledge of the composite Fourier transform of the amplifier, optics, and detector optical impulse functions, as well as the image signal-to-noise ratio makes optimal (minimum variance error) compensation of the image frequency content possible through Wiener theory.

However, techniques other than Wiener filters for MTF compensation exist. In addition, the signal-to-noise ratio of the original scene is sacrificed somewhat to regain the lost high-frequency energy. Consequently, generation of MTF-compensated imagery as a standard product is not advisable and should be relegated to special processing only. In any event, the intent of MTF-compensation is to regenerate the scene prior to the sensor aperture, whereas for change detection and spectral classification work, the scene as transferred to the sampler (post-sensor-aperture) is adequate. I. e., low signal-to-noise ratio is more important than increased high-frequency content. For special processing, several standard digital techniques exist.



Aperture correction refers to modification of the image samples to achieve constant resolution across the image in the face of varying aperture shape, such as occur in conical scan sensors and in pointable sensors when pointed off nadir. The conical scan sensors either rotate the detector cell relative to the spacecraft ground track, resulting in a varying detector aperture, or rotate the detector cell relative to the scan direction, giving constant detector aperture but space-variant amplifier equivalent aperture. Aperture correction can be implemented as a piecewise approximation to the appropriate MTF compensation function, constructed in hardwired algorithms. However, this process is required only for conical-scan thematic mappers with significant spacecraft ground track separation between passes in order to satisfy change detection requirements. Since the HRPI data will most likely not be used for change detection and since variable resolution is not a problem to spectral classification, this process is not considered a necessity for the central processing facility.

Scale expansion of output images must be generated by pixel replication or pixel interpolation if a laser-beam recorder (LBR) is used for photo generation, due to the LBR's fixed output scan raster. Pixel replication for scale expansion is equivalent to nearest-neighbor reconstruction of the continuous sensor aperture-degraded image and results in significant obscuration of scene content, due principally to extreme aliasing (for high-expansion factors) in the expanded image. TRW's cubic convolution process, however, closely reconstructs the continuous scene intensity surface, resulting in an expanded image that uses nearly all the information contained in the transmitted samples. The expanded scale images can be generated at the same time that geometric correction is being performed by appropriate modification of the geometric distortion coefficients. Accurate magnifications of up to 8:1 are practicable. Again, this procedure is relegated to special-order processing during slack periods in machine utilization. Nonstandard map projections should be generated directly from bulk uncorrected data to avoid multiple corrections and the corresponding compilation of residual errors. Available map projections are limited by storage capability of the across-scan skew buffer to handle scan line rotation to

the desired projection. Projections which are feasible, assuming the spacecraft is steered to align the roll axis along the ground track, include rotated UTM, tangential, and space oblique mercator (SOM). Again, throughput limitations of the image correction subsystem may relegate the less desired projections to special-processing status. The distortion estimation process generates the appropriate distortion coefficients to generate the map projection and its timing is independent of which one is selected.

Nonstandard gamma corrections are assumed required for photo products only and may be able to be generated in the LBR. If not, gamma correction is a post-processing step (i.e., not sensor detector specific) which can be accomplished at extremely high speed via table lookup during output product generation.

## 7.10 REGISTRATION CONTROL POINTS

The geometric accuracy requirements desired by users of EOS sensor data exceed those utilized by the most demanding of ERTS data users by almost a magnitude. In addition, registration accuracies between scenes on the order of  $1/4$  of a pixel dimension are design goals for the EOS image processing system. These demands require geometric accuracies greater than those achievable by controlling and measuring system-induced errors. Measurements independent of the sensor platform are necessary, and registration control points (RCPs) are these measurements.

Registration control points are derived from sensor image data. They, technically, are not points (though for visual registration schemes, they could be) but are neighborhoods with uniquely identifiable features. These features are used to correlate an image neighborhood with some reference neighborhood. The geometric attributes of each of the neighborhoods are known, and upon correlation of the two neighborhoods, their relative geometric relationship is established. This process is known as a registration control point location measurement. Using a number of registration control point location measurements, static and dynamic geometric errors, with respect to a reference image, can be measured and eliminated to produce an image approaching the same geometrical accuracy as the reference image. This process is referred to as the registration process. The registration process not only increases the accuracy of the image, but inherently registers the image to the reference image. If the process is designed with some care, the difference in location between similar pixels in each image (the registration error) can be kept below a maximum of  $1/4$  of a pixel.

Some differentiation must be made between a registration control point and the more traditional concept of a ground control point (GCP) — sometimes referred to as geodetic control points. Ground control points are locations in an image that are determined from measurements independent of the image. An example is the crossing of two highways in an image;

the geodetic location of the crossing is used as a measurement to locate the pixels of the image in some absolute reference frame. The registration control point process, however, uses another image (the reference image) as its absolute reference frame. All input image registered to this reference image will be inherently registered to each other. In addition, all input images will have the same absolute geometric accuracy as the reference image. Section 7.9, Image Processing Algorithms, discusses this point in detail and establishes the procedures for constructing and maintaining a registration control point file.

Geometric and geodetic accuracy in an image can be achieved by a number of time-dependent processes, ranging from subscene characteristics with durations of seconds, to the attributes of the complete spacecraft pass with durations to ten minutes. It was determined in Section 5.2.5, Pointing Error Budget Allocation, that control and measurement of error sources during the pass was the most satisfactory procedure for achieving error correction accuracies. This study determined the relative location and the number of control points necessary to meet desired accuracies; it assumed that the registration control points could be located to within a fraction of a pixel. It was also noted that for EOS-A, both the TM and HRP1 sensors would require the registration process. Hence, images from each sensor will be inherently registerable; note that the bands within each sensor are inherently registered by design. Details of that portion of this task are, therefore, not presented here, but more appropriately discussed in Section 5.2.5.

This section considers those aspects of registration control points that have not been addressed in the previously mentioned two sections. These considerations center around the registration control point location measurement process and address four topics: RCP characteristics, preprocessing, RCP search algorithms, and RCP correlation algorithms. The characteristics of registration control points determine the amount of preprocessing necessary to perform the subsequent search and correlation algorithms. The search algorithm is used to locate a registration control point to within one or two pixels and the correlation algorithm is used to obtain subpixel location accuracy.

### 7.10.1 Assumptions

The basic assumptions are:

- This task addresses the registration control point measurement process.
- The procedures for registration control point file generation and maintenance, and the use of registration control point location data for image processing is presented in Section 7.9, Image Processing Algorithms.
- The number and location of registration control points necessary to achieve required geometric accuracy in an image is presented in Section 5.2.5, Pointing Error Budget Allocation.

### 7.10.2 Analysis and Tradeoffs

Four topics are discussed below: RCP characteristics, preprocessing, RCP search algorithms, and RCP correlation algorithms. These topics are discussed in the context of the registration control point measurement process, and constitute consideration for obtaining rapid subpixel registration between images. Desirable characteristics of RCPs are discussed first.

Results with the automatic digital registration of ERTS images have been very sensitive to the characteristics of the RCPs used. Properties that enhance the location accuracy do not necessarily yield rapid implementations, and vice versa. Also, RCPs which have good visual properties do not necessarily have good properties when used with digital algorithms. There are also situations that show the difficulty of this problem. Because of seasonal changes, there can be a tremendous variation in the distribution of pixel intensities between cycles of the same scene. In fact, actual contrast inversions have been observed in scenes, i. e., relatively light and dark intensity regions reverse their relationship. Nevertheless, the problem of the choice of RCPs has some bounds. It has been determined from the ERTS experience that a 32 by 32 pixel region should be sufficient to achieve the final 1/4 pixel location accuracy. Note that this size region yields a 1024-point correlation calculation. Thus, the problem is the determination of 32 by 32 pixel regions in a reference image that has desirable RCP characteristics.

These characteristics include the following:

- Insensitivity to temporal changes
- Insensitivity to spatial changes, e. g., changes in land-water boundaries
- Ultimate subpixel correlation properties
- Initial geodetic position accuracy.

Experience with ERTS data has shown that the only way to insure the integrity of the registration process is to manually monitor the process. This requirement results from the variations observed in ERTS images over time. Changes in sun and viewing angle, seasonal variations on the ground, and degradation in sensor performance make the registration process a very dynamic one. Technical experience with data less than two years old has not been sufficient to predict with certainty all the characteristics needed for ERTS RCP digital registration, let alone those predicated on the class of sensors to be utilized with the EOS system.

Some desirable characteristics of RCPs can be stated. There does appear to be a window in the spectral region between  $0.5 \mu\text{m}$  and  $0.8 \mu\text{m}$  that has some desirable properties. The chlorophyll effect due to seasonal changes has been observed for wavelengths greater than  $0.8 \mu\text{m}$ . At the lower wavelengths, around  $0.5 \mu\text{m}$ , there is significant scattering in the atmosphere. Hence, the band between  $0.6$  and  $0.7 \mu\text{m}$  appears to have less sensitivity to seasonal and sun angle variations. Properties of distribution of pixel intensities within the RCP should possess good correlation characteristics, i. e., a sharp, unambiguous peak in its correlation function. A relatively noise-like appearance in the image, such as a race-track and its surroundings, can be very good for correlation purposes. Nevertheless, operator experience creating the RCP file will be the most valuable input in determining the best RCP characteristics. In addition, an operator in the loop can ascertain variations in the RCP images and determine methods to be used to compensate for their presence by using preprocessing techniques.

Preprocessing techniques are the tools used to enhance the speed and accuracy of the registration process. It is envisioned that the registration process monitor will use these techniques under command with the aid of an interactive display. Perhaps, the simplest technique is to use seasonal representations of the reference RCP images; this is very time consuming though, taking at least one year to create the file. The other preprocessing techniques require performing transformations on the pixel intensities. These techniques implement different goals depending on whether a search is being performed or the final correlation algorithm is to be processed. In the former, only a one or two-pixel accuracy is desired; hence, increased speed in implementing the sequential similarity detection algorithm (SSDA) (discussed below) to the desired preprocessing goal. Local averaging, normalization, and quantization procedures appear to have this characteristic. Edge detection schemes can also have some useful effects under certain conditions.

The correlation algorithms require preprocessing techniques which increase the accuracy of the resulting location determination. Schemes based upon pixel differences within an image such as gradient, laplacian, and edge detection techniques have application for this case. Another class of interesting schemes is based upon quantizing the pixel intensity distribution, and application of edge detection algorithms.

In addition to the above preprocessing consideration, there is a need to compensate for changes in the pixel intensity distribution between scenes due to intrinsic variations in sun angle, among other contributors. Regression analysis techniques are commonly used to remove this effect by using the pixel intensity distributions of each image. In general, this preprocessing technique will be required before the RCP search algorithms are implemented.

The most successful technique for rapidly registering two images to within one or two pixels of each other is the class of sequential similarity detection algorithms (SSDA). This technique uses the sum of the difference between pixels in the two images being registered to determine their point of similarity. This calculating process ceases when a given threshold is exceeded and another point of similarity is chosen to start a new sum of

differences until a minimum sum is found. The SSDA techniques exhibit superior performance in speed when compared to correlation and fast fourier transform algorithms. There is some work being performed on optimizing the threshold function, which will enhance the SSDA speed advantage even more. The SSDA technique is to be used for the RCP search algorithm. Its accuracy is only one or two pixels in location; hence, an RCP correlation algorithm is used after the completion of the search to achieve the subpixel registration accuracy.

Unfortunately, errors which can be considered negligible for the search algorithm become important during the correlation process to obtain subpixel registration accuracy. The SSDA addresses the problem of removing a translational difference between two images. There are other classes of errors between the two images to be registered: rotation, skew, and scale, as well as the previously mentioned pixel intensity variations. Excluding intensity variations, translational errors are dominant for the TM and HRP1 (within the field of view of the TM) for the search process. For the offset HRP1 outside the field of view of the TM, skew and scale errors increase and compensation must be made in the correlation process. There are even small rotational errors due to cross-track drift and small scale errors due to altitude changes for TM scenes. Scan non-linearities can also cause errors on the order of tenths of a pixel if not modeled properly in correction routines. Some care must be exercised when designing the correlation algorithm for the EOS sensors — sensors which have much higher resolution than the ERTS MSS and RBV.

There are two important approaches to obtaining subpixel registration:

- Interpolate the registration control points to obtain a refined set of pixels for the image, and then perform the correlation on the refined image
- Interpolate the correlation function of the two images to find the location of the correlation position.

The first approach has been used successfully on ERTS data using cubic convolution interpolation to refine the pixel spacing; the second approach requires much less calculation as the order of the interpolation kernel determines the number of correlation values that must be calculated



before the interpolation is performed. In either case, the desired goal is the same — to find the position of registration between the two images with the least error possible. Accuracies on the order of 1/4 pixel should be possible with either approach for the EOS images.

#### 7.10.3 Conclusions

As observed from the previous discussion, the final EOS registration control point measurement process algorithms will be determined by empirical results based upon algorithms derived from theoretical consideration and suggested by recent experience. TRW has been developing registration technology using ERTS data, and expects to extrapolate those results to satisfy the EOS requirements.

## 7.11 CDPF SYSTEM SYNTHESIS

This section presents a functional and hardware design for a CDPF computer system capable of handling the data volume corresponding to coverage of the entire U.S. from both the TM and HRPI sensor with no images rejected due to cloud cover. Processing time requirements are less than two (8-hour) shifts. Both uncorrected and corrected sensor data products are generated, with the relative geometric accuracy of the corrected product being better than  $\pm 1/4$  pixel. The system is structured in sufficient detail to allow accurate performance and cost estimation and to provide a reference for which the relative cost and performance tradeoffs of alternative EOS system designs can be assessed.

This section includes sizing and timing estimates and hardware tradeoffs to support the baseline CDPF design. Section 9.3 of this volume discusses the philosophy of design and qualitative design goals. The functional structure and interfaces of the CDPF are presented in Section 9.3, with this section containing quantitative justification for the resulting design. As discussed in Section 9.3.3, the Information Management System (IMS) does not require appreciable development, and thus is not discussed here, but in Section 7.8. Existing equipment and software are used for the IMS. The image processing system is discussed in detail with respect to sizing, throughput, and hardware design, followed by an analysis of operational considerations and a compilation of CDPF costs for the baseline design.

The dominant cost and throughput impact on the system is shown to be the output product generation, requiring mass storage for reformatting. The image correction process is relatively easily handled via special-purpose hardware techniques developed by TRW for correction of imagery such as ERTS using minicomputers for initialization and control.

### 7.11.1 Input/Output Characteristic Used for Sizing CDPF Design

The CDPF baseline configuration is designed to handle 50 thematic mapper users and 200 HRPI scenes (the equivalent number for 50 thematic mapper scenes) every day. This corresponds to 22.5 minutes of sensor operation each day for the baseline sun synchronous orbit of 717 km altitude. This represents an upper-bound on the processing load as there will

be at most 35 thematic mapper scenes per day covering CONUS. There are at most three passes over CONUS each day, with the maximum pass duration being on the order of 10 minutes. The rest of the scenes will cover data taken at the Alaska ground station and other available scenes taken outside CONUS from the Goldstone and NTTF ground stations. Considering the three CONUS passes and the Alaska ground station data, it is assumed that there is an average of five passes each day during which sensor data is acquired. Table 7-8 summarizes the characteristics of the CDPF input sensor data.

There are three types of CDPF output products: high density digital tapes (HDDT), computer compatible tapes (CCT), and film. There is also the requirement for an archival product to be used for sensor data storage and retrieval. NASA has specified that the HDDT products include both uncorrected and corrected sensor data. All of the CCT products are to be corrected. First-generation film products are to be positive and negative black and white images; the color positives and negatives are second-generation products. Photo processing will produce the additional black and white and color film products.

There are two levels of quality for the digital products, uncorrected and corrected. Clearly, it is desirable to obtain the highest quality necessary in an output product. TRW has taken the approach that there is not a significant cost savings by providing a range in the quality of the output products. Special-purpose hardware implementation of high-order error correction algorithms yields the same throughput as low-order algorithms; hence, there is no reason why a user should have to use data which is inherently less accurate than other output products. The conclusion is that output data product quality will be either uncorrected, i. e., reformatted sensor data, or it will be corrected to a quality which will satisfy the most demanding user requirement. Table 7-9 summarizes the data quality characteristics used for sizing the CDPF design.

Two principal user groups receive the output products: NASA principal investigators and EROS. The principal investigators are selected members of the scientific community who will require special and unique output product formats as well as the standard formats to satisfy their collective requirements. The output products that are shipped to EROS

Table 7-8. Characteristics of Input Sensor  
Data Used for Sizing CDPF Design

Input Sensor Product

Average daily number of sensor data ground station passes	5
Average total duration of sensor data	22.4 minutes
Maximum station pass duration	10 minutes
Number of HDMR tapes for each pass (one for each sensor)	2
Average daily number of HDMR tapes	10
HDMR tape format:	Each 14-inch, 9600-foot tape contains the data from each sensor and is recorded at 180 ips. The peak data rate is 128 Mbit/sec, and has a serial output. The average sensor data rates are 11.4 Mbytes/sec and 13.5 Mbytes/sec for the thematic mapper and HRPI, respectively, with 8 bits per byte representing each pixel.

Input Sensor Data Daily Volume

Thematic mapper scenes (1.22 x 10 inch bits)	50
HRPI scenes (1.47 x 10 inch bits)	200
Total average daily sensor data input	2.69 x 10 inch bits

Input Sensor Data Format Parameters

	<u>Thematic Mapper</u>	<u>HRPI</u>
Bits per pixel	8	8
Pixels per scan	8192	4800
Spectral bands (ground resolution)	(No. 1-6 30m, No. 7 120m)	4 (10m)
Swath width	185 km	48 km
Detectors per scan	100	19,456
Pixels stored to form line	813 K	58 K
Pixels per scene	306 M	92 M

Table 7-9. Output Data Quality Characteristics Used  
for Sizing the CDPF Design

Uncorrected Output Products: Quality commensurate with that inherent in the input sensor data; only processing is reformatting.

Corrected Output Products:

Attribute	Sensor	
	TM	HRPI
Pixel misalignment ( $3\sigma$ )	1/4 pixel	1/4 pixel
Band-to-band registration ( $3\sigma$ )	0.1 IFOV	0.3 IFOV
Position accuracy ( $1\sigma$ )	15 m	15 m
Relative radiometric accuracy ( $3\sigma$ )		
Visible Bands		
Tape	1.6%	1.6%
Film	5.0%	5.0%
Thermal Band		
Tape	1°K	not applicable
Film	3°K	not applicable

(or other similar facilities) will be used to satisfy the requirements of the general public and operational programs. The digital data interface to EROS should be the HDDT's because of their high data densities.

All the digital data contained on HDDT's can conveniently be contained in three formats: uncorrected, band-interleaved corrected, and band-separated corrected. All HDDT formats would have error correction coefficients and image annotation files as headers. The band-interleaved corrected format is the most useful for producing band-interleaved products such as magnetic tapes for classification routines. The band-separated product is the most cost-effective format for first-generation film production. It should be formatted with annotation to reduce subsequent processing costs and time. In addition, the band-separated product is the most economical form for producing band-separated magnetic tapes.

The format for the uncorrected HDDT should be the one which is most useful for subsequent processing. Uncorrected, band-interleaved data is a prime candidate for HDDT products sent to EROS, especially if correction

data is included on the tape. Thus, EROS can generate first-copy, single-correction data in non-standard formats by modifying the distortion coefficients and processing the uncorrected data with a similar facility to the CDPF IPS. Uncorrected HDDT data should have the same format as that used for input to the error correction process. Furthermore, of the two formats, band-interleaved and band-separated, the most useful format in terms of subsequent scene processing is the band-interleaved product. This follows because it takes less time and storage volume to produce a band-separated image than to perform the converse, i.e., band-separated to band-interleaved. These considerations lead to the recommendation that the uncorrected data HDDT be band-interleaved.

To estimate the data volume for the three HDDT formats, some assumptions must be made to define the process. It is assumed that the equivalent of all the input sensor data will be stored in each of the three formats. One copy of each of the formats will be sent to EROS and one copy of each will be retained by the CDPF for archiving. In addition, the equivalent of two copies of the uncorrected HDDT (with the error correction information in the header) will be sent to LCGS users for their unique processing requirements. This results in a daily data volume of  $1.1 \times 10^{12}$  bits for uncorrected HDDT's and the same for the corrected HDDT's.

Two CCT technologies are used, 1600 and 6250 bpi. This will be the interface medium for digital data used by NASA principal investigators and a variety of formats are desirable. Standard formats should include band-interleaved, band-separated, pixel-interleaved by band, 1/16 of TM swath width (512 pixels for standard displays), quarter swath width TM (for use with HRPI data), and half- and quarter-swath width HRPI formats. It should be recognized that by the very nature of the work performed by the user community which utilizes the CDPF CCT output products, it is essential that there be enough flexibility to satisfy almost all formats anticipated. Clearly, the users of larger data volumes will capitalize on the 6250 technology. One TM scene can be read onto four 2400-foot reels of 6250 bpi tape; the same medium can hold one HRPI scene. However, it requires at least nine 1600 bpi tapes to hold a TM scene and at least three tapes for an HRPI scene.

To size the CCT tape data volume, it is assumed that there are 100 NASA principal investigators. If each investigator is involved with a particular area (which is compatible with the ERTS experience), then, recognizing the 17-day cycle for the baseline orbit, it can be assumed that there are on the average six investigators requesting data each day. To get an upper bound on the data volume, assume each investigator requests the equivalent data of one TM scene. The resulting daily CCT tape data volume for the equivalent of six TM scenes is  $1.5 \times 10^{10}$  bits. Figure 7-35 shows the possible mix between the number of 1600 bpi and 6250 bpi tapes for this average daily volume. The case of all 6250 bpi tapes corresponds to a 1/4 swath format on each tape and the case of all 1600 bpi tapes corresponds to a 1/16 swath format (512 pixels).

There is a requirement for both positive and negative first-generation black and white transparency film products. The products will consist of all scenes of each sensor. This results in 50 TM and 200 HRPI scenes per day for a total of 1150 images generated per day. Color positive and negative transparencies are specified to be second-generation products. The film products are specified to have a 241 mm (9.5 inch) size. A number of

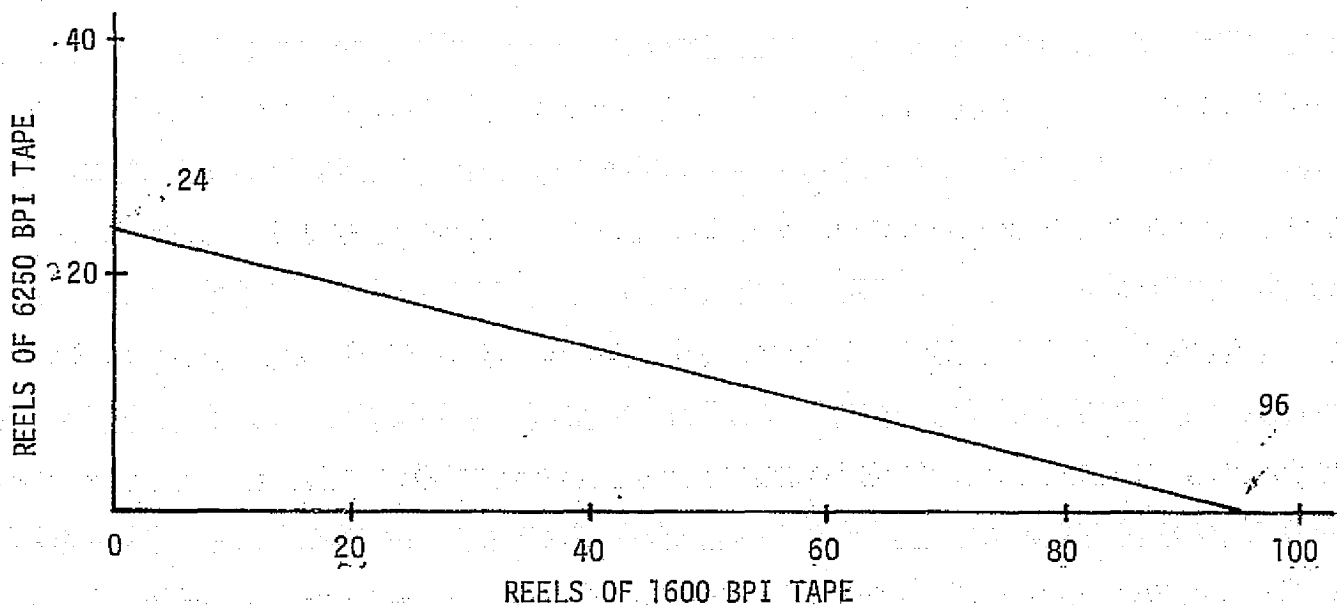


Figure 7-35. Mix of 1600 and 6250 bpi Tape Reels to Satisfy Average Daily CCT Output Product Volume



output formats are desirable. Because the frame size of the TM is equivalent to the ERTS MSS frame size, it is anticipated that there will be a continuation of the existing formats for enlargement to standard map scales, e.g., 1:1,000,000. The HRPI scene can be enlarged about four times the TM scene because of its reduced field of view and the fixed 241 mm film size.

To estimate the photographic product volume, proportions for various output film products were derived from the ERTS capability using the reference\* cited below. Table 7-10 summarizes these proportional factors for estimating the quantity of output film products using the number of images as a basis. The proportional factor is multiplied by the number of daily images to calculate the average number of output products indicated.

Table 7-11 summarizes the output product volume. It uses the average daily load as the basis for its presentation. This approach represents a conservative estimate for sizing the daily output product generation requirements and its hardware implementation. These estimates also represent the upper bound on the data volume specifications generated by NASA.

Table 7-10. Factors for Calculating Average Daily Output Film Products from the Number of Daily Images

<u>Production Output Format</u>	<u>Proportional Factor</u>	(multiply factor times the number of daily images to calculate output product volume)
First-generation black and white	2	
Black and white		
Positive transparency	5	
Negative transparency	10	
Positive print	0.5	
Color		
Positive transparency	0.05	
Negative transparency	0.10	
Positive print	0.07	

\*NASA document, "NASA Support Plan, Earth Resources Technology Satellite A and B", Contract NAS5-11320, dated June 1, 1971, revised March 22, 1974. See pages 4310.14 and 4310.15.



Table 7-11. CDPF Output Characteristics for Sizing Product Generation

Product	Average Daily Data Volume	Format	Comments
HDDT			Error correction and image annotation information used as header on all HDDT products
Uncorrected	$1.1 \times 10^{12}$	band-interleaved	Four copies of all data
Corrected	$1.1 \times 10^{12}$ bits	band-interleaved and band-separated	Band-separated product annotated and formatted for film generation
CCT	$1.5 \times 10^{10}$ bits	1600 and 6250 bpi	Equivalent to 6 TM scenes; flexibility in generation to satisfy all formatting needs
Film		all 241 mm (9.5 inch) film size	Formats include enlargements to standard map scales including 1:1, 000, 000 1:1, 500, 000, and 1:250, 000
First-generation black and white	2300 images		Positive and negative transparency of all error corrected scenes; 50 TM, 200 HRPI
Black and white positive transparency	5750 images		
Black and white negative transparency	11500 images		
Black and white positive prints	575 images		
Color positive transparency	58 images		
Color negative transparency	115 images		
Color positive print	80 images		
Archive Material: One copy each of the three HDDT formats ..... 8.3 x 10 inch bits (data volume included in HDDT volumes above)			

The archive material is one copy each of the three formats of the HDDT. These HDDT's represent master copies and are used to generate requested output products. After 70 days (4 cycles of data), it is assumed that EROS will have completed its archive preparation with the equivalent data. Subsequent requests then could be satisfied by EROS.

#### 7.11.2 Image Processing System Functional Design

The processing requirements and resulting functional structure of the CDPF Image Processing System (IPS) are discussed in Section 9.3. The primary functions are shown in Figure 9-10 and consist of input reformatting, distortion calculation, image correction, and output product generation. The bases of this functional structure are: (1) the user requirements discussed above in terms of products, formats, and quantities; (2) the sensor data formats and rates, discussed below; and (3) image distortion measurement and correction techniques successfully employed by TRW for ERTS data correction, extrapolated to EOS, and discussed in Section 7.9.

The downlinked TM and HRPI data is multiplexed and recorded on wideband tape (HDMR) in a format determined by the sensor design. For the Te sensor, 16 lines in each of 6 bands and 4 lines in a seventh band (corresponding to one mirror scan) are all transmitted simultaneously in parallel (pixel-interleaved). For the Hughes sensor, the multiplexing format is further complicated by alternate mirror scans being in the opposite direction (reverse pixel order). The Honeywell TM scans similarly to the Te, except that the scan is highly nonlinear (conical). The Westinghouse HRPI has 4800 detectors in each of 4 bands, corresponding to the individual pixels across-track, and samples them in a scrambled order determined by a sampling rate limits on adjacent detector cells.

On the other hand, image correction techniques and output product generation require line-sequential data in pixel-ordered format. Some output products require band interleaved data, such as HDDT for spectral classification users. Other products with band-separated data are also required, such as LBR-generated photo products. Consequently, reformatting of the input sensor data is required to generate the pixel-ordered, line-sequential data.

A primary system tradeoff is whether the bands should be separated on a per-scene basis in the input reformatting, thus requiring less buffer storage in the image correction process and directly generating band-separated output products, or the bands should be interleaved on a line-by-line basis, thus minimizing input reformatting buffer storage and directly generating band-interleaved output products. In either case, output reformatting is required to generate separated or interleaved products from the opposite correction processor output product. For a minicomputer-based system, image correction buffer requirements would indicate preference for input band-separation reformatting and band-separated image correction. However, midicomputer systems' greater core addressability and a high-cost in input reformat buffer size and throughput limitations indicate preferability of band-interleaved processing.

Also recorded on the HDMR is auxiliary data, especially radiometric calibration measurements, multiplexed in the sensor scan retrace period. This data must be extracted from the input tape and analyzed prior to in-line radiometric correction of the input pixel intensities. Similarly, before the image data can be corrected geometrically to the required precision, geodetic control points (GCP) must be located in the incoming image and combined with a priori data on the spacecraft and sensors to measure the geometric distortion. GCPs from an entire pass are required for the distortion calculation process before image correction can commence, in order to minimize geometric discontinuities between adjacent scenes. Consequently, an initial pass is made through the HDMR to extract GCP and calibration data for use by the distortion calculation process.

The distortion calculation process generates coefficients which define the image distortion, radiometric correction coefficients, and image annotation tables. This data is utilized by the image correction processor to correct the imagery as it comes out of the input reformatter on a second pass through the HDMR. Only two passes are made through each HDMR. The correction processor generates uncorrected and corrected HDDTs, both containing the correction coefficients. These tapes are then sent to the output product generator which produces duplicate HDDTs, CCTs in 1600 and 6250 bpi, and first-generation photocopy. Both band-interleaved and band-separated output products are generated.

The uncorrected HDDTs are the primary product sent to the EROS Data Center for dissemination to users. The EROS Data Center can then produce first-generation corrected data in standard and non-standard formats (projections, gammas), the latter by appropriate modification of the distortion coefficients included on the uncorrected HDDTs. The corrected HDDTs and first generation photocopy can also be sent to EROS for ease of reproducing standard products.

The overall processing structure of the IPS is highly parallel; i. e., implementable as a pipeline, or assembly-line, process. Consequently, in light of TRW's experience with correction of ERTS imagery on a minicomputer, a multiple minicomputer architecture was a strong contender for the IPS. This architecture would include two minicomputers for each correction system, one minicomputer for the distortion estimator, and several minicomputers for input reformatting and output product generation. However, the low hardware cost, parallel operation, and existing estimation and correction software are offset by more complicated process control, lack of multiprocessor real-time operating systems, limited core addressability and independent memory ports, and operational limitations such as moving image tapes and data bases between processors.

Consequently, a more conservative architecture was selected for the baseline design, based on a typical midicomputer (i. e., low-cost, 32-bit, multiport memory). The particular hardware selected is not optimized for low cost, but is representative of a straightforward design, capable of handling the specified throughput and accuracies with substantial margin. Modularity is stressed so that, when input/output specifications evolve in the light of this study and future EROS involvement, corresponding cost efficiencies can be realized via design optimization. The IPS system is divided between three processors: one for image correction and two for output product generation. One of the output product generation processors can be deleted if EROS generates and disseminates products for all users, including NASA principal investigators, from corrected or uncorrected HDDTs (the IPS will still generate HDDTs and one photocopy for every scene).

#### 7.11.2.1 Input Reformatting and GCP Extraction Sizing

The wideband sensor data recorder (HDMR) tapes contain multiplexed sensor data recorded in real-time from the sensor downlink at the ground receiving stations. For the TM baseline, samples from 100 detectors are multiplexed in parallel corresponding to each mirror scan, with 80 percent mirror scan efficiency (i.e., 20 percent of scan period (retrace) does not contain image data). During the 20 percent retrace period, calibration measurement data is added by the spacecraft. Separate recorders are assumed for the HRPI and TM data.

For the baseline Te and Honewell TM, the image size is nominally 8192 samples per line for 16 lines/scan of bands 1 through 6 and 2048 samples per line for 4 lines/scan of band 7. The baseline Hughes TM reverse scan has slightly fewer samples. Total data per mirror scan is 795 Kbytes at 1 byte per sample. Assuming a Kel factor of 1.33 for no line overlap across-scan at 30 m IFOV, a 185 km scene requires 6167 lines. At 385 mirror scans per scene, 6160 lines are collected in bands 1 through 6 per scene. A 717 km orbit corresponds to approximately 27.45 seconds per 185 km along ground track, giving 14.03 mirror scans per second, or 11.15 Mbyte/sec average image data rate. At a scan efficiency of 80 percent, the peak data rate recorded on the HDMR is 13.94 Mbytes/sec, or 97.6 Mbits/sec at 7 bits/byte; total image data volume per scene (all bands) is 306 Mbytes.

The TM radiometric calibration data is assumed comprised of 6 calibration point measurements per detector at 10 bits precision. Thus, 6 Kbits are required to be extracted during scan retrace. The data is buffered by the interface and represents an average real-time collection data rate of 84 Kbits/sec. Stored in 2 bytes per sample by the interface, this translates to 1200 bytes of calibration data.

The baseline HRPI design is comprised of 75 chips of 64 detectors each in each of 4 bands for a total of 19,200 detectors. Sampling every 10 m on the ground results in  $12.94E6$  samples/sec. At 7 bits/sample, this is  $90.6E6$  samples/sec. A 48 km by 185 km swath requires 355 M bytes at 1 byte/sample. A HRPI scene is hereafter defined as one-fourth of this data volume, i.e., 48 km x 46.25 km (or 88.75 Mbyte). Thus,

though the data rate from the HRPI is approximately the same as for the TM, the scene rate is four times as great. Consequently, if HRPI scenes are taken continuously, a total of 200 scenes per day would yield 40 TM scenes and 160 HRPI scenes, sufficient for complete CONUS coverage every 17 days. The line-sequential reformat process in the case of the HRPI is concerned with putting pixels in scan order, as well as band separation. As this would require prodigious CPU capability at the desired throughput rates, the pixel-ordering is assumed hardware-assisted by the interface/controller. Total reformatting buffer requirement (double-buffered) is 38.4 Kbytes (two lines of each of four bands), compatible with core buffering.

The HRPI radiometric calibration data is assumed to consist of 2 measurement points per detector at 10 bits each, or 384 Kbits. Transferred as two-byte words, this requires 76.8 Kbytes. To reduce bandwidth required, calibration for 12 chips (768 detectors) is assumed to accompany each scan line (674 scans/sec), representing a data rate (average) of 1.04 Mbyte/sec. If the detectors are sufficiently stable, this can be reduced to 1 chip (64 detectors) per scan line. The former rate corresponds to approximately one calibration update every 4 HRPI scenes (25 sec) for each detector. The time required for transmission of this calibration data and any status data determines the scan efficiency of the HRPI.

Input reformatting to line-sequential, pixel-ordered, band-interleaved-by-line data is accomplished in special-purpose hardware buffers included in the HDMR interface to the GDPF computers. The alternative concepts of reformatting buffering in core memory or rotating mass storage were discarded due to buffer size requirements and throughput limitations and processor involvement for rotating memories.

Line reformatting in core memory would require at least one mirror scan of storage and, more realistically, two, that is, 1.6 Mbyte. Since the HDMR is not record formatted, it cannot be shuttled back and forth for either average data rate reduction or line reformatting. Addressability constraints of available midcomputers would require



addition of rotating memory, preferably double-buffered fixed-head disks (FHD), if special hardware reformatting were not available. In the best of circumstances, disks are capable of sustaining approximately 500 Kbits/sec average transfer rate. However, considerable core data shuffling is still required and disk transfer efficiencies will be considerably reduced by the disk formatting required. Differential transfer rates of the HDMR and disk further reduce effective transfer rates. Consequently, special-purpose hardware buffers containing 1.6 Mbyte are utilized.

The HDMR interface/controller formats data such that the CPU can recognize bytes by the position relative to "start-of-record" and "end-of-record." The HDMR playback speed determines processor throughput and processor bandwidth requirements, as shown in Table 7-12.

Geodetic control point neighborhoods are extracted from the HDMR data stream and stored. Required lines and pixels are calculated pre-pass from spacecraft data on the Master Digital Data Tape and the GCP list. A priori knowledge of GCP locations from attitude, ephemeris, and alignment measurements is accurate to better than  $\pm 500$  m. Consequently, a  $32 \times 32$  GCP will be contained within a 65 line by 75 pixel search neighborhood, or 4875 bytes per GCP neighborhood. At a maximum of 5 candidate GCPs per scene, this requires 24 Kbytes. A maximum requirement of 20 candidates per pass requires 100 Kbytes of output storage. Bandwidths are negligible relative to the image data.

Table 7-12. Processor Throughput and Bandwidth Requirements

Playback Ratio	TM Scenes Per 12 Hrs.	Peak Data BW	Average Data BW	Scan Rate	Line Rate
8	197	1743 Kbps	1394 Kbps	1.753 sec <sup>-1</sup>	170
12	131	1162	929	1.169	113
16	98	871	697	0.877	85
24	66	581	465	0.584	57
32	49	436	348	0.438	43

### 7.11.2.2 Image Correction Sizing

The image correction process performs radiometric and geometric correction on the TM and HRPI data according to calibration and distortion coefficients input from disk or tape. Input data is from the HDMR as reformatted by the hardware input line reformatter.

Radiometric and geometric corrections are performed in hard-wired algorithms to off-load the central processors. Throughput rates of two pixels/ $\mu$ sec are achievable with core memory cross-scan skew buffer and minicomputer control and initialization. Radiometric correction is accomplished in the hardware via point-slope (multiply and add) for the HRPI and table-lookup for the TM. Correction data is updated and loaded once per scene. Along- and across-scan geometric corrections are performed by recursive distortion estimation and interpolation of pixel intensities via limited convolution with an appropriate interpolation function (TRW cubic convolution) as a minimum. Geometric correction is performed in two passes: along-scan followed by across-scan. This increases throughput and allows correction for mirror-scan-length and nonlinearities and for commutation skew between detectors.

The cross-scan-skew buffer retains a sufficient number of input scan lines to subtend at least one complete output (corrected) line. Total buffer storage per band, as a function of maximum direction rotation (yaw) from desired, is shown in Table 7-13. Throughput of the cross-scan-skew buffer is determined by the number of independent memory parts and memory cycle time. For dual-ported, 600  $\mu$ sec memory, rates greater than 1 E6 pixels/sec can be achieved, i.e., over 100 TM scenes per 12 hour day.

Table 7-13. Total Buffer Storage Per Band (As a Function of Maximum Direction Rotation)

Max Yaw	TM Pixels (1 band)	HRPI Pixels (1 band)	TM (7 bands)	HRPI (4 bands)
.03°	65.6 KB	33.6 KB	398 KB	135 KB
.05°	81.9 KB	43.2 KB	497 KB	173 KB
.10°	123 K KB	62.4 KB	746 KB	250 KB



Corrected image data is output to HDDT. Zero fill on the HDDT is used to equalize HDMR input transfer rates and HDDT output transfer rates. Both corrected and uncorrected HDDT products are generated. HDDT output buffer requirements are two TM lines, or 16 Kbytes.

The CPU performs initialization and control of the hardware image correction. Once per pass the radiometric calibration coefficients are loaded into a random-access memory (RAM) in the correction hardware. Total RAM storage requirement is 256 bytes per detector for the TM and 2 bytes per detector for the HRPI. TM RAM storage can be reduced by reloading coefficients at the start of every line at an execution time penalty of less than 5 seconds per TM scene.

#### Distortion Estimation Sizing

Timing requirement for each of the distortion estimation steps is discussed in Section 7.9. Throughput limit is the manual steps required to add new GCPs to the Control Point Library. If most of the GCPs are already in the Control Point Library, the throughput limit is the distortion coefficient calculation process.

The distortion estimation process is based upon the image distortion measurement and correction techniques developed by TRW for ERTS digital image processing. The memory size of the process is equivalent to 32K words. The distortion coefficient calculation, which limits the throughput, is an iterative algorithm with its running time determined by the accuracy desired. Extrapolation of ERTS timing results yields an estimate of 10 seconds per scene for the accuracy required by the EOS data quality requirements. The timing estimate for the total pass processing is estimated to be 30 minutes per sensor for a total of one hour per day.

#### 7.11.2.3 Output Product Generation Sizing

##### 7.11.2.3.1 Magnetic Tape Output Product Generation Sizing

There are two types of magnetic tape output products: high density digital tapes (HDDT's) and computer compatible tapes (CCT's). Daily data volume for each are  $2.2 \times 10^{12}$  and  $1.5 \times 10^{10}$  bits, respectively, for the HDDT's and CCT's. The sizing of the HDDT output generation is considered first.

The HDDT's are specified to have 28 tracks of which 24 are data tracks. The linear packing density is 13.9 Kbits/inch yielding a data rate of 20 Mbits/sec at 60 Ips, a rate compatible with the LCGS tape recorder requirement. The data rate can be changed to any value by using an alternate clock. A 14 inch reel of 9200 feet of tape will hold  $4.6 \times 10^9$  bytes, sufficient volume so that the maximum HDMR tape data volume (10-minute pass of 22 TM scenes or 88 HRPI scenes) can be contained in two reels. This yields a minimum of eight reels of HDDT to cover each day's HDMR volume. Assuming that the pass data for each sensor is to remain physically separated on different HDDT's, the worst case volume distribution (three passes greater than 5 minutes over CONUS), requires eight reels of HDDT tape for each sensor or 16 reels per day on the average to hold each day's total data volume.

The HDDT's are assumed to have three formats: uncorrected, corrected band-interleaved, and corrected band-separated. Assuming the uncorrected HDDT format requires that separate passes be allocated to different tapes, the four copies of HDDT data needed for output products are contained on 64 reels each day on the average. The corrected band-interleaved HDDT can be more efficiently packed without the pass requirement to obtain an average daily volume of 16 reels for two copies required. Band-separated corrected HDDT's contain the image annotation in a format for direct reproduction of the data on the LBR filmwriter. This additional data results in the need for four reels to cover the TM scenes and an increase to five reels to store the HRPI scenes. The required two copies result in the need for an average of 18 reels per day. Table 7-14 summarizes the average number of HDDT reels needed each day.

Table 7-14. Sizing Summary for the Average Number of HDDT Reels Required Each Day

	TM	HRPI	Copies	Total
Uncorrected (band-interleaved)	8	8	4	64
Corrected (band-interleaved)	4	4	2	16
Corrected (band-separated)	4	5	2	18
Average number of HDDT reels per day . . . . .				98

Two HDDT drives are used with each controller and interface to eliminate the rewind and mount/dismount time. Actually, all the HDDT transports will be combined with a matrix switch to increase their redundancy. The uncorrected HDDT generation is obtained as part of the error correction process. It is generated at a nominal transfer rate of 500 Kbytes/sec which results in 8.6 hours of recording time. Assuming five minutes setup time for each of the eight tapes, there is a total of 9.3 hours to obtain the original copy. Using 180 ips to duplicate the tape, the time to make three more additional copies is 54 more minutes for each of the eight tapes with seven minutes used to rewind and mount a new reel. This results in a total of 7.2 hours for output product generation. The corresponding times for the HRPI are  $10.1 + 0.7 = 10.8$  hours for the original copy, and 7.2 hours for copying. The original copy of the corrected band-interleaved HDDT is obtained as the output of the error correction process. Hence, the times for the uncorrected copy apply except that only two copies are necessary reducing the 54 minutes of HDDT transport time to 18 minutes. This results in a copy time of 2.4 hours.

The corrected band-separated HDDT is in a format suitable to be used by an LBR filmwriter. This implies that there will be a 20 percent increase in data volume to provide spacing and annotation. This increased volume results in the need for two additional reels of tape per day, but reduces and simplifies filmwriter processing requirements at EROS and other similar facilities which generate film products. A double-buffer disk system is used to produce the band-separated format; ten 100-Mbyte drives (86 Mbyte formatted) are used for the TM and four drives for the HRPI. This buffer is required to hold all bands of a scene plus 20 percent of the volume for image annotation and spacing. The input rate for the process is 460 Kbytes/sec and the output rate is 500 Kbytes/sec. This yields 9.6 hours for recording and 20 minutes for setup time for the four HDDT tapes for the TM; in addition, 18 minutes per tape for copying the second copy yields 1.2 hours. The HRPI HDDT tapes require  $11.0 + 0.4 = 11.4$  hours for the original copy and 1.5 hours for producing the second copy.

Table 7-15 summarizes the HDDT sizing requirements. The last item, CCT output generation, anticipates the estimate established for the

Table 7-15. HDDT Sizing Estimate

	Reproducing (hrs)	Setup (hrs)	Sum (hrs)
<u>Uncorrected generation</u>			
Master copy	8.6	0.7	9.3
TM	8.6	0.7	9.3
HRPI	10.1	0.7	10.8
Copies			
TM	4.4	3.8	7.2
HRPI	4.4	3.8	7.2
Subtotal . . . . .	34.4 hours		
<u>Corrected band-interleaved generation</u>			
Master copy			
TM	8.6	0.7	9.3
HRPI	10.1	0.7	10.8
Copy			
TM	1.4	1.0	2.4
HRPI	1.4	1.0	2.4
Subtotal . . . . .	24.9 hours		
<u>Corrected band-separated generation</u>			
Master copy			
TM	9.6	0.3	9.9
HRPI	11.0	0.4	11.4
Copy			
TM	0.7	0.5	1.2
HRPI	0.9	0.6	1.5
Subtotal . . . . .	24.0 hours		
CCT output product generation subtotal = 8.0 hours			
Total average HDDT transport operating time per day = 105.3 hours (Copy generation requires two transports)			

worst-case timing. It is observed that the average daily HDDT transport operating time is 105.3 hours. Based upon a 12-hour work day, there is a minimum requirement for nine transports to satisfy the average loading. The baseline configuration uses 20 transports, two drives with each of the ten units. An increased number of transports increases the reliability. The addition of a manual HDDT matrix switch coupling all the transports increases the average redundancy from a factor of 20:9 to 11:1 based upon the above loading analysis.

The generation of CCT output products will now be discussed. There are two tape technologies used for output CCT tape products: 1600 and 6250 bpi. Within each tape density, a number of formats should be made available. The 6250 bpi will be used for the larger volume formats and the 1600 bpi for the smaller. Table 7-16 describes the baseline capability. For sizing purposes, two cases will be considered. The first case is 1/16 of a TM scene, 512 pixels for each line, on a 1600 bpi tape for all the CCT products, a total of 96 reels. The second case is 1/4 of a TM scene on a 6250 bpi tape for all CCT products, a total of 24 reels.

All reels are assumed to be a standard 2400-foot length. Hence, the 125 ips drives require 230 seconds to reproduce and the 250 ips require 115 seconds. It is assumed that three minutes are necessary between reel replacements to setup the CCT format software used; two drives per controller allow simultaneous rewind and mount/dismount during tape production. Table 7-17 summarizes the timing estimates for the two cases. It is observed that CCT tape production can be accomplished in 8 hours (one shift) using just the one 1600/6250 unit with two drives.

Table 7-16. Characteristics of Magnetic Tape Units  
for Output Product Generation

---

One combined 1600/6250 bpi unit: 2 drives; 400 Kbytes/sec at 250 ips for 1600 bpi; 780 Kbytes/sec at 125 ips for 6250 bpi; 45 sec rewind time

Three 800/1600 bpi units: 2 drives; 125 ips yields 100 Kbytes at 800 bpi and 200 Kbytes/sec for 1600 bpi; 114 sec rewind time; shared with system and other applications

---

There are a variety of formats possible. Band-separated products are most efficiently generated using band-separated HDDT's and the equivalent statement holds for band-interleaved products. The worst-case, then, for buffering and processing occurs when band-interleaved products are required in pixel sequential, rather than line-sequential, order. This results in a buffer requirement of 102 Kbytes, using a double buffering technique and the TM as an upper bound, which can be easily accommodated in 32 K words of storage (2 16 K word increments). It is to be noted that the large dual access TM 1000-Mbyte disk is only used for

Table 7-17. Output Tape Generation Timing Estimates

---

Case One: 96 1600 bpi tapes

Reproduce:

One unit (400 Kbytes/sec)	3.1 hours
Two units (200 and 400 Kbytes/sec) . . .	2.5 hours

Setup time (average of 3 minutes/tape)	<u>4.8</u> hours
--	------------------

Worst-case total	7.9 hours
------------------	-----------

Case Two: 24 6250 bpi tapes

Reproduce:

One unit (780 Kbytes/sec)	1.5 hours
---------------------------	-----------

Setup time (average of 3 minutes/tape)	<u>1.2</u> hours
--	------------------

Worst-case total	2.7 hours
------------------	-----------

Worst-case CCT generation . . . . . 7.9 hours

---

10 hours during the band-separated corrected HDDT product generation. This means that these disks will be available for 2 hours during a 12-hour work day for CCT formatting use. This capability provides the answer to the pixel-interleaved, band-interleaved CCT formatting processing.

#### 7.11.2.3.2 First-Generation Film Production Sizing

There is a requirement for film output products. Positive and negative first-generation master copies of all images processed are needed to produce the other film products required by investigators. Consideration of the production of film products from these master copies is contained in Section 7.7.

Principally because of the specified 9.5 inch film format, a laser beam recorder (LBR) is to be used for the filmwriter. Electron beam recorders using present technology have a field of view well below 9.5 inches, something on the order of 5 inches. The film format transfer rate and resolution requirements also preclude consideration of CRT technology when compared to LBR technology.

The LBR has two potential modes for generating the first-generation film products for the band-separated corrected HDDT: either directly from the formatting process or from the HDDT containing the formatted

data. In either case, minimal processing is required by the LBR as the sensor data is already formatted for film production, having been merged with the image annotation data during the band-separation formatting process. In the direct mode, the continuous film transport of the LBR allows the film images to be generated at the same data rate as the HDDT corrected, band-separation format data is recorded. This requires 9.9 hours for the TM and 11.4 hours for the HRPI to produce one of the types of first-generation products, say the negative transparency. The LBR can have data rates much larger. Therefore, the second mode can be recorded with the HDDT running at 120 ips for an input data rate of 5.0 Mbyte/sec. This yields a total processing time for the generation of the positive transparency of 1.9 hours for the TM and 2.0 hours for the HRPI.

To achieve the maximum throughput through the LBR, the HDDT input is played twice to get the positive and negative transparency for the second mode of production. This requires a total time of 3.8 hours for the TM and 4.0 hours for the HRPI. This represents only 7.8 hours of required LBR operation per day and could easily be satisfied by one unit. This is the preferred approach because it requires only one LBR, and still has the flexibility to produce special film product after the 7.8 hours of required recording time.

#### 7.11.3 Image Processing System Hardware Design

The section presents the image processing system hardware design. The actual hardware configuration is presented first, followed by a discussion of the design implementation of hardware required to support the CDPF baseline.

The image processing system hardware consists of three Xerox 550 computer systems with standard peripherals, special system peripherals, special purpose hardware, and high density magnetic tape recorder systems. These computers are in the medium-scale 32-bit class of general purpose computers. It was chosen to be the basic building block for the subsystem implementation of the four basic processing functions because it offers the computational capacity necessary for each of the functions while offering the input/output flexibility and memory structure of a larger system. This flexibility is essential to support the extensive use of special purpose hardware in the baseline design.

Figures 7-36, -37, and -38 present the hardware configuration of the three computer systems. The three systems are referred to as the error correction subsystem; the estimation, formatting and film generation subsystem; and the formatting and tape generation subsystems. The error correction subsystem is allocated the function of performing the image correction on the TM and HRPI raw data and generating the primary output product, corrected HDDT's. The error correction subsystem is based on a single Xerox 550 CPU, 176K 32-bit words of main memory, a set of support peripherals and the special-purpose hardware necessary to support the TM and HRPI image correction streams.

The basic Xerox 550 system with 32K of memory is used to support the process control for the two image correction chains. The throughput required is quite low with an average rate of less than 0.15 MIPS required to support the process control functions. This is well within the 0.35 MIPS capacity of the Xerox 550.

There are two separate image correction chains. One each for the TM and HRPI. Each image correction chain consists of a HDMR system interface, a hardware line reformatter, along- and across-scan correction hardware, a segment of 32-bit main memory and a pair of HDDT systems. The magnetic tape systems have only control interfaces to the Xerox 550 system for this configuration. All data flow is via direct data buses between the magnetic tape systems and the special-purpose hardware. The large core across-scan skew buffers are configured as part of the Xerox 550 system. However, this core is normally not used by the CPU except as a means of loading the large radiometric calibration constant arrays into the along-scan correction hardware. The normal use of these core modules is via dedicated memory ports and direct memory access controllers to the TM and HRPI image correction chains. The assignment of separate ports to the CPU modules and each of the image processors allows interference free use of the memory as separate buffers but still allows access by the main CPU if necessary.

The distortion correction coefficients, calibration data, and annotation data are passed to the error correction subsystem via cartridge disk packs. One cartridge is generated for each HDMR tape.



The estimation, formatting, and film generation subsystem is allocated the error measurement data extraction, distortion calculation and film output product generation functions. This configuration is supported by a single Xerox 550 CPU with 128K words of 32-bit main memory, standard peripherals and the special-purpose hardware required to support the HDMR and HDDT systems.

The computational workload on this system is modest. The major tasks of prepass setup, GCP extraction and processing, distortion estimation, and calibration data management require less than 0.10 Mps capacity for a two-shift operation at the system loading specified in Section 7.11.4. The data base maintenance tasks for calibration data and the GCP library are low throughput tasks once the initial data base is established.

These tasks also would not normally be run during first-pass processing since they would compete with the GCP processing for the display system. The remaining tasks are basically input/output related and are limited by the available permutations of peripherals to accomplish low volume output generation.

The system memory configuration was sized to support the basic system software, pass one application software, and adequate input/output buffers to allow output product generation during pass one.

The first-pass processing of the sensor raw data tape is supported by the MIOP interface to the GCP extraction hardware and HDMR subsystem. This is the primary hardware interface for this function.

The GCP processing and distortion estimation processing are supported by the display system, 100 Mbyte of direct access for the GCP library and a cartridge disk system for distortion correction coefficients and calibration data.

The output product generation tasks involve the use of an HDDT either as an input and/or output medium. The HDDT systems have two independent data interfaces: one high rate port for use with the LBR and other HDDT's, and a separate MIOP interface for providing a maximum data rate of 750 Mbyte/sec into the CPU memory. The control interface is via the direct input/output lines. An HDDT-to-HDDT tape duplication operation, then, would only involve the control interface and the data

flowing directly between the tape controllers. High data rate LBR operation would use the high-speed bus from the HDDT controller although an image could be sent to the LBR from the main memory and/or large disk store via the MIOP interface.

The generation of band-separated images and special editing of the image data tapes is supported by the use of the 1000 Mbytes disk system. This disk system is also provided with dual data paths to allow scene-by-scene processing at throughput rates approaching the average bandwidth of the disks.

The formatting and tape generation subsystem is allocated the function of performing the output product formatting and generating the output tape. This configuration is supported by a single Xerox 550 CPU with 128K words of 32-bit words of main memory, standard peripherals, and a dual density 1600/6250 bpi high performance tape system.

The computational workload on the system is also modest. The major band-separated task and generation of user requested CCT require less than 0.10 Mips capacity for a two-shift operation. The generation of band-separated images is again supported by the 1000 Mbyte disk system in the same manner as the previous subsystem. This additional capability is necessary to satisfy the throughput requirement for a first-generation film product of each image. User requested CCTs may be generated at either 1600 or 6250 bpi via the dual density tape system. Editing may be done to or from the 1000 Mbyte disk system.

The selection of the Xerox 550 for use as the baseline computer was almost a direct fallout of the baseline design concept of using special purpose hardware for the image processing. The special purpose hardware removes the requirement for a CPU with a high throughput. Without the requirement for a fast CPU, the use of minicomputers becomes an attractive solution, both from a cost viewpoint and the high degree of parallelism possible in the processing stream. Unfortunately, the modularity of a minicomputer system also causes several problems. The cost of the process control software can be considerably higher than in a more integrated system. This is partially due to the lack of mature, sophisticated real-time operating systems for the mini's. The minicomputer

systems also tend to have small memory address spaces which tend to further fragment the systems. Further, the current systems tend to be limited in the I/O structures possible due to single-ported memories offered by the manufacturers.

Rather than attempt to deal with these problems as part of the baseline design, a more conservative design approach was taken. This was done to provide a more straightforward design even though it might not necessarily represent the lowest cost approach. The decision was made to use a midicomputer approach as the baseline.

The midicomputer hardware currently available provides a fairly narrow choice for a system design that is concerned with reasonable cost but requires a flexible system with good I/O capabilities. The selection is usually made from systems built by Xerox, System Engineering Laboratories (SEL) or DEC.

SEL has one basic family of 32-bit machines with two CPU's (the 8500 and 8600), offering a 30 percent spread in throughput. The SEL 85 is roughly equal to the Xerox 550 in speed and the SEL 86 has slightly less machine power than a Xerox  $\Sigma 9$ . The SEL machines have several drawbacks that effectively eliminated them from consideration. First the memory size is limited to a maximum of 128K words. This would have required a fourth machine in the baseline configuration. Second, the selection of peripherals on the SEL hardware is much more limited than either Xerox or DEC. The 100 MB disk system, in particular, offered by SEL is limited to a maximum capacity of 800 MB/system. Finally, the I/O structure of SEL 85 and 86 would have required the development of a special MIOP since the standard MIOP cannot be used with 100 MB disks or high speed CCT systems.

The DEC PDP-10 class machines have many of the desirable features necessary to support the CDPF. The PDP-10 offers two basic processors — a large memory space (4M words) and a large selection of peripherals. However, the lack of direct byte addressability in the memory and high minimum configuration costs discouraged this approach.

The Xerox line of 32-bit machines presented three apparent choices for the baseline design. The Sigma 9 series machines have all the

desired features in CPU, I/O structure and large memory space. However, the CPU power is much greater than required and costs accordingly. The 500 series machines offer two basic CPUs, the 550 and 560 which have a CPU power of 0.35 MPS; this is in the right range. The 560 is basically a business and time-sharing oriented machine with several features, such as a decimal instruction set, that are not required for the IPS functions. The 550, then, was selected as providing the necessary CPU speed, adequate address space and a flexible multi-ported I/O structure to be used in the IPS baseline.

The major peripheral subsystems for the IPS are discussed in the following section. The basic considerations for each function are presented and the equipment chosen to support each function briefly discussed. A short description of the Xerox CPR operating system is also presented in Section 7.11.3.8.

#### 7.11.3.1 HDMR Subsystem

The HDMR subsystem provides the main interface into the image processing system for sensor data from the EOS ground stations. This subsystem provides the capability to playback the HRPI and TM sensor data tapes and format the data into a line-sequential, band-interleaved format with a minimum of CPU intervention. The resultant savings in CPU time is consistent with the IPS baseline design goal of removal of high data rate processes from general-purpose hardware. A functional overview of the HDMR subsystem is shown in Figure 7-36.

##### 7.11.3.1.1 HDMR Recorder/Reproducers

The HDMRs used in the image processing system are the same basic design, the Ampex FR-2042, as used in the ground stations.

Three FR-2042 HDMRs are configured in the image processing system providing one HDMR for each sensor data processing chain and one for the error measurement data extraction. This quantity represents the minimum number of recorders that will support the operational time-line discussed in Section 7.11.4.

A matrix switch system, provided between the input HDMRs and the image processing system, allows the HDMRs used to support the first pass processing to be used in the second pass to provide

ORIGINAL PAGE IS  
OF POOR QUALITY

7-157

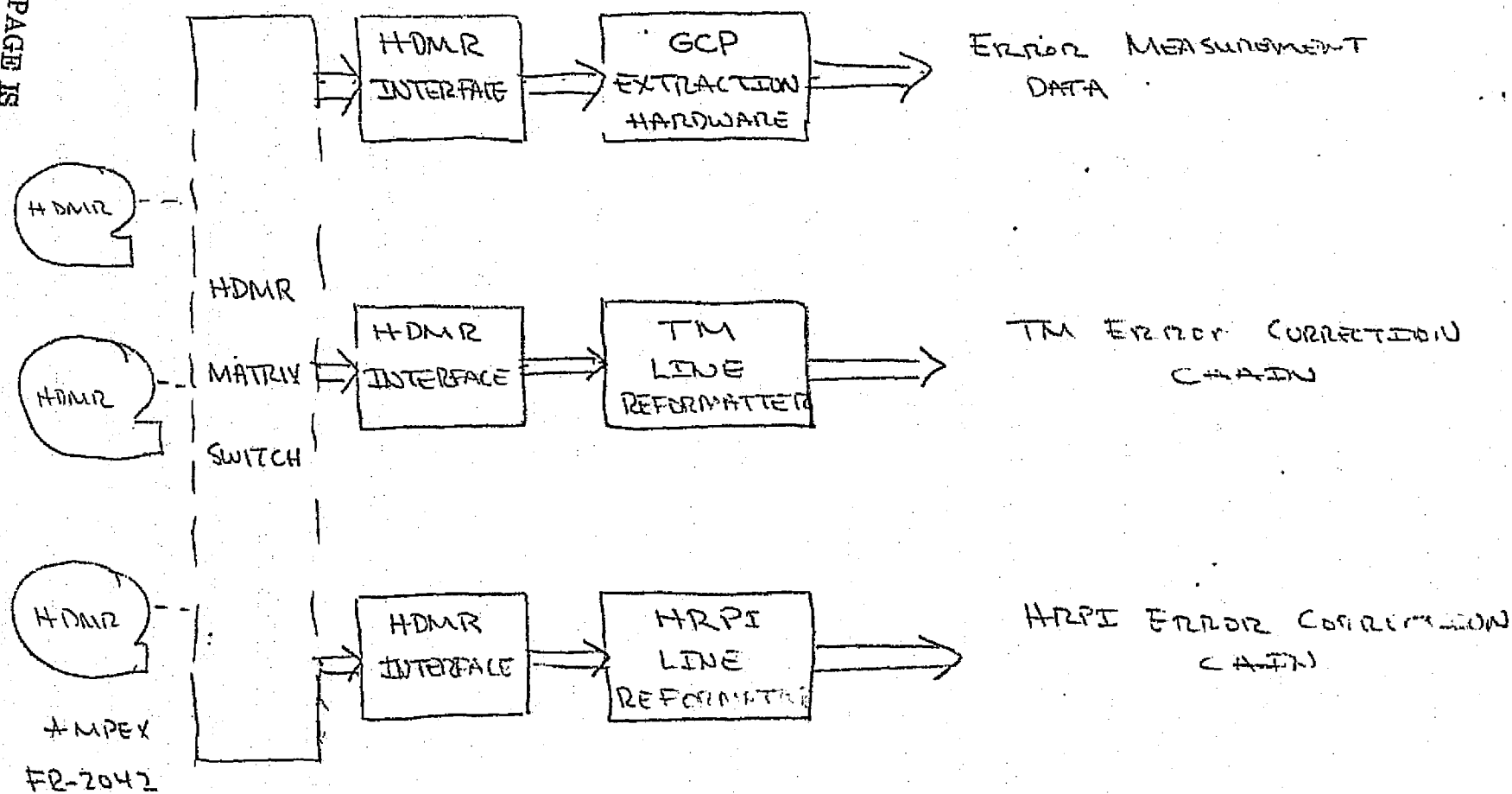


Figure 7-36. HDMR Subsystem

operational overlap of tape rewind and loading operations. This matrix switch also allows the use of any HDMR as the input device for any of the processing functions. Additional HDMRs may be added to the HDMR pool at any time to improve system availability or throughput.

Each of the HDMRs is configured to include a full complement of record/reproduce electronics. The rationale for this is discussed in the section on HDDTs, Section 7.11.3.7.

#### 7.11.3.1.2 HDMR Matrix Switch

The HDMR matrix switch accepts the serial bit streams from the reproduce electronics of the HDMRs and routes it to the HDMR interface associated with each processing system. The matrix switch is a simple manual switch based on conventional wideband video technology for the serial data lines and T-bar switching for the control interface.

#### 7.11.3.1.3 HDMR Interface

The HDMR interface is the basic interface between the serial HDMR data stream from the matrix switch and the sensor data formatting hardware. The interface accepts the serial data stream and clock from the HDMR reproduce electronics and performs the basic frame synchronization on the data stream. The frame-synchronized data is passed to the decommutating section where the data is broken down into line/band serial streams for the line reformatting and GCP extraction hardware.

The HDMR interface is the same for each sensor. The sensor decommutating pattern and data rate are manually selected according to the type of sensor data (TM or HRPI) being reproduced by the HDMR. The spectral band to be used for GCP data is selected by a programmed interface.

The HDMR interface is controlled from the host Xerox 550 system via the direct input/output (DIO) line. This DIO interface also provides the programmed control function for the HDMR transport via the HDMR I/F and the matrix switch.

#### 7.11.3.1.4 GCP Extractor

The formatting system is provided with a special front-end processor to extract GCP search regions and calibration data from the raw sensor data. The GCP extractor allows the first-pass processing to take place at a data rate much higher than would be feasible if the data editing were done in software. For a playback speed of one-sixth real-time, the data bandwidth required for GCP extraction is reduced from 2.5 Mbyte to 2.5 Kbyte.

The GCP extractor operates on the decommutated data received from the HDMR I/F in two ways. First, the GCP search regions are pulled out of a single band on a scan-by-scan basis using control information provided by the prepass setup processing. This data is blocked into an internal holding buffer and passed to the formatting CPU via an MIOP whenever a specified search region is completed. The second type of processing on the input stream is the extraction of the sensor calibration for each band. This data is also blocked and sent via the MIOP to the CPU.

The GCP extraction hardware is designed to process either the baseline TM or HRPI. The difference in sensor data format is compensated for by changing the hardware control tables used to direct the demultiplexing process. This is a manual control interface. The actual control tables defining the boundaries of the GCP search regions are sent to the GCP hardware via the same MIOP interface used by the pixel data.

The calibration data for the two classes of sensors is handled in a slightly different fashion. The TM calibration data is removed from the data stream during the mirror retrace time and transmitted periodically to the calibration data base. The baseline HRPI does not have the equivalent repetitive calibration function as the TM; that is, the current design requires the HRPI to be placed in a calibration mode periodically and the resultant data sampled by the GCP extraction hardware. This periodic sample would be sent to the calibration data base.

#### 7.11.3.1.5 Line Reformatter

Each of the image processing chains in the image correction system has a hardware line reformatter to provide a line-sequential, band-interleaved sensor data stream. This data stream is double-buffered internally in a dedicated memory. The output from the buffer is placed on a parallel data bus for use by the along-scan correction hardware. The HDDT system, tasked to generate any required uncorrected HDDT image tapes, is also attached to this data bus.

The line formatter accepts the partially demultiplexed sensor data from the HDMR I/F and sorts it into the internal buffers under control of hardware control tables. A set of control read-only memories (ROM) is required for each sensor data format. Normal use of the line reformatter will have one unit dedicated to each sensor.

The major difference between the TM and HRPI line reformatters will be in the amount of buffer memory required. The HRPI will require a buffer size of 60 Mbytes to reformat the baseline HRPI; whereas, the TM baseline sensor will require a buffer of 1.6 Mbytes or 200 lines. The sensitivity of the buffer size to sensor design is discussed in the sizing analysis.

The control interface to the line reformatters is provided via a DIO interface to the host Xerox 550. Control information is limited to initialization and status data.

The output data bus is designed to provide a synchronous, parallel interface to the across-scan error correction hardware and to an HDDT controller.

#### 7.11.3.1.6 Interactive CRT Display

An interactive image display CRT is included for the purpose of Control Point Library Maintenance; that is, addition, deletion, and modification of control points in the Control Point Library. The CRT contains an internal refresh memory to minimize CPU interaction requirements. The Comtal 8000 series is typical of the required display, containing sufficient storage for several 512 x 512 images of up to 256 gray level intensities. Hardware contrast enhancement is available (as well as color



density slicing). A trackball or joystick, together with hardware-generated cursor, allows manual designation of image feature locations to the CPU. An entire 512 x 512 image can be replaced by the CPU in less than 2 seconds. A state-of-the-art fixed-head disk (Data Disk) is used as refresh store.

Alternative image displays are available using solid-state refresh memory, however, with substantially lower performance and flexibility at slightly higher cost.

#### 7.11.3.2 Image Correction Hardware

The baseline image processing system uses special purpose hardware throughout the image correction processing string for each sensor. The use of special purpose hardware allows the baseline design to process two sensor data strings in parallel at a minimum rate of 3  $\mu$ s per pixel. The main CPU is required only to perform the process control functions and serve as the host for the core buffer memories for each string.

The baseline design image correction hardware would be designed and fabricated for the EOS application. This hardware would be based on the prototype CCI now operational at TRW. The used commercial hardware for these functions was investigated but none was found satisfactory for a variety of reasons. See Section 7.11.3.2.4 for additional discussion.

The functional structure of the image correction chain is shown in Figure 7-37. Each sensor chain is essentially the same in processing performed. The TM and HRPI chains differ mainly in the radiometric calibration module and the sizing of the skew buffer. The following discussion would be applicable to both sensors except as noted in the text.

##### 7.11.3.2.1 Analog Scan Corrector

The along scan corrector (ASC) performs the first step of the sensor image correction processing. This processing includes receiving the raw sensor data from the line reformatter data bus, radiometrically calibrating each pixel, applying the along scan correction and placing the corrected pixel into the skew buffer for use by the across scan corrector (CSC).

ORIGINAL PAGE IS  
OF POOR QUALITY

7-162

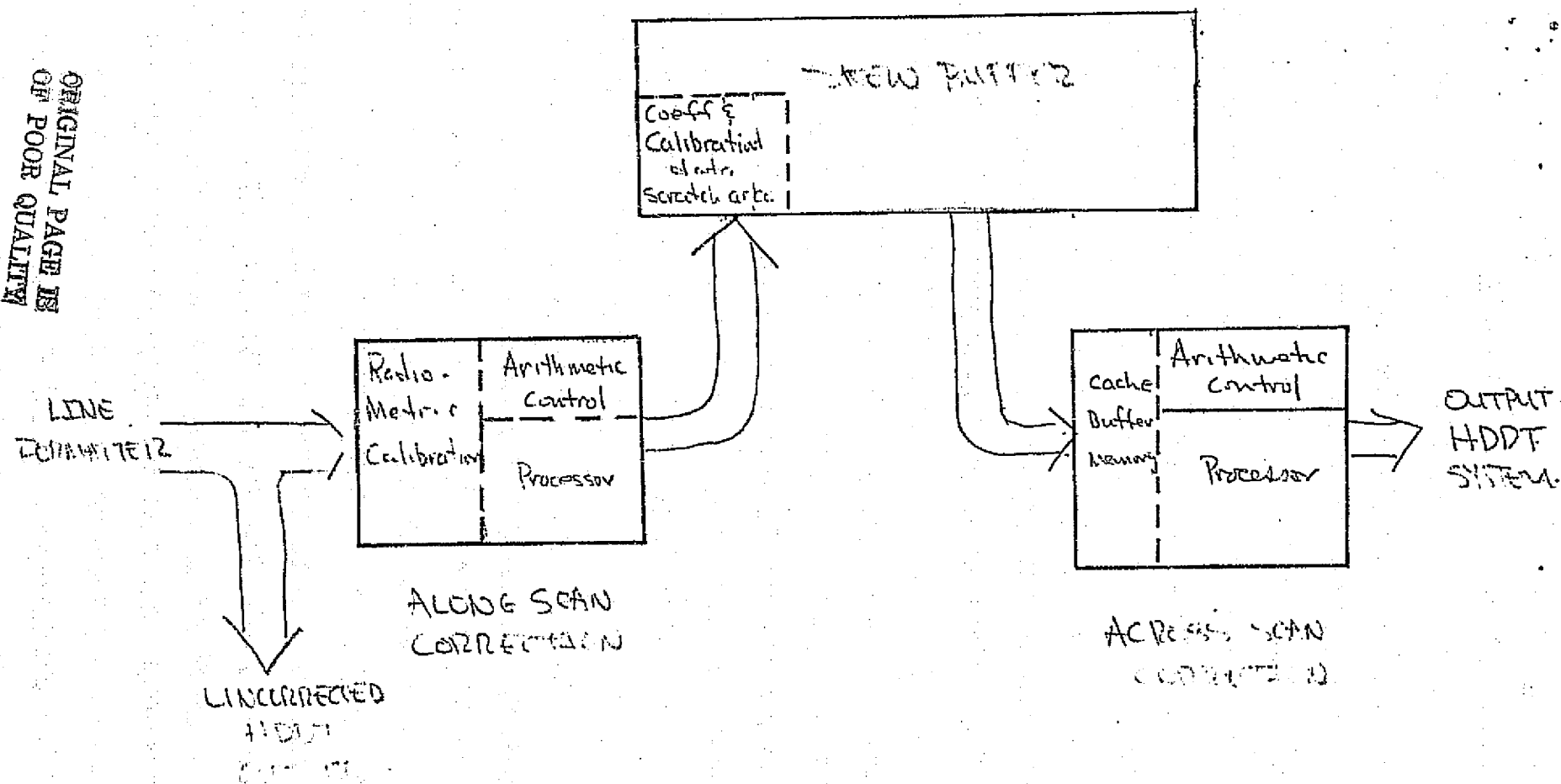


Figure 7-37. Image Correction Chain

The ASC is composed of three major sections: input data interface, radiometric calibration, correction and output data interface.

#### 7.11.3.2.2 Skew Buffer Memory

The skew buffer bulk memory is provided to store sufficient along scan corrected data to allow the across scan skew corrections to be performed as an inline process. The sizing of the buffer differs for the TM and HRPI. The configured memory for the baseline HRPI is 48K 32 bit words and 96K words for the baseline TM. These sizes represent the sizing estimates discussed in Section 7.9 and Section 7.11.4 of this task rounded to the next highest 16K word increment of memory.

Each buffer memory is configured with a pair of dedicated ports for use solely by the image correction string attached to it. This configuration is shown in Figure 7-37. The dedicated ports are bussed together to form an input bus and output bus each attached to a DMP. This separation of the input and output paths provides the minimum memory access interference for a continuous flow process such as image correction.

#### 7.11.3.2.3 Across Scan Corrector

The across scan corrector (CSC) performs the final step of the image correction process. The CSC reads pixel data from four adjacent lines at a time from the skew buffer and generates one continuous output line. The processed output lines are passed directly to the output HDDT system via a parallel data bus.

The structure of the CSC is similar to that of the ACS consisting of an input and output data interface, corrector module but no radiometric calibration module.

#### 7.11.3.2.4 Alternative Hardware Solutions

The TRW cubic convolution interpolation algorithm has been under development for some time as part of an effort to develop improved image processing techniques. During this development cycle the algorithm has been implemented in software on several computer systems, notably the CDC 6500 and DEC PDP 11/45. As the software development progressed, a parallel investigation was carried out as to the feasibility and/or desirability of using dedicated hardware to perform the convolution interpolation to achieve the best cost/performance for image correction.

The choices for this hardware implementation seemed to lie between a completely hardwired algorithm box, a microprogrammed minicomputer, or one of several special purpose signal processing systems then beginning to become available. The design goal was a processing speed of one pixel per microsecond.

The microprogrammed minicomputers were eliminated due to lack of processing speed on the machines then available. A secondary problem occurred in the memory porting and I/O architecture not being able to support the data rates on a sustained basis.

The special purpose signal processors showed a potential for a solution but were not being delivered in the time frame we required.

The resultant decision was to build a prototype dedicated processor for the cubic convolution algorithm. The design was to incorporate the maximum parallelism in processing and have a number of special I/O interfaces to allow research into system configurations utilizing the DEC PDP 11/45. The finished hardware was integrated into the TRW signal processing facility and operates at an internal rate of 0.6  $\mu$ s/pixel.

As a result of this experience, the baseline design for the IPS image correction was based on dedicated hardware processors. The same basic tradeoffs exist now as before for the implementation of the cubic convolution algorithm. However, in the case of the along scan correction, it does not appear that a cost competitive alternative is available to the hardwired processor. The across scan system does, however, have some additional complexity that may have several potential solutions in commercial hardware.

The most promising candidates are the Culler Harrison AP-120 and the Signal Processing Systems SPS-81. Both of these devices have the basic design flexibility in I/O and processing capability to perform the across scan correction but cannot achieve the desired throughput without modifications.

#### 7.11.3.3 Large Disk Store

A large direct access storage system is provided each formatting system to allow manipulating of the image data. The two primary editing

and reformatting requirements, as discussed in Section 7.11.2.3, are the generation of band separated image data and the creation of edited data for CCTs. The scene buffer for the band separation process sets the size requirement for the disk system. This will require a minimum of 300 Mbytes per buffer for the TM and 360 Mbytes per buffer on the HRPI.

The disk buffer selected for the baseline design is the standard Xerox 7276 high density disk system. This system will support a maximum of  $1.3 \times 10^9$  bytes for a 15 spindle system. Each disk drive has a formatted capacity of 86 Mbytes. The standard Xerox format is based on a 1024-byte sector. Using this sector size gives each spindle the capacity of 10.5K TM lines or 16.9K HRPI lines without resorting to special formatting. The total number of spindles required to provide a full double buffer are 10 for the TM and 4 for the HRPI using the baseline sensor design.

The disk drives are provided with a dual access feature to allow each drive to be attached to two separate disk controllers (see Figure 7-35). This feature is necessary to allow simultaneous access to both halves of the double buffer via two separate MIOPs on separate I/O clusters. This dual access increases the net data bandwidth through the disk buffer to near the track average of 678 Kbyte/sec.

A possible alternative implementation for the large disk storage system would be based on the STC Super Disk system. These disk drives are based on a module having a storage capacity of 800 Mbyte on four double density spindles. The basic system as it currently exists has a maximum capacity of  $6.4 \times 10^9$  bytes with the same basic characteristics as the single spindle system but with improved access time. The real improvement in performance would come with the increase of the transfer rate which could be accomplished by the addition of a dual transfer mode using two spindles or by increasing the recording bit density. Both solutions would require controllers and drive development.

#### 7.11.3.4 Computer Compatible Tape

The capability to generate image products for small volume users or those users unable to justify a HDDT system will require a conventional

CCT system for the IPS. The nominal industry standard today in CCTs is based on 800 bpi NRZI and 1600 bpi PE tape technology. The anticipated growth in tape technology over the next 2 to 5 years will be expanded to include the 6250 GCR technology now entering commercial practice.

The CCT subsystem chosen to meet the CCT output product requirements is a dual density 1600/6250 bpi PE/GCR drive and matching controller. This class of drive is currently being delivered by two vendors, IBM and Storage Technology Corp. (STC), and will undoubtedly be produced by others as the use of 6250 bpi spreads. The baseline design uses a drive supplied by STC. STC currently seems to be the most likely vendor to be used by Xerox to supply their 6250 drives. (STC currently is designing an interface for the  $\Sigma 9$  although Xerox will not commit to a direct quote for the 550 systems.) The STC tape drive is a dual speed unit as well as dual density. The highest speed, 250 ips, is used at 1600 bpi to yield a transfer rate of 400 Kbit/sec and a tape copy time of less than 2 minutes/2400 feet. The 125 ips speed is used at 6250 bpi to give a high transfer rate of 780 Kbit but still remain within the MIOP bandwidth of 1 Mbyte.

#### 7.11.3.5 Cartridge Disk System

The output from the first pass on the sensor raw data tape is a set of distortion correction coefficients, calibration data and annotation files all of which are used in the second pass on the image data. Since the processing time for the first pass is less than that for the actual image correction processing, some method must be provided for the storage of the first pass output between the execution of pass one and two. Further, these data files must be physically moved along with the sensor tape from one processing system to another with some in-transit storage delay.

The use of an on-line shared data base between the three processors in the image processing system did not appear worth the cost of the additional direct access storage, peripheral switch gear, and software development. A further potential difficulty with the shared data base is the access contention problem associated with one or two disk drives being shared in a time-critical environment. A removable media device kept with the corresponding HDMR tape seemed a better approach.

A cartridge disk was chosen, predicated mainly on convenience and reliability, over magnetic tape as the file transport mechanism. The performance requirements are certainly within the range of tape or disk systems. However, our experience with cartridge disk drives has been far superior to that with tape drives within the same price range. This is based on usage in several in-house minicomputer installations. The additional cost associated with the disk cartridges was felt to be outweighed by the operator convenience and easier file design afforded by the disk.

The formatting system is provided with a single Xerox 3242 5 Mbyte cartridge disk drive and Xerox 3211 controller. The image correction system has a single controller and a pair of drives, one for each sensor processing chain. The resultant 5 Mbyte capacity per cartridge is more than adequate to carry the 3 Mbyte coefficients, calibration data and annotation data for each pass tape.

#### 7.11.3.6 Filmwriter (LBR)

There is a requirement for first-generation positive and negative transparencies with a 241 mm (9.5 inch) film format. The film has to be generated from digital data and will be presented in a standard output coordinate system. Three technologies were investigated: cathode ray tube (CRT), electron beam recorder (EBR), and laser beam recorder (LBR).

The CRT technology does not have the resolution or filmwriting speed that the other two technologies possess and, hence, was eliminated from consideration. The EBR technology does not have the capability to satisfy the 241 mm film format presently being limited to around 175 mm. Therefore, by process of elimination, the LBR is the technology to use. Fortunately, it has the capability to satisfy the output film production requirements.

Three companies were contacted: Goodyear, CBS, and RCA. Since there was a procurement for an LBR system being initiated by GSFC during this same period of time, there understandably was some reluctance by the parties to discuss their LBR system in detail. Nevertheless,

sufficient information was obtained to validate the design concept for the utilization of an LBR for the filmwriter.

The characteristics of the LBR are as follows. It would have high resolution, 50 percent MTF at 40 lp/mm, with f/32 optical size. Its bandwidth could support a rate of 5.0 Mpixels/sec with up to 8 bits of grey level. The long-term position accuracy would be on the order of 0.1 percent, using a spinning mirror approach (as opposed to a galvanometer) for line formation. The 241 mm film would be provided on a continuous transport. An intercept-driven line buffer would be an integral part of the LBR, with a capability of storing a number of lines of digital data. Technology appears to exist to develop such an instrument.

#### 7.11.3.7 High Density Digital Tape Subsystem

The high density digital tape subsystem provides the means of generating the digital image tapes required for archival purposes, input to film product generation and large volume data users. It also provides a tape format interface for the LCGS users. These tapes are produced as primary products by the image correction system and as secondary products during output product generation. The types and format of the HDDT output products are discussed in Section 7.11.2.3.1. The major elements of the HDDT subsystem are discussed in the following sections.

##### 7.11.3.7.1 HDDT Matrix Switch

The HDDT subsystems utilize a matrix switch between the tape drive record/reproduce electronics and the controller interface similar to that used in the HDMR subsystem as described in Section 7.11.3.1.2. The switch is particularly important to the HDDT system since, without some method of HDDT drive reconfiguration, at least 6 additional drives would be necessary to maintain an acceptable system availability.

##### 7.11.3.7.2 High Density Digital Tape Transports

The tape transports selected to support the high density digital tape requirement are the next generation of the AMPEX FR-1928 drives used in the ERTS program. The FR-2000 is primarily an improvement in the basic mechanical design of the transport. These improvements result in reduced dynamic skew, flutter and timing errors compared to the FR-1900



series. One major change was in the top plate design to allow the use of 16-inch tape reels. This increases the maximum tape capacity for standard tape to 12.5K feet, an increase of 40 percent from the FR-1900. This could reduce the number of tapes required by some HDDT users although it does not impact the standard output products.

The HDDT system uses the FR-2000 drive in a 28 track configuration. The standard wideband electronics are used in conjunction with the AMPEX Miller code digital electronics to achieve a high density digital system. The 28 track configuration is allocated as 24 digital data tracks, 2 sync tracks, and 2 auxiliary tracks; one for tape servo control and the other for tuning and annotation data.

The baseline bit density is nominally 14K bpi. This density with the 24 data tracks gives a transfer rate of 20 Mbits/sec at a tape speed of 60 ips; this is one of the design interface speeds to the LCGS. This data density also yields the nominal 500 Kbit/sec data transfer rate at 15 ips used in image correction processing; overhead data volume allows this division by 4 to get the nominal rate. The data transfer rates from the HDDT are directly controlled by the tape loop servo system. The basic speed range for the HDDTs is set by using a maximum speed of 120 ips and then using binary division of that speed. However, an additional reference oscillator will be provided to allow an 180 ips top speed for use in tape to tape copy operations. The extra speed derived from this reference (90 ips, 45 ips, etc.) may be used to provide additional throughput rates when the tape and sensor formats are finalized.

All of the HDDTs in the system are configured with a full set of record/reproduce electronics even though some position may require only record on playback capability. This was done in the baseline for several reasons. First, the full complement of electronics allows any HDDT to be placed in any position via the matrix switch for complete reconfiguration flexibility. This is a convenience, but considering the number of HDDTs in the system some restrictions in this area would not be critical. However, the crux of the matter is system maintenance and tape interchangeability. AMPEX feels that a system with many drives in several locations (LCGSs) has fewer maintenance and set up problems if each

system has the full set of electronics. The most reliable and quickest setup procedures are based on the use of a reference tape and closed loop alignment of the drives. Both of these procedures require a dedicated set of electronics. AMPEX has considered the development of a special test set for the wideband electronics and the Miller encoder/decoder dropped the project as not being cost effective for the total number of systems in the field.

#### 7.11.3.7.3 HDDT Controller/Interface

Each HDDT position is equipped with an HDDT controller. This controller supports a two-drive interface into the HDDT matrix switch and two data interfaces. The controller will support one data transfer operation from one data port to one tape drive. Control operations may be performed on the drive not engaged in data transfer operations.

The controller design is based on the use of a Xerox System Control Unit (SCU) as the principle element. The SCU is microprogrammed and is used to provide not only control functions and data buffering for the HDDTs but also to act as a subsystem controller for the HDDT-LBR systems for output film product generation. The micro-coded control software will be stored in the SCU read only control memory. Special functions will be loaded into the SCU RAM control memory via the CPU interface. The baseline controller will contain a 32 Kbyte buffer memory. This will support a minimum of two formatted TM lines or five HRPI lines.

The controller interface with the CPU is via a MIOP. This interface will support a maximum transfer rate of 1 Mbyte/sec or 70 percent of the maximum SCU bandwidth. The secondary data interface has two paths through the controller. The buffered path is used by the parallel data bus that supports the interface to the image correction hardware. The unbuffered interface is used to support data rates greater than 1.4 Mbyte/sec and is used to support the high speed HDDT to LBR and HDDT to HDDT copy operations.

#### 7.11.3.8 Systems Software

The Xerox Control Program for Real-Time (CPR) is the basic operating system typically used by the Xerox 550 systems. It provides all of the basic features required to support the IPS. The primary requirements of the IPS are support of multiple real-time programs for the output product generation, management of the total memory space and minimization of system overhead.

CPR provides all of these features in the support provided for primary and secondary real-time tasks. Primary real-time programs (tasks) are connected to and scheduled by hardware interrupts and typically have a response time of less than 100 microseconds. Secondary real-time programs are software scheduled in a multitask environment, and operate in the mapped mode. Batch programs, also mapped, execute during periods not required for foreground processing and are scheduled as the lowest priority secondary task.

Additional features of CPR include:

- Multiprogramming — Support is provided for up to 32 jobs (one background).
- Dynamic Real Memory Management — CPR provides services to manage pools of dynamic real memory among primary and secondary real-time tasks.
- Task Scheduling — Primary tasks are scheduled through the external interrupt structure of the 550 System Control Processor. Secondary tasks are priority scheduled and dispatched at multiple dispatcher levels upon the completion of I/O, logical events, wakeup, and timer intervals, or upon demand by other foreground tasks.
- Complete Memory Protection — All secondary (including background) tasks are isolated virtually through memory access protection as established by the memory map. Primary tasks are protected by the memory write locks.
- Roll-In/Roll-Out — All secondary tasks, unless they request to be "locked" in memory, may be rolled out by CPR to make room for higher priority tasks.
- File Management — CPR provides for dynamic cataloging of files (allot and delete) and also for file sharing through enqueue/dequeue services. All files are addressed by name and can be read or written in several modes: compressed, sequential, and random.

- Device Input/Output — CPR input/output may be either device-dependent or device-independent. The user may refer to I/O devices by symbolic designators or by I/O device address in order to perform I/O. All I/O services are FORTRAN callable.
- Input/Output Queueing — All input/output requests are queued on the basis of task priority as opposed to first-in/first-out (FIFO).
- Symbiont Input/Output — The optional symbiont facilities provide disk-spooled I/O for Xerox card readers and line printers concurrent with batch job processing. Flexible operator controls assure efficient management and utilization of these peripheral devices.

The normal system utilities and media conversion routines are also provided. Language processors include extended ANSI FORTRAN IV and a Macro Assembler.

The minimum core requirements for the CPR system are about 11K words but will vary for the peripheral configuration for each system and the number of resident device handlers desired.

#### 7. 11. 4 Image Processing Operational Considerations

The operational considerations for the image processing system of the CDPF are presented in this section. The operational aspects of the data management functions of the CDPF are essentially a continuation of the equivalent ERTS NDPF functions. The applicability of the ERTS process to EOS is discussed in some detail in Section 4.7, Applicability of ERTS Equipment, and Section 7.8, Software Functions. These activities are monitored by the Sigma 5 computer system, and it is assumed that this implementation will continue to be utilized for EOS. Thus, these considerations address the operational time line for the image processing system, and discuss the operation of the three Xerox 550 computer systems as they process the image data.

The image processing begins as a pass-tape oriented system and ends with scene and image products. A master digital data tape (MDDT) generated for spacecraft telemetry, meteorology, and ephemeris data in the Sigma 5 and the HDMR ground station pass tapes represent the inputs to the image processing system. The MDDT contains all the relevant

pass data for correcting the image data and producing output products. The HDMR tape contains the sensor data for one pass. The operational time line considered here will assume the worst case, which is a 10 minute pass, i.e., 23 TM scenes.

There are four functions performed: input reformatting, distortion calculation, image correction, and output product generation. Figure 7-38 presents a time line for performing all these functions to process one 10-minute pass tape. It is observed that on the order of 13.4 hours is needed to complete the process. Actually, the operational timeline is a continuous process incorporating parallel operations. Two days would nominally be required for complete processing, with the break generally occurring after the image correction process. Efficiencies resulting from the parallel operations actually will reduce the total elapsed time necessary to process a pass tape. The overall CDPR production timeline is discussed in detail in Section 7.8 mentioned above. Users will receive their products within one cycle time, i.e., within 17 days of the sensor data pass.

Any timeline for processes which have computers, their peripherals, and tape recorders must be concerned with the concept of operational availability and its ramifications. To assess this parameter, TRW utilized the services of Xerox to run their availability model program using the three 550 computer systems as input. The results are presented in Table 7-18. While the operational availability figures are very impressive, it should be noted that the two-shift requirement allows one shift (on an overtime basis) to rectify any production line delays. The largest contributor to unavailability is the HDMR magnetic tape recorders. The matrix switch concept allows the use of redundancy to increase the availability of these systems which use the HDMRs from 0.025 to 0.050 units. The same effect was observed for the HDDT matrix switch case. The values in Table 7-18 corresponds to the baseline system which uses the matrix switches.

There should be some concern over the number of magnetic tape reel replacements needed to process one day's volume of sensor data. Using a worst case estimate, there are a total of 20 HDMR replacements,

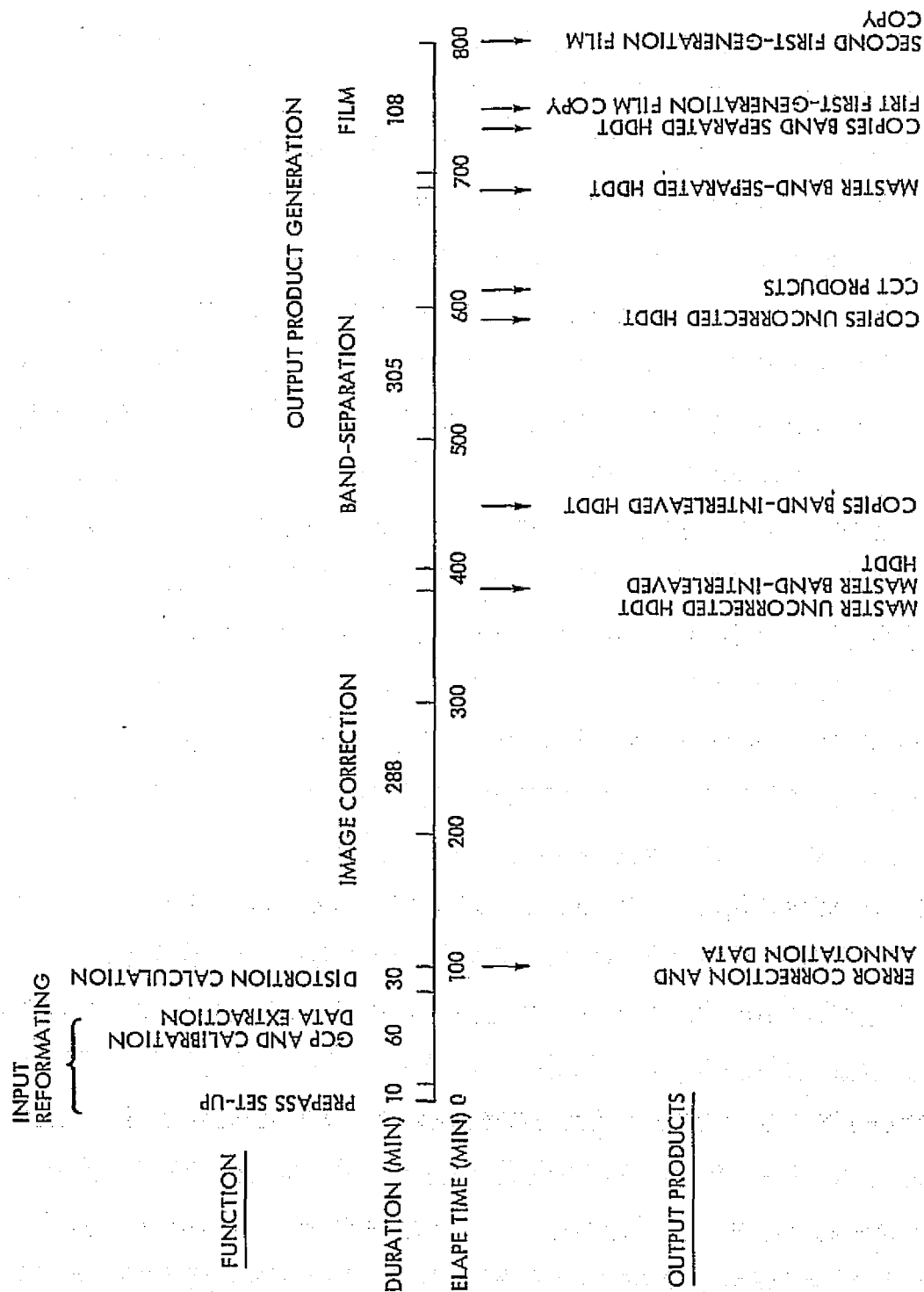


Figure 7-38. Maximum Pass Time HDMR Operational Timeline

Table 7-18. Image Processing System Operation Availability Results

	Error Correction	Estimation, Formatting and Film Production	Formatting and Tape Generation
Operational Availability	0.985	0.977	0.983
Mean Time Between Corrective Maintenance Actions (hrs)	28.62	28.58	31.27
Mean Time to Repair (hrs)	1.33	1.47	1.44
Corrective Maintenance Time per Week (hrs)	7.78 (5.18)	8.66 (5.77)	7.73 (5.15)

NOTE: The above analysis is based upon 24 hours, 7 days a week operation; numbers in parenthesis are estimates derived from Xerox data for a two-shift, 16 hour per day operation.

132 HDDT replacements, and 96 CCT reel replacements. Therefore, there are 248 reel replacements per day, worst case. This implies an average of 5.2 tape replacements per hour for each data handler during an equivalent 12 hour image processing day, or a tape replacement per data handler every 11.5 minutes. Note that there are four data handlers for each shift.

To summarize, the operational characteristics of the image processing systems have been derived for a system designed to satisfy the throughput requirements in a 12 hour, two-shift day. The nominal operational schedule will result in a delay of one day because of the two-day processing cycle. These timing estimates are conservative in two respects. First, a 12-hour day instead of a 16-hour day was used for sizing, and second, if incidental production delays are encountered for some reason, there is overtime capability available to get back on schedule.



## 7.12 DATA PROCESSING FOR OTHER MISSIONS

CDPF data processing requirements for post EOS-A sensors are considered based on the mission payloads defined in Reference 1 and the CDPF servicing cases defined in Reference 2. Reference 2 implicitly considered post EOS-A sensors and Table 7-19 lists the sensor payloads of interest while Figure 7-39 indicates on-orbit schedules. It is obvious from the table that ER and EP missions probably will require STADAF support due to high data rates. OM missions might best be serviced by LCGS. Indeed, some of the low data rate EP sensors might be serviced by LCGS. It might also be the case that EP and OM data processing missions would be supported by agencies other than NASA.

However, in order to consider worst-case data processing conditions, it is assumed for this study that all EOS missions will be supported by the CDPF. Additionally, the ER gap filler mission to bridge ERTS and EOS will be serviced by the CDPF.

Data processing for the gap filler mission, a typical ERTS technology application, can be supported by a low-cost minicomputer implementation possibly at the CDPF such as that developed by TRW\* - total cost of such an implementation would be in the neighborhood of \$ 900K. This minimal investment would free existing ERTS hardware for conversion to support the EOS effort.

The converted and augmented ERTS NDPF equipment becomes the nucleus of the EOS CDPF. Figure 7-40 shows a cartoon of the TRW multi-mission data processing concept. Realization of this concept for EOS-A is discussed elsewhere; the point here is to show how multimission data processing would be implemented, and from there discuss peculiar sensor impacts on the baseline design. The concept shown in the cartoon is not unique; indeed, one realization would be a CDC 7600. TRW's approach is to use lower priced systems.

---

\* Operational implementation of the demonstrated image processing capability of TRW's Signal Processing Facility which currently supports research work of an ERTS principal investigator.

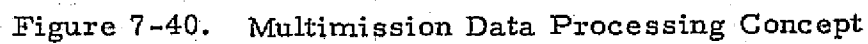
Table 7-19. Sensor Payloads

Mission	Generation	Payload		Downlink Data Rate (Mb/s)
		Sensor Complement	Flight	
Earth Resources (ER)	1	Thematic mapper (TM) High resolution pointable imager (HRPI)	EOS-A	200
	2	High resolution multispectral point scanner (HRMPS) Pointable imager (PI) Synthetic aperture radar (SAR)	EOS-A'	368 368 300
	3		EOS-A''	
	1	Particulate-measuring sensor (PMS) Gas-measuring sensor (GMS) Water pollution sensor (WPS) Vertical temperature sender (VTS) Very high resolution radiometer (VHRR) Side-looking radar (SLR)	EOS-B	200
	2	Laser particulate sensor (LPS) Laser plankton profiler (LPP) Multispectral polarimeter (MP)	EOS-B'	300
Environmental- pollution (EP)	3		EOS-B''	
Oceanography and meteorology (OM)	1	Advanced atmospheric sounder (AAS) Oceanic scanning spectral- photometer (OSS) Sea surface temperature imaging radiometer (SSTIR) Passive multichannel microwave radiometer (PMMR) Constant resolution meteo- logical scanner (CRMS) Cloud physics radiometer (CPR)	EOS-C	1
	2	AAS; advanced OSS; advanced PMMR; advanced CRMS	EOS-C'	2
	3		EOS-C''	
	1	Five-band multispectral scanner		30

MISSION	1977	1978	1979	1980	1981	1982	1983	1984
EROS EOS-A AND A' (MSS + TM) EOS-B AND B' (TM AND HRPI)			A ▲	A' ▲	B ▲	B' ▲	TWO-SATELLITE OPERATIONAL SYSTEM → 1990	
MARINE AND WATER RESOURCES AND POLLUTION EOS-C (TWO TM + ONE HRPI + SAR)				C ▲				
OCEAN DYNAMICS AND SEA ICE EOS-D (SEASAT-B)					D ▲			
WEATHER AND CLIMATE EOS-E (TIROS-O)						E ▲	OPERATIONAL SYSTEM →	
OTHER		SMM ▲ SEASAT-A ▲		EOS-TEST ▲ SHUTTLE 6	SEOS-A ▲			SEOS-B ▲

Figure 7-39. Mission Model

7-180



The modularity concept allows individual data streams to be processed in accordance with their peculiar requirements (e.g., differing data rates/data volumes, individualized special-purpose preprocessing and processing hardware, special user support services). Incremental procurements of required software and hardware modules to format and correct a new sensor's imagery (one of the pipes shown in the cartoon) permits phased growth of the EOS program. Indeed, TRW's baseline design for EOS-A is predicated on future incremental growth: the baseline computer configuration operates on the order of 50 percent capacity, with respect to both memory and processing rate.

This operating condition permits addition of new error correction modules through EOS-A'. Second generation error correction modules would replace the first generation modules should the sensor characteristics change. It is expected that the 1984 computer configuration will handle EOS-B' and EOS-C'.

#### References:

- 1) TRW IOC EOS-52, "Mission Model (EOS, SEOS, SEAT, SM, %-Band MMS)," P. E. Romo, 20 May 1974.
- 2) TRW IOC EOS-92, "Task DP-6 Software Functions; Task LU-6 Operational Support," D. M. McKinnon, 31 May 1974.

### 7.13 GROUND WIDEBAND TAPE RECORDERS

A study was made to review and cost alternative 120/240 megabit tape recorder approaches including modular options for reduced data rates on other missions.

#### 7.13.1 Problem Discussion

The high data rate bit stream from the wideband downlink receivers must be recorded (digitally) by a tape recorder. The recording data rate requirements for EOS-A are 120 mbps in each of the data channels. The maximum playback rate is 20 mbps. Tape recorders that meet these requirements, as well as a necessarily low bit error rate, represent state-of-the-art design. Because there is no recorder presently available off the shelf that meets these requirements, the survey must evaluate potential designs and predict performance, cost and availability. A transparent tape recorder system is probably the most cost effective: off-the-shelf tape systems usually include bit synchronizers as well as the multiplexing/de-multiplexing circuits. These systems accomplish the multiplexing without synchronizing to the downlink data frame.

#### 7.13.2 Assumptions

- (a) The record data rate will be limited to 128 mbps per system.
- (b) The bit error rate from all causes must be less than  $10^{-6}$ .

#### 7.13.3 Analysis and Tradeoffs

Five tape recorder manufacturers were surveyed: Ampex, Bell and Howell, RCA, Honeywell and Sangamo. Three of these companies produced (or will produce) machines that will record digital data at the required 128 mbps rate. A requirement/capabilities table (Table 7-20) lists the capabilities of the three candidate suppliers as a function of the ground station requirements. Table 7-21 lists the salient features for the three systems.

The three candidate systems all use multiple track recording heads. The bit synchronization, error correction, de-skew and the data multiplexing/de-multiplexing electronics is provided by each of the manufacturers as a

Table 7-20. High Density Digital Tape (HDDT) Recorders

REQUIREMENT	CAPABILITY			COMMENTS
	14 Tracks per 1" Tape System A	42 Tracks per 1" Tape System B	164 Tracks per 2" Tape System C	
Record Rate: 120 MBPS per Recorder	3 unit required	1 unit required	1 unit required	System A produces 3 simultaneous tapes that must be reproduced synchronously.
Record Time: 10 minute minimum	16 minutes	10 min 40 sec	10 min	Based on 9600 ft of tape on a 14-inch reel, all data can be recorded for 95 percent of the passes.
Reproduce Rate: 10 - 120 MBPS	Meet	Meet	Meet	Selectable in 2:1 steps or controlled by external clock.
Bit Error Rate: $10^{-6}$	$10^{-8}$	$2 \times 10^{-7}$	$2 \times 10^{-6}$	Trackwidth limitation - Figure 7-41.
Tape Interchange- ability	Yes	Yes	Difficult, due to tracking	Close tolerances preclude tape inter- change between recorders.
Expected downtime due to maintenance (during a pass)	None	None	None	80 minutes between passes should suf- fice for all normal maintenance.
Head Life: 1000 Hours	Meet	Meet	Meet	Ferrite or Alfecon construction. Pic- ture degradation at 1000 hours should be negligible.
Bit Synchronization Electronics	Yes	Yes	Yes	Tape recorder is operated as a "Transparent" system
Error Detection and Correction	Yes	Yes	Yes	Detection is used as indicator of health.
Start Time: 10 Sec Maximum	8 Sec	8 Sec	TBD	BER above includes correction improvement.
High Quality Tape Required	Yes	Yes	Yes	System A requires scraping and cleaning off off-the-shelf tapes.
GRME Instrumentation				

Table 7-21. HDDT Recorder Features

	14 Tracks per 1" Tape	42 Tracks per 1" Tape	164 Tracks per 2" Tape
Tape Width	1 inch	1 inch	2 inches
Tape Length	9600 ft	9600 ft	TBD
Tape Speed	120 IPS	180 IPS	120 IPS
Packing Density	33 KBits/Inch/Track	18.5 KBits/Inch/Track	~25 KBits/Inch/Track
Bits per Square Inch	$.33 \times 10^6$	$.66 \times 10^6$	$.66 \times 10^6$
Record Encoding	ENRZ	MILLER	Double Density
Heads	Ferrite	Ferrite	Alfecon
Track Width	.050 inch	.018 inch	.008 inch
Basic Transport	Bell & Howell VR-3700 B Honeywell "Ninety-Six" Sangamo "Sabre IV"	Ampex FR-2000	TBD (RCA)
Size	4 full racks	2 full racks	3 racks
Cost per 120 MBPS			
System		187	
Recurring	240K (B&H)	187K (Ampex)	TBD
Non-Recurring	- (B&H)	50K (Ampex)	TBD
Delivery Time	210 - 270 Days	210 Days	TBD
Present Customers	NASA	TRW	Devel. to NASA



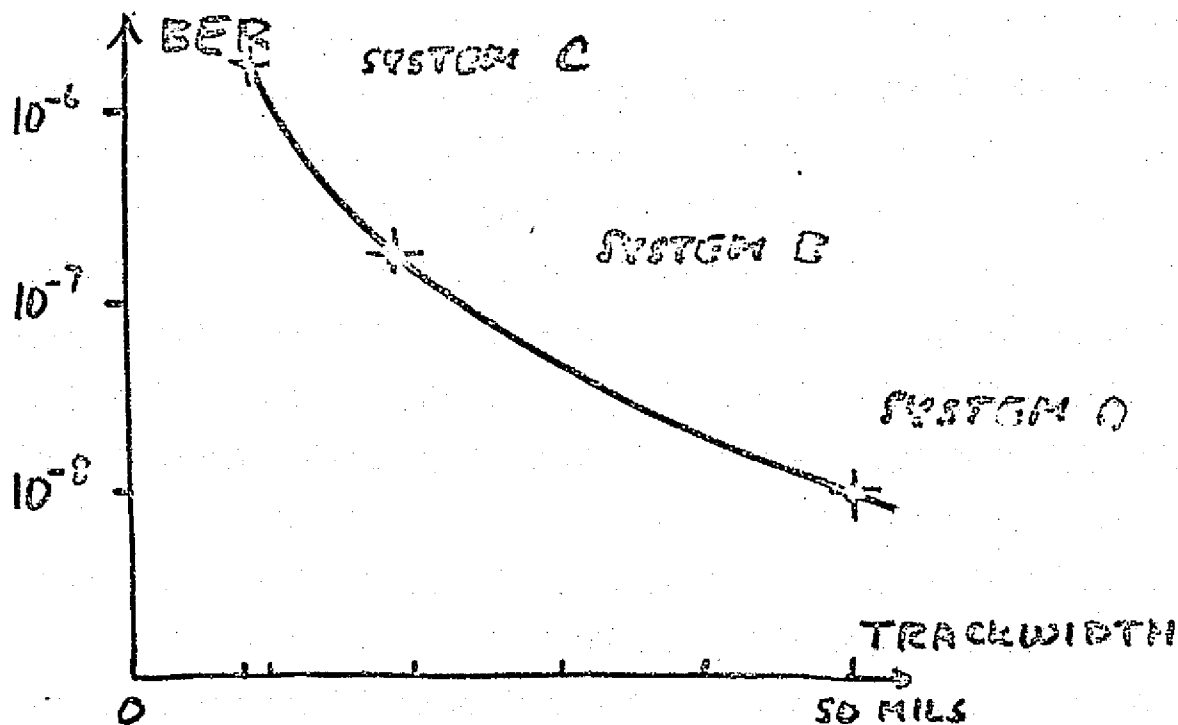


Figure 7-41. Bit-Error-Rate as a Function of Trackwidth. Tape Surface Imperfections cause Dropouts that on the Average Correspond to A signal-Loss Area of 25 mils in Diameter. This will Cause Complete Data Loss in a Narrow Track System, with Resulting Higher BER

part of the tape recorder package. The capabilities of each supplier is predicated on the use of their entire system, e.g., the bit error rate is based on the tape recorder, all electronics, and tape in each case.

#### 7.13.4 Conclusions

The 42 track tape recorder is chosen for the baseline system for the following reasons:

##### A. Standardization

42 tracks recording on 1" wide tape is IRIG standard.

##### B. Experience

A 42 track 80 MB/S system similar to system B has been operated successfully by TRW for one year.

##### C. Operational Characteristics

System B is built around a standard FR-2000 transport, familiar to all ground stations.

System A stores the data on sets of 3 reels of tape, which is an operational disadvantage.

System C requires precise tape tracking due to the many narrow tracks making machine-to-machine interchangeability questionable.

Bit error rate of the 42 track recorder is well within specification ( $2 \times 10^{-7}$  vs  $1 \times 10^{-6}$ ) (see Figure 7-41).

## 7.14 LCGS CONFIGURATION

A study was made to configure LCGS facility for several cost/performance options, identify and cost all hardware and software, and consider upgraded low-cost ground stations, using a computer for data processing and reformatting.

### 7.14.1 Problem Discussion

The Low-Cost Ground Station concept makes earth observation data available to users in a timely manner in a format which allows processing to their unique needs. Sensor data will be transmitted directly to a ground station over an X-band channel at a reduced rate with respect to the data acquired at NASA ground stations. This reduced rate allows a relatively low cost for implementation without significantly degrading the data quality.

The design for the implementation of the LCGS concept has been completed in sufficient detail to allow analysis and tradeoffs to be performed on the EOS-A spacecraft regarding the technical and cost impact. The design consists of two basic configurations: the direct display and the record and process. Figure 7-42 presents a functional block diagram of the design approach. The direct display configuration is the lowest cost, but only provides a film output product. The record and process configuration allows recording of the downlink data and subsequent computer-based image processing; the data quality is potentially commensurate with the output product quality of the CDPF. Each of the basic configurations are broken down into hardware subsystem components, and costs associated with each of the components and software are presented.

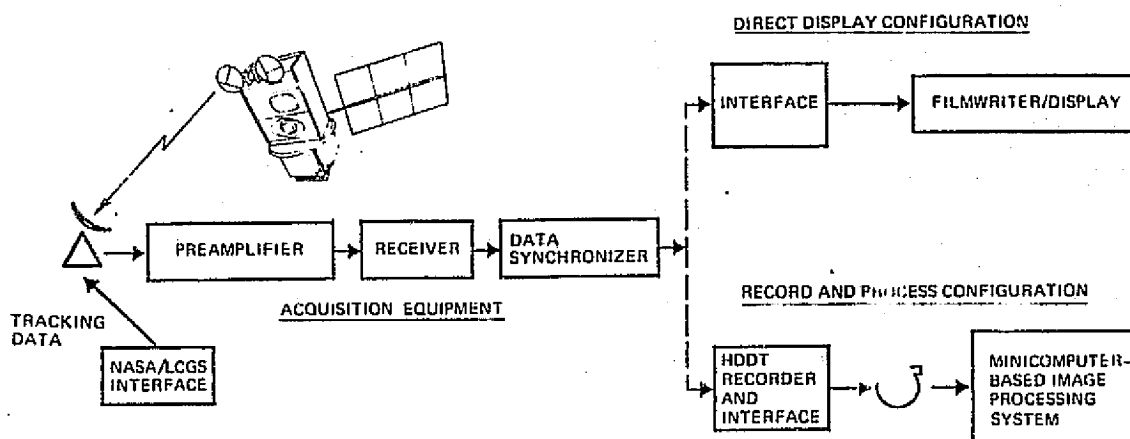


Figure 7-42. LCGS Functional Block Diagram

#### 7. 14. 2 Assumptions

The basic assumptions are:

- Only thematic mapper data is transmitted to the LCGS
- All error correction processes and sensor edit options which do not significantly impact the spacecraft cost will be performed on-board
- Low-cost is the driving consideration for implementing the LCGS design
- Recurring LCGS subsystem component cost figures are based upon ten units initially required
- The direct display configuration will not perform any radiometric calibration or geometric correction

#### 7. 14. 3 Analysis and Tradeoffs

The first consideration is the available LCGS formats for the GSFC compaction alternatives. It was determined that all alternatives were achievable, see Figure 7-43. If one preprocessing scheme is chosen for the implementation of Option 4, the reduced resolution option, an additional option could be implemented which would consist of any linear combination of the data, e.g., an output consisting of the principal components of a combination of bands. In addition, it was also determined that on-board detector calibration could be performed on the LCGS data (see Section 5, Volume 3).

<u>Option</u>	<u>Swath Width (km)</u>	<u>Bands</u>	<u>Downlink Rate (Mbps)</u>	<u>Resolution (M)</u>
1	185 (full)	Any 1	20	30
2	90 (1/2 full)	Any 2	20	30
3	45 (1/4 full)	Any 4	20	30
4	185 (full)	All	20	90

Figure 7-43. LCGS TM Compaction Alternative

The RF equipment is common to each of the configurations. Its analysis and costs are presented in Section 7.19, LCGS RF Equipment, and will only be summarized in the discussion below. Likewise, the considerations for the direct display configuration, the filmwriter/display and its interface, are identified in Section 7.16, Filmwriter Technology. Section 7.16 also contains the analysis and trades for the HDDT recorder and interface used in the record and process configuration.

The record and process configuration design and lowest-cost implementation is based upon TRW's Signal Processing Facility, presently being used to digitally process ERTS sensor data. Figure 7-44 presents a minimal minicomputer configuration for processing EOS data. This configuration is capable of producing output products with the same data quality as the CDPF.

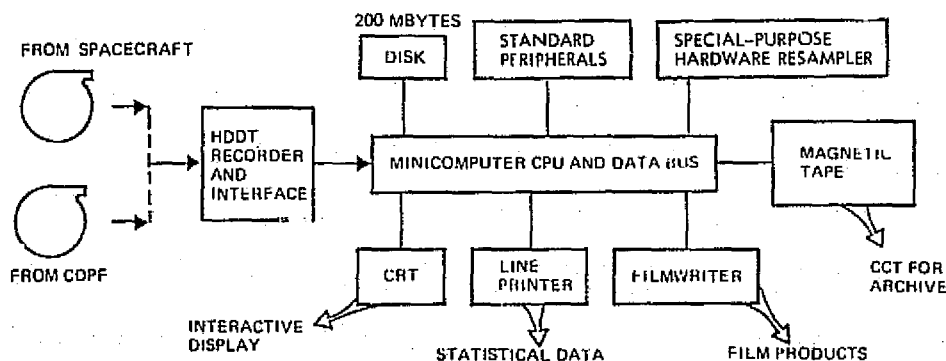


Figure 7-44. LCGS Minimal Cost Record and Process Configuration

Table 7-22 summarizes hardware and software components and their associated non-recurring and recurring costs. Also presented are estimates for systems engineering and integrations tasks and required

facilities for each of the two configurations. Note that the recurring costs are based upon ten initial units.

#### 7.14.4 Conclusions

A Direct Display Configuration represents a substantial savings in cost over the Record and Process Configuration, \$217K in recurring hardware/software costs alone. The user, however, will only have available film output products for analysis. If more precise data is needed, then it will be available at an additional cost for its implementation.

Table 7-22. LCGS Cost Breakdown

Subsystem Element	Non-Recurring (\$K)	Recurring (\$K)		
RF Equipment:				
LCGS antenna, mount, drive and tape reader	20	56		
X-band preamplifier	5	15		
X-band biphase demodulator	15	16		
Data synchronizer - bit synchronizer and decommutator	50	15		
Total	90	102		
Direct Display Configuration:				
Filmwriter/Display and interface	200	60		
Record and Process Configuration:				
HDDT recorder and interface	0	80		
Minicomputer CPU and standard peripherals	0	50		
Filmwriter	0	20		
CRT display	0	40		
Disk storage	0	40		
CCT tape recorder and interface	0	12		
Special purpose hardware - resampler	0	25		
Software development	100	0		
Total	100	277		
Total Hardware/Software Costs:				
Direct Display Design	290	162		
Record and Process Design	190	379		
Additional Costs for System Engineering and Integration:				
	Direct Display Design Non-Recurring (\$K)	Direct Display Design Recurring (\$K)	Record and Process Non-Recurring (\$K)	Record and Process Recurring (\$K)
Management and Engineering	50	10	100	30
Quality Assurance	0	10	0	5
Integration and Test	5	2	10	5
Facilities	10	30	20	70
Total	65	52	130	110
Total LCGS System Costs			Non-Recurring (\$K)	Recurring (\$K)
Direct Display Configuration			355	214
Record and Process Configuration			320	490

## 7.15 TAPE FORMAT COMPATIBILITY

A study was made to evaluate magnetic tape format compatibility with CDPF products to maximize benefits to LCGS.

### 7.15.1 Problem Discussion

There are a number of reasons why it is desirable that the LCGS have a high density magnetic tape format which is compatible with a CDPF product. Some of these reasons are off-loading capability for CDPF image processing, availability of increased input TM data volume and HRPI data for LCGS users, and economies derived from utilizing the CDPF high density tape recorder technology to meet the LCGS input tape recorder requirements. An investigation was made to determine which forms of magnetic tape formats would have desirable features and how they could be implemented in the most cost-effective manner.

### 7.15.2 Assumptions

The basic assumptions are:

- An HDDT tape format for both corrected and uncorrected sensor data at the CDPF is required.
- The CDPF HDDT tape format requires frame synchronization, i.e., it is unformatted with respect to CCT specifications.
- The maximum input rate to the LCGS is 20 Mbits/sec.

### 7.15.3 Analysis and Tradeoffs

The Direct Display Configuration processes the data in real-time and will not have a tape recorder associated with its implementation. Therefore, only the LCGS Record and Process configuration has the potential for tape format compatibility with the CDPF.

It has been determined that the most cost-effective ground station tape recorder format is a serial in, serial out process, i.e., the HDMR will be transparent in the sensor data stream. This factor and its higher cost because of the high performance requirements, e.g., 120 Mbit/sec record rate, imply that it is not a suitable candidate for tape format compatibility with the LCGS. At the other end of the performance spectrum,



CCT's do not have the high data volumes desirable for efficient transfer of sensor data. For example, 6250 bpi technology can store on the order of 120 Mbytes on a 2400 foot reel of tape, less than the equivalent of two LCGS thematic mapper scenes for the sensor edit options.

There is a specification for both uncorrected and corrected HDDT formats for the CDPF output products. Furthermore, HDDT formats utilize performance specifications which can also satisfy the LCGS input tape recorder requirements, i.e., data volumes exceeding 10 thematic mapper scenes per reel and data rates up to 2.5 Mbytes/sec (20 Mbits/sec.) The HDDT tape format is the candidate for tape compatibility between the LCGS and CDPF by a process of elimination.

The LCGS input tape recorder must operate at a rate of 20 Mbits/sec and have a data volume equivalent to at least 10 thematic mapper images with overhead, 680 Mbytes for any of the four LCGS sensor edit options. The Ampex FR-2000 series technology can satisfy both the requirements for the CDPF HDDT and the LCGS input tape recorder. With a linear bit packing density of 17 Kbi and using an extension of the ERTS FR-1928 approach (28 tracks with 24 data channels), the maximum LCGS data volume can be recorded on 1350 feet of tape using a recording rate of 49 ips. The linear bit packing density is the same as that of the baseline HDMR (see Task GS-3, Wideband Tape Recorders); to decrease the bit error rate to less than  $10^{-6}$ , the density can be reduced to 13.9 kbi which corresponds to a recording rate of 60ips, a standard rate. With this density for the HDDT's, a 14-inch reel holding 9200 feet of tape will handle a data volume of  $4.61 \times 10^9$  bytes, or almost 15 full thematic mapper scenes. This corresponds to a ground station pass of 6.5 minutes, less than the maximum of around 11 minutes. Nevertheless, the tape volume is well within the limits for holding any HDMR input on two HDDT reels.

Thus, it is apparent that the HDDT format can satisfy both the LCGS and CDPF requirements. Furthermore, mod 2 slowdown ratios can be used to obtain lower data rates for the CDPF generated HDDT products being processed in the LCGS. For example, a tape speed of  $7 \frac{3}{4}$  ips will yield a transfer rate of 312 Kbytes/sec, well within the performance capability of a minicomputer-based image processing configuration with special purpose hardware. The CDPF can generate an HDDT with the same format

that the spacecraft transmits to the LCGS, allowing the same processing to be used. In addition, the Option 1 format, one band at full data volume, can be used to process band separated data generated at the CDPF data which utilizes all bands. Furthermore, with additional cost devoted to the LCGS HDDT interface, the band inter-leaved products, i.e., one line of one band, then the same line for the second band, etc., could be processed. In all these formats, the HDDT would be used as a serial, in, serial out process. The interface used for frame synchronization also is used to demux the data stream. Using the Option 1 as a baseline for the frame synchronization, all TM or HRPI data processed by the CDPF can be utilized by the LCGS through its input tape recorder and interface. See Section 4.6.4, High Speed Buffer, for the details of this format.

#### 7.15.4 Conclusions

The required HDDT format for the CDPF is found to be a suitable interface with the LCGS through its use of the HDDT for its input tape recorder. Utilizing band separated processing with the format for Option 1 of the LCGS TM compaction alternative used for frame synchronization, no additional cost is necessary for the LCGS to process CDPF data. If the LCGS user desires HDDT data in another format such as band inter-leaved data, then only modification of the HDDT interface is necessary, a modification which should run no more than \$10K.

## 7.16 FILMWRITER TECHNOLOGY

A study was made to evaluate existing filmwriter/image display technology and medium-rate tape recorders and trade off cost of direct imaging recording versus recording and slowdown.

### 7.16.1 Problem Discussion

The cost of the direct display configuration (see Section 7.14, LCGS configuration for system design costs) is determined by the cost of implementing the Filmwriter/Display and its interface. This approach requires technology that can process the images in real-time. To insure that this is the lowest cost implementation, the cost of this approach is compared to recording the data and processing it with a relatively low cost filmwriter operating at a reduced rate.

### 7.16.2 Assumptions

The basic assumptions are:

- The downlink data rate is 20 Mbits/sec, with each pixel represented by 8 bits, and only thematic mapper data available.
- There are four formats transmitted to the LCGS:
  - i) any one band, 8192 pixel line
  - ii) any two bands, 4096 pixel lines (maximum)
  - iii) any four bands, 2048 pixel lines (maximum)
  - iv) seven bands, six having 2731 pixel lines and the seventh having 683 pixels
- All formats are transmitted band inter-leaved, at an 80 percent scan efficiency (see Task WD-3, High Speed Buffer for details of the formats).
- A maximum of ten scenes are available for processing
- Recurring cost figures are based upon ten units initially required
- The Direct Display configuration will not perform any radiometric calibration or geometric correction

### 7.16.3 Analysis and Tradeoffs

The cost of the Direct Display configuration is determined by the Filmwriter/Display and its interface. Three technologies were investigated for low-cost implementation: cathode-ray tube, electron beam recorder, and laser beam recorder. It was determined that the electron beam recorders cannot meet the low-cost requirements, being in excess of \$100K, and, hence, were ruled out of contention.

The cathode-ray tube technology, while operating near the limits of its capability in terms of both resolution and transfer rates, can satisfy the requirements with some qualifications. It cannot display all seven bands of the reduced resolution option, but can display three bands. Furthermore, about 10 percent of the data will be lost during the time necessary to advance the film to a new position because of its output framing requirements. However, one company, Dicomed, states that they should be able to deliver a cathode-ray tube filmwriter and interface with the above characteristics for \$54K per unit on a recurring cost basis, and an effective non-recurring cost of \$114K.

Laser beam recorders represent the best filmwriter technology with respect to combined performance and cost. It can meet all the TM compaction alternatives, using a 9 1/2 inch film format, a format compatible with the GDPF film product. To implement the recorder with a low-cost design requires some care in the design of the laser beam scanning operation. CBS recommends a galvanometer approach, while Goodyear recommends a scanning mirror for low-cost implementation. It appears that in either case, laser beam recorders could be developed for a non-recurring cost of \$200K and recurring cost of \$60K per unit, including interface.

Because the downlink rate is 20 Mbits/sec, the tape recorder technology associated with the ERTS program is applicable to the LCGS requirements. Discussions with Ampex regarding their FR-1928 led to the choice of the equivalent FR-2000 transport technology using a 28-track tape format. This technology, recognizing the GDPF requirements and desirable LCGS-GDPF tape format compatibility (see Section 7.15, Tape Format Compatibility), represents a good compromise between lower cost designs and higher performance. In addition, this technology has been demonstrated in the field at rates substantially higher than the LCGS requirement, and, hence,

represents minimal non-recurring cost and a conservative estimate for recurring costs. In fact, the non-recurring cost will be borne by the CDPF requirements. The recurring cost for the tape recorder and electronics is estimated to \$60K.

With a record speed of 120 ips and a reproduce speed of 15/16 ips, a slowdown ratio of approximately 120:1 can be achieved. This implies a transfer data rate of 20 kBytes/sec and the applicability of relatively inexpensive flying spot scanner technology. The estimated recurring cost is \$30K for the scanner and \$15K for the interface with the tape recorder, resulting in a total recurring cost of \$45K for the filmwriter and its interface. The non-recurring cost is suggested to be \$10K to cover hardware integration and software development.

The alternative to the real-time film recording process results in a total recurring cost of \$105K and a non-recurring cost of \$10K. Clearly, the Direct Display configuration is more economically implemented with a real-time filmwriter based upon the analysis of recurring cost. To record the data and utilize relatively low-cost filmwriter technology results in a recurring cost of \$45K over the real-time system.

Some comment is appropriate on the format of the output film product. The LCGS sensor data is transmitted line sequential, one line of one band, then the equivalent line of the next band. This holds for all four formats. The implementation of the Direct Display configuration presents each line across the film, one band at a time. Additional resolution capability is required by the filmwriter over the other options to incorporate the reduced resolution option, seven bands across the film. The laser recorders have this capability, and, hence, all options are available for real-time film product generation.

#### 7.16.4 Conclusions

It has been determined that the cost of direct image recording is substantially less than the cost of recording the data and processing at a slowdown rate. The recurring cost differential is \$45K based upon a direct image recording cost of \$60K. There is a non-recurring cost of \$200K associated with development of an inexpensive filmwriter and interface. The technology exists to meet the performance requirements.

## 7.17 IMPACT OF OTHER SYSTEM ELEMENTS

The three existing stations that support ERTS (Alaska, Goldstone, NTTF) are required to provide tracking, commanding and telemetry and X-band readout and recording of EOS spacecraft and sensor data. Although the intent of the EOS Phase B Study is to derive a system definition that has a minimal impact on these stations, some is inevitable.

### 7.17.1 Assumptions

Those of Section 7.1, Control Center System Analysis and Design.

### 7.17.2 Analyses and Tradeoffs

With the given pointing accuracy of the spacecraft and payload, it is essential that the tracking stations provide data, that when smoothed will give an in track accuracy of no more than  $\pm 50$  meters for the baseline EOS configuration and orbit if the specific final product positional accuracy of  $\pm 170$  meters without ground control points is to be obtained.

ERTS tracking antennas, feeds and amplifiers must be modified for both S- and X-band operation. X-band receivers and synchronizers must be installed. Wideband tape recorders must be provided to replace ERTS equipment.

The existing tracking station equipments are adequate to receive, display and transmit all planned real time telemetry data to the Central Control Center, requiring only the proper set up of the station decodms and brush recorders.

The 642B computers are adequate to handle both telemetry data and command interfaces with NASCOM although limited software development will be required.

The NASCOM links as configured are adequate to handle EOS telemetry, commands and voice.

The ERTS station spacecraft command consoles could be used as-is to uplink three (decimal) digit EOS backup commands, although provision must be made to handle a 2 Kbit command link with no sub-bit encoding.

The ERTS station manning and procedures are adequate to support EOS operations.

It is difficult to assess the impact of EOS on TDRS (and TDRS on EOS) without a definitive plan for TDRS implementation. TDRS can potentially support EOS in several areas that are currently not supported.

- Payload readout outside North America.
- Telemetry readout and real time commanding anywhere in the world.

In general, foreign nations are not going to accept payload operations over their countries with the data channeled through the U.S. The principal area of interest is then that of being able to receive real time telemetry data 24 hours a day at the EOS Control Center. The ability to command in real time throughout the world is desirable but is not a requirement.

In the EOS baseline system, TDRS would only be used internationally to provide extended telemetry coverage, possibly limited to passes where payloads were in operation. If telemetry coverage were to be provided internationally, the very narrow band real time command link would presumably be included. In gross, this would require TDRS relatively narrow band support for a maximum of 3 hours daily.

As the existing U.S. ERTS stations provide full coverage of the U.S. (except Hawaii), TDRS only could potentially serve two functions.

- Relay all payload data in near real for processing and analysis.
- Replace the existing ERTS tracking stations.

If TDRS is to assume these roles, then TDRS must, in the baseline EOS mission, provide telemetry and real time command support approximately 3 hours daily and broad band support approximately 30 minutes daily.

EOS-A must still have very accurate positional data which will require ground based tracking and ranging at sufficiently close intervals to support best fit ephemeris computation.

TDRS must also make certain portions of payload data available to the CDPF in very near real time which almost dictates an earth terminal at Goddard.

The requirement for communications between the EOS Control Center and the spacecraft when the latter is docked with the Shuttle have not been clearly established.

The Shuttle crew will be in constant voice communication with JSC through either STDN or TDRS so voice communications between the EOS Control Center and Shuttle technical personnel are clearly feasible. Although it is also technically feasible to directly read out payloads and telemetry while docked, it appears unrealistic. On spacecraft servicing missions, test equipment will be installed in the Shuttle to permit functional check of replaced modules. If desired, EOS spacecraft telemetry can be multiplexed onto the Shuttle's downlink and routed through NASCOM to the EOS Control Center. The EOS spacecraft can be kept in the near vicinity of the Shuttle while any required system checks are commanded from the EOS Control Center and telemetry and payload readouts observed.

If TDRS is fully operational in this period, spacecraft checkout can be accomplished over any area of the world. If TDRS is not operational, final spacecraft checks will be within line of sight of the NTTF at Goddard.

### 7.17.3 Conclusions

TDRS could replace the payload and telemetry readout stations of North America. Direct ground tracking would probably still be required to provide the accurate ephemeris predictions and positional data required for mission support and wide band processing.

TDRS would be valuable in providing full international telemetry coverage but its use is not absolutely essential.

If TDRS is used to handle broadband data, it may be necessary to provide some portion of that data in near real time to the Control Center for payload control.

TDRS would be valuable in support of checkout and orbit insertion maneuvers.

EOS could have a tremendous impact on TDRS. TDRS would not have a large impact on EOS.



## 7.18 ORBIT DETERMINATION

Spacecraft past and predicted positions are required to support:

- Acquisition and tracking information for U.S. multipurpose or foreign regional stations.
- Acquisition and tracking information for U.S. and foreign low cost stations.
- Antenna pointing information for spacecraft antennas.
- Payload processing.

The first three of these requirements are all for predictive data. The last requirement is for measured and corrected data.

### 7.18.1 Analyses and Tradeoffs

Our link calculations have indicated that wideband antennas, both on the ground and on the spacecraft, should be pointed with an accuracy of approximately 0.1 degree. This requires that in track predicted accuracy of the spacecraft must be 700 meters. The requirement to transmit reformatted ephemeris data to the various stations determines the period for which the prediction must be valid. In the U.S. where communications are relatively easy, the prediction need only be valid for 48 hours. For remote foreign stations, the prediction must be valid for a period equal to the maximum communication time (1 to 2 weeks).

To reduce the scheduling and communication problems of the EOS Control Center, it would be highly desirable if a 14 day prediction could be obtained, accurate to an in track 700 meters.

The Central Data Processing Facility will require a daily input containing the accurately measured positions of the spacecraft at precise times. Assuming that the pointing error of the spacecraft payload is a constant with time, the more accurate the measured positional data, the fewer ground control points need be used and the shorter the payload processing span.

The EOS Phase B RFP stated that in 1978, in-track measured data would be accurate to 50 meters and cross-track to 30 meters. This accuracy, combined with spacecraft and payload pointing error of a maximum of 37 arcseconds, yields a worst case position accuracy of 175 meters which is slightly greater than the specified positional accuracy without the use of ground control points.

As the potential errors in spacecraft payload pointing are over twice as large as the errors in the ground based measurement system, ground control points cannot be fed back into orbit determination with sufficient accuracy to improve ephemeris predictions. Unless spacecraft attitude rigidity and instrument pointing angle may be determined to an accuracy of something better than a total of approximately 15 arcseconds.

Although an absolute requirement does not exist to process payload data in real time, data will be available from the NTTF, or TDRS, in near real time. It would be highly desirable that corrected ground measurement data of spacecraft position be available to the CDPF in the same day that the measurements were taken.

#### 7. 18. 2 Conclusions

- NASA Orbit Determination Group Support requirements.

Output	Period	Accuracy
14 Day predicted ephemeris	14 Days	In-track $\pm 700$ meters
Measured data report of all real time tracking data.	Daily	In-track $\pm 50$ meters Cross-track $\pm 30$ meters

- If foreign readout stations are to receive positional data to the  $\pm 170$  meters accuracy without ground control points, best fit ephemeris data to the accuracies of measured data must be provided.
- The use of ground control points to improve ephemeris prediction does not appear realistic.

## 7.19 LCGS RF EQUIPMENT

The low cost ground station (LCGS) provides a class of EOS-A users with the means for receiving a selected subset of the satellite thematic mapper (TM) data. This data is transmitted from the satellite on a 20 Mbit/sec biphase modulated X-band carrier. A key requirement for the LCGS is that it be configured in a way that minimizes the costs for constructing and maintaining the station. To this end, the ground station X-band reception equipment has been designed and selected.

The link power budget and the choice of the modulation format and rate was determined in Section 4.6 of Appendix A. It was shown there that an adequate  $E_b/N_0$  could be achieved at the LCGS by using an 8-foot program-pointed antenna and a 1.5-dB noise figure uncooled parametric amplifier. This combination of antenna size and preamplifier noise figure results in a link margin that is 6.6 dB above the 9.5 dB theoretical SNR required to achieve a BER of  $10^{-5}$ . The antenna size is the maximum that can be computer pointed, thus avoiding a very costly auto-track system.

The equipment required to track and demodulate the received PSK signal is contained in the RF equipment section of the LCGS. This equipment, shown in Figure 7-45, must be capable of coherently demodulating the suppressed carrier signal and deriving bit synchronization from the detected data. The demodulator and bit synchronizer shown in Figure 7-45 perform these functions. These units must achieve near theoretical performance with a signal close to threshold. This requirement can be met by a variety of equipments and implementation techniques. However, not all designs will provide reliable operation consistent with low cost. The baseline design, described below, uses a reliable modulation wipeoff technique to recover the data and a commercially available bit synchronizer for data detection.

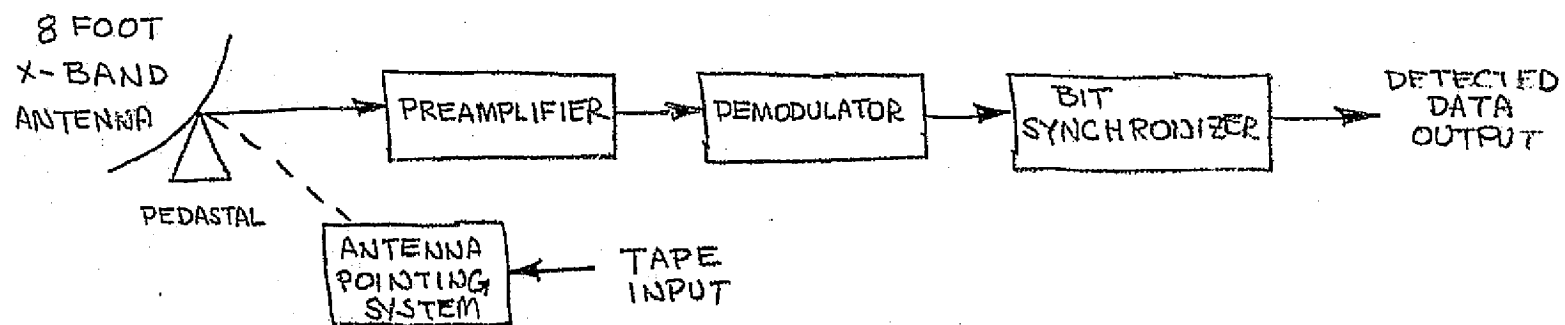


Figure 7-45. X-Band Reception Equipment

### 7.19.1 Equipment Description

#### 7.19.1.1 Antenna and Pedestal

The antenna design recommended consists of an 8-foot diameter parabolic reflector using a crossed dipole feed. The reflector will be constructed from fiberglass having a maximum RMS surface tolerance of less than 0.015 inch. A fiberglass support ring will be incorporated in the layup to support the reflector and provide a mounting surface to the pedestal. The feed consists of unequal length crossed dipoles fed from a split tube balun and backed by a cupped splashplate. This feed will be supported from a center fed air dielectric coaxial boom extending from the vertex of the parabolic reflector.

The antenna has a peak gain of 43.5 dB with respect to a right hand circular polarized isotropic antenna and a beamwidth of approximately 1.1 degree.

A tradeoff of antenna diameter versus tracking technique was performed. Using a paper tape antenna pointing configuration, a pointing accuracy of  $\pm 0.2$  degree can be accomplished at low cost. This is approximately 1/5 of a beamwidth of an 8-foot diameter reflector and results in a 0.5 dB pointing loss. Therefore, to use an appreciably larger reflector will cause a greater pointing loss which only defeats its purpose. To increase gain would require a more costly pointing or tracking mode such as monopulse or conical scan.

The pedestal, which is commercially available and shown in Figure 7-46, is an elevation-over-azimuth design that includes spur gears with adjustable backlash. It is a low cost versatile pedestal which is ideally suited for fixed- or mobile-ground based installations. The pedestal operates under environmental conditions such as those encountered in coastal, tropical, and desert environments. All assemblies are enclosed and protected by gasketed covers providing quick access to all critical components. Typical Specifications are as follows:

Wind (operating)	40 knots
Velocity	10 deg/sec
Acceleration	30 deg/sec

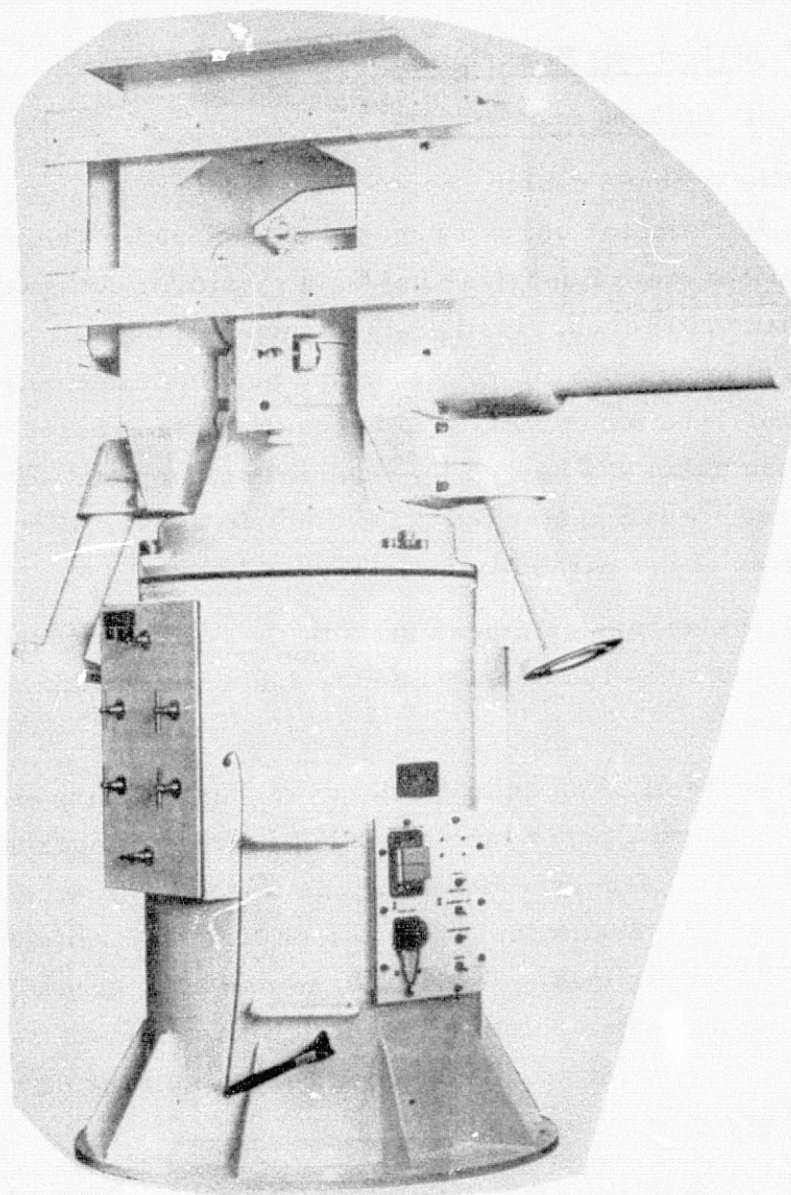


Figure 7-46. LCGS Antenna Pedestal

Azimuth travel	±420 degrees
Elevation travel	-10 to +190 degrees
Backlash	0.30 degree
Orthogonality	0.02 degree
Weight	900 lb

#### 7.19.1.2 Antenna Pointing Equipment

The antenna pointing equipment consists of the drive electronics, servos, and paper tape reader. These items will be purchased as existing equipment from a local vender. Figure 7-47 is a blockdiagram of the pointing equipment.

In the position mode, the digital comparator computes the relative difference between two digital angle input signals to provide a DC output. When the angular difference between the actual and the commanded position is larger than 10 degrees, a constant DC output is generated which slews the positioner toward the commanded position by the shortest angular distance (unless commanded to go in a specific direction). When the angular difference becomes less than 10 degrees, the amplitude of the output signal is directly proportional to the difference in the angle inputs. In this way the commanded position will be approached at a decreasing rate of speed, resulting in little or no overshoot and extremely accurate positioning.

In the rate mode, the digital comparator is used to drive the positioner at a variable, programmed rate of speed. When the rate mode is selected, a DC output voltage, proportional to the commanded velocity, is provided. The command input is provided from a paper tape. The digital comparator is compatible with speed regulated SCR controls.

#### 7.19.1.3 X-Band Preamplifier

The noise figure of the preamplifier, along with the antenna temperature, determines the received signal threshold level for the LCGS. As stated above, a preamplifier noise figure of 1.5 dB is required to avoid a large and costly antenna system. This noise figure can be achieved with

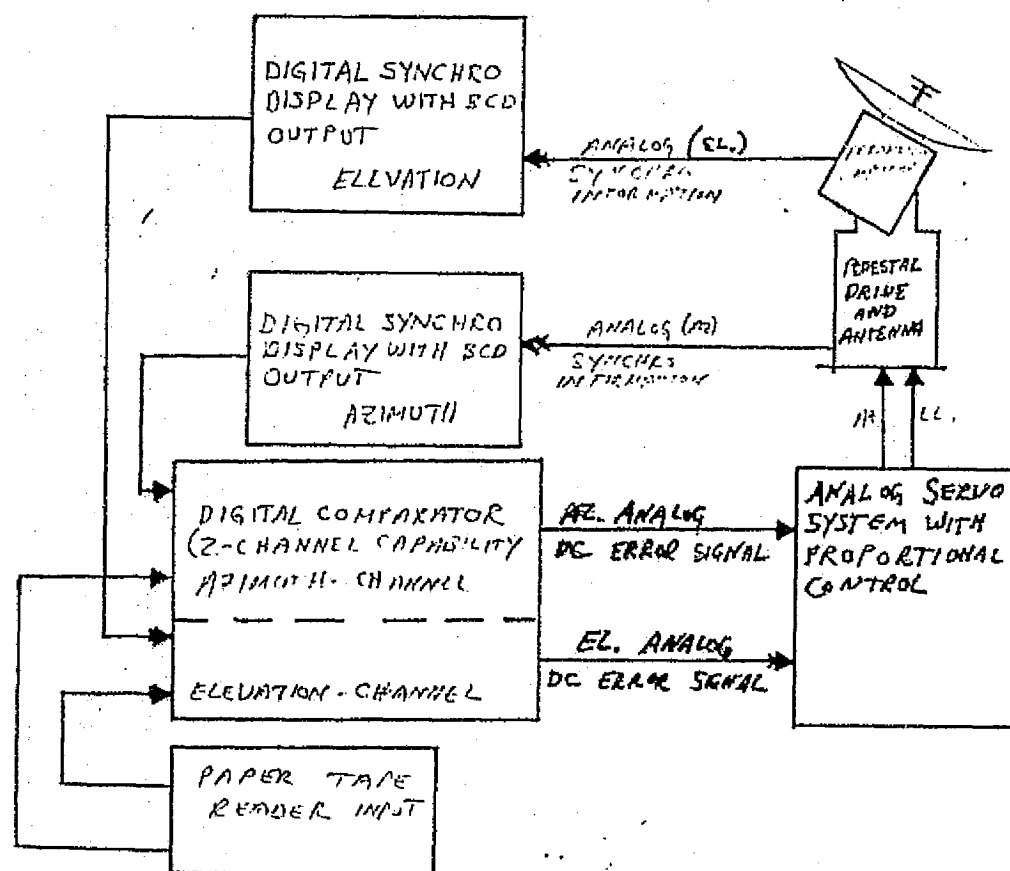


Figure 7-47. Block Diagram of Pointing Equipment



an uncooled parametric amplifier as a minimum. Less costly amplifier techniques will not meet the 1.5 dB requirement. For example, a gallium arsenic FET amplifier using a  $1\mu$  gate width will only yield a 4-dB noise figure.

#### 7.19.1.4 20-Mbit/sec PSK Demodulator

The demodulator shown in Figure 7-45 is essentially an X-band receiver which reconstructs and tradeoffs the suppressed carrier of the received PSK signal and recovers the binary data. While there are many ways to configure this type of receiver, careful consideration must be given to achieve a reliable low cost design. TRW has studied three basic demodulation techniques for the receiver implementation. These are: the 1) Costas demodulator; 2) the data wipeoff technique; and 3) the frequency doubler (X2) approach.

The Costas demodulator is well known and will not be described here. The frequency doubler demodulator design employs a X2 circuit to convert the biphase PSK modulation to a CW carrier which is tracked by a phase-lock loop. The loop VCO signal is divided by two in frequency and used as a coherent reference to detect the PSK data. In the data wipeoff demodulator approach, Figure 7-48, the PSK data is coherently detected using a reference oscillator and used to remodulate the reference. The remodulated signal is then used as a coherent reference, along with a delayed version of the received signal, to form a tracking error signal for a phase-lock loop.

The data wipeoff demodulator is the recommended design for the LCGS. Its main advantage over the other two approaches is its simplicity and relative ease of assembly and test. The main disadvantage of the Costas loop is the need for a wideband (20 MHz) DC coupled correlator and wideband DC amplifiers. The high degree of DC balance required makes these items costly and difficult to construct. DC balance is necessary to keep the loop stress to a minimum, especially in the presence of a threshold level signal. The main disadvantage of the frequency doubler demodulator is the requirement for implementing the additional IF circuitry following the X2 circuit. In addition, this IF needs a narrow-band filter ahead of the loop phase detector to reduce the added noise produced by the frequency multiplication process.

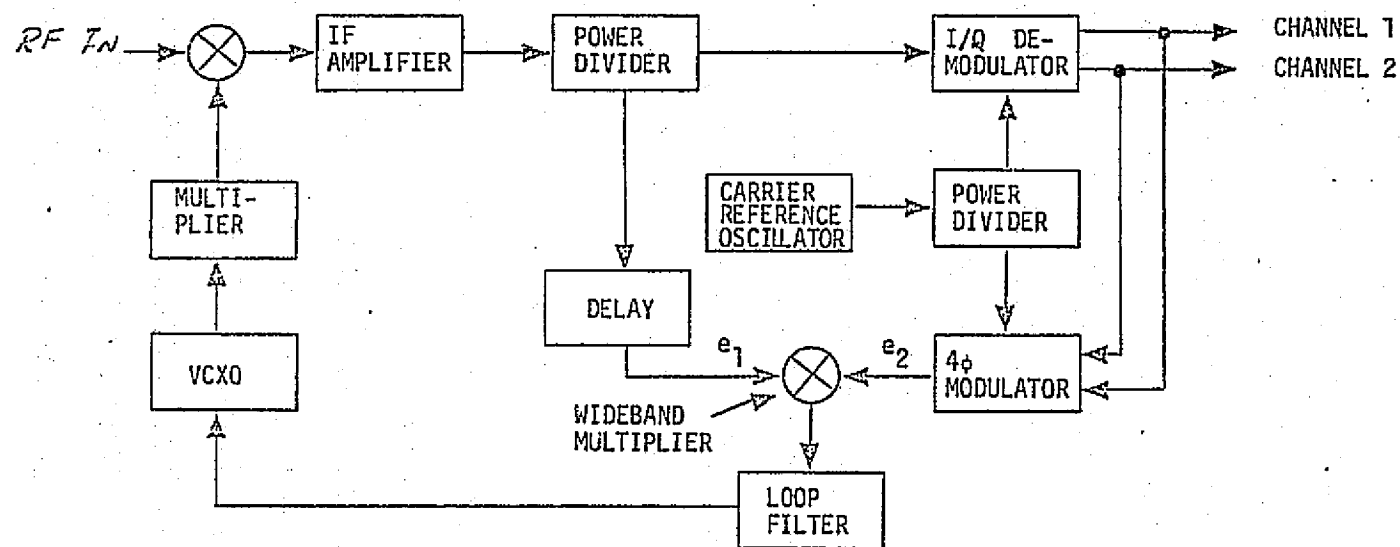


Figure 7-48. X-Band Data Wipeoff Demodulator

In addition to the data recovery section, Figure 7-48 shows a complete single conversion X-band receiver. As shown, a phase-lock loop is formed by driving the mixer and multiplier chain with the loop VCO. This design, employing a 1.5 GHz IF, has been successfully used at X-band by TRW. This IF frequency limits the significant spurious products produced in the mixer to seventh and ninth order and these are down by 70 to 80 dB in the mixer.

#### 7.19.1.5 Bit Synchronizer

A bit synchronizer similar to the General Dynamics-18347 (Dynatronics) is recommended. This bit synchronizer is adaptive to input signal conditions over a certain class of phenomena and range of values as shown in Table 7-23. The adaptive nature of the synchronizer ensures best signal recovery characteristics under all conditions of noise, jitter, frequency offset, and baseline offset.

The bit synchronizer is housed in a standard 19-inch rack. The front panel is shown in Figure 7-49. The unit is constructed to withstand military level shock and vibration tests.

Orbital characteristics of the synchronizer are tested as shown below:

- Acquisition curves as a function of offset with SNR at 15, 10, 5, 0, and -5 dB.
- Phase error as a function of frequency and amplitude of deviation (for  $\Delta f = 0.1, 0.5, 1$  and 2 percent).
- Probability of slip as a function of noise with various source jitter (for  $\Delta f = 0.1, 0.5, 1$  percent; and  $f_m = 1, \text{ and } 5$  percent).
- AGC and offset correction will be measured, at SNR 15, 10, 5, 0, and -5 dB.
- Slip threshold as a function of jitter and transition density (for transition densities of 0.1, 0.25, and 0.5).
- Bit error rates as a function of SNR with various source jitter (1 dB steps from 0 to 15 dB with  $\Delta f = 0.1, 0.5, \text{ and } 1$  percent).

Table 7-23. Bit Synchronizer Adaptive Characteristics

Phenomena	Possible Causes	Mal-Effects	Bandwidth Action Required to Combat Mal-Effect
Transiently poor signal to noise	Burst noise, Fading, Interferences, Changing L. O. S. in channel	Loss of sync with attendant magnification of BER until frame sync is reacquired.	Make the loop narrow.
Frequency Offset	Initial acquisition and/or reacquisition after loss of sync. Sudden shift in data frequency (due to shock). Initial unknown error in source or bit sync frequency, (drift, doppler). Tape Recording. High G stress on data source clock. High doppler, noise injected into clock source.	Large loss of data until acquisition or reacquisition is achieved.	Initially make the loop wide until acquisition then decrease bandwidth for bit detection.
Jitter	Transient noise causing large initial errors in the loop. Asynchronous multiplexing of data sources.	Loss of sync or large increase of BER above that expected from Gaussian probability curves.	Widen the loop to track the jitter. As jitter decreases, make the loop narrower.

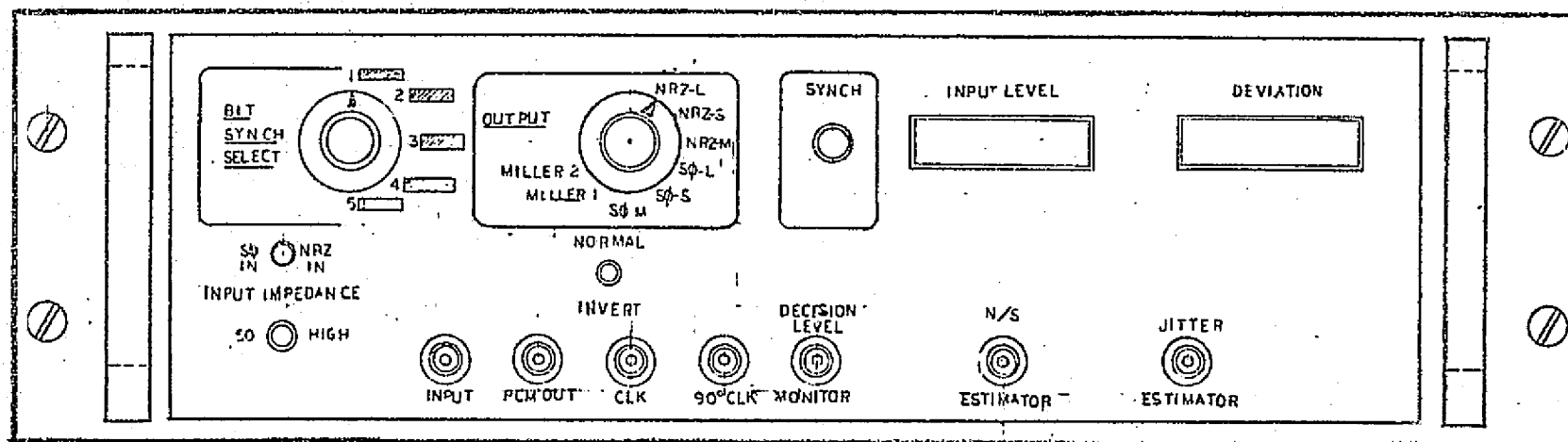


Figure 7-49. Bit Synchronizer Front Panel